Fakultät für Mathematik, Informatik und Naturwissenschaften | RWTH AACHEN UNIVERSITY

Engineering topological superlattices and their epitaxial integration in selectively grown hybrid nanostructures via MBE

Von der Fakultät für Mathematik, Informatik und Naturwissenschaften der RWTH Aachen University zur Erlangung des akademischen Grades eines Doktors der Naturwissenschaften genehmigte Dissertation

vorgelegt von

Abdur Rehman Jalil, M.Sc.

aus

Rawalpindi, Pakistan

Berichter*:* *Prof. Dr. Detlev Grützmacher*

Prof. Dr. Markus Morgenstern

Tag der mündlichen Prüfung*:* *07.06.2022*

Forschungszentrum Jülich GmbH

Peter Grünberg Institute 9 (PGI-9)

Jülich Aachen Research Alliance for

Fundamentals of Future Information Technology (JARA-FIT)

Jalil, Abdur Rehman:

Engineering topological superlattices and their epitaxial integration in selectively grown hybrid nanostructures via Molecular Beam Epitaxy

PhD Thesis, Forschungszentrum Jülich GmbH,

Peter Grünberg Institute 9, 2022

Dedication

I would like to dedicate this work to my lovely mother, who after the sudden demise of my father in 1993, dedicated her life and struggled alone in a developing country of Pakistan to make sure that I along with my siblings get proper education. She also taught me a lesson “never to give up in life”. It is only due to her tiring efforts in the past that I am able to finish this work.

I would also like to acknowledge the sacrifices of my wife and kids, who have given me enough time to focus on my work. Also, I am sorry to them for living far away and not being able to perform my duties as a family man due to visa problems. I hope we can be together soon.

I would also like to thanks my elder brother who has always supported me morally and economically. Finally, I am obliged to Prof. Grützmacher, Dr. Mussler and my colleagues in PGI-9 who always supported me and treated me with patience particularly in my case when I was not able to perform my work for days due to serious health conditions on several occasions.

It would not have been possible for me to finish this work without the efforts and support of all the above mentioned people and thus, this work is dedicated to all of them.

Declaration of originality

I certify that the work in this thesis has not previously been submitted for a degree nor has it been submitted as part of requirements for a degree except as fully acknowledged within the text.

I also certify that the thesis has been written by me. Any help that I have received in my research work and the preparation of the thesis itself has been acknowledged. In addition, I certify that all information sources and literature used are indicated in the thesis.

_____

Abdur Rehman Jalil

Jülich, 24th November 2021

Contents

Abstract

The realization of advanced spintronics applications including the topological quantum computation, spin manipulation for data storage, dissipationless ballistic transport for ultra-fast quantum devices and topological switching for low energy memory applications etc. became more feasible with the experimental discovery of 3D topological insulators (TIs). The incorporation of exotic spin-momentum locked Dirac surface states (of 3D TIs) into these futuristic complex quantum devices requires not only the growth of high crystal quality epilayers but also the fabrication of pristine nanostructures, topological band engineering, ultra-smooth and defect-free surfaces, and atomically transparent epitaxial interfaces.

This work deals with a systematic study of epitaxial growth of convention 3D TIs via molecular beam epitaxy (MBE) and atomic-scale structural characterization via scanning transmission electron microscope (STEM) to explore the above mentioned requirements. At first, the relation between the growth parameters and the defect density in the Van-der-Waals (VdW) based layered structures is investigated. The optimum growth parameters are extracted and the defect-free epilayers are prepared. Later, the technique of selective area epitaxy (SAE) is explored to develop a platform to achieve a scalable nano-architecture. Utilizing CMOS compatible fabrication technology, Si (111) substrates with crystalline and amorphous combinational surfaces are prepared. The precisely controlled growth parameters facilitated the realization of selectively grown topological structure. Based on statistical analysis, a generalized growth model is established that provided control over structural defects through the effective growth rate at the nanoscale and assisted in achieving high quality nanostructures.

Based on conventional 3D TIs, the capabilities of VdW epitaxy are exploited further with the growth of topological-trivial heterostructures. The stoichiometric adjustment in these heterostructures is utilized as a tool to control the strength of spin-orbit coupling (SOC) and to engineer the topological band structure. Two such systems are explored including Bi_xTe_y = $(Bi_2)_m(Bi_2Te_3)_n$ and GST/GBT = $(GeTe)_n(Sb_2Te_3/Bi_2Te_3)_m$. With the continuous addition of Bi_2 bilayers and GeTe (materials that exhibit trivial phase) into 3D TIs, the stoichiometric modulations are achieved. Moreover, the modification of growth parameters is conducted to incorporate these stoichiometries with the pre-patterned substrates and selectively grown nanostructures of the corresponding alloys are prepared. Assisted by the atomic-scale structural characterizations, the phenomenon of VdW reconfiguration is explored to observe the transformation of layer architecture; the key mechanism in the evolution of interfacial phase change materials (IPCMs). Moreover, the systematic alterations in the atomic interaction and resulting changes in bond lengths within a pristine and hybrid VdW stacks are investigated.

The focus is then shifted towards surfaces where the stability (inertness) of TI epilayers in the ambient conditions via structural and compositional investigations, is analyzed. An undeniable evidence of the aging effect in all material systems is obtained where a non-saturating oxidation process at the (0001) surfaces with a continually decreasing oxidation rate is witnessed. Using the *in situ* thin film deposition of Al (2 nm), the top surfaces are passivated and the aging effect is neutralized. The phenomenon of charge transfer due to band alignment at the Si (111) - TI bottom surface is investigated with a comparative growth, structural and transport analysis of TI epilayer prepared on HfO_2 substrate. Finally, the interfaces between TIs and various s-wave superconductors (SCs) are explored. The challenges to achieve the induced superconductivity in TI-SC hybrid junction and highly transparent interfaces are addressed. The issue of metal diffusion into the TI epilayer and the resulting formation of Schottky-like barriers is avoided with the introduction of a thin metallic film as a diffusion barrier. Using the natural tendency of transition metals to transform into their corresponding di-chalcogenides (TMDCs) at the exposure to TI surfaces, atomically well-defined and VdW assisted epitaxial interfaces are engineered. The newly evolved interfaces assisted in achieving the induced superconductivity that was a huge limitation in realizing the complex functional devices.

List of Publications

2017 and Earlier:

1. Peter Schüffelgen, Daniel Rosenbach, Chuan Li, Tobias Schmitt, Michael Schleenvoigt, **Abdur Rehman Jalil**, Jonas Kölzer, Meng Wang, Benjamin Bennemann, Umut Parlak, Lidia Kibkalo, Martina Luysberg, Gregor Mussler, Alexander Golubov, Alexander Brinkman, Thomas Schäpers, Detlev Grützmacher, "*Boosting Transparency in Topological Josephson Junctions via Stencil Lithography*", arXiv preprint arXiv:1711.01665. (2017) https://arxiv.org/abs/1711.01665

2. **Abdur Rehman Jalil**, Hao Chang, Vineeth Kumar Bandari, Peter Robaschik, Jian Zhang, Pablo F. Siles, Guodong Li, Danilo Bürger, Daniel Grimm, Xingyuan Liu, Georgeta Salvan, Dietrich R. T. Zahn, Feng Zhu, Haibo Wang, Donghang Yan, Oliver G. Schmidt "*Fully Integrated Organic Nanocrystal Diode as High Performance Room Temperature NO_2 Sensor*", Advanced Materials, 28: 2971-2977 (2016) https://doi.org/10.1002/adma.201506293

3. Vineeth Kumar Bandari, Lakshmi Varadharajan, Longqian Xu, **Abdur Rehman Jalil**, Mirunalini Devarajulu, Pablo F Siles, Feng Zhu, Oliver G Schmidt "*Charge transport in organic nanocrystal diodes based on rolled-up robust nanomembrane contacts*", Beilstein Journal of Nanotechnology. (2017), 8, 1277–1282. https://doi:10.3762/bjnano.8.129

4. Peter Schüffelgen, Daniel Rosenbach, Michael Schleenvoigt, Tobias W Schmitt, Chuan Li, **Abdur Rehman Jalil**, Martin P. Stehno, Gregor Mussler, Lidia Kibkalo, Martina Luysberg, Christian Weyrich, Benjamin Bennemann, Stefan Trellenkamp, Elmar Neumann, Thomas Schäpers, Alexander Brinkman, Detlev Grützmacher, "*In-situ Fabrication of Topological-Superconducting Hybrids*", IEEE/CSC & ESAS superconductivity, (2017)

2018:

5. **Abdur Rehman Jalil**, Michael Schleenvoigt, Stefan Trellenkamp, Benjamin Bennemann, Thomas Schäpers, Tobias Schmitt, Gregor Mussler, Peter Schüffelgen, Daniel Rosenbach, Martina Luysberg, Detlev Grützmacher, "*In-Situ Fabricated Low-Dimensional Topological Insulator-Superconductor Hybrid Junctions: A Platform for Majorana Fermions*", 658. WE-Heraeus-Seminar on 'Spins out of equilibrium: Manipulating and detecting quantum magnets', WE-658, Bad Honnef. (2018)

6. Thomas Schäpers, Christian Weyrich, Daniel Rosenbach, Jonas Kölzer, Tobias Schmitt, Peter Schüffelgen, Gregor Mussler, Michael Schleenvoigt, **Abdur Rehman Jalil**, Hans Lüth, Detlev Grützmacher, "*Phase-coherent transport in topological insulator nanocolumns and nanoribbons*", SPIE Proceedings Volume 10732, Spintronics XI; 107320V (2018) https://doi.org/10.1117/12.2322720

2019:

7. Ankita Anirban, **Abdur Rehman Jalil**, Yunbo Ou, Mirko Rocci, Gregor Mussler, Jagadeesh Moodera, Crispin Barnes, Christopher J. Ford, "*Selective Contact and Patterning of Topological Surface States*

by Interfacing with Trivial and Ferromagnetic Insulators", APS March Meeting (2019); Y03. 009 https://ui.adsabs.harvard.edu/#abs/2019APS..MARY03009A/abstract

8. Peter Schüffelgen, Tobias Schmitt, Michael Schleenvoigt, Daniel Rosenbach, Pujitha Perla, **Abdur Rehman Jalil** Gregor Mussler, Mihail Lepsa, Thomas Schäpers, Detlev Grützmacher, "*Exploiting topological matter for Majorana physics and devices*", Solid-State Electronics, 155;99-104 (2019) https://doi.org/10.1016/j.sse.2019.03.005.

9. Vijay Narayan, P. C. Verpoort, J. R. A. Dann, D. Backes, CJB Ford, M Lanius, **Abdur Rehman Jalil**, Peter Schüffelgen, Gregor Mussler, G. J. Conduit, Detlev Grützmacher, "*Long-lived nonequilibrium superconductivity in a noncentrosymmetric Rashba semiconductor*", Physical Review B 100, 024504 (2019), DOI: 10.1103/PhysRevB.100.024504

10. Peter Schüffelgen, Daniel Rosenbach, Chuan Li, Tobias W Schmitt, Michael Schleenvoigt, **Abdur Rehman Jalil**, Sarah Schmitt, Jonas Kölzer, Meng Wang, Benjamin Bennemann, Umut Parlak, Lidia Kibkalo, Stefan Trellenkamp, Thomas Grap, Doris Meertens, Martina Luysberg, Gregor Mussler, Erwin Berenschot, Niels Tas, Alexander A Golubov, Alexander Brinkman, Thomas Schäpers, Detlev Grützmacher, "*Selective area growth and stencil lithography for in situ fabricated quantum devices",* Nature nanotechnology 14, 825–831 (2019) https://doi.org/10.1038/s41565-019-0506-y

11. Peter Schüffelgen, Daniel Rosenbach, Chuan Li, Tobias W Schmitt, Michael Schleenvoigt, Sarah Schmitt, **Abdur Rehman Jalil**, Jonas Kölzer, Lidia Kibkalo, Martina Luysberg, Benjamin Bennemann, Umut Parlak, Doris Meertens, Stephan Trellenkamp, Gregor Mussler, Thomas Grap, Meng Wang, Erwin J Berenschot, Niels R Tas, Alexander A Golubov, Alexander Brinkman, Thomas Schäpers, Detlev Grützmacher, "*Exploiting topological matter for Majorana physics and devices via molecular beam epitaxy (Conference Presentation)*", SPIE Proceedings Volume 11090, Spintronics XII; 110902D (2019) https://doi.org/10.1117/12.2527294

2020:

12. Daniel Rosenbach, Nico Oellers, **Abdur Rehman Jalil**, Martin Mikulics, Jonas Kölzer, Erik Zimmermann, Gregor Mussler, S. Bunte, Detlev Grützmacher, Hans Lüth, Thomas Schäpers, "*Quantum transport in topological surface states of Bi2Te3 nanoribbons*", Advanced Electronic Materials, 6 (8), 2000205 (2020), https://doi.org/10.1002/aelm.202000205

13. Arthur Leis, Michael Schleenvoigt, **Abdur Rehman Jalil**, Vasily Cherepanov, Gregor Mussler, Detlev Grützmacher, F Stefan Tautz, Bert Voigtländer, "*Room temperature in-situ measurement of the spin voltage of a BiSbTe3 thin film*", Scientific Reports, 10, 2816 (2020). https://doi.org/10.1038/s41598-020-59679-9

14. Jonas Kölzer, Daniel Rosenbach, Christian Weyrich, Tobias W. Schmitt, Michael Schleenvoigt, **Abdur Rehman Jalil**, Peter Schüffelgen, Gregor Mussler, Vincent E Sacksteder IV, Detlev Grützmacher, Hans Lüth, Thomas Schäpers, "*Phase-coherent loops in selectively-grown topological insulator nanoribbons*", IOP Nanotechnology, 31 325001 (2020)

15. Tobias W. Schmitt, Malcolm R Connolly, Michael Schleenvoigt, Chenlu Liu, Oscar Kennedy, José M Chávez-Garcia, **Abdur Rehman Jalil**, Benjamin Bennemann, Stefan Trellenkamp, Florian Lentz, Elmar Neumann, Tobias Lindström, Sebastian E de Graaf, Erwin Berenschot, Niels Tas, Gregor Mussler, Karl D Petersson, Detlev Grützmacher, Peter Schüffelgen, "*Integration of topological insulator Josephson junctions in superconducting qubit circuits*", arXiv preprint arXiv:2007.04224 (2020)

16. Jinzhong Zhang, **Abdur Rehman Jalil**, Pok-Lam Tse, Jonas Kölzer, Daniel Rosenbach, Helen Valencia, Martina Luysberg, Martin Mikulics, Gregory Panaitov, Detlev Grützmacher, Zhigao Hu, Jia Grace Lu, Thomas Schäpers, "*Proximity-Effect-Induced Superconductivity in Nb/Sb2Te3-Nanoribbon/Nb Junctions*", Annalen der Physik, 532, 2000273 (2020). https://doi.org/10.1002/andp.202000273

2021:

17. Danhong Huang, Godfrey Gumbs, Martin Lanius, **Abdur Rehman Jalil**, Peter Schüffelgen, Gregor Mussler, Detlev Grützmacher, Vijay Narayan, "*Quantum Boltzmann equation for non-reversible transient transport in Rashba-Landau coupled low-dimensional GeTe systems*", Physics Letters A 411, 127550 (2021). https://doi.org/10.1016/j.physleta.2021.127550.

18. Daniel Rosenbach, Tobias W Schmitt, Peter Schüffelgen, Martin P Stehno, Chuan Li, Michael Schleenvoigt, **Abdur Rehman Jalil**, Gregor Mussler, Elmar Neumann, Stefan Trellenkamp, Alexander A Golubov, Alexander Brinkman, Detlev Grützmacher, Thomas Schäpers, "*Reappearance of first Shapiro step in narrow topological Josephson junctions*", Science Advances 7 (26), eabf1854 (2021). https://doi.org/10.1126/sciadv.abf1854

19. Daniel Rosenbach, Kristof Moors, **Abdur Rehman Jalil**, Jonas Kölzer, Erik Zimmermann, Jürgen Schubert, Soraya Karimzadah, Gregor Mussler, Peter Schüffelgen, Detlev Grützmacher, Hans Lüth, Thomas Schäpers, "*Gate-induced decoupling of surface and bulk state properties in selectively-deposited Bi2Te3 nanoribbons*", arXiv preprint arXiv:2104.03373 (2021).

20. Tobias Schmitt, Malcolm Connolly, Michael Schleenvoigt, Chenlu Liu, Declan Burke, Oscar Kennedy, Tobias Lindstrom, Sebastian de Graaf, **Abdur Rehman Jalil**, Benjamin Bennemann, Stefan Trellenkamp, Florian Lentz, Elmar Neumann, Erwin Berenschot, Niels Tas, Kristof Moors, Gregor Mussler, Karl Petersson, Detlev Grützmacher, Peter Schüffelgen, "*Timons: superconducting gatemon qubits based on proximitized topological insulators*", Bulletin of the American Physical Society, APS March Meeting (2021), C31.00010.

21. Jinzhong Zhang, Pok-Lam Tse, **Abdur Rehman Jalil**, Jonas Kölzer, Daniel Rosenbach, Martina Luysberg, Gregory Panaitov, Hans Lüth, Zhigao Hu, Detlev Grützmacher, Jia Grace Lu, Thomas Schäpers, "*Flux periodic oscillations and phase-coherent transport in GeTe nanowire-based devices*", Nature communications 12 (1), 754, 1-8 (2021). https://doi.org/10.1038/s41467-021-21042-5

Chapter – 1
Introduction to Topological Materials

1.1 Topological insulators (TIs)

Topology[1] is a mathematical terminology. It deals with the study of geometrical objects where the properties remain preserved through continuous deformations such as twisting and stretching as long as they are not damaged through tearing or cutting. For example, topologically an ellipse, a sphere, an ellipsoid and a square are all equivalent to a circle that can be transformed through continuous deformations into each other[1, 3].

In solid state physics, topology is related to specific features in electronic band structure. The most prominent features of topology can be observed in materials that exhibit strong spin orbit coupling (SOC) where the swapping of opposite parity orbitals across the Fermi level leads to the phenomenon of band inversion[3, 4, 5, 6]. The connectivity of inverted with the non-inverted bands results in the formation of linearly dispersed energy states with Dirac cone like formation (also known as topological states) that exhibit several exotic features including the helical spin-momentum locking[4, 5, 6]. This phenomenon of band inversion and resulting evolution of gapless states introduced a new class of materials in condensed matter known as topological insulators (TIs). Bi_2Te_3, Bi_2Se_3, Sb_2Te_3 and SnTe are a few examples of TIs[5, 6]. In general, all TIs can be categorized in 2 major groups:

- 2-dimensional topological insulators (2D TIs) exhibit 1D exotic topological states that reside at the edges of the material (edge estates), also called quantum spin Hall (QSH) insulators for example (Hg,Cd)Te quantum wells[7, 8].
- 3-dimensional topological insulators (3D TIs) host 2D topological states on the surface of the material called topological surface states (TSS) for example Bi_2Te_3, Bi_2Se_3 and Sb_2Te_3[5, 6].

Topology in 3D materials can be categorized into various sub-classes with novel topological phases. In order to understand the difference among various 3D topological phases, the phenomenon of band inversion and the origin of topological surface states (TSS) is necessary to understand.

1.1.1 Band inversion and the origin of topological surface states (TSS)

The origin of TSS in the electronic structure and the band inversion at the Γ-point in Bi_2Se_3, Bi_2Te_3, and Sb_2Te_3 can be understood with the help of different stages in the evolution of energy levels of atomic p-orbitals. For example, in Bi_2Se_3 the inversion occurs between the neighboring Bi (6p) and Se (4p) atomic orbitals due to three stages of evolution as described by Zhang *et al.*[4] and depicted in Figure 1.1.

- ***Chemical bonding:*** In the first stage, according to molecular orbital theory, the atomic p-orbitals split into bonding (+) and anti-bonding (-) orbitals due to hybridization during chemical bonding where the anti-bonding orbitals always exhibit higher energy levels. This step brings Se anti-bonding orbital $(P2^-_{X,Y,Z})$ and Bi bonding orbital $(P1^+_{X,Y,Z})$ closer in energy. "+/-" symbols represent "even/odd" parity of orbitals respectively.
- ***Crystal field splitting:*** The anisotropy in crystal field i.e. the difference in the structure along xy-plane and z-orientation causes further splitting of Se $(P2^-_{X,Y,Z})$ orbital into $(P2^-_Z)$ and $(P2^-_{X,Y})$ while Bi $(P1^+_{X,Y,Z})$ orbital splits into $(P1^+_Z)$ and $(P1^+_{X,Y})$. P_X and P_Y orbitals stay degenerate due to in-plane symmetry of the layered crystal. This step brings Se $(P2^-_Z)$ and Bi $(P1^+_Z)$ orbitals energetically closer.

- ***Spin-orbit coupling:*** The moving electrons in the vicinity of positively charged nuclei experience an effective magnetic field, which couples to their spin orientation. This effect is called spin-orbit coupling (SOC) that leads to a repulsion between energy levels with opposite spin orientation, e.g. in Bi for $P1_Z^+ \uparrow$ and $P1_{X+iY}^+ \downarrow$. As this effects directly related to the number of protons per nucleus, SOC is stronger in heavy elements e.g. Bi. It splits $P1_{X+iY}^+ \downarrow$ and $P2_{X+iY}^- \downarrow$ orbitals while deflects Bi $(P1_Z^+)$ downwards and Se $(P2_Z^-)$ upwards that results in the crossover of orbitals with opposite parity around the Fermi level.

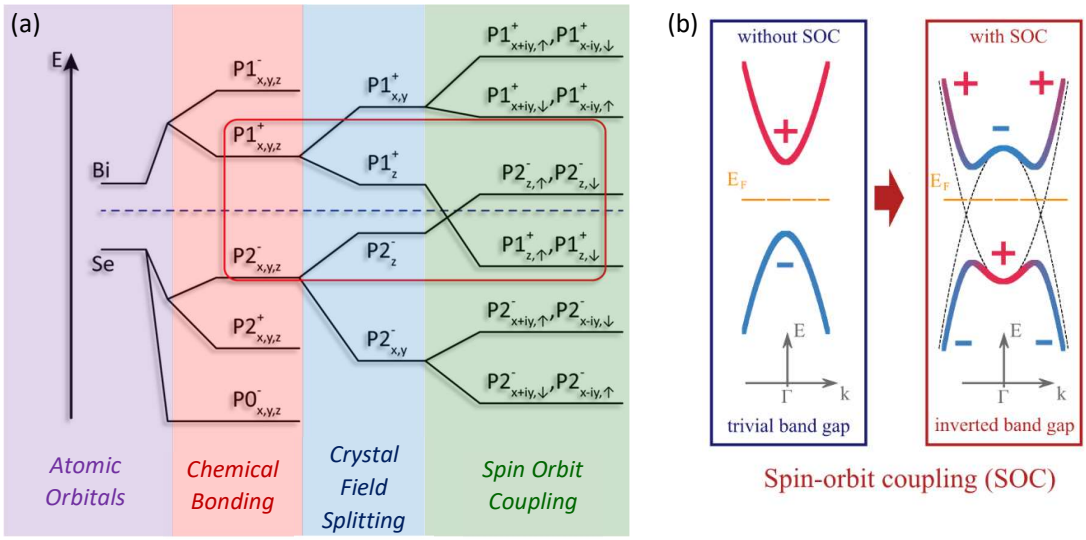

Fig. 1.1: Multi-step band structure evolution in Bi_2Se_3. (a) Chemical bonding, crystal field splitting and spin orbit coupling (SOC) affect the energy levels of Bi and Se $\mathbf{p}$-orbitals. In each step band with opposite parity (odd "-" orbital of Se in valance band and even "+" orbital of Bi in conduction band) come closer and finally, SOC inverts the band structure across the Fermi level at the Γ-point (orbitals of interest are marked with red box). (Adopted from Zhang et al.[4] with permission) (b) Without considering SOC, the order of the bands remains trivial throughout the whole Brillouin zone. By taking the effect of SOC into account, the inversion of the bands makes the valence band with even parity (electron-like) and the conduction band with odd parity (hole-like) in the vicinity of the Γ-point (simulation image is provided by Irene Aguilera)[9].

Passing through the above mentioned three stages of evolution, the odd parity orbital of Se $P2_Z^- \downarrow, P2_Z^- \uparrow$ and even parity orbital of Bi $P1_Z^+ \downarrow, P1_Z^+ \uparrow$ swap their relative positions on the opposite side of Fermi level leading to the phenomenon of band inversion in Bi_2Se_3 (Figure 1.1). The conduction band after inversion exhibits odd (-) while the valance band exhibits even (+) parity, the exact opposite behavior demonstrated by any normal insulator/semiconductor. This phenomenon is depicted in Figure 1.1b where the parity inversion of bands, before and after SOC, can be visualized around the Γ-point. For other high symmetry points F, K, M, L, Z etc. the effects of band evolution are not strong enough for an inversion in Bi_2Se_3 and hence, the bands remain topologically trivial within the residual Brillouin zone[4].

Origin of TSS: When a material with an inverted band structure (topological insulator) e.g. Bi_2Se_3 gets in contact with another material having non-inverted band structure (normal insulator/semiconductor) e.g. Si, the parities of conduction and valence band have to switch across the interface in order to fulfil the requirement of continuation of parity. The parity alignment across the Fermi level results in a transition region with very sharp band closing and reopening at the interface with the evolution of linearly dispersed metallic states called topological surface states (TSS)[4, 6]. This effect is also visually described in an earlier study by Schüffelgen *et al.*[10] TSS are different from conventional surface states that appear in materials with non-inverted band structure mostly due to structural defects whereas, TSS evolve as a result of parity

alignment to link the inverted and non-inverted bands. Other than being metallic in nature, TSS exhibit several exotic features among them a few are introduced here:

- ***Helical spin-momentum locking[5, 6]:*** TSS exhibit spin-momentum locking due to parity conservations. This feature makes TIs very promising candidate for advanced spintronics[11, 12, 13] such as fault-tolerant quantum computation[14, 15, 16] and high speed data storage applications at the room temperature.
- ***Robust against disorders[17, 18]:*** TSS are protected by time-reversal symmetry (TRS) that makes them very robust against perturbations and disorders as long as they are non-magnetic. Magnetic impurities allow for spin-flip, break TRS and the protection of TSS[19].
- ***Prohibited backscattering[17, 18]:*** Spin-momentum locking of TSS does not allow quasiparticles to switch/reverse spin without the relative change in momentum and hence, elastic backscattering is prohibited[6]. This features facilitates ballistic transport of TSS[20] that makes them prominent for low energy applications.

In general, this model describes how the strength of SOC leads to the band inversion of orbitals and the evolution of surface states in topological materials such as Bi_2Se_3, Bi_2Te_3 and Sb_2Te_3. It also explains that Sb_2Se_3 is not a TI because SOC is too weak to invert the bands[4]. However, in order to understand cases where materials exhibit complex topological phases, a model presented by Fu and Kane for the inversion symmetric crystals[21] explains this phenomenon in more detail and discussed in the next section.

1.1.2 Topological invariants for 3D systems

Fu and Kane[21] introduced a model to characterize various 3D topological systems hosting surface states (topology) with a set of variables $v_0; (v_1 v_2 v_3)$ known as Z_2 invariants. In case of 2D materials the topological invariant v_0 alone is utilized to identify the system being topological ($v_0 = 1$) or trivial (v_0 = 0)[21]. In 3D materials however, ($v_0 = 0$) does not necessarily means that the system is trivial rather the combination of all topological invariants $v_0; (v_1 v_2 v_3)$ define the topological state of the system[21].

According to Kramers theorem[22], if the Hamiltonian H of a system is invariant under time-reversal (exhibit TRS), every state $|\psi n(k, \uparrow)\rangle$ and the state with opposite spin and wave vector $|\psi n(-k, \downarrow)\rangle$ are eigenstates of the same Bloch energy and the Kramers pairs (KP) are at least two-fold degenerate due to the two possible spin directions of a fermion[21]. As observed earlier (Figure 1.1), the spin-orbit coupling (SOC) lifts this degeneracy and splits the states depending upon their spin. However, the states remain degenerate at some points in the Brillouin-zone, where the momentum is invariant under time-reversal called time-reversal invariant momenta (TRIM)[21]. The TRIM points (Γ_{ij}) are also called the Dirac points. Fu and Kane[21] demonstrated for the inversion symmetric crystals that topology of a 3D system (the Z_2 invariant v_0) is determined by the parity product of the occupied bands at the bulk TRIM points[21]. Taking an example of a cubic system v_0 and v_k (weak indices) could be evaluated using following equations.

$$(-1)^{v_0} = \prod_{i=1}^{8} \delta_i = \prod_{i=1}^{8} * \prod_{m=1}^{n} \xi_m(\Gamma_{ij}) \tag{1.1}$$

$$(-1)^{v_k} = \prod_{n_k=1;\, n_{k\neq j}\,=\,0,1} \delta_{i=\,(n_1 n_2 n_3)} \tag{1.2}$$

Here, ξ_m represents the parity eigenvalue (ξ_m = ±1) of the occupied band m at the TRIM point Γ_{ij} where i and j represent spatial identification, as depicted in Figure 1.2a and δ_i represents the parity invariant in the bulk. This means that for every Γ_{ij} a parity invariant δ_i is attributed, which is either 1 or -1 (-1 represents an inverted band structure).

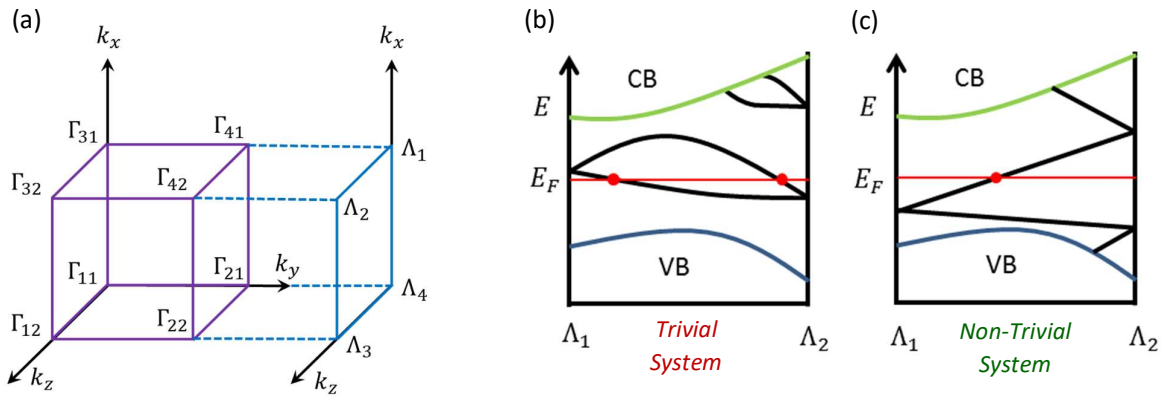

Fig. 1.2: (a) Schematic representation of the TRIM points (Γ_{ij}) of a cubic crystal structure. Projection of the TRIM points at the (010) surface (Λ_i) is displayed. Schematic representation of the energy levels and states between two surface TRIM projections Λ_1 and Λ_2 for a trivial insulator (b) and a topological insulator (c). In case of (b) the states always connect even number of crossings with the Fermi level, which indicates the trivial system with non-inverted bands while in (c) the states connect switching partners (opposite parity). Due to this switching, the Fermi level crosses the surface states always in an odd number, resulting in a metallic connection between valence and conduction bands. (Adopted from Fu and Kane[21])

1.1.3 Strong topological insulator (STI)

Considering a cubic crystal structure, as depicted in Figure 1.2a, if the bulk values are projected to the surface TRIM points Λ_i by $\pi_a = \delta_{i=(a1)}\delta_{i=(a2)}$ there can be two cases discussed below.

- First, if there is no change in the surface parity invariant between the two surface TRIM points ($\pi_1\pi_2 = 1$), the Fermi level cuts these states in an even number[23, 24] (Figure 1.2b). This corresponds to a trivial insulator ($v_0 = 0$) with the non-inverted and gapped band structure.
- Second, if there is a change in the surface parity invariant $\pi_1\pi_2 = (-1)$, the system is a topological insulator ($v_0 = 1$). In this case, the Fermi level always cuts the states in an odd number[23, 24], which means there is a connection between valence and conduction band and therefore the system is metallic (Figure 1.2c).

A material is called "***strong topological insulator***" (STI)[21], if the product of parity at the TRIM points projected on the surface i.e. $\pi_1\pi_2\pi_3\pi_4 = (-1)$ and the Fermi arc encloses Λ_i only once as depicted in Figure 1.3. Considering the case of cubic crystal, it means that either one or odd number of TRIM points should exhibit odd parity $\delta_i = (-1)$ to ensure that the product remains (-1) and material exhibits strong topology with the presence of TSS on all facets. All the conventional 3D TIs i.e. Bi_2Se_3, Bi_2Te_3 and Sb_2Te_3 exhibit Z_2 invariants $v_0; (v_1v_2v_3) = 1; (000)$ and belong to the category of STI. Another example Z_2 invariant with STI phase is $1; (111)$ exhibited by HgTe[7, 25], Sb[8, 21, 26] and Bi_4Te_3 (discussed in section 4.8.2).

1.1.4 Weak topological insulator (WTI)

Weak topological insulator is a unique phase of 3D topology when Z_2 invariant v_0, according to equation 1.1, becomes 0. As mentioned earlier, in case of 2D topology $v_0 = 0$ represents the trivial phase; however, in 3D systems it is possible that some surfaces exhibit topologically trivial phase named "dark surfaces"[27, 28] while other surfaces exhibit topological protection. Such a material is called "***weak topological insulator***" (WTI) [27, 28, 29].

According to Fu and Kane model[21], when $v_0 = 0$, the topology is determined by vector G_v (equation 1.3) where the weak indices v_k are evaluated using equation 1.2.

$$G_v = v_1b_1 + v_2b_2 + v_3b_3 \qquad (1.3)$$

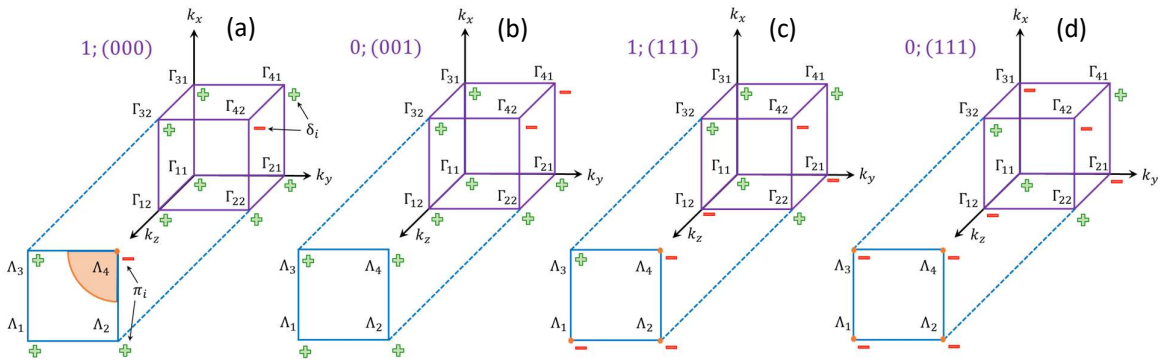

Fig. 1.3: A few examples for cubic Brillouin zones (represented with purple color) along with the projections of (001) surfaces (represented with blue color) of strong and weak topological insulators with 1, 2, 3 and 4 TRIM points. All TRIM points are allocated with a green or a red color sign for even i.e. $\delta_i = (+1)$ or odd i.e. $\delta_i = (-1)$ parities respectively. The parity projections on the (001) surface TRIM points Λ_i by $\pi_a = \delta_{i=(a1)}\delta_{i=(a2)}$ are also marked with similar rules. (a) An example of STI with Z_2 invariants $\nu_0; (\nu_1\nu_2\nu_3) = 1; (000)$, with one projected surface TRIM point Λ_4 with odd parity $\pi_4 = (-1)$ confirming the case $\pi_1\pi_2\pi_3\pi_4 = (-1)$. The orange curve represents the Fermi surface enclosing one Dirac point with odd parity. (b) An example of WTI with all $\pi_i = (+1)$, giving raise to trivial (001) surface. Fermi surface encloses no Dirac points (gaped band structures). (c) Another example of STI with a large Fermi surface where three Λ_i with odd parity confirm $\pi_1\pi_2\pi_3\pi_4 = (-1)$. The Fermi surface is not plotted. (d) A random example of possible WTI phase with all $\pi_i = (-1)$ resulting in $\pi_1\pi_2\pi_3\pi_4 = (+1)$ giving raise to trivial (001) surface. (Adopted from Fu and Kane[21])

Mathematically, when $G_\nu \neq 0$, it represents a WTI[21]. As mentioned earlier, a STI exhibits $\nu_0 = 1$ by satisfying the situation $\pi_1\pi_2\pi_3\pi_4 = (-1)$. It is only true when one or in general, odd number of TRIM points demonstrate odd parity $\delta_i = (-1)$ as depicted in Figure 1.3a and c. In case of WTI, the structure exhibits $\nu_0 = 0$ with any surface $\pi_1\pi_2\pi_3\pi_4 = (+1)$. This implies that even number of TRIM points demonstrate odd parity $\delta_i = (-1)$. In such a case, there can be two possibilities:

- Surfaces that contain all π_i with same parity i.e. $(+1)$; it is true when $G = G_\nu \; mod \; 2$. These surfaces are trivial and do not exhibit topologically protected surface states (dark surfaces) as depicted in Figure 1.3b where all π_i exhibit even $(+)$ parity resulting in dark (001) surface while it will not be the case at (010) surface. A similar model with the opposite parity case is depicted in Figure 1.3d where all π_i exhibit odd $(-)$ parity resulting in $\pi_1\pi_2\pi_3\pi_4 = (+1)$.
- Surfaces for which two of the Λ_a's are positive and two are negative, $G \neq G_\nu \; mod \; 2$. For those surfaces, the Fermi arc encloses two Λ_a's which have the same sign for π_a. Here, it is important to notice one major difference in WTI from STI. In STI, the Fermi arc encloses only one Dirac point while in case of WTI, the Fermi arc always enclose an even number of Dirac points. The (010) and (100) surfaces, in the system introduced in Figure 1.3b, will exhibit such a behavior.

The term "weak" was proposed as the system was claimed to have less protection against disorders or perturbations[30, 31, 32]; however, several studies have shown the robustness of WTIs via magneto-transport investigations. The main importance of WTI phase is realized after the proposal for its utilization to design materials with novel topological phases[2], discussed in section 1.2. $Bi_{14}Rh_3I_9$[27] , $ZrTe_5$[30], Bi_1Se_1[32, 33] and Bi_1Te_1[29] are a few examples of WTIs.

1.1.5 Topological crystalline insulator (TCI)

In case of strong and weak topological insulators, discussed above, the topology is always protected by time-reversal symmetry (TRS). No disorder or perturbations can destroy TSS as long as TRS remains intact. Topological crystalline insulator (TCI)[34, 35, 36, 37], on the other hand, is a unique phase of topology in 3D

systems where topology is not protected by TRS. Rather one or a combination of crystal symmetries (CS) including mirror, reflection and rotational etc. (spatial symmetries) define and protect topology.

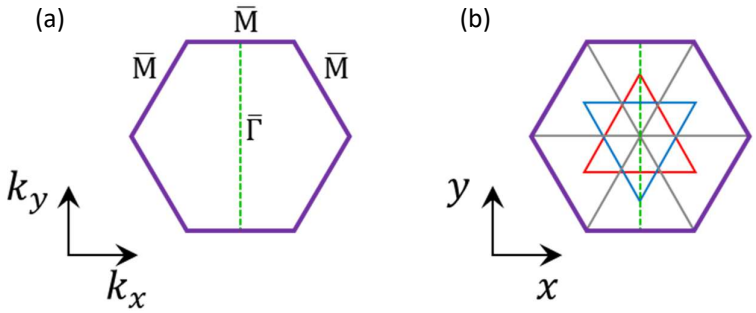

Fig. 1.4: Schematic representation of bismuth (Bi) Brillouin zone in the reciprocal (a) and real space (b), respectively. The mirror plane is displayed in both images as dashed green line. In b) the three different stacked layers of Bi are displayed in purple, red, and blue colors. (Adopted from Lanius et al.[38])

In the first generation 3D TIs, several Dirac points were observed in the band structure calculations of Bi_xSb_{1-x}[39, 40, 41] that somehow could not be explained by the presented model of Fu and Kane[21] for TRS protected inversion symmetric objects, discussed in section 1.1.3 and 1.1.4. Teo, Fu and Kane[41] established another theory to define the topological state that do not originate from TRS but are protected by the mirror symmetry of the crystal and thus, in addition to Z_2 invariants another topological invariant named the "*mirror Chern number*" $n_{\text{ɱ}}$ is introduced.

In Bi_xSb_{1-x}, the mirror plane resides at $k_x = 0$ between TRIM points $\bar{\Gamma}$ and $\bar{M}$, as depicted in Figure 1.4. The mirror reflection M (marked with green color) can be redefined in terms of a spatial inversion P and a two-fold rotation symmetry C_2 as $M(\hat{x}) = PC_2(\hat{x})$, which inverts the x-coordinate. The eigenvalues of $M(\hat{x})$ are $\pm i$ and $M^2 = 1$, it means that the mirror eigenvalues of the states in the mirror plane can be labeled with $\pm i$. According to Fu and Kane's TCI model[41], the mirror Chern number $n_{\text{ɱ}}$ can be evaluated using equation 1.4, by connecting the occupied bands in this mirror plane to a Chern invariant $n_{\pm i}$.

$$n_{\text{ɱ}} = \frac{n_{+i} - n_{-i}}{2} \tag{1.4}$$

In the presence of time-reversal symmetry (TRS), a total Chern number of the system must be zero[42] i.e. $n = n_{+i} + n_{-i} = 0$. It means, for $n_{\text{ɱ}} \neq 0$, even if there are no TRS protected surface states (topologically trivial surface), Dirac cones protected by the mirror symmetry can be found. The numerical value of the mirror Chern number $n_{\text{ɱ}}$ (an integer) is equal to the number of Dirac cones along the mirror plane in the first Brillouin-zone where the sign (±) of $n_{\text{ɱ}}$ called mirror chirality, gives the direction of the edge states.

Unlike the case of TRS protected topology, the Dirac points originated from crystal symmetry (mirror symmetry[34, 42] or other point-group symmetries of the crystal lattice[34, 42]), are not envisaged at surface projections of the TRIM points, rather can be observed on the mirror plane[29] or other high symmetry crystal surfaces[34, 42] depending upon the exact symmetry responsible for topological protection. The mirror symmetry is a property of the crystalline structure of the material. It can be broken by distortions or structural defects and therefore, it is characterized as a weak symmetry; however, experiments have shown that TCI states are robust[35, 37, 43] similar to other states originated from TRS protected STI or WTI phases.

The first TCI that was theoretically predicted and experimentally confirmed via ARPES is SnTe[35, 36, 44, 45]. Later, Eschbach *et al.*[29], reported the experimental realization of Bi_1Te_1 a dual TI (WTI + TCI) where (0001) surface being topologically dark (trivial surface of WTI) facilitated the experimental confirmation of CS originated Dirac cone away from the $\bar{\Gamma}$ point along the $\bar{M}$ plane. Similarly, theoretical studies have revealed

that Bi_2Te_3 and Bi_4Te_3 (discussed in section 4.8.2) also exhibit TCI characteristics[46] but due to being STI in nature, the surface states overlap at the $\bar{\Gamma}$ point and TCI behavior cannot be observed via ARPES.

1.1.6 Higher order topological insulator (HOTI)

Higher order topological insulator (HOTI)[45, 47, 48, 49] is a novel topological phase of 3D systems where materials do not exhibit 2D metallic surface states (witnessed in TRS protected STI and WTI phases and CS protected TCI phase) but rather host 1D topologically protected gapless hinge states[45, 47, 48, 49] or even lower-dimensional corner states. In HOTI, topology is protected by spatiotemporal (TRS + CS) symmetries and can be classified in the following categories also depicted in Figure 1.5.

- ***Chiral HOTIs:*** Topology is protected by the combination of TRS and CS (n-fold rotation symmetry $\widehat{C_n}$ or mirror symmetry). They exhibit hinge states with chiral modes[50, 51] while the bulk topology is Z_2-classified.
- ***Helical HOTIs:*** Topology is protected mainly by crystal symmetries (CS) while in some cases TRS is also involved. They exhibit helical hinge states that come in Kramers pairs while the bulk topology is Z-classified.

Several materials previously regarded as trivial insulators according to the Z_2-classifications, have started to exhibit HOTI phases in theoretical calculations, by extending the topological classification to the Z_4 invariants. One such example reported earlier is the bulk bismuth (Bi)[48, 52] that according to Z_2-classification exhibits topologically trivial surfaces with Z_2 invariants $\mathbf{0;(000)}$; however, CS facilitates the appearance of hinge states at the corners of the bulk (depicted in Figure 1.5c) demonstrating topological bulk–boundary correspondence[48]. Similarly, a recent discovery of helical edge states in Bi_4Br_4[49] is also reported confirming the important of Z_4 classification to determine HOTI phases. HOTI phases are also observed in SnTe[45] and predicted to appear in Bi_2TeI, Bi_1Se_1, and Bi_1Te_1[45].

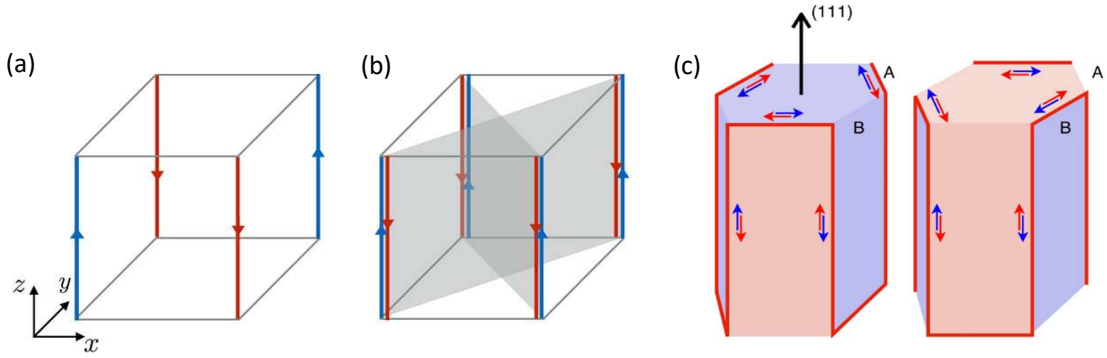

Fig. 1.5: A theoretical representation of HOTIs with topologically protected hinge states of second order 3D TIs. (a) A model representing chiral hinge modes along the corners of a cubic crystal protected by 4-fold rotational symmetry along z-axis ($\widehat{C_4^z}$) preserving bulk termination in z-direction. (b) Time-reversal invariant model with anti-propagating and degenerate hinge states where the highlighted planes in gray represent mirror planes that protect the hinge states via crystal mirror symmetry along xy-plane ($\widehat{M_{xy}}$) and $x\bar{y}$-plane ($\widehat{M_{x\bar{y}}}$) respectively. (c) Schematics of the helical hinge states of a hexagonally shaped HOTI in bismuth, oriented along the trigonal [111] axis with $\widehat{C_3}$ and inversion symmetry. Red lines represent a single one-dimensional Kramers pair of gapless protected modes. (Taken with permission from Schindler et al.[45, 48])

1.1.7 Topological semi-metal (TSM)

Topological semi-metal is not a well-defined term and utilized for systems with different classes of materials. In general, TSM can be divided into following three categories:

- An ordinary (trivial) semi-metal that contains separate electron and hole pockets compensating each other; however, the parity switching between the conduction and valence bands, discussed in section 1.1, gives rise to a nontrivial Z_2 topology and resulting in TSS. An example of such a system is pure Sb[8, 21], a trivial semimetal with TSS, where the topology is characterized by Z_2 invariants with $1; (111)$.
- A zero bandgap semiconductor (semi-metal) with strong SOC and band inversion. Similar to the first category, these materials also exhibit TSS with trivial bulk but unlike the first category, the inverted bandgap in such materials can be introduced by lowering the CS. The most prominent example is HgTe, a TSM that readily evolves into a 3D TI via applying a uniaxial strain to the bulk[7, 8, 53, 54, 55] by growing a HgTe layer on a lattice mismatched substrate[56]. The tensile strain lowers the CS, lifts the band degeneracy and opens an inverted bandgap.
- This category represents the true term of TSM with bulk topology including Dirac semi-metal (DSM)[2, 57, 58, 59, 60, 61, 62] and Weyl semi-metal (WSM)[2, 63, 64, 65, 66, 67]. In a Weyl semimetal due to SOC, the valence and conduction bands touch each other at isolated points around which the band structure forms non-degenerate 3D Dirac cones (not necessarily on high symmetry points). The apex of this 3D Dirac cone is called a Weyl node (non spin degenerated). Weyl nodes always appear in pairs and exhibit fascinating physics where a pair of Weyl nodes give rise to an arc of zero-energy excitation (Fermi arc) to connect them in the projected surface of Brillouin zone that hosts Weyl fermions[68, 69] as depicted in Figure 1.6. The crucial ingredient for the realization of a WSM is the presence of SOC and either TRS or inversion-symmetry (IS) must be broken. In contrast, when both TRS and inversion-symmetry are preserved, the system exhibits a Dirac cone with a Kramers double degeneracy and therefore, it is called a Dirac semi-metal (DSM). The most prominent examples of a DSM is Na_3Bi[57] with preserved TRS and a WSM is TaAs[66, 68, 70] with broken TRS. There are several proposals to design DSM and WSM from 3D TIs using topological phase transition, discussed in section 1.2.

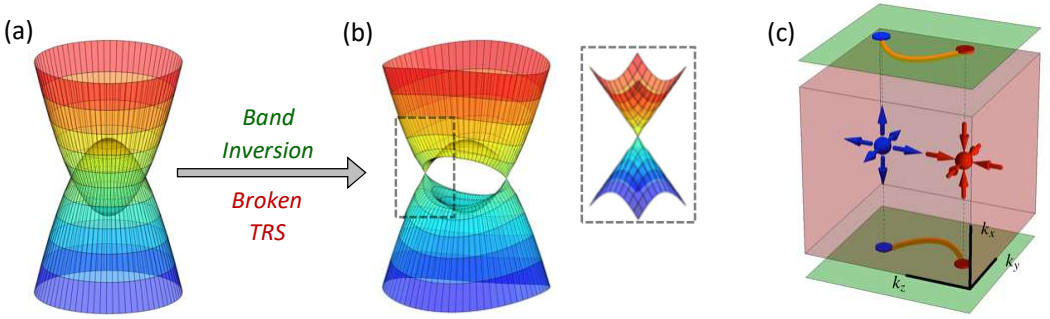

Fig. 1.6: A model representing the formation of a WSM. (a) Electronic band structure with overlapping conduction and valence bands due to parity inversion imposed by the strength of SOC. (b) The emergence of Weyl semi-metallic phase with the evolution of non-spin-degenerate Weyl nodes and band structure with the broken TRS. (c) An illustration of the simplest Weyl semimetal state that has two single Weyl nodes with the opposite (±1) chiral charges in the bulk where the zero energy excitations will give rise to the evolution of the Fermi-arc. (Adopted from Xu et al.[68])

1.2 Topological phase transition

Topological transition is a technique to engineer band structure in which the current topological phase of the material can be transformed into another topology or switched to topologically trivial phase. Such a transition can be achieved by two different methods:

- ***Physical modifications:*** This method deals with the modification of physical characteristics such as thickness of the crystal, stress in the epilayer and the applied pressure. Theoretical studies[71] and experimental observations[71, 72] have proved that 3D TIs can be transformed into 2D TIs by carefully

reducing the epilayer thickness below 5 nm[72]. Topological phase and texture modifications by mechanical strain in Bi_2Se_3 crystal have been reported[73] where the 3D topology is modified by varying the strength of applied tensile strain. Another example of topological phase transition using uniaxial strain is already mentioned where HgTe can be transformed from TSM phase to 3D TI[7, 8, 53, 54, 55]. This methods is mostly limited to 2D ↔ 3D transitions and topological ↔ trivial transformations. It does not provide stable and precise transformations among various 3D topological phases for the van der Waals (vdW) assisted layer based materials.

- ***Chemical variations:*** Chemical variations in the crystal i.e. the compositional changes[74] or the stoichiometric tuning[29], is more precise and suitable method to tune 3D topological phases. Using this method, the stoichiometry of a topological material "base", is altered with the addition of a topologically trivial material "additive". The accumulation of "additive" in "base" results in the reduced strength of spin orbit coupling (SOC) that in result alters the band structure.

One such model with an attempt to classify various 3D topological phases and to develop a link between 3D TIs and semi-metallic phases (TSMs), is presented by Yang *et al.*[2] The approach of chemical variation, according to the proposed model, can be adopted to engineer compositional alloys with the desired topology where the path of topological transformation particularly the topology at the critical point (when bandgap reaches 0 eV) is dictated by the topological state of the "base" (i.e. the symmetries exhibited by the starting 3D TI) while the electronic features of the "additive" (trivial material) impose the relative alterations in SOC and thus, in the band structure.

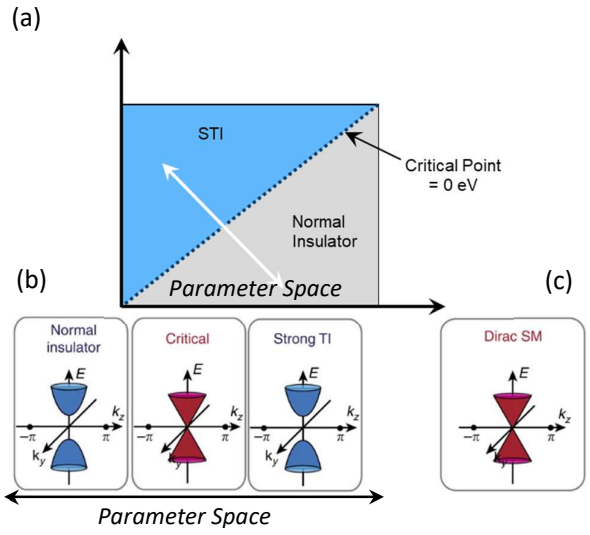

Fig. 1.7: A model representing phase transition in a STI, induced by band crossing when a single control parameter is varied in the system. (a) The generic phase diagram of a system with TRS and IS but lacks rotational symmetry (RS), categorizing various topological phases and the topological transition path based on the control parameter (White arrow). The control parameter along the x-axis is modifying the strength of SOC and the size of inverted/non-inverted bandgap. The dotted line represents the topological-trivial transition critical point with 0 eV bandgap (phase boundary). (b) System with trivial semi-metallic phase at the critical point with TRS and IS but lacking the RS. (c) Possibility of a DSM when an additional uniaxial RS is included (Adopted from Yang et al.,[2]).

Engineering DSM: Alloys/materials with DSM phase can be engineered when "base" exhibits STI phase protected by TRS and inversion symmetry (IS) as depicted in Figure 1.7. Continuous accumulation of "additive" into "base" will result in reduced strength of SOC in the stoichiometric states causing inverted bandgap to shrink until it will reach the critical point of 0 eV. Here, the alloy can take following possible paths depending upon the formation of the Dirac point.

- If the Dirac point forms at TRIM (crystal exhibits uniaxial rotational symmetry), the resulting alloy will exhibit DSM phase (Figure 1.7c).
- If the Dirac point does not exhibits uniaxial rotational symmetry; however, it exhibits TRS and IS, the alloy will exhibit type-1 TSM with trivial bulk band and TSS e.g. Sb (discussed in section 1.1.7).
- Irrespective to the position of the Dirac point formation, if the strength of SOC is too low to support the band inversion, the alloy will lose its topological features[2] resulting in a trivial semimetal (Figure 1.7b at the critical point).

With further addition of additive, the non-inverted bandgap will start expanding until the alloy reaches the electronic state of "additive" (a trivial insulator).

Engineering TDSM: Alloys/materials with topological DSM (TDSM) phase can be engineered when "base" exhibits WTI/TCI phase protected by TRS/CS respectively, as depicted in Figure 1.8. The continuous accumulation of "additive" will reduce the strength of SOC causing inverted bandgap to shrink until it will reach the critical point of 0 eV. Such materials, as pointed out in the diagram, exhibit two critical points.

- At the first critical point, facilitated by WTI/TCI phase, the formation of a pair of Dirac points will take place away from the TRIM points $\bar{\Gamma}$ that will exhibit degeneracy depending upon the rotation symmetry of the crystal. They will exist along the rotation axis and exhibit the TDSM phase until the material will reach the second critical point.
- At the second critical point, the Dirac points will meet at the TRIM points $\bar{\Gamma}$. With the reduced strength of SOC, the band inversion will stop and the alloy will lose its topological features[2] resulting in a trivial semimetal.

Once again, with the further addiction of additive, the non-inverted bandgap will start expanding until the alloy reaches the electronic state of "additive" (a trivial insulator).

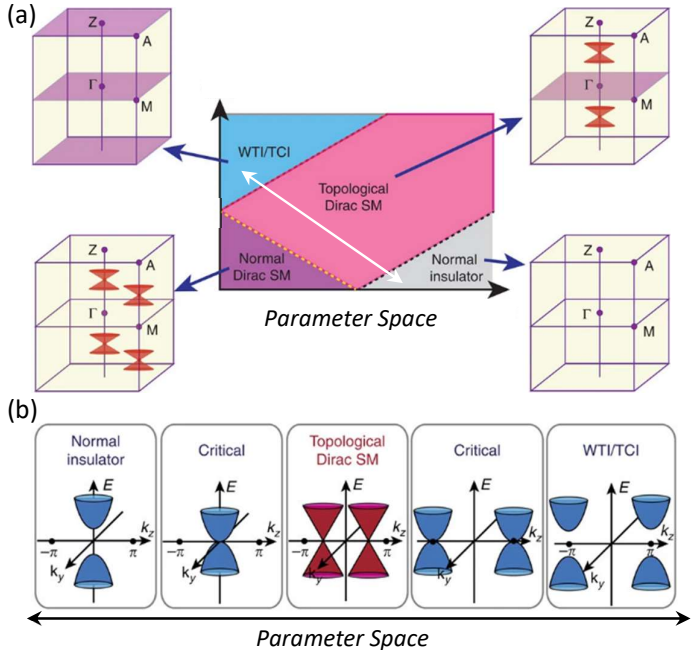

Fig. 1.8: A model representing phase transition in a WTI/TCI, induced by band crossing when a single control parameter is varied in the system. (a) Generic phase diagram of the system with TRS, RS and IS categorizing various topological phases and the topological transition path based on the control parameter (white arrow). The control parameter along the x-axis modifies the strength of SOC and the size of inverted/non-inverted bandgap. The two dotted lines on the transition path represent phase boundaries. (b) Topological DSM phase appears when the control parameter is tuned between two critical points that mediates the transition between a normal insulator and a WTI/TCI. (Taken with permission from Yang et al.,[2]).

Engineering WSM: WSM phase can be engineered with the following three methods. The first two approaches deal with breaking the TRS and the IS of a DSM respectively[75, 76, 77, 78, 79, 80, 81, 82].

- The evolution of WSM was theoretically demonstrated in several Bi based DSMs[75, 80] (Na_3Bi, K_3Bi, Rb_3Bi) by breaking the TRS and tuning the compounds at the topological phase boundary (the critical point). The degenerate Dirac points were enforced into the transformation of non-degenerate Weyl points along with the appearance of non-trivial Fermi-arc on the surface[75]. The topological stability of these compounds was ensured by the CS. Similar simulations were later reported for DSM Cd_3As_2[76] where WSM phase was engineered by breaking the TRS as well.
- Unlike the TRS, several proposals to break the IS in DSM to evolve WSM phases were also reported. It was proposed that engineering alloys that contain layer-by-layer growth of topological-trivial sequences would result in breaking the IS. One such model was theoretically demonstrated by Hassan's group[77] where the stacking sequence of $TlBi(S_{1-x}Se_x)_2$ and $TlBi(S_{1-x}Te_x)_2$ alloys were proven

to break the IS and Weyl points were realized. A similar model with HgTe/CdTe multilayer structure[78] was also proposed. With all these successfully demonstrated theoretical models to engineer WSM[82], till date no experimental realization of such a system using the technique of topological phase transition, has been achieved.

- The third approach to engineer a WSM phase is also via growing topological-trivial heterostructures; however, in this case the standard topological material is replaced with a magnetic TI[83]. The addition of trivial insulator spacer-layer stacked between magnetic TI layers helps managing the strength of SOC and breaking the IS of the compound that eventually, similar to the case of TDSM depicted in Figure 1.8, at the phase boundary (critical point), evolves in WSM phase[83]. Similar transformations are also reported in rare earth compound $Y_2Ir_2O_7$ as well[84, 85].

1.2.1 Topological band engineering using conventional 3D TIs

TSMs (DSM, TDSM and WSM) with bulk topology are favored over conventional 3D TIs due to enhanced density of states that possess topological protection. 3D TIs exhibit TSS that even in the best scenario (i.e. Fermi level in the bulk gap and low carrier concentration) suffer from deviations in the Fermi level (not homogeneous throughout the whole system) and the limited contribution in the electronic transport of the crystal due to confined density of states while major contributions are done by the bulk (trivial) carriers. In comparison to 3D TIs, TSMs exhibit higher mobility[86, 87] and enhanced magneto-effective responses[86, 87, 88]. They also exhibit novel zero-energy excitations with fascinating physics (Fermi-arc, Nodal line etc.)[64, 68, 85, 89, 90] that are not exhibited by 3D TIs. It does not imply 3D TIs are not effective rather, the aim is to find better possibilities to enhance the overall influence of topological states in the electronic transport particularly for the quantum applications.

Based on above mentioned points (Section 1.2), various TSM phases can be engineered from conventional 3D TIs (Bi_2Te_3, Bi_2Se_3 and Sb_2Te_3) using the technique of chemical variation (stoichiometric tuning) where the addition of a trivial material would help in managing the strength of SOC and protecting/breaking spatiotemporal (TRS, IS and CS) symmetries of the alloy. Considering conventional 3D TIs, the topological state of the starting material "base" defines the distinct path of topological transformations (band engineering) that can be adopted to engineer TSMs. A few of such possibilities are introduced below:

Transformations from STI to DSM: The transformation path is introduced in Figure 1.7. Among conventional 3D TIs, all materials exhibit STI phase and thus can be utilized as "base". Some of the "base + additive" combinations are discussed below:

- ***$Bi_{2-x}Sb_xSe_3 = Bi_2Se_3 + Sb_2Se_3$:*** $Bi_{2-x}Sb_xSe_3$ can be an example of classical phase transformation[91]. Bi_2Se_3 exhibits STI phase; however due to weak SOC, Sb_2Se_3 demonstrates non-inverted band structure with trivial phase[4, 92]. The only limitation in this compositional alloy ($Bi_{2-x}Sb_xSe_3$) is the structural stability of the alloy when Sb contents increases from 25%. Sb_2Se_3[93] does not exhibit the trigonal crystal structure[4, 94] like Bi_2Se_3. With increasing Sb contents, the crystal structure of alloy converts into the orthorhombic crystal[92, 93] which makes the realization of topological phase transformations difficult to achieve.
- ***$Sb_xTe_y = Sb_2Te_3 + Sb_2$:*** Sb_xTe_y is another example of topological phase transformation. In this system, the stoichiometric alloys exist naturally in form of $(Sb_2)_m(Sb_2Te_3)_n$ superlattices and thus, structural stability is not a limitation[95, 96]; however, the issue lies in the electronic features[97] of the "additive" i.e. Sb. It is not only a semi-metal but also a non-trivial entity (STI). The topology of both materials being STI and semi-metallic nature of Sb make the transformation range quite limited and the topological phase projections very complex.
- ***$Bi_xSe_y = Bi_2Se_3 + Bi_2$:*** Bi_xSe_y series, similar to Sb_xTe_y, exhibit compatible crystal structure; however, unlike Sb_2, the "additive" Bi_2 is a topologically trivial semi-metal (Bi_2 exhibits HOTI phase[48] while as bulk, it is still considered trivial). The trivial attributes of Bi_2 allow to achieve phase transformations;

however, it can only be achieved in a limited range as Bi_2 being a semi-metal does not allow stoichiometric states to reach the trivial insulator phase.

- ***$Ge_xSb_yTe_z$ = Sb_2Te_3 + GeTe:*** $Ge_xSb_yTe_z$ (GST) stoichiometric series lack both problems encountered in the above mentioned systems. The crystal structural stability[98, 99, 100] and trivial insulating attributes of the "additive". GeTe exhibits +0.6 eV non-inverted bandgap[101, 102] that allows GST stoichiometric states to explore the complete range to topological phase transformations according to Figure 1.7.

Transformations from TCI to TDSM: The transformation path is introduced in Figure 1.8. Among conventional 3D TIs, only Bi_2Te_3 exhibits TCI phase and thus can be utilized as the "base". Some of the "base + additive" combinations are discussed below:

- ***Bi_xTe_y = Bi_2Te_3 + Bi_2:*** Bi_xTe_y is a complex example of topological phase transformation because Bi_2Te_3 is a dual TI that exhibits STI and TCI phases and therefore, the transformation process will impact both paths i.e. one with STI towards DSM and other from TCI towards TDSM simultaneously. Both candidates i.e. Bi_2Te_3 and Bi_2 exhibit similar crystal structure (trigonal) and thus, the structural compatibility does not pose a problem[103, 104]. The electronic features of Bi_2 as a semi-metal limit the range of transformation and will not let alloys to reach the trivial insulator phase. One interesting feature that can be expected from Bi_xTe_y transformations is the richness of topological phases as both TRS and CS based transformations will occur at the same time. Some predicted phases in Bi_xTe_y series range from STI to WTI[29], TCI[29, 46] to HOTI[45, 48] and TSM[105].
- ***$Ge_xBi_yTe_z$ = Bi_2Te_3 + GeTe:*** $Ge_xBi_yTe_z$ (GBT) stoichiometric series similar to GSTs is an example of classical phase transformation where the "base" is replaced from Sb_2Te_3 to Bi_2Te_3. Once again, the dual nature of Bi_2Te_3 will allow multiple paths of transformation and the restriction imposed by semi-metallic features of Bi_2 in Bi_xTe_y, will be encountered by the trivial insulator GeTe. GBT is one of the most promising transformation series, as it allows to explore the complete range of phase transformations (topological ↔ TSM ↔ trivial) in Bi_2Te_3.

Transformations from WTI to TDSM: All conventional 3D TIs exhibit only STI phase, WTI phase is not exhibited by any compound. The discovery of WTI phase[29, 32] in modified conventional 3D TIs i.e. Bi_1Se_1 and Bi_1Te_1, members of Bi_xSe_y and Bi_xTe_y series make them quite promising and unique to investigate for the probable realization of TDSM phases.

Transformations from MTI/STI to WSM: The path to engineer WSM phase through magnetic TIs[106] is also achievable via ($MnBi_2Te_4$ + Bi_2) and ($MnBi_2Te_4$ + GeTe) heterostructures; however, the stoichiometric tuning of these alloys can be quite complicated and hard to achieve. Another possibility to obtain WSM phase is via conventional 3D TIs and magnetic insulator heterostructures. A few such examples are (Bi_2Se_3 + MnSe)[107, 108], (Bi_2Te_3 + MnTe)[109, 110], (Sb_2Te_3/Bi_2Te_3 + YIG)[111], (Bi_2Se_3 + EuO)[111, 112] and (Bi_2Se_3 + $Y_3Fe_5O_{12}$)[113]. The details of magnetic TIs based phase transformations can be found in Burkov *et al.*[83] while a few first principles based calculations are reported in Zou *et al.*[114]

1.3 Topological superconductor (TSC)

One of the most promising and immensely desired application of topology[115] is the fault tolerant quantum computation[14, 116, 117, 118] based on spatial braiding[14, 15, 119, 120] of Majorana quasiparticles (MQPs). MQPs are exotic massless entities that always emerge in pairs[14, 121, 122] where one particle acts as an antiparticles of the other with the cumulative effect of the pair is equivalent to one fermionic state (e^-)[118]. They obey non-Abelian statistics[14, 116, 123] and therefore, could be used as a robust building blocks in the quantum computation. MQPs are predicted to emerge in the vortex of a topological superconductors (TSC) as a zero energy excitation called Majorana zero mode (MZM)[14, 123, 124]. A TSC is an odd-parity p-wave superconductor $(p_x + ip_y)$[123] with topological protection that rarely exists in nature. Till date no such

existing materials are reported in literature though, a few potential candidates are under investigation[123]. This phenomenon limits the probable realization of MQPs and thus, the topological quantum computation.

The search for MQPs was suddenly boosted in 2008 with the proposed model of Fu and Kane[121] to artificially engineer a TSC based on a normal s-wave superconductor-semiconductor heterostructure[125]. It was proposed that the superconducting proximity effect in a material with strong SOC for example a STI, will result in the induced superconductivity of TSS (helical spin-momentum locked states) forming an artificial TSC. Though, there are certain requirements that must be fulfilled before the emergence of MQPs in an odd-parity p-wave artificial TSC will be witnessed. In order to explore Majorana physics, the topological community rapidly adopted this alternative approach and a race to observe topological superconductivity in semiconductor-SC hybrid junctions was started[126, 127, 128]. At first, most of the successful attempts were conducted with 2-dimensional electron gas (2DEG) in III-V semiconductors based junctions due to their pre-established high quality epitaxial interfaces where the signatures of topological superconductivity were observed[129, 130, 131, 132, 133]. In 2012, for the first time, the induced TSC was witnessed in a conventional 3D TI-SC hybrid junction[134] where Bi_2Se_3 QLs (STI) were placed on top of an unconventional s-wave superconductor $NbSe_2$. Later, the artificial TSC was also reported in Bi_2Te_3 – $NbSe_2$ hybrid junctions[135, 136].

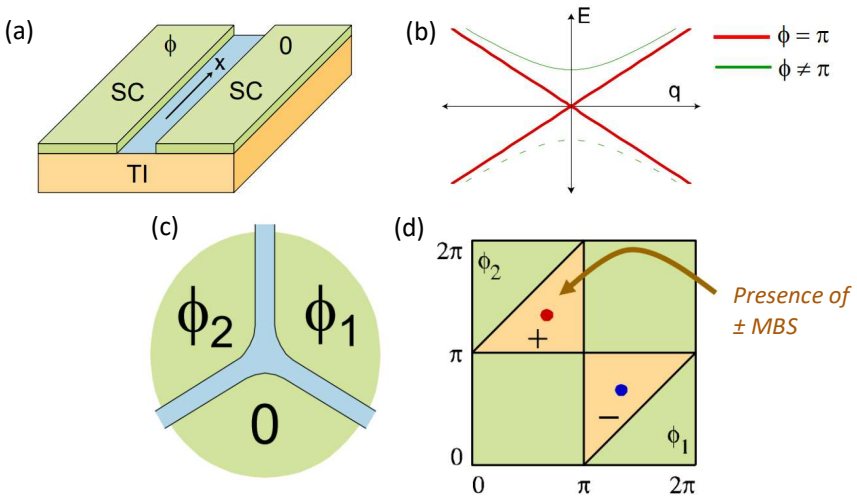

Fig. 1.9: Fabrication of an artificial TSC. (a) SC-TI-SC linear Josephson junction. (b) Spectrum of a linear junction as a function of momentum for various in-plane applied flux (ϕ). The red lines show the Andreev bound states for $\phi = \pi$ while the bound states for $\phi = 0$ merge with the continuum, indicated by the green lines. (c) A linear network based on multi-terminal topological Josephson junctions between three superconductors. (d) Phase diagram for the tri-junction with orange regions indicating a ± MBS at the junction.(adopted from Fu and Kane[121])

As discussed earlier, the first part of Fu and Kane model[121] introduced an alternative approach via TI-SC hybrid junctions to fabricate an artificial TSC, the second part of the model presented an idea of utilizing the artificially engineered TSC in form of linear junctions i.e. Josephson junctions (JJs) at the nanoscale where MQPs appear in form of Majorana bound states (MBS)[121, 137, 138]. Also an electronic circuit based on these topological JJs can be utilized to create, fuse (annihilate) and manipulate MBSs[137] to realize a topological Qubit as depicted in Figure 1.9. Till date, numerous studies are conducted to fabricate a topological Qubit without any reported success; however, a few of them have described the observation of 4π-periodic phase relation of MBS[139, 140, 141, 142, 143] in topological JJs, the basic step towards the realization of topological Qubit.

1.3.1 Building blocks of a topological superconductor (TSC)

Various theoretical models[122, 144, 145, 146] and mathematical calculations[14, 15, 139, 141, 147] have confirmed the idea presented by Fu and Kane[121]. Recently, an experimental replica of this model via phase sensitive measurements based on Pb-Bi_2Te_3 multi-terminal junctions is demonstrated[148] though, no experimental realization of Majorana braiding has yet been achieved[115]. This phenomenon of relatively slow progress in obtaining the proposed target can be linked to non-ideal material characteristics (deviations from the theoretical models) and other restraining issues that must be resolved in order to continue the quest towards the realization of fault-tolerant topological Qubit.

The simplest topological Qubit system comprises of a multi-terminal JJ as depicted in Figure 1.9b. The smallest unit of such a system is a single topological JJ while the basic entity of a topological JJ is a TI-SC hybrid structure. A TI-SC hybrid junction consists of 3 building blocks, depicted in Figure 1.10, that are:

- superconductor (SC)
- weak link (topological material)
- interface between SC and topological material

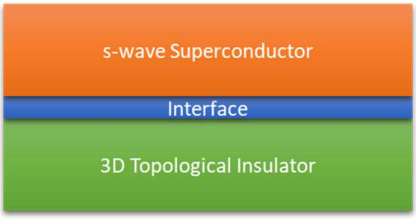

Fig. 1.10: A representation of the building blocks of a TI-SC hybrid junction i.e. s-wave superconductor, 3D topological insulator and the interface that connects them.

There are certain requirements that must be fulfilled by all entities of a TI-SC hybrid junction, in order to obtain an odd-parity p-wave artificial TSC suitable for the realization of a topological Qubit.

Superconductor (SC): The key requirements of the superconducting material are as follow:

- SC must exhibit Cooper pairs condensation with spin-singlet order[149, 150] (total spin = 0) in s-wave pairing[123, 124, 142, 149]. Example of the single element based SC include Sn, Nb, Al and Pb while the compound SC materials $NbSe_2$[135, 136] and $PdTe_2$[151] exhibit s-wave pairing. The proximity-induced TSC on a d-wave superconductor has also been reported[152]; however, they are more suitable to engineer higher-order topological superconductor (HOTSC)[153].
- SC must exhibit 2e periodic supercurrent[154, 155, 156] and stable ground state with even parity[154]

Topological material: The requirements from the topological materials are as follow:

- TSS must exist on the particular surface in contact with the SC, the (0001) surface, irrespective of the topological phase being STI[142], WTI[157] or TSM[158]
- Enhanced contribution of TSS (in case of STI and WTI) via growth of defect-free high quality epilayers exhibiting low bulk carrier density, high mobility and enhanced phase coherent length of the quasiparticles
- Fermi level of the material (in case of STI and WTI) along with the Dirac point is preferred to reside in the bulk bandgap

Interface between SC and TI: Interface is the most critical entity that links the SC with the topological material. The interface quality determines characteristics such as the strength of the induced superconductivity (size of the induced gap Δ') and the superconducting coherence length (ξ) of quasiparticles within the weak link (topological material). In most of the cases, the interface is analyzed through the superconducting JJ measurements by evaluating the transparency (τ) of the junction[143, 147].

With the increasing interest in TI-SC based artificial TSC for the controllable utilization of MQPs, a great deal of research on the functional interfaces is ongoing. With the cumulative understanding of interfaces, the requirements are constantly evolving[128, 138, 159, 160, 161, 162, 163]. The major requirements include:

- The interface is preferred to be epitaxial[123] without any inter-diffusion between TI and SC. The SC is preferred to exhibit compatible crystal structure with the similar lattice parameters of TI or should exhibit vdW based epitaxial stacking to avoid the formation of any dislocations or other strain related defects.
- The morphology at the interface must be atomically clean to avoid the formation of any traps and Schottky defects (e.g. oxides) that may lead to quasiparticle poisoning[123]. Hence, if possible, the interface must be prepared *in situ* to avoid any contamination from the ambient conditions. This parameter also assists in achieving low resistance noise at the junction during electronic investigations[160, 163].
- The interface should exhibit near perfect transparency ($\tau \rightarrow 1$) and large $I_C R_N$ product[160, 163] where I_C represents the critical current and R_N represents the normal state resistance of the junction.

If the selected material systems and their interaction at the interface fulfill all the corresponding above mentioned requirements, the restraining issues that are mostly encountered in TI-SC hybrid junctions will be avoided and the realization of MQPs based topological Qubit will be promptly achievable.

1.4 Scope of this work

This work is almost in continuation of the earlier reported studies by Borisova *et al.*[164] Lanius *et al.*[38] and Kampmeier *et al*.[165] where the preliminary growth foundations of conventional 3D TIs on Si (111) substrates via molecular beam epitaxy (MBE) were laid that paved the way to fabricate topological JJs with the successful realization of MBSs as reported by Schüffelgen *et al.*[10, 142]

The objective of this thesis is to perform a systematic growth optimization of crystals via MBE through detailed structural characterization using the techniques of high resolution X-ray diffraction (HR-XRD) and aberration corrected scanning transmission electron microscopy (STEM) and extend the growth capabilities from conventional 3D TIs to materials with other novel topological phases. Utilizing detailed structural characterization, the growth feasibility study for several topological-trivial heterostructures combinations, is performed. The technique of selective area epitaxy (SAE) is exploited as a tool to develop a scalable platform in order to fabricate pristine topological nanostructures. The impact of surface oxidation and substrate induced effects on the structural and electronic characteristics of the crystals are investigated and finally, the interface engineering in several hybrid structures is conducted to realize epitaxial interfaces between 3D TIs and s-wave superconductors; as the realization of epitaxial interfaces is a bottleneck in the fabrication of Majorana based functional devices. The entire study can be divided into three sections while each section is sub-divided into two chapters.

Section 1: This section focuses on the growth optimization and structural characterization of conventional 3D TIs and the realization of topological nanostructures.

- In chapter 2, based on a systematic growth and STEM study, challenges of van der Waals (vdW) epitaxy are addressed. The correlation between the growth parameters (substrate temperature and thin film growth rate) and the defect density is investigated. Various structural defects and their impact on the material's electronic characteristics are discussed. The optimum growth parameters are extracted and the defect-free high crystal quality epilayers of all Te based 3D TIs are prepared.
- To fulfil the demand of high-quality crystalline nanostructures in the pristine form (unaffected from fabrication chemicals and the ambient conditions), a platform to support the scalable nano-

architecture using the technique of selective area epitaxy (SAE), is established in chapter 3. The fabrication and strain related issues of the pre-patterned substrates are addressed. Based on the statistical study, a growth model is developed to evaluate and control the effective growth rate of nanostructures. Finally, with the assessed optimum parameters, high structural quality pristine nanostructures of all conventional 3D TIs are obtained. The electronic characterization of nanostructures via magneto-transport investigations is performed where novel features of TSS in the transport analysis are witnessed.

Section 2: This section focuses on the epitaxial growth of topological-trivial heterostructures using the proposed model of topological phase transitions in conventional 3D TIs to achieve other novel 3D topological phases including TSMs.

- Among all conventional 3D TIs, only Bi_2Te_3 exhibits CS protected TCI phase along with STI, protected by TRS. To investigate materials at the path of TCI based topological phase transformations, the growth of Bi_xTe_y stoichiometric alloys is conducted in chapter 4. $Bi_xTe_y = (Bi_2)_m(Bi_2Te_3)_n$ stoichiometric alloys arrange themselves in the natural order of Bi_2 bilayers and Bi_2Te_3 QLs where the relative presence (m:n) determines the stoichiometry while the stacking sequence determines the unit cell length and topology of the alloy. The epitaxial growth and the detailed structural characterizations of several stoichiometric states are performed and the stacking sequences of the key states are confirmed via STEM investigations. The unique presence of hybrid vdW stacking and its impact on the structural properties of the crystal, is investigated. Finally, nanostructures on the pre-patterned substrates using the technique of SAE, are realized.
- In chapter 5, a growth study of a couple of topological-trivial heterostructures combinations in form of GST and GBT stoichiometric alloys, is conducted with the trivial insulator GeTe to explore the entire topological transformation range of Sb_2Te_3 and Bi_2Te_3 respectively. Epilayers of various stoichiometric alloys ranging in topological and trivial phases are prepared. The detailed structural investigations are performed and finally using SAE, the nanostructures of compositional alloys are fabricated.

Section 3: This section focuses on the structural characterization of surfaces and interfaces.

- The influence of changes in (0001) surfaces on the structural and electronic characteristics of the crystal is investigated in chapter 6. At the exposure to ambient conditions, the surface oxidation and ageing effects of conventional 3D TIs, Bi_xTe_y stoichiometric states, GST and GBT compositional alloys and GeTe epilayers are examined and the corresponding structural reconfigurations are observed via STEM investigations. A comparative analysis between passivated and non-passivated surfaces is conducted. Finally, the substrate induced effects on the electronic properties of the materials such as band bending at substrate-TI interface and the electronic doping into the TI epilayer, are explored by conducting a comparative analysis by growing the TI epilayers and performing magneto-transport investigations on different substrates.
- In chapter 7 at TI-SC hybrid junctions, transition metal dichalcogenides (TMDCs) assisted self-epitaxial interfaces are engineered for their utilization in quantum applications. The challenges of Al diffusion into 3D TIs and the resulting formation of Schottky barrier are addressed with the introduction of a few transition-metal thin films including Nb, Ti, Pt and Pd as inter-diffusion barrier. The structural characterization of interfaces is conducted via STEM investigations where the transformation of transition metals into their corresponding TMDC structure and their self-alignment in epitaxial order with the underlying TI epilayer, is witnessed. The blocking of Al from diffusion is confirmed via energy dispersive X-ray (EDX) spectroscopy. This behavior assisted in obtaining strain-free, high-quality and well defined epitaxial interfaces.

Chapter – 2

Growth Optimization of Conventional 3D TIs

It has been a decade since the experimental discovery of the first 3-dimensional topological insulators (3D TIs)[1, 2]. Theoretical calculations of these crystals had predicted exotic features offered by topologically protected surface states (TSS) that would open new possibilities for advanced applications. Among them ballistic and dissipationless transport for high mobility applications[3], spinless surface states for advanced spintronic devices[4, 5, 6] and Majorana quasi particles in TI-Superconductor hybrid systems[7, 8, 9, 10, 11] for topological quantum computation[12, 13, 14] hold the key importance. Surprisingly, the progress towards the application based devices is unexpectedly slow. This behavior can be linked to the encountered deviations in physical and electronic characteristics of conventional 3D TIs from the ideal predictions, provided by the theoretical models. The major deviations include:

- Narrow bulk band gap i.e. a semiconducting material instead of an ideal insulator
- Non-intrinsic behavior of crystals exhibiting higher carrier concentration of trivial bulk carriers suppressing the effects/contributions of topological surface states (TSS)

Despite these challenges, some remarkable milestones have been achieved[8, 15, 16, 17, 18, 19, 20]. However, the in-depth understanding of growth mechanism including the formation of structural defects, suppressing the source of unexpectedly high carrier concentration[21, 22], topological phase engineering[23, 24], electronic band alignment at the substrate[25, 26] and the realization of epitaxial interfaces are the key factors in these materials that affect the progress speed to reach the final goal.

The most promising 3D TIs are the chalcogenide based binary compounds of Bi and Sb including Bi_2Se_3, Bi_2Te_3 and Sb_2Te_3. Over the period, these topological crystals have been prepared by various methods including the Bridgeman technique[27, 28], chemical vapor deposition (CVD)[29, 30, 31], sputter technology[32, 33, 34], pulsed laser deposition (PLD)[35, 36, 37] and molecular beam epitaxy (MBE)[21, 38, 39, 40, 41, 42, 43, 44]. Among them MBE is the most sophisticated technique. It allows to grow high quality crystalline films with precise thickness control and the least defect density.

Economically, the successful industrial utilization of any new material demands its compatibility with the CMOS fabrication technology. The incorporation of these TI materials into CMOS industry depends on its reliability to grow in high crystal quality on silicon (Si). Several studies have reported the successful growth of 3D TIs on Si (111)[45, 46, 47]; however, all of them have witnessed an unexpectedly high charge carrier density and an unintentional shift in the Fermi level[48, 49, 50, 51]. Due to very narrow bulk bandgap of 170 meV[52], 210 meV[38, 53, 54] and 320 meV[55, 56] in Sb_2Te_3, Bi_2Te_3 and Bi_2Se_3 respectively, the Fermi shift results in the extrinsic n-type in Bi_2Se_3 and Bi_2Te_3 and p-type behavior in Sb_2Te_3. The Fermi level can be tuned precisely by alloying n-type Bi_2Te_3 and p-type Sb_2Te_3 binary compounds and controlling their relative concentrations to form ternary $Bi_xSb_{2-x}Te_3$ alloys[57, 58, 59]. In earlier reports, the high carrier concentration in MBE grown topological films is directly linked to the Te/Se thermal vacancies[45, 60] and other structural defects such as rotational twins[61] and domains.

This chapter focuses on a systematic study to realize the high quality epitaxial growth of 3D TIs via MBE. The entire crystal growth process is divided into several building blocks to study the effect of each parameter individually. Subsequently, the impact of these parameters on the structural properties of the crystal is investigated. These parameter include:

- substrate characteristics, cleaning and pre-conditioning mechanism
- interface quality of TI with the substrate
- growth rate (R_{TF}) i.e. the direct beam flux of individual element

- growth/substrate temperature (T_{sub})

A detailed study of the above mentioned parameters and their co-dependency is carried out. Based on these parameters, the epilayers are investigated to observe changes in structural defects (the formation twin and antiphase domains, screw dislocations and stacking faults) along with the identification of the point defects (vacancies, antisite defects and the intercalation of adatoms in the layers) and the surface morphology (Section 2.2). The analysis is started with the binary compounds and later extended to ternary alloys. One of the key factors in the process of growth optimization is reproducibility. Numerous growths of each binary and ternary compounds with diverse range of growth conditions, are conducted and based on those results a statistical analysis is performed. The sources of structural defects are identified and the relation between the growth conditions and the defect density is explored. Finally, the optimized parameters for each compound to obtain high crystal quality epilayers with ultra-smooth surfaces are extracted and their reproducibility study is performed.

2.1 Interface with Si (111) and *van der Waals* (vdW) epitaxy

All 3D TIs exhibit a rhombohedral crystal structure with 3-fold rotational symmetry[56, 62]. Silicon exhibits a cubic crystal structure with 4-fold rotational symmetry and hence, would not support the growth of defect-free epilayers of crystals exhibiting the rhombohedral structure. On the other hand, Si (111) surface exhibits a hexagonal geometry with 6-fold rotational symmetry and thus, can act as a base for the epitaxial growth of 3D TIs; however, the issue of lattice mismatch must be addressed. The lattice constants for all binary and ternary compounds along with the corresponding calculated in-plane lattice mismatch with Si (111) surface are listed in Table 2.1. Considering the classical heteroepitaxy, the lattice mismatch leads to strain[63]. The subsequent strain relaxation results in the formation of dislocations and defects. Thus, the defect free epitaxial growth with high lattice mismatch is nearly impossible.

Table 2.1: An overview of the crystal structure and space groups of chalcogenide based 3D TIs with their in-plain and out of plain lattice parameters and the corresponding in-plain lattice mismatch with Si (111) hexagonal surface.

Material System	Crystal Structure	Space Group	In-plain lattice constant (Å)	Out of plain lattice constant (Å)	Lattice mismatch with Si (111)
Bi_2Se_3	Rhombohedral	R-3mH (166)	4.14[45, 56]	28.64[45, 56]	7.8%
Bi_2Te_3	Rhombohedral	R-3mH (166)	4.38	30.49	14.06%
Sb_2Te_3	Rhombohedral	R-3mH (166)	4.28	30.45	11.45%
$Bi_xSb_{2-x}Te_3$	Rhombohedral	R-3mH (166)	4.28 - 4.38	30.45 - 30.49	11.5 - 14%
Si (111)	Hexagonal	-	3.84	-	0%

The *van der Waals* (vdW) epitaxy, on the other hand, provides a platform that allows materials with relatively large lattice mismatch to grow without strain[64, 65]. Rotational alignment with the substrate, strain free growth and no misfit dislocations are the characteristics of vdW epitaxy[64, 65]. The key is formation of a wetting layer, a monolayer of atoms that saturates the dangling bonds of substrate at the surface and facilitates the growth of subsequent adsorbents in layer based structure. These layers are only weakly bonded with the passivated layer and henceforth, do not experience any strain imposed by the lattice mismatch with the substrate. Thus, the wetting layer provides a base for vdW epitaxy that evades the strain at the interface and allows materials with relatively large lattice mismatch to grow without misfit dislocations[64, 65]. Understanding the growth of 3D TIs on Si (111) surface via vdW epitaxy and the optimization of growth parameters to fabricate high quality thin films is the goal of this chapter.

Prior to the assessment of the best passivation material for vdW epitaxy of 3D TIs on Si (111), the selection of substrate is carried out. The characteristics of substrate is one of the key factor in the process of growth optimization as it directly relates to the formation of substrate induced defects (Figure 2.14) and the

electronic band alignment at the interface (Section 6.3). This study is conducted using highly resistive Si (111) wafers with the resistivity of 2000 Ωcm. The wafers utilized were n-doped with 0.5˚ misorientation angle which results in the periodic silicon step edges with terrace length of approx. 45 nm. The wafers were spin coated with photoresist, diced into 1 cm x 1 cm pieces and the cleaning process, discussed in Table 2.2, is carried out. For the purpose of reliability and ease of data analysis, all growths are carried out using the same cleaning process.

Table 2.2: An overview of substrate wet cleaning process steps. The organic contaminations are removed with multi-step processing starting from the solvent treatment to RCA cleaning. Prior to epitaxial growth, the native oxide is removed with HF wet etching to expose the pristine Si (111) surface.

Step No.	Process Name	Chemicals	Duration	Comments
1	Resist Removal	Acetone	5 mins	Pre Cleaning - 1
2	Acetone Removal	Isopropanol	5 mins	Pre Cleaning - 2
3	Rinsing	DI Water	10 mins	-
4	RCA Cleaning	H_2SO_4 (96%) : H_2O_2 (37%) = 1:1	20 mins	Removal of Organic Contaminations
5	Rinsing	DI Water	20 mins	Removal of Piranha solution
6	SiO_2 Etching	HF 1%	3 mins	Removal of native silicon oxide and dangling bonds termination with Hydrogen
7	Rinsing	DI Water	5 mins	HF removal and the preservation of H-terminated bonds

After the cleaning process, samples are loaded into the MBE chamber with the vacuum of approx. 5 - 11 x 10^{-10} mbar and the pre-conditioning step is carried out (the details of the MBE chambers can be found in several previous studies[66, 67] and in Appendix 2A). The sample is baked out at 700˚C for 10 minutes where the dangling bonds at Si (111) surface are exposed by thermally removing the terminating hydrogen atoms. Later, sample is cooled down to the growth temperature at approx. 300˚C. A number of tests with different pre-conditioning times are conducted and statistically the best growth results are obtained with the baking and the post-bake cooling durations of 25 minutes for each step. After pre-conditioning, the activation step is conducted where a monolayer of atoms passivated the dangling bonds at Si (111) surface via 1 x 1 reconstruction and formulated a base for vdW epitaxy. In order to find the most suitable materials for the passivation/wetting layer, growth tests are conducted where the Si dangling bonds are passivated by the elements including Bi, Sb, Te and Se.

It has been observed that all elements have successfully saturated the dangling bonds; however, epilayers prepared with Bi passivation exhibited the most defective epilayer while growing 3D TIs. This phenomenon can be explained with relatively stronger reactivity of chalcogenide atoms[68, 69] towards Bi. The incoming Te/Se atom tends to react with the passivated Bi, creates a covalent bond by deforming the wetting layer that leads to the formation of defective and inhomogeneous layers. No such deformations and defects are observed when pristine Bi_2 epilayers are grown on Bi passivated Si (111) surfaces[70] as depicted in Figure 2.1d.

- In case of Sb passivation, no major structural defects are observed[71] but via STEM and EDX based investigations, it has been found that with time Te atoms replace Sb atoms at the interface. These observations are also found to be in agreement with the earlier reports[72, 73, 74]. In addition, it is also observed that epilayers with Sb passivation tend to house more twin domains in comparison to Te passivated films (confirmed via XRD φ-scans). The reason for this behavior is still unknown.

To prevent any defect formation at the interface and to reduce the overall defect density in all forthcoming growths, Te based binary and ternary compounds are passivated with Te monolayer while Se atoms are utilized to saturate Si dangling bonds while growing Bi_2Se_3.

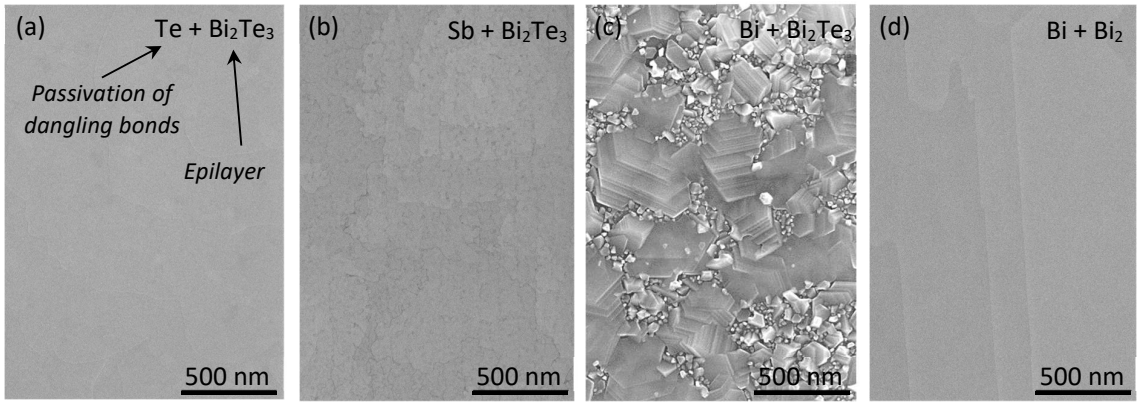

Fig. 2.1: Investigation of the optimum saturation material to facilitate vdW epitaxy. SEM images of Bi_2Te_3 films grown with different wetting layers including (a) Te, (b) Sb, (c and d) Bi atoms. It is evident that Bi is not a suitable candidate to saturate Si dangling bonds while growing 3D TIs. On the other hand, Bi does not exhibit any defects while growing pure Bi films on Si (111) as depicted in (d).

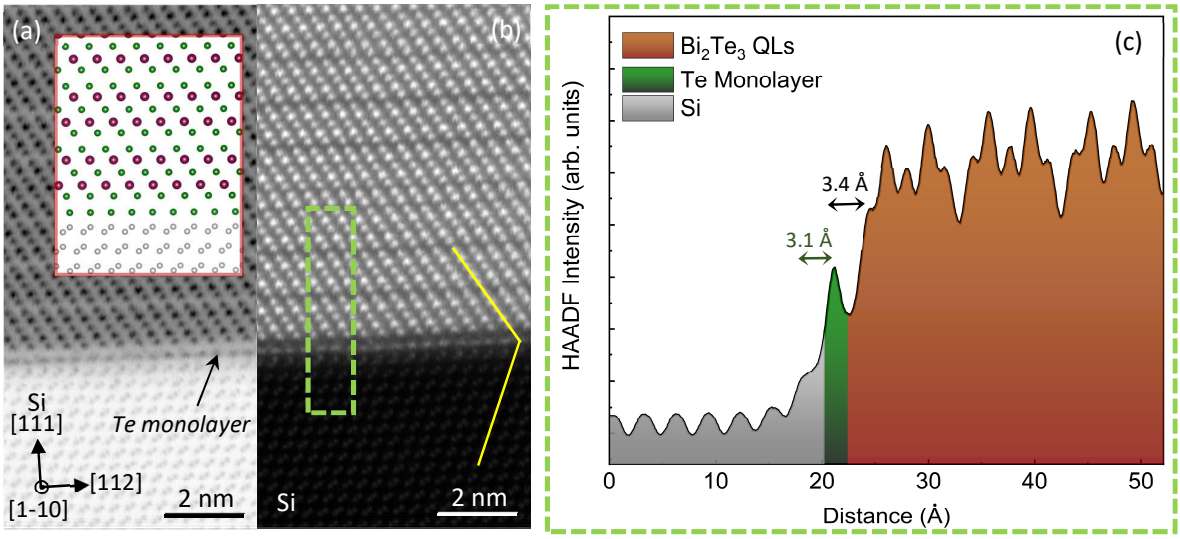

Fig. 2.2: A cross-sectional overview of 3D TI epilayer grown on Si (111) substrate acquired with the help of (a) bright field, (inset) the atomic model and (b) HAADF STEM images along Si [1-10] projection. The distance between the Si and Te monolayer is 0.31 nm while the distance between Te atoms across the vdW gap is 0.34 nm, evaluated and depicted with a line profile in (c).

Figure 2.2 depicts STEM bright field (BF) and HAADF images of TI epilayer grown on Si (111) substrate. The image is captured along Si [1-10] projection. An atomically flat interface between TI quintuple layer (QL) and Si atoms is observed where the dangling bonds on the Si (111) surface are saturated by a monolayer of Te atoms. The distance between Si and the passivated Te atom is found to be 3.11 $\pm$ 0.02 Å which is equal to the projected distance between two Si atoms. The distance between the Te monolayer and the first Te atomic row (of a QL) is found to be 3.39 $\pm$ 0.02 Å which indicates the presence of weak vdW interaction as the length of covalent bond in Te based compounds is always in the range of 2.4 - 3.1 Å[75]. Figure 2.2c depicts a line profile at the interface along with the marked area in (b) and displays atomic intensity w.r.t. their spatial ordering.

The growth process of topological epilayer starts with the formation of nucleation sites containing sub-layer islands of approx. 0.35 to 0.45 nm in height as reported earlier[46, 76]. The vdW interactions facilitate these islands to float on the passivated Si (111) surface where they grow and coalesce to form a closed layer[46, 76]. Room temperature STM studies have shown that Bi_2Te_3 forms fewer islands with larger

diameter compared to Sb_2Te_3 which tends to form numerous islands with relatively smaller diameter[46]. This behavior corresponds to a larger lateral diffusion length of Bi adatoms compared to Sb on the passivated Si (111) surface[76].

One of the challenges an adatom faces during the initial growth process is the presence of a potential barrier that exists at the edge of a layer between the lower and top terraces of an island. This potential is called the Ehrlich-Schwöbel barrier[77] and it limits the mobility of adatoms to cross-over the island and to form a closed film[78]. This barrier is overcome by providing thermal energy to adatoms on the substrate. It has also been observed that adatoms exhibit higher mobility on a closed epitaxial layer in comparison to Si (111) surface[66]. That is why, the growth mode that starts with the islands like formation after reaching a critical thickness of approx. 4 nm switches to *Frank–van der Merwe* (FM) mode and follows 2D step flow[46, 76]. The controlled ratio of incoming adatoms to the thermal energy provided at the substrate is the key to grow smooth epitaxial films.

2.2 Structural characterization of topological thin films

Theoretical calculations and ARPES measurements have shown that the critical thickness to observe 3D topological features in tetradymite crystals (Bi_2Te_3, Bi_2Se_3, Sb_2Te_3 etc.) is approx. 6 nm[21]. Therefore, this study is limited to films varying in the thickness from 6 nm up to 70 nm. Initial films are grown with parameters extracted from the previous studies[66, 79, 80, 81] at T_{sub} = 290 ℃ with elemental parameters of T_{Bi} = 480 ℃, T_{Sb} = 470 ℃, T_{Te} = 330 ℃ and T_{Se} = 110 ℃. The corresponding beam fluxes of all individual temperatures are tabulated in Appendix 2B. Structural characterization of thin films is performed via XRD and STEM investigations while the topography analysis is conducted via SEM and AFM. Thickness of each epilayer is measured via XRR and the thin film growth rate (R_{TF}) is evaluated. Figures 2.3 depicts two XRR scans of Bi_2Te_3 epilayers exhibiting different thicknesses.

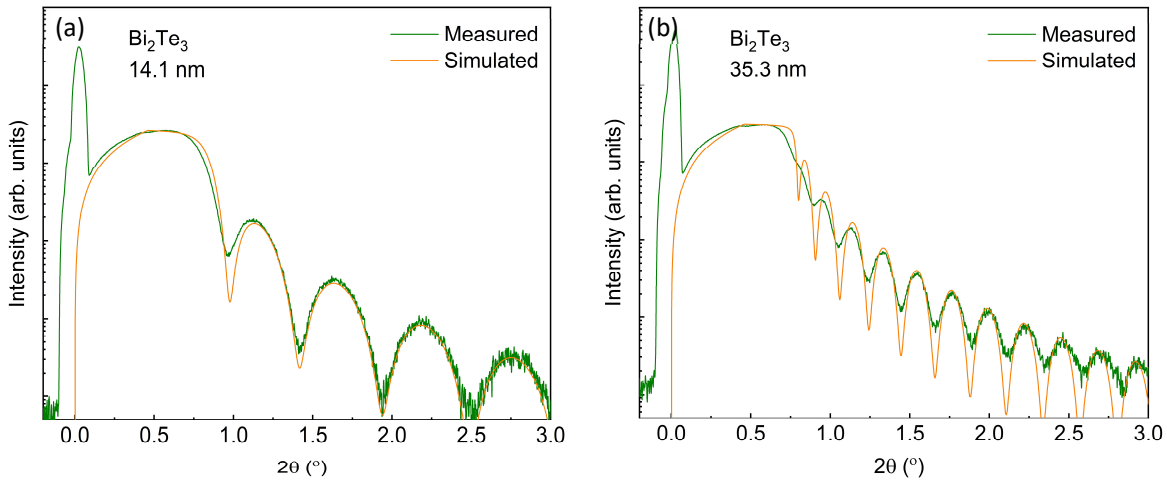

Fig. 2.3: XRR scans ranging from -0.2˚ to 3˚ along with the simulated data to measure the epilayer thickness and to evaluate the thin film growth rate (R_{TF}). The measured and simulated XRR plots of (a) 14.1 nm and (b) 35.3 nm thick epilayers of Bi_2Te_3 are depicted.

Figures 2.4(a-d) depict SEM images of approx. 25 nm thick epilayers of Bi_2Te_3, Sb_2Te_3, BST alloy and Bi_2Se_3 respectively, grown via MBE on Si (111) substrate with an estimated rate of 12 nm/h. SEM images signify the full coverage of grown films on the substrate. The contrast variations in images indicate relatively high surface roughness of Sb_2Te_3 and Bi_2Se_3 epilayers compared to Bi_2Te_3. This behavior is also observed in previous studies of Sb_2Te_3[66, 80] and Bi_2Se_3[81] indicating the tendency of these materials to form epilayers[46, 79] with high surface roughness that requires major improvements. The optimization of surface roughness for all 3D TI epilayers and the topography analysis is discussed in Section 2.3.

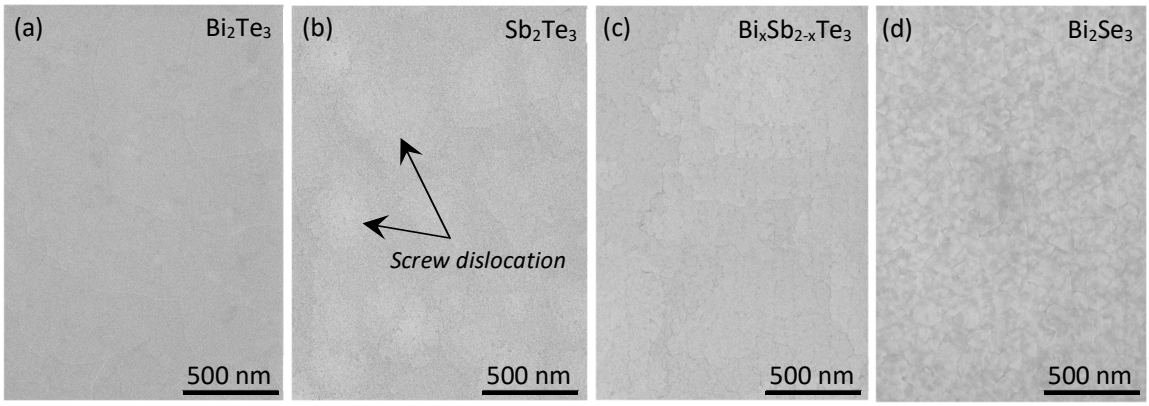

Fig. 2.4: SEM images of 25nm thick epilayers of (a) Bi_2Te_3 that exhibits relatively smooth surface without any visible topographical defects in comparison to (b) Sb_2Te_3 with relatively rough surface with visible layer steps and screw dislocations, (c) BST alloy with improved surface from Sb_2Te_3 and (d) Bi_2Se_3 with fully covered but rough morphology.

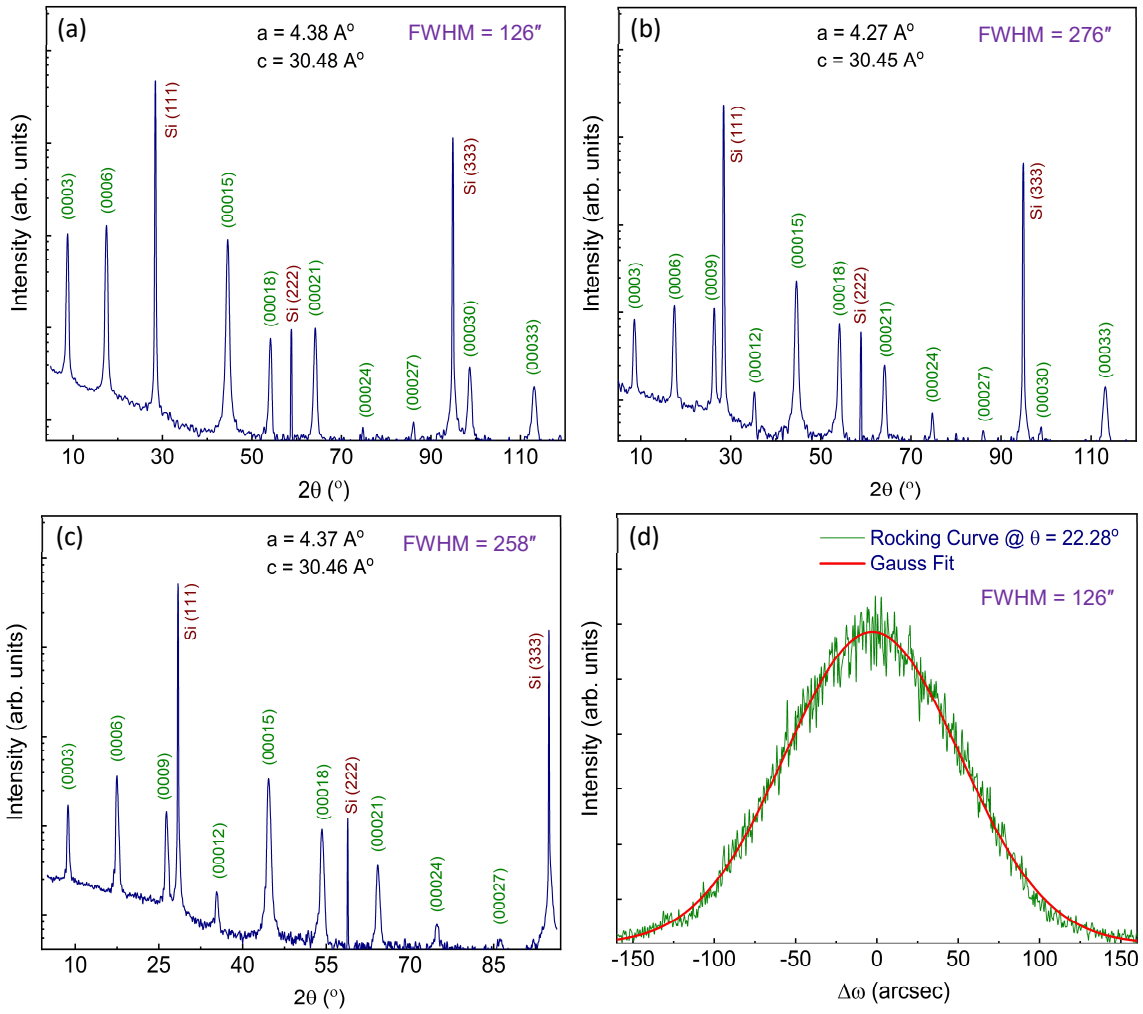

Fig. 2.5: XRD 2ϑ-ω scans of 25nm thick epilayers of (a) Bi_2Te_3, (b) Sb_2Te_3 and (c) $Bi_{0.5}Sb_{1.5}Te_3$ alloy. The relative intensity of the (000 9) diffraction peak in BST alloy (c) indicates the presence of higher Sb contents. The qualitative analysis is performed with Δω scans and FWHM values of the rocking curves are indicated in respective plots. (d) Displays the rocking curve (Δω) scan of Bi_2Te_3, acquired at the (000 15) peak, along with Gaussian fitting.

Figure 2.5 displays XRD 2θ-ω scans of all Te based 3D TIs depicted in Figure 2.4. The single crystalline fully relaxed films are evident by XRD patterns.

- 2θ-ω scan also assists in the compositions analysis of BST alloy as the (000 9) diffraction peak which is forbidden for Bi_2Te_3 (Figure 2.5a), is clearly visible in Sb_2Te_3 epilayer (Figure 2.5b). It indicates that the (000 9) peak intensity in BST alloys (Figure 2.5c) depend upon the relative contents of Sb in the epilayer. With this feature, (000 9)/(000 15) peaks ratio can be utilized as a swift approach to estimate (with ±1 % tolerance) the relative composition of the ternary system[59] (BST alloy) with being zero for Bi_2Te_3.
- Along with the compositional analysis, 2θ-ω/2θ-θ scan also provides information about the unit cell dimensions with ultra-high precision (± 0.001 Å); however, is limited only to the out-of-plane lattice "c". 2θ-ω/2θ-θ scans do not probe the in-plane structure and therefore cannot provide any information about the in-plane lattice constant "a". It can be, however, measured via reciprocal space map (RSM) as depicted in Figure 2.6. The lattice parameters are evaluated using 2θ-θ and RSM techniques for all 3D TIs are mentioned in Figure 2.5.
- The shape and strength of XRD peaks depend heavily on the thickness of the epilayer as thin films suffer from the natural broadening[82] in XRD 2θ-ω/2θ-θ scans. Therefore, the qualitative analysis independent of the epilayer thickness, is performed with the rocking curve (Δω) investigations. Δω scan probes the in-plane structural defects[83] of the epilayer and provides a qualitative figure of merit in terms of full width half maxima (FWHM) measured in arcsecond (″). Smaller value of FWHM indicates the higher crystal quality of the epilayer as the presence of defects leads to the peak broadening. Figure 2.5d displays the rocking curve of Bi_2Te_3 epilayer, acquired at the (000 15) peak, along with the Gaussian fitting with FWHM value of 126″.

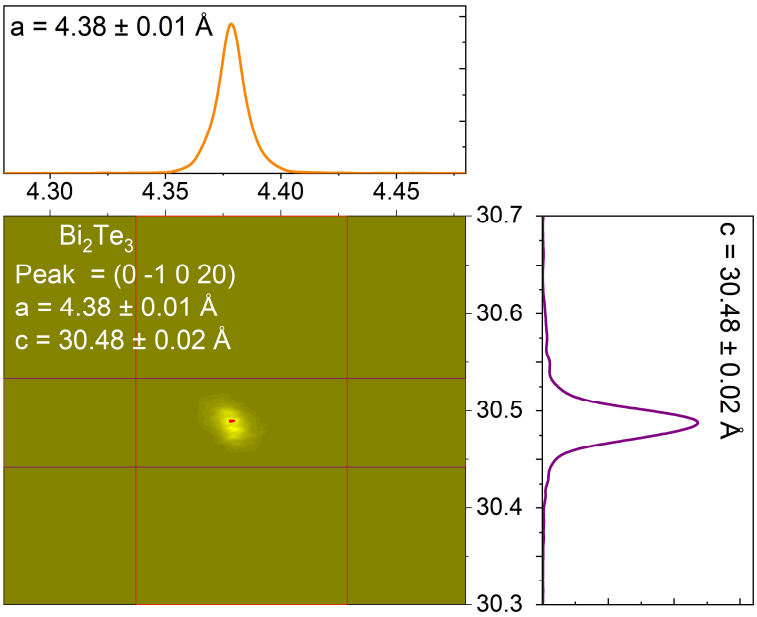

Fig. 2.6: Investigation of lattice parameters via reciprocal space map (RSM) measurement of Bi_2Te_3 acquired along the (0 -1 0 20) peak indicating lattice constants "a = 4.38 Å" and "c = 30.48 Å". The profiles along x and y-axis are also depicted.

2.2.1 Substrate temperature (T_{sub}) vs. growth rate (R_{TF})

In the growth process of 3D TIs, the chalcogenide flux is always kept an order of magnitude higher than pnictogens (Group 5A elements = Bi/Sb) [84, 85, 86]. Considering the stoichiometric stable growth conditions, the growth rate (R_{TF}) is governed solely by pnictogens. Chalcogenides do not influence the growth rate (R_{TF}) of epitaxial films. Thus, R_{TF} is controlled and limited by the individual fluxes of Bi, Sb and the accumulative flux of both (Bi + Sb) during the growth process of Bi_2Te_3, Sb_2Te_3 and BST alloys respectively.

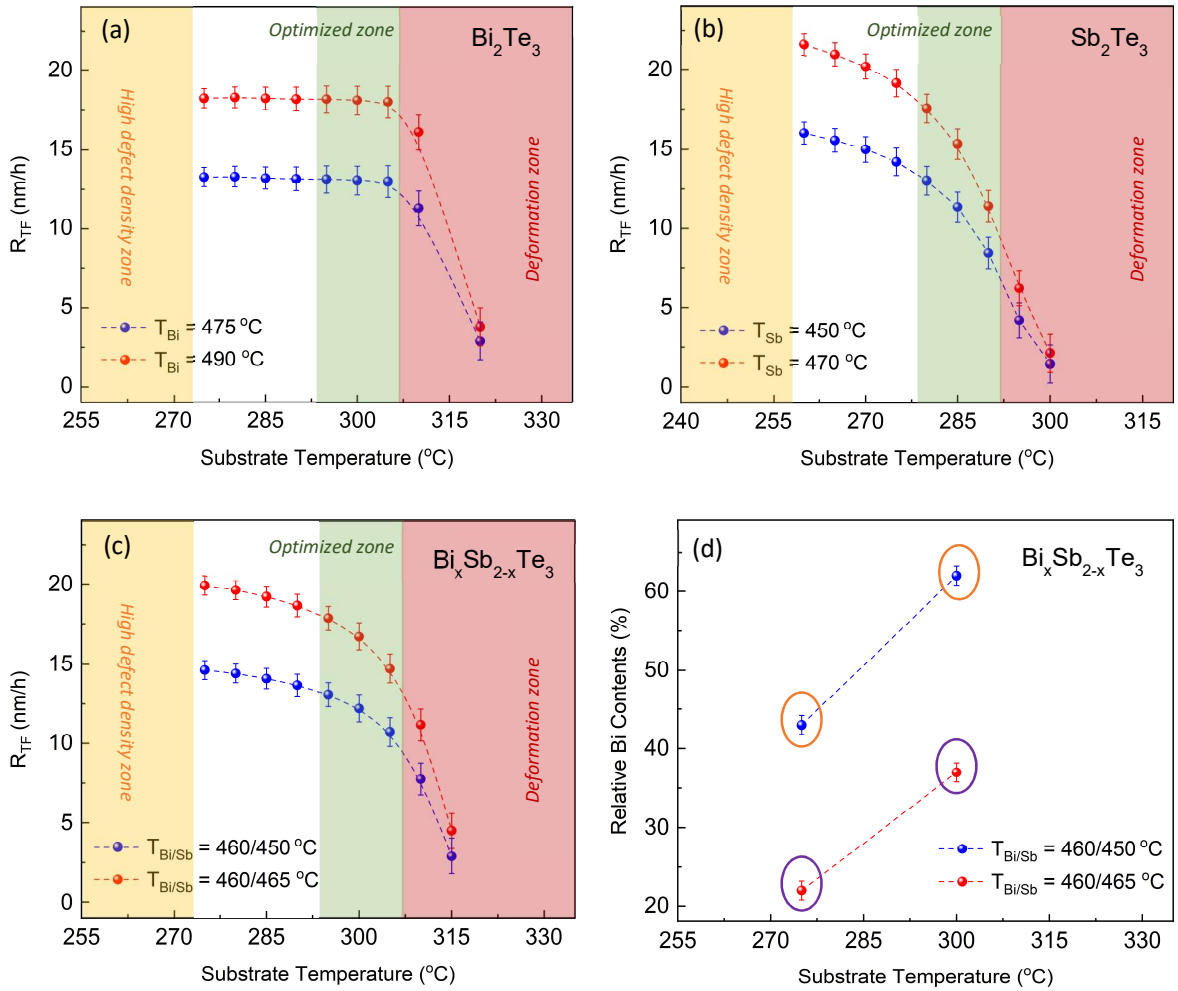

Fig. 2.7: Growth rate (R_{TF}) vs. T_{sub} behavior of (a) Bi_2Te_3, (b) Sb_2Te_3 and (c) $Bi_xSb_{2-x}Te_3$ alloys representing ADR dependency of Bi and Sb on T_{sub}. Yellow, green and red colors represent high defect density, optimum temperature and deformation zones respectively. Plot (d) represents the trend of increased Bi contents with increasing T_{sub} for the corresponding alloys in (c) due to higher Sb desorption in BST epilayers.

It is observed that the growth rate (R_{TF}) of TI epilayers is influenced by the growth temperature (T_{sub}) as well. It can only be possible if there are variations in the effective flux of rate controlling elements reaching the substrate. As, the individual fluxes are kept constant, the observed variations in R_{TF} must have originated from the changes in the adhesive strength of Bi and Sb adatoms with the corresponding changes in the substrate temperature. This trend is observed in all Te based compounds. In order to evaluate the individual and cumulative effects of Bi and Sb dependency on T_{sub} and the resulting effects on the growth of 3D TIs thin films, a series of experiments is conducted. In each experiment, all the growth parameters are set to the pre-ordained values and kept constant while T_{sub} is varied over a wide range to observe variations in R_{TF}. In the next step, the growth parameters are changed to the new values and (in order to confirm the trend at different R_{TF}) and the experiments with changing T_{sub} are conducted once again for Bi_2Te_3, Sb_2Te_3 and BST alloys. The results are summarized in Figure 2.7.

- It has been observed that with the increasing T_{sub} the adsorption to desorption ratio (ADR) of the Bi adatoms did not change. This is the reason that the growth rate (R_{TF}) of all Bi_2Te_3 epilayers remained approx. constant with the increasing T_{sub} as shown in Figure 2.7a. This trend continued until T_{sub} reached a critical point where ADR of Bi suddenly dropped and the epilayer started to deform.

- Unlike Bi, Sb adatoms did not exhibit constant ADR. An indirect relation of $ADR_{(Sb)}$ with T_{sub} is observed. This behavior can be explained with the weak adhesive strength of Sb with Si (111) surface at higher temperatures[87]. With increasing T_{sub}, ADR of Sb kept on dropping and due to this reason, a continuous drop in the growth rate (R_{TF}) of the Sb_2Te_3 films is observed as depicted in Figure 2.7b.
- In the growth process of BST alloy, Bi adatoms provided support and increased the adhesive strength of Sb. In other words, Sb adatoms exhibited higher adhesive strength with Bi than Si. A similar behavior is also observed in other Sb based alloys including GSTs and Ti_xSb_{1-x}[87]. With no ADR dependency of Bi on T_{sub} (Figure 2.7a) and the increased adhesion of Sb, the overall ADR dependency of BST alloy on T_{sub} decreased. That is why, in comparison to R_{TF} of Sb_2Te_3, the growth rate of BST alloy decreased rather slowly with increasing T_{sub} as shown in Figure 2.7c *(please notice the change along x-axis of Figure 2.7b and c).*

It is worth noticing that the decreasing R_{TF} of BST alloy with the increasing T_{sub} is mainly caused by the desorbing Sb adatoms and that is why an increment in the growth temperature (T_{sub}) will always cause the reduced Sb contents in the epilayer. This trend is also observed during the above mentioned experiments conducted on BST alloys. The rising Bi contents in BST epilayer with the increasing T_{sub} are observed and confirmed via Rutherford backscattering spectrometry (RBS)[88, 89] and depicted in Figure 2.7d. The RBS spectrum can be observed in Appendix 2C. Based on these observations, any change in T_{sub} will alter the stoichiometry of BST alloy. Thus, for the optimization and reproducibility purposes, BST alloy with the desired stoichiometry must always be prepared at a fixed temperature (T_{sub}).

In order to extract the optimum growth temperature (T_{sub}) based on the results obtained by XRD and SEM, Figure 2.7 is categorized into three colored zones.

- The *"yellow zone"* corresponds to the low temperatures. At this temperature range formation of closed films are achieved but most of the epilayers are found to exhibit polycrystalline phases or crystals with numerous structural defects (Δω scans revealed FWHM values >> 400"). With the increasing growth temperatures the defect density reduced and films with better crystal quality are achieved.
- The *"green zone"* indicates the best temperature range for the crystalline growth of the epilayers. XRD 2θ-ω and Δω scans have revealed this zone to be the least defective and therefore must house the optimum growth temperature (T_{sub}). (Δω scans revealed FWHM values < 400")
- The *"red zone"* highlights the deformation zone. At this temperature range, the desorption rate of the growth controlling adatoms (Bi, Sb) exceeds their adsorption rate (extremely low ADR). It resulted in the deformed layers that eventually evaporated entirely leading to the failed epitaxy.

Based on these experiments, the optimum temperatures (T_{sub}) of 300℃, 285℃ and 300℃ are extracted for the epitaxy of Bi_2Te_3, Sb_2Te_3 and BST alloys respectively, for all future growth experiments.

2.2.2 Structural defects in epitaxial layers

The growth rate of an epitaxial film (R_{TF}) plays a significant role in the realization of defect-free crystal formation. The analysis of the data obtained from section 2.2.1 indicates that R_{TF} influences the crystal quality by affecting the defect density in the crystal. To further understand the impact of R_{TF} on structural deformations, a systematic study is conducted. Samples of Te based TIs are prepared at the corresponding optimum T_{sub}, extracted from the analysis of Figure 2.7, with relatively slow, moderate and high R_{TF} of 5 nm/h, 12 nm/h and 20 nm/h respectively. The detailed structural characterization is performed with the aberration corrected HR-STEM, XRD φ-scans to identify the rotational twin domains and Δω scans to probe in-plane structural defects of the epilayers.

(Note: The information about STEM system, utilized in this study, can be found in Appendix 1)

Domains: Among all structural defects the most common are domains[90, 91] and particularly the rotational twin domains[22, 91, 92]. All chalcogenide based 3D TIs exhibit trigonal crystal structure with 3-fold rotation symmetry of 120̊. While growing on Si (111) hexagonal surface with 6-fold rotational symmetry, the substrate offers a 60̊ rotational freedom to the starting crystallites. Hence, the rotational domains formulate at the starting layer of the growth process. The domains with exactly 60̊ rotational off axis are called *"twin domains"* while the domains with all other rotational misalignment are known as *"non-twinning domains"* or grains[68, 93] in general.

3D TIs grow in form of quintuple layers (QLs) where a unit cell comprises of three vertically stacked QLs that differ spatially in the lateral arrangement of atoms. During the growth when two islands having layers with different spatial arrangement coalesce, the atoms in these layers readily arrange themselves without deforming the epitaxial film. If the merging islands differ in collinearity (rotation alignment), however, a rotational domain can form depending upon the adsorption rate of incoming adatoms and the available thermal energy in form of the substrate temperature (T_{sub}). The type and the density of rotational domains depends upon the growth rate (R_{TF}) of the epitaxial film[94].

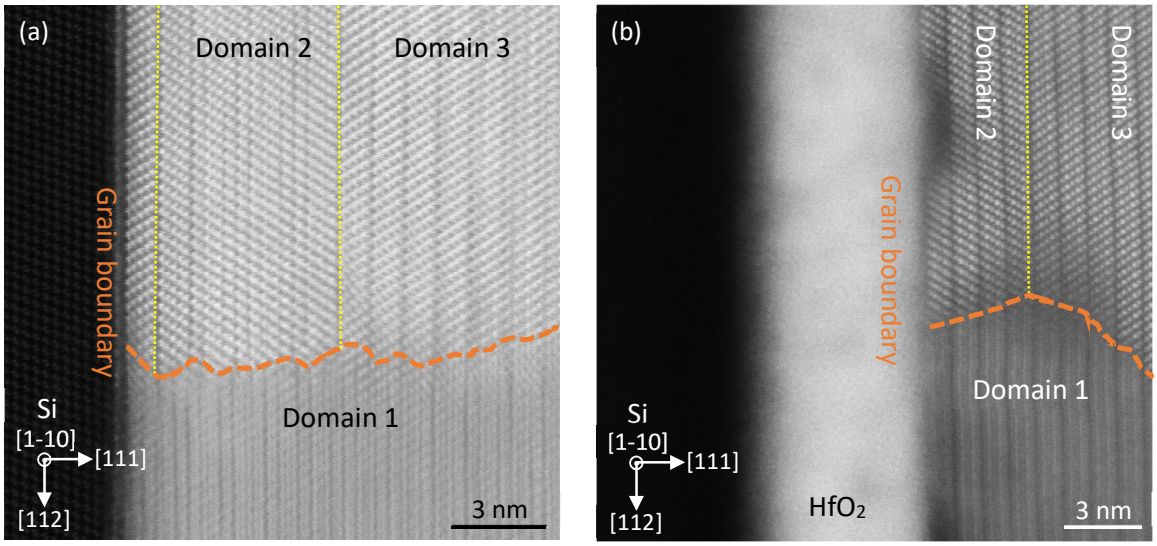

Fig. 2.8: STEM-HAADF images acquired along Si [1-10] projection containing grains/non-twinning domains. (a) Sb_2Te_3 epilayer grown with high R_{TF} = 20 nm/h exhibits high defect density with grains boundaries (orange line) and TSFs (yellow lines) as well. (b) $Bi_1Sb_1Te_3$ epilayer grown with medium R_{TF} = 12 nm/h on amorphous substrate of HfO_2 also exhibits high defect density with similar defects.

The growth rate (R_{TF}) limits the average thermal energy per adatom. Upon merging, if the adatoms that belong to the first island do not have enough energy to re-orient themselves corresponding to the second merging island, it will always result in the formation of a rotational domain.

- At very high growth rates i.e. $R_{TF} \geq 20$ nm/h, *non-twinning rotational* domains are observed in Sb_2Te_3 and BST alloys as depicted in Figure 2.8 however, no such domain is observed in Bi_2Te_3 epilayer when prepared even at higher growth rates.
- At the moderate growth rate i.e. R_{TF} = 12 nm/h, without the presence of grains, only rotational twin domains are observed in all topological materials. XRD φ-scans have revealed that twins always form collinear to either Si (311) or Si (220) as reported in previously studies [36, 79, 94]. In all TI epilayers prepared via MBE, irrespective of the material, the domain collinear to Si (311) is found to be the dominant one[79, 94]. Previous reports have indicated that the twin domain boundary can continue up to several layers until annihilated by the dominant one[79, 94]. This study has revealed that twins do form at moderate growth rates but are limited to only 1 QL. The dominant domain annihilates the other domain in the second QL as depicted in Figure 2.9. The reason for this

behavior can be linked to the selection of optimum T_{sub} in comparison to the previous studies. The presence of a twin defect always gives rise to another defect known as the translational shear fault (TSF), identified in Figure 2.9 and discussed in the next section.

- No twin-like defects are observed in Bi_2Te_3 growths performed at low rate i.e. R_{TF} = 5 nm/h and below, whereas heavily suppressed twins are still observed in Sb_2Te_3. The twinning, in case of BST alloys prepared at low R_{TF} depends upon Bi contents in the epilayer. Alloys with more than 50 % Bi contents are successfully grown without any twins; however, epilayers with higher Sb contents exhibited suppressed twins similar to the case of Sb_2Te_3. The results of the twin defects measured via XRD φ-scans for all 3D TIs and their dependency on the R_{TF} are summarized in Figures 2.10-2.12. It can be clearly seen that with continuously decreasing growth rates the density of twin defects reduces and the domain collinear with Si (311) dominates.

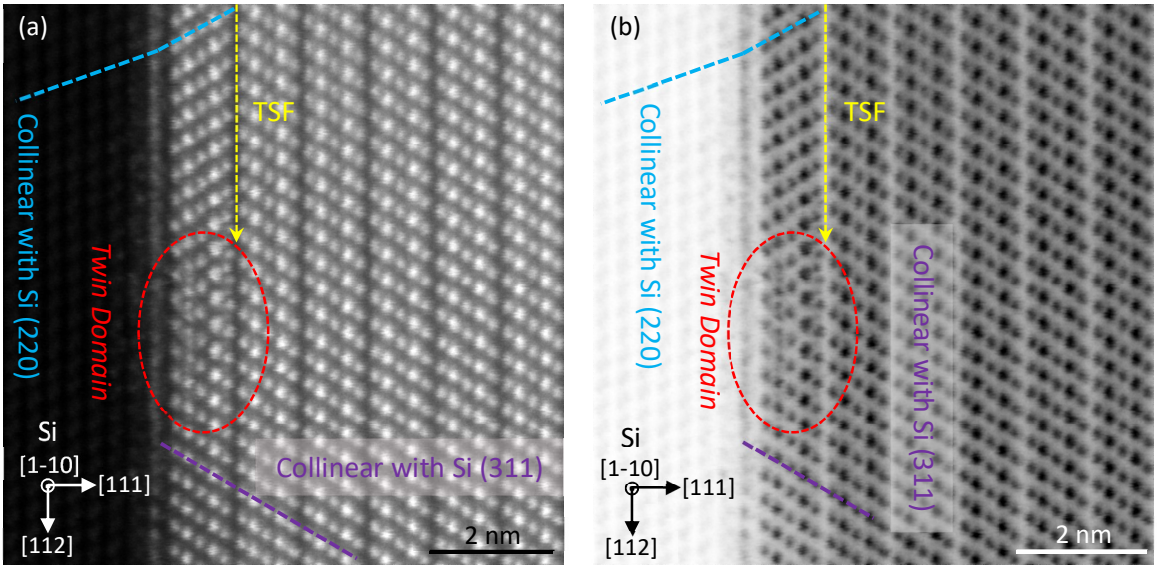

Fig. 2.9: STEM images acquired along Si [1-10] projection depicting twin domains. (a) HAADF image of Bi_2Te_3 epilayer grown with moderate R_{TF} = 12 nm/h exhibits heavily suppressed rotational twin domain to only one QL and being dominated by the domain collinear with Si (311). (b) The corresponding BF image indicating the orientation of both domains and the formation of TSF at the twin coalescence.

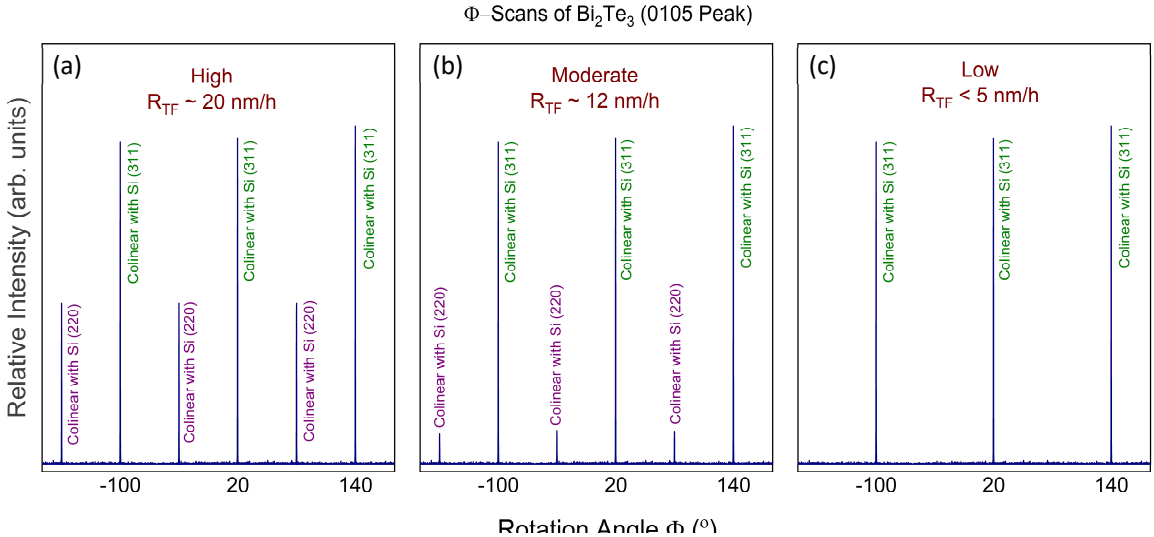

Fig. 2.10: Analysis of rotational twin domains via XRD φ-scan for Bi_2Te_3 epilayers acquired at the (0 1 0 5) peak along with their relative intensity collinear with Si (311) and (220) orientations. (a) Epilayers prepared at higher R_{TF} exhibited high density of twin defects. (b) Suppressed twin domains along Si (220) with the relative abundance of 1:9 is observed

in epilayers that were prepared at moderate R_{TF}. (c) Twin free epilayers collinear only with Si (311) are obtained when prepared at low R_{TF}.

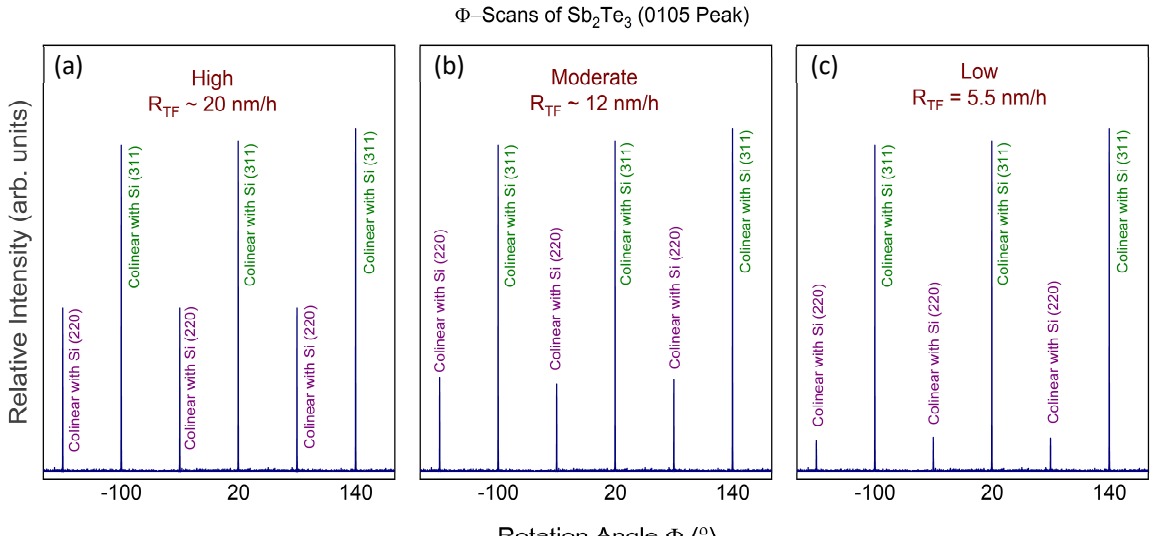

Fig. 2.11: Analysis of rotational twin domains via XRD φ-scan for Sb_2Te_3 epilayers acquired at the (0 1 0 5) peak along with their relative intensity collinear with Si (311) and (220) orientations. (a) Epilayers prepared at high R_{TF} exhibited high density of twin defects. (b) Slightly suppressed twins, yet in relative abundance of 1:3 are observed in epilayers that were prepared at moderate R_{TF}. (c) Heavily suppressed twin domains along Si (220) with the relative abundance of 1:10 are witnessed in epilayers that were prepared at low R_{TF} with Si (311) being the dominant orientation.

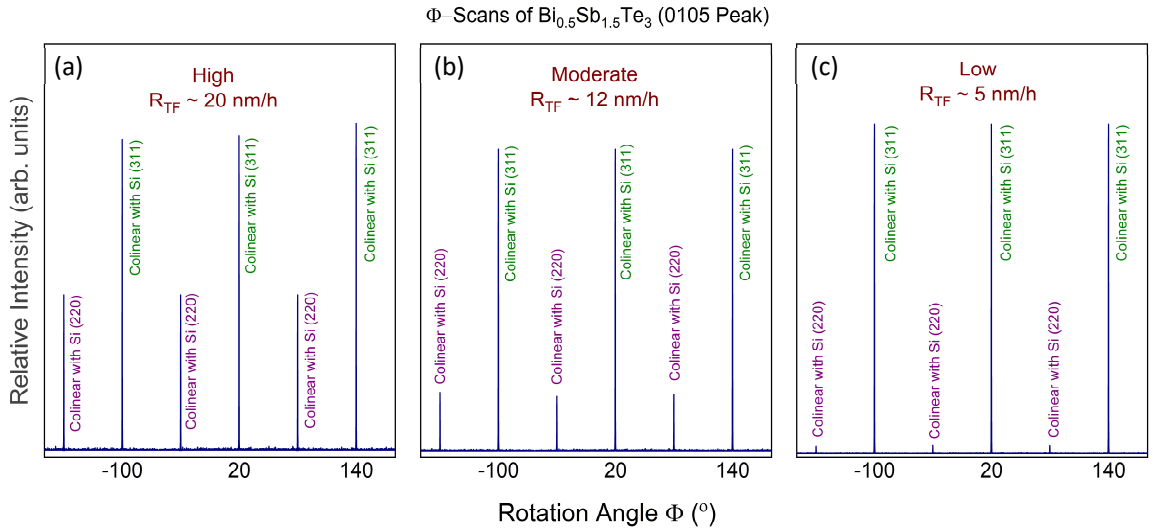

Fig. 2.12: Analysis of rotational twin domains via XRD φ-scan for BST alloys acquired at the (0 1 0 5) diffraction peak along with their relative intensity collinear with Si (311) and (220) orientations. (a) Epilayers prepared at high R_{TF} exhibited high density of twin defects. (b) Slightly suppressed twins, yet in relative abundance of 1:5 is observed in epilayers that were prepared at moderate R_{TF}. (c) Heavily suppressed twin domains along Si (220) with the relative abundance of 1:25 is witnessed in epilayers that were prepared at low R_{TF} with Si (311) being the dominant orientation.

Twining is one of the most common defects exhibited by 3D TIs during the epitaxial growth on Si (111) substrates. The remedy to avoid twins, is to reduce R_{TF} at 5 nm/h and to select the optimum T_{sub}, as discussed above. There are, however, possibilities to grow epilayer with relatively high R_{TF} without any considerable increase in twin defects. This can be achieved with the selection of substrates that exhibit small lattice mismatch with 3D TIs for example, Bi_2Te_3 on sapphire[95, 96] and Bi_2Se_3 on InP (111)[81, 97] where lattice mismatch in comparison with Si (111) reduces from 14% to 8% and from 8% to 0.3% respectively.

Stacking fault: It is a planar defect that forms during the crystallization process. Any disruption in the periodic arrangement of atoms leads to disorder in the crystallographic planes. Such a planar defect is called the *stacking fault*[98, 99, 100]. After rotational twins, stacking fault is the second most common defect in vdW based layered materials[98, 99, 100]. In this study, due to precisely controlled growth parameters, none of the conventional stacking faults have been observed. However, in nearly 70% of all samples investigated (prepared at moderate and high R_{TF}), the presence of translation shear fault (TSF)[101, 102, 103] is witnessed. TSF differs from the conventional stacking faults as it does not alter ABC-ABC stacking periodicity of atoms, it alters only the angular order. In simple term, It can merely be explained as the combination of out-of-plane mirroring along with the shift operation parallel to the fault; and it appears mostly due to shear stress in the crystallographic plane[101]. TSF behavior investigated in MBE grown topological epilayers can be summarized in the following points.

- It is observed that TSF originates at another defects, mostly at the coalescence of rotational domains in the crystal. When the dominant domain annihilates a subordinate domain, it results in the origination of a TSF as depicted in Figure 2.9 (yellow arrow indicates the origin of a TSF). The other crystal defects such as lattice strain due to substrate induced defects also lead to the formation of a TSF (for details visit chapter 5, Figure 5.7 and 5.24).
- In Bi based compounds TSFs appear mostly near the substrate. It can be linked to the presence of twin domains at the Si interface extending to only one QL (Figure 2.9).
- In Sb based systems they also have been observed far from the substrate due to Sb tendency of forming Sb_{Te} and Te_{Sb} antisites assisted bilayer defects and screw dislocations. Such bilayer defects introduce localized lattice strain in the crystallographic planes that, in some cases trigger TSF (Figure 5.7). Figure 2.8a depicts such defects in Sb_2Te_3 while Figure 2.8b and 2.13 represent these defects in BST alloys (indicated by yellow lines/arrows).

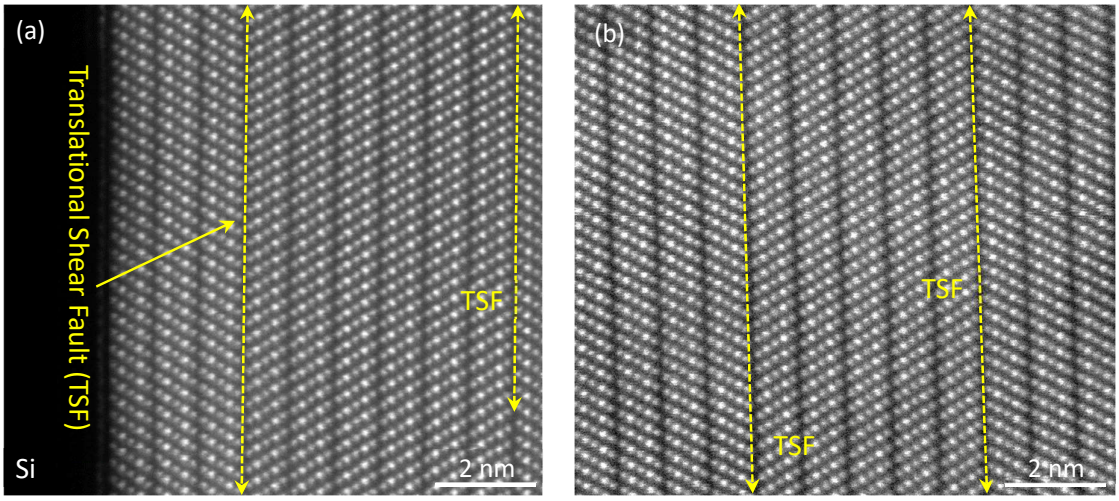

Fig. 2.13: STEM-HAADF images acquired along Si [1-10] projection of BST alloy where epilayers are prepared with (a) moderate and (b) high R_{TF} indicate the presence of translational shear faults (TSFs).

Antiphase domains & screw dislocations: These are unique interlayer structural defects that entirely depend upon the surface quality of the substrate. The Si (111) wafer suffers from the natural misorientation angle on the surface that results in the appearance of periodic step edges of approx. 0.4 nm in height. The periodicity of these steps is determined by the misorientation angle of the wafer. Si wafers used in this work have miscut angles ranging from 0.05° to 0.5° that brings the periodic step edges approx. 450 nm to 45 nm apart, respectively. These step edges during the epitaxial growth facilitate the development of dislocations.

During the growth of 3D TIs, the atomic arrangements of atoms (collinearity of the epilayer) at the planar step edge dictates the type of structural defect. In all Te based TIs, a QL comprises of five covalently bonded atomic layers sequenced as Te_{out} – Bi/Sb – Te_{in} – Bi/Sb – Te_{out}. The height of the bottom three atomic layers from Te_{out} to Te_{in} is approx. 0.43 nm (0.429 ± 0.004 nm measured via STEM) that is close to the height of the Si step edge. The merger of epitaxial film at the step edge between the upper and the lower facets is determined by the coalescence arrangement of the remaining two atomic layers. It has been observed that this arrangement in the MBE grown epilayers depends upon the dominant rotational domain present at the edge. It brings one of the following two possibilities:

- When the dominant domain is collinear with Si (311) as depicted in Figure 2.14a, the Bi/Sb atomic layer at the lower facet merges with the Bi/Sb layer on the upper side and the Te_{out} layer does the same (follow the blue lines in the image). This arrangement requires higher energy to stabilize and results in the formation of an antiphase type domain. The epilayers prepared at the optimum temperatures with relatively low R_{TF} have exhibited this phenomenon.
- The second possibility is when the domain present at the edge is collinear with Si (220) as described in Figure 2.14b. At merger, the Bi/Sb atomic layers and Te_{out} layers from the upper and bottom facets have to swap their relative positions (follow the blue lines in the image). This arrangement requires the antisite swapping between Bi/Sb and Te atoms that always result in screw type dislocations. Mainly Sb_2Te_3 and BST while in some cases Bi_2Te_3 epilayers (prepared at very high R_{TF}) exhibit the formation of screw dislocations.

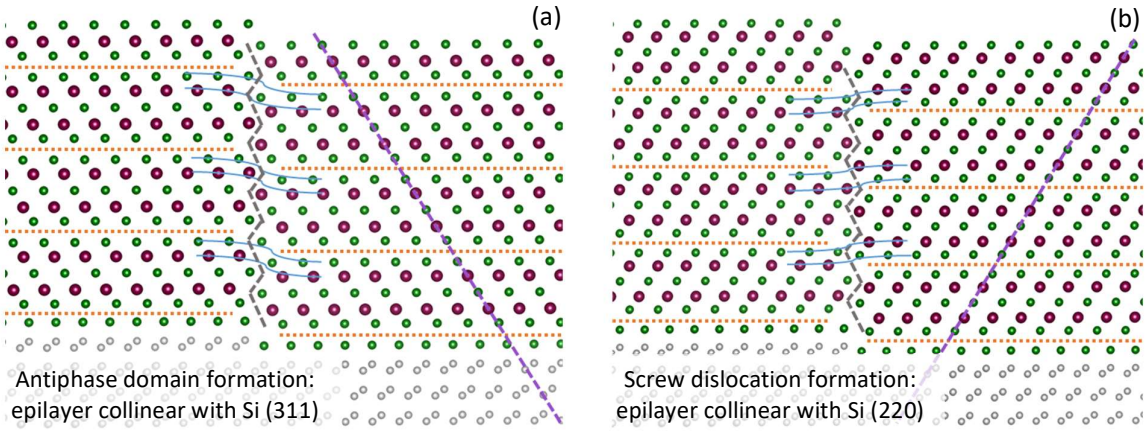

Fig. 2.14: 2D atomic model along Si [1-10] projection representing structural defects formation at Si step edge with two possible cases. (a) The epilayer collinear with Si (311) encounters a hard boundary and rearrange atoms without any antisite defects or atomic layer swapping forming an antiphase domain. (a) The epilayer collinear with Si (220) utilize antisite defects for atomic layer swapping while encountering a step edge and forms a screw dislocation.

Figure 2.15 depicts STEM images acquired at the cross-section of a screw type dislocation formed at the Si step edge in a BST epilayer prepared with R_{TF} = 20 nm/h. In conventional 3D TIs (based on QL architecture), the formation of such defects at Si step edges cannot be avoided. A step edges always hosts either an antiphase domain or a screw dislocation depending upon the domain collinearity. Experiments have shown that by preparing epilayers at low growth rates (R_{TF}) and at optimum T_{sub}, the density of the screw dislocations in Sb_2Te_3 and BST alloys can be reduced as the domain density collinear with Si (220) reduces. It causes screw dislocations to transform into antiphase domains, collinear with Si (311).

Summary: It has been observed that the structural defect density has a direct relation with the substrate temperature (T_{sub}) and the growth rate (R_{TF}). By keeping T_{sub} constant at the optimum value, the influence of R_{TF} is investigated and it is observed that most of the structural defects including domains and stacking faults can be avoided by reducing R_{TF} to 5 nm/h. The defect formation at Si step edges i.e. the antiphase domains and screw dislocations cannot be avoided in 3D TIs; however, the defect density can be minimized

by improving surface quality of the substrate. This can be achieved with the selection Si wafers exhibiting the lowest possible misorientation angle.

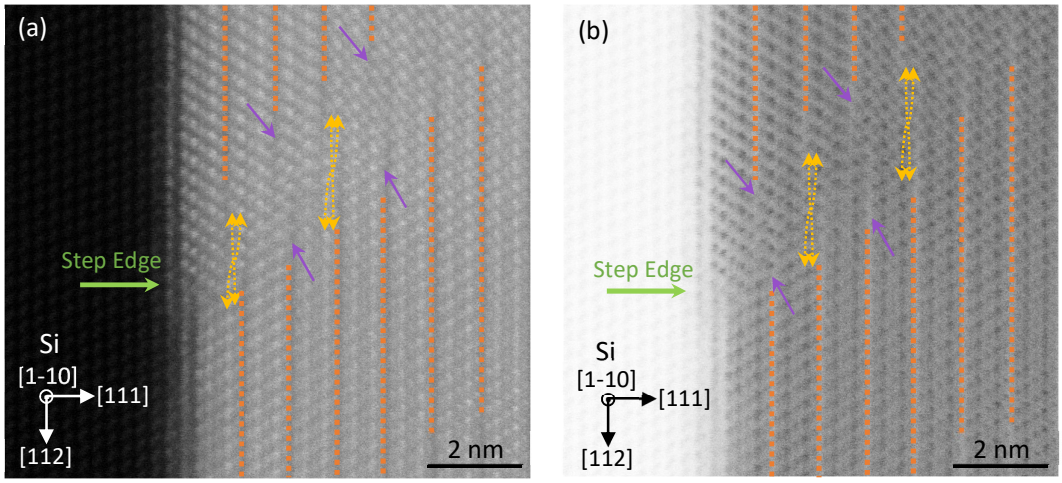

Fig. 2.15: STEM images acquired along Si [1-10] projection at the cross section of a screw dislocation in BST epilayer. (a) HAADF image representing the screw dislocation formed at a Si step edge. Epilayer at bottom and top terraces of the step edge exhibit twins where top terrace, collinear with Si (220), dominates the other domain and proceed with antisite defects assisted layer swapping (follow yellow arrows) forming a screw dislocation and confirming the model represented in Figure 2.13b. (b) Bright field image of (a) represents the same information with the inverted contrast.

It has also been observed that these step defects act as a limiting factor for the phase coherent length of the quasiparticle in magneto-transport investigations of 3D TIs[3] (discussed in chapter 3, Table 3.3). Though in conventional 3D TIs, these substrate induced defects cannot be avoided because of QL architecture. The defect density, however, can be heavily reduced during the epitaxy of Bi_xTe_y alloys where, the layer architecture comprises of bilayer (BL) structures along with QLs (discussed in chapter 4, Figure 4.34). Moreover, these defects can be completely avoided in multilayer architecture of GST/GBT alloys via vdW reconfiguration mechanism (discussed in chapter 5, Figure 5.7) and also in the layer-free architecture of GeTe (Figure 5.25).

2.2.3 Point defects in 3D TIs

The largest source of unintentionally high carrier concentration in 3D TIs is the atomic defects in crystalline films[37, 104, 105, 106]. Due to the nature of these defects it is nearly impossible for most of them to spatially identify their presence. The point defects include vacancies, antisite defects and intercalated adatoms.

Vacancy defects: As the name suggests, vacancies are unoccupied lattice sites (atomic voids) that form due to unavailability of atoms during the crystal formation. This phenomenon leads to unsaturated bonds with the neighboring atoms and possibly to higher carrier concentration. Vacancies always exist and are the temperature dependent defects. All 3D TIs suffer from Te vacancies (V_{Te}) especially Bi_2Te_3 due to its relatively higher optimum growth temperature. Te vacancies (V_{Te}) result in the appearance of non-bonded electrons and thus act as n-type dopants[107]. Depending upon the concentration of vacancy defects the Fermi level in Bi_2Te_3 shifts inside or very close to the bulk conduction band resulting in n-type behavior[37, 104, 105, 106]. Sb_2Te_3 also suffers from Te vacancies but the cumulative effect of the vacancy defects is heavily reduced by the dominant antisite defects[107, 108].

Antisite defects: During the crystal growth, the swapping of lattice sites between two different elements leads to the antisite defects. In Bi based TIs, due to the difference in the atomic radii between Bi (1.51Å)[109] and Te (1.36 Å)[109], a relatively higher energy ΔE = 0.67 -1.12 eV[110, 111, 112] is required to realize Bi_{Te} (Bi occupying Te lattice site) antisites and therefore, these defects occur with less probability. However, in Sb

based TIs where the atomic radii of Sb (1.38 Å)[109] and Te (1.36 Å) are almost similar and Sb_{Te} antisite energy ΔE = 0.35 eV[113, 114] is relatively smaller than Bi_{Te}, Sb_{Te} antisites occur with higher probability. That is why, these defects are most commonly found in form of bilayer switching defects at the screw dislocations in Sb_2Te_3 and BST epilayers as observed in Figure 2.15. They are also responsible for the vdW reconfiguration through the layer architecture switching in GSTs (Chapter 5, Figure 5.7). In 3D TIs, the antisite defects act as dopants with two possible swapping schemes.

1. The first case is where a chalcogenide atom (Te) takes the lattice site of a pnictogen atom (Bi/Sb). In this scenario, the chalcogenide atom after completing bonds with the neighboring pnictogen atoms ends up with one free electron. Thus, Te antisite defect at Bi/Sb position (Te_{Bi} and Te_{Sb}) results in n-type doping. As Te naturally suffer from the thermal vacancies (V_{Te}), this case is the less probable one[112, 113].
2. In the second case of antisite defects, a pnictogen atom takes the lattice position of a chalcogenide and after saturating the bonds with the neighboring chalcogenide atoms; it ends up with an electron deficiency that acts as a hole. Thus Bi/Sb antisite defect at Te position (Bi_{Te} and Sb_{Te}) results in p-type doping.

As mentioned earlier, 3D TIs suffer heavily (1-3 %)[115] from thermal vacancies of Te (V_{Te}). It causes excess of electron with n-type charge carriers. Due to less availability of Te atoms (high Te vacancies), Te_{Bi} and Te_{Sb} antisite swapping are less probable. Bi_{Te} antisites in Bi_2Te_3 epilayer, as discussed above, are energetically also less favorable to occur. Thus, due to the cumulative effect of heavy Te vacancies (V_{Te}) and less favorable Bi_{Te} antisite, Bi_2Te_3 crystal always exhibits n-type behavior. On the other hand, Sb_2Te_3 with energetically favorable Sb_{Te} antisites exhibits high density of atomic switching where Sb fills most of Te thermal vacancies (V_{Te}) in the lattice resulting in p-type carriers and neutralizing n-doping of V_{Te}. That is why, naturally Sb_2Te_3 exhibits p-type behavior assisted by Sb_{Te} antisite defects.

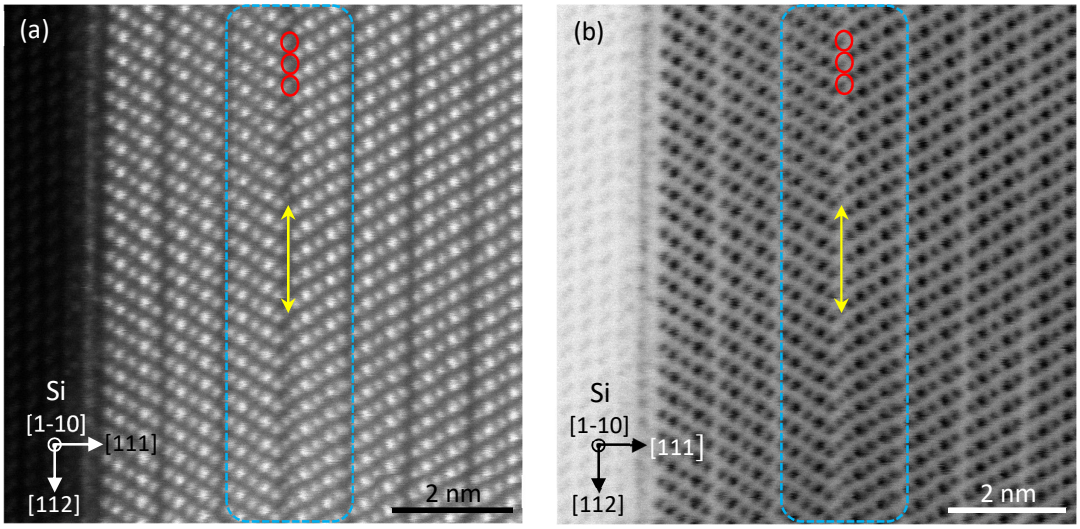

Fig. 2.16: STEM images acquired along Si [1-10] projection at high defect zone in Bi_2Te_3 epilayer. (a) HAADF image depicting the intercalated adatoms (red circles) at a TSF (yellow arrow) in highlighted area (blue box). (b) BF image of (a) represents the same information with the inverted contrast.

Intercalation of adatoms: These are point defects that occur due to the presence of additional interstitial atoms at the high defect zones and thus, are hosted by the structural defects in the crystal. These defects include rotational domains, stacking faults, TSFs, antiphase domains and the screw dislocations. Near these defects, the crystal lattice deforms and adatoms do not take the conventional lattice positions. An example of this behavior can be seen in Figure 2.9 where twin domains are merging and due to periodic inhomogeneity in the lattice plane, additional atoms have intercalated. Another example is depicted in

Figure 2.16 where atoms have intercalated at a high defect zone forming a TSF. These defects are random in nature and cannot be predicted; however, can be avoided altogether with the growth of defect free crystalline epilayers.

All crystal defects including the extended and the point deformations that occur during the epitaxial growth of conventional 3D TIs via MBE along with their resulting effects are summarized in Table 2.3.

Table 2.3: An overview of all possible crystal defects during the epitaxial growth of conventional 3D TIs via MBE, their resulting effects and optimum solution.

Defect	Category	Effects	Solution
Non Twinning Domains	Extended Defect	• Limits phase coherent length of quasiparticles • Increases carriers concentration	Growth at optimum T_{sub} and R_{TF} ~ 5 nm/h
Twin Domains			
Stacking Faults			
TSFs		Limits phase coherent length of quasiparticles	
Antiphase Domains			Cannot be avoided but reduced with the improvement in Si (111) surface misorientation angle along Si [112] and Si [110]
Screw Dislocations		• Increases carriers concentration	Growth at optimum T_{sub} and R_{TF} ~ 5 nm/h
V_{Te}	Point Defect	Increases n-type carrier concentration	Cannot be avoided, although can be reduced by adjusting T_{sub}
V_{Sb}, V_{Bi}		Increases p-type carrier concentration	Cannot be avoided, although can be reduced by adjusting Bi/Te and Sb/Te flux ratios
Te_{Bi} & Te_{Sb} antisites		Increases n-type carrier concentration	Energetically less favorable to occur due to V_{Te} and relatively higher optimum T_{sub}
Bi_{Te} antisite		Increases p-type carrier carriers	Energetically less favorable to occur
Sb_{Te} antisite			Energetically favorable, can be reduced by optimizing epitaxy at higher T_{sub}
Intercalation of Adatoms		Increases carriers concentration	Growth at optimum T_{sub} and R_{TF} ~ 5 nm/h

2.3 Morphology and surface roughness

Topology, in 3D TIs, is a surface related attribute where surfaces exhibit topological *Dirac* states. Effective utilization of these materials, for advanced quantum and spin related applications, demands atomically clean and epitaxial interfaces with metallic electrodes. Thus, the optimization of surface roughness holds a key importance in achieving high quality crystalline growth of TI epilayers.

The growth optimization process, discussed in section 2.2, brings the average surface roughness of 3D TIs to the rms value of approx. 1 nm. With minimal optimization, the surface quality (smoothness) can be further improved. As, most of the growth parameters during the structural optimization process are already tuned to their optimum values to obtain the least defective crystal quality; any change in those parameters including T_{sub} or Bi/Sb beam fluxes would cause the deviation from those optimum conditions and would result in structural defects. That is why, neither T_{sub} nor Bi/Sb beam fluxes can be modified and the attempts for surface treatment are carried out by modifying only Te beam flux (T_{Te}).

As mentioned earlier, Te flux does not influence the epitaxial growth rate (R_{TF}) of 3D TIs and is always kept an order of magnitude higher than Bi/Sb flux. However, it is observed that Bi/Te flux ratio plays a crucial role in controlling the morphology of the epitaxial film. With the controlled reduction in Te flux (increased Bi/Te flux ratio), the surface roughness of the epilayer can be improved below 1 nm rms values. Here, one must be careful while reducing the Te flux as it may also result in drastic structural and stoichiometric changes. During the surface optimization, the following points hold the critical importance.

- It is extremely important not to reduce Te flux below the critical value that results in the stoichiometric shift of the material. For example in case of Bi_2Te_3 epitaxy, the reduced Te flux shifts the stoichiometric state containing 40% Bi contents (Bi_2Te_3) to higher values of Bi_xTe_y states such as Bi_1Te_1 and Bi_4Te_3 (for details visit chapter 4).
- The lowered Te flux might also lead to high vacancy defects (V_{Te}) and possibly to higher unintentional carrier concentration that exhibit trivial features and would suppress the contribution of topological surface states (TSS) even more.

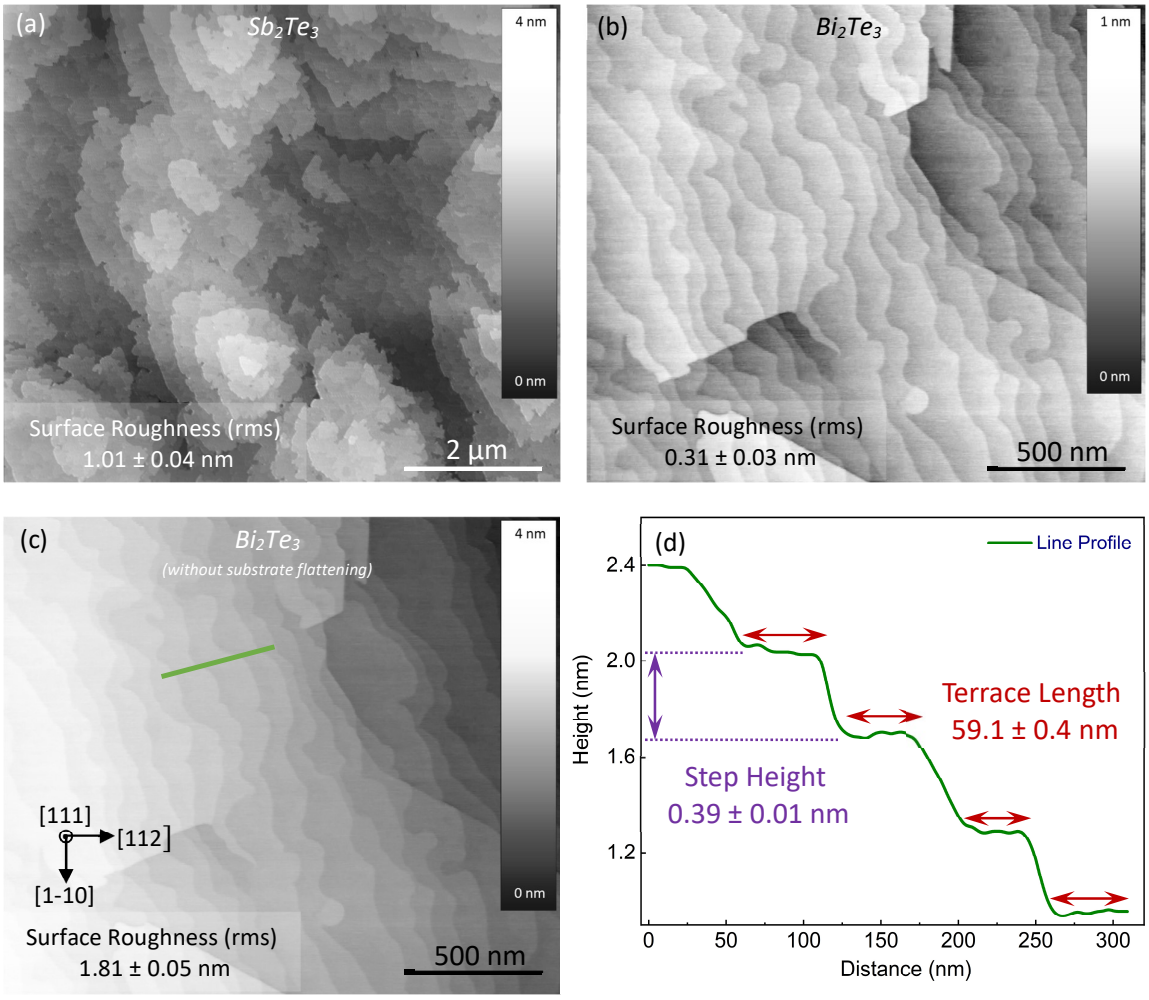

Fig. 2.17: AFM images depicting the morphological information of (a) Sb_2Te_3 and (b) Bi_2Te_3. (c) Represents Bi_2Te_3 epilayer without the planar correction performed in (b) following the misorientation induced substrate steps on Si (111) surface along Si [112] and Si [110]. (d) Represents the line scan in (c) depicting unequal terraces with average terrace length of 59nm.

Figure 2.17 depicts AFM topographic images of Bi_2Te_3 and Sb_2Te_3 epilayers prepared on Si (111) substrate with T_{Te} = 310℃ (green zone in Figure 2.18). The impact of Si misorientation angle on the epilayer surface and the formation of terraces with the increased surface roughness can also be witnessed in Figure 2.17c.

Figure 2.18 illustrates the trend in the surface roughness for all Te based TIs with the affective change in the Te flux (T_{Te}). The data is obtained for the growth rate (R_{TF}) of approx. 5 nm/h. The red zone indicates the "*stoichiometric variation zone*" with T_{Te} resulted in the stoichiometric changes while the green zone represents the optimum Te flux range for best surface quality without affecting the stoichiometry. However, as mentioned earlier that decreasing the Te flux may result in the increased density of Te vacancies (V_{Te}). In the end, it is a tradeoff between the high Te vacancies (V_{Te}) and the improved surface quality of the epitaxial films.

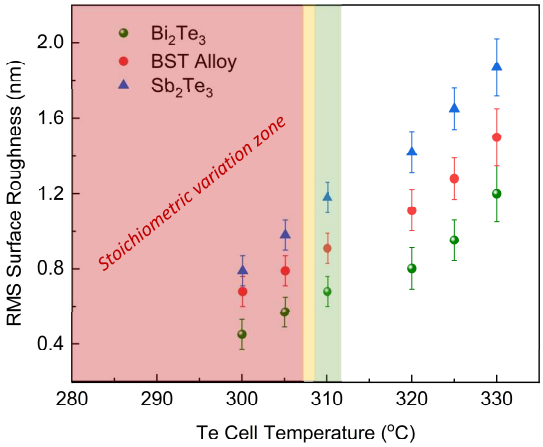

Fig. 2.18: The trend of average surface roughness with changing Te flux. The red zone indicates the critical T_{Te} where Bi/Te or Sb/Te flux ratios cross the limit and result in the altered stoichiometry. The green zone indicates the lowest possible T_{Te} that provides the best (lowest) surface roughness while keeping the stoichiometry intact.

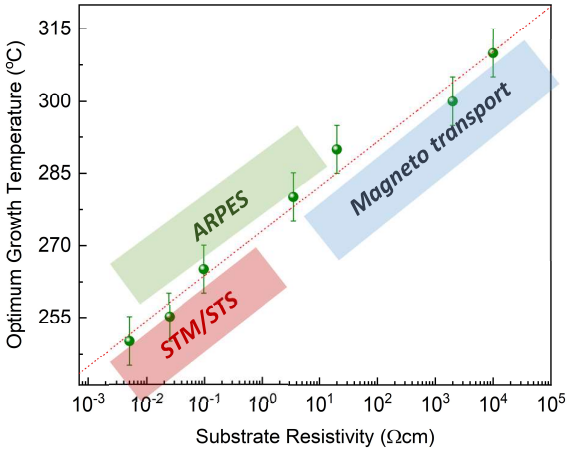

Fig. 2.19: The trend in the optimum T_{sub} measured with the changes in electronic resistivity of the substrates are depicted. With the increasing resistivity, optimum T_{sub} is observed to increase. The preferred ranges of various substrate conductivity for the specific characterization tool along with the optimized T_{sub} are also marked.

2.4 Effect of substrate resistivity on growth parameters

Dynamic characterization tools and measurement techniques demand substrates with various electronic conductivities. Low temperature STM and STS investigations require highly conductive substrate, ARPES prefers relatively moderate to low resistive range while for the electronic transport investigations of topological epilayers, the highly resistive substrates are necessary. An advantage of conducting the epitaxial growths on Si substrates is that high quality wafers with a wide range of resistivity are readily available.

Due to the requirements of performing several above mentioned characterizations, the growth optimization of 3D TIs is performed on substrates with a wide range of resistivity. It has been observed that with the increase in electronic conductivity of the substrate, the thermal conductivity also increases

and correspondingly the optimum growth temperatures (T_{sub}) decreases. In order to evaluate the optimum growth parameters on substrates with different resistivity and to avoid structural optimization individually all over again, all the growth parameters are fixed to their optimum values (to achieve R_{TF} = 5 nm/h) while the growth temperature (T_{sub}) alone is adjusted until the desired structural quality of the epilayer is achieved. The qualitative analysis of the grown epilayers is performed with Δω scans. Figure 2.19 illustrates the trend of optimum growth temperature (T_{sub}) obtained with the varying resistivity of Si (111) substrates.

2.5 Summary

The realization of futuristic quantum applications based on the exotic spin-momentum locked Dirac surface states of 3D TIs, requires the growth of high crystal quality epilayers with ultra-smooth and defect-free surfaces. Conventional 3D TIs are vdW assisted layer based materials that are prone to suffer from the high density of structural defects. A systematic study on the epitaxial growth of convention 3D TIs via MBE and the atomic-scale structural characterization via STEM, is performed to explore the growth challenges. At first, the passivation of Si dangling bonds is conducted with different elements and Te is found to be the optimum candidate. Later, Si-TI interface is investigated where an atomically clean, well defined, epitaxial and yet, an incoherent interface between the Te atomic layers (the passivated monolayer and the QL) across the vdW gap, is observed. The presence of an incoherent interface confirms the strain-free stacking of TI epilayer on the silicon substrate. By conducting a series of experiments, a relation between the growth parameters and the structural defect density in the epilayers is identified. The selection of optimum growth temperature (T_{sub}) and the control over thin film growth rate (R_{TF}) = 5 nm/h have facilitated the achievement of defect-free and high structural quality epilayers of Te based 3D TIs. All structural (extended) defects including twin domains, stacking faults and TSFs are successfully evaded; however, the formation of substrates induced defects i.e. antiphase domains and screw dislocations, bound to appear on Si step edges, cannot be avoided. Finally, the surface morphology is optimized by managing the Bi/Te and Sb/Te flux ratios. The ultra-smooth epilayers with the surface roughness of 0.30 ± 0.02 nm rms values are achieved. The achievement of defect-free epilayers has paved a path towards the realization of pristine topological nanostructures, discussed in the next chapter.

Chapter – 3
Selective Area Epitaxy (SAE) of 3D Topological Nanostructures

Chapter 2 was dedicated to achieve successful epitaxy of Te based 3D TIs including Bi_2Te_3, Sb_2Te_3 and $Bi_xSb_{2-x}Te_3$ (BST) alloys on planar Si (111) substrates where epilayers were prepared with high crystal quality. The detailed structural characterizations were performed and the optimum growth parameters for each topological material, were extracted. Though, high crystal quality epilayers were achieved, the utilization of exotic features offered by topological surface states (TSS) in advanced applications and their incorporation into quantum devices demand the availability of defect-free topological nanostructures.

Topological nanostructures, other than attracting attention for fundamental research on quantum effects[1, 2, 3, 4] and material properties[3, 4, 5, 6, 7], lay a foundation for realizing several potential applications including:

- Topological switching[9] and steering effect of TSS[10] in quantized (quasi-1D) multi-terminal junctions[11] (discussed in Section 3.6.2)
- Low energy dissipation electronics such as single electron transistors[12]
- Majorana quasi particles and Majorana zero modes in TI-SC hybrid nanostructures[13, 14, 15, 16, 17]
- Quantum spintronics[18], including spin valves[19], TI-ferromagnetic hybrid structure assisted quantum anomalous Hall insulator (QAHI)[20, 21] and topological antiferromagnetic spintronics[21]
- Enhancement for figure of merit in topological thermoelectrics[22, 23, 24, 25]
- Fault tolerant quantum computation[26, 27]

The importance of scalable nano-architecture can be realized from a few above mentioned potential applications. These applications not only demand high crystal quality but also require pristine and ultra-smooth surfaces to achieve defect-free epitaxial interfaces. Therefore, the realization of topological nanostructures requires the development of a platform with certain methodology/approach that must fulfill the following criteria:

- ***Reliability:*** The approach to prepare nanostructures must not harm the topological material in any way. Oxidation via exposure to ambient conditions (discussed in Chapter 6) and chemical treatment during fabrication etc. are a few examples that may alter, damage or affect physical and electronic characteristics of the material.
- ***Reproducibility:*** Each cycle of the technique with which the crystal growth and fabrication of nanostructures is performed must always produce equivalent results if conducted with similar parameters. This criterion ensures that results obtained from various samples do not provide any unintended digression.
- ***Dimensionality:*** The platform must be adaptable. It must be capable of providing structures with a wide range of dimensions (from micro to nanoscale) that could be adopted without any complexity. Hence, when and if required, the controlled changes in dimensions could be achieved.
- ***Scalability:*** The platform must be scalable for nano-architecture. It must be capable of providing structures of the desired dimensions in any complexity of design that could be readily implementable on any size of substrate. It must also support multi-step fabrication especially lithography processes with ultra-high alignment precision.

3D TIs exhibit TSS, this feature allocates a critical importance to surfaces and interfaces. Nanostructures, in comparison to bulk crystals and thin films, exhibit enormously increased surface to volume ratio that also grants surfaces a key role. This role magnifies immensely in topological nanostructures where both

surface related entities i.e. the material (TI) and the nano-architecture merge. Thus, the impact of any factor that harms, damages, alters or affects surfaces in any way would massively increase in topological nanostructures.

Studies have illustrated that surface oxidation of 3D TIs, at the exposure to ambient conditions, is a critical problem[28, 29, 30, 31, 32] (for details visit chapter 6). As topological states are protected by TRS, the surface oxidation or other non-magnetic impurities cannot destroy them rather bury them under the oxidized layer. This phenomenon increases the complexity of forming atomically clean and defect-free interfaces between the buried TI surfaces and metallic electrodes, required in most quantum devices. It has also been demonstrated that surface oxidation can be prevented by appropriate encapsulation or surface passivation with a thin oxide layer[6, 33] e.g. Al_2O_3 or HfO_2. Due to surface oxidation and challenges to attain atomically clean interfaces, reliability is one of the most important criteria for developing a platform to prepare topological nanostructures.

There are several approaches that can be utilized to prepare topological nano-architecture. All of them can be categorized in following four groups. Based on the required criteria to fabricate topological nanostructures discussed above, pros and cons of these approaches are discussed and the best approach is adopted.

- ***VLS nanowires:*** Among all approaches, VLS grown nanowires exhibit the best structural quality of TIs[34, 35, 36, 37] and are extremely reproducible. However, this approach lacks control over dimensions and reliability as the surface passivation is complicated to achieve. Also, VLS nanowires have very limited application capability as they are not adaptable or scalable for complex architecture.
- ***Exfoliated crystals:*** Crystals prepared via zone melt and Bridgman methods can only be utilized via exfoliation[38, 39, 40]. High quality crystals can be prepared and exfoliation conducted in controlled environment can also protect surface states. Still, the formation of nanostructures requires lithography and etching processes that brings challenges to reliability. This approach provides no support for dimensionality and scalability.
- ***Mesa structures:*** Epilayers prepared via MBE, CVD, VPE, sputter deposition and PLD etc., all require fabrication process to create nanostructures. This is the most utilized approach by the topological and the thermoelectric communities[41, 42, 43] where TI mesa structures are created via lithography and etching processes (*ex situ*). With the optimized parameters, reproducible epilayers can be prepared. Even if surfaces are protected by in situ passivation, exposure to fabrication chemicals create reliability issues that may be negligible in microstructures but cannot be disregarded for nano-architecture. Thus, in this approach reliability becomes an issue when dimensions reach at nanoscale while scalability is not a problem.
- ***Selective area epitaxy (SAE):*** SAE is an inverse approach of the mesa structures and can be adopted with any of the above mentioned growth techniques; however, it is best suited for MBE. In this approach, at first patterns with the desired dimensions are transferred to the substrate via lithography and fabrication processes. Later, the controlled epitaxy is performed on the pre-patterned substrate to obtain high quality nanostructures[6, 7, 17, 44]. This approach[45, 46] provides reliable, dimensionally controllable and scalable nano-architecture. Reproducibility can also be achieved via optimization of growth parameters.

Among all the above mentioned techniques, SAE is the most promising approach to fabricate structures at nanoscale as it fulfils all the necessary requirements including reliability, dimensionality and scalability. However, this technique is relatively new for topological materials and still under development by several research groups. That is why, SAE is adopted and explored in this study to develop a platform to fabricate nanostructures of all conventional 3D TIs, investigated in chapter 2. Initially, the working principles of SAE are explored, the fabrication challenges of pre-patterned substrates are addressed and the issues of selectivity are resolved. Finally, with the understanding of growth dynamics, high-quality selectively grown

topological nanostructures of all Te based 3D TIs are prepared and characterized via structural and magneto-transport investigations.

3.1 What is SAE?

SAE is a technique that allows epitaxial growth of the desired crystal locally only on one of the two involved surfaces belonging to different materials. The combination of these surfaces is ratified based on two key requirements.

- ***Crystal compatibility:*** One of the two surfaces must not favor the epitaxial growth of crystal and should not necessarily but preferably, be amorphous in nature. This surface is named the blocking surface while the other is called the epitaxial surface.
- ***Thermal compatibility:*** The second requirement is the selective thermal compatibility of the blocking surface with respect to the epitaxial surface. It means that at the optimum growth temperature (T_{sub}) of the desired crystal, the blocking surface must has a very low adsorption to desorption ratio (ADR). This parameter confirms the quality of selectivity.

As this work focuses on Si (111) for the epitaxial surface, SiO_2 and Si_3N_4 are the most suitable candidates for the blocking materials. Other compatible materials that fulfil the above mentioned requirements, such as Al_2O_3 and HfO_2 are also tested. Based on the preliminary growth experiments, SiO_2 and Si_3N_4 are found to be relatively better than other material systems due to reasons discussed below and therefore, are selected to fabricate the blocking surfaces for SAE of 3D TIs.

- Both materials i.e. SiO_2 and Si_3N_4, remain amorphous even at high temperatures ($T_{sub} \geq 700$ ℃) during the substrate degassing and activation processes, discussed in chapter 2 (Section 2.1). In contrast, Al_2O_3 and HfO_2 start to transform in polycrystalline phase after the thermal treatment[47, 48].
- SiO_2 and Si_3N_4 are easily accessible and also compatible with the standard fabrication chemicals and tools. Al_2O_3 and HfO_2 also offer similar features; however, the control over precise etching rate of Al_2O_3 and HfO_2 that is required prior to epitaxy, is more challenging than for SiO_2.
- High quality thin films of SiO_2 and Si_3N_4 with precisely controlled thicknesses and without unintentional cross contamination can be prepared using several deposition techniques.

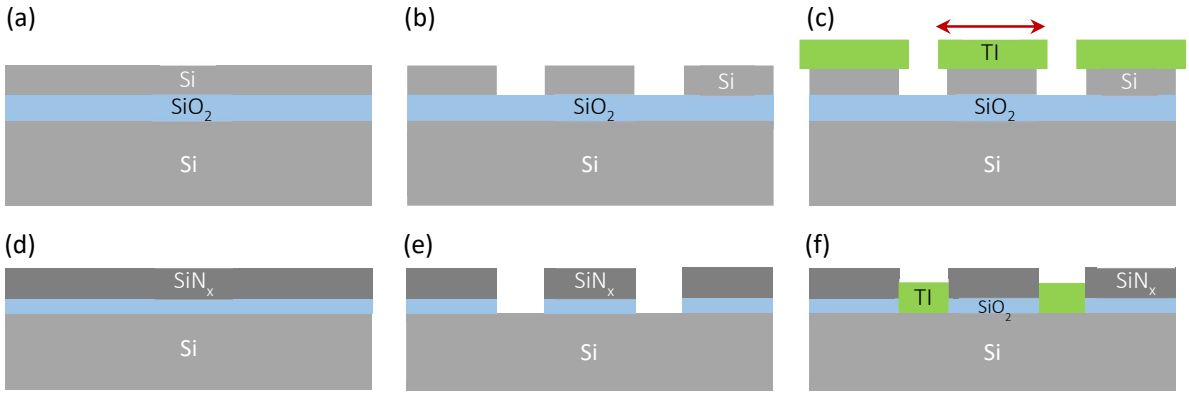

Fig. 3.1: A model representing positive (a-c) vs. negative (d-f) selective masks. (a) SOI wafer with Si (111) surface on SiO_2 layer. (b) Patterned Si (111) surface as a positive mask. (c) TI epilayer selectively grown only on Si (111) surface exceeding the dimensional limits due to non-availability of side walls. (d) Si (111) wafer deposited with SiO_2 and Si_3N_4 as blocking materials. (e) Negative patterned in transferred by etching the blocking material into desired structures. (f) SAE of TI on exposed Si (111) surface confined by the wide walls of the blocking material.

3.1.1 Positive vs. negative masks for SAE

There are two formats in which Si (111) as an epitaxial and SiO_2/Si_3N_4 as a blocking surface can be structured and are discussed below:

- ***Positive selective mask:*** This is the first format. The fabrication requires Si (111) mesa structures that after processing stands higher than the blocking surface of SiO_2. This arrangement is only possible with a specific type of substrates known as silicon on insulator (SOI). Positive masking is not possible with conventional Si (111) wafers. Other than the requirement of the specific substrate, this format also lacks with the following mentioned features.
    - After growth, as soon as the substrate is taken out of MBE chamber the epilayer is exposed to the ambient conditions due to unprotected side surfaces, even if the top surface is passivated with a thin layer of Al, a technique developed in an earlier study[49, 50]. This problem, however, can be solved by using the *in situ* conformal passivation via ALD.
    - The epilayer over extends the dimensional limits of the pattern due to the unavailability of hard boundaries at the edges. Therefore, it is not possible to obtain patterns with sharp boundaries particularly at the nanoscale (Figure 3.2 c-d).

Successful growth of Bi_2Te_3 epilayer on Si (111) mesa structures prepared with positive selective mask on SOI substrates is reported in previous studies[44, 51] that confirms the above mentioned issues, as depicted in Figure 3.2. This technique, despite all drawbacks provides an advantage of being utilized as the back gate-able substrate for the advanced measurements e.g. in-situ STM and dual gated magneto-transport investigations.

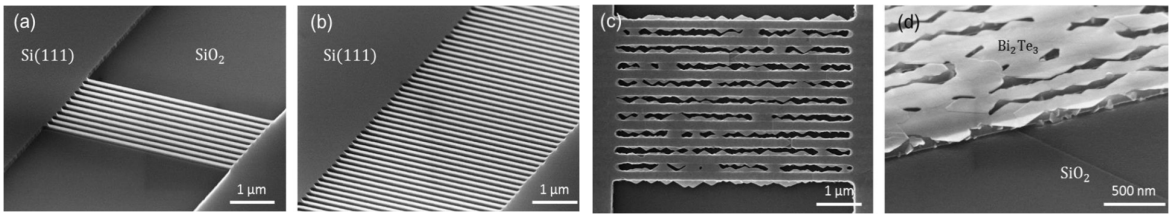

Fig. 3.2: Fabrication and SAE using positive selective mask on SOI wafer. (a) SOI wafer with 100nm wide suspended Si (111) patterned nanoribbons while SiO_2 layer is wet etched, (b) similar to (a) but on large scale repetitive structures. (c) Bi_2Te_3 epilayer selectively grown only on Si (111) surface exceeding the dimensional limits due to non-availability of side walls as modeled in Fig. 1(c), (d) angular SEM image depicting extended growth and the limitation of positive selective mask for nanostructures. (Taken from Lanius et al.[51])

- ***Negative selective mask:*** In this technique the conventional Si (111) wafer is covered with thin layers of SiO_2/Si_3N_4 to prepare the blocking surface. Later, via lithography processes, trenches of the desired dimensions are etched to expose the buried Si (111) epitaxial surface. This technique addresses both issues encountered with the positive masked substrates. The epitaxial film grows in the etched trenches where the shape of the geometrical pattern is always preserved and the protection of epilayer side walls from the ambient exposure is guaranteed by SiO_2/Si_3N_4 trench walls as long as the epilayer thickness remains smaller than the trench depth.

Using the negative mask technique, several devices are fabricated where the electronic investigations are performed including nano-Hallbar[6], transmission line model (TLM) nanoribbons[7] and superconducting Josephson junction (JJ)[17]. However, the lack of in-depth understanding of the growth dynamics and the relation between T_{sub} vs. R_{TF} (Figure 2.7), had limited the fabrication of high quality nanostructures with precise thickness control. Moreover, this technique exhibits certain critical requirements and strain related issues that must be addressed in order to obtain high quality pristine nanostructures. The fabrication of pre-patterned substrates and the related issues are discussed in section 3.2 and 3.3 respectively.

3.2 Fabrication of the pre-patterned substrates

This section focuses on the fabrication challenges related to the pre-patterned substrates for SAE. At first, Si (111) surface must be covered by the blocking material before the negative selective mask could be fabricated.

3.2.1 Selection of the blocking material

It has been mentioned earlier that among all materials, SiO_2 and Si_3N_4 are the best candidates to fabricate the blocking surface. For SAE of nanostructures, the selection of a blocking material is of critical importance and certain aspects must be considered before the final selection including:

- ***Interface protection:*** The removal of the blocking material in the trenches to expose the buried Si (111) surface for epitaxial growth must not harm the interface.
- ***HF Resistant:*** Before loading the sample into MBE system for epitaxy, Si native oxide (SiO_2) on the epitaxial surface must be etched by HF and therefore, the blocking material must be resistant to HF etching to preserve the pattern dimensions.
- ***Stress at the Interface:*** The blocking material must not exhibit any stress/strain with Si (111) surface so that the quality of epitaxial growth remains unaffected.

SiO_2 as the blocking surface: SiO_2 can be prepared via dry and wet thermal oxidation, rapid thermal annealing (RTA), low pressure chemical vapor deposition (LPCVD), plasma enhanced chemical vapor deposition (PECVD), pulsed laser deposition (PLD) and atomic layer deposition (ALD). Irrespective of the tool being used, SiO_2 at Si (111) interface exhibits compressive strain[52]. The strength of the strain in SiO_2 differs from one tool to another and it can also be managed by changing the deposition/oxidation parameters. The films prepared with dry thermal oxidation above 900˚C exhibit the least strain[52] and the best structural and electronic characteristics. SiO_2 exhibits stress at Si interface but due to being compressive in nature, it does not affect the epitaxial growth. While the Interface and the stress criteria are fulfilled by SiO_2, it fails to provide the dimensional integrity. During the HF etching process, the isotropic etching of SiO_2 results in the increased structural dimensions. Moreover, the continuous HF etching of SiO_2 causes the reduced thickness of the blocking layer. Hence, SiO_2 is not a reliable blocking material for nanostructures.

Si_3N_4 as the blocking surface: Si_3N_4 can be prepared via LPCVD and PECVD. Being deposited by both methods it exhibits high tensile strain at the Si (111) interface which, to some extent, can be reduced with the parameter adjustment[53] but cannot be entirely neutralized[54]. Si_3N_4 deposited by LPCVD offers better structural quality and is resistant to HF etching and thus, provides the dimensional protection to the pattern at the nanoscale. Si_3N_4 with anisotropic profile is more effectively etched via dry etching; however, the dry etching via plasma treatment can always harm Si (111) surface. Damage to the epitaxial surface and high strain at the interface are the factors that do not allow Si_3N_4 to be a reliable blocking material.

These issues can be addressed with the combinational layer stack of SiO_2 and Si_3N_4 to fabricate the blocking surface. A very thin layer of SiO_2 at Si (111) interface would protect the interface from the use of any strong chemical treatment as well as from any stain related problems while a relatively thicker Si_3N_4 layer on top of thin SiO_2 would protect the pattern dimensions due to its resistance towards HF etching.

3.2.2 Preparation of blocking surfaces with the combinational layer stack

The first step in the fabrication of combinational layer stack is the selection of deposition methods. SiO_2 is prepared via dry thermal oxidation due to its optimum structural characteristics and uniformity even in a few nm thin film. As far as Si_3N_4 is concerned, the highest quality films can be prepared via LPCVD. However, due to unavailability of LPCVD, Si_3N_4 films are prepared via PECVD utilizing *Oxford instruments* reaction

chamber. There are certain challenges involved in PECVD deposited Si_3N_4 that must be addressed before its utilization as the blocking surface. There challenges include:

- Strong tensile strain (ranging in GPa) that would not allow the epitaxial growth of 3D TIs on Si (111) surface particularly in the nanostructures (for details visit Section 3.3.3).
- Irresistance towards HF etching (due to H^+ ions in the deposited SiN_x film) would practically limit its utilization as the blocking material.

The solution of above mentioned problems rests in understanding PECVD deposition processes and in the identification of key process controlling parameters.

Strain management: The stoichiometric deposition of Si_3N_4 via PECVD always results in high tensile strain[53, 55]. In order to manage the strain it is decided to deviate from conventional high radio frequency (HRF) plasma to low frequency (LRF) treatment for the following reasons:

- At HRF = 13.56 MHz, ions do not respond to radio frequency (RF) field. Films with stoichiometric Si_3N_4 with high tensile strain are obtained.
- At LRF = 100-350 KHz, ions respond and provide ion bombardment of the growing film. This feature changes the density of the films with slight stoichiometric shifts resulting in SiN_x. Films prepared with only LRF field exhibit highly compressive strain.

Thus, the best possibility is to prepare the films with mixed frequency PECVD process. Mixing of high (HRF) and low frequency (LRF) powers allow control over ion bombardment and hence, control over the film density and strain. Numerous deposition tests with varying HRF/LRF ratios are conducted (Figure 3.3) where the strain is evaluated by measuring the bow (curvature of the wafer profile) before and after SiN_x deposition using the Dektak profiler. The best results are obtained with 70% HRF providing high surface quality films with slight tensile strain.

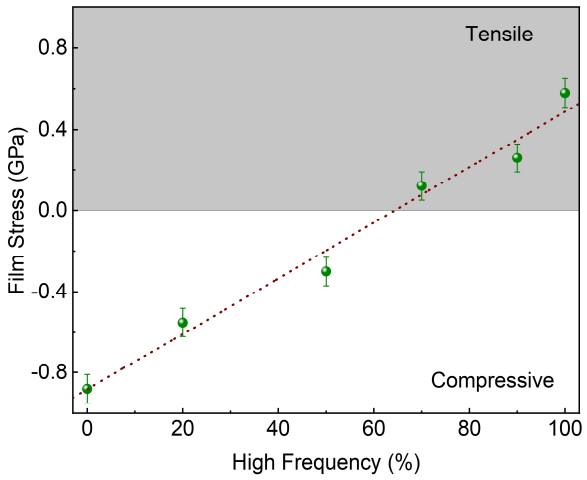

Fig. 3.3: The trend of stress in mixed frequency PECVD deposited SiN_x films. It is evident that with the increasing HRF fraction stress in the film shifts from compressive to tensile. The best quality films are produced with HRF around 70%. HRF fraction can be evaluated via $HRF = \frac{T_{HRF}}{T_{HRF}+T_{LRF}} \times 100\%$, *where T_{HRF} and T_{LRF} stand for the time duration in which high and low frequencies are applied in the film deposition process.*

Irresistance towards HF: The strain management in PECVD deposited SiN_x films is conducted; however, the films still exhibited irresistance in HF solution with the etching rate of approx. 25 ± 2 nm/min. The reason for this behavior is the presence of high concentration of H^+ ions in SiN_x film. The etching rate of SiN_x in HF-based solutions strongly depends on Si/N ratio[56, 57, 58] and on H^+ ion density in the film[56, 59], as described by Knotter's reaction mechanism[60, 61]. As discussed earlier, adjusting the deposition conditions can tune the film composition, while the thermal treatment after deposition can decrease H^+ concentration and increase the density of the film, thereby improving the etching resistance of SiN_x in HF based solutions[61, 62]. In order to improve the etching selectivity of SiN_x in HF based solutions, films prepared via PECVD are thermally treated via RTA ranging from 500℃ to 1000℃. Slight improved etching resistance is observed in

films annealed at 800℃; however, the optimum results are obtained with films annealed at 1000℃ for 5 mins in N_2 environment. The annealing process reduced H^+ concentration in SiN_x films and in result decreased the etching rate of SiN_x from 25 nm/min to 1.2 nm/min in the buffered HF.

After both major issues related with PECVD SiN_x i.e. tensile strain and irresistance in HF solution are resolved, the fabrication process of the blocking surfaces is continued with the following processing steps.

- A 4-inch Si (111) wafer is processed via RCA cleaning steps (discussed in Table 2.2) to eliminate ionic particles and organic contaminations.
- After native SiO_2 removal in HF solution, the wafer is loaded into the *tempress* oxidation furnace and dry thermal oxidation is performed at 900℃ for 5 minutes to obtain 7 nm thermally grown high quality SiO_2.
- Oxidized wafer is then loaded into the Oxford PECVD chamber and 30 nm of SiN_x is deposited at 350℃ with HRF/LRF mixed frequency process discussed above. The detailed recipe with exact parameters of pre-conditioning and SiN_x deposition steps is described in Appendix 3A.
- SiN_x deposited wafer is annealed via RTA at 1000℃ for 5 mins in N_2 environment with the flow of 5 liter/min and naturally cooled down with N_2 flow of 0.5 liter/min till 150℃.

Now, the Si (111) wafer containing combination layer stack is ready for the fabrication steps to create patterns for SAE. The process is executed in the following steps.

- Global alignment markers are written via e-beam lithography (EBL). After resist development, negative markers (700 nm deep in Si) are prepared with dry reactive ion etching (RIE). The global markers are necessary to write forthcoming lithography steps with precise alignment. Wafer is cleaned with Piranha, spin coated for protection and diced into smaller pieces (e.g. 7 x 7 mm^2).
- Each diced samples is passed through another EBL step to transfer the desired pattern in form of trenches (negative selective mask). Samples are developed and dry etched via RIE with precise thickness control until SiN_x is completely etched and a few nm of SiO_2 is left (a buffer for surface protection).
- Now, each processed sample contains the desired patterns and it must be cleaned with Piranha and etched in HF solution to expose Si (111) surface before loading into MBE chamber to perform SAE.

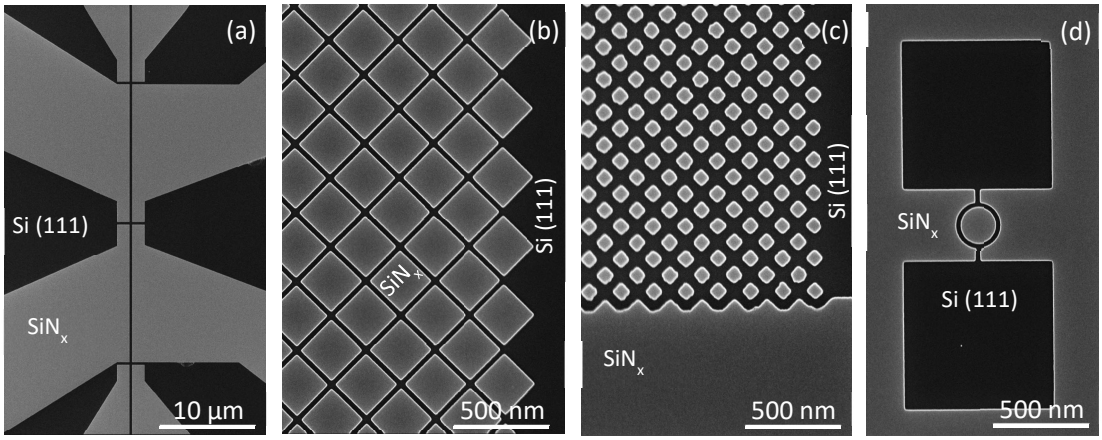

Fig. 3.4: (a-d) SEM images of a few pre-patterned substrates with pattern dimensions ranging from micro to nanoscale. The dark and light (grey) contrasts represent the exposed Si (111) surface and the blocking surface of SiN_x (the combinational layer stack) respectively.

Figure 3.4 depicts a few negatively patterned structures for SAE. The detailed fabrication processes including all steps of EBL, resist development and dry etching for LPCVD based SiNx are discussed already

in a previous study[63]. Due to slightly different characteristics of SiN_x prepared via PECVD, all the modified parameters along with the summary of all fabrication steps are described in Appendix 3B.

3.3 Selective growth of 3D TIs

The efforts to achieve selective area growth of the 3D TIs on the pre-patterned substrates are initiated in the similar fashion as on the bare Si (111). A set of growth parameters with T_{sub} in a close proximity of the corresponding optimum value (± 10˚C) along with the R_{TF} ranging from 20 nm/h (high) to 5 nm/h (low) are opted to conduct SAE of each 3D TI. The optimum growth parameters for planar epitaxy (R_{TF} = 5 nm/h) are listed in Appendix 2B. The growth on an epitaxial surface, into the etched trench, should work similar to the planar substrate with the nucleation of islands that grow laterally, coalesce and form a closed layer. On the other hand, the blocking surface (SiN_x) is amorphous in nature and does not provide any support for the epitaxial growth. It does not mean that the growth on an amorphous substrate is not possible. The crystalline growth of Bi_2Se_3 (3D TI) on the amorphous SiO_2 substrate is reported earlier[64, 65]. Moreover, the growth of Te based TIs on ALD prepared high-K Al_2O_3 and HfO_2 amorphous substrates is conducted and discussed in chapter 6 (Figure 6.11).

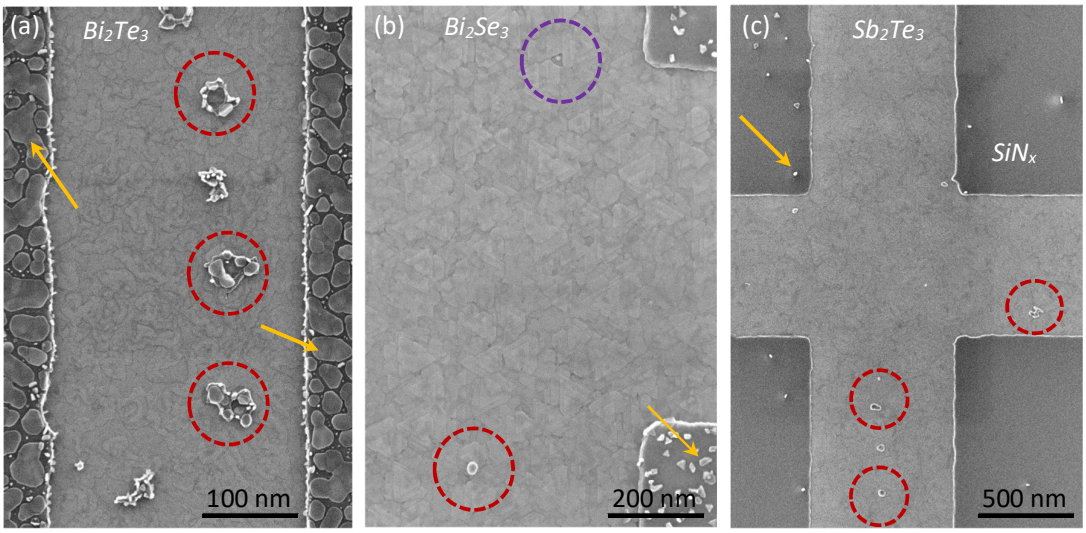

Fig. 3.5: SEM images depict the first SAE attempts of (a) Bi_2Te_3 conducted at T_{sub} = 290˚C and R_{TF} = 8 nm/h, (b) Bi_2Se_3 conducted at T_{sub} = 295˚C and R_{TF} = 8 nm/h and (c) Sb_2Te_3 conducted at T_{sub} = 285˚C and R_{TF} = 10 nm/h. Orange arrows indicate the bad selectivity in (a) that is heavily improved in (b) by increasing T_{sub} by 5˚C while keeping T_{Bi} constant and in (c) Sb_2Te_3 due to low ADR exhibits the best selectivity even at T_{sub} = 285˚C. Red circles indicate fabrication defects while purple circle points to the growth defect due to residual oxide on Si (111) surface.

If TIs can be grown on amorphous substrates then what is meant by the above mentioned statement *"no epitaxial support is provided by an amorphous substrate"*. The reality is, 3D TIs grow on amorphous substrates in form of islands that are highly unordered and exhibit a high defect density as the substrate does not provide any azimuthal or rotational alignment to the nucleating QLs. Similarly, parameter adjustment to achieve the coalescence of these islands to form an entirely closed layer is a complicated process. That is why, the optimum growth parameters on the amorphous substrates are entirely different from the crystalline surfaces. At the optimum growth parameters according to Si (111) surface, most of the amorphous substrates do not exhibit any considerable growth; that is why, amorphous materials provide the best blocking surfaces with the selective epitaxy only on Si (111) surface. Figure 3.5 depicts SEM images of the first SAE attempts of 3D TIs including Bi_2Te_3, Bi_2Se_3 and Sb_2Te_3.

The initial SAE tests have demonstrated several fabrication issues and growth deficiencies that are required to be addressed first. Later, the structural optimization of selectively grown nanostructures will be

performed. The key issues, that are required to be addressed before successful SAE on the nanostructures can be achieved, are discussed below:

- Selectivity of the epilayer
- Fabrication defects in the patterned substrates
- Strain issues of the blocking material

3.3.1 Selectivity of the epilayer

The selectivity is a qualitative attribute of epitaxy on the patterned substrate. It describes the relative partiality of the crystal to grow on one of the two surfaces i.e. Si (111) or SiN_x. The sample without any growth on the blocking surface (SiN_x) exhibits the best selectivity. In the growth of 3D TIs, the selectivity can be tuned by the compound adjustment of T_{sub} and R_{TF}. Keeping R_{TF} constant, the desorption rate of the incoming adatoms increases at the higher T_{sub} that stops the formation of nucleation on SiN_x. While at the lower temperatures, ADR increases and the selectivity fails.

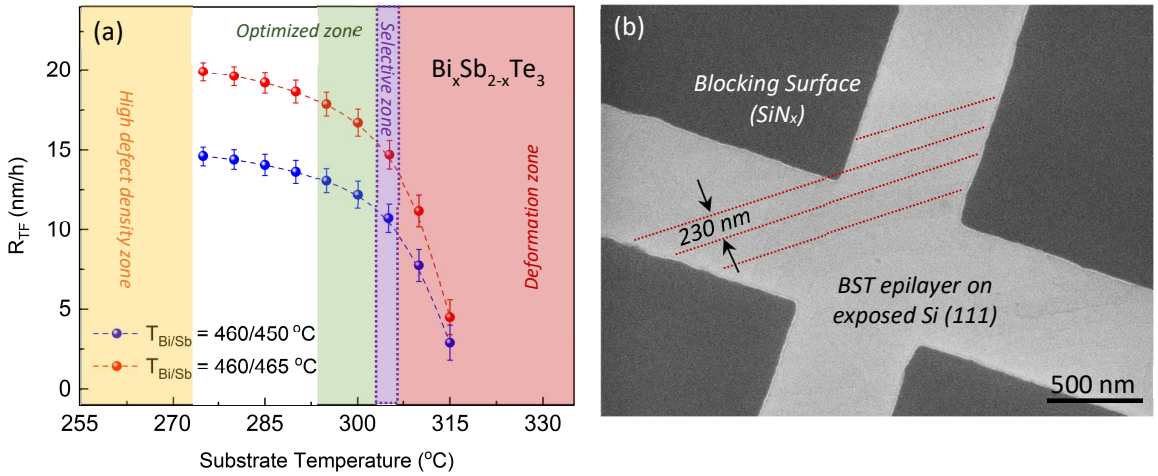

Fig. 3.6: Temperature range for best selectivity. (a) Growth rate (R_{TF}) vs. T_{sub} behavior of $Bi_xSb_{2-x}Te_3$ alloy representing the selective zone at the border of the optimum and the deformation zones (purple color). (b) SEM image depicts SAE of BST alloy with perfect selectivity while T_{sub} is tuned in the selective temperature zone (T_{sub} = 305 ˚C) with R_{TF} = 5.5 nm/h. The red lines indicate some of the 2D defects originating from Si step edges periodically after 230 nm.

Among 3D TIs, Sb_2Te_3 exhibits the best selectivity due to relatively higher desorption rate of Sb even at higher R_{TF}; however, this is not the case with Bi based compounds. Bi based TIs due to the higher adhesion coefficient of Bi exhibit dramatic change in selectivity even with minor changes in R_{TF} and T_{sub}. In case of Bi_2Te_3, Bi_2Se_3 and BST alloys the best selectivity is obtained with T_{sub} at the border of the optimum zone (green color) and the deformation zone (red color) according to Figure 2.6 and replotted in Figure 3.6 where the purple marked zone identifies the temperature range for the best selectivity of BST alloy. An example of SAE of BST alloy with R_{TF} = 5.5 nm/h at T_{sub} = 305 ˚C (conducted in the purple zone) is depicted in Figure 3.6b.

Any attempt to perform SAE outside the purple marked (selective) temperature zone results in either failed or bad selectivity. A few examples are depicted in Figure 3.5 where (a) depicts the growth of Bi_2Te_3 epilayer with very poor selectivity (orange arrows). Due to the higher R_{TF} and the lower corresponding T_{sub} several large islands can be observed on the surface of SiN_x. Bi_2Se_3 growth, depicted in Figure 3.5b, indicates that the size and the density of islands are decreased due to increased T_{sub} (closer to purple zone) and hence, the selectivity is improved. While Figure 3.5c shows near perfect selectivity of Sb_2Te_3.

3.3.2 Fabrication defects in the patterned substrates

The largest and the most common source of defects in patterned substrates is a fabrication cycle. A general fabrication cycle consists of two main steps:

- Lithography
- Etching / Deposition + Resist removal (Lift off)

The defects can originate at both steps but statistically, the lithography process has higher probability as it contains several sub-steps including samples cleaning, spin coating, soft/hard resist baking, optical/e-beam writing and resist development. Any defect originated during the lithography process cannot be avoided during etching or deposition steps. Moreover, the shape and type of defects appear during lithography process depend entirely on the resist system in use. Figure 3.7 depicts some of the fabrication defects that are finalized in the dry etching step via RIE but are originated during the lithography process of pattern transfer.

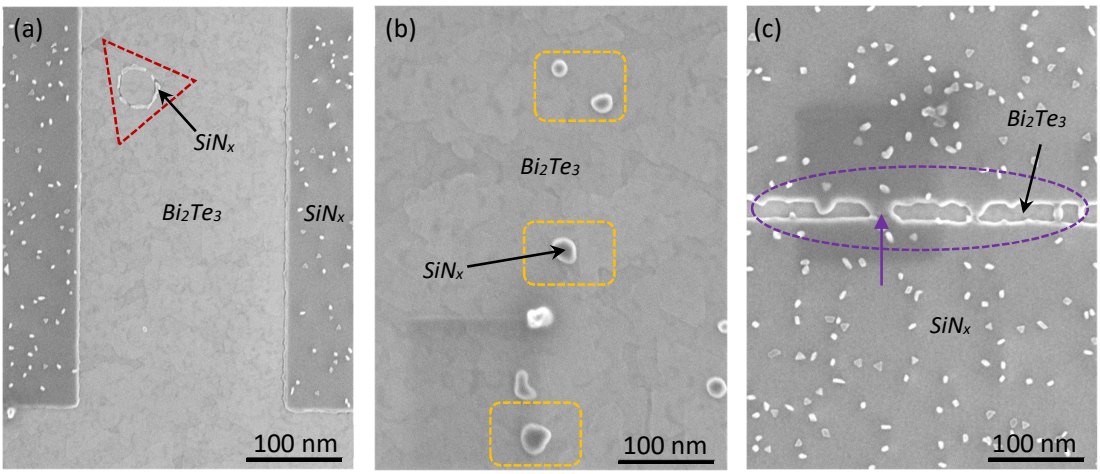

Fig. 3.7: SEM images depict fabrication defects in patterned substrates that originated in lithography process but finalized in etching step. (a) Red triangle indicates residual SiN_x ring left in the etching process due to trapped air bubble in the resist while spin coating, (b) Yellow boxes indicate SiN_x pillars left standing after RIE due to hard particles in the resist that failed to develop and (c) purple marked area depict an example of a damaged structure where desired pattern transfer failed due to underexposure or underdevelopment of resist in the lithography process.

- The red triangle in Figure 3.7a indicates the presence of an air bubble in the resist that was trapped during the spin coating process. It took the shape of a circular ring during the resist soft baking step as the air was released. It got hardened with thickness variations and did not get exposed and developed properly and thus, left its footprint on the substrate during the etching process. This ring is the left over nitride circular wall that failed to be etched and now acts as a boundary defect in the crystal growth process.
- The presence of hard particles in the resist left their marks on SiN_x surface during the etching process, similar to the case of air bubbles in the resist. They took the shape of SiN_x pillars that caused defects and restricted the growth of homogenous epilayer as shown in Figure 3.7b.
- The inhomogeneous spin coating of the resist and the inappropriate exposure parameters during the e-beam lithography (EBL) resulted in an underexposed and underdeveloped structure, depicted in Figure 3.7c. With such defects the proper shape of the pattern cannot be transferred to the substrate.

Other than these defects, there are also several critical parameters in the lithography process related to EBL such as coarse vs. fine exposure, beam defocus, dose factor and the proximity effect correction etc.

that, if not optimized properly, may lead to other defects or unintended changes in the patterns dimensions. Similarly during the etching process, the optimization of etch rate and the etching profile of side walls with the control over chemical vs. physical etching in the RIE process is also critical. A summary of all the fabrication processes along with the detailed steps and the optimum parameters, is described in Appendix 3B.

3.3.3 Strain management in the combinational layer stack

As discussed in Section 3.2, SiO_2 and SiN_x exhibit compressive and tensile strain respectively. SiO_2 fails to provide dimensional protection while SiN_x exerts strain onto the epitaxial film and causes structural damages. Hence, both of them cannot be utilized as the blocking material individually; however, with the fabrication of combination layer stack (SiO_2 + SiN_x), strain-free blocking surfaces can be prepared quite efficiently. The blocking surfaces prepared with the combinational layer stack are observed to exhibit a delicate stress balance where the thickness ratio between SiO_2:SiN_x controlled the overall strain. It is witnessed that the thickness ratio of 1:4 is the maximum that allows epitaxy of 3D TIs without any exerted strain or structural damages in the epilayer. It means that combinational layer with the thickness of 7 nm SiO_2 can have a maximum 28 nm of SiN_x. Any reduction in the thickness of SiO_2 or an additional thickness in SiN_x film will lead to stress misbalance that would affect the structural quality of the epilayer.

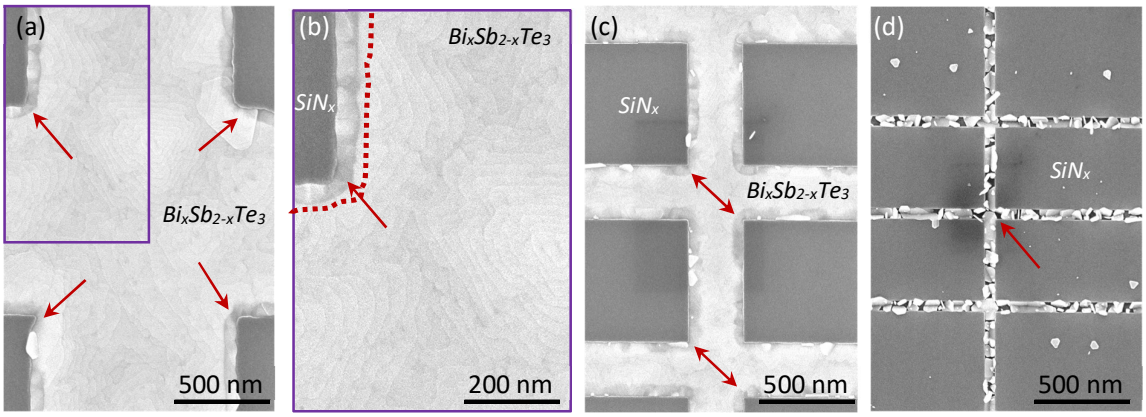

Fig. 3.8: SEM images illustrate the effects of tensile strain exerted by SiN_x (red arrows) in pre-patterned substrates prepared with SiO_2:SiN_x = 1:7 with lateral effects up to 80 nm. (a) Pattern with 1000 nm width exhibit damaged epilayer limited only to the edges, (b) enlarged area selected in (a) depicts the damaged layer and lateral extent of tensile strain, (c) strain damage became more significant in 500 nm wide structure although in central areas epitaxy is still successful, (d) Strain in 100 nm wide structure exceeded the critical value, so that epitaxy entirely failed.

Figure 3.8 displays SEM images of SAE containing BST alloy, conducted on a pre-patterned substrate with SiO_2:SiN_x thickness ratio of 1:7, with SiO_2 thickness kept at 7 nm. The tensile stress of 50 nm SiN_x overcame the compressive stress and exerted strain on the substrate that affected the epitaxial film. It is observed that the extent of the exerted strain on the epilayer is limited laterally to approx. 70 nm. Further than that, the growth continued conventionally without any impact of strain induced defects. Figures 3.8a, c and d depict the effect of lateral strain on the epilayer in 1 µm, 500 nm and 100 nm wide trenches respectively. The damage to the crystal structure due to tensile strain is clearly visible in 1 µm wide pattern that increased with the reducing dimensions in 500 nm. Moreover, in 100 nm wide pattern, the epitaxial growth has entirely failed due to excessive lateral strain. Hence, if the total thickness of the blocking layers is required to increase, it is necessary to control the compressive/tensile strain balance with the optimization of SiO_2:SiN_x thickness ratio.

3.3.4 Micro to nanostructures

The achievement of defect and strain free fabrication of patterned substrates resolved major obstacles for the successful SAE. By adjusting T_{sub} to the respective optimum values in the selective zone i.e. 300℃ for Bi_2Te_3, 285℃ for Sb_2Te_3 and 305℃ for BST ternary alloy, the selectivity is ensured and the growth of 3D TIs on pre-patterned substrate is acquired.

SAE on micrometer scaled patterns worked without any noticeable difference in comparison to planar substrates (Figure 3.6b); however, it has been observed that trenches smaller than 1 µm in width exhibited textures of higher growth rate. This trend became more obvious with the continuous reduction in the trench width. For example, consider the case of 50 nm wide structure (Figure 3.9c) where the epitaxial growth rate was so high that 30 nm deep trench was entirely filled by the epilayer in just 90 minutes. That brings the epitaxial growth rate (R_{eff}) in 50 nm wide trench to approximately 20 nm/h while the applied growth rate (R_{TF}) was kept at 8 nm/h.

Figure 3.9 depicts a few examples of overgrown trenches in the patterned nanostructures. Figure 3.9a displays a 500 nm wide trench with Sb_2Te_3 SAE performed at R_{TF} = 12 nm/h. The trench is entirely filled and later started to grow laterally, indicated by orange arrows. Figure 3.9b displays SAE of BST alloys in 200 nm wide trench with R_{TF} = 10 nm/h. The crystal has overgrown and due to higher effective growth rate (R_{eff}) multiple twin domains have formed and are clearly visible, indicated by red and blue triangles. Figure 3.9c shows SAE of Bi_2Te_3 in 50 nm wide diamond array structure with R_{TF} = 8 nm/h. The effective growth rate (R_{eff}) was so high that after entirely filling the trenches, TI overgrew laterally to the extent that a suspended sheet of TI (Bi_2Te_3) film is formed being supported by the Bi_2Te_3 pillars in the trenches. All the stated examples have confirmed that SAE conducted at nanoscale alters the effective growth rate (R_{eff}).

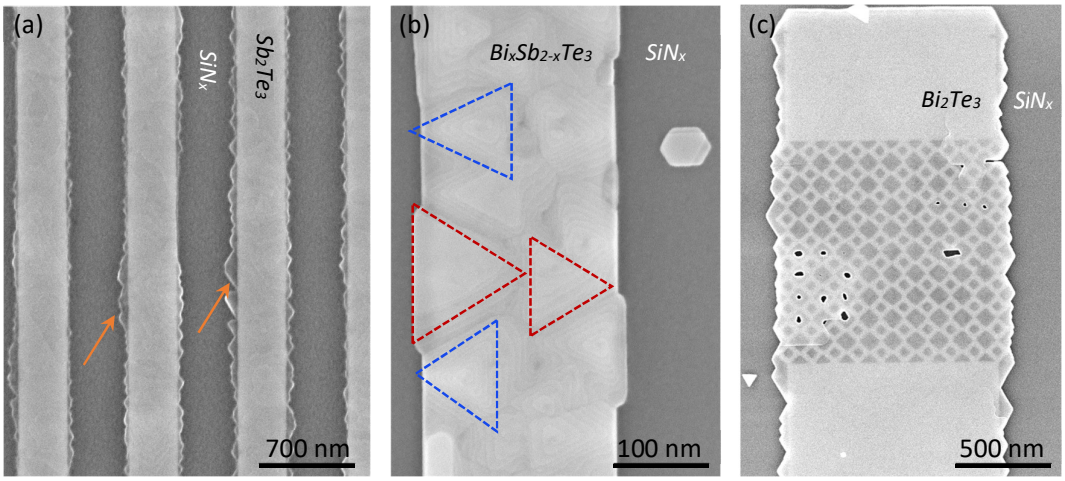

Fig. 3.9: SEM images depict a few examples of overgrown epilayers in patterned substrates indicating the change in effective growth rate than applied R_{TF}. All samples are grown for 90 minutes where (a) represents 500 nm wide trench with Sb_2Te_3 SAE with R_{TF} = 12 nm/h, (b) SAE of BST alloys in 200 nm wide trench with R_{TF} = 10 nm/h, (c) SAE of Bi_2Te_3 in 50 nm wide diamond array structure with R_{TF} = 8 nm/h. All trenches exhibited relatively high effective growth rates although the narrowest structure among all, depicted in (c), experienced highest effective changes in R_{TF}.

As the fabrication defects, strain management and selectivity challenges are addressed, SAE on micro and nanoscale structures is successfully achieved with one remaining issue that must be resolved. It is the structural optimization of the epilayer in the nanostructures that is directly related to growth rate of the crystal, as discussed in chapter 2. The higher effective growth rates (R_{eff}) in the nano-trenches lead to higher defect density. In order to optimize the crystal quality in nanostructures, the relation between pattern dimensions and the effective growth rate (R_{eff}) must be identified.

3.4 Growth dynamics in the nanostructures

In SAE, the estimation of effective growth rate (R_{eff}) is a bottleneck for the crystal optimization of topological nanostructures. For this purpose, a systematic study is carried out with hundreds of growths and a statistical analysis is performed to develop a model and formulize the effective growth rate (R_{eff}). The dependency of R_{eff} on the applied growth rate (R_{TF}) and on the dimensional changes in the pattern is evaluated. In the first step, all structural parameters and material variables that may affect the epitaxial growth are identified.

- The structural parameters include trench dimensions i.e. width (W), length (L), perimeter (P) and surface area (A). All the trenches, in this study, exhibit similar depth and therefore, the depth is not included as a structural variable for the analysis.
- The material parameters include the applied thin film growth rate (R_{TF}) and lateral diffusion length of adatoms on the blocking surface (L_D).

L_D is a temperature dependent parameter however, its dependency on temperature is also not considered for the analysis as T_{sub} is kept constant in all experiments (at the corresponding selective T_{sub}) due to very narrow window of selectivity. For R_{eff} dependency analysis, the growths are conducted with three different values of R_{TF} including 5 nm/h, 10 nm/h and 15 nm/h.

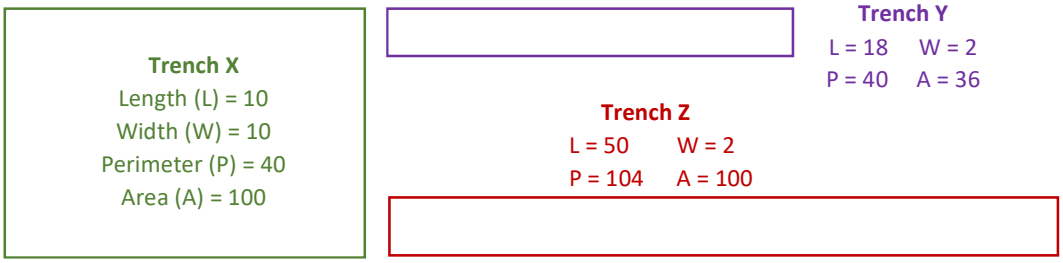

Fig. 3.10: A model represents three different trenches X, Y and Z. All trenches have different dimensions where X and Y exhibit same perimeter (P) and different surface area (A) while X and Z exhibit different perimeters but equivalent surface area.

Structural dependency: Based on statistical results, it is observed that two trenches with similar perimeter (P) but different surface areas (A) exhibit different growth rates. For simplicity, Figure 3.10 depicts the top view of three different trenches where trench X and Y have similar perimeter of 40. The results have shown that R_{eff} in the trench Y with smaller surface area (A = 36) is higher than the trench X containing the larger surface area i.e. A = 100. Hence, R_{eff} exhibits inverse proportionality with the surface area (A) of the trench, as described in equation 3.1. Later results have shown that if the surface area of the trench is kept similar as in trench X and Z, R_{eff} exhibits direct proportionality to the perimeter (P) of the trench and that is why, R_{eff} in trench Z (P = 104) will be higher compared to the trench X (P = 40). Equations 3.2 and 3.3 summarize the structural dependency of the R_{eff}.

$$R_{eff} \propto {}^{1}/_{A} \tag{3.1}$$

$$R_{eff} \propto P \tag{3.2}$$

$$R_{eff} \propto {}^{P}/_{A} \quad \leftrightarrow \quad R_{eff} \propto 2\left(\frac{1}{W}+\frac{1}{L}\right) \tag{3.3}$$

Material dependency: It is obvious that R_{eff} must have a direct proportionality with R_{TF}. It has been observed that the lateral diffusion length of the adatoms on the blocking surface (L_D) is the key parameter that impacts heavily on the effective growth rate (R_{eff}) as summarized in equations 3.4.

$$R_{eff} \propto R_{TF} \times L_D \tag{3.4}$$

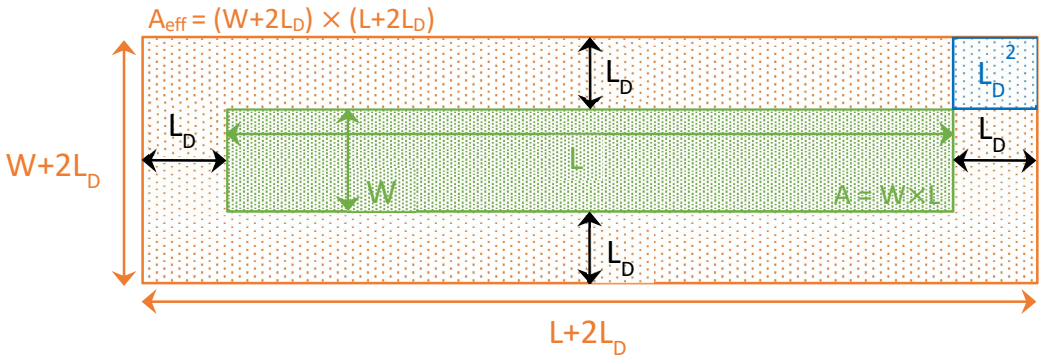

Fig. 3.11: A model represents the lateral diffusion length (L_D) in nanostructures. The impact of L_D on the effective growth rate (R_{eff}) can be visualized in this way that the trench with surface area ($A=W\times L$) experiences the effective influx of adatoms from $A_{eff} = (W+2L_D) \times (L+2L_D)$ based on the applied rate (R_{TF}).

Figure 3.11 depicts a model, specific for a rectangular pattern that indicates how L_D impacts R_{eff} of the epilayer during SAE. In order to evaluate the effects of material and structural parameters on R_{eff} quantitatively, the relation can be summarized in form of equation 3.5.

$$\frac{R_{eff}}{R_{TF}} = \frac{A_{eff}}{A} \tag{3.5}$$

$$R_{eff} = R_{TF}\left[\frac{(L+2L_D)(W+2L_D)}{W\times L}\right] \tag{3.6}$$

$$R_{eff} = R_{TF}\left(\frac{W\times L}{W\times L} + \frac{2L_D L}{W\times L} + \frac{2L_D W}{W\times L} + \frac{4L_D^2}{W\times L}\right) \tag{3.7}$$

$$R_{eff} = R_{TF}\left(1 + \frac{2L_D}{W} + \frac{2L_D}{L} + \frac{4L_D^2}{W\times L}\right) \tag{3.8}$$

The term $4L_D^2/A$ is too small to have any considerable impact on R_{eff} and therefore, can be ignored. Moreover, the length scale of most of the trenches investigated in this study is in micrometer scale which brings the parameter $1/L << 1$ and can also be ignored. The final formula, summarized in equation 3.9, indicates that major parameters affecting R_{eff} other than R_{TF} are the width of the trench (W) and the lateral diffusion length of the adatoms (L_D).

$$R_{eff} = R_{TF}\left(1 + \frac{2L_D}{W}\right) \tag{3.9}$$

The first requirement is to evaluate L_D for each element i.e. Bi, Sb and Te. L_D is extracted from the measured value of R_{eff} using equation 3.9 while R_{eff} is evaluated from the measured thickness of the epilayer in the trench using SEM images, acquired at the cross-section of selectively grown nanoribbon prepared via focused ion beam (FIB) as reported in Rosenbach *et al.*[6] and via AFM discussed in Appendix 3C. The extracted values have indicated that Bi has much smaller lateral diffusion length ($L_{D\text{-}Bi}$ = 12 ± 0.5 nm) than Sb ($L_{D\text{-}Sb}$ = 20 ± 0.5 nm) on SiN_x surface which is an opposite behavior compared to Si (111), reported in earlier studies[66, 67]. This is why, nanostructures during the growth of Sb_2Te_3 and BST alloy experienced elevated changes in R_{eff} compared to SAE of Bi_2Te_3. Equation 3.9 holds true as long as the pattern length (L) remains > 1 µm; however, as soon as the length of the pattern drops below 1 µm, the assumption $1/L << 1$ does not hold true and cannot be ignored anymore. In that case R_{eff} can be described using equation 3.10 and the resulting changes in R_{eff} at nanoscale occur more rapidly. An example of such a change in effective growth rate can be seen via SEM image in Figure 3.9c where both dimensions i.e. width and length of the trench reached at the nanoscale (< 100 nm).

$$R_{eff} = R_{TF}\left[1 + 2L_D\left(\frac{1}{W} + \frac{1}{L}\right)\right] \tag{3.10}$$

Figure 3.12a and c (purple colored zones) represent the corresponding changes in R_{eff} with the applied rates i.e. R_{TF} = 5 nm/h (green), 10 nm/h (red) and 15 nm/h (blue), when the trench width (W) is reduced from 250 nm down to 30 nm for Bi_2Te_3 exhibiting L_D = 12 nm and Sb_2Te_3 with L_D = 20 nm respectively. The circular points represent the measured R_{eff} values from the selectively grown nanostructures while the dotted lines in the corresponding colors represent the fitting of these measured values according to the model presented in equation 3.9, ignoring the length scale ($1/L << 1$). Similarly, the effect of decrement in length (L) on R_{eff} is also measured and depicted in Figure 3.12b and d (orange colored zones) for Bi_2Te_3 and Sb_2Te_3 respectively. In order to observe the effect more prominently, the trench width is fixed to W = 50 nm while the trench length (L) is gradually decreased from 250 nm down to 30 nm. The dotted lines here represent the fitting of the measured values according to the model presented in equation 3.10, taking the length (L) of pattern into account.

It can be observed that the decrement in both structural parameters (W and L) simultaneously impacts heavily on R_{eff} where, the values can reach as high as $R_{eff} \geq 3 \times R_{TF}$ (Figure 3.12d). The colored zones in Figure 3.12 also assist in comparing the effect of L_D along with the dimensional changes. The purple colored zones represent the trend of R_{eff} for Bi_2Te_3 (Figure 3.12a) and Sb_2Te_3 (Figure 3.12c) with the changing widths; however, the effect is much pronounced in Sb_2Te_3 due to higher value of $L_{D\text{-}Sb}$. Similarly, the orange colored zones represent changes in R_{eff} when both dimensions (W and L) are at nanoscale. Once again, the higher value of $L_{D\text{-}Sb}$ impacted more prominently in Sb_2Te_3 (Figure 3.12d) than Bi_2Te_3 (Figure 3.12b).

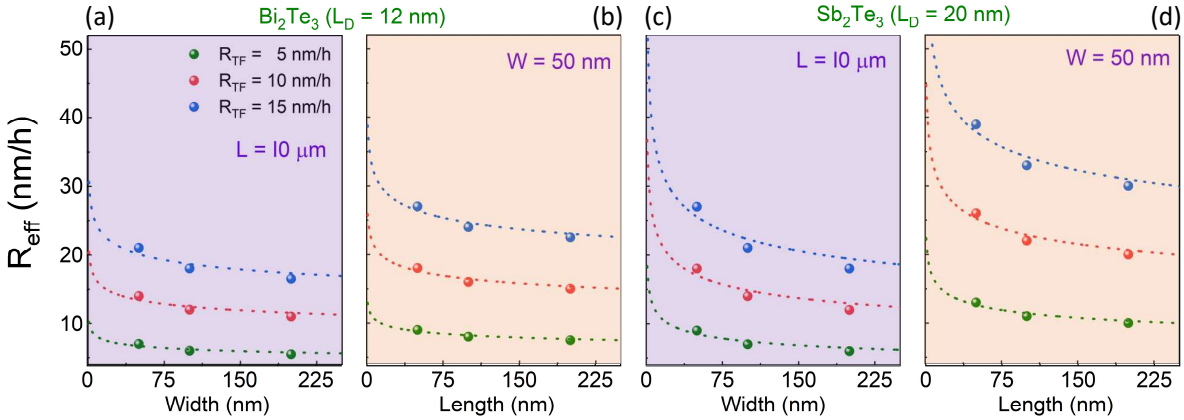

Fig. 3.12: Dependence of effective growth rate (R_{eff}) on structural dimensions and lateral diffusion length (L_D). Trend in resulting R_{eff} for different applied R_{TF} with decreasing trench width for (a) Bi_2Te_3 with L_D = 10 nm and (c) Sb_2Te_3 with L_D = 20 nm while 1/L << 1. The drastic enhancement in R_{eff} with the decreasing trench length along for (b) Bi_2Te_3 and (d) Sb_2Te_3 while the width (W) is kept constant at 50 nm.

Table 3.1: An overview of resulting R_{eff} with the changing width of patterns for $Bi_1Sb_1Te_3$ (L_D = 16 nm) SAE with different applied rates (R_{TF}). Higher applied rates (R_{TF}) result in rapid increment of R_{eff} particularly in narrow trenches.

$Bi_1Sb_1Te_3$ L_D = 16 nm	Trench Width (nm)				
	50	100	200	500	1000
R_{eff} (nm/h) for R_{TF} = 8 nm/h	13.1	10.6	9.3	8.5	8.3
R_{eff} (nm/h) for R_{TF} = 15 nm/h	24.6	19.8	17.4	16	15.5

The fitting curves according to the model presented in equation 3.10 are in good agreement with the measured values as witnessed in Figure 3.12 and therefore is opted to adjust the growth parameters to tune R_{eff} = 5 nm/h. As for binary compounds the proposed model can be utilized straight forward as Te does not take any part in determining the growth rate; however, this feature limits the evaluation of L_D for Te. The value of $L_{D\text{-}Te}$ can only be evaluated in cases where the Te flux will start influencing the growth rate (R_{TF}). It will be possible with SAE of Bi_xTe_y stoichiometric alloys. The study of such compounds is out of

scope of this section; however, the detailed discussions can be found in chapter 4. In case of compositional alloys such as BST, the effective value of L_D depends upon the exact stoichiometry of the material (i.e. relative presence of rate controlling elements). For example, in case of $Bi_1Sb_1Te_3$ the effective values of L_D will be the average of Sb and Bi with L_D = 16 nm. The experimentally measured values of R_{eff} during the growth of $Bi_1Sb_1Te_3$ in trenches with various dimensions for the applied thin film rates (R_{TF}) of 8 nm/h and 15 nm/h are summarized in Table 3.1.

Based on numerous conducted SAE runs and the analysis with the proposed model, the key observations are summarized in the following points:

- When the width (W) of the pattern is in nanoscale whereas the length (L) is large enough to hold the condition ($1/L << 1$) true, R_{eff} can be approximated via equation 3.9.
- When both W and L are in the nanoscale, the condition ($1/L << 1$) does not remain true and R_{eff} can be approximated using equation 3.10.
- When both W and L are in the nanoscale and reaching values so small that the condition $W \leq 2L_D$, the term $4L_D^2/A$ cannot be ignored and R_{eff} can be approximated correctly using equation 3.8.

The model discussed here is specific only to rectangular and square patterns. The same model can be adopted to other geometries such as circular, elliptical and triangular etc. as well and discussed further in Appendix 3D.

3.5 Structural optimization of topological nanostructures

In the light of detailed structural characterization conducted on 3D TIs thin films (Section 2.2), it has been established that nearly all defects, other than antiphase domains and screw dislocations bound to appear at the substrate step edges, can be avoided by conducting growth at optimum T_{sub} and relatively low R_{TF} of approx. 5 nm/h. The same principle is applied to the selectively prepared topological nanostructures to avoid any structural defects.

In SAE, the choice of T_{sub} is always optimum by default, as the selectivity can only be achieved if T_{sub} resides in the "*selective temperature zone*" (Section 3.3.1). However, the selection of suitable R_{TF} can be particularly challenging as R_{eff} varies with changing dimensions of the pattern. It can be even more problematic if the pre-patterned substrate contains trenches with a variety of widths ranging from micrometer to nanometer scale. For instance, R_{eff} can upsurge by a factor of 3 of the applied rate (R_{TF}) in very narrow trenches as observed in Figure 3.12d while remains effectively unchanged at micrometer scale. The statistical model presented in equations 3.9 and 3.10 provided quite accurate estimations of the resulting R_{eff} in nanostructures. In order to obtain defect-free nanostructure (R_{eff} = 5 nm/h) of a particular dimension via SAE, the applied rate (R_{TF}) can be tuned according to equation 3.10, without any complication. However, the selection of R_{TF} can still be challenging if the pre-patterned substrate contains structures with various sizes as each pattern will experience different R_{eff} according on its dimensions.

Table 3.2: An overview of resulting R_{eff} with optimum selected applied rate (R_{NS}) for SAE of each 3D TI. R_{NS} is opted in such a way that the resulting R_{eff} = 5 nm/h in trenches with W = 150 nm for Bi_2Te_3 and 100 nm for Sb_2Te_3 and BST alloys to avoid structural defects in nanostructures.

3D TIs	Trench Width (nm)				
	50	100	200	500	1000
R_{eff} for Bi_2Te_3 when R_{NS} = 4.3 nm/h	6.38	5.34	4.82	4.52	4.41
R_{eff} for Sb_2Te_3 when R_{NS} = 3.97 nm/h	7.16	5	4.78	4.29	4.14
R_{eff} for BST alloy when R_{NS} = 3.8 nm/h	6.54	5	4.48	4.08	3.82

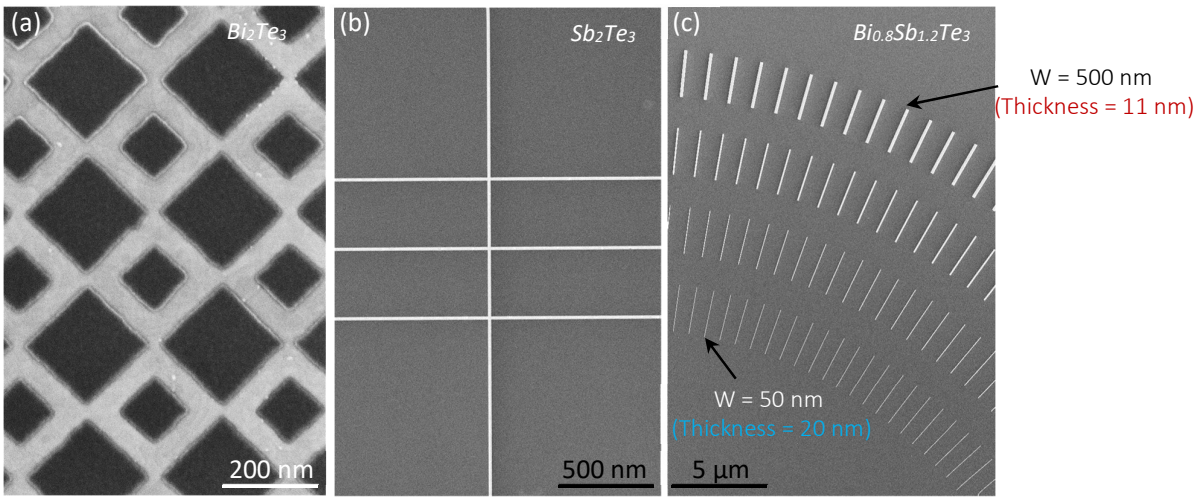

Fig. 3.13: SEM images represent SAE of 3D TIs with optimized applied rate (R_{NS}) for nanostructures. (a) Bi_2Te_3 diamond array structures with W = 50 nm and L = 200 nm, (b) Sb_2Te_3 nano-hallbar with W = 50nm and L = 5 µm, (c) BST alloy nanoribbons with width (W) ranging from 50 nm to 500 nm resulting in different R_{eff} and different thickness.

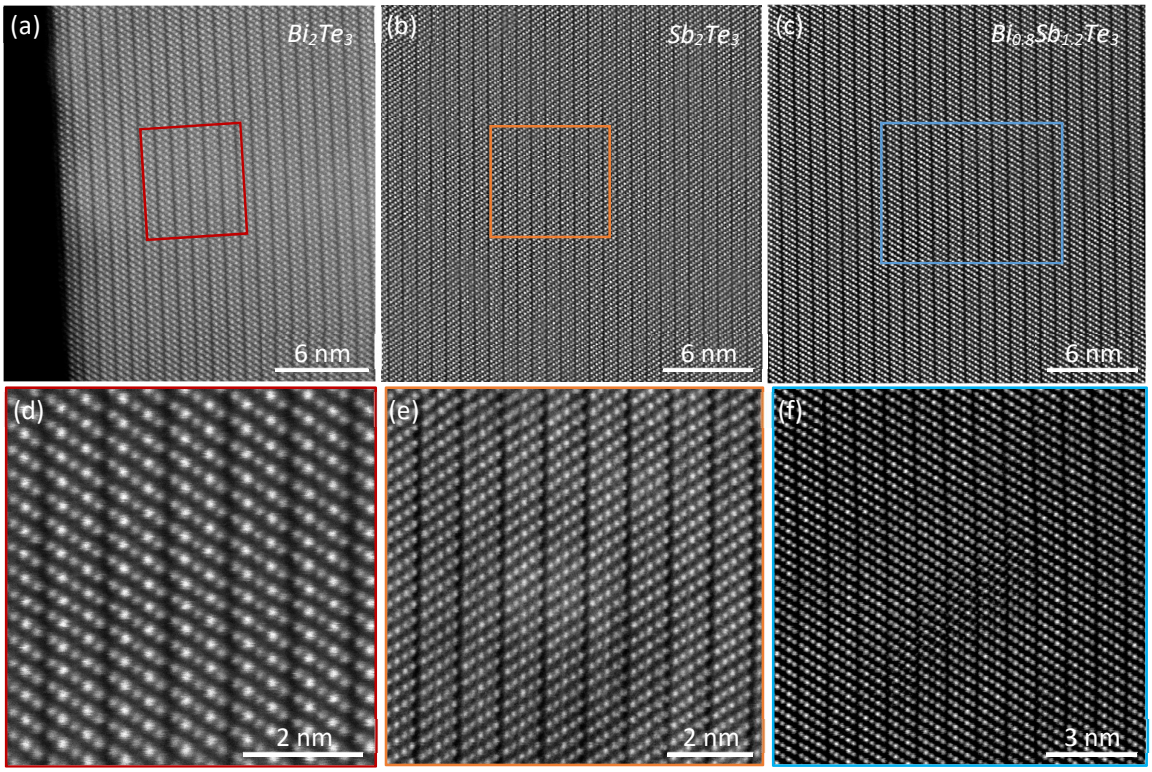

Fig. 3.14: STEM-HAADF images of selectively grown 3D TIs acquired at the cross-section of 200 nm wide nanoribbons along Si [1-10] projection. (a) Defect-free and relaxed stacking of Bi_2Te_3 QLs are evident while (d) represents the enlarged area marked in (a). Similarly (b and e) represent Sb_2Te_3, while (c and f) depict defect free structure of $Bi_{0.8}Sb_{1.2}Te_3$ QLs.

In this study, the pre-patterned substrate are fabricated with trenches ranging in width from 10 µm down to 30 nm. The growth rate for the best crystal integrity in the nanostructures (R_{NS}) is adopted to fulfill the rate requirements of all pattern dimensions and therefore, based on L_D of Bi_2Te_3, Sb_2Te_3 and BST alloy of approx. 12 nm, 20 nm and 16 nm respectively, R_{NS} for SAE of each material system are evaluated. R_{NS} is the evaluated equivalent R_{TF} for a specific trench width (R_{NS} = R_{TF} at a specific width) when R_{eff} = 5 nm/h. For this purpose, the trench width of 150 nm is chosen as a standard for Bi_2Te_3 while due to relatively high

value of $L_{D\text{-}Sb}$ in Sb_2Te_3 and BST alloy, the standard width is selected as 100 nm. R_{NS} for all 3D TIs is calculated (equation 3.11 is specific for Bi_2Te_3) and the resulting values of R_{eff} for the key dimensions are listed in Table 3.2.

$$R_{eff} = R_{TF}\left(1+\frac{2L_D}{W}\right) \quad \rightarrow \quad 5 = R_{NS}\left(1+\frac{2\times 12}{150}\right) \text{ for } Bi_2Te_3 \tag{3.11}$$

Due to quite narrow dimensions, structural investigations of the crystal in nanostructures is not possible with XRD and is only limited to STEM investigations. After the evaluation of optimum values of R_{NS} for all TIs (Table 3.2), SAE of topological nanostructures is performed. Highly selective and smooth epilayers of nanostructures containing Bi_2Te_3, Sb_2Te_3 and BST alloy can be observed via SEM images depicted in Figure 3.13a, b and c respectively. Later, STEM investigations are carried out at the cross-section of 500 nm wide nanoribbons of each TI material. Figure 3.14 depicts HAADF images of Bi_2Te_3 (a, d), Sb_2Te_3 (b, e) and BST alloy (c, f) acquired along Si [1-10] projection where the high crystal quality of nanostructures without any structural defects and dislocations, is evident.

3.6 Electronic characterization of topological nanostructures

Finally, the electronic characterization of the topological nanostructures is performed via magneto-transport investigations. The magneto-transport is a very vast field of electronic characterization that facilitates diverse analysis techniques with various structural designs.

The in-depth transport investigations of various topological nanostructures are performed; however, they are not the subject of discussion in this study. Here, a short summary of major results is presented to compare different material systems with the help of overall carrier concentration (η) and the relative contribution of TSS. In order to analyze topological materials, the following three types of measurements are performed.

- Hall effect (electronic characteristics of the material system)
- Topological switching via steering effect of resistance in multi-terminal junctions (T and Y junctions to identify the contribution of TSS)
- *Aharonov–Bohm* (AB) oscillations[8, 68, 69] in a single O-ring and array structures (to identify the contribution of TSS)

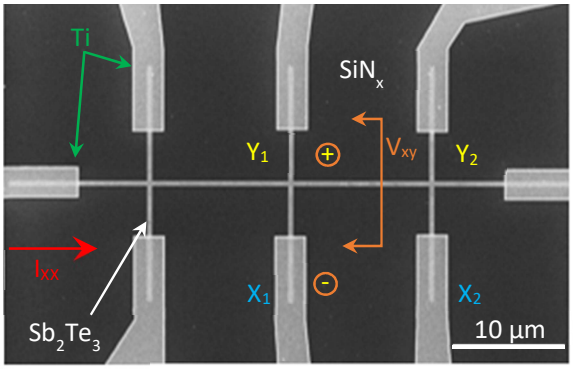

Fig. 3.15: SEM image depicting 1 µm wide selectively grown Hallbar of Sb_2Te_3 with Ti electrodes. X_1 and X_2 are the input longitudinal terminals with I_{XX} applied current between the vertical outer contacts. Hall voltage is measured between terminals Y_1 and Y_2.

3.6.1 Hall effect

The Hall effect arises due to the deflection of moving charge carriers because of the *Lorentz* force in an applied magnetic field where the periodic oscillations in the resistance can be observed because of the quantization of energy levels[69, 70]. The Hall measurement are performed to evaluate the electronic properties of topological materials. The details of measurement setup and the relevant theoretical background can be found in an earlier reported study i.e. Weyrich *et al.*[70] Various selectively grown Hallbars of 3D TIs (Bi_2Te_3, Sb_2Te_3 and BST alloys) having widths (W) of 50 nm, 100 nm, 200 nm, 500 nm, 1 µm and

10 µm are investigated. The summary of the performed measurements and the analysis with an example of 1 µm wide hallbar of Sb_2Te_3 is discussed below.

- The longitude resistance R_{xx} is measured between terminal X_1 and X_2 according to Figure 3.15 where the temperature dependent magnetoresistance is observed (Figure 3.16a) along with the weak anti-localization (WAL) effect at low magnetic fields of ± 1T (Figure 3.16b). WAL is a quantum correction to the classic conductance that is caused by self-interference of charge carriers when they are coherently scattered in such a way, that they return to the same position after many scattering events. WAL can be observed in systems exhibiting strong spin-orbit coupling (SOC)[70]. The sheet resistance (R_{sheet}) is also evaluated using equation 3.12 and is plotted in Figure 3.16c.
- Utilizing Hikami-Larkin-Nagaoka (HLN) model[70] described in equation 3.13, WAL data is fitted and the phase coherent length (l_Φ) of charge carriers and factor (α) are evaluated and plotted in Figure 3.16d.
- Transverse voltage V_{xy} is measured between terminal X_1 and Y_1 (according to Figure 3.15) and the Hall resistance ($R_{xy} = R_H$) is plotted in Figure 3.16e. Using equation 3.14, the Hall constant (A_H) and the 2D charge carrier density (η_{2D}) are extracted. As the obtained η_{2D} does not take the sample thickness (d) into account, 3D carrier concentration (η_{3D}) and mobility (μ) are evaluated using equation 3.15 and 3.16 respectively.

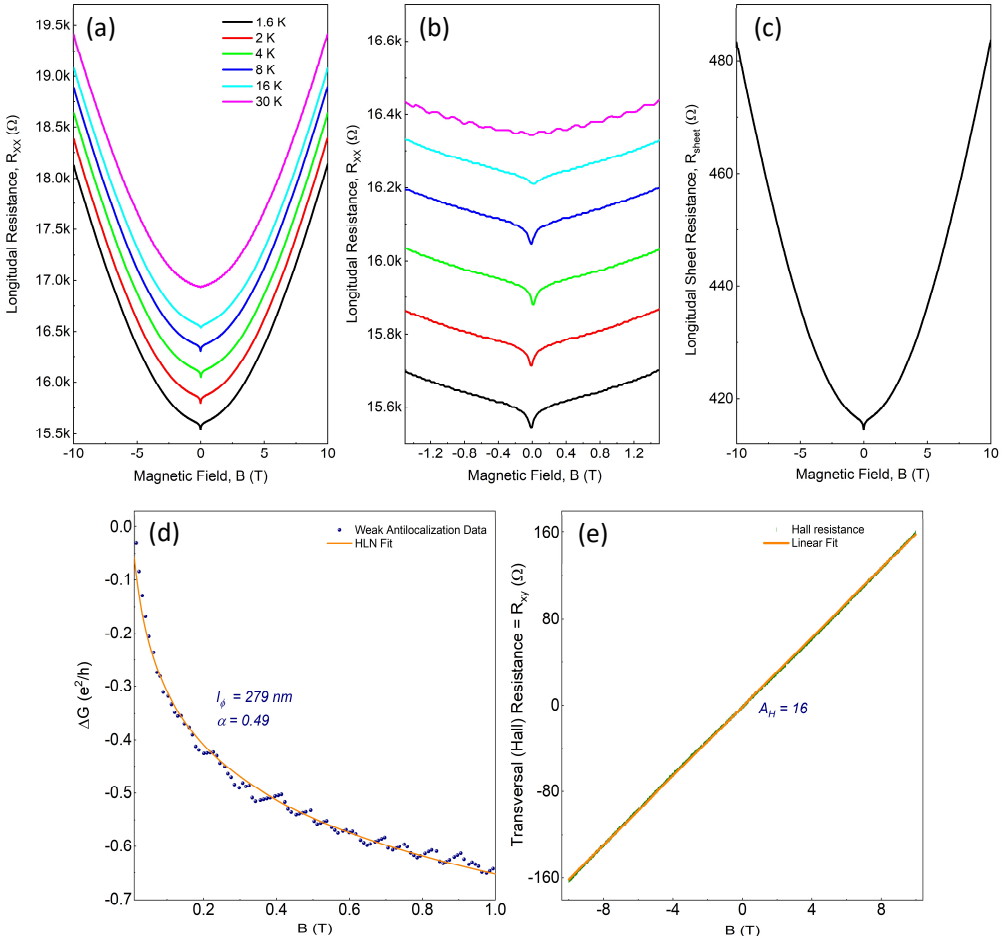

Fig. 3.16: Hall measurement data. (a) Temperature dependent trend in longitudinal resistance (R_{xx}) vs. applied magnetic field (B). (b) Temperature dependent trend of weak anti-localization in R_{xx} at lower magnetic fields. The oscillations at 30 K appear due to the fluctuations in the PID loop of the heater. (c) Sheet resistance at base temperature of 1.6 K. (d) Exemplary HLN fitting of weak anti-localization to extract l_Φ and α. (e) Hall resistance vs. applied field to extract Hall constant (A_H) in order to evaluate mobility (μ) and carrier concentration (η_{2D}) of the material system.

$$R_{she} = R_{xx}\frac{W}{L} \tag{3.12}$$

Here, W and L are the width and the length of the Hallbar respectively.

$$\Delta G_{HLN}(B) = -\alpha\frac{e^2}{2\pi^2\hbar}\left[ln\left(\frac{B_\phi}{B}\right) - \Psi\left(\frac{1}{2}+\frac{B_\phi}{B}\right)\right] \tag{3.13}$$

Here, ΔG_{HLN} is the measured change in the magneto-conductance, whereas α is a pre-factor that determines the strength of the magnetic coupling. A value of α = 0.5 represents one TI channel. Every additional channel will result in an addition of 0.5. B_ϕ is the magnetic field associated with the phase coherence length via $B_\phi = \frac{\hbar}{8e\pi B l_\phi}$ while Ψ represents the digamma function.

$$R_H = R_{xy} = \frac{V_H}{I_{xx}} = A_H\frac{B_z}{d} \quad \rightarrow \quad A_H = \frac{1}{q\eta_{2D}} \tag{3.14}$$

Here, R_H and V_H are the Hall resistance and Hall voltage. I_{xx} is the longitudinal/applied current, B_z is the applied out-of-plane magnetic field and d is the thickness of the sample. A_H represents the Hall constant, q is the universal charge while η_{2D} and η_{3D} represent 2D and 3D charge carrier density respectively.

$$\eta_{3D} = \frac{\eta_{2D}}{d} \tag{3.15}$$

$$\mu = \frac{A_H}{R_{she}} \tag{3.16}$$

Discussion: Following the above mentioned scheme, samples of various dimensions belonging to all Te based 3D TIs are investigated. The results obtained from each category of the samples are summarized in Table 3.3 and the best results are highlighted. The key observations are discussed below:

- Unexpectedly, despite the fact of achieving high crystal quality selectively grown topological nanostructures, high carrier concentration in Hallbars belonging to each material system is observed where the lowest carrier density is witnessed in Bi_2Te_3 nanostructures with approx. 2 x 10^{19} cm^{-3}.
- In BST alloys, the carrier density is supposed to be further improved from Bi_2Te_3 due to the neutralization effect of p- and n-type carriers exhibited by Sb and Bi respectively; however, the carrier concentration measured in BST epilayer is found to be higher than Bi_2Te_3.
- Though, the overall carrier density is improved by almost 1 order in comparison to earlier reports including Lanius *et al.*[51] and Weyrich *et al.*[70] with the utilization of SAE and the *in situ* surface passivation. Still, the unexpected high carrier density in all material systems including BST alloys indicate the problem must reside somewhere other than the topological epilayers themselves. The issue may arise from the substrate or at the interface between Si-TI epilayers. In order to evaluate this problem, the structural investigations and the magneto-transport analysis of the substrate-TI interface is conducted with the growth of BST epilayers on another substrate and a comparison with Si (111) is conducted. The details can be found in chapter 6 (Section 6.3.3).
- A noticeable difference in carrier density among the *in situ* capped (passivated) and the non-capped samples is observed (Table 3.3).
- An important feature about the phase coherent length (l_Φ) of charged particles in Bi_2Te_3 epilayers is observed to be linked with the misorientation angle of Si (111) surface. As discussed earlier, Bi_2Te_3 epilayer forms an antiphase domain at the Si step edge. It seems that the antiphase domain acts as a barrier and limit l_Φ of the charged particles. An example of this behavior can be observed in Table 3.3 where two Bi_2Te_3 Hallbars of same dimensions are prepared with similar growth parameters on different surfaces quality (miscut angle), have exhibited different results. The Hallbar prepared at the substrate with 0.5° miscut angle exhibited l_Φ = 63 nm while, the other Hallbar belonging to substrate with the misorientation angle of 0.1° exhibited l_Φ = 230 nm. These

values are matching perfectly with the terrace length of periodic steps at Si (111) surface corresponding to the miscut angle. The terrace length has also been confirmed via AFM and depicted in Figure 2.17 (Chapter 2). This trend is witnessed in all Bi_2Te_3 samples; however, it does not seem to impact Sb_2Te_3.

Table 3.3: The summary of all material parameters extracted from Hall measurements. MR represents the percentage change in the magnetoresistance in R_{XX} between B = 0 T and B = 10 T.

Topological Material	Carrier	Width (nm)	η_{2D} (x 10^{13} cm^{-2})	η_{3D} (x 10^{19} cm^{-3})	l_Φ (nm)	μ (cm^2 /Vs)	Si Miscut Angle (˚)	MR @ 10 T (%)	Comments
Bi_2Te_3	n-type	10,000	6.2	4.3	324	213	0.07	89	*In situ* capped
		1,000	9.4	7.8	154	124	0.2	54	-
		500	4.1	2.3	230	324	0.1	98	*In situ* capped
		500	6.9	8.6	63	136	0.5	38	*In situ* capped
		200	5.9	4.1	232	315	0.1	93	*In situ* capped
		100	3.9	2.5	234	342	0.1	88	*In situ* capped
		50	3.4	2.2	231	312	0.1	87	*In situ* capped
Sb_2Te_3	p-type	10,000	7.2	5.3	418	442	0.1	64	*In situ* capped
		1,000	10.8	8.4	279	246	0.5	21	-
		1,000	7.7	5.4	364	386	0.2	42	*In situ* capped
		500	11.3	9.8	214	220	0.5	36	-
$Bi_xSb_{2-x}Te_3$	-	10,000	7.9	5.4	212	386	0.2	54	*In situ* capped
		1,000	10.3	8.9	109	156	0.5	28	-
		1,000	8.7	6.9	169	212	0.2	44	*In situ* capped
		500	11.1	9.5	98	87	0.5	23	-

Surface transport investigations via SdH and AB oscillations: All the measured parameters listed in Table 3.3 describe the bulk electronic characteristics of materials. The surface transport contribution can only be witnessed with advanced analysis techniques. TSS can be simply envisioned as a 2-dimensional electron gas (2DEG) with a special property that electrons experience spin-momentum locking and *Dirac* dispersion. Their presence and contribution in the electronic transport can be identified with the presence of periodic oscillations in the resistance profile with the out-of-plane applied magnetic field. This phenomenon is known as *Shubnikov-de Haas* (SdH) effect[70]. SdH oscillations are witnessed in 500 nm wide Hallbar of Bi_2Te_3 where the detailed analysis is performed and reported in Rosenbach *et al*.[6] However, in 200 nm, 100 nm and 50 nm wide structures SdH oscillations are not witnessed due to the absence of TSS as the structures entered into the quasi-1D regime.

In narrow structures, the Berry phase at the cross-section of the nanoribbon becomes trivial as soon as the perimeter of the nanoribbon becomes < $2l_\Phi$. This regime is known as quasi-1D and results in opening the gap and diminishing TSS as depicted in Figure 3.17a. As listed in Table 3.3, l_Φ = 230 nm for Bi_2Te_3, this results in 500 nm wide structures to be topological while 200 nm and below structures fulfill the requirement of quasi-1D regime and lose topological protection. That is why, SdH oscillations are not witnessed in any structure smaller in width than 500 nm. The gap in quasi-1D structures can be closed again with the appearance of TSS by applying the in-plane field (B) equivalent to the flux $\varphi/2$ as depicted in Figure 3.17 where φ depends upon the cross-sectional area (A) of the nanoribbon and can be calculated using equation 3.17[8, 68, 69].

$$\varphi = A \times B \tag{3.17}$$

As soon as the in-plane applied field fulfills the requirements and the flux becomes equivalent to $\varphi/2$, the evidence of TSS can be witnessed through periodic quantum interference effects (oscillations in resistance profile). This phenomenon is known as *Aharonov–Bohm* (AB) oscillations[8, 68, 69] and can be observed in

nanostructures where the surface to volume ratio is high enough to overcome the bulk contributions and manifest surface effects. As mentioned above, structures with width of 200 nm and below exhibited quasi-1D effects. With the applied in-plane magnetic field, AB oscillations in 200 nm, 100 nm and 50 nm wide nanoribbons, with a distinct frequency matching the corresponding cross-sectional areas of the structures, are witnessed. The details of AB oscillations analysis in all the structures is reported in Rosenbach *et al*[6].

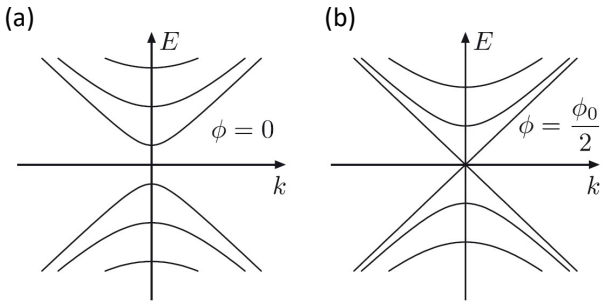

Fig. 3.17: (a) The nontrivial Berry phase causes a gap at zero flux in a TI nanowire (quasi-1D). (b) Applying a flux of φ/2 restores the gapless mode. (Taken from [8])

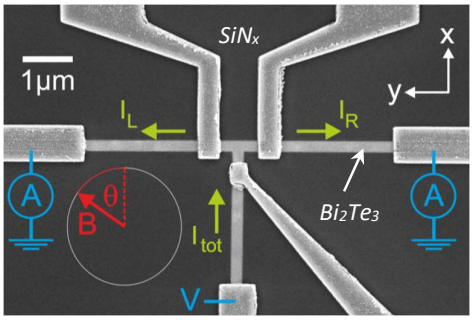

Fig. 3.18: SEM image of selectively grown T junction of Bi_2Te_3 representing the basic measurement setup where I_{tot} represent the total current flowing from the central leg. I_L and I_R represent the individual currents in left and right legs where the current variations are measured with the changes in the applied field orientation.

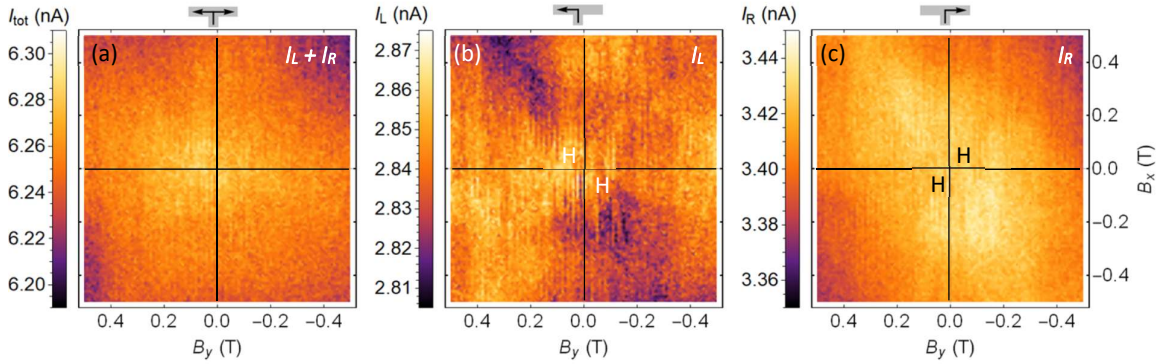

Fig. 3.19: Currents through the T-shaped tri-junction as a function of in-plane magnetic field components. (a) The current is measured from the bottom leg to both output legs and individually to the left leg (b) and right leg (c). The coordinates exhibiting higher resistance are identified with letter "H". The sketches on top of the plots indicate the current paths. The difference in leg resistance can be observed in the opposite diagonal coordinates for I_L and I_R where H represents the high resistance zone.

3.6.2 Resistance steering effect in multi-terminal junctions

A unique phenomenon in a quasi-1D multi-terminal nanoribbon structure where the surface current exhibits dependency on the in-plane magnetic field orientation with a distinct steering pattern was proposed by Moors *et al.*[10] In order to confirm this proposed phenomenon of TSS, a multi-terminal T-junction is prepared via SAE as depicted in Figure 3.18 where the effect of current steering with the in-plane magnetic field orientation is investigated. It has been observed that with changing the orientation of

in-plane field, this current steering originates from the orbital effect, trapping the coherent 3D TI surface states in the different legs of the junction on opposite sides of the nanoribbon and breaking the left-right symmetry of the transmission across the junction. The detailed analysis of the observed distinct pattern of the current steering is reported in Kölzer *et al.*[11] An examples of distinct current pattern belonging to different legs of the junction in diagonal coordinates can be observed in Figure 3.19b and c. An important point to notice here is the heavy suppression of the steering effect due to high density of trivial bulk carriers (4×10^{19} cm^{-3}) that do not exhibit steering rather enhance the background noise of the measured effect.

3.6.3 Aharonov–Bohm (AB) oscillations in the ring structures

AB oscillations measured in quasi-1D nanoribbons of Bi_2Te_3 with the in-plane applied field are discussed in Section 3.6.1. Here, a different geometrical structure in form of a ring, depicted in Figure 3.20, is fabricated to investigate AB oscillations in the perpendicular (out-of-plane) applied field. As mentioned above that AB oscillations can only be observed in a structure when the length of interference path $< 2l_{\Phi}$. In ring structures, this path is equivalent to the half of circumference of the ring radius.

The ring structures of BST alloy with various sizes are prepared via SAE and the investigations are performed[71]. An example of selectively grown BST ring structure with 50 nm radius is depicted in 3.20a. Among all the samples, only two structures with radii 50 nm and 70 nm have fulfilled the requirement of phase dependent quantum interference and therefore, in both structures two distinct frequencies in the Fourier spectrum of magneto-conductance measurements are observed. The observed oscillation and the FFT spectrum of 50 nm ring are depicted in Figure 3.20 (b-c). The peak values can be translated back to certain radii within the finite width of the ring. For both rings a peak at the frequency corresponding to the inner surface as well as a peak at the frequency corresponding to the mean path (mean radius, middle of the ring) are observed. The frequency of the oscillation corresponding to the inner surface can be attributed to an interference of electrons occupying TSS on the inner side of the ring, whereas the other peak can be attributed to a bulk contribution. The details about the experimental setup and measurements can be found in Behner *et al.*[71] A comparative analysis, with the help of AB oscillations in ring structures, between BST alloy (STI) and Bi_1Te_1 (WTI) is conducted in chapter 4 (Section 4.9).

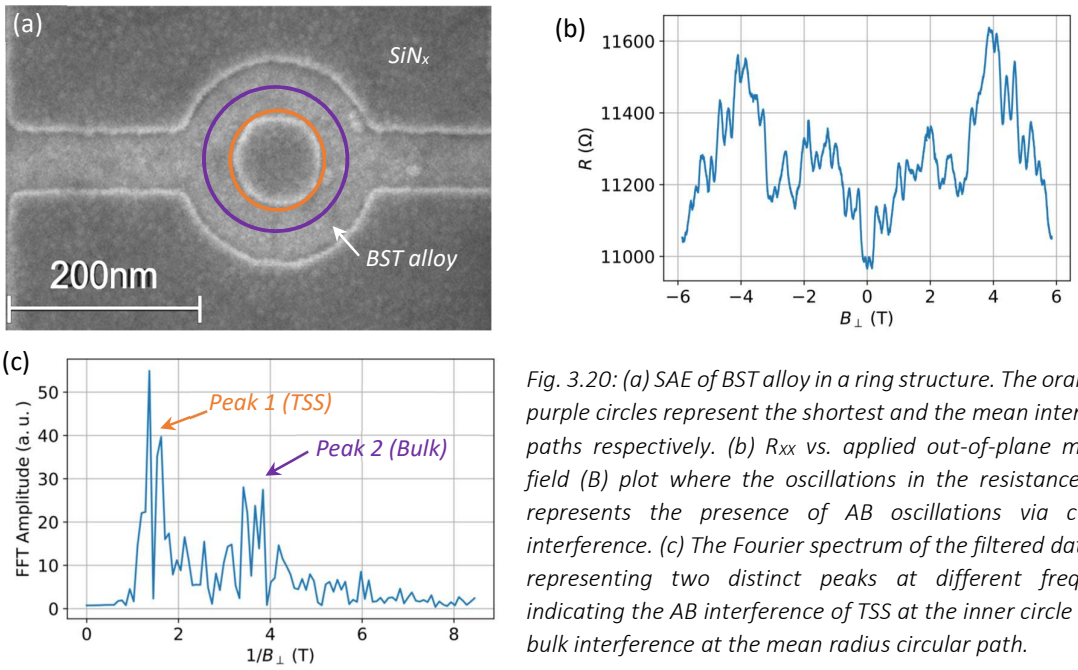

Fig. 3.20: (a) SAE of BST alloy in a ring structure. The orange and purple circles represent the shortest and the mean interference paths respectively. (b) R_{XX} vs. applied out-of-plane magnetic field (B) plot where the oscillations in the resistance profile represents the presence of AB oscillations via coherent interference. (c) The Fourier spectrum of the filtered data of (b) representing two distinct peaks at different frequencies indicating the AB interference of TSS at the inner circle and the bulk interference at the mean radius circular path.

With the help of magneto-transport investigations, the electronic characterization of 3D TIs is performed. The presence of unexpected high density of bulk carriers is a massive drawback that heavily suppressed the contribution of TSS; however, the high crystal quality of topological nanostructures have allowed to observe several unique and distinct effects of TSS in form of SdH and AB oscillations along with the steering effect in multi-terminal junctions. With the attenuation of high concentration of trivial (bulk) carriers, the exotic effects, offered by TSS would, be more pronounced.

3.7 Summary

This chapter is dedicated to the development of a scalable nano-architecture to fulfill the demands of integratable and pristine nanostructures with adaptable dimensions. Utilizing CMOS compatible fabrication technology, Si (111) substrates with crystalline and amorphous combinational surfaces are prepared. The development of PECVD SiN_x to be resistant in HF based solutions has enabled the realization of blocking surfaces and subsequently, the patterned substrates. The fabrication challenges in the patterned substrates and the strain related issues in the combinational blocking surfaces are systematically addressed. Later, the optimum growth parameters (T_{sub} and R_{TF}), extracted from the high quality planar growths of 3D TIs, are subjected to the pre-patterned substrates. The technique of SAE has facilitated the achievement of high quality selectively grown structures at the macroscale (> 1 µm); however, the nanostructures have exhibited the high defect density. The encountered challenges of crystal defects in selectively grown nanostructures are addressed with the development of a specialized growth model. This model, by incorporating the pattern dimensions into account, has provided control over the effective growth rate (R_{eff}) of the crystal, and in succession, has facilitated the preparation of defect-free structures at the nanoscale. Atomic scale structural characterizations conducted on selectively grown topological nanostructures have confirmed the high-quality of the grown crystals. Moreover, the magneto-transport investigations have revealed the improved electronic properties of 3D TIs, particularly the bulk carrier density (2 x 10^{-19} cm^3) is observed to decrease by almost 1 order, compared to the earlier reports (5 x 10^{-20} cm^3)[44, 51, 70, 72, 73]. Though, the improved results are obtained, the observed carrier density is still at least 2 orders higher than the utilizable conditions (10^{-17} cm^3)[74, 75] for most of the advanced quantum applications. This deficiency in electronic properties could not be associated to the crystal quality of 3D TIs, as almost defect-free nanostructures are realized. Despite the limitation of high density of trivial bulk carriers, distinct phenomena in magneto-transport due to the presence of TSS including the weak anti-localization (WAL) effect, the Shubnikov-de Haas (SdH) and the Aharonov–Bohm (AB) oscillations, and the resistive steering effect are witnessed. The observation of these effects can be associated to the high crystal quality of the selectively grown topological nanostructures and the *in situ* passivation of surfaces that prevented them from oxidation and other aging effects. The realization selectively grown nanostructures with adaptable dimensions and scalable architecture has facilitated the fabrication of complex quantum devices with pristine and high quality layers of 3D TIs which was not easily attainable in the past.

Chapter – 4
Topological-Trivial Heterostructures: Bi_xTe_y Stoichiometric Family

The topological state of a 3D material can be modified using the technique of topological phase transformation[2], introduced in chapter 1 (section 1.2). Applying this technique via stoichiometric tuning[3], various compositional alloys consisting of "*base"* (topological) and *"additive"* (trivial) heterostructures can be prepared. The stoichiometry of such materials can be tuned by controlling the relative contents of "*base*" and "*additive*" that assist in engineering the electronic band structure of the alloy to achieve novel 3D topological phases. Among them, one of the most desired phase is the topological Dirac semi-metal (TDSM) that can be engineered if the "*base*" material exhibits the topology of weak topological insulator (WTI) or topological crystalline insulator (TCI), introduced in section 1.2 (Figure 1.8). None of the conventional 3D TIs exhibit WTI phase; however, Bi_2Te_3 is the only member of 3D TIs that exhibit dual topology[4] i.e. TCI features along with the strong topological insulator (STI) phase. This phenomenon renders Bi_2Te_3 to utilize in topological-trivial heterostructures to engineer TDSM phase.

The one possibility of achieving topological transformation of Bi_2Te_3 is via Bi_xTe_y stoichiometric alloys where Bi_2Te_3 quintuple layer (QL) and Bi_2 bilayer (BL) act as "*base*" and "*additive*" respectively. Bi_xTe_y alloys exist naturally in form of $(Bi_2)_m(Bi_2Te_3)_n$ superlattices where (m:n) represents the relative abundance of BLs and QLs respectively. These alloys attract a lot of attention and curiosity of material scientists and physicists for their utilization in future applications. The importance of this stoichiometric family can be estimated from the experimentally proven and theoretically predicted topological phases from STI to WTI[3], TCI[3, 4] to HOTI[5, 6] and TSM[7].

Bismuth (Bi_2 BL) as an "*additive*" is not truly a trivial neither purely a topological material. According to Z_2-classifications, bismuth is trivial with invariants $0;(000)$ and does not exhibit 3D topological states protected by time-reversal symmetry (TRS). However, recent studies have shown the crystal symmetry (CS) protected 1D helical hinge states in Bi_2 crystals[8] i.e. the higher-order topological insulator (HOTI) phase, observed via STM at ultra-low temperatures[6, 9]. Still, in bulk bismuth is categorized as a trivial material and therefore, is utilized as an "*additive*" in this study. Due to well-known thermoelectric properties of Bi chalcogenides[10], some members of the Bi_xTe_y stoichiometric series have already been prepared via zone melt, Bridgeman method[10, 11, 12], sputter deposition[7], PLD[13] and MBE[3]. During the preparation of Bi_xTe_y alloys for thermoelectric applications, the exact stacking sequence of QLs and BLs in a particular stoichiometric state, is not important as the only purpose is to alter the composition[11]. In the topological transformation; however, it is critically important for the particular stoichiometric state to exhibit the corresponding stacking sequence periodically to ensure the CS. The importance of CS in a material can be estimated from the recent studies that indicate a higher tendency of a crystal to host HOTI phase[5, 6, 9, 14, 15] if it exhibits TCI features. This can be quite challenging to control via MBE as Bi_xTe_y crystals, depending upon the relative presence of Bi contents, naturally arrange themselves in an arbitrary order without any particular stacking sequence.

This chapter is dedicated to study the growth feasibility of $Bi_xTe_y = (Bi_2)_m(Bi_2Te_3)_n$ stoichiometric states via MBE. To investigate the individual topological phases of these alloys via ARPES is beyond the scope of this work. The aim is to conduct a systematic study on the epitaxial growth of Bi_xTe_y alloys on planar Si (111) substrates, to investigate the extent of possibilities in tuning the composition (how precisely stoichiometry can be tuned), the periodicity of the stacking sequences and the stability/reproducibility of these stoichiometric states. In order to do so, the detailed structural characterizations of the grown epilayers are

performed via XRD and the stacking sequences are confirmed via STEM. The stoichiometric tuned parameters are then subjected to the pre-patterned substrates and via SAE, the defect-free nanostructures are fabricated. Thus, when required, any targeted stoichiometry (the desired 3D topology) can be incorporated into the nano-architecture to fabricate the quantum devices.

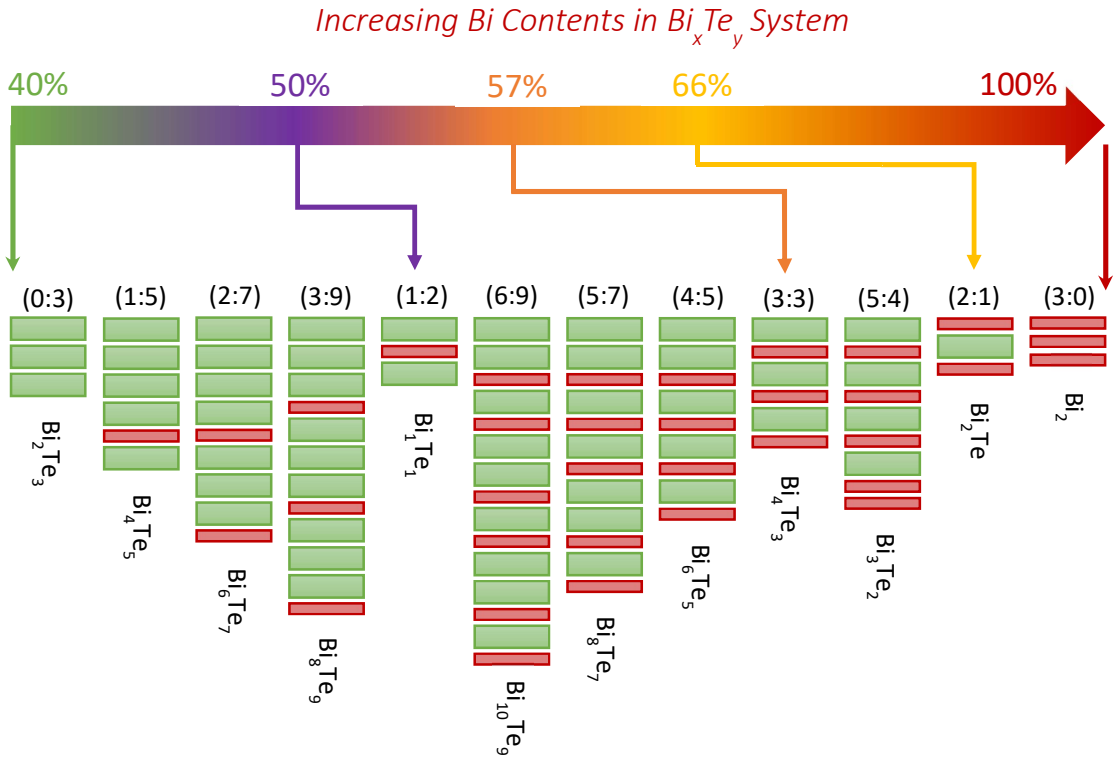

Fig. 4.1: An overview of unit cells representing $Bi_xTe_y = (Bi_2)_m(Bi_2Te_3)_n$ key stoichiometric states along with the stacking sequences. Difference in the color of blocks represents the change in layer architecture where the green block indicates the presence of Bi_2Te_3 QL while the red block represents a Bi_2 bilayer. On top of the stacking sequences of each stoichiometry, the relative presence of BLs and QLs are indicated by the values (m:n).

4.1 Bi_xTe_y: Layer architecture and nomenclature

Bi_xTe_y family is a layered based system supported by vdW interactions that exhibits a unique phenomenon of keeping the layer architecture of "*base*" and "*additive*" intact unlike other layer based stoichiometric systems such as GST/GBT[16, 17, 18, 19, 20, 21, 22] and MST/MBT[23, 24] alloys, where "*base*" and "*additive*" lose their individual layer structure, amalgamate and form new compound layers (for details visit chapter 5). As mentioned above, Bi_xTe_y stoichiometric states naturally arrange themselves in $(Bi_2)_m(Bi_2Te_3)_n$ superlattices where any stoichiometry can be identified by (m:n)[25] = (number of BLs: number of QLs) in a unit cell of that specific alloy as depicted in Figure 4.1 along with the corresponding stacking sequences. Some of Bi_xTe_y alloys were studied by the thermoelectric community[10] were primarily synthesized using the Bridgeman method[10, 11, 12] that occasionally did not exhibit the periodic stacking sequences (mixed states). Due to this reason, Bi_xTe_y alloys are identified by different nomenclature in the literature. These nomenclature include:

- ***Normalized unit cell***[25]***:*** This is the most common form that identifies the formula unit or characteristic unit cell for example Bi_2Te_3, Bi_1Te_1 and Bi_4Te_3 etc.
- ***Entire unit cell***[26, 27]***:*** This is the least common form used; however, it helps to identify the total number of BLs and QLs in the unit cell. For example Bi_2Te_3 would be named Bi_6Te_9 (3QLs), Bi_1Te_1 as Bi_6Te_6 (2QLs + 1BL) and Bi_4Te_3 as $Bi_{12}Te_9$ (3QLs + 3BLs).

- ***Atomic fraction***[26, 28, 29]***:*** This is the second most common form that mostly used when the crystal contains mixture of two or more stoichiometric states (non-periodic stacking sequences). It identifies the relative contents of elements in the crystal. For example Bi_2Te_3 would be named $Bi_{40}Te_{60}$, Bi_1Te_1 as $Bi_{50}Te_{50}$ and Bi_4Te_3 as $Bi_{57}Te_{43}$.

4.2 Epitaxy & stoichiometric analysis of Bi_xTe_y alloys

The growth of any Bi_xTe_y stoichiometric state demands the incorporation of Bi_2 BL in the layer stack. This can be acquired with the increment in Bi/Te flux ratio to enrich Bi contents in the crystal that would lead to the formation of Bi_2 BL. The tuning of Bi/Te flux ratio can be achieved with two different approaches discussed below. Both approaches have their pros and cons.

- Approach 1: Increasing Bi flux while Te flux and T_{sub} are kept constant.
- Approach 2: Decreasing Te flux while Bi flux and T_{sub} remained unchanged.

Approach 1: In the MBE growth process, the individual beam fluxes are controlled by adjusting the effusion cell temperatures of the corresponding elements. The search for stoichiometric alloys is conducted with the first approach where Bi/Te flux ratio is tuned by increasing the Bi flux (T_{Bi}) during epitaxy while the Te flux is kept constant. In order to do so, T_{Bi} is gradually increased from 470 ℃ (parameters extracted from Bi_2Te_3 optimized growth in chapter 2) while T_{Te} and T_{sub} are kept constant at 320 ℃ and 300 ℃ respectively.

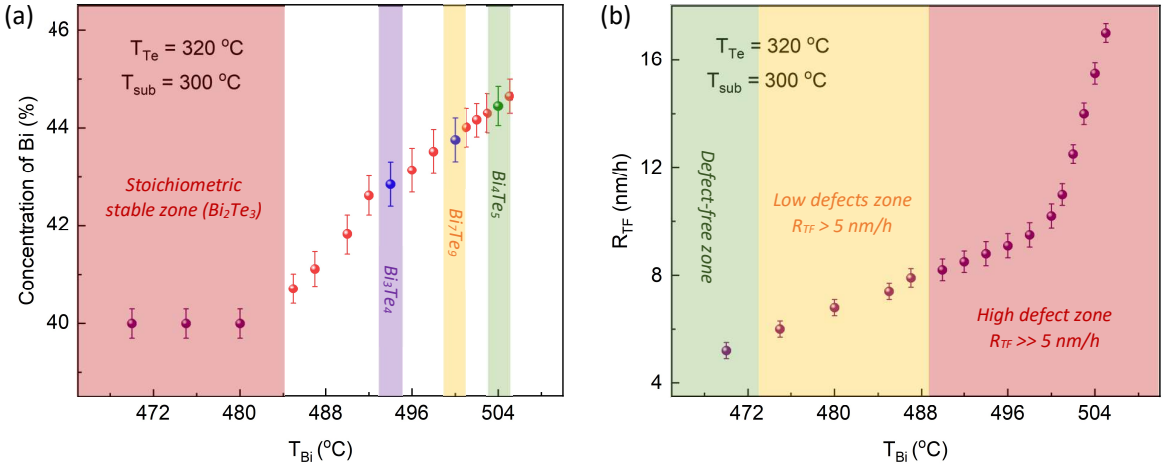

Fig. 4.2: The search for Bi_xTe_y stoichiometric states with the variable parameters T_{Bi}. (a) The trend of increasing Bi contents in the epilayer with the increment in the applied Bi flux (T_{Bi}) can be observed. After T_{Bi} = 485 ℃, the presence of Bi bilayer with the increased Bi contents in the epilayer is evident. The Bi contents in the epilayer are measured via RBS. (b) The corresponding change in the thin film growth rate (R_{TF}) of the epilayer with the increasing T_{Bi}, measured via XRR.

It was established in chapter 2 that thin film growth rate (R_{TF}) is solely controlled by Bi flux and Te flux does not have any influence on it. That is why, during the growth of 3D TIs, Te flux is always kept relatively higher than the required ratio to avoid Te thermal vacancies (V_{Te}) in the epilayer. Starting from the base state of Bi_2Te_3 at T_{Bi} = 470 ℃, with the gradual increment in T_{Bi} (Bi flux) the corresponding R_{TF} of the epilayer kept on increasing while Bi contents in the epilayer remained constant with the stoichiometric state of Bi_2Te_3 (Bi = 40 %). This phenomenon can be explained by the availability of auxiliary Te atoms that were present due to the additional Te flux applied to keep Te vacancies at minimum. The incoming Bi atoms kept on using the excess Te until the Bi flux reached a critical point at T_{Bi} = 485 ℃ where the availability of Te atoms was not sufficient to form a QL. Eventually, extra bismuth adatoms formed a Bi_2 BL and the formation of stoichiometric alloys started (see Figure 4.2). With further increment in T_{Bi}, the density of Bi_2 BL in the film

started to increase. Hence, by controlling Bi/Te flux ratio using the first approach, the desired stoichiometry can be achieved.

Figure 4.2a depicts the observed trend of Bi fraction in the epilayer due to appearance and increasing density of Bi_2 BLs in the layer stack. The bismuth contents in the epilayer are measured via *Rutherford backscattering spectroscopy* (RBS) where T_{Bi} is systematically increased. As soon as T_{Bi} reached 485 ℃, the presence of first Bi_2 BL in the layer stack is identified with the sudden increment in Bi contents. It is also observed with the slight shifts in XRD 2θ-ω characteristic peaks of Bi_2Te_3. With the continuous increment in T_{Bi}, the density of Bi_2 BLs in the layer stack kept on increasing until a BL periodically appeared after eight QLs at the applied T_{Bi} = 495 ℃. At this point $(Bi_2)_m(Bi_2Te_3)_n$ with (m:n) = (1:8) resulted the stoichiometric state of Bi_3Te_4, identified in Figure 4.2a. Similarly, with the further increment in T_{Bi} other stoichiometric states, having higher Bi contents, are also obtained. The corresponding trend in R_{TF} with the increasing T_{Bi} is depicted in Figure 4.2b.

Following the first approach, several stoichiometric states including Bi_3Te_4, Bi_7Te_9 and Bi_4Te_5 are successfully achieved as identified in Figure 4.2a but two main challenges hindered the growth quality and the reproducibility of these states. These challenges include the unintentional high R_{TF} and the compositional stability of the stoichiometric alloy.

- T_{Bi} controls R_{TF} in Bi_2Te_3. It has been established that all epitaxial growths with R_{TF} > 5 nm/h (T_{Bi} > 470 ℃) are prone to suffer from structural defects (see Figure 2.10). Bi_xTe_y states require Bi contents > 40% and, therefore, are obtained at T_{Bi} >> 470 ℃ that corresponds to R_{TF} >> 5 nm/h (Figure 4.2b). This trend also predicts further increase in R_{TF} with increasing T_{Bi} while reaching for the stoichiometric states with higher Bi contents. It would lead to the epitaxial growth of nearly all members of Bi_xTe_y with very high defect density.
- The higher R_{TF} may also disrupt the periodic stacking sequence of QLs and BLs in the epitaxial film that would result in the altered stoichiometry and in the broken/damaged crystal symmetry (CS).
- The higher R_{TF} would also lead to the failed selectivity; furthermore, the fabrication of nanostructures via SAE would not be possible.
- The reproducibility is critical for any epitaxial growth. The trend in Figure 4.2a depicts the very narrow tolerance in the Bi flux (T_{Bi}) for stable stoichiometric state. Any variation is Bi flux may lead to a stoichiometric shift that will become more problematic with the increasing T_{Bi}. It can be witnessed with the reduced stability window in Bi_4Te_5 vs. Bi_3Te_4 in Figure 4.2a. Therefore, more appropriate parameters are essential for the stable and reproducible epitaxy of these stoichiometric alloys.

In some way all of these challenges are directly linked to the high values of R_{TF}. Summarizing from the results of Figure 4.2, it can be deduced that T_{Bi} is not the correct variable to tune stoichiometry as it directly affects R_{TF}. The lower R_{TF} can only be obtained at the lower T_{Bi} and therefore, T_{Bi} must be fixed to the optimum value, extracted from Bi_2Te_3 epitaxy i.e. 470 ℃ to achieve defect free growths. Thus, using the first approach stoichiometry can be tuned; however, the defect free growth will not possible.

Approach 2: The focus is shifted to the second approach where Te flux is used as a variable parameter while Bi flux is kept constant to avoid any drastic changes in R_{TF}. This approach is expected to fix the above mentioned issues as Te flux does not affect R_{TF} and therefore, tuning stoichiometry with changing Te flux (approach 2) is more appropriate than changing Bi flux (approach 1). The Te flux unlike Bi suffers from adsorption to desorption ratio (ADR) and is heavily dependent on T_{sub}. Any change in T_{sub} would result in an altered Bi/Te flux ratio and hence, for simplicity T_{sub} must also be fixed to the optimum value. After fixing T_{Bi} = 470 ℃ (for R_{TF} control) and T_{sub} = 300 ℃ (to keep ADR constant), T_{Te} is systematically reduced from 320 ℃ to tune the Bi/Te flux ratio in search of Bi_xTe_y stoichiometric alloys.

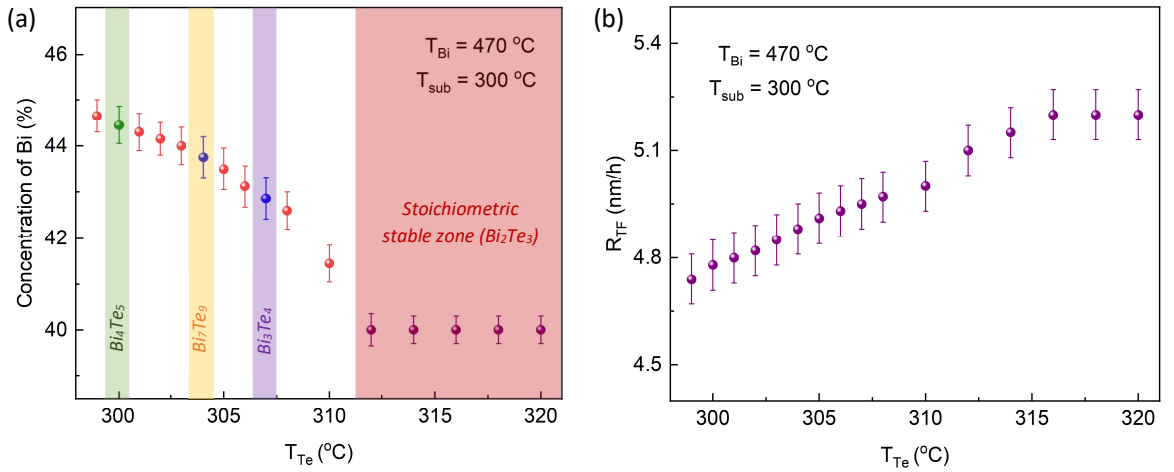

Fig. 4.3: The search for Bi_xTe_y stoichiometric states with the variable parameters T_{Te}. (a) The trend of increasing Bi contents in the epilayer with the gradual decrement in the applied Te flux (T_{Te}) can be observed. As soon as T_{Te} drops below 312°C, the presence of Bi bilayer with the increased Bi contents in the epilayer can be witnessed. The Bi contents in the epilayer are measured via RBS. (b) The corresponding change in the thin film growth rate (R_{TF}) of the epilayer with the decreasing T_{Te}, measured via XRR.

With the reduced incoming Te flux, the availability of Te atoms to form Bi_2Te_3 QL decreased and eventually extra Bi adatoms formed a Bi_2 BL. As soon as T_{Te} dropped below 312°C, the presence of Bi_2 BL is identified via RBS and XRD similar to the first approach. Figure 4.3a illustrates the trend of increasing Bi fraction in the epilayers with the gradual reduction in T_{Te}. The appearance of several stoichiometric states with the continuous reduction in Te flux is also evident. It can be clearly seen, the two major challenges that limited the first approach where T_{Bi} is used as the variable parameter to tune the stoichiometry, are now fixed with the replacement of T_{Te}. Figure 4.3b illustrates that R_{TF} always resides in the optimum range (≤ 5 nm/h) and further growth optimization to reduce the structural defects is not required. Also, the stability of the stoichiometric states is much improved as the parameter window is now more tolerant to the fluctuations in Bi/Te flux ratio. Hence, the reproducibility of stoichiometric states is not an issue anymore. Depending upon the above mentioned conclusions, the growth process of Bi_xTe_y family is conducted with a systematic approach in three different stages. These stages are divided on the basis of parameter utilized as a variable to tune the Bi/Te flux ratio and discussed in detail in the next sections. The stages are:

- Stage 1: From Bi_2Te_3 to Bi_1Te_1
- Stage 2: From Bi_1Te_1 to Bi_4Te_3
- Stage 3: Bi_4Te_3 to Bi

Each stage focuses on a group of stoichiometric alloys with key members where the epitaxial growth and the structural characterization of each member is individually performed in the following two steps.

- In the first step, the growth optimization of epitaxial thin film on Si (111) planar substrate is conducted. The stoichiometric stacking sequence based structural characterization is performed with XRD 2θ-ω scans as each member has its own characteristic diffraction peaks. The lattice parameters are evaluated using the Braggs law via XRD $2\theta/\theta$ and RSM scans. The presence of twin defects and the quality of the epilayer is investigated with φ and $\Delta\omega$ scans respectively.
- In the second step, the optimized parameters are applied to the pre-patterned substrates and SAE is performed to fabricate nanostructures. Due to limitations of XRD at the nanoscale, structural characterization is performed via STEM where the stacking sequences are identified and the lattice parameters (unit cell length, vdW gap and bond lengths etc.) are evaluated.

4.3 Stage 1: Bi_2Te_3 to Bi_1Te_1 - Epitaxy and structural characterization

The epitaxial growth of the Bi_xTe_y members performed in this stage are summarized in Table 4.1, where m and n indicate the total number of Bi_2 BLs and Bi_2Te_3 QLs in a unit cell respectively. The increasing number of Bi_2 BLs in a unit cell increases the relative contents of Bi in the corresponding alloy. The varying fractions of Bi and Te in each alloy are also tabulated. Among the tabulated parameters is also the in-plane lattice constant "a" that increases approx. 1.1 % from Bi_2Te_3 to Bi_1Te_1 due to the presence of Bi bilayers[11, 12]. The predicted out-of-plane lattice constant "$c_{predicted}$" is evaluated using the equation 4.1 where c' and c'' indicate the unit cell length of Bi_2 = 11.86 Å[11] and Bi_2Te_3 = 30.48 Å[11, 30, 31, 32, 33] respectively.

$$c_{predicted} = \frac{1}{3}(mc' + nc'') \quad (4.1)$$

Table 4.1: An overview of Bi_xTe_y stoichiometric alloys prepared via MBE in the stage 1. For each state the relative contents of individual elements i.e. Bi and Te, the total number of individual layers of additive (m) and base (n) in a unit cell, the in-plane lattice constant (a) and the out-of-plane predicted ($C_{predicted}$) and measured (C_{actual}) lattice constants are listed. Alloys for whom SAE is performed and STEM investigations are conducted, are also identified.

Bi_xTe_y	m	n	Comments	Bi (%)	Te (%)	a (Å)	$c_{predicted}$ (Å)	c_{actual} (Å)	STEM Analysis	SAE
Bi_2Te_3	0	3	Reference	40.00	60.00	4.38	30.47	30.48	Yes	Yes
Bi_3Te_4	1	8	QL-BL stacks	42.85	57.15	4.40	85.23	84.98	No	Yes
Bi_3Te_4	0	3*	SL stacks	42.85	57.15	4.38	42.72	-	-	-
Bi_7Te_9	3	18	Multiple of 3	43.75	56.25	4.41	194.74	193.98	No	Yes
Bi_4Te_5	1	5	-	44.45	55.55	4.42	54.74	54.47	Yes	Yes
$Bi_{22}Te_{27}$	6	27	Multiple of 3	44.90	55.10	4.42	298.04	296.6	No	No
Bi_5Te_6	3	12	Multiple of 3	45.45	54.55	4.42	133.78	133.02	No	Yes
Bi_6Te_7	2	7	-	46.15	53.85	4.42	79.03	78.51	Yes	Yes
Bi_7Te_8	5	16	Long period	46.66	53.34	4.42	182.32	-	No	Yes
Bi_8Te_9	3	9	Multiple of 3	47.06	52.94	4.43	103.28	102.58	Yes	Yes
Bi_9Te_{10}	7	20	Long period	47.37	52.63	4.43	230.98	-	No	No
$Bi_{14}Te_{15}$	6	15	Multiple of 3	48.28	51.72	4.43	176.12	174.72	Yes	Yes
Bi_1Te_1	1	2	-	50.00	50.00	4.43	24.27	24.01	Yes	Yes

Before the individual stoichiometric states are discussed, there are a few important points that must be addressed in order to comprehend Table 4.1.

- ***Multiple of 3:*** The dramatic change in $c_{predicted}$ (unit cell length) from one stoichiometric state to the next. The reason is the periodic arrangement of atoms (ABC-ABC stacking order) in a unit cell of a trigonal lattice can only be achieved if the total number of atoms, along "c" direction (out-of-plane), is a multiple of 3. For example, Bi_2Te_3 unit cell comprises of 3 QLs where each QL is a characteristic unit that contains 5 atomic layers but cannot be a unit cell as it does not ensure the ABC-ABC stacking order. 5 being not a multiple of 3, a QL has to repeat itself 3 times with 15 atoms to ensure the periodicity of the stacking order to complete a unit cell with 3 QLs. Similarly, the unit cell of bismuth comprises of 3 BLs with a total of 6 atoms. Simply stating, in Bi_xTe_y stoichiometric alloys, the total no of layers (m+n) must be a multiple of 3. Otherwise, the complete layer stack must repeat itself 3 times to complete a unit cell. For example Bi_4Te_5 with (m+n) = (1+5) is a multiple of 3 and therefore, it acts as a complete unit cell. On the other hand, Bi_8Te_9 with (m+n) = (1+3) is not a multiple of 3. The complete stack (1+3) has to repeat 3 times to ensure the stacking sequence and thus, a unit cell of Bi_8Te_9 contains (m+n) = (3+9) with $c_{predicted}$ = 102.90 Å.
- ***Long stacking sequence:*** Another reason for the unexpected high values of $c_{predicted}$ in some stoichiometric states is the presence of unprecedentedly long stacking period in a unit cell. Examples of such states are Bi_7Te_8 and Bi_9Te_{10} with (m:n) = (5:16) and (7:20) respectively. Another

state $Bi_{22}Te_{27}$ suffers from both issues. It has a long period of (2:9) which is not a multiple of 3 and therefore, it ends up with the period of (6:27) in a unit cell with $c_{predicted}$ = 298.04 Å.

- ***Multilayer architecture:*** Some of Bi_xTe_y alloys are predicted to exist in the septuple layer (SL) architecture[7, 34, 35] similar to GST-124 (discussed in chapter 5). Bi_3Te_4 is the ground state of SL architecture just as Bi_2Te_3 is the ground state of QL architecture. Bi_3Te_4 alloy grown in this study is found to be comprised of one BL and eight QLs. The presence of SL architecture is not observed. Similarly, all the other stoichiometric alloys grown in this study are always found to be a composition of BL and QL multiples and none of the structures with SL architecture is observed.

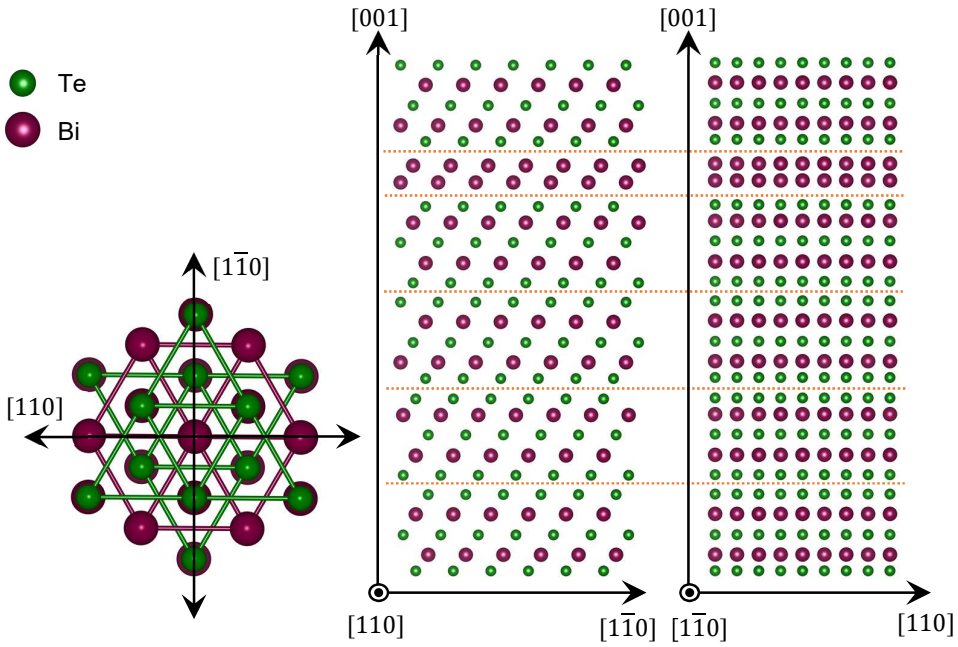

Fig. 4.4: A model representing Bi_4Te_5 unit cell and the layer stacking sequence along $[001]$, $[110]$ *and* $[1\bar{1}0]$ *orientations. The red color represents Bi atoms while the green color indicates the locations of Te atoms. The stacking order of QQQQBQ along* $[001]$ *orientation is evident where Q and B represent Bi_2Te_3 quintuple layer and Bi_2 bilayer respectively. The dotted orange lines are indicating the presence of van der Waals interactions (vdW gaps).*

4.3.1 Epilayer thickness vs. stoichiometry

It is observed that XRD peaks of several epilayers prepared with similar stoichiometric parameters and having different thicknesses, exhibited minor deviations. These deviations are mostly observed in alloys having Bi fraction between 41 % - 47 % and are found to be associated with the presence of an incomplete unit cell in the epilayer. An incomplete unit cell does not conserve stoichiometry of a complete unit cell as both Bi_2Te_3 and Bi_2 preserve their individual layer structure and therefore, epilayers having different thicknesses that are prepared with similar parameters may end up having different stoichiometry. For example, Bi_4Te_5 with (m:n) = (1:5) has a unit cell length of 54.33 Å (5.43 nm)[36]. The stacking sequence and the lattice information of Bi_4Te_5 can be seen in Figure 4.4. Bi_4Te_5 epilayers with 10.86 nm, 16.29 nm and 21.72 nm, in general any films having the thickness that is a multiple of its unit cell length will not exhibit any deviation in XRD as the stoichiometry remains conserved. However, an epilayer with thickness of 8 nm (not a multiple of the unit cell length) contains 1 complete unit cell (conserved stoichiometry with 44.45% Bi) while the remaining thickness 8 nm - 5.43 nm = 2.57 nm contains only QLs (40 % Bi). The resulting stoichiometry of the epilayer changes. Hence, for reliable characterization via XRD, this issue can be avoided by either growing films where the thickness is always a multiple of its unit cell length or the thickness is large enough to contain multiple unit cells. In this way the stoichiometric variation due to the

presence of an incomplete unit cell will be ignorable. For example, a 50 nm thick Bi_4Te_5 film contains 48.87 nm with conserved stoichiometry (Bi = 44.45 %) while the remaining 1.13 nm contains only 40 % Bi contents. The overall Bi contents will become (44.45 x 48.87 + 1.13 x 40)/50 = 44.35 % where the deviations will be ignorable. Due to this reason the structural characterization via XRD, in this section, is limited to the stoichiometric states with unit cell length ≤ 15 nm and the films are prepared with approx. 60nm to minimize any stoichiometric deviations.

4.3.2 Bi_3Te_4 and Bi_4Te_5

As depicted in Figure 4.3, with gradually decreasing Te flux, the first BL appeared in the layer stack at T_{Te} = 310℃. With the further controlled reduction in Te flux, the density and periodicity of Bi_2 BL is controlled. At T_{Te} = 307℃, the stoichiometric state of Bi_3Te_4 is obtained. Bi_3Te_4 ($Bi_{18}Te_{24}$) comprises of (m:n) = (1:8) with out-of-plane lattice parameter "c_{actual}" = 84.98 Å. In literature, the information is available only for SL architecture[34, 35], any crystallographic reference for QL-BL stacks of Bi_3Te_4, to our knowledge, is not available[37]. The high quality epitaxial films of Bi_3Te_4 are prepared and characterized. The XRD 2θ-ω scan is depicted in Figure 4.5a.

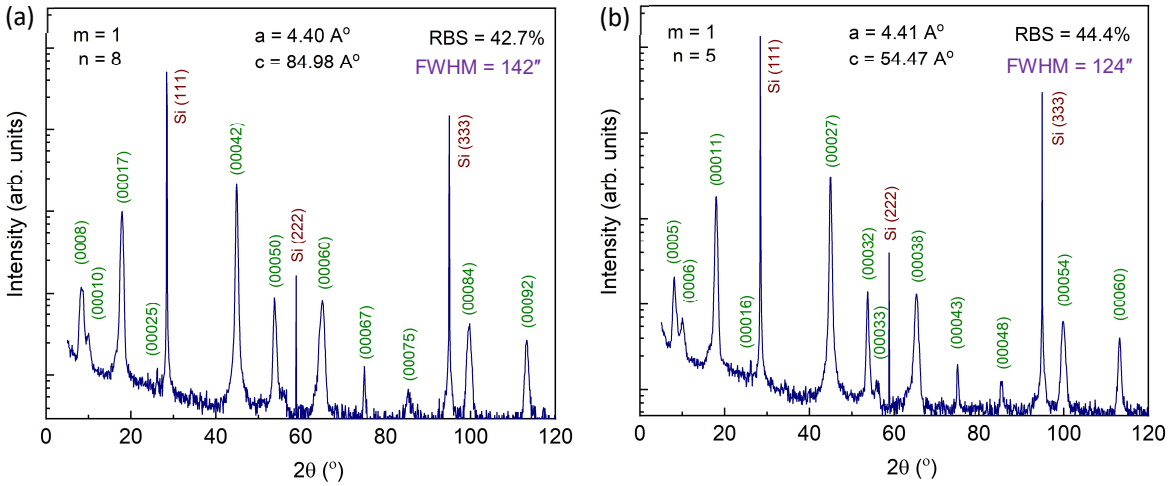

Fig. 4.5: XRD 2ϑ-ω scans. (a) Bi_3Te_4 consists of (m:n)=(1:8) exhibiting the unit cell length c_{actual} = 84.98 ± 0.01 Å. Δω scan revealed FWHM values of 142″ obtained at the (000 42) peak indicating high structural quality of the epilayer. (b) Bi_4Te_5 consists of (m:n)=(1:5) exhibiting the unit cell length c_{actual} = 54.47 ± 0.01 Å. Δω scan revealed FWHM values of 124″ obtained at the (000 27) peak.

The stoichiometric state Bi_4Te_5 ($Bi_{12}Te_{15}$), as described above, comprises of (m:n) = (1:5) with the stacking sequence of (QQQQBQ) where Q and B represent QL and BL respectively as depicted in Figure 4.4. Bi_4Te_5 exhibit a trigonal crystal structure with P-3m1 (164) space group[29, 36]. The detailed crystallographic information of this state is not readily available in the literature; however, a few studies have reported the crystal preparation via Bridgeman method[11, 34] where the lattice parameters were investigated for $Bi_{43}Te_{57}$[29, 36]. Bi_4Te_5 state is also been observed to appear as a defect after the annealing process of Bi_2Te_3[13, 38, 39]. In the process of stoichiometric tuning via MBE, Bi_4Te_5 state is obtained with the further reduced Te flux at T_{Te} = 300℃ with R_{TF} = 4.8 nm/h. Figure 4.5b displays the XRD pattern of 60nm thick epilayer of Bi_4Te_5.

Based on XRD 2θ-θ scan, the unit cell length is evaluated using the Bragg diffraction law[40], stated in equation 4.2. The relation between the diffraction index (n) and Sin(θ_n) is plotted in Figure 4.6a where θ_n represents the angle of incidence[40] corresponding to the particular diffraction index. The unit cell length is found to be "c_{actual}" = 54.469 ± 0.001 Å which deviates slightly from the reported value of 54.9 Å[12, 36]. It also deviates from the theoretical value of "$c_{predicted}$" = 54.74 Å. In order to confirm the observed deviation, the

unit cell parameters are measured again via XRD reciprocal space map (RSM) using the (0 -1 0 37) peak, depicted in Figure 4.6b. The values obtained via RSM matched perfectly with XRD 2θ-θ scan and confirmed that the observed deviation in the unit cell length is not an artifact. The reason for this deviation can only be identified with the atomic scale structural investigations via STEM and is conducted later. The φ-scan, similar to the Bi_2Te_3 obtained with $R_{TF} < 5$ nm/h and depicted in Figure 2.10, confirmed the absence of twin domains while the rocking curve ($\Delta\omega$) analysis with FWHM value of 124″, ensured the high structural quality of the epilayer as the parameters reside in the defect free zone ($R_{TF} < 5$ nm/h).

$$Sin(\theta_n) = \frac{n\,\lambda}{2c} \tag{4.2}$$

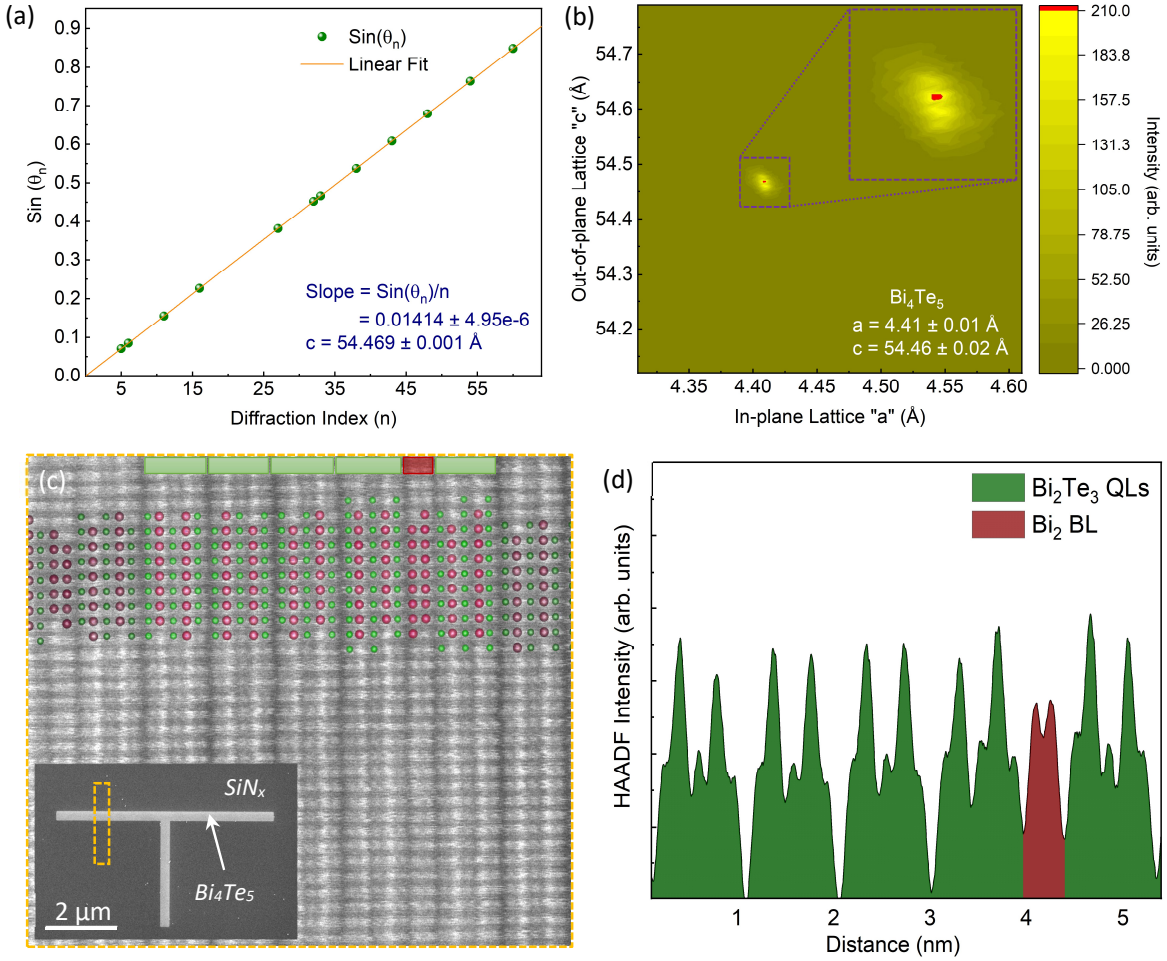

Fig. 4.6: Investigation of lattice parameters for Bi_4Te_5. (a) The evaluation of unit cell length "c" according to Bragg diffraction principle via XRD 2ϑ/ϑ scan. The plot depicts the trend between the diffraction index (n) and the angle of incidence (ϑ_n). (b) The reciprocal space map of Bi_4Te_5 acquired via XRD along the (0 -1 0 37) peak indicating the unit cell length "c_{actual}" in good agreement with the value obtained via XRD 2ϑ/ϑ scan. (c) STEM HAADF image acquired along Si [211] projection. The lamella is extracted at the cross section of 500 nm wide T-junction (inset) of selectively grown Bi_4Te_5. The image represents a unit cell with the stacking sequence of QQQQBQ with (m:n) = (1:5) where red and green color dots are representing Bi and Te atoms respectively. (d) The line profile of HAADF image, depicted in (c), representing a Bi_4Te_5 unit cell.

Selective area epitaxy (SAE): After the epitaxial growth and XRD characterization of Bi_4Te_5 epilayers on planar Si (111) substrates, the parameter are transferred to the pre-patterned substrates in order to achieve SAE. Based on the discussion in chapter 3, there are two key parameters i.e. R_{eff} and T_{sub} that must be tuned for the growth of high quality nanostructures via SAE. R_{eff} is combinedly controlled by R_{TF} and L_D

(lateral diffusion length of adatoms) that determines the crystal quality while T_{sub} ensures the selectivity. Due to the pre-optimized parameters, SAE of Bi_4Te_5 is successfully achieved and the structural characterization in large area structures is conducted via XRD. Observations have indicated slight deviations in XRD characteristic peaks in comparison to the planar epilayers. At first it was being associated with the presence of an incomplete unit cell effect, discussed in section 4.3.1; however, after the characterization of several growths having thickness a multiple of its unit cell length, it became obvious that the observed stoichiometric deviations are real and have another origin. A factor that alters stoichiometry (the Bi/Te effective flux ratio) of Bi_xTe_y stoichiometric states while remains ineffective during the SAE of the ground state (Bi_2Te_3).

Based on numerous SAE growths including several stoichiometric states, it is discovered that the lateral diffusion length (L_D) of Te on the blocking surface is different from Bi. This factor has no influence in the SAE of 3D TIs (Bi_2Te_3, Sb_2Te_3 and BST alloy); however, it changes the effective Bi/Te flux ratio during the SAE of Bi_xTe_y alloys. The effective change in the flux ratio is not enormous; however, it is enough to alter the layer stacking sequence. The analysis has revealed that L_D for Te is 14 nm (evaluated using equation 3.10) slightly higher than L_D for Bi = 12 nm and due to this reason SAE of Bi_4Te_5 exhibited slightly higher Te contents. This factor does not affect the Bi/Te flux ratio for the planar epitaxy, however, must be tuned separately for the SAE. The correct Bi/Te flux ratio for SAE is obtained at T_{Te} = 299 ℃, decreased by 1 ℃. From this corrected parameters the growth of Bi_4Te_5 nanostructures is achieved and the structural characterization is performed via STEM. Figure 4.6c and d depict STEM-HAADF images of Bi_4Te_5 acquired at the cross-section of a 500 nm wide T-junction along [211] projection and the extracted line profile of a unit cell respectively.

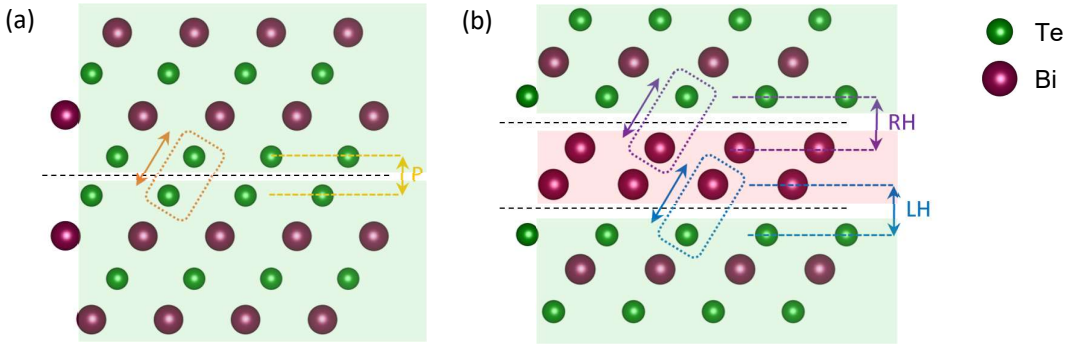

Fig. 4.7: A model representing the vdW based layer structures with pristine (P) and hybrid (H) gaps. (a) Layer stacking with pristine vdW interactions between QLs where the vdW gap is highlighted with the yellow arrow while the orange arrow is representing the projected bond length between neighboring Te atoms on both sides of the vdW gap. (b) Hybrid stacking with left hybrid (LH) vdW (between Te-Bi atoms) and right hybrid (RH) vdW interactions (between Bi-Te atoms) are highlighted with the blue and purple arrows along with the projected bond length respectively.

Reduced dimensions of the unit cell: As mentioned earlier, the length of Bi_4Te_5 unit cells (c_{actual}), measured via XRD, is found to be slightly less than theoretically evaluated value ($c_{predicted}$). The unit cell length is measured again via STEM line scan (depicted in Figure 4.6d) i.e. 54.48 ± 0.04 Å that is found to be in good agreement with the values obtained via XRD (54.469 ± 0.001 Å). The question arises, where the unit cell faces reduction in length to have slightly reduced c_{actual} than $c_{predicted}$. Is it happening in the vdW gaps or QLs themselves are having slightly reduced dimensions as well? Once again, STEM investigations have revealed that the lengths of a QL in Bi_2Te_3 (stated in Table 4.2) and Bi_4Te_5 are identical. As far as vdW gaps are concerned, the gaps of two reference materials i.e. Bi_2Te_3 and Bi_2 are taken into account for the calculations of $c_{predicted}$ in all stoichiometric alloys (equation 4.1). However, there is an important point to notice that vdW gaps in Bi_2Te_3 and Bi_2 are between Te – Te and Bi – Bi atoms, the similar elements. While,

in Bi_xTe_y stoichiometric alloys due to the presence of Bi_2 BL between QLs stack, now three types of vdW gaps exist including the pristine (P) Te – Te (between QLs) and two hybrid vdW gaps Te – Bi (between QL – BL) and Bi – Te (between BL – QL) named left hybrid (LH) and right hybrid (RH) respectively for the reference in future discussions.

In order to understand the relation between slightly reduced measured values of unit cell length (c_{actual}) and the effect of increasing density of Bi_2 BLs in the stacking sequence, the height of QL, all three types of vdW gaps (P, LH and RH) along with the corresponding projected bond lengths (highlighted in figure 4.7) are measured via STEM line scans for each stoichiometric state. The measured values of Bi_4Te_5 crystal are listed in Table 4.2. To have broader understanding, a comparative analysis of the reduced c_{actual} for all the stoichiometric states is combinedly performed in section 4.6. In order to avoid the repetitive structural information, only XRD 2θ-ω scans and STEM-HAADF images, confirming the stacking sequences of the corresponding alloy, will be presented in future while RSM, $\Delta\omega$ and φ-scans will not be presented for each stoichiometric state.

Table 4.2: An overview of the measured structural parameters via STEM-HAADF line profiles including the unit cell length (c_{actual}), the height of a QL, all vdW gaps (pristine and hybrid) and the corresponding projected bond lengths for the stoichiometric states of Bi_2Te_3 (reference), Bi_4Te_5 and Bi_6Te_7.

Parameter		Bi_4Te_5	Bi_6Te_7	Bi_2Te_3
c_{actual}	(Å)	54.48 ± 0.04	78.49 ± 0.03	30.48 ± 0.03
Height of QL	Te_{out}-Te_{out} (Å)	7.61 ± 0.03	7.60 ± 0.03	7.62 ± 0.03
vdW Gap (P)	QL – QL (Å)	2.52 ± 0.04	2.53 ± 0.04	2.55 ± 0.03
Projected Bond Length (P)	Te – Te (Å)	n/a: Si [211] orientation	2.86 ± 0.04	2.88 ± 0.04
vdW Gap (LH)	QL – BL (Å)	2.41 ± 0.04	2.40 ± 0.03	-
Projected Bond Length (LH)	Te – Bi (Å)	n/a: Si [211] orientation	2.71 ± 0.04	-
vdW Gap (RH)	BL – QL (Å)	2.42 ± 0.03	2.41 ± 0.03	-
Projected Bond Length (RH)	Bi – Te (Å)	n/a: Si [211] orientation	2.72 ± 0.05	-

4.3.3 Bi_6Te_7 and Bi_8Te_9

The stoichiometric state Bi_6Te_7 ($Bi_{18}Te_{21}$) contains 46.15 % Bi contents and exhibits a unit cell with (m:n) = (2:7) with the stacking sequence of (QQQB-QQQBQ) where Q and B represent QL and BL respectively. Bi_6Te_7 exhibits a trigonal crystal structure with P-3m1 (164) space group[12, 26]. Similar to Bi_4Te_5, the extensive structural information of Bi_6Te_7 alloy is not available in the literature; however, one study has reported the lattice parameters for $Bi_{45}Te_{55}$[12, 26] crystal prepared via the Bridgeman method. The epitaxial films of Bi_6Te_7 via MBE, are obtained at further reduced Te flux with T_{Te} = 294 ℃ with R_{TF} = 4.5 nm/h. Figure 4.7a displays XRD pattern of 47 nm thick epilayer of Bi_6Te_7. XRD measurements have revealed the unit cell length of MBE grown Bi_6Te_7 crystal (c_{actual}) = 78.51 ± 0.01 Å that is slightly reduced from $c_{predicted}$ = 79.03 Å similar to Bi_4Te_5. XRD φ-scan and $\Delta\omega$ analysis with FWHM = 128″ confirmed the high quality epilayer without the presence of twin defects.

As, all growth parameters (T_{sub} and R_{TF}) reside in the optimum zone of selectivity, the stoichiometric tuned parameters are subjected to the pre-patterned substrates and SAE is successfully achieved. As discussed earlier, to conserve the stoichiometry in selectively grown nanostructures due to slightly larger L_D of Te, the Bi/Te flux ratio is adjusted by reducing T_{Te} by 1 ℃ to 293 ℃. The nanostructures with various dimensions are prepared using T_{Bi}/T_{Te} = 470 ℃ /293 ℃ and the detailed structural characterization at the cross-section of 500 nm wide Hallbar structure is performed via STEM and the stacking sequence is identified. Figure 4.8b depicts HAADF image of Bi_6Te_7 epilayer acquired along Si [1-10] orientation. The unit cell length (c_{actual}) is extracted, all the vdW gaps and the corresponding projected bond lengths are measured and listed in Table 4.2.

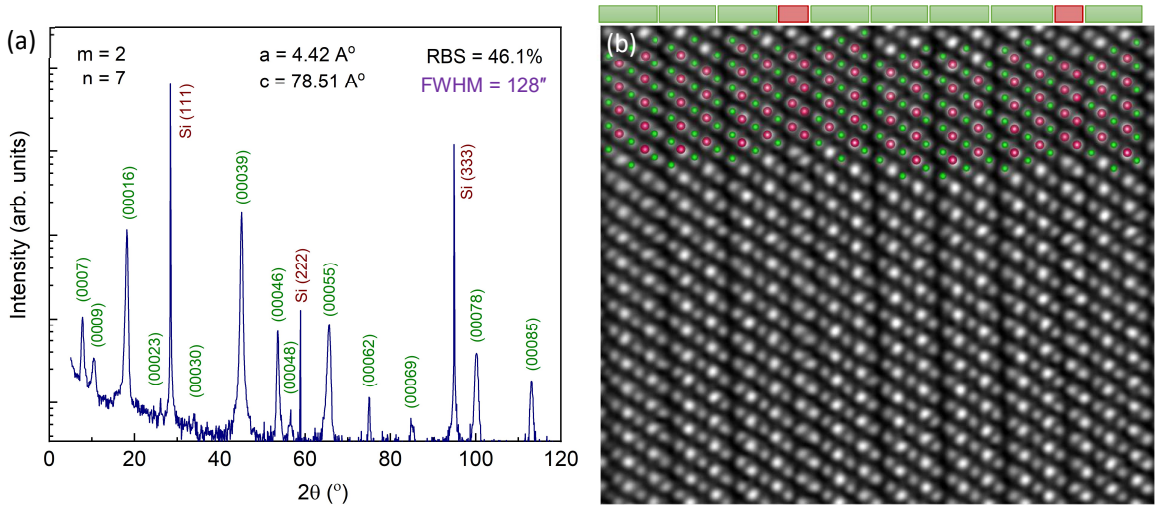

Fig. 4.8: (a) XRD 2ϑ-ω scan of Bi_6Te_7 epilayer, consists of (m:n)=(2:7) exhibiting the unit cell length c_{actual} = 78.51 ± 0.01 Å. Δω scan revealed FWHM values of 128″ obtained at the (000 39) peak. (b) STEM-HAADF image acquired along Si [1-10], confirms the stacking sequence of QQQB-QQQQB in Bi_6Te_7. The red and green color dots are representing Bi and Te atoms respectively.

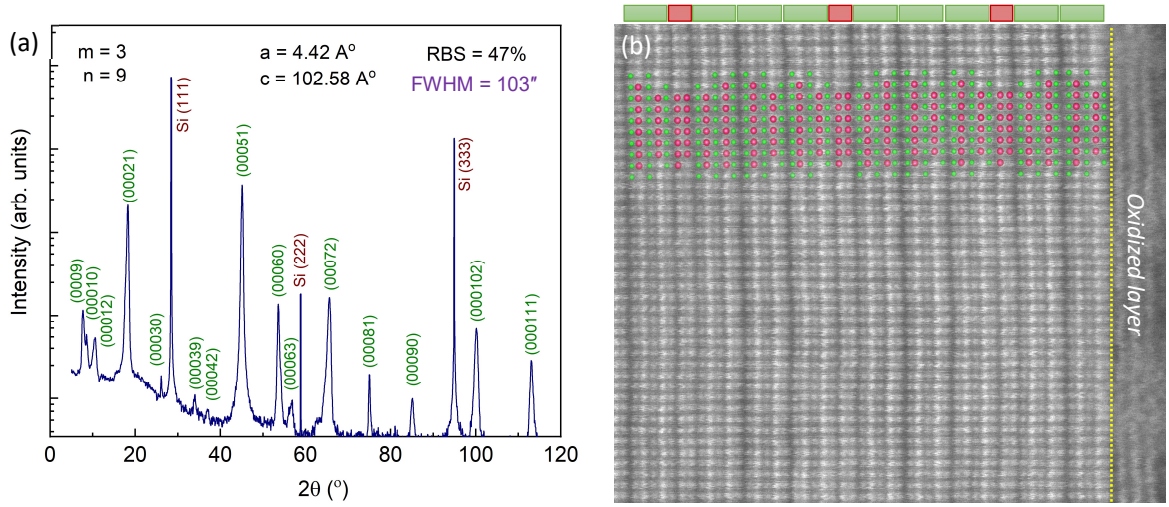

Fig. 4.9: (a) XRD 2ϑ-ω scan of Bi_8Te_9 epilayer, consists of (m:n)=(3:9) exhibiting the unit cell length c_{actual} = 102.58 ± 0.01 Å. Δω scan revealed FWHM values of 103″ obtained at the (000 51) peak. (b) STEM-HAADF image acquired along Si [211] orientation representing a unit cell of Bi_8Te_9 and confirms the stacking sequence of QBQQ-QBQQ-QBQQ. The red and green color dots are representing Bi and Te atoms respectively. The yellow dotted line indicates the interface with the oxidized layer.

The stoichiometric state Bi_8Te_9 ($Bi_{24}Te_{27}$) contains 47.06 % Bi contents and exhibits a characteristic cell with (m:n) = (1:3) with the sequence of (QQBQ); however, it suffers from multiple of 3 issue and therefore, a complete unit cell comprises of (m:n) = (3:9) with the sequence of (QQBQ-QQBQ-QQBQ). The display of the stacking sequence along [001], [110] and [1-10] orientations can be seen in Appendix 4A. The epitaxial films of Bi_8Te_9 are prepared via MBE at T_{Te} = 289℃ with R_{TF} = 4.2 nm/h. Figure 4.9a displays XRD 2θ-ω scan of 73 nm thick epilayer of Bi_8Te_9. The φ-scan revealed domain free growth and $\Delta\omega$ analysis with FWHM = 103″ confirmed the high structural quality of the epilayer. Bi_8Te_9 belongs to a rhombohedral crystal structure with R-3m (166) space group[41, 42] with $c_{predicted}$ = 103.28 Å. The literature contains several reported values of Bi_8Te_9 unit cell length from 102.99 Å[42], 103.57 Å[41] to 103.90 Å[12] where crystals were prepared via the Bridgeman method. The unit cell length of MBE grown Bi_8Te_9 crystal measured by XRD diffraction

pattern is found to be c_{actual} = 102.58 ± 0.01 Å that does not exactly match with any reported values and similar to other stoichiometric states is also found to be slightly less than $c_{predicted}$.

The nanostructures of Bi_8Te_9 crystal are prepared via SAE by applying the stoichiometric adjusted parameters T_{Bi}/T_{Te} = 470 ℃/288 ℃ to the pre-patterned substrates (T_{Te} is reduced by 1 ℃ to conserve the stoichiometry). The detailed structural investigations are conducted via STEM at the cross-section of 500 nm wide nanoribbon of Bi_8Te_9, the stacking sequence is confirmed and depicted in Figure 4.9b. Due to limitations of structural investigations i.e. the projected bond length measurements along Si [211] orientation, further investigations are conducted with a new lamella extracted along Si [1-10] orientation (A bright field image of Bi_8Te_9 epilayer along Si [1-10] can be observed in Figure 4.33a). The unit cell length c_{actual} = 102.58 ± 0.04 Å is extracted from STEM line scan that is found to be in good agreement with the value obtained via XRD. For further analysis, all vdW gaps and the corresponding projected bond lengths are measured and listed in Table 4.3.

4.3.4 $Bi_{14}Te_{15}$ and Bi_1Te_1

The stoichiometric state $Bi_{14}Te_{15}$ contains 48.28 % Bi contents with a very large unit cell having $c_{predicted}$ = 176.12 Å. It exhibits a characteristic cell with (m:n) = (2:5) with the sequence of (QQBQQQB); however, similar to Bi_8Te_9, it suffers from the multiple of 3 issue and a complete unit cell comprises of (m:n) = (6:15) with the sequence of (QQBQQQB-QQBQQQB-QQBQQQ). $Bi_{14}Te_{15}$ belongs to a rhombohedral crystal structure with R-3m (166) space group and is reported to be synthesized via zone melt method by several groups[42, 43, 44, 45]. Yet, the structural details or any other crystallographic information is not available in the literature. The epitaxial films of $Bi_{14}Te_{15}$ are obtained via MBE at T_{Te} = 285 ℃ with R_{TF} = 3.90 nm/h. Figure 4.10 displays the XRD pattern of 52 nm thick epilayer of $Bi_{14}Te_{15}$. The unit cell dimensions, measured by XRD, are found to be in good match with the suggested value by Mansour *et al.*[44], though slightly less than $c_{predicted}$. The crystal quality of the epilayer is confirmed by $\Delta\omega$ scan with FWHM = 105″. The selectively grown nanostructures of $Bi_{14}Te_{15}$ are successfully achieved by applying the compositional tuned parameters with T_{Bi}/T_{Te} = 470 ℃/284 ℃ to the pre-patterned substrates. Figure 4.10b depicts the HAADF image of the characteristic cell (QQBQQQB), acquired at the cross-section of 200 nm wide nanoribbon. The unit cell length (c_{actual}) and all the vdW gaps along with the corresponding projected bond lengths are measured and listed in Table 4.3

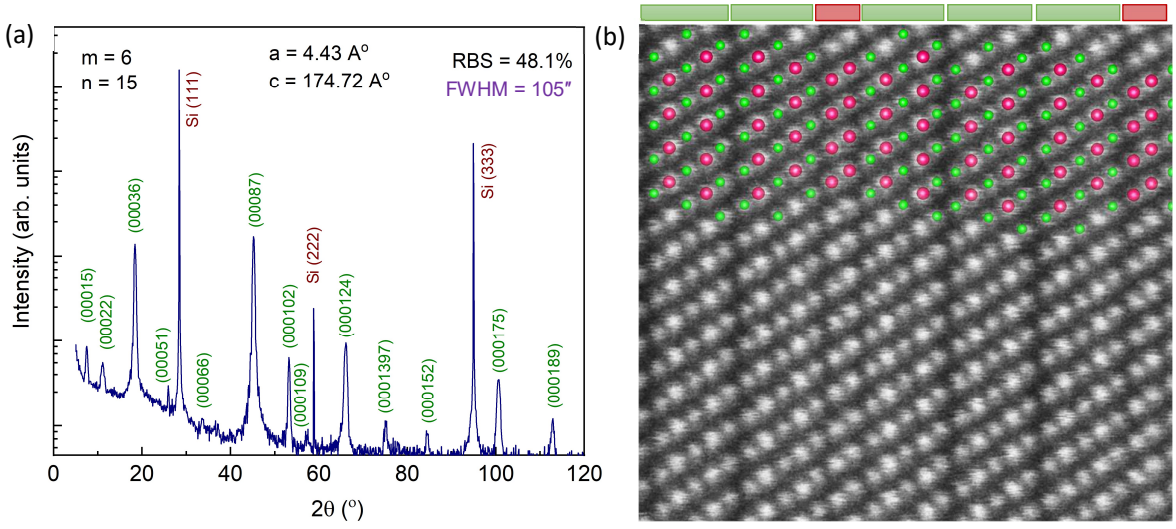

Fig. 4.10: (a) XRD 2ϑ-ω scan of $Bi_{14}Te_{15}$ epilayer, consists of (m:n)=(6:15) exhibiting the unit cell length c_{actual} = 174.72 ± 0.01 Å. Δω scan revealed FWHM values of 105″ obtained at the (000 87) peak. (b) STEM-HAADF image acquired along Si [1-10] orientation representing a characteristic cell of $Bi_{14}Te_{15}$. It confirming the stacking sequence of QQB-QQQB. The red and green color dots are representing Bi and Te atoms respectively.

Bi_1Te_1 (Bi_6Te_6) is one of the most studied stoichiometric state after Bi_2Te_3 due to its outstanding thermoelectric characteristics[11, 13, 28, 42, 46, 47, 48]. The crystal contains even contents of Bi and Te with the smallest unit cell among all the stoichiometric states investigated till now with $c_{predicted}$ = 24.27 Å. The unit cell comprises of (m:n) = (1:2) with the stacking sequence of QBQ indicating a BL sandwiched between two QLs. The stacking sequence along [001], [110] and [1-10] orientations can be seen in Appendix 4A. Bi_1Te_1 exhibits a trigonal crystal structure with P-3m1 (164) space group[46]. Several studies have reported the crystal preparation via zone melt and Bridgeman methods[12, 27, 28, 46] where the lattice parameters were investigated for $Bi_{49}Te_{51}$[28], Bi_1Te_1[46] and Bi_2Te_2[27] with the unit cell length of 24 Å, 24.22 Å and 24.33 Å respectively. There are also a few reports on the crystal preparation via PLD[13], sputter deposition[7], MOVPE[49] and a recent study on Bi_1Te_1 epitaxial thin film growth via MBE[3]. This report includes the preliminary structural characterization via STEM. It also confirmed the trivial (0001) surface of the predicted WTI phase[3] in Bi_1Te_1, where the investigations were performed via the spin-polarized ARPES[3].

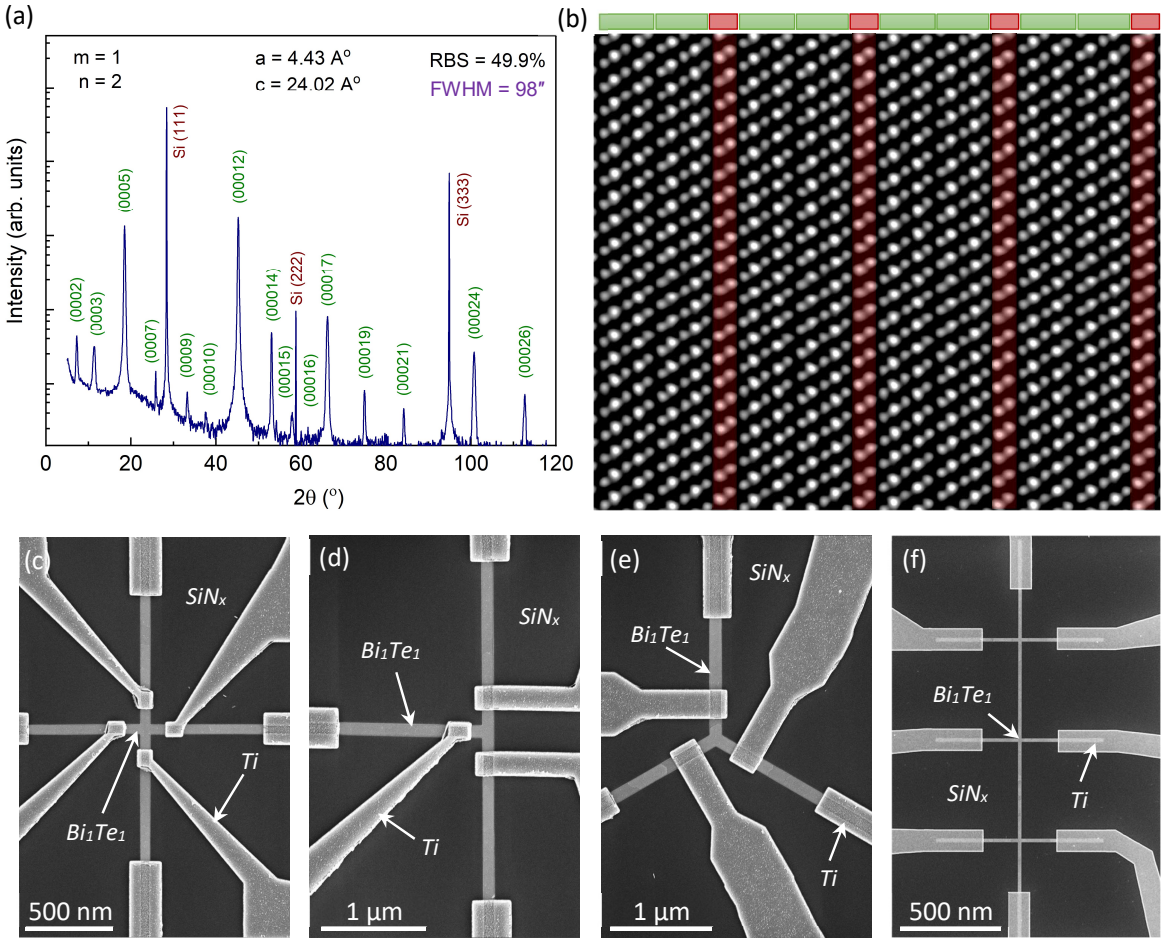

Fig. 4.11: (a) XRD 2ϑ-ω scan of Bi_1Te_1 epilayer, consists of (m:n)=(1:2) exhibiting the unit cell length c_{actual} = 24.02 ± 0.01 Å. Δω scan revealed FWHM values of 98″ obtained at the (000 12) peak. (b) STEM-HAADF image acquired along Si [1-10] orientation of Bi_1Te_1 confirms the stacking sequence of QQB. The presence of Bi_2 bilayers is highlighted with red color. (c-f) SEM images of several selectively grown nanostructures of Bi_1Te_1 with Ti contact lines.

The growth parameters are tuned and Bi_1Te_1 stoichiometric state is obtained with the Bi/Te flux ratio at T_{Te} = 280℃ with R_{TF} = 3.5 nm/h. Figure 4.11 displays the XRD pattern of 48 nm thick epilayer of Bi_1Te_1. The lattice parameters, observed via XRD (c_{actual} = 24.02 ± 0.01 Å), are found to be in agreement with the earlier report[3]. The trend of slightly reduced c_{actual} than $c_{predicted}$ remains true in Bi_1Te_1 as well. The absence of twin domains, observed via φ-scan, and RC analysis with FWHM = 98″ confirmed the high crystalline quality of

the epilayers. After XRD characterization, the stoichiometric tuned and modified parameters with T_{Bi}/T_{Te} = 470℃/279℃ (L_D neutralization of Te) are subjected to the pre-patterned substrates and selectively grown nanostructures are obtained as shown in Figure 4.11(c-f). The structural investigations are performed via STEM at the cross-section of 200 nm wide Hallbar along Si [1-10] orientation, also depicted in Figure 4.11b. The unit cell length c_{actual}, all the vdW gaps and the corresponding projected bond lengths are measured and are listed in Table 4.3.

With the Bi_1Te_1 stoichiometric growth, the stage 1 has completed. All Bi_xTe_y stoichiometric alloys of this stage with their corresponding Bi contents, the required Te flux (T_{Te}) and the growth rates (R_{TF}) are summarized in Figure 4.12.

Table 4.3: An overview of the measured structural parameters via STEM-HAADF line profiles including the unit cell length (c_{actual}), the height of a QL, all vdW gaps sizes (pristine and hybrid) and the corresponding projected bond lengths for the stoichiometric states of Bi_8Te_9, $Bi_{14}Te_{15}$ and Bi_1Te_1.

Parameter		Bi_8Te_9	$Bi_{14}Te_{15}$	Bi_1Te_1
c_{actual}	(Å)	102.58 ± 0.04	174.72 ± 0.04	24.02 ± 0.03
Height of QL	Te_{out}-Te_{out} (Å)	7.62 ± 0.03	7.60 ± 0.03	7.61 ± 0.03
vdW Gap (P)	QL – QL (Å)	2.54 ± 0.03	2.53 ± 0.04	2.53 ± 0.04
Projected Bond Length (P)	Te – Te (Å)	2.87 ± 0.04	2.87 ± 0.03	2.86 ± 0.04
vdW Gap (LH)	QL – BL (Å)	2.40 ± 0.05	2.39 ± 0.04	2.39 ± 0.05
Projected Bond Length (LH)	Te – Bi (Å)	2.71 ± 0.04	2.71 ± 0.04	2.71 ± 0.04
vdW Gap (RH)	BL – QL (Å)	2.41 ± 0.05	2.40 ± 0.05	2.40 ± 0.04
Projected Bond Length (RH)	Bi – Te (Å)	2.72 ± 0.05	2.71 ± 0.04	2.71 ± 0.04

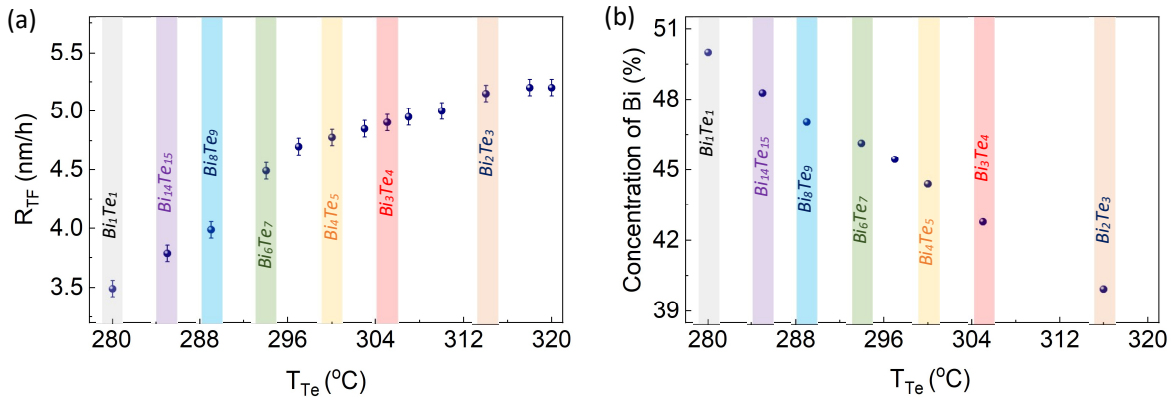

Fig. 4.12: An overview of the key Bi_xTe_y stoichiometric states belong to Stage 1. The stoichiometric alloys are obtained by tuning the Bi/Te flux ratio by gradually decreasing T_{Te} (the only variable parameter) while all the other parameters are fixed to the corresponding optimum values including T_{Bi} and T_{sub} at 470℃ and 300℃ respectively. (a) The decrement in the thin film growth rate (R_{TF}) with the decreasing T_{Te} is evident. R_{TF} is measured via XRR. (b) The trend of Bi contents with decreasing T_{Te}, measured via RBS of the corresponding epilayers mentioned in (a). The drop in T_{Te} from 320℃ to 280℃ resulted in the stoichiometric shift from 40 % (Bi_2Te_3) to 50 % (Bi_1Te_1) in bismuth contents.

4.4 Stage 2: Bi_1Te_1 to Bi_4Te_3 - Epitaxy and structural characterization

Bi_xTe_y stoichiometric states in this stage contain Bi contents from 50 % to approx. 57 % and nearly all of them are scarcely studied in the literature. The reason to separate this stage from the previous one is the necessity to alter the approach of flux tuning in order to search for the next stoichiometric states. In the previous stage, T_{Te} is utilized as a variable parameter to tune the Bi/Te flux ratio. If the similar approach is continued to grow the stoichiometric alloys of this stage, T_{Te} will be required to drop below 240℃ with extremely low R_{TF}. The growth parameters and their stability vary from one growth chamber to another

and it has been noticed through several growth tests that in the current system (*BST-MBE in PGI-9*), the homogeneity of Te flux does not remain intact as soon as T_{Te} drops below 270℃. That is why, for the stable growth conditions, search for next stoichiometric states is switched to the first approach where T_{Te} is kept constant and T_{Bi} is utilized as a variable parameter to tune the Bi/Te flux ratio. The epitaxial growth of Bi_xTe_y alloys, performed in this stage, are summarized in Table 4.4 where the expected unit cell length ($c_{predicted}$) is evaluated using the equation 4.1.

Table 4.4: An overview of Bi_xTe_y alloys prepared via MBE in the stage 2. For each state the relative contents of individual elements Bi and Te, the total number of individual building blocks/layers of additive (m) and base (n) in a unit cell, the in-plane lattice constant (a) and the out-of-plane predicted ($C_{predicted}$) and measured (C_{actual}) lattice constants are listed. Alloys for whom SAE is performed and STEM investigations are conducted, are also identified.

Bi_xTe_y	m	n	Comments	Bi (%)	Te (%)	a (Å)	$c_{predicted}$ (Å)	c_{actual} (Å)	STEM Analysis	SAE
Bi_1Te_1	1	2	Reference	50.00	50.00	4.43	24.27	24.01	Yes	Yes
$Bi_{16}Te_{15}$	9	15	Multiple of 3	51.61	48.39	4.43	187.98	186.11	Yes	Yes
$Bi_{14}Te_{13}$	8	13	Long period	54.85	48.15	4.43	163.71	162.07	No	Yes
$Bi_{12}Te_{11}$	7	11	Long period	52.17	47.83	4.43	139.43	137.91	No	Yes
$Bi_{10}Te_9$	6	9	Multiple of 3	52.63	47.37	4.43	115.16	113.96	Yes	Yes
Bi_9Te_8	11	16	Long period	52.94	47.06	4.43	206.05	204.4	No	No
Bi_8Te_7	5	7	-	53.33	46.67	4.43	90.89	89.91	Yes	Yes
Bi_7Te_6	9	12	Multiple of 3	53.85	46.15	4.44	157.5	155.76	Yes	Yes
Bi_6Te_5	4	5	-	54.54	45.46	4.44	66.61	65.91	Yes	Yes
Bi_5Te_4	7	8	-	55.55	44.45	4.44	108.95	107.85	No	Yes
Bi_4Te_3	3	3	Multiple of 3	57.14	42.86	4.45	42.34	41.89	Yes	Yes

The approach utilized for the stoichiometric growth and the structural characterization of stage 1 alloys can be summarized in following steps.

- thin film growth on planar Si (111) substrates
- structural characterization of Bi_xTe_y epilayer via XRD 2θ-ω, $\Delta\omega$, φ and RSM scans
- parameters correction for the stoichiometric tuning and SAE
- investigation of the stacking sequence via STEM in selectively grown nanostructures

Using this methodology, the epitaxial growths of all Bi_xTe_y stoichiometric alloys of stage 2, listed in Table 4.4, are conducted. The stoichiometric tuning is performed by keeping T_{Te} and T_{sub} constant at 280℃ and 300℃ respectively and utilizing T_{Bi} as a variable parameter. In order to avoid the repetitive information, only XRD and STEM data of the key states, is presented here.

$Bi_{16}Te_{15}$: The stoichiometric state $Bi_{16}Te_{15}$ ($Bi_{48}Te_{45}$) contains 51.6 % Bi contents and exhibits a characteristic cell of (m:n) = (3:5). Due to multiple of 3 issue, a complete unit cell consists of (m:n) = (9:15) with the sequence of (QQBQQBQB-QQBQQBQB-QQBQQBQB). It exhibits a rhombohedral crystal structure with R-3m (166) space group. To our knowledge, only one study has reported the crystal preparation of this alloy via the Bridgeman method[50]; however, the structural characterization is not performed.

$Bi_{16}Te_{15}$ state is achieved via MBE at T_{Bi}/T_{Te} = 476℃/280℃ with R_{TF} = 3.8 nm/h. Figure 4.13 displays the XRD pattern of 74 nm thick epilayer of $Bi_{16}Te_{15}$. The detailed structural investigations are performed via STEM at the cross-section of 1 µm wide selectively grown Hallbar along Si [1-10] orientation. The characteristic cell is depicted in Figure 4.13b and the measured structural parameters are listed in Table 4.5. One important observation worth mentioning here is the emergence of unequal gap lengths between the hybrid vdW stacks as soon as the alternating QL-BL stacks appear in the stacking sequence i.e. LH ≠ RH. This effect is most prominent in Bi_4Te_3 stoichiometry and is discussed in section 4.6.

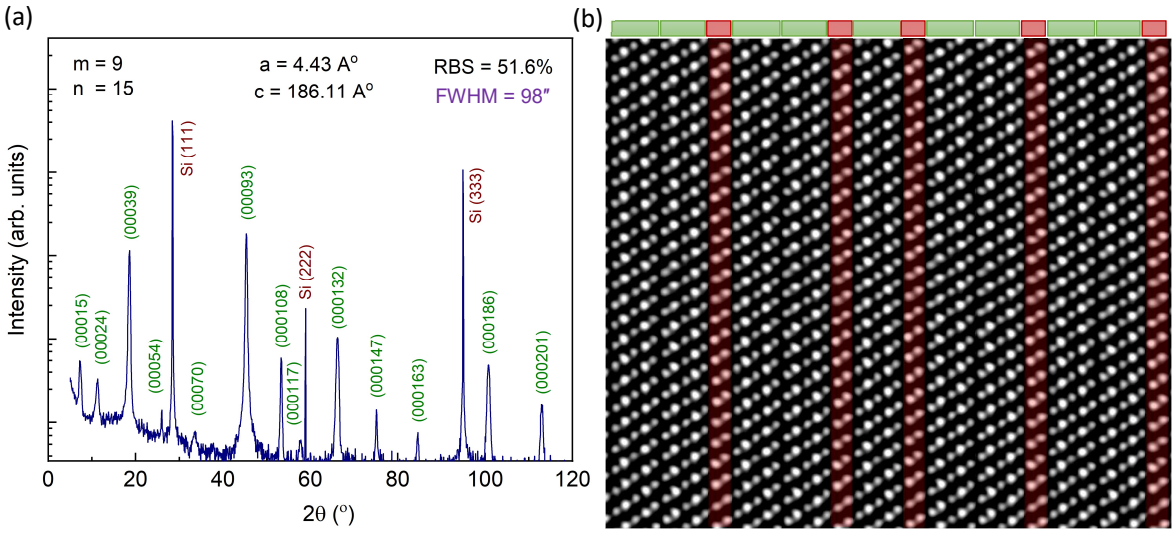

Fig. 4.13: (a) XRD 2ϑ-ω scan of $Bi_{16}Te_{15}$ epilayer exhibiting the unit cell length c_{actual} = 186.11 ± 0.01 Å. Δω scan revealed FWHM values of 98″ obtained at the (000 93) peak. (b) STEM-HAADF image acquired along Si [1-10] orientation representing a characteristic cell of $Bi_{16}Te_{15}$ and confirms the stacking sequence of QQBQQBQB. The presence of Bi_2 bilayers is highlighted with red color.

$Bi_{12}Te_{11}$: The stoichiometric state of $Bi_{12}Te_{11}$ ($Bi_{36}Te_{33}$) contain 52.2 % Bi contents. It exhibits a large unit cell of (m:n) = (7:11) with a long and non-repetitive stacking sequence of (QQBQB-QQB-QQBQB-QQBQB) and results in the unit cell length ($c_{predicted}$) = 139.43 Å. The state of $Bi_{12}Te_{11}$ is obtained at T_{Bi}/T_{Te} = 481℃/280℃ with R_{TF} = 4 nm/h. The unit cell length of MBE grown $Bi_{12}Te_{11}$ epilayer, measured via XRD, is found to be c_{actual} = 137.91 ± 0.01 Å that is as expected, similar to the other stoichiometric states, slightly less than $c_{predicted}$. Figure 4.14 displays the XRD pattern of 66 nm thick epilayer of $Bi_{12}Te_{11}$. To our knowledge, no study about the crystal preparation or the structural characterization of this alloy is reported until now.

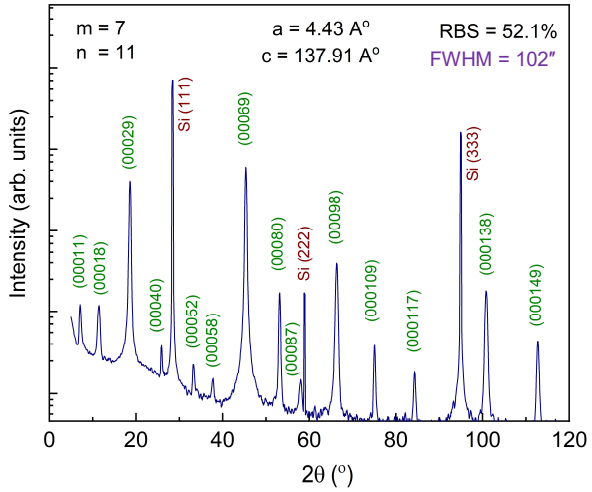

Fig. 4.14: XRD 2ϑ-ω scan of $Bi_{12}Te_{11}$ epilayer, consists of (m:n)=(7:11) exhibiting the unit cell length c_{actual} = 137.91 ± 0.01 Å. Δω scan revealed FWHM values of 102″ obtained at the (000 69) peak indicating high structural quality of the epilayer.

Instability of non-repetitive long stacking order: $Bi_{12}Te_{11}$ is an intermediate state between $Bi_{16}Te_{15}$ and $Bi_{10}Te_9$. Any stoichiometric state with such a long and non-repetitive stacking order such as $Bi_{12}Te_{11}$ (m:n)=(7:11), is prone to instability of maintaining the exact stacking sequence during the growth. This phenomenon is observed via XRD characterization of $Bi_{12}Te_{11}$ where several epilayers with similar parameters and thickness are prepared but only 70% of them exhibited the characteristic peaks of $Bi_{12}Te_{11}$ while the rest of them presented deviations in XRD 2θ-ω scans. RBS investigations of all those samples provided similar results with equal bismuth contents. These observations indicate the presence of non-

periodic stacking as RBS is insensitive to it while any change in the stacking sequence changes the out-of-plane lattice parameter and XRD is extremely sensitive to even small changes in the unit cell length. Hence, $Bi_{12}Te_{11}$ epilayers are grown with only 70% success rate and thus, it is categorized as an intermediate state.

$Bi_{10}Te_9$: $Bi_{10}Te_9$ ($Bi_{30}Te_{27}$) stoichiometric state contains 52.63 % Bi contents and exhibits a very simple characteristic cell of (m:n) = (2:3) with the sequence of (QQBQB); however, a complete unit cell comprises of (m:n) = (6:9) with the sequence of (QQBQB-QQBQB-QQBQB). It exhibits a rhombohedral crystal structure with R-3m (166) space group. $Bi_{10}Te_9$ is a stoichiometric states that is predicted by several groups[51] including Bos *et al.*[12]; however, the successful preparation of single crystalline phase, to our knowledge, is never reported. A few studies have reported the presence of $Bi_{10}Te_9$ crystal in a mixed state with Bi_4Te_3, prepared via MOVPE[48, 49] and the Bridgeman methods via extreme solid state refrigeration[52].

For the epitaxial growth of $Bi_{10}Te_9$ via MBE, the optimum Bi/Te flux ratio is achieved at T_{Bi}/T_{Te} = 484 ℃/280 ℃ with R_{TF} = 4.2 nm/h. The unit cell length of MBE grown epilayers, measured via XRD, is found to be c_{actual} = 113.96 ± 0.01 Å. Figure 4.15a displays the XRD pattern of 57 nm thick epilayer of $Bi_{10}Te_9$ and the RC analysis confirmed the high structural quality of the epilayer with the FWHM = 96″. SAE is achieved with the corrected parameters at T_{Bi}/T_{Te} = 484 ℃/278 ℃ with T_{Te} reduced by 2 ℃. The detailed structural investigations are performed via STEM at the cross-section of 600 nm wide selectively grown nanoribbon along Si [1-10] orientation. The HAADF image of the unit cell is depicted in Figure 4.15b while the measured structural parameters are listed in Table 4.5.

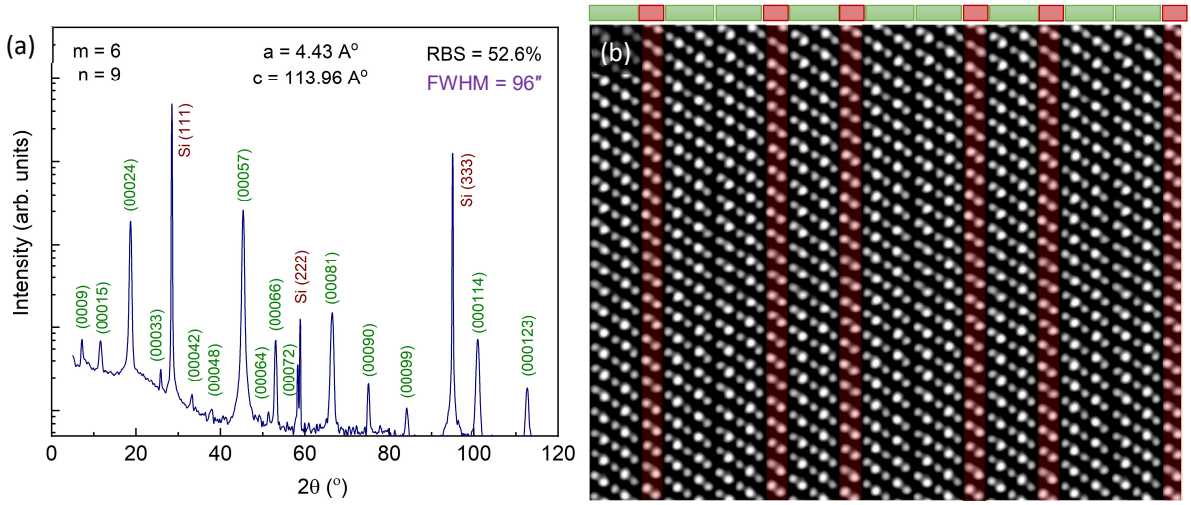

Fig. 4.15: (a) XRD 2ϑ-ω scan of $Bi_{10}Te_9$ epilayer, consists of (m:n)=(6:9) exhibiting the unit cell length c_{actual} = 113.96 ± 0.01 Å. Δω scan revealed FWHM values of 96″ obtained at the (000 57) peak. (b) STEM-HAADF image acquired along Si [1-10] orientation representing a unit cell of $Bi_{10}Te_9$ and confirms the stacking sequence of QBQQB-QBQQB-QBQQB. The presence of Bi_2 bilayers is highlighted with red color.

Table 4.5: An overview of the measured structural parameters including the unit cell length (c_{actual}), the height of a QL, all vdW gaps sizes (pristine and hybrid) and the corresponding projected bond lengths for $Bi_{16}Te_{15}$, $Bi_{10}Te_9$ and Bi_8Te_7.

Parameter		$Bi_{16}Te_{15}$	$Bi_{10}Te_9$	Bi_8Te_7
c_{actual}	(Å)	186.11 ± 0.04	113.96 ± 0.03	89.91 ± 0.04
Height of QL	Te_{out}-Te_{out} (Å)	7.61 ± 0.03	7.62 ± 0.03	7.61 ± 0.03
vdW Gap (P)	QL – QL (Å)	2.55 ± 0.03	2.54 ± 0.04	2.55 ± 0.03
Projected Bond Length (P)	Te – Te (Å)	2.87 ± 0.04	2.86 ± 0.04	2.87 ± 0.04
vdW Gap (LH)	QL – BL (Å)	2.39 ± 0.05	2.39 ± 0.04	2.39 ± 0.05
Projected Bond Length (LH)	Te – Bi (Å)	2.69 ± 0.05	2.69 ± 0.05	2.69 ± 0.05
vdW Gap (RH)	BL – QL (Å)	2.43 ± 0.05	2.44 ± 0.03	2.43 ± 0.05
Projected Bond Length (RH)	Bi – Te (Å)	2.77 ± 0.04	2.76 ± 0.04	2.77 ± 0.04

Bi_8Te_7: The stoichiometric state Bi_8Te_7 ($Bi_{24}Te_{21}$) with 53.33 % Bi contents, comprises of a large unit cell with (m:n) = (5:7) exhibiting the sequence of (QBQQB-QBQB-QQB). It exhibits a trigonal crystal structure with P-3m1 (164) space group[53]. The epitaxial growth of this state is achieved via MBE at T_{Bi}/T_{Te} = 487 ℃/280 ℃ with R_{TF} = 4.4 nm/h. XRD based structural characterizations are performed where the measured unit cell length is found to be c_{actual} = 89.91 ± 0.01 Å which is, similar to the other states, slightly less than $c_{predicted}$. Similarly, φ and $\Delta\omega$ scans with FWHM value of 91″ have confirmed the domain-free and high crystal quality of the epilayer. The structural quality of the crystal can also be witnessed via thickness oscillations at the (000 19) and the (000 45) peaks in XRD 2θ-ω scan of 27 nm thick epilayer of Bi_8Te_7, depicted in Figure 4.16a. Here, the thickness oscillations are observed, in comparison all previous measurements, due to very thin epilayer. With the increasing thickness of the epilayer, the oscillation period gets smaller until they start to merge together and disappear. After XRD characterization, nanostructures are prepared via SAE by applying the modified parameters with T_{Bi}/T_{Te} = 487 ℃/278 ℃ to the pre-patterned substrates. The detailed structural investigations are performed via STEM at the cross-section of 500 nm wide selectively grown nanoribbon along Si [1-10] orientation. The HAADF image of the unit cell is depicted in Figure 4.16b while the measured structural parameters are listed in Table 4.5. To our knowledge, no report about the crystal preparation or the structural characterization of this alloy, is available.

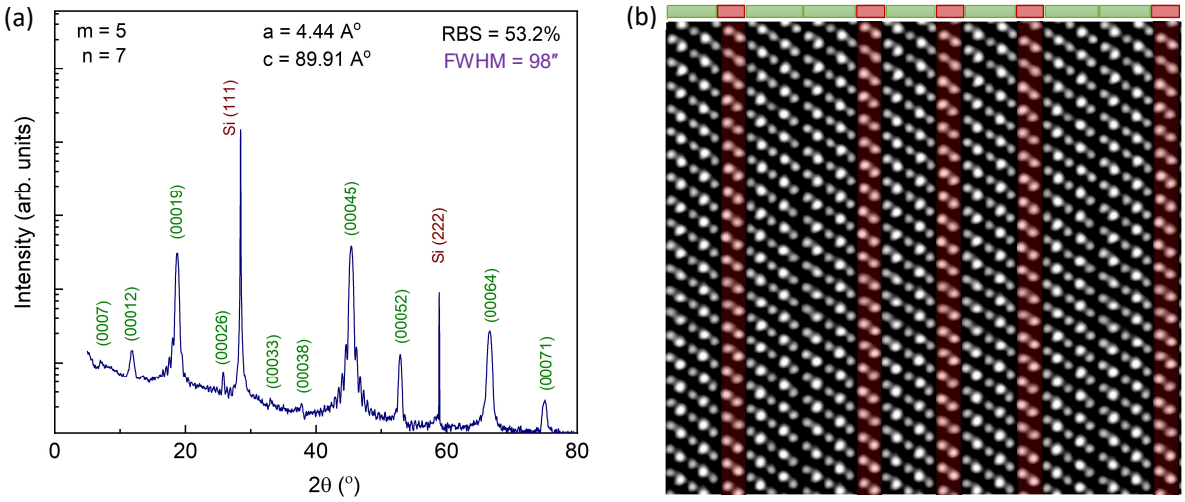

Fig. 4.16: (a) XRD 2ϑ-ω scan of Bi_8Te_7 epilayer, consists of (m:n)=(5:7) exhibiting the unit cell length c_{actual} = 89.91 ± 0.01 Å. Δω scan revealed FWHM values of 98″ obtained at the (000 45) peak. (b) STEM-HAADF image acquired along Si [1-10] orientation representing a unit cell of Bi_8Te_7 and confirms the stacking sequence of QBQQB-QBQB-QQB. The presence of Bi_2 bilayers is highlighted with red color.

Bi_7Te_6: The stoichiometry of Bi_7Te_6 ($Bi_{42}Te_{36}$) contains 53.85 % Bi contents. It exhibits the multiple of 3 issue and therefore, a unit cell comprises of (m:n) = (9:12) with the sequence of (QQBQBQB-QQBQBQB-QQBQBQB). It exhibits a rhombohedral crystal structure with R-3m (166) space group. Bi_7Te_6 has been extensively studied theoretically by several groups for its predicted outstanding thermoelectric features[44, 54] and phase change characteristics[55]. However, to our knowledge, there is not a single study reported about the crystal preparation or the structural characterization of this alloy.

Bi_7Te_6 epitaxial growth is achieved via MBE at T_{Bi}/T_{Te} = 489 ℃/280 ℃ with R_{TF} = 4.5 nm/h. The unit cell length of MBE grown epilayers measured via XRD is found to be c_{actual} = 155.76 ± 0.01 Å which is, similar to the other states, slightly less than $c_{predicted}$. Figure 4.17a displays the XRD pattern of 63 nm thick epilayer of Bi_7Te_6 and the RC analysis confirmed the high structural quality of the epilayer with FWHM = 88″. Later, nanostructures are prepared via SAE by applying the modified parameters with T_{Bi}/T_{Te} = 489 ℃/278 ℃ to

the pre-patterned substrates. STEM based structural investigations are performed at the cross-section of 600 nm wide nanoribbon along Si [1-10] orientation. The HAADF image is depicted in Figure 4.17b while the measured structural parameters are listed in Table 4.6.

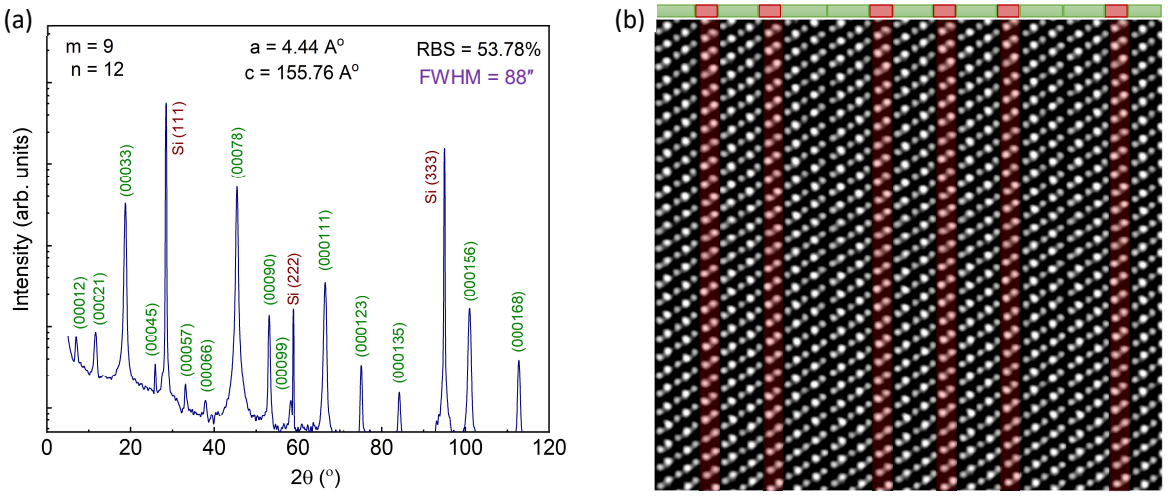

Fig. 4.17: (a) XRD 2ϑ-ω scan of Bi_7Te_6 epilayer, consists of (m:n)=(9:12) exhibiting the unit cell length c_{actual} = 155.76 Å. Δω scan revealed FWHM values of 88 obtained at the (000 78) peak. (b) STEM-HAADF image acquired along Si [1-10] orientation representing a unit cell of Bi_7Te_6 and confirms the stacking sequence of QQBQBQB-QQBQBQB-QQBQBQB. The presence of Bi_2 bilayers is highlighted with red color.

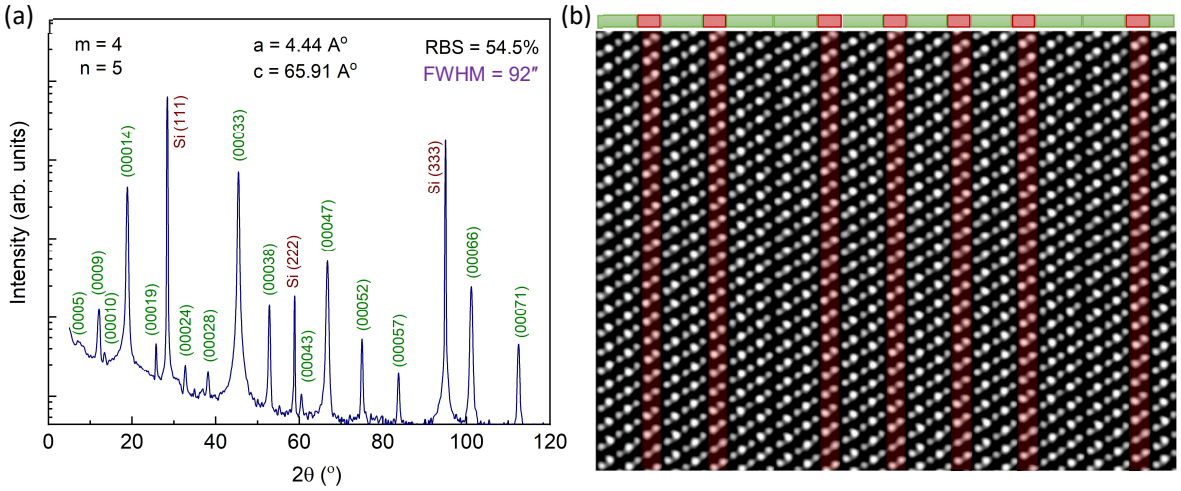

Fig. 4.18: (a) XRD 2ϑ-ω scan of Bi_6Te_5 epilayer, consists of (m:n)=(4:5) exhibiting the unit cell length c_{actual} = 65.91 ± 0.01 Å. Δω scan revealed FWHM values of 92″ obtained at the (000 33) peak. (b) STEM-HAADF image acquired along Si [1-10] orientation representing a unit cell of Bi_6Te_5 and confirms the stacking sequence of QBQB-QQBQB. The presence of Bi_2 bilayers is highlighted with red color.

Bi_6Te_5 and Bi_5Te_4: Bi_6Te_5 ($Bi_{18}Te_{15}$) contains 54.54 % Bi contents and exhibits a unit cell containing (m:n) = (4:5) with the sequence of (QBQB-QQBQB). Bi_5Te_4 ($Bi_{30}Te_{24}$), on the other hand, contains 55.55 % Bi contents and exhibits a unit cell of (m:n) = (7:8) with the sequence of (QBQBQB-QQB-QBQBQB). Both states exhibit the trigonal crystal structure with P-3m1 (164) space group. Bi_6Te_5, similar to Bi_7Te_6, is a stoichiometric state that has been theoretically studied by several groups for its thermoelectric features[44, 56, 57] and phase change characteristics[55]. A few studies have reported the synthesis of Bi_6Te_5 nanoparticles composite[44, 58]; however, the preparation of single crystalline films of Bi_6Te_5 and Bi_5Te_4, to our knowledge, has never been achieved[59, 60].

The stoichiometric states of Bi_6Te_5 and Bi_5Te_4 are obtained via MBE at T_{Bi}/T_{Te} = 492 ℃/280 ℃ and 497 ℃/280 ℃ where the epilayers are prepared with R_{TF} = 4.7 nm/h and 5 nm/h respectively. Figure 4.18a and 4.19 display the XRD patterns of 46 nm and 54 nm thick epilayers of Bi_6Te_5 and Bi_5Te_4 while the unit cell lengths, measured via XRD, are found to be c_{actual} = 65.91 ± 0.01 Å and 107.85 ± 0.01 Å respectively. Later, the pristine nanostructures of Bi_6Te_5 and Bi_5Te_4 are prepared via SAE by applying the modified parameters with T_{Bi}/T_{Te} = 492 ℃/278 ℃ and 497 ℃/278 ℃ to the pre-patterned substrates. The detailed structural investigations are performed via STEM at the cross-section of 500 nm wide T-junction of Bi_6Te_5 along Si [1-10] projection. The HAADF image of the unit cell is depicted in Figure 4.18b while the measured structural parameters are listed in Table 4.6. The stacking sequence and atomic scale structural investigations have failed for Bi_5Te_4 due to excessive damage to the lamella.

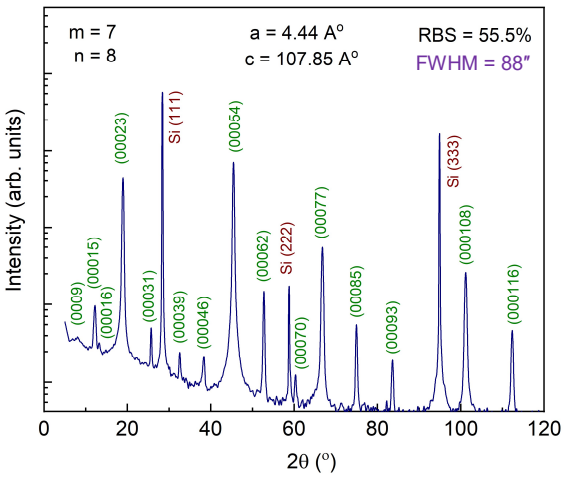

Fig. 4.19: XRD 2ϑ-ω scan of Bi_5Te_4 epilayer, consists of (m:n)=(7:8) with the stacking sequence of QBQBQB-QQB-QBQBQB exhibiting the unit cell length c_{actual} = 107.85 ± 0.01 Å. Δω scan revealed FWHM values of 88″ obtained at the (000 54) peak.

Table 4.6: An overview of the measured structural parameters via STEM-HAADF line profiles including the unit cell length (c_{actual}), the height of a QL, all vdW gaps sizes (pristine and hybrid) and the corresponding projected bond lengths for the stoichiometric states of Bi_7Te_6, Bi_6Te_5, Bi_4Te_3 and Bi_3Te_2.

Parameter		Bi_7Te_6	Bi_6Te_5	Bi_4Te_3	Bi_3Te_2
c_{actual} (Å)	-	155.76 ± 0.04	65.92 ± 0.03	41.90 ± 0.03	59.86 ± 0.03
Height of QL (Å)	Te_{out}-Te_{out}	7.61 ± 0.03	7.62 ± 0.03	7.61 ± 0.03	7.61 ± 0.03
vdW Gap (P)	QL – QL (Å)	2.55 ± 0.03	2.54 ± 0.04	-	2.48 ± 0.03
Projected Distance (P)	Te – Te (Å)	2.87 ± 0.04	2.86 ± 0.04	-	2.80 ± 0.03
vdW Gap (LH)	QL – BL (Å)	2.39 ± 0.05	2.39 ± 0.04	2.37 ± 0.04	2.42 ± 0.04
Projected Distance (LH)	Te – Bi (Å)	2.69 ± 0.05	2.68 ± 0.05	2.68 ± 0.05	2.73 ± 0.05
vdW Gap (RH)	BL – QL (Å)	2.43 ± 0.05	2.44 ± 0.05	2.47 ± 0.04	2.41 ± 0.04
Projected Distance (RH)	Bi – Te (Å)	2.77 ± 0.04	2.78 ± 0.04	2.79 ± 0.05	2.74 ± 0.05

Bi_4Te_3: The stoichiometric alloy Bi_4Te_3 ($Bi_{12}Te_9$) is the third most studied member of Bi_xTe_y family after Bi_2Te_3 and Bi_1Te_1 due to its outstanding thermoelectric properties and the only member of this stage to be explored in the literature[47, 49, 61, 62, 63]. It contains 57.14 % bismuth contents and exhibits a unique and the smallest characteristic unit of (m:n) = (1:1) with the stacking sequence of (QB); however, it suffers from multiple of 3 issue and therefore, a complete unit cell comprises of (m:n) = (3:3) with the sequence of (QB-QB-QB) and $c_{predicted}$ = 42.34 Å. The stacking sequence along [001], [110] and [1-10] orientations can be seen in Appendix 4A.

Bi_4Te_3 exhibits a rhombohedral crystal structure with R-3m (166) space group[61]. Several studies have reported Bi_4Te_3 crystal preparation using the Bridgeman method[11, 12, 34, 47, 64], PLD[13], sputter deposition[7], MOVPE[48, 49, 63] and MBE[62, 64]. Most of these reports have not dealt with the epitaxial layer growth of high quality thin films rather with bulk crystals or nanoparticles composites[62, 63] including nanowires[62, 63] and

nanoplates[49] etc. The structural characterizations have been performed by several groups where the lattice parameters are investigated for $Bi_{57}Te_{43}$ bulk crystals and Bi_4Te_3 layers having the unit cell length of 42.34 Å[34], 42.24 Å[59] and 41.89 Å[7, 47, 49, 61].

In order to obtain Bi_4Te_3 stoichiometry via MBE, T_{Bi} is gradually increased from 497 ℃ and at T_{Bi}/T_{Te} = 505 ℃/280 ℃, epitaxial growth of Bi_4Te_3 is successfully achieved with R_{TF} = 5.4 nm/h. Figure 4.20a displays the XRD pattern of 25 nm thick epilayer of Bi_4Te_3. The unit cell length of MBE grown Bi_4Te_3 epilayers, measured via XRD, is found to be c_{actual} = 41.889 ± 0.002 Å which is, similar to the other stoichiometric states, slightly less than $c_{predicted}$. Once again, the thickness oscillations, due to high crystal quality and small thickness of the epilayer, can be observed at the (000 21) peak. The structural characterizations are performed via φ and $\Delta\omega$ scans where the FWHM value of 68″ revealed the domain-free and highest quality of Bi_xTe_y crystal achieved yet. After XRD characterization on Si (111) planar substrates, the focus is turned towards the SAE and epitaxial nanostructures are obtained by applying the modified parameters with T_{Bi}/T_{Te} = 505 ℃/278 ℃ to the pre-patterned substrates. The detailed structural investigations are performed via STEM at the cross-section of the 600 nm wide nanoribbon along Si [1-10] orientation. The STEM-HAADF image, representing the stacking order, is depicted in Figure 4.20b. The unit cell length c_{actual}, all the vdW gaps along with the corresponding projected bond lengths are measured and listed in Table 4.6.

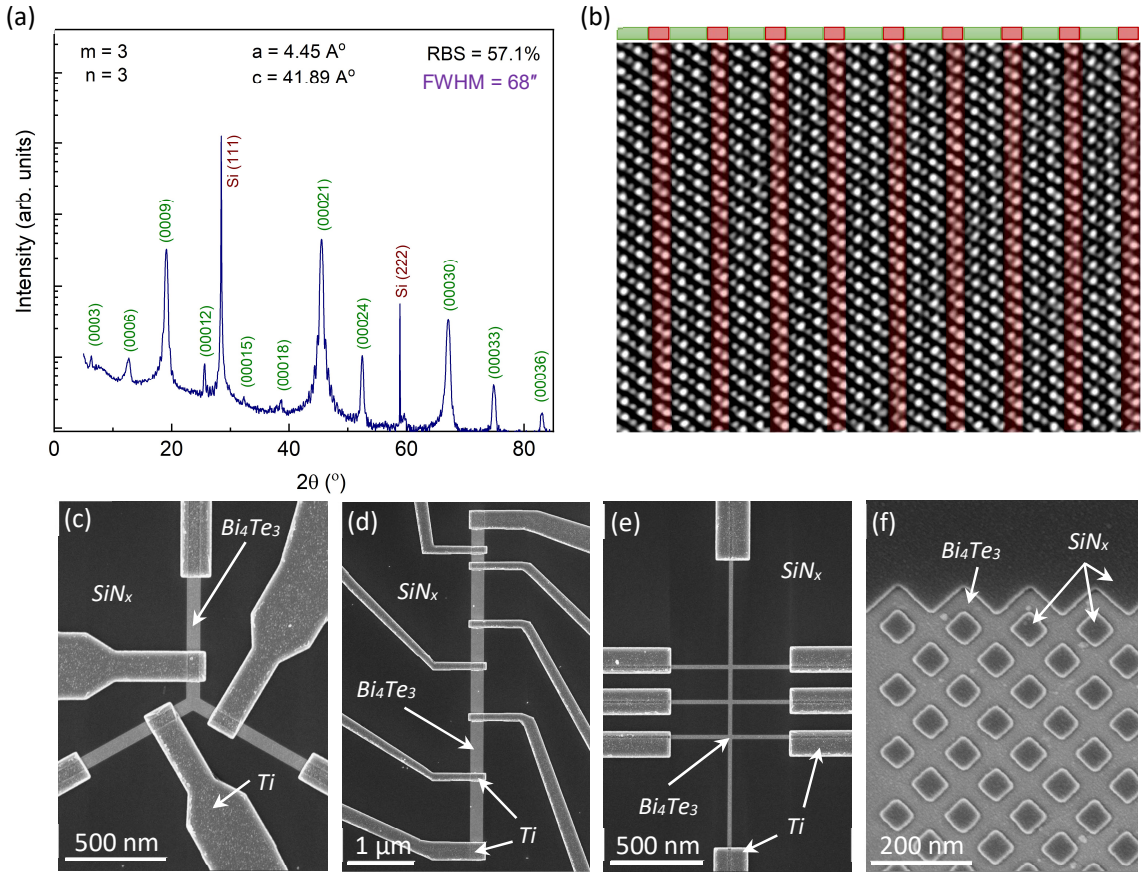

Fig. 4.20: (a) XRD 2ϑ-ω scan of Bi_4Te_3 epilayer, consists of (m:n)=(3:3) with the stacking sequence of QB-QB-QB exhibiting the unit cell length c_{actual} = 41.89 ± 0.01 Å. Δω scan revealed FWHM values of 68″ obtained at the (000 21) peak indicating high structural quality of the epilayer. (b) STEM-HAADF image acquired along Si [1-10] orientation of Bi_4Te_3 confirms the stacking sequence of QB. The presence of Bi_2 bilayers is highlighted with red color. (c-f) SEM images of several selectively grown nanostructures of Bi_4Te_3 with Ti contact lines.

Bi_4Te_3 is a very important stoichiometric state as it exhibits several unique structural and chemical features; some of them are mentioned below:

- Bi_4Te_3 is the equilibrium stoichiometric state between Bi_2 and Bi_2Te_3.
- Bi_4Te_3 is the only state that does not host any pristine vdW gap between Te-Te or Bi-Bi atoms. Any state with slightly higher or lower Bi contents must have at least one pristine vdW stack.
- Due to the alternating QL-BL stacking, Bi_4Te_3 exhibits the most diverse relation between the left handed (LH) and the right handed (RH) hybrid vdW gaps (discussed in section 4.6)
- Electronically Bi_4Te_3 crystal exhibits near semi metallic behavior[7, 59, 65, 66]. (discussed in section 4.8)
- The highly compressive crystal state with the presence of only hybrid vdW stacks makes Bi_4Te_3 a prime candidate for phase change material (PCM) particularly from one crystalline phase (trigonal) to another (cubic)[60, 67].
- Bi_4Te_3 exhibits superconductivity when applied to high pressure conditions[65].

With the successful planar and SAE of Bi_4Te_3 stoichiometric alloy, the stage 2 has completed. All stoichiometric alloys prepared in this stage with their corresponding Bi contents, the required Bi flux (T_{Bi}) and the growth rates (R_{TF}) are summarized in Figure 4.21.

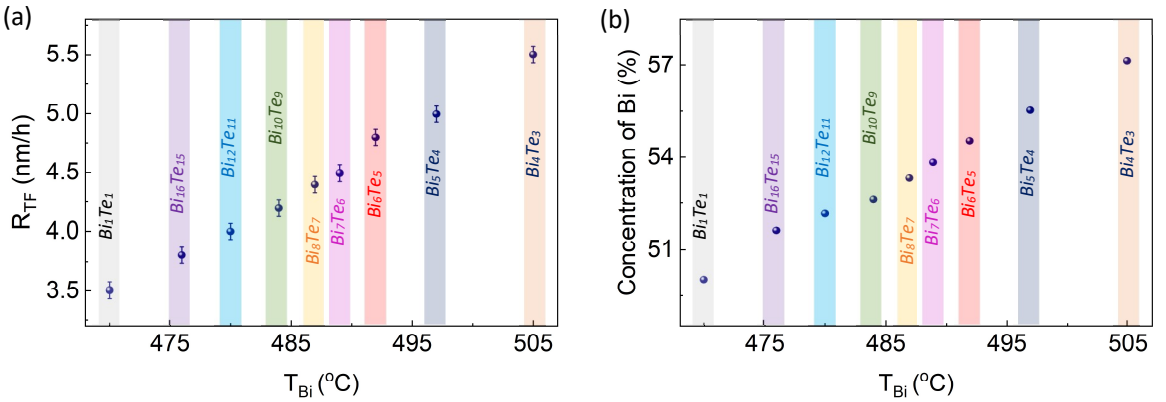

Fig. 4.21: An overview of the key Bi_xTe_y stoichiometric states belong to Stage 2. The stoichiometric alloys are obtained by tuning the Bi/Te flux ratio by gradually increasing T_{Bi} (the only variable parameter) while all the other parameters are fixed to the corresponding optimum values including T_{Te} and T_{sub} at 280˚C and 300˚C respectively. (a) The increment in the thin film growth rate (R_{TF}) with the increasing T_{Bi} is evident. R_{TF} is measured via XRR. (b) The trend of Bi contents with increasing T_{Bi}, measured via RBS of the corresponding epilayers mentioned in (a). The rise in T_{Bi} from 470˚C to 504˚C resulted in the stoichiometric shift from 50 % (Bi_1Te_1) to 57 % (Bi_4Te_3) in bismuth contents.

4.5 Stage 3: Bi_4Te_3 to Bi_2 - Epitaxy and structural characterization

This stage contains stoichiometric alloys with Bi contents from 57.1 % to 100 %. The range of Bi contents is so vast that hundreds of stacking combinations are possible and their systematic growth and structural investigations demand years of research. The reasons to separate this stage from other two stages are as follow:

- ***Diverse flux ratio:*** The preliminary growth tests indicated that for stoichiometric tuning of Bi_xTe_y members in this stage, none of the growth parameters T_{Bi}, T_{Te} and T_{sub} can be fixed. In other words, the requirement of Bi/Te flux ratio is so diverse that the stoichiometric growth cannot be achieved by adjusting a single variable parameter, an approach utilized in the previous two stages. The optimum Bi/Te flux ratio can only be achieved with the mutual adjustment of T_{Te} and T_{Bi}.
- ***Thermal stability:*** All stoichiometric states of this stage contain at least one dual Bi_2 BL in the stacking sequence. T_{sub} is required to drop with the increasing density of BLs due to the thermal instability of Bi rich films at higher temperatures. The extent of drop in T_{sub} can be estimated from

this fact that the epitaxial films of pure Bi crystal are achieved at T_{sub} < 70℃. If the epitaxial growth of the stoichiometric states are still conducted at higher temperatures it will result in epilayers with rough surfaces exhibiting high density of Bi crystallites.

- ***Challenges for SAE:*** Due to relatively higher requirement of Bi flux and poor thermal stability, SAE is extremely challenging to achieve.

The epitaxial growth of Bi_xTe_y members performed in this stage are summarized in Table 4.7 where the theoretical out-of-plane lattice constant ($c_{predicted}$) is evaluated using the equation 4.1. Due to above mentioned challenges, particularly the thermal instability, SAE is failed for most of the states, also mentioned in Table 4.7. The detailed structural characterizations are performed via XRD for all stoichiometric states; however, STEM investigations are conducted only for Bi_3Te_2, the last stoichiometric state that allowed SAE. The literature is quite silent about the members of this stage. The only information that can be found is about Bi_2Te and Bi_2 crystals. In comparison to stage 1, it is the least studied material group in the literature.

Table 4.7: An overview of the Bi_xTe_y stoichiometric alloys prepared via MBE in the stage 3. For each state the relative contents of individual elements Bi and Te, the total number of individual building blocks/layers of additive (m) and base (n) in a unit cell, the in-plane lattice constant (a) and the out-of-plane predicted ($C_{predicted}$) and measured (C_{actual}) lattice constants are listed. Alloys for whom SAE is performed and STEM investigations are conducted, are also identified.

Bi_xTe_y	m	n	Comments	Bi (%)	Te (%)	a (Å)	$c_{predicted}$ (Å)	c_{actual} (Å)	STEM Analysis	SAE
Bi_4Te_3	3	3	Multiple of 3	57.14	42.86	4.45	42.34	41.89	Yes	Yes
Bi_7Te_5	11	10	Long period	58.33	41.67	4.45	145.09	143.69	No	Yes
$Bi_{10}Te_7$	8	7	Long period	58.82	41.18	4.45	102.75	101.80	No	Yes
Bi_3Te_2	5	4	-	60	40	4.46	60.41	59.85	Yes	Yes
$Bi_{14}Te_9$	12	9	Multiple of 3	60.87	39.13	4.46	138.88	137.62	No	Failed
Bi_8Te_5	7	5	-	61.54	38.46	4.46	78.47	77.77	No	Failed
Bi_5Te_3	9	6	Multiple of 3	62.5	37.5	4.46	96.54	95.71	No	Failed
$Bi_{12}Te_7$	11	7	Long period	63.15	36.85	4.47	114.61	113.62	No	Failed
Bi_7Te_4	13	8	Long period	63.63	36.37	4.47	132.67	131.55	No	Failed
Bi_2Te_1	2	1	-	66.67	33.33	4.48	18.07	17.92	No	Failed
Bi_2	3	0	Multiple of 3	100	0	4.54	11.85	11.86	No	Failed

Approach to tune stoichiometric states: Due to the less demand of Te flux and keeping R_{TF} in defect free zone (< 5 nm/h), the search for next state after Bi_4Te_3 started with gradually decreasing T_{Te} from 280℃ (i.e. from Bi_4Te_3 parameters) while keeping T_{sub} and T_{Bi} constant at 300℃ and 505℃ respectively. The resulting effects of the increased Bi/Te flux ratio are immediately identified via SEM and XRD. It is observed that with the decreasing Te flux, the excessive Bi adatoms did not favor the formation of an additional Bi_2 BL rather kept the stoichiometric state stable at Bi_4Te_3 (confirmed via XRD) with the additional formation of Bi_2 crystallites on the surface as shown in Figure 4.22 (a-d). The density of crystallites changed according to the Te flux (T_{Te}) until the epilayer started to disintegrate.

The initial conclusion extracted from these observations is the thermal instability of Bi rich epilayer prepared with the reduced Te flux than T_{Te} = 280℃. This assumption also justifies the increased surface roughness and the epilayer degradation observed in Figure 4.22 (d). In order to confirm this theory, the growth parameters are tuned again where T_{Te} and T_{Bi} are kept constant at 280℃ and 505℃ respectively while T_{sub} is gradually increased from 300℃ to 315℃. At first, the surface roughness started increasing until T_{sub} reached 305℃ (Figure 4.22e). With the further increment in T_{sub}, the decreasing ADR of Te altered the Bi/Te flux ratio that, similar to the case observed in Figure 4.22 (a-d), resulted in the stable stoichiometry of Bi_4Te_3, whereas, the excessive Bi adatoms formed Bi_2 crystallites as can be seen in Figure 4.22 (f-h).

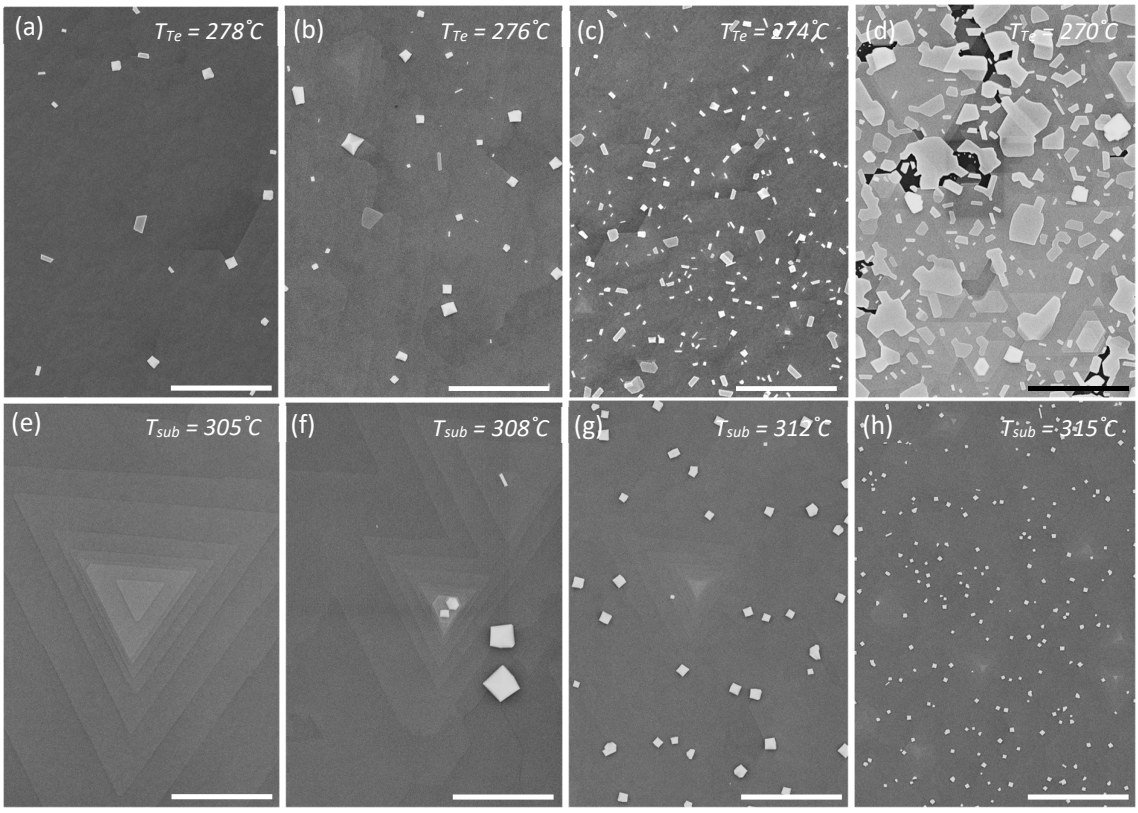

*Fig. 4.22: SEM images representing the attempts to obtain the stoichiometric growth of Bi_xTe_y states having Bi contents higher than Bi_4Te_3 (57 %). (a-d) The effect of decreasing Te flux on the surface morphology while keeping T_{sub} and T_{Bi} constant. With the continuously decreasing Te flux, the density of Bi crystallites are observed to increase until the epilayer started to destabilize. (e-h) The effect of increasing T_{sub} on the surface morphology while keeping T_{Te} and T_{Bi} constant. With the continuously increasing T_{sub}, the surface roughness kept increasing until Bi crystallites appeared. The density of Bi crystallites exhibited a direct proportionality with T_{sub}. (*scale bar = 1 µm)*

As both approaches i.e. variable T_{Te} and T_{sub} to obtain the next stoichiometric states have failed, the Bi/Te flux ratio is now adjusted by increasing the Bi flux (T_{Bi}) from 505℃ while keeping T_{Te} and T_{sub} constant at 280℃ and 300℃ respectively. Once again, the formation of Bi crystallites is observed; however, unlike the other two approaches, the shifts in the XRD characteristic peaks from Bi_4Te_3 stoichiometry are also witnessed. Hence with T_{Bi} as a variable parameter, the next stoichiometric states can be achieved; however, due to the thermal instability of Bi rich epilayers, the issue of Bi crystallite formation still remained unresolved. Based on the above mentioned experiments, the key observations are stated below:

- At T_{sub} = 300℃, Bi_4Te_3 is the most stable alloy that can be achieved with the defect-free epilayers while T_{Te} is kept at 280℃. The epilayers with higher Bi contents will result in the formation of Bi crystallites.
- The correct Bi/Te flux ratio is not the only factor to tune the stoichiometry anymore. The adjustment of minimum Te flux at the corresponding T_{sub} is also critical to avoid the formation of Bi crystallites.
- The formation of the Bi crystallites can be avoided at lower T_{sub}. The combined reduction of T_{Te} and T_{sub} can solve this problem; however, it may also result in high defect density in the epilayer and failed SAE.
- If T_{sub} must be kept close to 300℃, the stoichiometric growth of higher Bi contents demands T_{Te} > 280℃ and must be tuned accordingly. It will result in higher R_{TF} and therefore with the high defect

density; however, the defect density using this approach would be lower in comparison to the growths conducted at lower T_{sub}.

In order to avoid the formation of Bi crystallites in the next stoichiometric states, the growth experiments are conducted with new parameters where T_{sub} and T_{Bi} are increased to 305 ℃ and 520 ℃ respectively while T_{Te} is gradually increased from 280 ℃. The density of Bi crystallites, observed at T_{Te} = 280 ℃, kept on decreasing with the increasing Te flux until they completely vanished at T_{Te} = 285 ℃. The corresponding behavior can be witnessed in Figure 4.23. From this point onward, the flux ratio adjustment is conducted by increasing T_{Bi} while T_{sub} and T_{Te} are kept constant at 305 ℃ at 285 ℃ respectively.

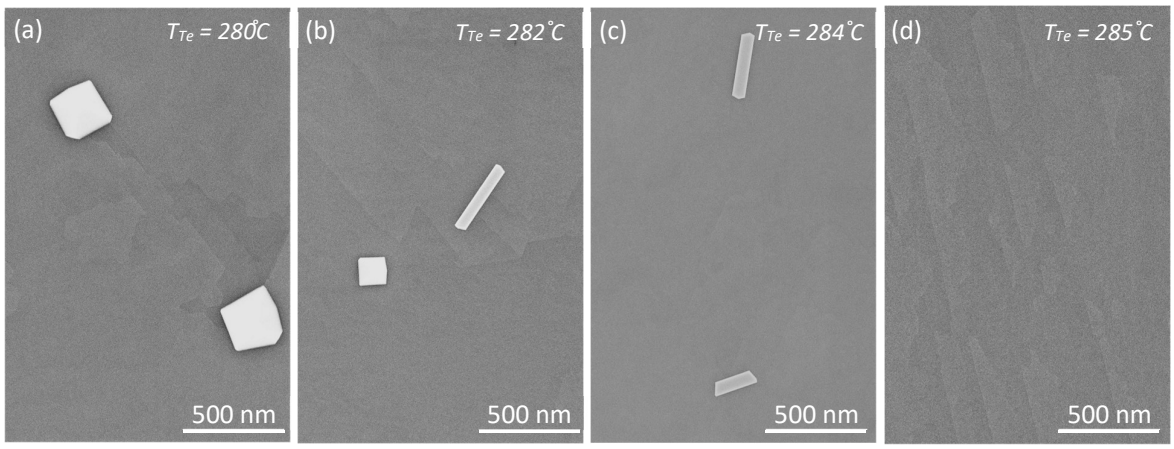

Fig. 4.23: SEM images representing the search of optimum T_{Te} to avoid the formation of Bi crystallites during the growth of Bi_xTe_y states having Bi contents higher than Bi_4Te_3 (57 %). (a-d) The effect of increasing Te flux on the surface morphology while keeping T_{sub} and T_{Bi} constant at 305 ℃ and 520 ℃ respectively. With the continuously increasing Te flux, the density of Bi crystallites are observed to decrease until they completely vanished at T_{Te} = 285 ℃.

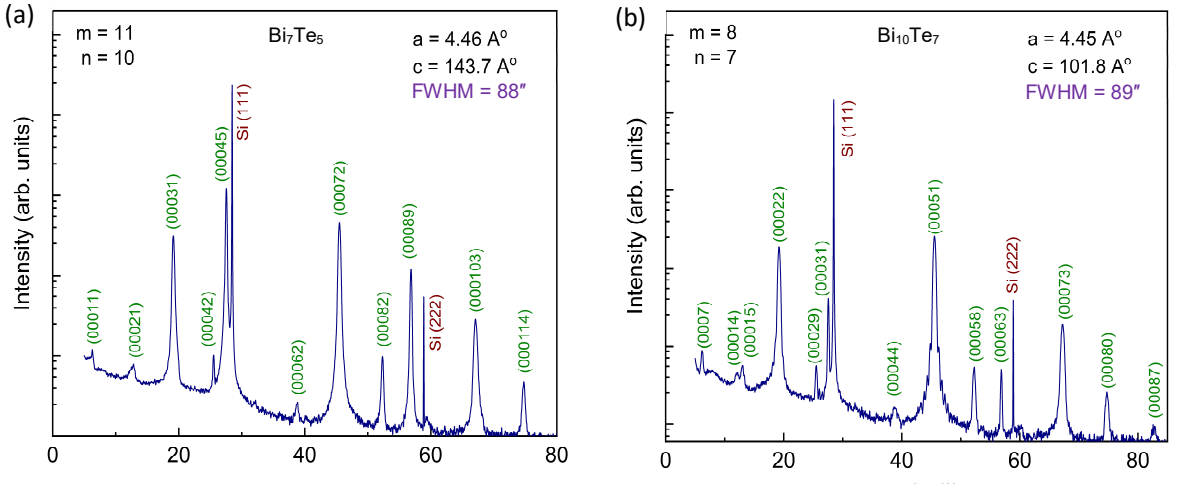

Fig. 4.24: XRD 2ϑ-ω scans. (a) Bi_7Te_5 epilayer, consists of (m:n)=(11:10) exhibiting the unit cell length c_{actual} = 143.7 ± 0.01 Å. Δω scan revealed FWHM values of 88″ obtained at the (000 72) peak indicating high structural quality of the epilayer. (b) $Bi_{10}Te_7$ epilayer, consists of (m:n)=(8:7) exhibiting the unit cell length c_{actual} = 101.8 ± 0.01 Å. Δω scan revealed FWHM values of 89″ obtained at the (000 51) peak.

Bi_7Te_5 and $Bi_{10}Te_7$: The stoichiometric states Bi_7Te_5 and $Bi_{10}Te_7$ contain 58.33 % and 58.82 % bismuth contents and exhibit unit cells comprise of (m:n) = (11:10) and (8:7) with the stacking sequences of (QBQBQB-QBQBB-QBQB-QBQBQB) and (QBQBQB-QBB-QBQBQB) respectively. Both states exhibit the trigonal crystal structure with P-3m1 (164) space group[11, 68]. These stoichiometric states are successfully achieved at T_{Bi}/T_{Te} = 515 ℃/285 ℃ and 518 ℃/285 ℃ with R_{TF} = 7.0 nm/h and 7.2 nm/h respectively while T_{sub}

is kept at 305℃. Figure 4.24a displays the XRD patterns of 59 nm thick epilayer of Bi_7Te_5 while Figure 4.24b depicts the diffraction pattern obtained from 31 nm thick epilayer of $Bi_{10}Te_7$. The unit cell lengths, measured via XRD, are found to be c_{actual} = 143.69 ± 0.01 Å and 101.80 ± 0.01 Å respectively. Both values are observed to follow the similar trend and are found be smaller than the predicted values. Later, SAE is successfully achieved for both states by applying the corrected parameters to the pre-patterned substrates with T_{Te} reduced by 3℃ and keeping T_{sub} at 305℃. To our knowledge, the crystalline growth or the structural characterization of both states are never reported until now.

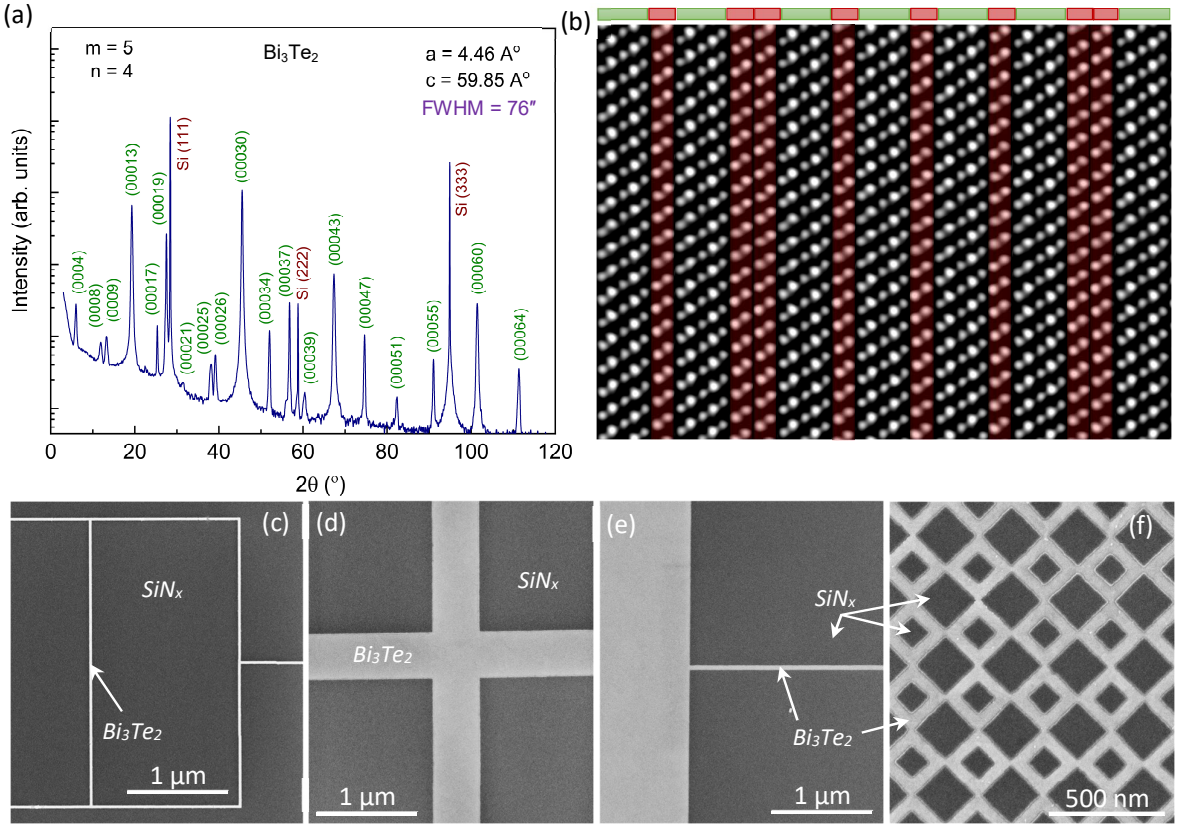

Fig. 4.25: (a) XRD 2ϑ-ω scan of Bi_3Te_2 epilayer, consists of (m:n)=(5:4) exhibiting the unit cell length c_{actual} = 59.85 ± 0.01 Å. Δω scan revealed FWHM values of 76″ obtained at the (000 30) peak. (b) STEM-HAADF image acquired along Si [1-10] orientation confirms the stacking sequence of QBQB-BQBQB. The presence of Bi_2 bilayers is highlighted with red color. (c-f) SEM images of several selectively grown nanostructures of Bi_3Te_2.

Bi_3Te_2: The stoichiometric state Bi_3Te_2 ($Bi_{18}Te_{12}$) contains 60 % bismuth contents and exhibits a unit cell of (m:n) = (5:4) with the stacking sequence of (QBQB-QBBQB). It exhibits a trigonal crystal structure with P-3m1 (164) space group[69] and $c_{predicted}$ = 60.41 Å. To our knowledge, there is only one study that reported the preparation of Bi_3Te_2 single crystal via the Bridgeman method[11]. There are also a couple of studies that have reported the preparation of nanoparticle composite for thermoelectric applications[70, 71]. Bi_3Te_2 is reported to exhibit outstanding thermoelectric features[11, 71] that are quite unique for low temperature applications[51, 70, 71, 72, 73, 74, 75] just as SiGe alloys are the best for high temperature applications[71, 76].

Bi_3Te_2 stoichiometry is achieved via MBE at T_{Bi}/T_{Te} = 522℃/285℃ with R_{TF} = 7.5 nm/h while T_{sub} is kept constant at 305℃. Figure 4.25a displays the XRD pattern of 44 nm thick epilayer of Bi_3Te_2. The unit cell length of MBE grown Bi_3Te_2 crystal, measured via XRD, is found to be c_{actual} = 59.85 ± 0.01 Å which is as expected slightly less than $c_{predicted}$. Due to relatively high growth rate (R_{TF} = 7.5 > 5 nm/h), twin domains are observed for the first time in any Bi_xTe_y stoichiometric state with the relative intensity of 1:39, measured via XRD φ-scan, where the dominant domain is observed to be collinear with Si (311), depicted

in Appendix 4A. Later, high quality nanostructures are prepared via SAE by applying the modified parameters with T_{Bi}/T_{Te} = 522℃/282℃ to the pre-patterned substrates. Once again, due to $L_{D\text{-}Te} > L_{D\text{-}Bi}$, the Bi/Te effective flux ratio is obtained with T_{Te} decreased by 3℃. The detailed structural investigations are performed via STEM at the cross-section of the 500 nm wide nanoribbon along Si [1-10] orientation. HAADF image of the unit cell along with SEM images of SAE are depicted in Figure 4.25. An important point to observe in HAADF image is the re-appearance of the pristine vdW stacking; however, it did not appear between QLs (Te-Te atoms) rather between BLs (Bi-Bi atoms). The unit cell length c_{actual}, vdW gaps along with the corresponding projected bond lengths are measured and listed in Table 4.6.

$Bi_{14}Te_9$: The stoichiometric state $Bi_{14}Te_9$ ($Bi_{42}Te_{27}$) contains 60.88 % Bi contents. Due to multiple of 3 issue, it exhibits a unit cell that comprises of (m:n) = (12:9) with the sequence of (QBQBBQB-QBQBBQB-QBQBBQB). It exhibits a rhombohedral crystal structure with R-3m (166) space group and $c_{predicted}$ = 138.88 Å. No report about the crystal preparation of $Bi_{14}Te_9$ is found in the literature.

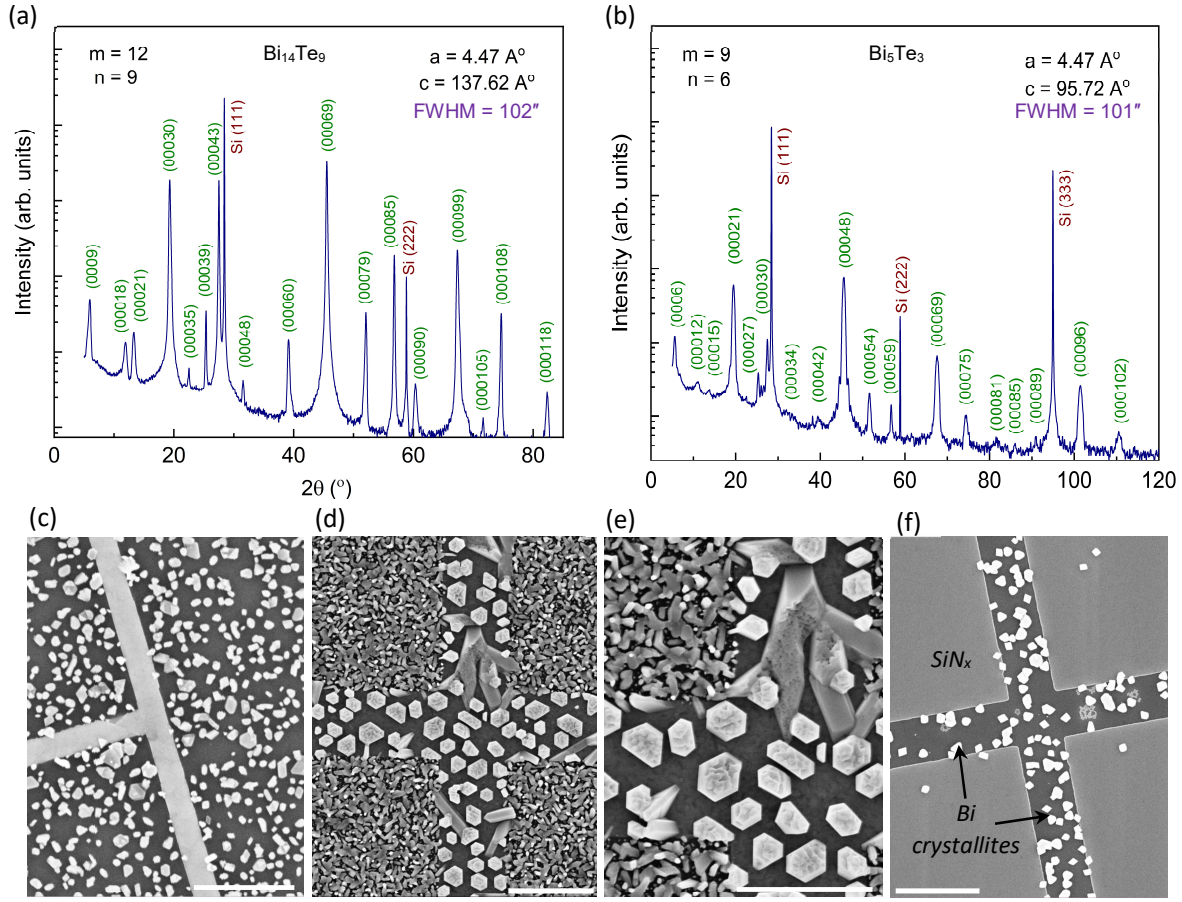

*Fig. 4.26: XRD 2ϑ-ω scans. (a) $Bi_{14}Te_9$ epilayer, consists of (m:n)=(12:9) exhibiting the unit cell length c_{actual} = 137.62 ± 0.01 Å. Δω scan revealed FWHM values of 102″ obtained at the (000 69) peak while φ-scan revealed the relative intensity of twins = 1:21. (b) Bi_5Te_3 epilayer, consists of (m:n)=(9:6) exhibiting the unit cell length c_{actual} = 95.72 ± 0.01 Å. Δω scan revealed FWHM values of 101″ obtained at the (000 48) peak. (c-f) SEM images representing the attempts of failed selectivity due to thermal instability of the epilayers at high T_{sub}. By increasing T_{sub}, epilayers disintegrate more quickly than the ADR drop to achieve selectivity (d and e). At T_{sub} >> optimum values, selectivity is achieved with the epilayer evaporated and only a few Bi crystals left in the patterned area (f). (*scale bar = 1 μm)*

During the epitaxial growth, the re-appearance of Bi crystallites has forced T_{sub} to be dropped at 290℃. The optimum Bi/Te flux ratio is achieved at T_{Bi}/T_{Te} = 520℃/275℃ with R_{TF} = 7.2 nm/h. Figure 4.26a displays the XRD pattern of 53 nm thick epilayer of $Bi_{14}Te_9$. The unit cell length of the epilayer, measured via XRD, is found to be c_{actual} = 137.62 ± 0.01 Å which is as expected slightly less than $c_{predicted}$. Unfortunately, due to

lower T_{sub}, the selectivity is not achieved. Various attempts are conducted to tune the Bi/Te flux ratio at higher T_{sub} to achieve selectivity; however, the poor thermal stability of Bi rich epilayer resulted in the damaged crystal and all attempts of SAE have failed, as depicted in Figure 4.26 (c-f).

Bi_5Te_3: The stoichiometric state of Bi_5Te_3 ($Bi_{30}Te_{18}$) contains 62.5 % bismuth contents and exhibits a very simple characteristic cell of (m:n) = (3:2) with the stacking sequence of (QB-QBB); however, as it suffers from multiple of 3 issue and a complete unit cell comprises of (m:n) = (9:6) with the sequence of (QBQBB-QBQBB-QBQBB). It exhibits a rhombohedral crystal structure with $c_{predicted}$ = 96.54 Å. The stoichiometric flux tuning of Bi_5Te_3 state is successfully achieved at T_{Bi}/T_{Te} = 525 ℃/275 ℃ with R_{TF} = 7.4 nm/h while T_{sub} is kept at 290 ℃. Figure 4.26b displays the XRD pattern of 28 nm thick epilayer of Bi_5Te_3. The unit cell length of Bi_5Te_3 epilayer, measured via XRD, is found c_{actual} = 95.71 ± 0.01 Å, slightly less than $c_{predicted}$.

$Bi_{12}Te_7$ and Bi_7Te_4: The stoichiometric states $Bi_{12}Te_7$ ($Bi_{36}Te_{21}$) and Bi_7Te_4 ($Bi_{42}Te_{24}$) contain 63.15 % and 63.63 % bismuth contents respectively. Both alloys belong to a trigonal crystal structure and exhibit unit cells with long stacking periods of (m:n) = (11:7) and (13:8) with the sequence of (BQBQB-BQBQB-BQB-BQBQB) along with the $c_{predicted}$ = 114.61 Å and (BQBQB-BQBQB-BQB-BQB-BQBQB) with $c_{predicted}$ = 132.67 Å respectively. The stoichiometric flux tuning of $Bi_{12}Te_7$ and Bi_7Te_4 states is successfully achieved at T_{Bi}/T_{Te} = 528 ℃/270 ℃ with R_{TF} = 7.9 nm/h and at T_{Bi}/T_{Te} = 532 ℃/270 ℃ with R_{TF} = 8.2 nm/h respectively while T_{sub} is dropped by 5 ℃ to ensure the thermal stability of epilayer and kept at 285 ℃. The unit cell length of $Bi_{12}Te_7$ epilayer measured via XRD, is found c_{actual} = 113.62 ± 0.01 Å while Bi_7Te_4 epilayer exhibited c_{actual} = 131.55 ± 0.01 Å, as expected, slightly less than $c_{predicted}$. To our knowledge, the single crystalline growth or the structural characterization are never reported for any of these stoichiometric states.

Bi_2Te: Bi_2Te (Bi_6Te_3) is the last stoichiometric state of Bi_xTe_y series that is investigated in this study. It contains 66.67 % bismuth contents and similar to Bi_1Te_1 exhibits the simplest unit cell of (m:n) = (2:1) with the stacking sequence of (BQB). The stacking sequence along [001], [110] and [1-10] orientations can be seen in Appendix 4A. Bi_2Te exhibits a trigonal crystal structure and belong to P-3m1, (164) space group[11, 12, 25, 58] with $c_{predicted}$ = 18.07 Å. Bi_2Te is reported to prepare by the Bridgeman method by a couple of studies[11, 12]. The stoichiometric flux tuning of Bi_2Te state is successfully achieved at T_{Bi}/T_{Te} = 542 ℃/260 ℃ with R_{TF} = 8.7 nm/h while T_{sub} is further decreased to 280 ℃. Figure 4.27 displays the XRD pattern of 45 nm thick epilayer of Bi_2Te. The unit cell length of Bi_2Te epilayer, measured via XRD, is found to be c_{actual} = 17.92 ± 0.01 Å that is also slightly less than $c_{predicted}$. Due to quite high requirement of Bi flux, Bi crystallites are also formed at the surface of the epilayer. The further optimizations are required to avoid the crystallites formation at lower T_{sub}; however, it are not conducted in this work. The achievement of high structural quality epitaxial growth of Bi_2Te via MBE will opens up possibilities to utilize this material for low energy and low temperature applications.

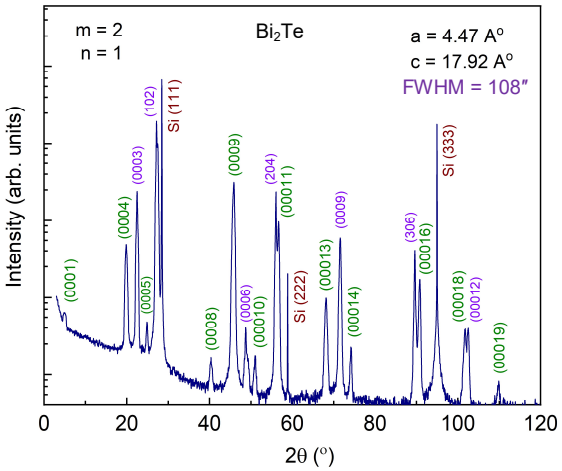

Fig. 4.27: XRD 2ϑ-ω scan of Bi_2Te_1 epilayer, consists of (m:n)=(2:1) exhibiting the unit cell length c_{actual} = 17.92 ± 0.01 Å. Δω scan revealed the FWHM values of 108″ obtained at the (000 9) peak indicating the high structural quality of the epilayer. Along with Bi_2Te_1 characteristic peaks, the diffraction peaks of bismuth are also observed, indexed with purple color, due to the presence of Bi crystallites on the Bi_2Te_1 epilayer surface.

A few characteristics of Bi_2Te stoichiometry are mentioned below:

- Bi_2Te (BQB) is the inverse equilibrium stoichiometric state of Bi_1Te_1 (QBQ).
- Bi_2Te crystal exhibits semi metallic behavior[7, 59, 65, 66] and similar to Bi_4Te_3 is a prime candidate for the PCM particularly from one crystalline phase to another crystal phase[60, 67, 77].
- Due to this characteristic stacking of sandwiched QL between two BLs, Bi_2Te is the only stoichiometric state after Bi_4Te_3 that exhibit superconductivity with T_c = 8.6 K[77] when applied to high pressure conditions.

Starting from the stoichiometry of Bi_2Te_3 (Bi = 40 %) till Bi_2Te_1 (Bi = 66.67 %), the epitaxial growth of 38 distinct phases (alloys) is achieved. Among them, 5 are found to exhibit the intermediate phases i.e. the instability due to long stacking period that either resulted in a mixed state or transformed into another close by stoichiometry and thus, are failed to be prepared with 100 % yield. The detailed structural characterizations are performed via XRD for the rest of 33 states while SAE is achieved successfully for 26 of them. The stacking sequences in unit cells along with the changes in vdW gaps at the atomic scale are investigated via STEM for 13 key states. The summary of all Bi_xTe_y states along with the growth parameters, the stacking sequences and the structural parameters are listed in Appendix 4B. The accumulative analysis of pristine vs. hybrid vdW gaps for Bi_xTe_y family is conducted in the next section.

4.6 Structural analysis: Interlayer gaps, bonding & unit cell dimensions

It was mentioned during the structural characterization of the individual states that all Bi_xTe_y alloys exhibited a trend of slightly reduced measured unit cell lengths (c_{actual}) then the calculated ($c_{predicted}$) ones. The presence of Bi_2 BL among QLs introduces hybrid vdW gaps (Figure 4.7). The atomic scale measurements via STEM have indicated the relatively short lengths of hybrid vdW stacks in comparison to the pristine gaps, listed in Tables 4.2, 4.3, 4.5 and 4.6 for all stoichiometric states. It is also noticed that the change in a unit cell length (Δc), according to equation 4.3, between the experimentally measured and the theoretically predicted values is not constant nor does it seem to be following any distinct pattern with the changing stoichiometry. In order to understand the resulting changes in unit cell length (Δc) due to hybrid gaps, it is necessary to understand the impact on the bonding with the appearance and increasing density of Bi_2 BLs in the stacking sequence.

$$\Delta c = c_{predicted} - c_{actual} \tag{4.3}$$

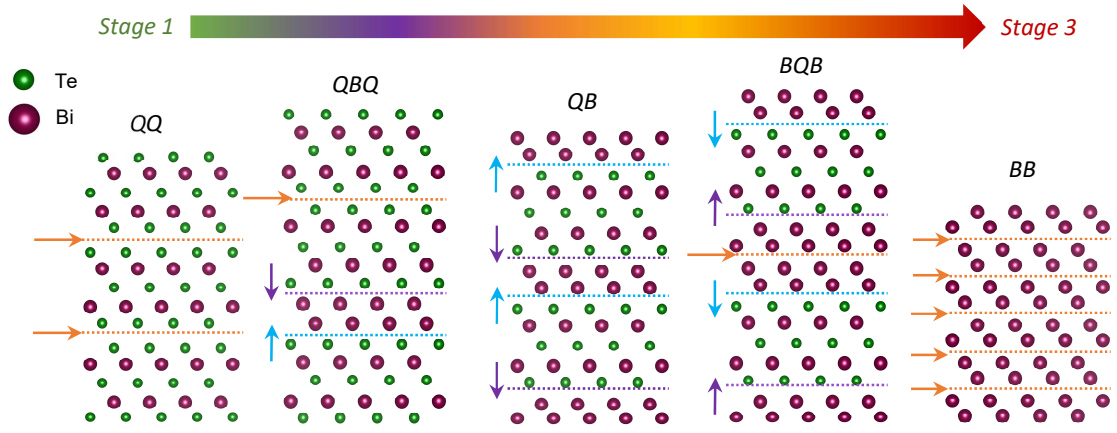

Fig. 4.28: A model representing the five unique structural blocks of Bi_xTe_y system that in various combinations provide all stoichiometric layer sequences. These building blocks are named QQ, QBQ, QB, BQB and BB. The red and green colors are representing Bi and Te atoms respectively. The orange arrows along with the dotted lines represent pristine (P) vdW stacking while the blue and purple color represent the hybrid, LH and RH gaps respectively.

Considering all the stacking sequences of Bi_xTe_y alloys, there are only five unique characteristic blocks, depicted in Figure 4.28, that by combining in various ratios facilitate any possible stacking order in $(Bi_2)_m(Bi_2Te_3)_n$ series. Hence, understanding the origin, inter-block transformation and bonding mechanisms of these five characteristic blocks is actually understanding the entire Bi_xTe_y family.

4.6.1 The QQ block

A QQ block (QQ stacking) exhibits only pristine vdW gaps between Te-Te atoms for example Bi_2Te_3. It facilitates the strain-free and relaxed stacking of layers. During the structural characterization of Bi_2Te_3, the interlayer gap between Te-Te atoms and the projected bond length were measured and listed in Table 4.2. The accuracy of the measured data can be confirmed with the evaluation of the angle of atomic arrangement in the crystal with the help of Pythagorean Theorem. It can also be visualized in Figure 4.29a.

The measured interlayer gap in a QQ Block between Te atoms (α) = Pristine vdW gap = 2.55 ± 0.03 Å
The measured projected bond length (β) = 2.88 ± 0.03 Å
The angle of atomic arrangement (θ) = Sin^{-1} (α/β) = 62.19° ± 0.04°

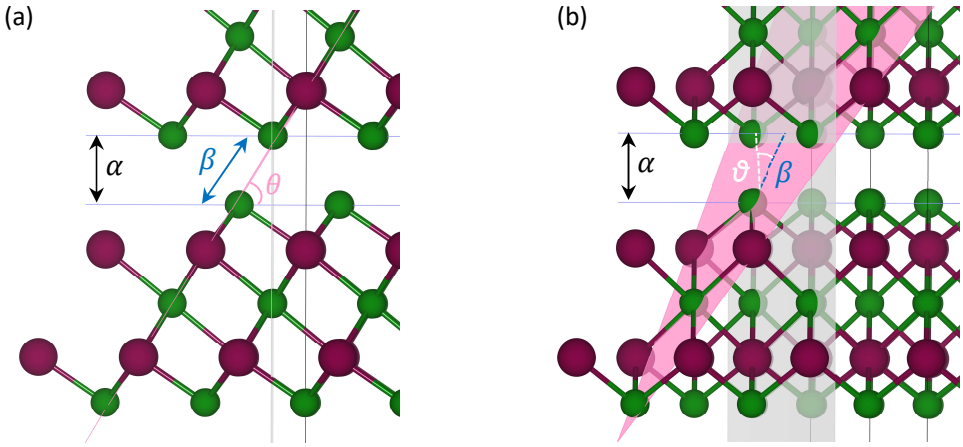

Fig. 4.29: A model representing (a) the vdW Gap in a QQ block between two QLs where α indicates the pristine vdW gap, β represents the projected bond length between neighboring Te atoms on the opposite side of the vdW gap and θ represents the angle of atomic arrangement. (b) The same QQ block rotated 30° around the z-axis to represent ϑ that indicates the in-plane angle between the Te atoms that was not possible to visualize in the projected image along the [110] orientation in (a). With ϑ the real bond length between Te atoms can be evaluated.

The evaluated angle fits perfectly with Bi_2Te_3 reported crystal structure[25, 78] and confirms the accuracy of the measured data. Now, using the projected bond length (β), the actual bond length between Te-Te atoms through the vdW gap can be evaluated. It is known from the theoretical models that the in-plane angle between two Te atoms is approximately 37° (represented by ϑ in Figure 4.29b where the plane is highlighted by the pink color), so according to Pythagorean Theorem:

The actual bond length (Te-Te) = the projected bond length / cos (37°) = 3.61 ± 0.04 Å

The bond length, reported for Sb_2Te_3, between Te-Te atoms across a pristine vdW gap in a QQ block is 3.63 Å[79, 80, 81, 82] that is in good agreement with the measured value for Bi_2Te_3 which also confirms the accuracy of the measurements. Thus, this method is adopted to evaluate the changes in bond length with the appearance and increasing density of Bi_2 BL in the stacking sequences e.g. in the blocks QBQ, QB and BQB. It will also assist in understand the changes in the bond strength and any effective change in lattice parameters.

4.6.2 The QBQ block (Stage 1 alloys of Bi_xTe_y)

A QBQ block can also be named as BQQ and QQB, represents a Bi_2 BL sandwiched between 2 QLs. It exhibits 3 interlayer gaps including one pristine and two hybrid named LH and RH, introduced in Figure 4.7.

- The pristine gap appears when a QBQ block stacks with another QBQ or a QQ block. It exhibits vdW gap between Te atoms with similar characteristics i.e. inter atomic interaction and bond length of a QQ block, discussed above for Bi_2Te_3. It can be visualized in Figure 4.28, represented by orange arrow along with a dotted line.
- Two hybrid gaps appear on both sides of the sandwiched Bi_2 BL between two QLs in QB and BQ stacking exhibiting vdW gaps between Te-Bi and Bi-Te atoms named left hybrid (LH) and right hybrid (RH) respectively. They are named to distinguish, if they exhibit identical or different behavior. LH and RH can be visualized in Figure 4.28, represented by blue and purple arrows along with a dotted lines respectively.

STEM measurements have indicated that both LH and RH gaps are identical in a QBQ block and listed in Table 4.8. It is also evident that both hybrid gaps are slightly smaller than the pristine gap. It can be directly linked to stronger interatomic interaction between Te-Bi atoms in comparison to Te-Te atoms. Due to these strong interaction both QLs are attracted towards Bi_2 BL resulting in reduced gap lengths while the pristine interlayer gap remained intact. This phenomenon creates the QBQ block, a unit with stronger intra-block interactions exhibiting hybrid gaps and weak inter-block interactions with the pristine gap (QQ stack).

Table 4.8: The measured structural parameters including the vdW gaps (pristine and hybrid) and the corresponding projected bond lengths via STEM in a QBQ block.

Interlayer Gap (Type)	Layer Stack (Order)	Interlayer Gap (Å)	Projected Bond Length (Å)	Bond Length (Å)
Pristine	QQ Stack	2.55 ± 0.03	2.88 ± 0.04	3.61 ± 0.04
Hybrid – LH	QB Stack	2.42 ± 0.04	2.73 ± 0.04	3.42 ± 0.04
Hybrid – RH	BQ Stack	2.43 ± 0.05	2.74 ± 0.05	3.43 ± 0.05

Bi_1Te_1 is the simplest example where a single QBQ block acts as a complete unit cell. The unit cell length of Bi_1Te_1, measured via STEM and listed in Table 4.3, is c_{actual} = 24.02 ± 0.03 Å while the theoretical predicted value without taking the hybrid interactions into account is $c_{predicted}$ = 24.27 Å. The overall difference imposed by the both hybrid gaps, in comparison to pristine gaps can be evaluated from Table 4.8, is 0.25 ± 0.04 Å that fits perfectly to the difference in unit cell length (Δc) of Bi_1Te_1. Hence, it became evident that the reduced bond length of hybrid gaps, due to the appearance of a Bi_2 BLs in stacking sequence, is the source of decrement in the unit cell length for all Bi_xTe_y crystals. That is why, c_{actual} is always observed to be slightly less than the $c_{predicted}$.

QQ to QBQ transformation: The transformation of QQ blocks into QBQ blocks can be observed in the stoichiometric alloys of stage 1, discussed in Section 4.3. As soon as a Bi_2 BL appeared in the stacking order, the QQ block transformed into a QBQ block resulting in a reduced unit cell length (c_{actual}) of the crystal. The transformations can be observed in Bi_3Te_4 with (QQ-QQ-QQ-QBQ), Bi_4Te_5 with (QQQ-QBQ), Bi_6Te_7 with (QBQ-QQQ-QBQ), Bi_8Te_9 with (QQ-QBQ-QQ-QBQ-QQ-QBQ) and ending at Bi_1Te_1 (QBQ) that contains only QBQ blocks.

Normalized compression: In order to compare the strength of compression in different stoichiometric states having diverse unit cell dimensions, the compression per unit length (normalized compression) is calculated according to equation 4.4. *(Note: The term compression here represents the decrement in the unit cell length due to enhanced inter-atomic interactions via hybrid stacks. No external physical parameter is involved.)* It is observed that the normalized compression in a crystal increases with the increasing

density of QBQ blocks in the stacking sequence. In other words, it increases with the increasing density of Bi_2 BLs in a unit cell.

$$Normalized\ compression\ = \left(\Delta c / c_{actual}\right) \times 100\ \% \tag{4.4}$$

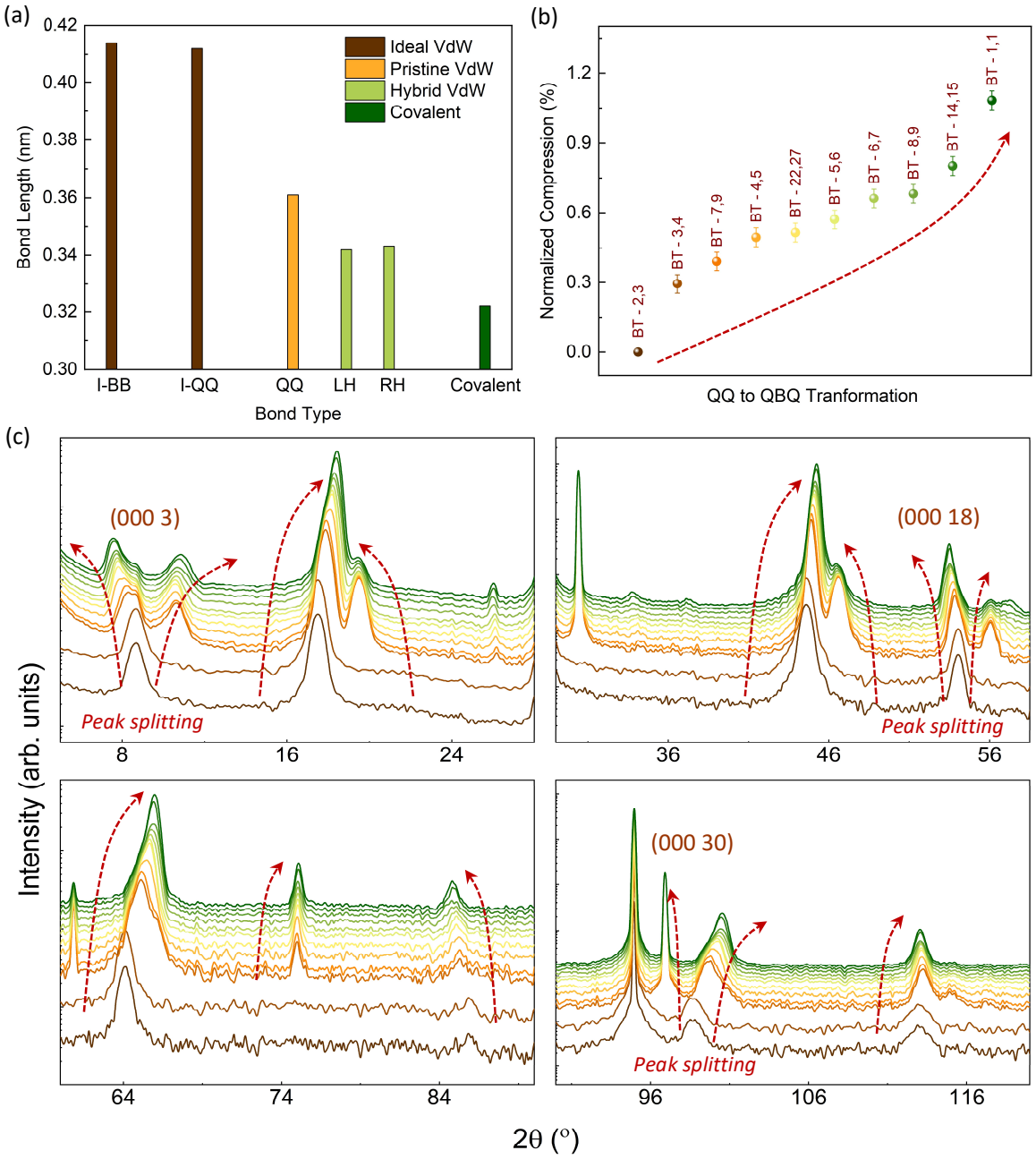

Fig. 4.30: The effect of Hybrid stacking on the unit cell length and the transformation from QQ to QBQ blocks. (a) An overview of the pristine ideal gaps between Te atoms (I-QQ), Bi atoms (I-BB) and the measured bond lengths of all three vdW stacks in a QBQ block. (b) A trend in the normalized compression of Bi_xTe_y unit cells of stage 1 alloys from Bi_2Te_3 to Bi_1Te_1 with the increasing density of Bi_2 BLs. (c) A cumulative XRD pattern of stage 1 alloys indicating the increment in normalized compression due to gradual transformation of QQ blocks into QBQ bocks and the resulting changes in the unit cell length. The (000 3) peak in Bi2Te3 at $2\vartheta = 8.64^{\circ}$ is observed to split (divide) into two separate peaks due to vertical compression. With the further increase in compression the divided peaks can be observed to move in the opposite directions. Similar trend can also be observed with other peaks bringing a ripple like behavior where the peak indices are marked according to Bi_2Te_3. For better visibility, follow the red arrows.

Figure 4.30a represents various ideal (according to definition) and measured vdW gaps along with the largest limit of the covalent bond length. An ideal vdW gap between two atoms is the sum of their individual vdW radii[79]. That is why, the ideal vdW gaps between two Bi atoms (I-BB) and two Te atoms (I-QQ) are almost identical as both atoms i.e. Bi and Te exhibit almost similar vdW radii. Any material that exhibits vdW gap smaller than the ideal case indicates the strong atomic interactions between atoms while the larger gap represents the weekly bonded layers. For further details of vdW bonding refer to [79, 80, 83, 84].

It is evident that all the measured vdW gaps exhibited stronger interactions than the ideal case however, the hybrid gaps (LH and RH) in comparison to the pristine gap (QQ), are much stronger and therefore, also shorter in length. Due to higher bond strength and strong atomic interactions in the hybrid stacking, the trend of increasing normalized compression with the increasing Bi contents in the epilayer (increasing density of BLs) and the resulting transformation of QQ blocks into QBQ blocks can be visualized in Figure 4.30b. The trend of normalized compression can also be observed via the cumulative XRD patterns of the stage 1 alloys from Bi_2Te_3 to Bi_1Te_1, depicted in Figure 4.30c (divided into four parts for better resolution). The introduction of Bi_2 BL in the stacking sequence compresses the (000 3) peak of Bi_2Te_3 and splits into two parts. Similarly, splitting of the (000 18) and (000 30) peaks can also be witnessed. With the continuously increasing strength of the normalized compression in the crystal, the peaks can be observed to move in opposite directions as indicated by the red arrows in Figure 4.30c.

Lateral strain: Bos *et al.*[11, 12] proposed another model to explain the compression in Bi_xTe_y crystals where a few Bi_xTe_y alloys were prepared via the Bridgeman method for the thermoelectric investigations. As, the structural investigations were not performed via STEM, the different interlayer gaps and the stacking blocks were not observed. That is why, the proposed model lacks the structural information about the hybrid gaps and the interatomic interactions were not considered as a factor to induce vertical compression in a unit cell. According to Bos *et al.*, the unit cell of Bi_xTe_y experiences compression due to exerted lateral strain by the Bi_2 BL as the in-plane lattice constant "a" of Bi_2 is larger than Bi_2Te_3 $a_{Bi_2}(4.57\ \text{Å}) > a_{Bi_2Te_3}(4.38\ \text{Å})$. With the incorporation of Bi_2 BL, the crystal experiences lateral strain and the out-of-plane lattice constant (c_{actual}) decreases. This theory could not justify changes in the unit cell for all stoichiometric states. Also, it does not explain the bond length differences in the pristine (QQ) and hybrid (QB) stacks and does not even identify the difference in behavior of the hybrid interlayer gaps in comparison to the pristine gaps. A recent study[85] has also reported the observation of lateral strain in the MBE grown Bi_xTe_y films prepared on the graphene layer. In this study, however, the detailed XRD characterizations and RSM measurements have confirmed the absence of any strain related effect in Bi_xTe_y crystals (For details visit Appendix 4B). According to this work, above mentioned factor ($a_{Bi_2} > a_{Bi_2Te_3}$) plays an important role in switching the growth mode from Stranski-Krastanov regime in Bi_2Te_3 to high quality 2D Frank–van der Merwe growth mode in Bi_xTe_y. It happens due to the enhanced interaction of Bi atoms with Te in the hybrid vdW stacking (QB and BQ). The appearance of Bi_2 BL stretches the crystal laterally forcing incoming adatoms to grow more uniformly and resulting in an improved surface roughness.

4.6.3 The QB block (Stage 2 alloys of Bi_xTe_y)

The QB block is a unique structural unit as it exhibits alternating QL-BL stacking and does not host any pristine interlayer gap. The only 2 interlayer gaps that exist are both hybrid in nature. Bi_4Te_3 is the ground state of the QB block. Similar to QBQ block, a BL attracts QLs at both interfaces however, the situation becomes different from a QBQ block as the attracted QLs are also being attracted by two other BLs on their opposite sides (depicted in Figure 4.28) whereas in a QBQ block they always remain in the relaxed state with QQ stacking. In other words, each layer (BL or QL) is being attracted by two layers of the opposite type on each sides i.e. a BL is being attracted by two QLs while each of those two QLs are also being attracted by other two BLs on the opposite direction.

QBQ vs. QB: As far as LH and RH gaps are concerned; based on the stacking sequence, it can be assumed that hybrid gaps in a QB block should be more relaxed (less compressed) than the hybrid gaps of a QBQ block. The reason are stated below.

- In a QBQ block, the BL attraction of both QLs is not challenged by any entity as both attracted QLs exhibit relaxed (QQ) stacking with neighboring QLs through weak interactions.
- In a QB block, when a BL attracts QLs at each side, both of those QLs are also being attracted by other BLs simultaneously. It can be imagined like a chain fully stretched, quite opposite to the case of QBQ block where a block is strong in itself, however, exhibits weak interactions with other blocks. Hence, according to this model, both hybrid gaps in a QB block are predicted to be equal in strength; although, a little stretched i.e. weaker and longer than the hybrid gaps in a QBQ block.

The observed reality is, however, completely opposite. It is witnessed via STEM measurements that both hybrid gaps are different in strength. The LH gap is observed to be much shorter than the estimated value while the RH gap is observed to be in more relaxed state as listed in Table 4.9. It seems that the anticipated stretched chain model does not apply to a QB block rather a trade-off agreement is witnessed to hold where one hybrid gap takes more strength with shorter interlayer gap while the other relaxes. The reason of this tradeoff is unknown and requires detailed chemical and structural analysis to enlighten the physics behind it. At the end, it results in a unit of two layers, a QB block that stacks with another QB block in a relatively weaker hybrid stacking though much stronger than the pristine QQ stack observed in QBQ blocks.

Table 4.9: The measured structural parameters including the vdW gaps (pristine and hybrid) and the corresponding projected bond lengths via STEM in a QB block.

Interlayer Gap (Type)	Layer Stack (Order)	Interlayer Gap (Å)	Projected Bond Length (Å)	Bond Length (Å)
Hybrid – LH	QB Stack	2.37 ± 0.04	2.68 ± 0.04	3.35 ± 0.04
Hybrid – RH	BQ Stack	2.47 ± 0.05	2.79 ± 0.05	3.49 ± 0.05

Transformation into QB blocks: A transformation from QBQ blocks into QB blocks happened in the stage 2 alloys, discussed in section 4.4. As soon as Bi contents increased from 50%, the stoichiometry with the additional Bi_2 BL forced the transformation of uniform QBQ blocks (Bi_1Te_1) into the QB blocks. Starting from Bi_1Te_1 with (QBQ), the gradual transformation took place through the major stoichiometric states of $Bi_{16}Te_{15}$ with (QBQ-QB-QBQ-QBQ-QB-QBQ-QBQ-QBQ-BQ), $Bi_{12}Te_{11}$ with (QBQ-QBQ-QB-QBQ-QB-QBQ-QB), $Bi_{10}Te_9$ with (QB-QBQ-QB-QBQ-QBQ-BQ), Bi_9Te_8 with (QBQ-BQ-BQ-QBQ-BQ), Bi_7Te_6 with (QB-QB-QBQ-QB-QB-QBQ-QB-QB-QB), Bi_6Te_5 with (QBQ-QB-QB-QB), Bi_5Te_4 with (QB-QB-QB-QQB-QB-QB-QB) and ending at Bi_4Te_3 with (QB-QB-QB), a ground state of the QB block.

The normalized compression: The transformation of a QB block from the QBQ annihilated the pristine QQ stacking (relaxed state) and introduced the hybrid QB stacking (compressed state) bringing the crystal in further compressed state. That is why after Bi_1Te_1, the vertical compression continued to increase until the density of the QB blocks became enough to stop the rising vertical compression through the tradeoff agreement between LH and RH (discussed above). The crystal started to rearrange itself and the vertical compression started to reduce until it reaches the periodic QB stacking in Bi_4Te_3. The normalized compression of stage 2 alloys is calculated according to equation 4.4 and depicted in Figure 4.31b. The similar behavior is also evident through the cumulative XRD patterns of stage 2 alloys from Bi_1Te_1 to Bi_4Te_3, depicted in Figure 4.31c. For better understanding, follow the red arrows where, at first the increasing and later the gradually decreasing strength of the normalized compression in the crystal forced the diffraction peaks to switch the direction.

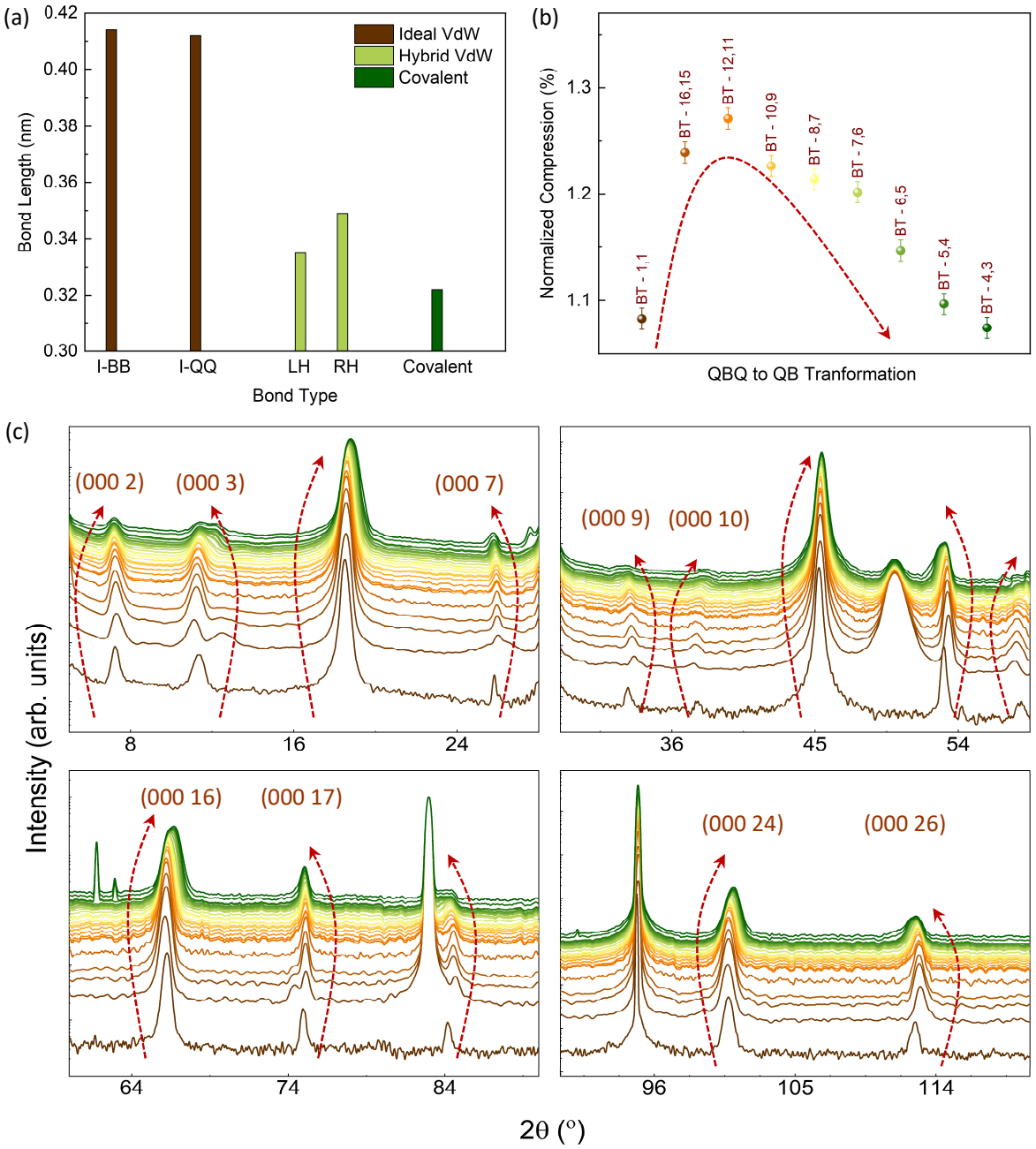

Fig. 4.31: The effect of Hybrid stacking on the unit cell length and the transformation from QBQ to QB blocks. (a) An overview of the pristine ideal gaps between Te atoms (I-QQ), Bi atoms (I-BB) and the measured bond lengths of both vdW stacks in a QB block. (b) A trend in the normalized compression of Bi_xTe_y stoichiometric states of the stage 2 alloys from Bi_1Te_1 to Bi_4Te_3 with the increasing density of Bi_2 BLs. (c) A cumulative XRD pattern of stage 2 alloys indicating the increment in normalized compression at the early stages due to gradual transformation of QBQ blocks into QB bocks and the resulting changes in the unit cell length. The trend of increasing compression is shifted after the stoichiometry of $Bi_{12}Te_{11}$ where the tradeoff agreement between LH and RH became dominant, the normalized compression started to decrease and eventually came back to the equivalent value in Bi_4Te_3 to Bi_1Te_1. This behavior of increasing the compression in early stages and later decreasing can be easily observed with the change in the direction of peak shifts by following the red arrows. The peak indices are marked according to Bi_1Te_1.

4.6.4 The BQB block (Stage 3 alloys of Bi_xTe_y)

The BQB block is just the exact opposite of a QBQ block, discussed in Section 4.6.2, with the role of QL and BL reversed. A BQB block can also be named as QBB and BBQ, represents a QL sandwiched between 2 BLs. It exhibits 3 interlayer gaps including one pristine and two hybrid.

- The pristine gap exists when a BQB block stacks with another BB or BQB block via BB stacking exhibiting the vdW gap between Bi atoms with similar characteristics i.e. inter-atomic interaction and bond length of a BB block in pure bismuth crystal. It can be visualized in Figure 4.28, represented by orange arrow along with a dotted line.
- Two hybrid gaps exist on both sides of the sandwiched QL between two BLs in BQ and QB stacking exhibiting RH and LH gaps respectively. The QL attracts both BLs reducing the interlayer gap and the bond lengths. STEM measurements have shown that similar to a QBQ block, both LH and RH gaps are identical in a BQB block and the measured values are listed in Table 4.10.

Table 4.10: The measured structural parameters including the vdW gaps (pristine and hybrid) and the corresponding projected bond lengths via STEM in a BQB block.

Interlayer Gap (Type)	Layer Stack (Order)	Interlayer Gap (Å)	Projected Bond Length (Å)	Bond Length (Å)
Pristine	BB Stack	2.48 ± 0.03	2.80 ± 0.04	3.51 ± 0.04
Hybrid – LH	QB Stack	2.42 ± 0.04	2.73 ± 0.04	3.41 ± 0.04
Hybrid – RH	BQ Stack	2.41 ± 0.03	2.74 ± 0.05	3.42 ± 0.05

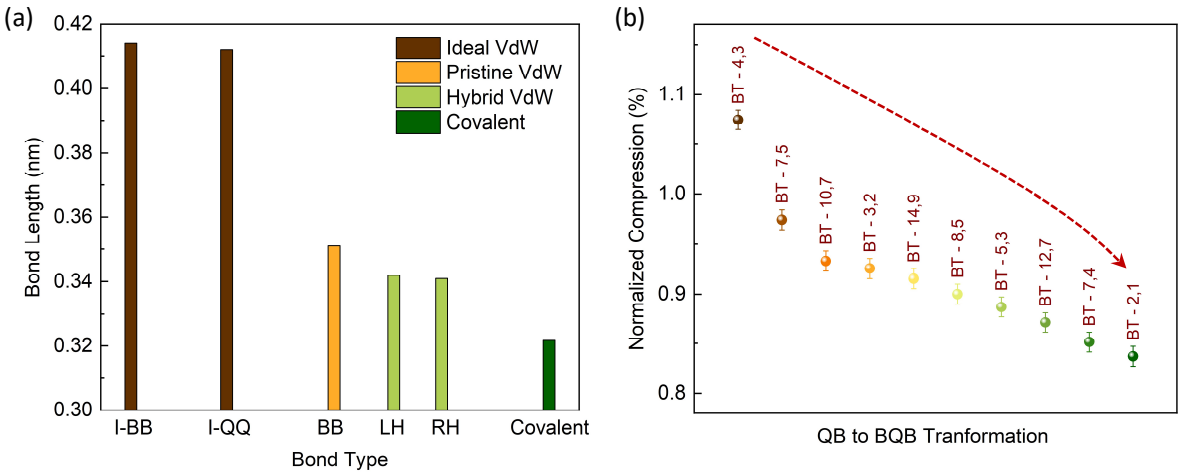

Fig. 4.32: The effect of Hybrid stacking on the unit cell length and the transformation from QB to BQB blocks. (a) An overview of the pristine ideal gaps between Te atoms (I-QQ), Bi atoms (I-BB) and all the measured bond lengths of vdW stacks in a BQB block. (b) A trend in the normalized compression of Bi_xTe_y stoichiometric states of the stage 3 alloys from Bi_4Te_3 to Bi_2Te_1 with the increasing density of Bi_2 BLs.

Transformation into BQB blocks: The transformation of QB blocks into BQB blocks occurred in the stage 3 alloys, discussed in section 4.5. With the continuous addition of Bi contents, natural stacking order forced the additional Bi_2 BL into the uniform QB stacking of Bi_4Te_3, transforming it into a BQB blocks. This phenomenon introduced, once again, the pristine interlayer gap; however, not in the form of QQ instead, in form of BB stacking between Bi atoms. Starting from Bi_4Te_3 with (QB-QB-QB), the gradual transformation into the BQB blocks took place through the major stoichiometric states of $Bi_{10}Te_7$ with (QB-QB-QB-QB-QB-QB-BQB), Bi_3Te_2 with (QB-QB-BQB-QB), Bi_8Te_5 with (QB-BQB-QB-BQB-QB), Bi_7Te_4 with (BQB-QB-BQB-BQB-QB-BQB-BQB-QB) and ending with Bi_2Te_1 (BQB), a ground state of the BQB block. With the increasing

density of transformation into BQB blocks, as mentioned above, the density of pristine gaps also increased and the overall compression in the crystal decreased. The normalized compression of the stage 3 alloys is calculated according to equation 4.4 and depicted in Figure 4.32. After Bi_2Te (BQB), the further addition of Bi_2 BL in the stacking order will gradually transform the BQB blocks into the BB blocks that will end at bismuth, comprises only of BB blocks.

4.7 Structural defects in Bi_xTe_y material system

It has already been established in chapter 2 that almost all structural defects in Bi_2Te_3 epilayers (other than the substrate induced effects) can be avoided just by controlling the growth rate (R_{TF}) ≤ 5 nm/h while keeping T_{sub} at the optimum value of 300℃. All growths of Bi_xTe_y alloys, discussed in Section 4.3 and 4.4, are conducted at the optimum T_{sub} while R_{TF} remained ≤ 5 nm/h. That is why, defect free epilayers are obtained for all the stoichiometric states from Bi_2Te_3 till Bi_3Te_2 (stage 3), confirmed by φ-scans while $\Delta\omega$ scans confirmed the high structural quality of the crystals (for details visit Appendix 4B). The epitaxial growths of stoichiometric states, having higher bismuth contents than Bi_3Te_2 (Bi = 60 %), exhibited suppressed twin domains as their growths are conducted at lower T_{sub} due to thermal instability of the epilayers. Before the development of building a platform, where only one variable parameter is utilized to tune the Bi/Te flux ratio, attempts to achieve the desired stoichiometric alloys were conducted with random parameters where in some cases, R_{TF} reached as high as 12 nm/h. During the structural investigations of these growths, conducted at high R_{TF}, a few structural defects were witnessed; however, the defect density in these crystals still remained quite low in comparison to conventional 3D TIs.

Domains: Observations have indicated that among all structural defects, the rotational twin domains are the first to appear. The relative intensity of twins in Bi_xTe_y system, measured via XRD φ-scans is observed to be 1:30, for the growths conducted at R_{TF} = 12 nm/h; however, as soon as R_{TF} dropped below 5 nm/h, the twin domains disappeared, exhibiting entire epilayer collinear with Si (311). In STEM investigations of all Bi_xTe_y system, twins are never witnessed. An example of STEM bright field image of Bi_8Te_9 epilayer at Si (111) interface is depicted in Figure 4.33a, where epilayer collinearity with Si (311) is evident.

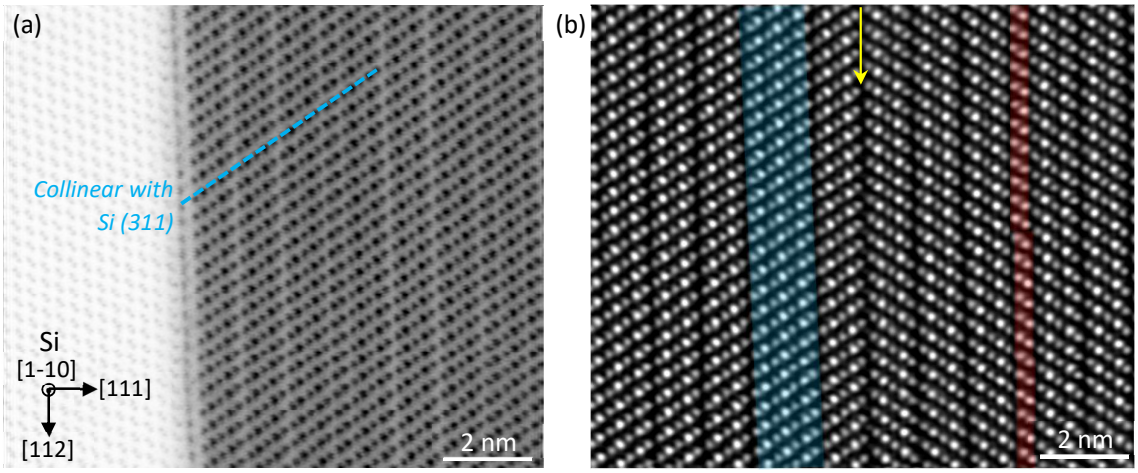

Fig. 4.33: A cross-sectional overview of Bi_8Te_9 epilayer prepared on Si (111) substrate acquired with the help of a bright field STEM images along Si [1-10] projection indicating an atomically sharp interface and the domain collinearity with Si (311). (b) HAADF image of Bi_4Te_5 epilayer, prepared with the non-optimized growth parameters with R_{TF} = 12 nm/h and T_{sub} = 285 ℃, indicating a couple of stacking faults including layer architecture defect with the appearance of SL (blue color) and a TSF (yellow arrow). The presence of bilayer is marked with the red color.

Stacking Faults: The main structural defect observed in Bi_xTe_y material system is the stacking fault. Among various types of stacking faults, three most common to this material system are the periodic stacking disorder, translation shear fault (TSF) and switching layer architecture.

- ***The stacking order***, also known as the periodic stacking sequence is unique for each stoichiometric state. Any variation in the periodic sequence results in stoichiometric deviation and forms the mixed phase crystal. Stacking order defect is the most complicated to control and can be avoided with the precise tuning of Bi/Te flux ratio and the optimum T_{sub}. It has been discussed in detail for each stoichiometric state in Sections 4.3 - 4.5.
- ***TSF*** is also known as the out-of-plane rotational domain and the stacking rotational disorder (SRD), already introduced in chapter 2 (Figure 2.13). This defect can also be avoided by reducing R_{TF} to 5 nm/h. Bi_xTe_y epilayers prepared with R_{TF} >> 5 nm/h exhibited TSFs. The most interesting fact about TSF in Bi_xTe_y material system is the location of its appearance. It has been noticed that only the weakly bonded stacks that exhibit characteristics closer to an ideal vdW bonding like QQ and BB stacks, host TSFs. Even in the QBQ and BQB blocks, TSFs only appear between the weakly bonded QQ and BB stacked layers with pristine vdW gaps. None of hybrid stacking (LH and RH), probably due to the relatively stronger atomic interactions, allow a TSF to develop. Figure 4.33b depicts a TSF, appeared between the QQ stacked layers of the stage 1 alloy, prepared with R_{TF} = 12 nm/h at T_{sub} = 285℃.
- ***Layer architecture defect*** is the deviation from the standard layer structure. In a few epilayers prepared at the non-optimized parameters i.e. R_{TF} >> 5 nm/h and T_{sub} lower than the optimum value, layer architecture defects are observed. At places, the formation of septuple layer (SL) in the layer stack instead of QL+BL is witnessed (Figure 4.33b) but only twice. Such defects disrupt the periodic staking order and alter the stoichiometry of the system. The epilayers prepared with optimum T_{sub} have never exhibited layer architecture defects. The formation of such defects is also reported during the epitaxial growth of Bi_2Te_3 crystal.

Antiphase Domain: According to discussions in chapter 2, the one and only category of structural defects that cannot be avoided even in the highest quality epitaxial growth of 3D TIs on Si (111) substrates is the step edge induced defects. It has also been discussed how these 2D step defects force QLs to form either an antiphase domain or a screw dislocation, depending upon the collinearity of the epilayer (Figure 2.13). In Bi_xTe_y material system, due to collinearity of epilayer with Si (311), only antiphase type domains are observed. The antiphase domain density that could not be avoided in Bi_2Te_3, can be naturally suppressed in Bi_xTe_y however, it depends entirely on the stacking order (stoichiometry) of the alloy. The most prominent case for QL architecture (Bi_2Te_3) is discussed in Figure 2.14, while the other three prominent cases with the presence of Bi_2 BLs are introduced here. The probability of an antiphase domain formation in all Bi_xTe_y is observed to change with the density of BLs in the stacking order, depicted in Figure 4.34e.

- The height of a Bi_2 BL (inclusive of hybrid gap) is approximately 3.95 Å[11, 12] that matches perfectly with the height of Si step edge. It suggests that with the presence of Bi_2 BL in the stacking sequence, the effects of Si step edges can be neutralized. As soon as the stacking sequence drops below (m:n) = (1:4), Bi_2 BL injects itself between lower and upper terraces and assists to overcome the step edge defect. Thus, the growth of uniform epilayer begins (Figure 4.34a). This phenomenon starts to overtake in Bi_5Te_6 state (section 4.3) and continues all the way through Bi_1Te_1 until Bi_7Te_6 (discussed in section 4.4). The one major drawback of this phenomenon is the disorder of stacking sequence in first few layers as depicted in Figure 4.34a particular for the state of Bi_1Te_1. However, epilayers after the first couple of disordered stacks can be grown with the perfect periodic sequence. On the bright side, phase coherent length of quasi-particle in the magneto-transport investigations which was observed to be limited by the antiphase domains[86] in Bi_2Te_3 can be much improved in Bi_xTe_y due to BL assisted blockage of the hard stacking shifts.
- With the increasing density of Bi_2 BLs, density of strongly coupled QB blocks with only hybrid stacking also increases. With this, assistance offered by Bi_2 BL to block step edge continuity gradually stops as hybrid stacking does not allow disordered sequences at all. This phenomenon is most prominent in Bi_4Te_3 that comprises only of QB blocks with the hybrid stacks. Keeping in mind

the strong interaction among QB blocks, the behavior of Bi_4Te_3 epilayer at Si step edge is predicted to be similar to Bi_2Te_3 (hard stacking shift). However, an interesting and unexpected phenomenon is observed. The hard stacking shift is energetically not favorable and layers, whenever possible, tend to avoid its formation. As mentioned in section 4.5 during the growth of stage 3 alloys that Bi has very low thermal budget and is not stable at high temperatures and form crystallites. In Bi_4Te_3, however, it is observed that due to the strong interaction of hybrid stacking, epilayer forces the formation of Bi_2 BL at the interface with Si (111) to overtake step edge and avoid hard stacking shift. This phenomenon is depicted in Figure 4.34 (b, d). This behavior indicates and confirms two key points, assumed earlier i.e. the energetically unfavorable hard stacking shift and the strength of QB stacking to inforce Bi_2 BL at the interface at high temperature. This phenomenon stops the step edge continuity; however, as soon as the epilayer reaches the next step edge, in order to preserve stacking order, QB block now has no option but to hard shift the entire stack forming an antiphase domain, as depicted in Figure 4.34c. Overall, QB stacks in Bi_4Te_3 neutralize one step defect and exhibit hard stacking on the next bringing the probability of the antiphase domain formation to the half (50 %).

- As soon as, the density of Bi_2 BL increases further and weakly bonded BB stacks appear in the stacking sequence and the probability of step edge induced antiphase domain formation drops exponentially. Particularly all states after Bi_2Te do not exhibit any antiphase domain at all.

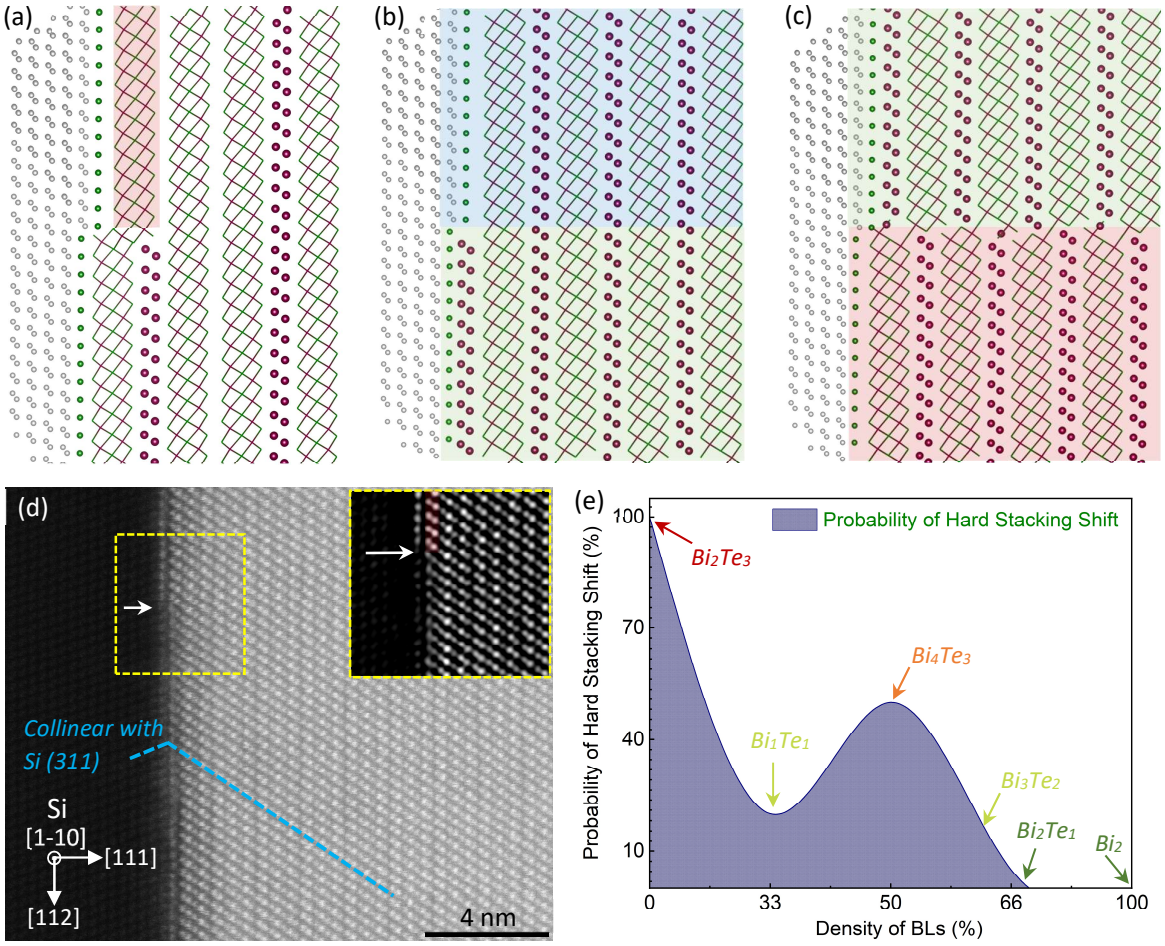

Fig. 4.34: 2D atomic model along Si [1-10] projection representing the defect formation at Si step edge with three probable cases. (a) In Bi_1Te_1, Bi_2 BL forces the stacking disorder in layer close to the interface with the substrate (red color), blocks the continuity of the antiphase domain and the epilayer continues to grow without further defects. (b) In Bi_4Te_3, The hybrid stack forces Bi_2 BL to get in contact with the interface and neutralize step defect (blue to green color) however, (c) the strong interaction of the hybrid stacking does not allow stacking disorder and the complete

epilayer had to hard shift creating an antiphase domain at the next Si step (green to red color). (d) The formation of Bi_2 BL at the interface with the neutralization of step defect (identified with white arrow), proposed in a model presented in (b) and can be visualized via HAADF image of Bi_4Te_3. (e) A trend of changing the probability to form antiphase domains with the increasing density of Bi_2 BLs in the stacking sequence.

4.8 Topology in Bi_xTe_y stoichiometric family

Bi_xTe_y family, with distinct combinations of Bi_2Te_3 and Bi_2, is proposed to be one of the richest material system in topology. The discovery of TCI phase in Bi_2Te_3 along with the conventional STI phase, the recent findings of Bi_1Te_1 as a dual TI with WTI phase along with TCI[3] and Bi_2 as a higher-order TI[6], attracts the attention of chemists and physics to this stoichiometric series for the probable discovery of TSM phases.

4.8.1 Bi_4Te_3: Electronic band structure

In an earlier study[3], the detailed electronic band calculations of Bi_1Te_1 was reported. In this study, the electronic band calculations of individual structural blocks, discussed in section 4.6, are performed in order to understand, the electronic transformation among various structural blocks. However, as all individual blocks exhibit a maximum length (along the "c" direction) of 2.5 nm, they do not qualify for 3D topology and therefore, are not presented here. Among the states after Bi_2Te_3 and Bi_1Te_1, Bi_4Te_3 (the bulk state of QB blocks) holds the key importance. Therefore, the electronic band calculations with various approximations to the exchange-correlation energy in density functional theory (DFT) are performed for bulk Bi_4Te_3. Using VASP, the bulk band structure of Bi_4Te_3 including spin-orbit coupling (SOC), is calculated and depicted in Figure 4.35.

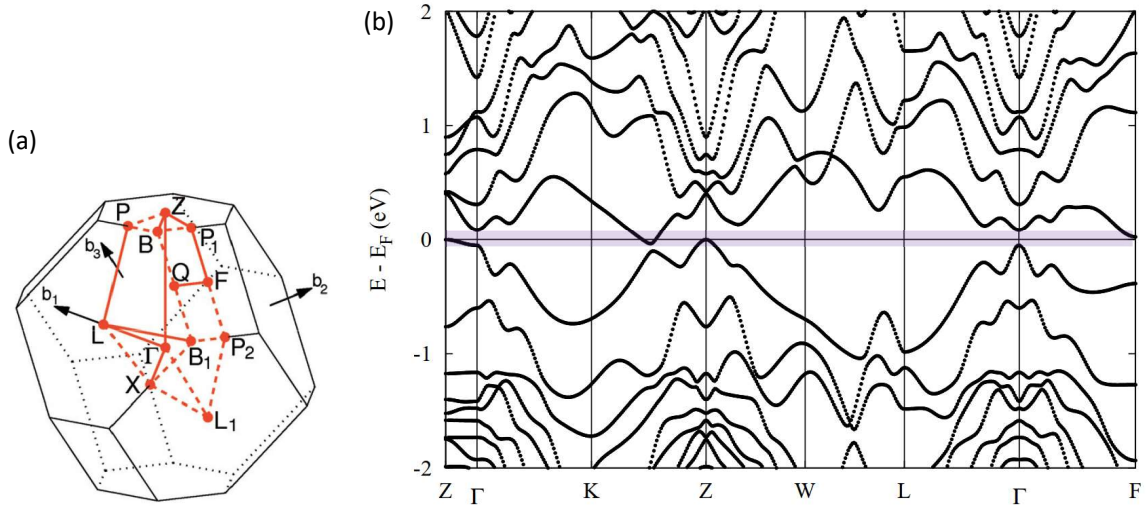

Fig. 4.35: (a) The Brillion zone of a trigonal crystal with R-3m (166) space group indicating the location of TRIM points. (b) The simulated electronic band structure of bulk Bi_4Te_3 using VASP. The bulk indicates the semi-metallic behavior with pockets of energy in valance and conduction bands overlapping between TRIM points Γ and Z and also between Z and K. *The overlap can easily be observed in the purple colored zone. Simulation results are kindly provided by Gustav Bhilmayer[87].*

The band structure, depicted in Figure 4.35, exhibits a gap at the TRIM point Γ; however, there are pockets of overlap between the valence and the conducted bands that can be observed between the TRIM points Γ and Z and also between points Z and K, for better visibility follow the purple color zone. These small overlap designate Bi_4Te_3 as a bulk semimetal with trivial attributes. In order to confirm the evaluated bands, the calculations are performed again using different approximations to the exchange-correlation energy including PBE, G_0W_0 (*Diag*), G_0W_0 using *Wannier* interpolation and G_0W_0 (full). The results are

depicted in Figure 4.36. According to the G_0W_0 (full) model, the valance and conduction bands are in very close proximity and exhibit a small and indirect band gap of approx. 2 meV (cannot be resolved in Figure 4.36).

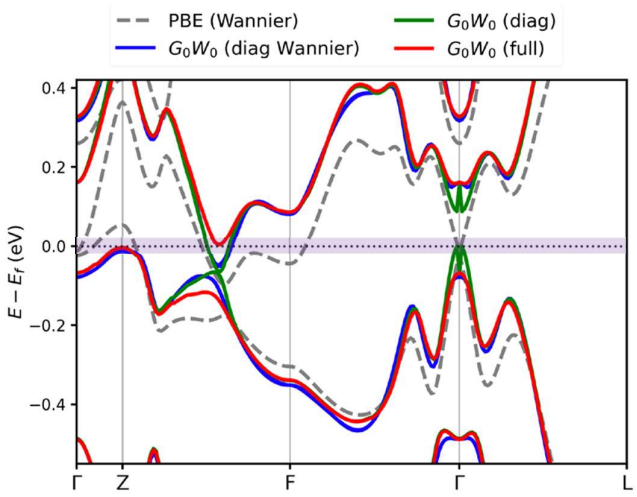

Fig. 4.36: The simulated electronic band structure of bulk Bi_4Te_3 using different approximations to the exchange–correlation energy including PBE, G_0W_0 (Wannier) using Wannier interpolation, G_0W_0 (diag) and G_0W_0 (full). The small changes in the band structures are evident where the overlap in the purple colored zone can be observed. The best approximations are achieved via G_0W_0 (full). Simulation results are kindly provided by Irene Aguilera[1].

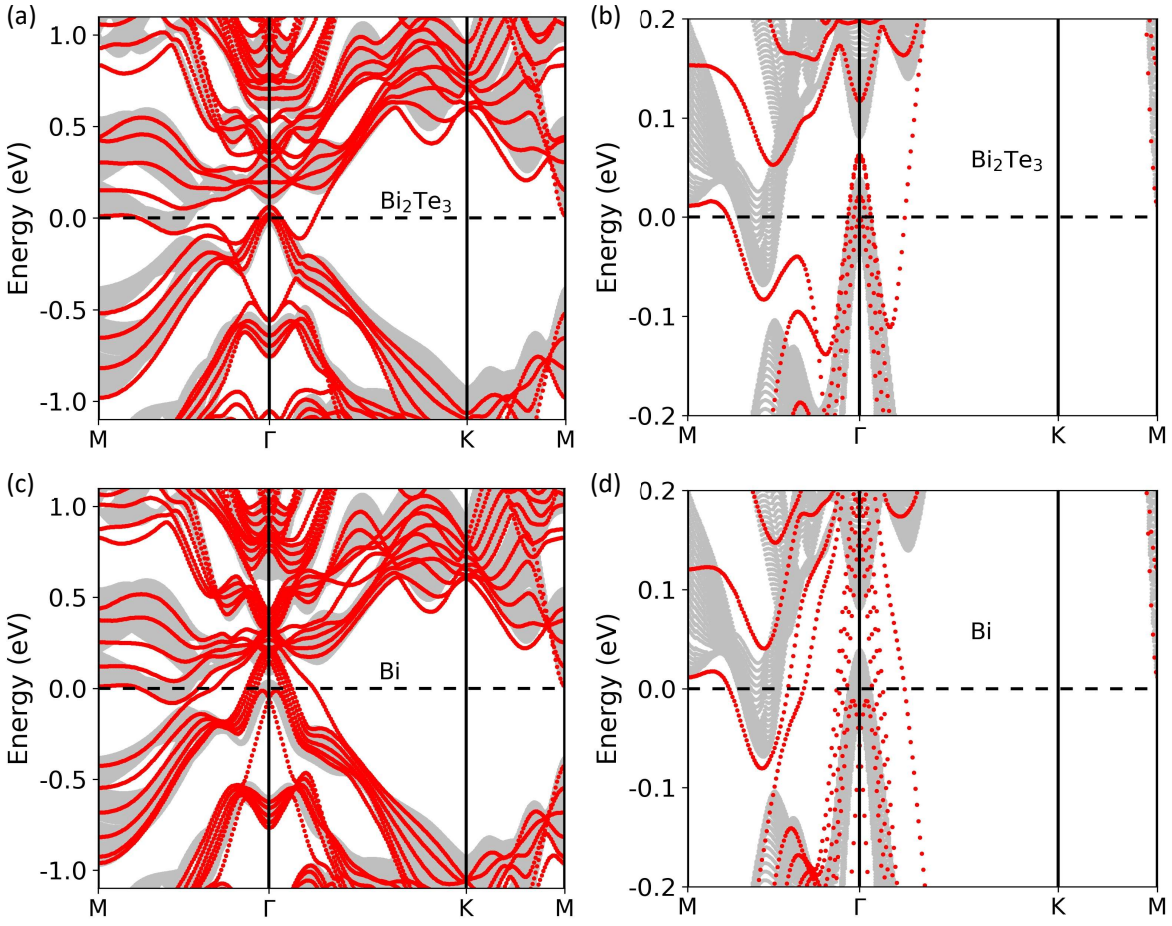

Fig. 4.37: The simulated surface states projected on the bulk bands of Bi_4Te_3 using FLEUR. The density of surface states (red color), depending upon the terminating layer being (a-b) Bi_2Te_3 QL and (c-d) Bi_2 BL, along with the projected bulk states (grey color), can be visualized. Simulation results are kindly provided by Gustav Bhilmayer[87].

4.8.2 Bi_4Te_3: Topology

In order to evaluate the topological attributes, the Z_2 invariants of Bi_4Te_3 are calculated and found to be $v_0; (v_1v_2v_3) = 1; (111)$. To calculate the Z_2 invariant, one Γ (0.0 0.0 0.0), one Z (0.5 0.5 0.5), three L (0.0 0.5 0.0), and three F (0.5 0.5 0.0) points are selected, while the corresponding parity products are found to be Γ (-1), Z (-1), F (-1), and L (+1) resulting in $\pi_\Gamma\pi_Z\pi_F\pi_L = (-1)$ confirming a strong topological phase in Bi_4Te_3 protected by time-reversal symmetry (TRS). Later, using FLEUR, the surface states are calculated and depicted in Figure 4.37. These calculations are in line with an earlier reported calculations of Bi_4Te_3 band structure by Saito *et al*.[7] where the evolution of surface states with the different top layer (Bi_2Te_3/Bi_2) and topological evaluations are not performed.

Surface States: It is observed that the surface states in Bi_4Te_3 vary in density based on the terminating layer on the (000 1) surface being Bi_2Te_3 or Bi_2. Bi_2Te_3 hosts limited number of surface states while the density of states is observed to be much high in case of Bi_2 termination, as depicted in Figure 4.37 where, the red color indicates topological surface states (TSS) while the grey color represents the projection of bulk states. Due to very small bulk bandgap of 2 meV in Bi_4Te_3, the contribution of TSS will be heavily suppressed.

Dual Topology: After the evaluation of time-reversal symmetry (TRS) protected topological attributes in Bi_4Te_3, the crystal symmetry (CS) based investigations are performed. It is observed that Bi_4Te_3, similar to Bi_2Te_3 and Bi_1Te_1, exhibits dual topology with a non-zero mirror Chern number ($n_\mathfrak{M} \neq 0$) and exhibits TCI phase as well. The mirror Chern number for Bi_4Te_3 is found to be $n_\mathfrak{M} = +1$ that represents the opposite chirality of the Dirac states compared to Bi_2Te_3 with $n_\mathfrak{M} = -1$ and Bi_1Te_1 with $n_\mathfrak{M} = -2$.

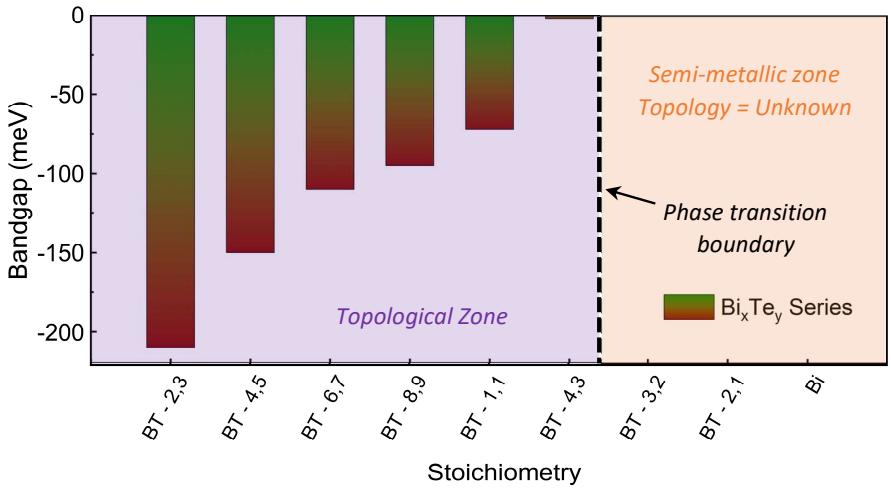

Fig. 4.38: The trend of decreasing bandgap vs. stoichiometry, plotted with data that is acquired from a few reported studies on Bi_xTe_y in literature. The increasing density of Bi_2 BLs with the changing stoichiometry resulted in weakening the strength of SOC and consequently in decreasing the inverted bandgap from -210 meV (Bi_2Te_3) to -2 meV (Bi_4Te_3). The stoichiometric states with higher Bi contents than Bi_4Te_3 such as Bi_3Te_2 and Bi_2Te_1 must exhibit semi-metallic behavior and therefore must pass through the critical point of 0 eV (phase transition boundary) and would most probably result in the formation of a topological Dirac semi-metal (TDSM).

4.8.3 Bi_xTe_y: Topological phase transformation

Applying the model of topological phase transition, introduced in chapter 1 (Section 1.2), to Bi_xTe_y stoichiometric family, the change in electronic band structure with the increasing density of Bi_2 BLs is evident and can be observed in Figure 4.38. The addition of trivial into a topological material i.e. Bi_2 into Bi_2Te_3 resulted in weakening the strength of SOC and consequently in decreasing the inverted bandgap from -210 meV (Bi_2Te_3) to -2 meV (Bi_4Te_3). The stoichiometry of Bi_4Te_3 with such a small bandgap indicates

that it resides very close to topological-trivial phase transition boundary (0 eV), as depicted in Figure 1.8. This trend also indicates that stoichiometric states with higher Bi contents than Bi_4Te_3 such as Bi_3Te_2 and Bi_2Te_1 must pass through the critical point of 0 eV (phase transition boundary) and would most probably result in the formation of a topological Dirac semi-metal (TDSM). That is why, these states hold a key importance for the topological investigations.

4.9 Magneto-transport investigations of Bi_xTe_y

At last, the electronic characterization of the selected few Bi_xTe_y stoichiometric states is performed via magneto-transport investigations. The Hall investigations are conducted to observe the change in carrier concentration with the decreasing inverted bandgap, plotted in Figure 4.38. After the Hall analysis, Aharonov–Bohm (AB) oscillations in ring structures are investigated to observe the dark (000 1) surfaces (trivial i.e. without topological surface states) of the weak topological insulator Bi_1Te_1 via magneto-transport investigations and compared with the strong topology of Bi_2Te_3[86] and BST alloy[88] (section 3.6).

4.9.1 Hall investigations of Bi_xTe_y alloys

The measurement setup and the analysis techniques are already introduced in chapter 3 (section 3.6), during the magneto-transport investigations of 3D TIs. The similar approach is utilized to perform preliminary investigation of several selectively grown Hallbars of Bi_1Te_1, Bi_6Te_5 and Bi_4Te_3. The SEM images of the Hallbars can be visualized in Figures 4.11 and 4.20. Figure 4.39a depicts the trend in the longitudinal resistance ($\mathbf{R_{xx}}$) vs. the perpendicular applied magnetic field ($\mathbf{B}$) in a 500 nm wide Hallbar of Bi_1Te_1. The weak anti-localization (WAL) effect can be observed at lower magnetic fields, highlighted with red color zone. Figure 4.39b depicts HLN fit (equation 3.13) of the WAL data to extract the coherent length (l_{Φ}) of the charged particles. Summary of the measured data is listed in Table 4.11. In comparison to Bi_2Te_3, two major differences are observed in Bi_1Te_1 characteristics and discussed below:

- The magneto-resistive change in Bi_2Te_3 was observed to reach 98 % at B = 10 T (Table 3.3). In Bi_1Te_1, due to lower bandgap, higher density of carriers and the weak topology with the trivial (000 1) surfaces, the magnetoresistance (MR) has dropped to only 4 %. Another factor that played an important role in this trend is the increase in the misorientation angle of the substrate. The MR is also observed to drop for Bi_2Te_3 from 98 % to 38 % when substrate misorientation angle changed from 0.1° to 0.5° (Table 4.11).
- In Bi_2Te_3, the coherent length (l_{Φ}) is observed to be limited by the misorientation angle of the substrate[89]. For example, the value of l_{Φ} is observed to drop from 230 nm to 63 nm (Table 4.11) when the misorientation angle is changed from 0.1° to 0.5° respectively. On the other hand, due to its natural ability to overcome the Si step defect by inserting a Bi_2 bilayer (Figure 4.34), l_{Φ} in Bi_1Te_1 is not limited by the miscut angle and exhibited an improvement from 63 nm (in Bi_2Te_3) to 460 nm.

Similarly, Bi_6Te_5 and Bi_4Te_3 Hallbars are also investigated. Figure 4.40a depicts the changes in $\mathbf{R_{xx}}$ when the perpendicular field ($\mathbf{B}$) varies from -7 T to 11 T in a 500 nm wide Hallbar of Bi_4Te_3. Unlike other Bi_xTe_y alloys, a novel phenomenon of negative magnetoresistance (NMR) is observed in thin Bi_4Te_3 epilayer. NMR is an unusual phenomenon that involves novel and fascinating physics and is reported to occur in three distinct cases[90] i.e. quenching of the Kondo effect[91, 92], the existence of the ferromagnetic metallic state (also known as colossal MR)[93] and the chiral anomaly in topological Dirac and Weyl semimetals under longitudinal magnetic field[94, 95, 96, 97]. None of these cases apply to Bi_4Te_3 and thus, there must be another factor responsible for such a unique behavior. It is also important to notice that NMR in Bi_4Te_3 is observed under the perpendicular magnetic field unlike the chiral anomaly in topological semimetals (TSMs).

Table 4.11: The summary of all electronic properties in the selected few Bi_xTe_y materials, extracted from the Hall measurements. MR represents the percentage change in the magnetoresistance in R_{XX} between B = 0 T and B = 10 T.

Topological Material	Carrier	Width (nm)	η_{2D} (x 10^{13} cm^{-2})	η_{3D} (x 10^{19} cm^{-3})	l_Φ (nm)	μ (cm^2/Vs)	Si Miscut Angle (°)	MR @ 10 T (%)	Comments
Bi_2Te_3 (Reference)	n-type	500	4.1	2.3	230	324	0.1	98	*In situ* capped
		500	6.9	8.6	63	136	0.5	38	*In situ* capped
Bi_1Te_1	n-type	1000	13.4	15.2	311	136	0.5	2.4	*In situ* capped
		500	11.5	13.2	460	154	0.5	3.8	*In situ* capped
		100	12.3	12.9	446	143	0.5	3.6	*In situ* capped
Bi_6Te_5	n-type	500	14.5	16.2	436	139	0.5	3.9	*In situ* capped
Bi_4Te_3	n-type	1000	98.4	153.2	113	187	0.5	9.8	*In situ* capped
		500	86.5	144.2	137	212	0.5	14.4	*In situ* capped
		100	87.3	132.9	124	176	0.5	12.3	*In situ* capped

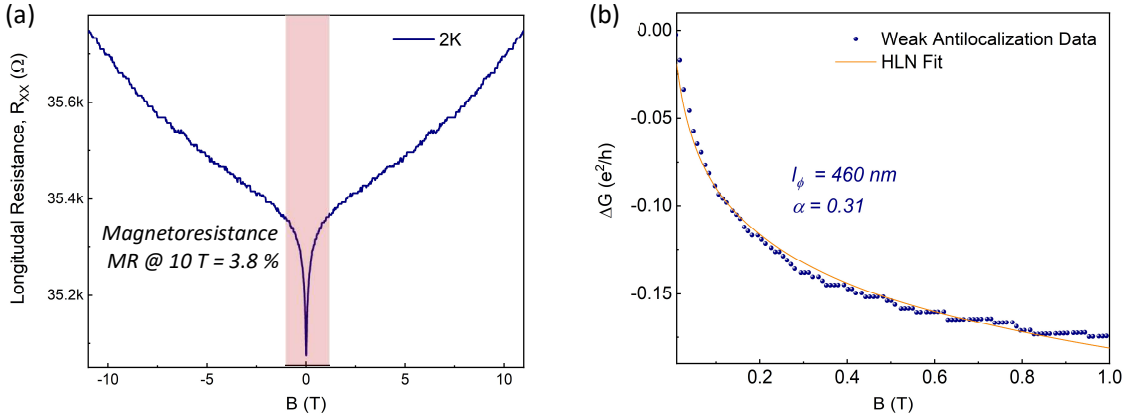

Fig. 4.39: Hall measurement data of Bi_1Te_1. (a) The trend in longitudinal resistance (R_{xx}) vs. applied magnetic field (B). The weak anti-localization can be observed at lower magnetic fields, highlighted with red color zone. (b) HLN fitting of weak anti-localization, red zone in (a), to extract the coherent length (l_Φ) and factor α.

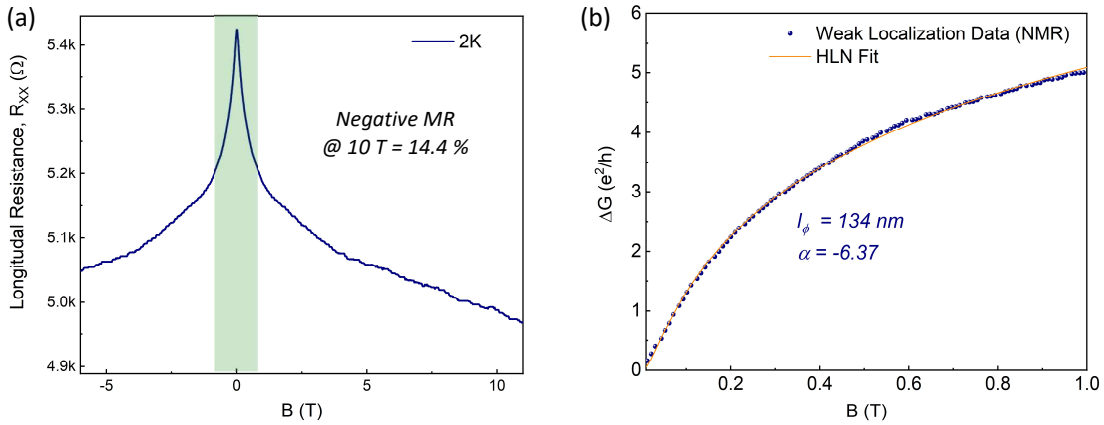

Fig. 4.40: Hall measurement data of Bi_4Te_3. (a) The trend in NMR, the longitudinal resistance (R_{xx}) vs. applied magnetic field (B). The weak localization can be observed at lower magnetic fields, highlighted with green color zone. (b) HLN fitting of weak localization, green zone in (a), to extract the coherent length (l_Φ) and factor α.

Recently, the phenomenon of NMR was reported in 3D TIs as well. Zhang *et al.*[98] reported NMR in CVD grown Bi_2Se_3 flakes due to the spatial inhomogeneity of carrier density and mobility in the crystal[99, 100]. Breunig *et al.*[90] reported NMR in TBST ($TlBi_{0.15}Sb_{0.85}Te_2$), Singh *et al.*[101] reported in $Bi_2Se_{3-y}S_y$ and Yadav *et al.*[102] reported in the sculpted nanowires of Bi_2Te_3 under the perpendicular magnetic fields. All reports

agreed on the common factor with the presence of spatial disorder in the crystal that led to the formation of electron puddles[103, 104] and altered the carrier concentration and mobility in the crystal[99, 100].

The NMR observed in Bi_4Te_3 somehow differs from the above mentioned reports as well. The magneto-resistive behavior reported in those studies exhibited WAL at low magnetic field and the trend later switched to NMR. In Bi_4Te_3, WAL is not observed rather a continuously increasing NMR is witnessed. Also, the presence of hybrid stacking and structural characterization via XRD and STEM have confirmed the defect-free epilayer (Figure 4.20). Thus, the defects induced localized variation in the carrier density cannot be a reason of NMR in Bi_4Te_3. Based on discussions in section 4.4, 4.6 and 4.8, there are two factor that may have impacted $\mathbf{R_{xx}}$ behavior in Bi_4Te_3 crystal, observed in Figure 4.40. The near semi-metallic band structure (high carrier density) along with the strong 3D topology with non-ending weak indices as the Z_2 invariants for Bi_4Te_3 are $1;(111)$ (Section 4.8). The stoichiometric location in topological-trivial phase diagram with a close proximity to the critical point (0 eV) i.e. the phase boundary with probable TDSM phase (Figure 4.38). Both of the above mentioned factors may have impacted the magneto-transport behavior of Bi_4Te_3. However, nothing can be said with certainty and further detailed and systematic electronic investigations are required to understand the physics responsible for NMR in Bi_4Te_3. Another important point to notice in Bi_4Te_3 epilayers, is the improvement of l_{Φ}, compared to Bi_2Te_3. This features confirms the structural ability of Bi_4Te_3 to suppress the Si step defect, depicted in Figure 4.34, with the reduced probability of antiphase domain formation to 50 %.

4.9.2 Aharonov–Bohm (AB) oscillations in ring structures

The presence of topological surface states (TSS) via AB oscillations originating in ring shaped structures of BST alloy under the perpendicular applied magnetic field, is already witnessed in chapter 3 (Figure 3.20). In order to confirm the dark (trivial) surface of WTI, the selectively grown ring structures of Bi_1Te_1 are investigated and the results, along with Bi_2Te_3, are depicted in Figure 4.41.

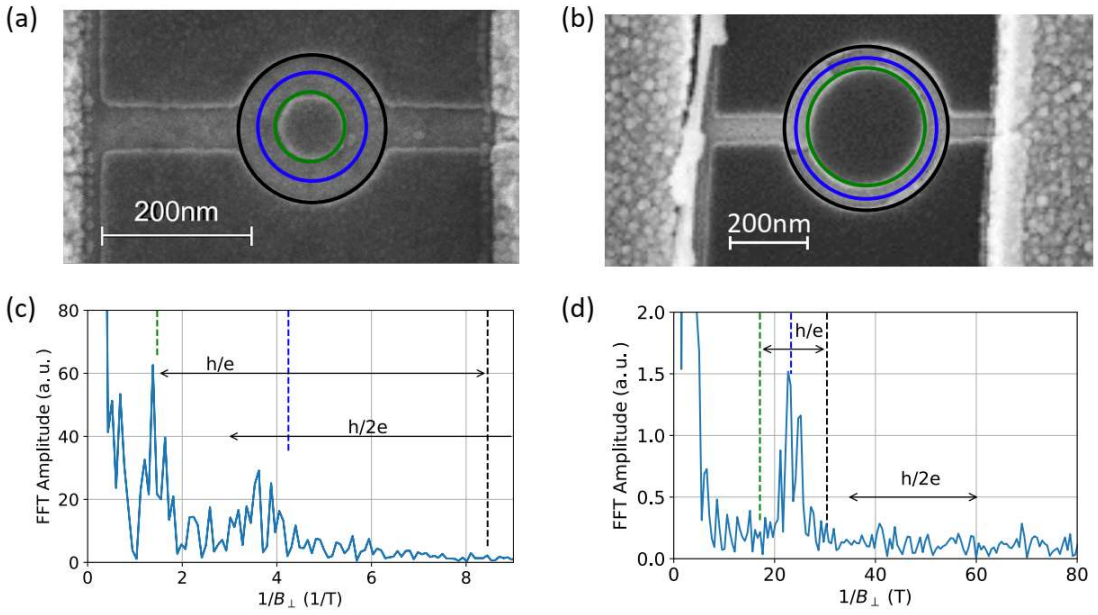

Fig. 4.41: Investigation of TSS on (000 1) surfaces via Aharonov–Bohm oscillations performed on the selectively grown ring structures of (a) BST alloy and (b) Bi_1Te_1. The green and blue colored circles represent the shortest and the mean radii of the ring structures respectively. (c) The Fourier spectrum of the filtered data measured on BST alloy ring i.e. the device presented in (a) representing two distinct peaks at different frequencies. (d) The Fourier spectrum of the filtered data obtained from Bi_1Te_1 ring representing only one distinct peak.

A comparative analysis between ring structures of BST alloy (STI) and Bi_1Te_1 (WTI) is conducted and the key observations are discussed below:

- The ring containing BST alloy (Figure 4.41a) due to presence of strong topology exhibited TSS. The Fourier spectrum of magneto-conductance (Figure 4.41c) revealed two distinct peaks where the frequency can be translated back to certain radii. The first one, marked with green color, is corresponding to the shortest radius of the ring (attributed to an interference of electrons occupying TSS at the inner surface of the ring). The second, marked with blue color, is corresponding to the mean radius (attributed to a bulk contribution)[105]. In Bi_1Te_1 ring structure (Figure 4.41b), however, the Fourier spectrum of magneto-conductance (Figure 4.41d) revealed only one peak that is corresponding to the mean path and thus, must have originated due to bulk contribution. While the spectrum position corresponding to the inner radius of interference path (due to TSS) exhibited no peak rather the residual background noise. This feature confirms the (000 1) surfaces of Bi_1Te_1 being dark (trivial) with the absence of TSS, just as witnessed via ARPES by Eschbach *et al*.[3]
- The investigation of AB oscillations in ring structures containing BST alloy were limited to a maximum radius of 70 nm. It was due to the requirement i.e. the interference path length < $2l_{\Phi}$ where l_{Φ} = 212 nm for the BST alloy (for details visit Table 3.3). Figure 4.41a displays a BST ring structure with the mean radius of 70 nm. Bi_1Te_1 on the other hand, exhibited highly improved l_{Φ} due to natural suppression of antiphase domains with the insertion of a Bi_2 bilayer between the top and bottom terraces at the Si step edge, observed during the Hallbar measurement and listed in Table 4.11. This property of Bi_1Te_1 facilitated the investigation of ring structures with the mean radius reaching up to 180 nm. Figure 4.41b displays a Bi_1Te_1 ring structure with the shortest radius of 150 nm while the mean radius is 175 nm.

The AB-oscillations based investigations on Bi_4Te_3 ring structures are not performed. Having strong topology with near semi-metallic band structure and exhibiting NMR behavior, the measurement of Bi_4Te_3 ring structures will shed further light into the fascinating physics of the material. The magneto-transport investigation, discussed in section 4.9, have provided the preliminary results. However, further detailed and systematic investigations including gated Hallbars and ring structures of various Bi_xTe_y alloys are required to be performed in order to understand the effects of changing spin-orbit coupling (SOC), the topology and the structural changes with the increasing density of Bi_2 bilayers in the stacking order.

4.10 Summary

To address the issue of high density of trivial carriers in conventional 3D TIs, the technique of topological band engineering (TBE) is adopted to transform the topological phase of materials into the TSMs (DSM, TDSM, WSM etc.), the phases that exhibit topologically protected bulk states. In order to do so, the capabilities of vdW epitaxy are exploited via MBE. A systematic study is performed where the epitaxial growth of topological-trivial heterostructures in form of Bi_2 bilayers and Bi_2Te_3 QLs is explored resulting in Bi_xTe_y stoichiometric alloys. The gradual and controlled accumulation of Bi_2 bilayers in the stacking order allowed the epitaxial growth of 38 distinct states of Bi_xTe_y family starting from Bi_2Te_3 and passing through the key compositions of Bi_4Te_5, Bi_6Te_7, Bi_8Te_9, Bi_1Te_1, $Bi_{10}Te_9$, Bi_8Te_7, Bi_6Te_5, Bi_4Te_3, Bi_3Te_2, and ending at Bi_2Te_1. The theoretical evaluations have revealed the existence of dual topological phases in the three key states including Bi_2Te_3 and Bi_4Te_3 with the STI and TCI phases while Bi_1Te_1 exhibits the WTI along with the TCI phase. The increasing contents of bismuth in these alloys impacts the strength of SOC and decreases the inverted bandgap from -210 meV (Bi_2Te_3) to almost 0 eV (Bi_4Te_3); however, most of these states are electronically and topologically unexplored. The detailed theoretical (DFT) investigations of all Bi_xTe_y alloys are required to have an overview of the trend in topology that would be able to provide an insight of the target stoichiometry that can be tuned exactly to engineer the electronic band structures of a TDSM phase.

For the first time, a systematic atomic-scale structural characterization (via STEM) of Bi_xTe_y alloys has facilitated the observation of unique stacking sequences of Bi_2 and Bi_2Te_3 layers along with the diverse variety of vdW interactions including the pristine (relatively weak) and the hybrid (relatively strong) stacking. The localized variations in the bond lengths due to the deviations in the atomic interactions with the changing vdW stack, and the resulting impact on the dimensional changes in the corresponding unit cells are explored. These observations can be extremely helpful in understanding the classification of bonding (pseudo-vdW, metavalent etc.) and their impact on the structural and the electronic properties of the layer based material systems. Once again, the support of theoretical calculations and the simulations of structural models are required.

Chapter – 5
3D TIs - GeTe Heterostructures: Towards Selective Nano-architecture

Thin film epitaxy on planar substrates and SAE of nanostructures on pre-patterned substrates of various Bi_xTe_y alloys, in form of $(Bi_2)_m(Bi_2Te_3)_n$ stoichiometric superlattices, are discussed in chapter 4. This chapter is dedicated to study the epitaxial growth of $(GeTe)_m(Bi_2Te_3/Sb_2Te_3)_n$ based heterostructures that materialize into stoichiometric GBT/GST ternary alloys respectively. The importance Bi_xTe_y alloys hold for their novel crystal symmetry (CS) based topological features[1, 2, 3] and outstanding thermoelectric properties[4, 5, 6, 7, 8, 9, 10], the equivalent importance is carried by GeTe based GST/GBT alloys for their time-reversal symmetry (TRS) based topological[11] and phase change characteristics (PCM)[12, 13, 14, 15, 16, 17, 18, 19, 20]. Based on discussions in chapter 1 (Section 1.2), the stoichiometric modulation assisted topological phase transitions are conducted once again with a new set of "*base*" (topological) – *"additive"* (trivial) material combinations. Here, GeTe is utilized as an "*additive*". GeTe is a semiconductor that exhibits topologically trivial attributes with 0.6 eV non-inverted bandgap[11, 12, 15, 21, 22] while one of the 3D TIs i.e. Sb_2Te_3/Bi_2Te_3, serves as the "*base*" formulating stoichiometric GST/GBT alloys. In GST/GBT stoichiometric alloys, with increasing contents of GeTe, the strength of spin orbit coupling (SOC) decreases causing the inverted bandgap to shrink until it reaches a critical point of 0 eV (becomes SM), breaks TRS and loses its topological features[23, 24]. With further addition of GeTe, the non-inverted bandgap with trivial attributes starts increasing until the material reaches the exact stoichiometry of GeTe.

The two stoichiometric material systems $Bi_xTe_y = (Bi_2)_m(Bi_2Te_3)_n$ (discussed in chapter 4) and GST/GBT = $(GeTe)_m(Sb_2Te_3/Bi_2Te_3)_n$ have a few similarities; however, they also exhibit unique differences as well. The key similarities and differences are discussed below:

- ***Multiple of 3 issue:*** Both systems belong to the trigonal (either H- or R- centered) crystal structure. Both systems exhibit ABC-ABC stacking order and therefore, the total number of atomic layers along the "c" lattice in a characteristic cell must be a multiple of 3 or the characteristics cell must repeat itself 3 times to complete a unit cell, as introduced in section 4.1.
- ***Layer architecture:*** In Bi_xTe_y stoichiometric system, both the "*base*" (Bi_2Te_3 QL) and the "*additive*" (Bi_2 bilayer) preserve their individual identity by not merging into each other and forming a new compound layer. In GST/GBT alloys, however, the "*base*" (Sb_2Te_3/Bi_2Te_3 QL) and the "*additive*" (GeTe) in most conditions form a composite super cell with 7, 9, 11, 13… atomic layers (depending upon the exact stoichiometric state) and lose their individual identity (Section 5.1).
- ***Nomenclature:*** Preserving the individual identity by "*additive*" and "*base*" in Bi_xTe_y family brings complications in comprehending various nomenclatures. $Bi_xTe_y = (Bi_2)_m(Bi_2Te_3)_n$ where (x,y) represents the normalized atomic contents and (m:n) represents the total number of BLs and QLs in a unit cell. The conversion of (x,y) into (m:n) can be quite complicated and not readily attainable. While, in GST/GBT alloys due to the formation of compound layer architecture or supercells, the nomenclature is relatively easy to understand and conversion is less complicated.
- ***Pristine vs. hybrid stacks:*** Bi_xTe_y family exhibits variety of layer stacking (pristine and hybrid) including QQ, QB and BB etc. (discussed in section 4.6) that results in different interlayer gaps. All of these different stacking orders make structural understanding quite unique and complicated at the same time. GST/GBT alloys other than IPCMs, always exhibit relatively weak stacking between Te atoms similar to QQ stack in Sb_2Te_3 and Bi_2Te_3 with pristine interlayer gaps.
- ***Topological protection via TRS vs. CS:*** Nearly all members of Bi_xTe_y exhibit topological protection, if not by TRS then via CS. Topologically, Bi_xTe_y is still a new material system that requires detailed

investigations. Lack of knowledge about topological effect on different stacking order and coupling of various blocks is the missing link. However, with upcoming new discoveries such as the recent findings of Bi as HOTI[3, 25], possibilities of topological features in Bi_xTe_y series are endless. On the other hand, GST system lacks such complexity and is an example of classical phase transformation. Sb_2Te_3 exhibits STI phase via TRS protection and with continuous accumulation of GeTe in the alloy, inverted bandgap of the stoichiometric state decreases that eventually switches to a non-inverted band with topologically trivial phase (the details can be found in chapter 1, section 1.2).

- ***Stoichiometric tuning:*** The stoichiometric tuning of GST/GBT alloys is more complicated than Bi_xTe_y as now three elements i.e., three different beam fluxes are involved in the optimization of a stoichiometric state. In Bi_xTe_y, the stoichiometry is tuned via only Bi/Te flux ratio while in GST system, all Ge/Sb, Ge/Te and Sb/Te flux ratios must be tuned to obtain the desired stoichiometry.

Due to the well-known amorphous ↔ crystalline phase transformation of Ge based chalcogenides[26, 27, 28, 29], GST alloys and GeTe are extensively studied; however, GBTs even after predicted of being a better PCM (fast conversion) than GSTs[30, 31], lack reported studies. This chapter is dedicated to perform the epitaxial growth of GST and GBT stoichiometric states along with pure GeTe via MBE on Si (111) planar substrates. Later, nanostructures via SAE are prepared by applying optimized parameters to the pre-patterned substrates and the detailed structural investigations are performed.

5.1 $(GeTe)_m(Sb_2Te_3)_n$ nomenclature and layer architecture

Unlike Bi_xTe_y, the nomenclature and conversion of GST alloys to their basic layer stacks i.e. GeTe and Sb_2Te_3 is not complicated as individual layers lose their identity and form supercells. In general, any GST stoichiometric state $Ge_xSb_yTe_z = (GeTe)_m(Sb_2Te_3)_n$ can also be represented in simplified version with GST-xyz. The values of (x, y, z) represent the normalized atomic contents while the values of (m:n) represent relative contributions of GeTe and Sb_2Te_3 in a unit cell. Similarly, the relation between the layer size (layer architecture) and the unit cell can be readily evaluated by checking if (x+y+z) or (m+n) is a multiple of 3 or not. Here are a few examples to explain this trend.

- GST-225 represents $Ge_2Sb_2Te_5$. It comprises of, as indicated by Ge (x = 2), Sb (y = 2) and Te (z = 5), with (m:n) = (2:1) as $(GeTe)_2(Sb_2Te_3)_1$. As (x+y+z) = (2+2+5) = 9 a multiple of 3, this stoichiometric state consists of periodic stacking of 9-atomic layers where each individual layer acts as a unit cell.
- GST-124 represents $Ge_1Sb_2Te_4$. It comprises of (m:n) = (1:1) as $(GeTe)_1(Sb_2Te_3)_1$. Because (x+y+z) = (1+2+4) = 7, this stoichiometric state comprises of periodic stacking of septuple layer (SL) and 7 being not a multiple of 3, a SL alone cannot act as a unit cell rather a unit cell in GST-124 comprises of (m:n) = (3:3) with 3 SLs.

Considering the stoichiometric pure growths of GST alloys, the layer architecture can be identified by the value of x (Ge) with the following rules.

- If x = 0, only QL architecture exists. Example: Sb_2Te_3
- If x < y, SL and QL architecture should exist. Example: GST-124 and GST-147
- If x = y, 9-atomic layer architecture exists. Example: GST-225
- If x > y, architecture must contain supercells with 11 or more atomic layers. The value of (x+y+z) provides information about layer architecture for example GST-326 comprises of 11 atomic layers.
- If y = 0, two distinct possibilities exist:
  - x = z, layer free architecture. Example: GeTe
  - x < z, trilayer (TL) architecture. Example: $GeTe_2$

The key members of GST stoichiometric states in a tri-elemental phase diagram along with their layer stacks in a unit cell are depicted in Figure 5.1

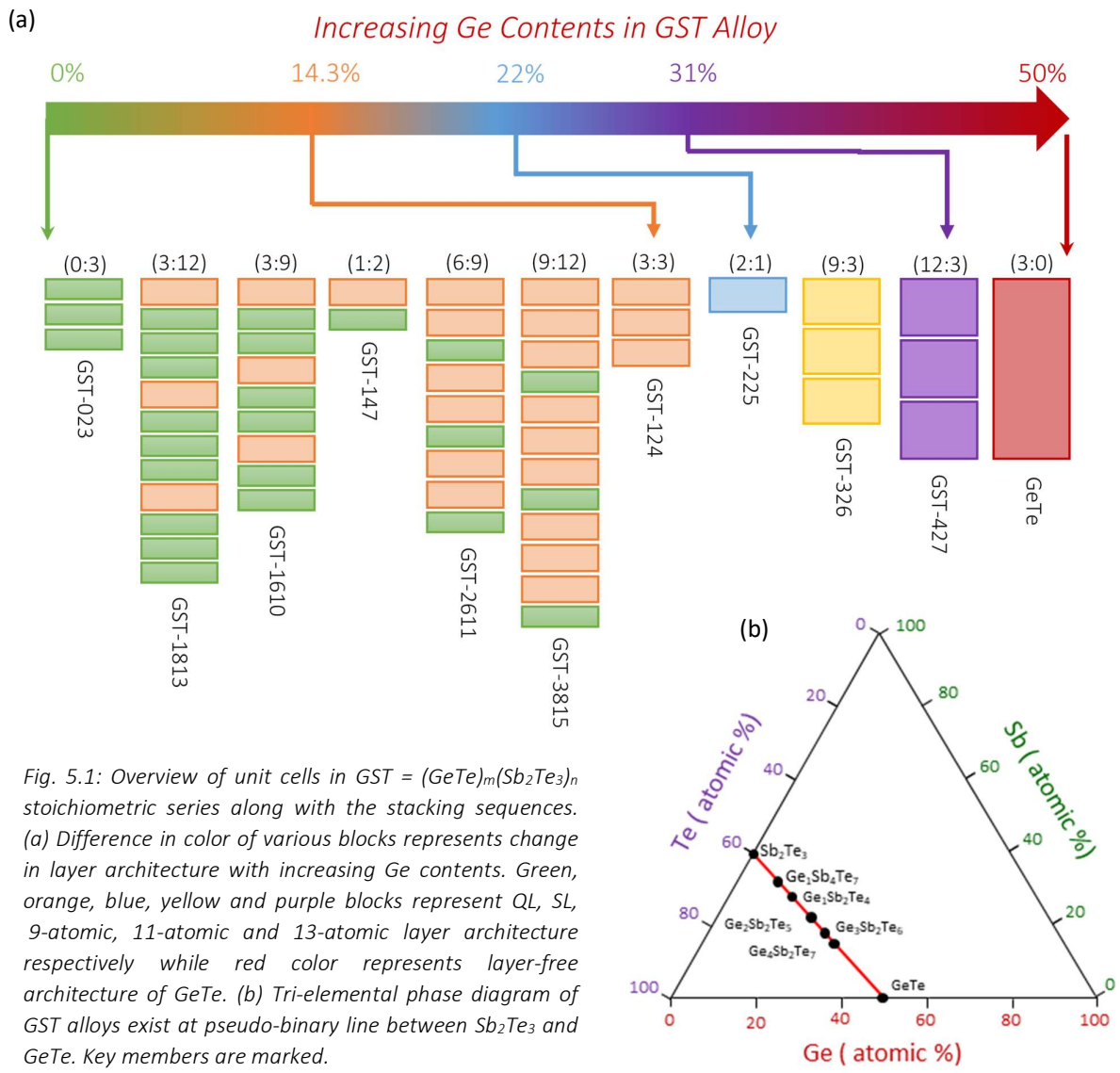

Fig. 5.1: Overview of unit cells in GST = $(GeTe)_m(Sb_2Te_3)_n$ stoichiometric series along with the stacking sequences. (a) Difference in color of various blocks represents change in layer architecture with increasing Ge contents. Green, orange, blue, yellow and purple blocks represent QL, SL, 9-atomic, 11-atomic and 13-atomic layer architecture respectively while red color represents layer-free architecture of GeTe. (b) Tri-elemental phase diagram of GST alloys exist at pseudo-binary line between Sb_2Te_3 and GeTe. Key members are marked.

5.2 Epitaxial growth of GST ternary alloys

The stoichiometric growth of GST ternary alloys, in comparison to Sb_2Te_3, requires additional tuning of Ge/Sb flux ratio and therefore, the initial attempts are started with the pre-optimized growth rate (R_{TF}) of Sb_2Te_3 (Figure 2.7). In order to simplify the process, only Ge flux (T_{Ge}) is used as a variable parameter. T_{sub}, T_{Te} and T_{Sb} are kept constant at 300 ℃, 320 ℃ and 470 ℃ respectively while T_{Ge} is gradually increased from 1180 ℃ in steps of 10 ℃. Unexpectedly, no change in the surface morphology of the epilayers is observed that are prepared with T_{Ge} from 1180 ℃ to 1220 ℃. XRD diffraction patterns also confirmed no changes in the stoichiometry of Sb_2Te_3. Nonetheless, the Ge flux is kept increasing and at T_{Ge} = 1250 ℃, the XRD pattern indicated single crystalline yet, mixed phase growth of GST alloy. The *Rutherford backscattering spectroscopy* (RBS) measurements revealed the presence of 18.7 % Ge in the epilayer which brings the stoichiometry between GST-124 (14.2 % Ge) and GST-225 (22.2 % Ge) states. In order to better understand the relation between the applied Ge flux (T_{Ge}) and the accumulation of Ge in the epilayer, a couple of growths are conducted with T_{Ge} at 1245 ℃ and 1255 ℃. XRD patterns revealed that the epilayer prepared at 1245 ℃ is still majorly Sb_2Te_3 with minor shifts in characteristic peaks (indicates very low accumulation of Ge) while the sample prepared at 1255 ℃ exhibited once again, the mixed phase crystal of GST alloy.

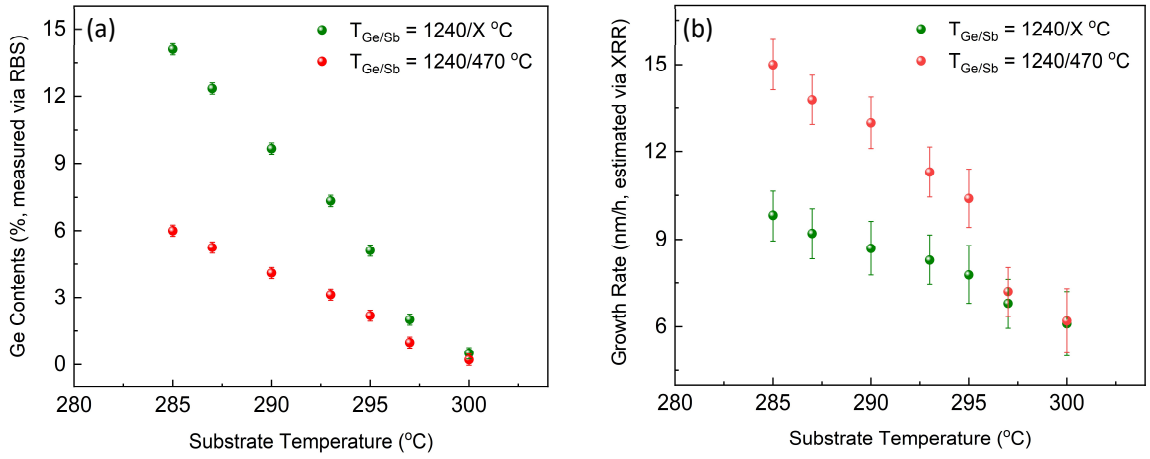

Fig. 5.2: T_{sub} - ADR dependency of Ge on T_{sub}. (a) The change in Ge contents with both modified (green with T_{Sb} = X˚C where X represents a variable value of T_{Sb} changed corresponding to T_{sub}) and unmodified (red with T_{Sb} = 470˚C) conventional approaches with gradually decreasing T_{sub} is depicted. The effect of ARD dependency of Sb and the resulting inaccuracy in Ge contents is evident in unmodified approach which is corrected with modified Sb flux and the effective change can be associated directly to Ge accumulation in the epilayer. (b) The corresponding changes in R_{TF} of epilayer discussed in (a). The constant T_{Sb} in unmodified conventional approach resulted in drastic increase in R_{TF} with decreasing T_{sub} as both Sb and Ge exhibit ADR dependency while in modified conventional approach Sb contents are influentially kept constant by correspondingly reducing T_{Sb} and Ge accumulation is the only feature that resulted in gradual increment in R_{TF}.

The above mentioned experiments indicated abrupt, rather than gradual accumulation of Ge contents in the epilayer. Such a behavior points towards the higher adsorption to desorption ratio (ADR) dependency of Ge adatoms on T_{sub} just like Sb, observed during Sb_2Te_3 growth (discussed in chapter 2). In order to tune the gradual accumulation of Ge in the epilayer, ADR dependency on T_{sub} must be investigated. The investigations are conducted using the following approaches:

- ***Flux variation:*** Keeping T_{sub} constant at 300 ˚C and assisting Ge accumulation in the epilayer by increasing R_{TF} with the additional Sb flux (increasing T_{Sb}). The average thermal energy per adatoms will decrease and Ge enriched epilayers could be achieved. This approach is not recommended due to two reasons. First is the unavailability of the growth rate (R_{TF}) reference points at higher Sb fluxes as in all previous experiments (conducted in chapter 2), T_{Sb} is never increased from 470 ˚C. Dealing with two unknowns i.e. Ge and Sb beam fluxes will simply increase the complexity of analysis. Second reason is the unnecessary increment in R_{TF} that would lead to high defect density.
- ***Temperature variation:*** This approach is the conventional one, where dependency can be simply investigated by keeping all fluxes T_{Ge}, T_{Sb} and T_{Te} constant and altering T_{sub} in gradual steps. Due to very high ADR dependency of Sb on T_{sub} (Figure 2.7), the conventional approach also will not provide accurate results. As with gradual decrement in T_{sub}, Sb contents in epilayer will increase and it will not be possible to identify changes in R_{TF} due to additional Ge contents precisely. This phenomenon can be visualized in Figure 5.2b (red data points) where it is also compared with the modified approach (green) to evaluate the accurate changes in Ge contents discussed below.
- ***Modified temperature variation:*** The above mentioned conventional approach with minor modifications can be used to realize the precise changes in Ge contents. The idea is to lower T_{Sb} with the decreasing T_{sub} to keep Sb accumulation in the epilayer constant (R_{TF} due to Sb); so that the resulting changes in R_{TF} can be attributed directly and only to Ge. To execute this scheme, the availability of reference data of changes in Sb accumulation with varying T_{sub} is mandatory. As ADR dependency study of Sb with T_{sub} is conducted in chapter 2, the corresponding reference data is available and exploited with this approach to evaluate ADR of Ge with T_{sub}.

Hence, T_{sub} - ADR dependency of Ge is conducted where T_{Ge} and T_{Te} are kept constant at 1240℃ and 320℃ respectively while T_{sub} is gradually decreased along with the corresponding reduced T_{Sb} (for details please refer to Figure 2.7). At T_{sub} = 300℃, the epilayer that exhibited pure Sb_2Te_3 state (confirmed via XRD) presented minor shifts in characteristic peaks that indicates the Ge accumulation while prepared at T_{sub} = 295℃. Ge contents in the epilayer kept increasing but mostly in mixed states until crystalline near single state is obtained at T_{sub} = 285℃ with T_{Sb} = 460℃. This trend of changing Ge accumulation in the epilayer is depicted in Figure 5.2 along with unmodified conventional approach. The extent of ADR dependency of Ge on T_{sub} can be visualized from this experiment where 15℃ decline in T_{sub} has transformed the stoichiometry from pure Sb_2Te_3 state (0 % Ge) to near GST-124 with 14.28 % Ge.

Based on these results, all epitaxial growths of GST alloys are conducted at T_{sub} = 285℃. Epitaxial thin films of key GST members that are successfully achieved in this study are summarized in Table 5.1, where m and n indicate the total number of GeTe blocks and Sb_2Te_3 QLs in a unit cell. The varying fractions of Ge, Sb and Te in each alloy are tabulated. The predicted out of plane lattice constant ($c_{predicted}$) is evaluated using the equation 5.1 where c' and c'' indicate the out of plane lattice constants of GeTe = 10.47 Å[12, 32, 33] and Sb_2Te_3 = 30.45 Å respectively.

$$c_{predicted} = \frac{1}{3}(mc' + nc'') \quad (5.1)$$

Table 5.1: An overview the GST stoichiometric alloys prepared via MBE. For each state the relative contents of individual elements Ge, Sb and Te, the total number of individual building blocks/layers of additive (n) and base (m) in a unit cell, the in plane lattice constant (a) and the out of plane predicted ($C_{predicted}$) and actual (C_{actual}) lattice constants are listed.

GST-xyz	m	n	Comments	Ge (%)	Sb (%)	Te (%)	a (Å)	$C_{predicted}$ (Å)	C_{actual} (Å)
GST-023	0	3	Reference	0	40.00	60.00	4.26	30.45	30.46
GST-1610	3	9	Multiple of 3	5.88	35.29	58.82	4.25	101.8	101.74
GST-147	1	2	-	8.33	33.33	58.33	4.25	23.79	23.82
GST-2611	6	9	Multiple of 3	10.53	31.58	57.89	4.25	112.25	112.29
GST-3815	9	12	Multiple of 3	11.53	30.77	57.69	4.24	142.78	142.72
GST-124	3	3	Multiple of 3	14.28	28.57	57.14	4.24	40.96	40.97
GST-225	2	1	-	22.22	22.22	55.55	4.22	17.12	17.17
GST-326	9	3	Multiple of 3	27.27	18.18	54.54	4.21	61.79	61.81

The last set of experiment assisted to evaluate optimum values of T_{sub} = 285℃ and T_{Sb} = 460℃ for the growth of GST alloys while T_{Te} is kept constant at 320℃. Unlike Bi_xTe_y but similar to the growth of 3D TIs, T_{Te} does not take any part in determining the growth rate. In GST alloys, the accumulative beam flux of Ge and Sb controls the growth rate (R_{TF}). This behavior can also be seen clearly in Figure 5.2 that indicates the rate of increasing R_{TF} is higher when T_{Sb} is kept constant at 470℃ (unmodified conventional approach) in comparison to the modified conventional approach where ADR of Sb is kept constant and only Ge flux was responsible for increasing R_{TF}. The tuning of GST stoichiometric states is started with the last growth parameter of T_{Ge} = 1240℃ that exhibited the Ge contents in the epilayer close to 14.8 % (Figure 5.2).

5.2.1 Epitaxial growth of GST-124

The stoichiometric state GST-124 contains 14.28 % Ge contents. It exhibits a characteristic unit cell of (m:n) = (1:1) where a single GeTe block merges with a QL and forms a septuple layer (SL). As it suffers from multiple of 3 issue, a complete unit cell comprises of (m:n) = (3:3) with 3 SLs. GST-124 exhibits a rhombohedral crystal structure with R-3m (166) space group and unit cell length $c_{predicted}$ = 40.96 Å[34, 35, 36]. After GST-225, it is the most extensively studied stoichiometry in literature as PCM[11, 27, 34, 37, 38, 39, 40]. GST-124 is reported to be prepared via Bridgeman and zone-melt methods[11, 41, 42], CVD[42], MOVPE[43, 44, 45],

sputter deposition[46, 47, 48], PLD[49] and MBE[50, 51]. Among all of them, MBE is the least studied technique. Though it provides the best crystal quality, it is not favored in PCM community due to a relatively slower and expensive technique to prepare epilayers. Also, the stoichiometric control via MBE is relatively more challenging in comparison to all other methods. Despite all of these challenges, epilayers prepared via MBE exhibit an order or two reduced defect density[52] (reduced carrier concentration) in comparison to other techniques which designates it as the best tool to prepare high quality crystals for quantum applications.

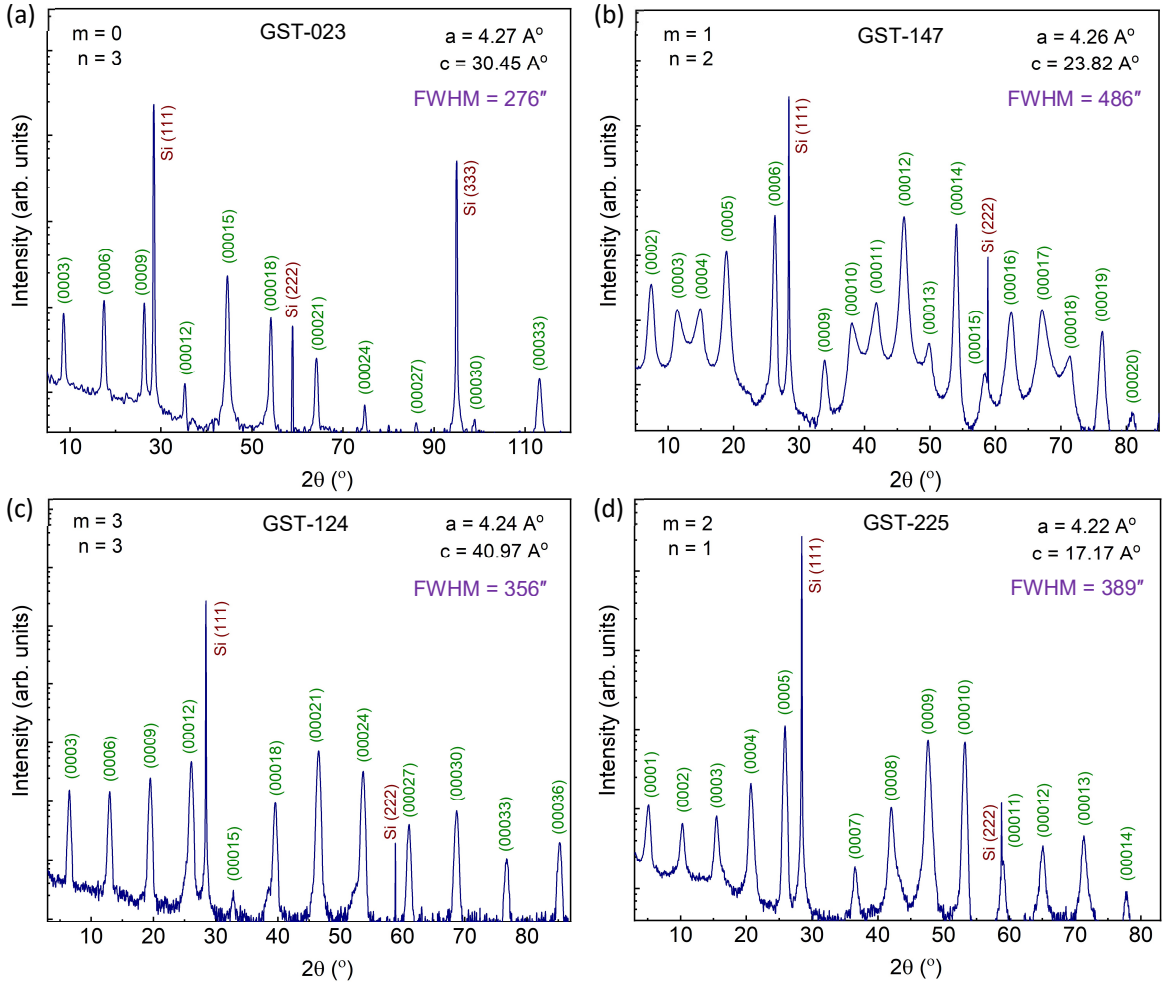

Fig. 5.3: XRD patters of key members of GST alloys according to hexagonal crystal lattices. (a) Diffraction peaks of Sb_2Te_3 (GST-023) with (m:n)=(0:3) matching perfectly with c = 30.45 Å. Δω scan revealed FWHM values of 276″ obtained at 2ϑ=44.45° (000 15) peak indicating high crystal quality. (b) Diffraction peaks of GST-147 with (m:n)=(1:2) exhibiting c = 23.82 Å. Δω scan revealed FWHM values of 486″. (c) Diffraction peaks of GST-124 with (m:n)=(3:3) exhibiting c = 40.96 Å with FWHM values of 356″. (d) Diffraction pattern of GST-225 with (m:n)=(2:1) exhibiting c = 17.28 Å. Δω scan with FWHM values of 389″ obtained at 2ϑ=47.25° (000 9) peak.

The tuning of GST-124 stoichiometric state is started with T_{Ge} = 1240 ℃ while all other fluxes and T_{sub} are kept constant at the corresponding optimum values. With gradual decrement of Ge flux, the accurate Ge/Sb flux ratio is obtained at T_{Ge} = 1236 ℃ and single crystalline epilayer of GST-124 is achieved with R_{TF} = 9.2 nm/h. Figure 5.3c displays XRD 2θ-ω scan of 78 nm thick epilayer of GST-124. The unit cell dimensions measured via XRD RSM and 2θ/θ diffraction pattern, displayed in Figure 5.4, are found c_{actual} = 40.97 ± 0.02 Å that is in agreement with the earlier reports[34, 39]. It is really interesting to notice here that the measured unit cell length c_{actual} does not deviate from the theoretical value $c_{predicted}$ unlike Bi_xTe_y stoichiometric states. It can be associated to the absence of hybrid stacking in GST-124. XRD φ-scan

indicated the presence of suppressed twin domains with the relative intensity of (1:11) and dominant domain collinear with Si (311), depicted in Appendix 5B. With further growth optimization, twins can be entirely avoided; although, here the presence of twins can be directly linked to R_{TF} > 5 nm/h. The structural quality of epilayer is investigated via rocking curve (Δω) analysis with FWHM value of 356".

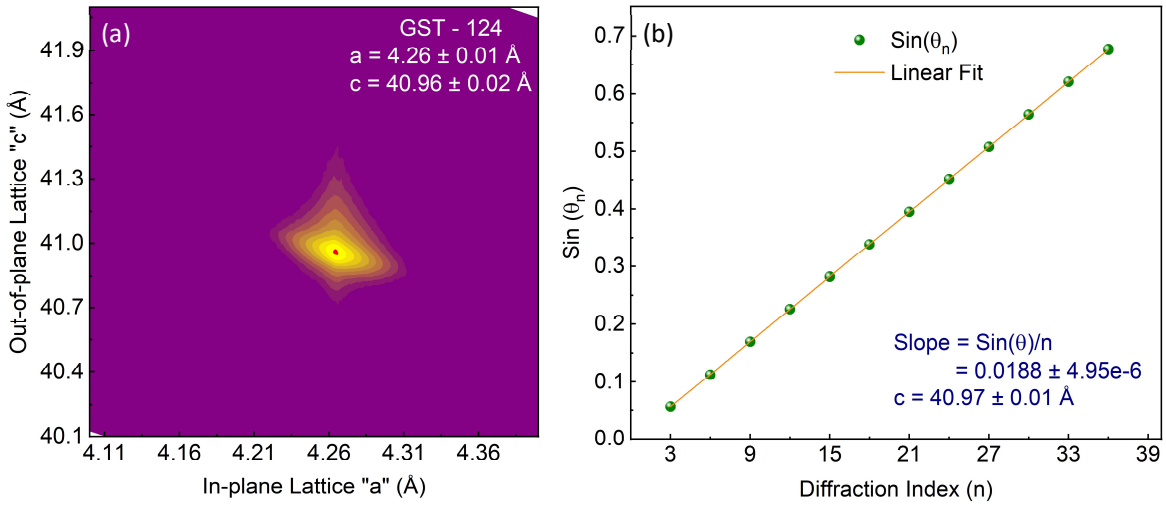

Fig. 5.4: Investigation of lattice parameters via XRD. (a) Reciprocal space map (RSM) of GST-124 acquired along the (0 -1 0 23) peak indicating lattice constants "a" and "c" in good agreement with $c_{predicted}$. (b) Evaluation of unit cell length "c" according to Bragg diffraction principle via XRD 2ϑ/ϑ scan.

5.2.2 Epitaxy from GST-124 to Sb_2Te_3 (GST-023)

Several stoichiometric states exist that contain either higher or lower Ge contents than GST-124 (Ge = 14.28 %). The search for next stoichiometric states started with the lower Ge contents towards Sb_2Te_3 because of their topologically non-trivial attributes and stacking variety[16, 36, 53]. Keeping all parameters constant, T_{Ge} is gradually decreased from 1236℃ and a couple of stoichiometric states including GST-3815 at T_{Ge} = 1229℃ and GST-2611 at T_{Ge} = 1221℃ with characteristic cells of (m:n) = (3:4) and (2:3) respectively, are achieved (for details visit Table 5.1). Both stoichiometric states exhibit the multiple of 3 issue and their complete unit cells comprise of (m:n) = (9:12) and (6:9) with the stacking sequences of SSSQ-SSSQ-SSSQ and SSQ-SSQ-SSQ where S and Q represent SL and QL respectively. Similar to the structural characterization of GST-124, depicted in Figure 5.4, XRD 2θ/θ and RSM investigations for both states i.e. GST-3815 and GST-2611 are performed and the lattice parameters are confirmed. None of these alloys are comprehensively studied in literature and no explicit report about their crystal preparation or structural characterization, is available.

GST-147: Gradually decreasing T_{Ge} from 1221℃, the optimum Ge/Sb flux ratio is obtained at T_{Ge} = 1215℃ with the stoichiometry of GST-147 that contains 8.33 % Ge. It exhibits a unit cell with (m:n) = (1:2) with the stacking sequence of SQ and unit cell length $c_{predicted}$ = 23.79 Å. GST-147 is not as commonly studied as GST-124; however, in the last few years a lot of attention is attracted by this state due to its topological and PCM characteristics[35, 54, 55, 56]. GST-147 is reported to be prepared via Bridgeman[55, 56]and zone-melt methods[11, 41, 42], CVD[42], sputter deposition[46, 47, 48, 57], PLD[20, 26, 58, 59, 60, 61] and MBE[62]. It exhibits a trigonal crystal structure with P-3m1 (164) space group[35, 63, 64, 65]. Figure 5.3b displays XRD 2θ-ω scan of a 88 nm thick epilayer of GST-147. The unit cell dimensions evaluated via RSM and XRD 2θ/θ diffraction pattern, depicted in Appendix 5B, are found to be in good match with the literature[66, 67] having c_{actual} = 23.82 ± 0.02 Å. Once again, no deviations between c_{actual} and $c_{predicted}$ are observed. XRD φ-scan (plotted in Appendix 5B) indicated the presence of heavily suppressed twins with relative intensity of (1:18) where the dominant domain is found collinear with Si (311). Though GST-147 epilayer exhibited the single crystalline state, the

quality of epilayer investigated via rocking curve (Δω) analysis with FWHM value of 486″ indicated the presence of a few interlayer defects (possible stacking sequence disorder) as other GST epilayers exhibited FWHM values close to 300″.

T_{Ge} is gradually decreased further from 1215 ℃ (state of GST-147) and at 1203 ℃ stoichiometric state of GST-1610 with the characteristics cell (m:n) = (1:3) is successfully achieved. It exhibits the multiple of 3 issue and thus, a unit cell comprises of (m:n) = (3:9) with the stacking sequences of SQQ-SQQ-SQQ respectively. It also exhibits the trigonal crystal structure; however, the literature holds no report about the crystal preparation or structural characterization of this alloy. With the continuous decrement in Ge flux, XRD characteristic peaks shifted to Sb_2Te_3 as soon as T_{Ge} reached 1195 ℃ indicating the absence of Ge in the epilayer. Here, the term absence of Ge implied to the absence of SL architecture as Ge atoms may still be present in the epilayer as dopants or as antisites in small quantities.

5.2.3 Epitaxy from GST-124 to GeTe

After reaching the lowest limit of Ge contents in GST alloys i.e. Sb_2Te_3 (GST-023), the search for stoichiometric states with higher Ge contents is initiated. In order to do so, T_{Ge} is set to the value of GST-124 with T_{Ge} = 1236℃. All parameters T_{Sb}, T_{Te} and T_{sub} are kept constant while T_{Ge} is gradually increased. Passing through several mixed phase states at T_{Ge} = 1252 ℃, the stoichiometric state of GST-225 is successfully achieved. GST-225 contains 22.22% Ge and exhibits the smallest unit cell length among all GST alloys with $c_{predicted}$ = 17.18 Å and (m:n) = (2:1). The layer stack and the relative atomic distribution of Ge and Sb in a GST-225 unit cell are depicted in Appendix 5A.

GST-225 is the most extensively studied material in the PCM community. It is reported to be prepared using all crystal preparation methods including Bridgeman[12, 46, 68, 69], CVD[42], sputter deposition[70], PLD[26, 58, 59, 60, 61, 71, 72] and MBE[16, 54, 62]. GST-225 exhibits a trigonal crystal structure with P-3m1 (164) space group[73]. Figure 5.3d displays the XRD pattern of a 73 nm thick epilayer of GST-225. The unit cell dimensions evaluated from RSM and XRD 2θ/θ diffraction pattern, depicted in Appendix 5B, are found be in good match with the literature[73]. The quality of the epilayer is investigated via Δω scan with the FWHM value of 389″. Structurally, GST-225 is one of the most interesting stoichiometric states. It consists of 9-atomic layer stacks in a trigonal lattice. The 9-atomic cell readily transforms itself into various isomers that exhibit several phase change properties including:

- ***Conventional bulk PCM:*** GST-225 acts as a bulk PCM[18, 68, 69]. It transforms between crystalline (low resistive) ⟷ amorphous (high resistive) states and is one of the most suitable candidate for non-volatile memory applications[12, 35, 46, 54, 68, 70].
- ***Crystalline bulk PCM:*** Based on the applied probe, GST-225 transforms into a cubic crystal structure (c-GST)[74] through vdW gap reconfiguration technique[75] and demonstrates three times higher conductivity (low resistive state) in comparison to the trigonal crystal structure (t-GST) (high resistive state).
- ***Interfacial PCM:*** Among all GST alloys, it is one of the best reported candidate for the interfacial PCM (IPCM)[76, 77, 78]. Within the trigonal crystal structure (t-GST), various configurations exist where 9-atomic super cell transforms into a group of 5 atomic QL and 4 atomic block of $(GeTe)_2$. These configurations with different arrangements of Ge/Te atoms in $(GeTe)_2$ block, depicted in Appendix 5A, result in different electronic states and are often recognized by their explicit names including Kooi[79, 80, 81], Petrov[82, 83, 84], inverse Petrov[69, 85] and Ferro[76, 86]. These inter-configuration changes (interfacial transformations) in GST-225 result in low ⟷ high resistive states formulating IPCM. Structurally, these configurations also introduce hybrid vdW stacks between Te and Ge atoms of QL and $(GeTe)_2$ blocks of GST-225.

- ***Topological switches:*** The above mentioned interfacial configurations not only vary in their electronic resistivity but also transform through topologically trivial and non-trivial states as well[83, 86] and therefore, can be utilized as topological switches[83, 86].

IPCMs due to low energy consumption are the future of conventional bulk PCMs. Realization and utilization of IPCMs require defect free, reliable and scalable nano-atrchitecture[76] for low energy applications. Understanding the structural transformations and individual electronic states of bulk and different interfacial phases in GST-225 is beyond the scope of this work; however, it is important to mention the potential applications that drive the demand of high quality epitaxial growth. Fabrication of high quality nanostructures and the control over interfacial configurations for IPCMs is still an ongoing research for GST-225[76, 77, 87, 88, 89].

GST-326: After attaining GST-225 at T_{Ge} = 1252 ˚C, T_{Ge} is gradually increased once again and the stoichiometric state of GST-326 is achieved successfully at T_{Ge} = 1265˚C. It contains 27.27 % Ge and exhibits the characteristic cell with (m:n) = (3:1) and comprises of 11-atomic layer supercell. Due to facing multiple of 3 issue, a complete unit cell consists of (m:n) = (9:3) with the unit cell length of $c_{predicted}$ = 61.79 Å. GST-326 state is not favored in the topological community due to its topologically trivial i.e. non-inverted bandgap[52, 90, 91]; however, is extensively studied in literature as a conventional bulk PCM[35, 52, 90, 91]. GST-326 exhibits a rhombohedral crystal structure with R-3m (166) space group[35, 52, 90, 91]. The quality of the epilayer is investigated via Δω scan with FWHM value of 373″.

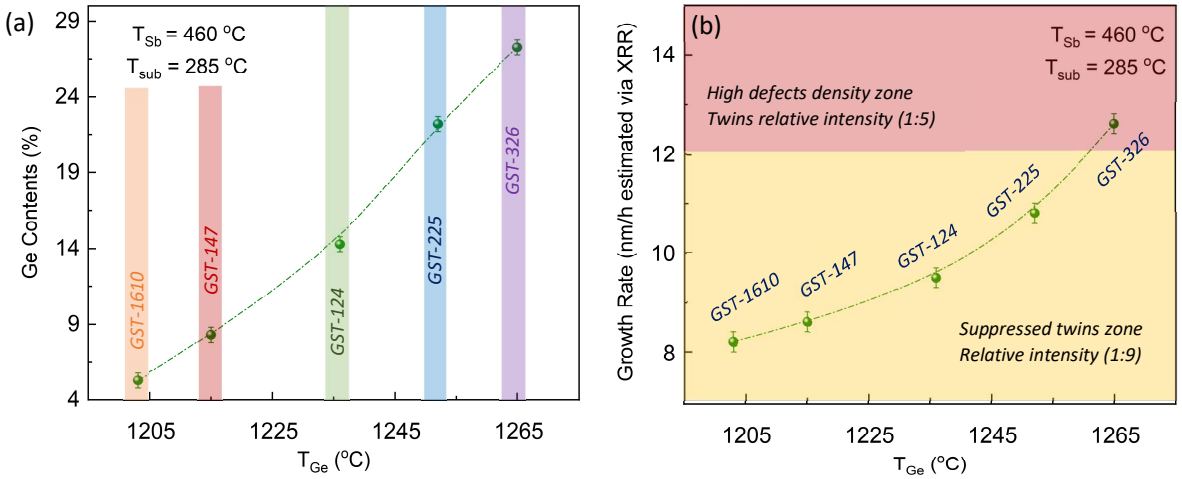

Fig. 5.5: An overview of epitaxial thin film growths of targeted GST stoichiometric states via MBE. (a) The trend of increasing Ge contents in the epilayer with variable T_{Ge} while all the other parameters are fixed to optimum values including T_{Sb} and T_{sub} at 460˚C and 285˚C respectively. The stoichiometric states of GST-1610, GST-147, GST-124, GST-225 and GST-326 are obtained with T_{Ge} at 1203 ˚C, 1215 ˚C, 1236 ˚C, 1252 ˚C and 1265 ˚C respectively. (b) The corresponding epilayers mentioned in (a) are achieved with the growth rate (R_{TF}) of 8.1 nm/h, 8.6 nm/h, 9.2 nm/h, 10.8 nm/h and 12.6 nm/h respectively. The rate map is divided into 2 zones: yellow zone with the suppressed twin domains ranging 5 nm/h < R_{TF} < 12 nm/h and high defect density red zone for R_{TF} > 12 nm/h. All alloys, except GST-326 reside in the yellow zone and exhibit suppressed twin domains.

After GST-326, the search for next stoichiometric states with higher Ge contents such as GST-427, 528 etc. is not conducted. The trend of Ge contents in the epilayer with the applied T_{Ge} along with the corresponding R_{TF}, during the epitaxial growth of key GST stoichiometric alloys, is displayed in Figure 5.5. The increment in R_{TF} with the rising Ge contents in alloys is obvious as the pursuit of these stoichiometric states requires Ge/Sb flux tuning which is achieved with the variable T_{Ge} while T_{Sb} is kept constant. Based on previous extensive structural investigations of 3D TIs (chapter 2 and 3) and Bi_xTe_y family (chapter 4), it can be concluded that higher R_{TF} (> 5 nm/h) steers towards higher probability of twin domains presence.

The XRD ϕ-scans conducted for all GST alloys exhibited almost identical results with the presence of suppressed twins exhibiting dominant domain collinear with Si (311). In order to avoid twin domains, R_{TF} must be brought down to 5 nm/h that demands the decrement in total flux while keeping Ge/Sb flux ratio intact. It can be achieved; however, it requires extensive set of experiments. Due to limited availability of time, the focus is shifted towards SAE to prepare nanostructures while R_{TF} optimization is postponed for the future studies.

5.2.4 SAE of GST nanostructures

Motivation: High structural quality nanostructures of GST alloys, particularly GST-225, are extremely desired and long awaited in the PCM community for ultra-fast phase transitions and low power applications[26, 76] via IPCMs. Being at topological-trivial transition critical point[23, 83, 92] with almost 0 eV bandgap[54, 69, 93, 94], GST-225 attracts attention of topological community as well, particularly in transformable IPCMs[29, 53, 95] for topological switching[83, 86]. GST-225 can also be utilized as a topological switch while acting as non-conventional bulk PCM where in trigonal crystal structure (t-GST) it exhibits the topologically non-trivial[16, 24, 93, 94, 96, 97, 98, 99, 100] while in cubic structure (c-GST) it exhibits the trivial features[85, 94, 101]. Similarly, all GST phases with lower Ge contents than GST-225, including GST-124[29, 36, 53, 102, 103] and GST-147[29, 53] are proposed to exhibit topologically non-trivial attributes. Hence, the successful fabrication with reliable, reproducible and scalable nano-architecture of GST alloys will open new paths for the advanced application research in the fields of phase-change and topological communities.

Selectivity: The stoichiometric tuned parameters of several GST alloys, mentioned in Figure 5.5, are now applied one by one to the pre-patterned substrates to prepare selectively grown nanostructures. As discussed in chapter 3, the strong ADR dependency of Sb on T_{sub} helps in attaining selectivity of Sb_2Te_3 in comparison to Bi_2Te_3 even at low T_{sub}. In GST alloys, strong ADR dependency of Ge on T_{sub} (discussed in section 5.1) along with Sb, assisted in achieving 100 % selectivity. Thus, without the requirement of further optimization for selectivity, nanostructures of GST alloys are successfully achieved.

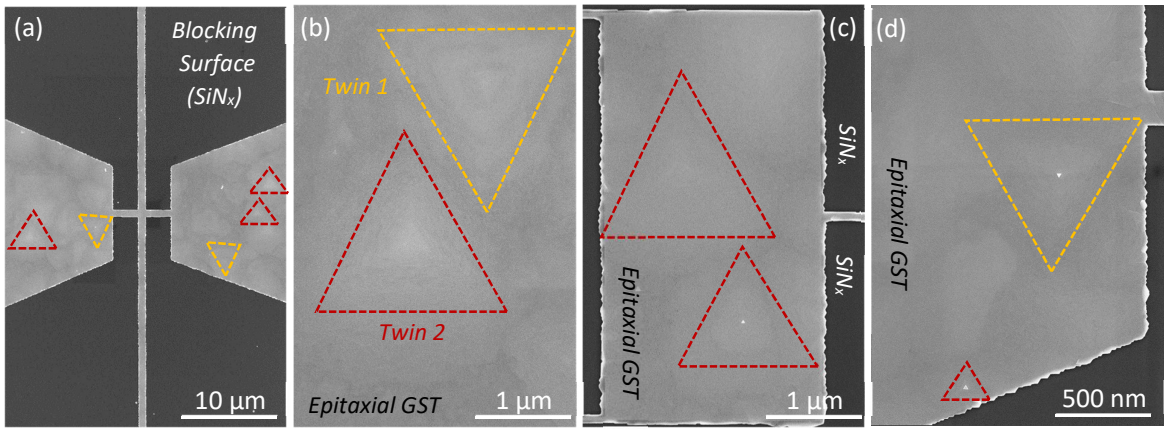

Fig. 5.6: SEM images depicting SAE of GST-225 on pre-patterned substrates. The darker contrast points to the blocking surface of SiN_x while the lighter contrast represents the epitaxial growth of GST alloy on Si (111) surface. (a) SAE of 1 µm wide Hallbar with much wider contacting lines. (b) Better resolved image of contacting lines of the Hallbar displayed in (a) with large twin domains. (c) SAE in the combinational structure with a narrow (100 nm) and wide pattern (5 µm). (d) Similar to (c) yet better resolved image of the epitaxial growth in a wide structure.

SAE of GST-225: The first attempt to prepare nanostructures via SAE is performed with the stoichiometric state of GST-225. Having R_{TF} = 10.8 nm/h (Figure 5.5), the expected R_{eff} = 11.67 nm/h is evaluated for 500 nm wide nanoribbon using SAE model stated in equation 3.10, considering L_D for Ge is equal to Sb. The epitaxial growth is performed for 2:30 hours (150 minutes) to achieve 30 nm deep trenches entirely filled. It is observed that the obtained thickness of epilayer is approx. 39 nm (measured via FIB and AFM,

discussed in Appendix 3C) while, the epilayer in 50 nm wide trench is excessively overgrown just as observed during the growth of 3D TIs depicted in Figure 3.9c (Chapter 3). The higher obtained values of the epilayer thickness and the enhanced R_{eff} than the estimated value, can be directly associated to the fact that assumed L_D for Ge is not equal rather higher than Sb. This assumption is also confirmed via observed deviations in XRD characteristic peaks in large area growth indicating the epilayer with mixed stoichiometric state containing higher Ge contents than the targeted state of GST-225. Figure 5.6 displays SEM images of the first attempt of SAE for GST-225 in various large structures of pre-patterned substrate. Due to relatively high R_{eff}, twin domains are formed and are clearly visible, indicated by maroon and orange triangles.

SAE of GST-124: In order to confirm this behavior and to evaluate the precise L_D of Ge, which according to the initial estimations seems higher than Sb, SAE of another stoichiometric state i.e. GST-124 is performed with T_{Ge} = 1236 ℃. The repeated growth experiment exhibited similar results with higher Ge contents in the epilayer and confirmed the hypothesis $L_{D\text{-}Ge} > L_{D\text{-}Sb}$. Quantitatively, based on the epilayer thickness measured at the cross-section of 500 nm wide nanoribbon via FIB, the exact value of $L_{D\text{-}Ge}$ is extracted using equation 3.10. It is interesting to know that $L_{D\text{-}Ge}$ is found to be 39 ± 0.5 nm that is approx. double than $L_{D\text{-}Sb}$ = 20 nm. This is why, the SAE of both GST alloys resulted in higher R_{eff} than the estimated values. Moreover, the phenomenon of difference in the lateral diffusion lengths (ΔL_D) of rate controlling elements i.e. Ge and Sb is the source of stoichiometric shift observed during SAE of GST-225 and GST-124. This phenomenon is named the ***selective stoichiometric shift (SSS)***. SSS is an enormous obstacle in obtaining the selectively grown nanostructures of the desired stoichiometry in GST alloys and must be addressed.

The effect of material parameters on stoichiometry: As discussed in chapter 3, during SAE changes in R_{eff} are determined by two factors i.e. structural dimensions and L_D of rate controlling elements (equation 3.10). In order to resolve the issue of higher R_{eff} and the phenomenon of SSS, the impact of each factor must be analyzed individually. At first, the focus is turned towards the material parameter L_D and assessing its impact on SAE.

- ***L_D vs. R_{eff}:*** In binary TIs, the impact of L_D is quite simple to assess as only one element controls R_{TF} (as discussed during SAE of 3D TIs in chapter 3); however, the influence of L_D in compositional alloys is more complicated and must be assessed separately for each stoichiometry. In case of alloys, the cumulative L_D can be evaluated by the compositional average of individual L_D exhibited by each element. For example GST-225 contains equal amount of Ge and Sb and as Te does not influence R_{TF}, the cumulative L_D will be (50x39 + 50x20)/100 = 29.5 nm which is the average values of both elements. While in case of GST-427, the cumulative L_D will change to (66.7x39 + 33.3x20)/100 = 32.63 nm and to 26.33 nm for GST-124. Hence, any change in composition will always result in an altered cumulative L_D that eventually will affect R_{eff}.
- ***L_D vs. SSS:*** The differential L_D (ΔL_D) between rate controlling elements (Ge, Sb) in an alloy (GST), not only influences R_{eff} as discussed above, it also alters the effective flux ratio (Ge/Sb) that leads to the stoichiometric shift in the epilayer (the phenomenon of SSS). The complexity enhances further as above mentioned stoichiometric shift does not remain constant rather varies with the compositional changes. It means, if SAE of GST-225 (with 22.22 % Ge) shifts Ge contents in the selectively grown structures to 28.22% with 6% additional Ge, the stoichiometric shift during SAE of GST-124 will not be similar rather it will change depending upon the Ge contents of each stoichiometric state. Where ΔL_D enhances the complexity of achieving nanostructures with the desired stoichiometry, the dynamics of SAE (equation 3.10) offers a solution. With the help of pre-evaluated L_D of Ge and R_{eff} combinedly, the required change in Ge flux (T_{Ge}) can be evaluated that will ease the tuning of correct flux ratio during SAE of the desired stoichiometry and will neutralize the phenomenon of SSS. The only drawback is the requirement of tuning the optimum Ge/Sb flux ratio individually for the planar epitaxy and for the selectively grown nanostructures.

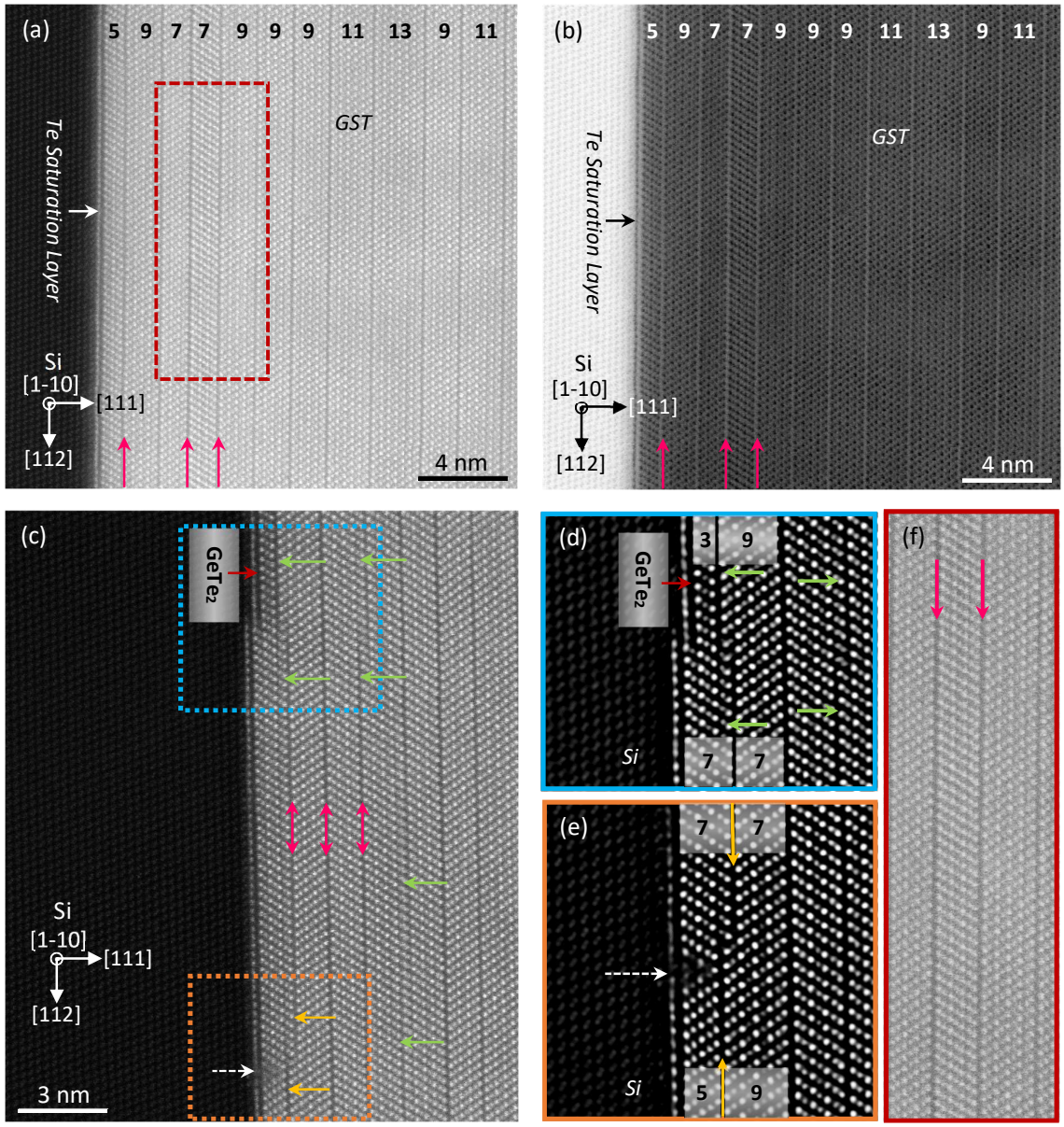

Fig. 5.7: STEM images acquired along Si [1-10] projection. The lamella is extracted at the cross section of 500 nm wide Hallbar of selectively grown GST alloy on Si (111) surface. (a) HAADF image acquired at Si (111)-GST interface. No defects, other than a few TSFs close to the interface (indicated with pink arrows), are observed. (b) The corresponding bright field (BF) image of (a). (c) HAADF image focusing the defects at the interface and the resulting inter-layer transitions occurring at Si step edge (better resolved in d, blue box) and the rotational twin domain coalescence (better resolved in e, orange box). Pink, green and yellow arrows indicate TSFs, bilayer switching and Ge vacancy layer assisted vdW reconfiguration. (d) Low-pass filtered HAADF image at Si step edge. Sb-Te antisite assisted bilayer switching transforming 7-7 atomic layer stack to 3-9 layer stack. (e) Low pass filtered HAADF image at the rotational twin domain coalescence. SL via Ge vacancy layer assisted vdW reconfiguration (yellow arrows) converts into QL. (f) Better resolved image of an area from (a) depicting a sandwiched SL between two TSFs.

For the detailed structural investigations and to observe the phenomenon of selective stoichiometric shift (SSS) at the atomic scale, a lamella at the cross-section of 500 nm wide selectively grown nanoribbon of GST-124 (SL architecture) is extracted and STEM measurements are performed. The results are depicted in Figure 5.7 while the key observations based on STEM results are mentioned below:

- The growth is started with only Sb flux for the first 2 minutes before Ge shutter is opened for the epitaxial growth of GST. This is why the formation of Sb_2Te_3 QL is observed at Si (111) interface. To achieve homogenous stacking, this step is reduced to only 30 seconds in all future growths.
- According to applied Ge flux, only SL architecture should have existed (assuming $L_{D\text{-}Ge} = L_{D\text{-}Sb}$). The observations have indicated that most of the blocks comprise of 9 and 11-atomic layers where one block even contains 13-atomic cell confirming the higher accumulation of Ge in the trench (enhanced Ge/Sb flux ratio as $L_{D\text{-}Ge} > L_{D\text{-}Sb}$) and resulting in mixed phase growth of GST.
- Due to relatively higher $R_{eff} \approx 12$ nm/h, the rotational twin domains are witnessed (white arrow in Figure 5.7c, e); however, the selection of optimum T_{sub} limited them to only one layer stack before getting engulfed by the dominant domain originating a translational shear fault (TSF).
- A few TSFs are witnessed, some originated at the twins coalescence while the origin of others could not be identified. The presence of all TSFs is limited to approx. first 5 nm of epilayer (indicated by pink arrows in Figure 5.7a, b and f).
- Inter-block transition (transformation of one layer architecture into another) is not observed in the defect-free zones; however near defects, transitions are witnessed via vdW reconfiguration[75] mechanisms including Sb-Te antisite assisted bilayer switching[78] (indicated by green arrows in Figure 5.7c and d) and Ge vacancy (V_{Ge}) layer assisted vdW transformation (indicated by yellow arrows in Figure 5.7c and e). Ge vacancy (V_{Ge}) exhibits the lowest formation energy of approx. 0.1 eV in GSTs[51, 87, 89]. That is why, V_{Ge} assisted vdW reconfiguration is the key mechanism in crystal ↔ amorphous phase transformation in GST and GBT alloys[77, 87, 88, 89].
    - At coalescence of twin domains, a TSF rearranged itself at lower energy state via V_{Ge} layer assisted vdW reconfiguration transforming 7-7 layer blocks into 5-9 layer blocks (Figure 5.7e).
    - Ge, with the capability of vacancy layer assisted vdW switching transformed into a stable trilayer (TL) formation of $GeTe_2$[104] at Si step edge witnessed in Figure 5.7c. The vdW switching is also observed at twin domain coalescence (yellow arrows in Figure 5.7d).
- The formation of antiphase domains and screw dislocations at Si step edge, one of the major defect observed in 3D TIs that limits the phase coherent length of quasi-particles in magneto-transport[105] and acts as bottleneck for some applications, is not witnessed in GST alloys. The step edge defect continuity is blocked combinedly with Sb-Te antisite assisted inter-block transition from 3-9 into 7-7 (2 additional atomic layers appeared due to the step edge height) and Ge vacancy layer assisted formation of $GeTe_2$ (Figure 5.7c and d).

The deviation from SL architecture, observed in Figure 5.7, can only be linked to higher Ge contents in the epilayer that confirms the phenomenon of selective stoichiometric shift (SSS). To obtain the target stoichiometry, the Ge/Sb flux ratio is tuned again with the reduced Ge flux (T_{Ge}) according to equation 3.10 (Chapter 3) and SAE of GST-124 is performed again. Figure 5.8 depicts SEM images of a few selectively grown GST-124 nanostructures. STEM investigations have confirmed that, the substrate induced defects including antiphase domains and screw dislocations are entirely avoided assisted by the natural phenomenon of inter-layer transitions (vdW reconfiguration) in GST alloys. Twin domains are observed however suppressed to only one layer similarly a few TSFs are also witnessed. Both of these defects can be directly associated to higher R_{eff} and can be avoided by conducting the growth at lower R_{eff}.

The effect of dimensional changes on stoichiometry: After assessing the effects of material parameter L_D on SAE of GST alloys, the effects of dimensional changes on R_{eff} and the stoichiometry are investigated.

- ***R_{eff} vs. pattern dimensions:*** The effect of dimensional changes on R_{eff} are discussed earlier in chapter 3 (Section 3.4) where it has been witnessed that R_{eff} is inversely proportional to the pattern's surface area. In binary compounds, the dimensional changes impact only R_{eff}; however, in compositional alloys any change in dimensions not only impacts R_{eff}, it also influences the

stoichiometry by altering the effective flux ratios. Stoichiometric variation only occurs when the rate controlling elements exhibit different L_D ($\Delta L_D \neq 0$) such as GSTs.

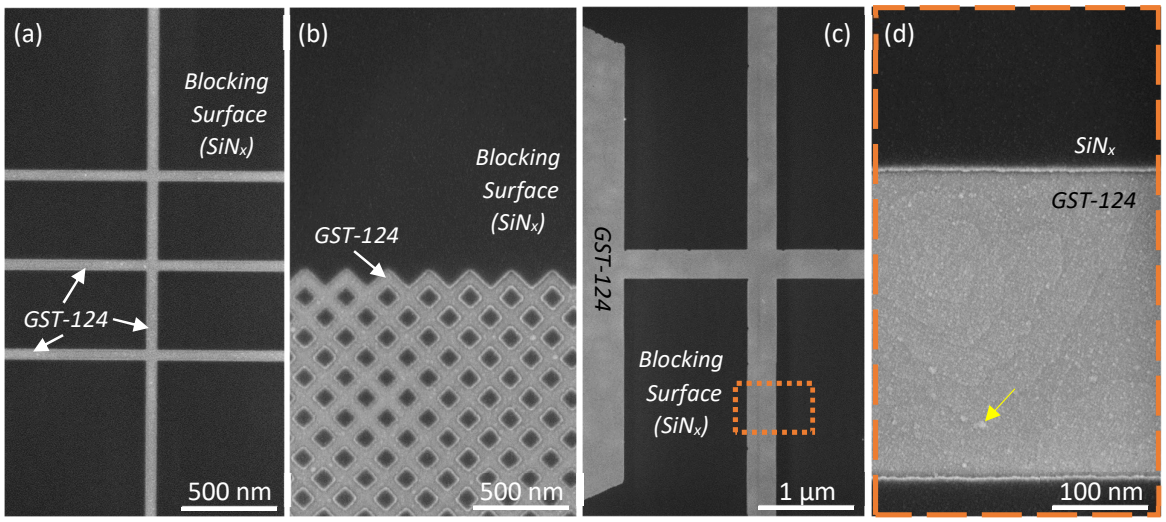

Fig. 5.8: SEM images of selectivity area epitaxy of GST-124 crystal on pre patterned substrates. (a) SAE of 100 nm wide Hallbar with ultra-smooth crystalline surface and 100% selectivity. (b) SAE of 100 nm wide array of diamond shaped structure with 100 nm gaps. It can also be visualized as the 100 nm wide pillars of SiN_x with 200 nm pitch piercing through the epilayer and forming an array of square shaped structures. (c) Selectively grown 500 nm wide Hallbar of GST with much wider contacting lines. (d) Better resolved image of the marked area depicted in orange dotted shape in (c) indicating high quality epitaxial growth and surface roughness of approx. 1 nm (rms). The bubbles on the surface appear due to Al capping layer (yellow arrow).

- ***ΔL_D vs. pattern dimensions:*** In case of compositional alloys where $\Delta L_D \neq 0$ such as GSTs with ΔL_D = 19 nm between Ge and Sb (rate controlling elements), SAE results in SSS, discussed above. Based on the corrections provided by dynamics of SAE, the issue of SSS can be resolved by reducing the Ge flux (T_{Ge}) in such a way that effective flux will keep the targeted Ge/Sb flux ratio intact for the desired stoichiometry and any unintentional stoichiometric shift will be avoided (neutralization of ΔL_D). This solution, however, has a limitation for changes in pattern dimensions. The corrected Ge flux (T_{Ge}) corresponds only to a specific set of dimensions (length and width). Any change in those dimensions, even after the corrected parameters for SSS, will result in an altered stoichiometry. Hence, the stoichiometric tuning to obtain selectively grown nanostructures with the targeted state of GST alloy can be performed as long as the pattern dimensions remain intact (partial neutralization of dimensional issue). In other words, the desired stoichiometry of GST alloy can be achieved via SAE for any dimensions; however, the flux tuning has to be performed individually for each of them and if SAE will be required to perform on two patterns with different dimensions at the same time, both patterns will exhibit different stoichiometry. This phenomenon where the stoichiometric shift occurs due to structural changes even after the correction of Ge flux for SSS, is named the ***selective dynamic stoichiometry (SDS)***. SDS can also be viewed as a 2nd order effect of SSS specific to dimensional changes.

Similar to the investigations of SSS, the phenomenon of selective dynamic stoichiometry (SDS) is also investigated. In order to do so, SAE of GST-147 is conducted where Ge/Sb flux ratio modifications to avoid any stoichiometric shifts are performed by changing T_{Ge} from 1215 ℃ to 1202 ℃ according to 1 µm wide pattern (SSS neutralization). In order to observe the probable stoichiometric shifts due to dimensional changes (the phenomenon of SDS), three lamellae are extracted at the cross-section of 200 nm, 500 nm and 1 µm wide nanoribbons from the same substrate i.e. prepared with similar parameters (T_{Ge} = 1202 ℃). STEM investigations are performed where the stoichiometry of GST-147 is observed, as

intended, in 1 µm wide structure confirming the neutralization of SSS. The STEM-HAADF image is depicted in Appendix 5B while the images acquired at the cross-section of other two nanoribbons i.e. 200 nm and 500 nm are displayed in Figure 5.9. STEM investigations have confirmed the deviations in both structures from the target stoichiometry of GST-147 confirming the phenomenon of SDS. According to dynamics of SAE, the extent of compositional deviation depends upon changes in pattern dimensions i.e. effective flux change in 200 nm wide pattern should be higher than the pattern with 500 nm width. GST-147 (Ge = 8.33 %) exhibits the stacking sequence of SQ while STEM investigations, depicted in Figure 5.9, confirmed that 200 nm wide structure exhibited SSSQ-SSSQ stacking of GST-3815 (Ge = 11.53 %) with higher compositional deviation than SSQ-SSQ stacking of GST-2611 (Ge = 10.53 %) observed in 500 nm structure.

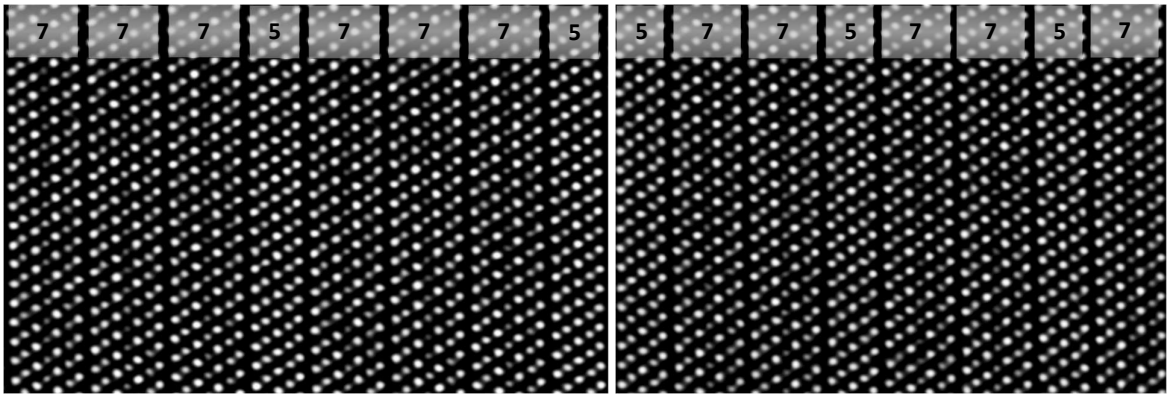

Fig. 5.9: STEM images acquired along Si [1-10] projection from selectively grown structures of GST-147 alloy. (Left) HAADF image acquired at the cross-section of 200 nm wide structure. Layer stacking of SSSQ-SSSQ is evident confirming the stoichiometric shift from GST-147 state to GST-3815. (Right) HAADF image belong to 500 nm wide structure grown together with the structure having width of 200 nm. Layer stacking of SSQ-SSQ confirm relatively smaller stoichiometric shift from GST-147 stoichiometric state to GST-2611.

Based on all STEM investigations conducted on selectively grown GST nanostructures, the key observations are summarized below:

- For all GST alloys, SAE of the desired stoichiometry is possible; however, the flux tuning for planar and selective growths are required to be performed separately. (SSS neutralization)
- The flux tuning for SAE is always limited to a specific set of dimensions. Any change in dimension would result in altered stoichiometry and therefore, the stoichiometric SAE on different dimensions cannot be achieved on the same substrate (same growth run). (SDS limitation)
- The growth tests, required to perform the stoichiometric flux tuning for each different dimension, are not necessary. Based on the dynamics of SAE, a couple of growths can help to evaluate the right set of parameters to tune the stoichiometry for all dimensions.
- SDS is a limiting factor that does not allow SAE of multiple dimensions without changing the stoichiometry of the alloy. However, it can be applied as a useful tool to explore the in-plane physics of quantum wells and fabricate novel devices such as topological switches (section 5.4).

5.3 Epitaxy and structural characterization of GBT alloys

Structurally GBTs and GSTs are alike, only difference is the replaced Sb atoms with Bi. Though their physical and electronic characteristics strongly overlap, they also exhibit slight deviation from each other such as:

- Relatively strong spin-orbit coupling (SOC) in Bi_2Te_3 compared to Sb_2Te_3, results in higher band inversion in GBTs than GSTs. In GSTs, as discussed in section 5.2, all stoichiometric states with lower Ge contents than GST-225 exhibit topologically non-trivial features with inverted band structures. With GST-225 being at the critical point, all states above GST-225 including GST-326

and GST-427 exhibit non-inverted trivial band structures. GBTs, on the other hand, exhibit relatively strong topology[54, 103, 106, 107, 108, 109]. The strength of SOC offered by Bi_2Te_3 shifts the critical point from 225 state in GSTs to 326 stoichiometry in GBTs. Based on all reported and predicted electronic features of GST and GBT states, the band gaps vs. stoichiometry data is replotted in Figure 5.10 that provides a relatively better overview of topological ↔ trivial phase transition. *Note: The values plotted in Figure 5.10 are just rough estimates that are acquired from different sources. The idea is to demonstrate the trend of changing bandgap. For the exact value of bandgap belonging to any stoichiometry, more precise calculations are recommended.*

- Topologically another difference in GBTs from GST is the presence and evolution of crystal symmetry (CS) protected TCI features introduced by Bi_2Te_3. Sb_2Te_3 and, therefore, GSTs do not exhibit TCI characteristics (for details visit chapter 1).
- GBTs just like GSTs exhibit PCM characteristics[28, 31, 110, 111, 112] not just as bulk but also as IPCMs. Studies have shown structural similarity of 225 stoichiometric state in GBT and GST with the transformation into a cubic crystal structure[113] (c-GBT) exhibiting crystalline bulk PCM. Relatively higher Bi_{Te} antisite energy than Sb_{Te} (discussed in chapter 2), restricts bilayer switching mechanism in GBTs that increases the probability of transformation into interfacial layer stack in GBT-225 than GST-225. This property predicts GBTs as more promising candidate for IPCMs than GSTs.

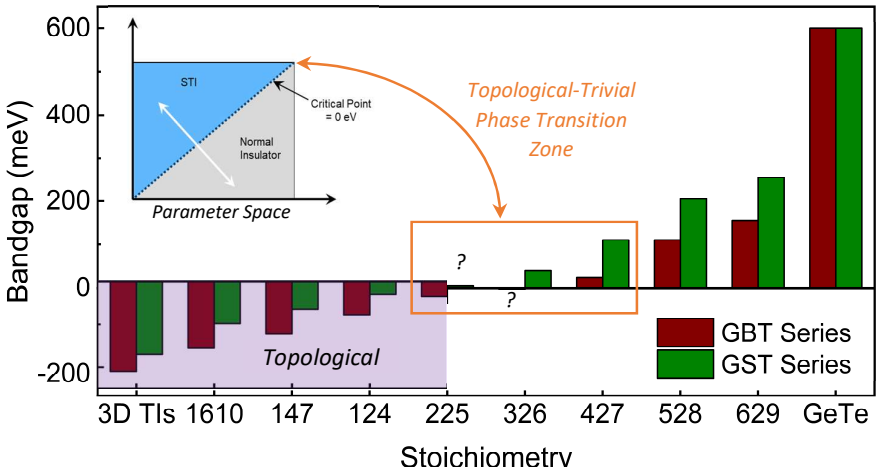

Fig. 5.10: The trend of changing band gaps vs. stoichiometry, plotted with data acquired from various reported studies about GSTs and GBTs in literature. It is interesting to observe relatively higher spin-orbit coupling (SOC) strength in Bi_2Te_3 that results in inverted bandgap of -210 meV in comparison -170 meV in Sb_2Te_3. With Ge accumulation in alloys, the decreasing strength of SOC brings the critical point (0 eV) in GSTs around the stoichiometric state of 225 while in GBTs relatively stronger SOC shifts it around the state of 326 (orange box). After passing through the critical point, alloys lose time-reversal symmetry (TRS) based topological protection and exhibit continuously increasing non-inverted bandgaps with relative increase in Ge contents. (Inset) The theoretical model of topological trivial phase transition[23].

5.3.1 Stoichiometric tuning of GBTs

The growth parameters for GBT alloys cannot be adopted from pre-optimized parameters of GST alloys due to two main reasons, both are related to Bi_2Te_3 epitaxy and are mentioned below:

- Based on the discussion in chapter 2, Bi_2Te_3 crystal exhibits high defect density if growth is conducted at T_{sub} < 300 ℃.
- Bi_2Te_3 exhibits a narrow window of temperature (298 ℃ < T_{sub} < 302 ℃) for optimum SAE. If GBT stoichiometric tuning on planar substrates is conducted at lower T_{sub} (285 ℃), SAE will fail and in order to improve selectivity T_{sub} would be required to increase. This step will alter the targeted stoichiometry due to strong ADR dependency of Ge on T_{sub} (Figure 5.2).

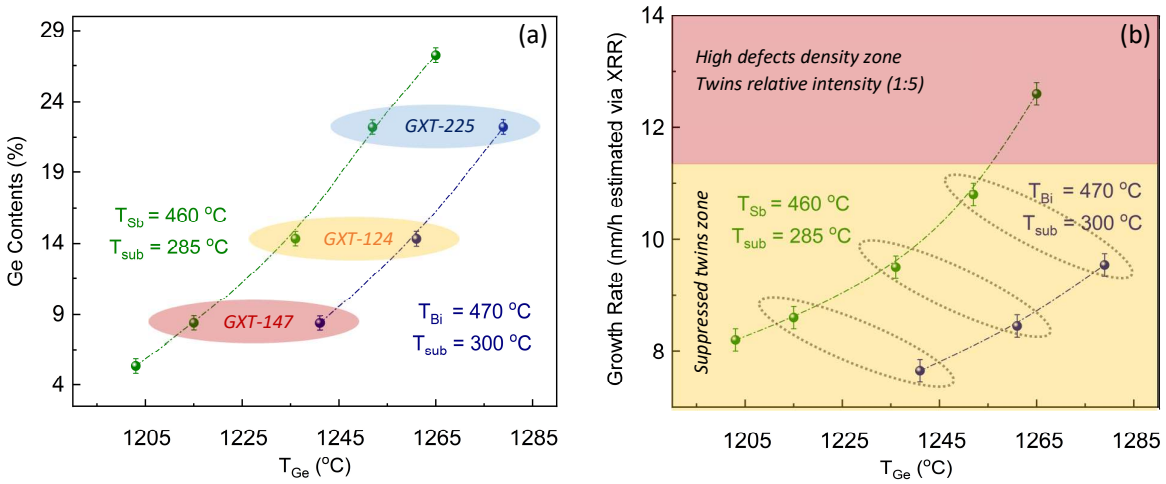

Fig. 5.11: A comparative overview of thin film growths of targeted GBT vs. GST stoichiometric states via MBE. (a) The trend of increasing Ge contents in the epilayer of GBTs with variable T_{Ge} is apparent. The GBT states are realized at higher T_{Ge} than their equivalent GST states due to increased T_{sub} from 285°C for GSTs to 300°C for GBTs. (b) The growth rates of GBTs and GSTs corresponding epilayers mentioned in (a). According to the standard zones of the rate map, all GBT epilayers are obtained with rates in yellow zone (suppressed twin zone) although with the reduced values than their GST equivalent despite the fact of higher applied T_{Ge}.

Considering both above mentioned points, the Ge/Bi flux tuning for the epitaxial growth of GBT alloys is started with the optimum parameters of Bi_2Te_3 epitaxy (adopted from chapter 2) at T_{sub} = 300°C. Keeping in mind the required Ge flux for the GST-124 (T_{Ge} = 1236°C) and the increased T_{sub} from 285°C to 300°C, the stoichiometric flux tuning for GBTs is started with T_{Ge} = 1240°C. After a series of tests and failed attempts to tune the flux ratio, finally the stoichiometric states GBT-147, GBT-124 and GBT-225 are successfully achieved at T_{Ge} = 1242°C, 1261°C and 1279°C respectively. The structural characterization of GBT epilayers is conducted with XRD 2θ-ω scans. Due to near identical unit cell length of Sb_2Te_3 (30.45 Å) and Bi_2Te_3 (30.48 Å), XRD diffraction peaks of GST and GBT are almost identical (see Figure 5.3) and therefore, are not explicitly depicted here. However, Δω scans revealed slightly improved crystal quality of GBT-124 and GBT-225, in comparison to their GST equivalents, with FWHM values of 255″ and 273″ respectively, due to the epitaxial growth performed at higher T_{sub}.

Figure 5.11 depicts the required values of Ge flux (T_{Ge}) for GXT stoichiometric states where X represents Sb for GSTs and Bi for GBTs. It is important to notice the effect of ADR dependency of Ge on T_{sub} with the increased demand of Ge for GBTs even though the corresponding R_{TF} of GBTs in comparison to their GST equivalents are quite low (Figure 5.11b). After the structural characterization of epilayers via XRD, stoichiometric tuned parameters are subjected to the pre-patterned substrates and nanostructures of various dimensions are prepared via SAE. Figure 5.12 depicts SEM images of planar and selectively grown nanostructures of GBT-124 and GBT-225 stoichiometric states. The phenomena of SSS and SDS, observed during SAE of GST alloys, have also been witnessed during the SAE of GBTs, and are investigated via STEM.

5.3.2 GBTs: Structural characterization via STEM

In order to investigate layer stacking sequences and to observe the phenomena of SSS and SDS, STEM investigations are performed on a lamella extracted at the cross-section of selectively grown 500 nm wide Hallbar of GBT-225. Based on previous STEM investigations of GST-124 and 147, the phenomenon of SSS i.e. the increased Ge contents in selectively grown epilayer due to enhanced Ge/Sb flux ratio, is expected to shift the stoichiometry from GBT-225 to another state with higher Ge contents. The flux ratio modifications to neutralize the effects of SSS are not performed. The aim is to investigate the extended

effects of ΔL_D when SAE is conducted at higher T_{sub} and enhanced T_{Ge}. Unfortunately, two factors have limited the detailed structural analysis of this sample:

- The lamella is extracted along Si [211] orientation. It not only projects high density of atoms but also limits the information of twin domains and TSFs.
- During STEM investigations, strong mechanical vibrations due to construction work in the lab, hindered the acquisition of high quality atomic resolution images and EDX spectra.

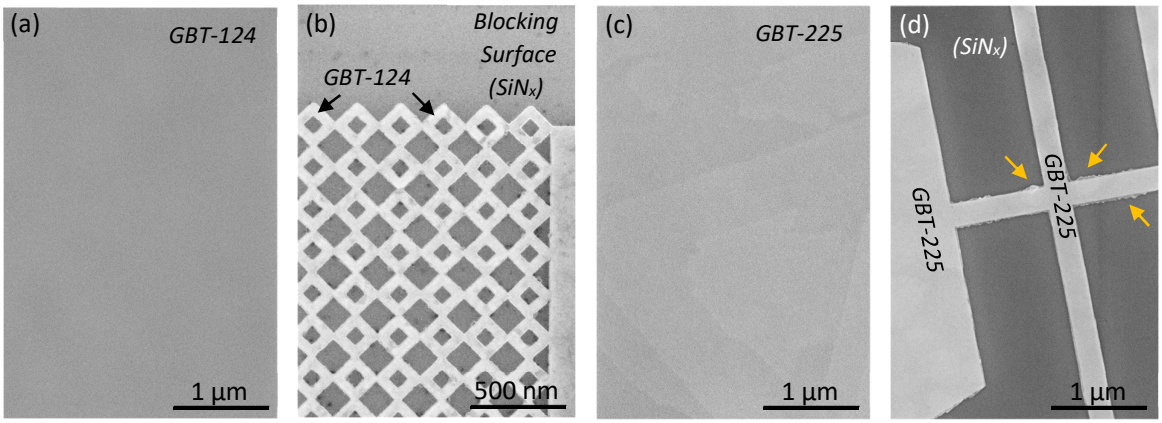

Fig. 5.12: SEM images of planar and selective area epitaxy of GBT alloys on Si (111) non-patterned and patterned substrates. The darker contrast points to the blocking surface of SiN_x while the lighter contrast represents the epitaxial growth of GBT alloy. (a) Ultra-smooth GBT-124 epilayer on planar Si (111) substrate. (b) SAE of GBT-124 upon the patterned substrate containing 50nm wide array of diamond shaped ring structure with 100 nm gaps. (c) GBT-225 epilayer on planar Si (111) substrate. (d) SAE of GBT-225 on 500 nm wide Hallbar with large connecting pads. After entirely filling the trench, the overgrown epilayer started to expand laterally (indicated with yellow arrows)

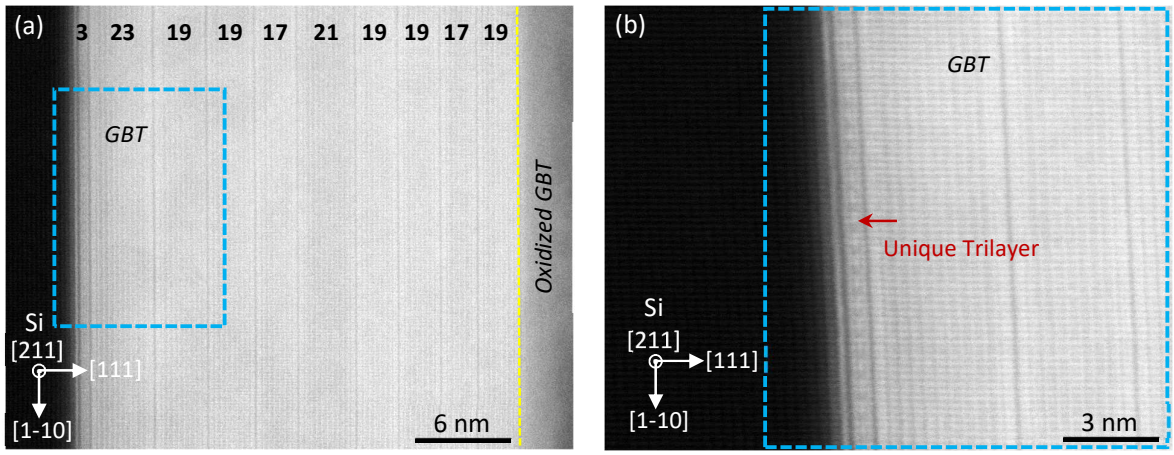

Fig. 5.13: STEM images captured along Si [211] projection. The lamella is extracted at the cross-section of 500 nm wide Hallbar of epitaxial and selectively grown GBT-225 on Si (111) surface. (a) HAADF image acquired at Si (111)-GBT interface. The monoatomic Te layer passivated Si dangling bonds. An unexpected trilayer structure is observed between Te passivation layer and the GBT layer stacks. The relatively high ΔL_D between Bi and Ge enhanced the effective flux ratio during SAE and altered the targeted 9-atomic layer architecture of GBT-225 into larger cells with 17, 19, 21 and 23 atomic layers indicating the phenomenon of selective stoichiometric shift. (b) The better resolved area of (a) marked with red rectangle, to observe the structure of this unexpected trilayer with unique periodic contrast variations.

The acquired STEM images of GBT-225 are depicted in Figure 5.13 displaying the overall stack in the epilayer while Figure 5.14 depicts the appearance of a unique trilayer structure at the interface with Si (111). Based on STEM measurements, the key observations are stated below:

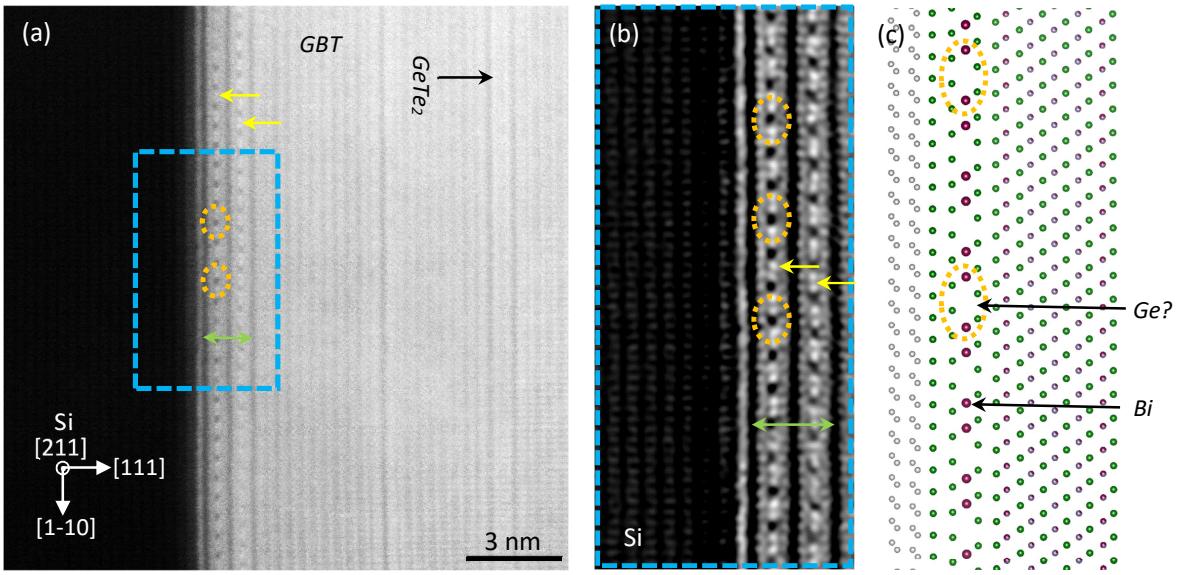

Fig. 5.14: STEM images captured along Si [211] projection of selectively grown GBT-225 on Si (111) surface. (a) HAADF image indicating dual stacked exotic trilayer structure at the interface. Another trilayer with homogeneous contrast is also observed that indicate the presence of $GeTe_2$. (b) The better resolved and low pass filtered images of area marked in (a) with blue rectangle, to observe the structure of dual stacked trilayer with unique periodic contrast variations. The atomic contrast indicates the presence of heavier element (Bi) in the central atomic layer (indicated with yellow arrows). The detailed observations indicate the periodic sequence of two adjusted Bi atom with one hole/vacancy spot with relatively dark contrast (indicated by orange circles). (c) An atomic model representing the observed structure of exotic trilayer with probable holes along Si [1-10] projection.

- As expected, the phenomenon of selective stoichiometric shift (SSS) is witnessed in GBTs as well. The effective Ge flux has pushed the targeted stoichiometric state of GBT-225 (Ge = 22.22 %) with 9-atomic layer architecture to a composition with approx. 37 % Ge contents and layer architecture containing mostly 19 and 21-atomic blocks (Figure 5.13).
- It is also observed that the stoichiometric shift in GBTs is much more pronounced than in GSTs. It can be associated to relatively high ΔL_D between Ge and Bi in GBTs than Ge and Sb in GSTs as Bi exhibits smaller $L_{D\text{-}Bi}$ = 12 nm than $L_{D\text{-}Sb}$ = 20 nm (evaluated in section 3.4). This factor slightly enhanced the effective Ge/Bi flux ratio but not as drastic as observed in Figure 5.13. An interesting point to notice here is the temperature dependency of $L_{D\text{-}Ge}$. The value of $L_{D\text{-}Ge}$ = 39 nm is evaluated for T_{sub} = 285 ℃ for GSTs while at T_{sub} = 300 ℃ for SAE of GBTs, the value of $L_{D\text{-}Ge}$ will be slightly higher and thus, it has influenced the Ge/Bi flux ratio even more.
- The major compositional shift, however, occurred due to the requirement of higher demand of Ge flux for GBT-225 (T_{Ge} = 1279 ℃) than the equivalent GST state (T_{Ge} = 1252 ℃) due to the growth of GBT at higher T_{sub}. Hence, with high L_D of Ge and higher applied flux (T_{Ge}), the resulting impact on the effective Ge/Bi flux ratio was also higher.
- Based on conclusions from STEM investigations of GST alloys (Figure 5.7), Bi shutter is opened only for 30 seconds prior to opening Ge shutter to avoid the formation of Bi_2Te_3 QL at the interface. As intended unlike GST, no QL is observed at the interface with Si (111); however, a unique trilayer structure with apparent periodic holes/vacancies (or the probable presence of relatively light atoms such as Ge) is witnessed as depicted in Figure 5.13 and 5.14.
- The atomic contrast in a couple of better resolved images indicates the higher contrast presumably caused by the presence of Bi atoms at the center of the observed exotic trilayer (yellow arrows in Figure 5.14 and 5.15) sandwiched between Te atomic layers on both sides. To our knowledge, no such layer structure is reported in the literature for Bi chalcogenides.

- There are several questions regarding the atomic arrangement, the composition and the formation of such an exotic trilayer architecture. Since neither the detailed atomic structure (due to Si [211] orientation) nor the exact atomic composition are known, further STEM and EDX investigations including the image simulations are required. At present, the atomic model presented in Figure 5.14c is only a rough guess based on the assumption that the bright atomic contrast arises from Bi atomic rows. So far the driving force for the formation of this exotic interface structure (trilayer architecture) is unknown and can only be speculated about.

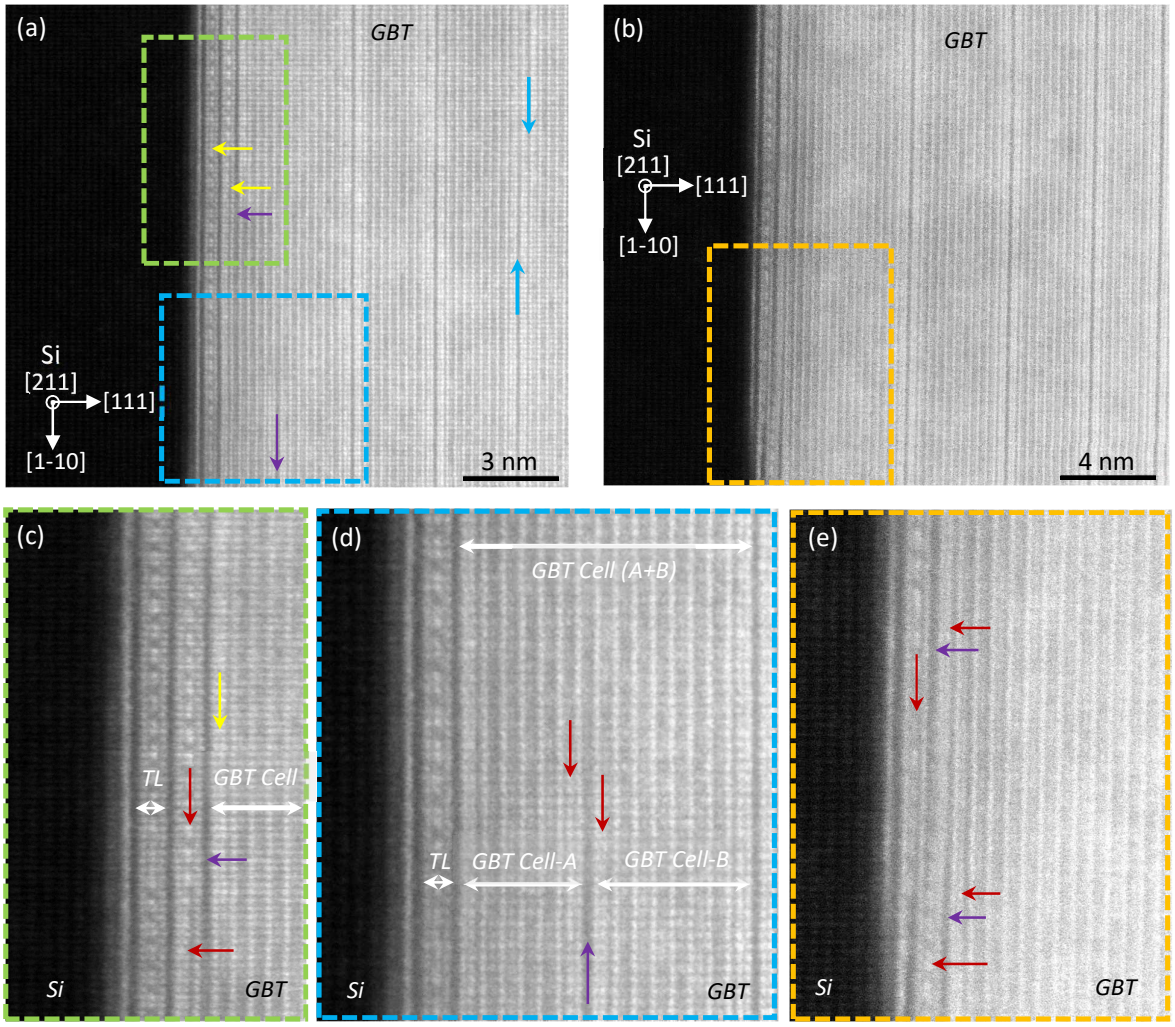

Fig. 5.15: A set of STEM images belong to GBT-225 selective area epitaxy on Si (111) surface captured along Si [211] projection depicting inter-layer transition mechanisms and structural changes at defects. (a) HAADF image representing all mechanisms of inter-layer transition including merging of exotic trilayer with GBT supercell (green box), Ge vacancy layer assisted conversion of a large supercell into two smaller supercells (blue box) and the vdW reconfiguration (indicated by two opposing blue arrows). (b) HAADF overview image indicating the behavior of layer transition at Si step edge. (c) A better resolved image of an area marked with green box in image (a) representing the merger of exotic trilayer with GBT supercell. The position of Bi layer in GBT cell (marked with yellow arrow) is taken by Ge. The vdW gap is annihilated by Ge accumulation (marked with purple arrow) and the central atomic layer of exotic trilayer takes the position of Bi layer in new GBT supercell (marked with maroon arrows). (d) A better resolved image of an area marked with blue box in image (a) representing the merger of two GBT supercell into a larger cells and vice versa. The vdW gap between two cells (marked with purple arrow) is annihilated by Ge atoms while the position of the two bordering Bi atomic layers (marked with red arrow) is also taken by Ge atoms forming a larger cell. (e) A better resolved image of an area marked with orange box in image (b) representing the merger and separation of the exotic trilayer with GBT cell while passing through Si Step edge.

- An interesting feature observed about the exotic trilayer structure is its ability to merge with the neighboring GBT layer and transforming back into itself after passing through the defects such as Si step edges (Figure 5.15e)
- Due to relatively higher Bi-Te antisites energy in comparison to Sb-Te antisites, GBTs do not readily form antisite defects and therefore, the antisite assisted bilayer swapping, the key inter-layer transition mechanism in GSTs, is not observed in GBTs (Figure 5.13-5.15). The inter-layer transition in GBTs is mainly observed to occur via Ge vacancy layer/Ge accumulation layer assisted vdW switching. Following are a few observed examples of such inter-layer transitions.
    - The exotic trilayer, at lower availability of Bi atoms, lost its identity and merged with neighboring GBT layer (Figure 5.15c). The central atoms of trilayer (predicted to be Bi) occupied the Bi slot in a GBT cell (maroon arrows) while the Te layers kept their relative positions. The vdW gap between trilayer and GBT layer vanished by the Ge accumulation (purple arrow) as depicted in Figure 5.15c.
    - Opposite to the first mechanism, the Ge layer discontinued and generated a vacancy layer that allowed Bi atoms to accumulate at both sides of the vacancy layer, dividing a relatively large GBT layer into two smaller layers. The creation of vacancy layer is indicated by the purple arrow while Bi accumulation is represented by maroon arrows in Figure 5.15d.
    - Ge with the help of vacancy /accumulation layer generated and obliterated vdW gaps that allowed atomic layers from one supercell (layer) to slide and merge with the other supercell as depicted in Figure 5.15a (two opposing blue arrows indicate the switching of vdW gap).
- The antiphase domains and screw dislocations are not observed. Once again, at Si step edge, the exotic trilayer deformed itself by merging with the neighboring GBT layer, impeded the step continuity and restructured itself after passing through the step edge. (Figure 5.15e)
- At places the appearance of $GeTe_2$ trilayer architecture is also observed (Figure 5.14a) which quickly merged with the supercell and lost its identity.

For the first time, STEM assisted structural characterizations of GBT alloy on Si (111) substrate are performed. The formation of layer stacks along with the phenomena of inter-layer transition, changes in layer architecture at defects and the formation of exotic trilayer structure is observed. The deep understanding of GBT structural features require further growth studies and structural characterization via STEM and EDX, particularly along Si [1-10] orientation to observe the effects at atomic scale without the limitations of crystal orientation.

5.4 Selective dynamic stoichiometry: limitations and applications

The phenomenon of selective dynamic stoichiometry (SDS) became evident during the structural characterization of selectively grown nanostructures of GST and GBT compositional alloys, discussed in section 5.2 and 5.3 respectively. SDS is a bottleneck to obtain the stable stoichiometric state in nanostructures if substrate contains patterns with different dimensions. The relatively larger L_D of Ge in comparison to Sb and Bi alters the Ge/Sb and the Ge/Bi flux ratios depending upon the structural dimensions leading to stoichiometric variations. While this phenomenon increases the growth complexity and adds limitations to dimensional changes for stoichiometric growth, it can be utilized for some novel conceptual applications as well.

It is known that stoichiometric states with changing Ge contents exhibit subsequent changes in the electronic bandgap, depicted in Figure 5.10. These stoichiometric variations not only impact the electronic band structure, they affect the strength of SOC in the alloys as well resulting in the transformed topological attributes. Utilizing this feature (i.e. SDS), a number of novel applications can be designed. The experimental realization of these applications requires extensive research and experience to control the targeted stoichiometry while here, just a few key ideas are presented.

Electronic characterization and understanding the physics of changes to the in-plane band structure. The lateral structures with gradual and abrupt dimensional changes can be fabricated to study the variations in material's electronic properties with the continuous or immediate changes in the electronic bandgap. (Figure 5.16a, b)

- The fabrication of in-plane quantum well (QW). Assisted by SDS, pattern with sudden large dimensional variations can be designed in such a way that the stoichiometry can be tuned to fabricate the in-plane QWs (Figure 5.16c). This technique can help to improve the performance of device with higher carrier concentration at low temperatures by limiting their paths physically and confining them in certain targeted areas.
- Topological-trivial switch array. Inverse of the in-plane QW design, SDS can be tuned in such a way that the confined and surrounding areas end up with stoichiometry containing non-inverted and inverted bandgap respectively. Such in-plane topological-trivial junctions can be utilized in superconducting quantum applications for example, Majorana box qubit[114]. (Figure 5.16d)

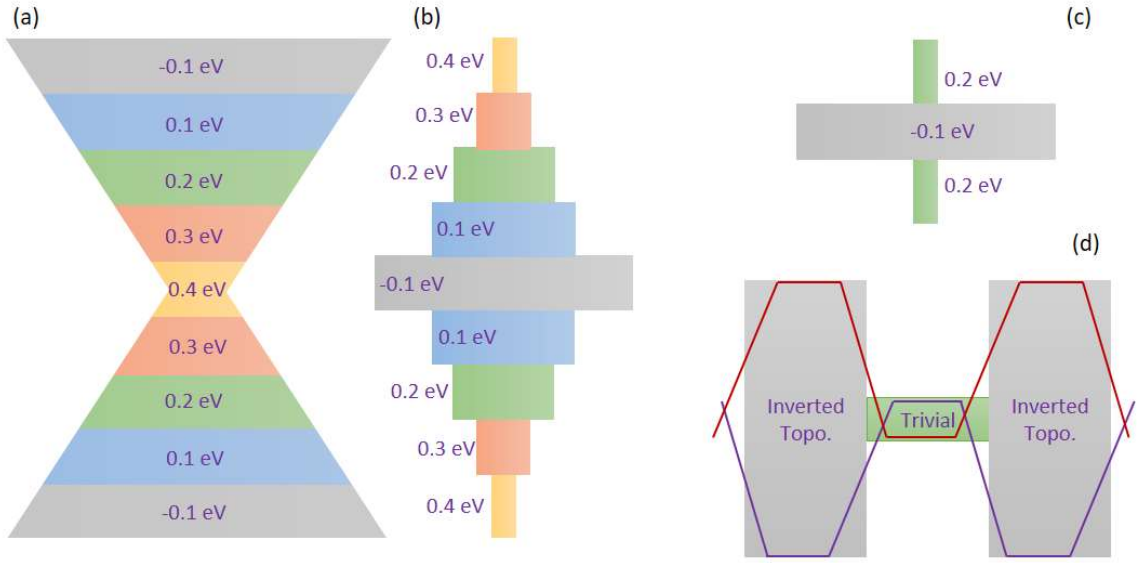

Fig. 5.16: A few models presenting the top view of patterns for the in-plane electronic band engineering utilizing the phenomenon of selective dynamic stoichiometry (SDS). Any change in pattern dimensions will alter Ge/Sb or Ge/Bi flux ratio where each different width will accumulate different amount of Ge resulting in localized changes in the electronic band structure. Pattern with smallest dimensions will accommodate highest Ge contents and will exhibit relatively largest non-invested gap depending upon the targeted stoichiometry. The in-plane band engineering can be designed in two different ways such as (a) where largest band is in the center and (b) while smallest gap in surrounded by relatively larger localized gaps. These changes in the electronic band structure can be gradual or abrupt just as depicted in (c) for in-plane quantum well design. Similar design can be utilized as the in-plane topological-trivial switches by designing the topologically trivial and non-trivial heterostructures as depicted in (d).

5.5 GeTe: Epitaxy and structural characterization

GeTe, as mentioned in the beginning of this chapter, exhibits topologically trivial features with non-inverted structure; however, the unique interatomic bonding[32, 115, 116, 117, 118] and strong SOC makes it gem of a material with characteristics ranging from bulk PCM[11, 15, 17, 18, 20, 71, 119] to Rashba semiconductor[120, 121, 122]. It also exhibits thermoelectricity[6, 20, 26, 123], ferroelectric features[15, 32, 124] along with the conventional superconductivity below 300 mK[125]. It is theoretically predicted[120] and experimentally demonstrated to be a non-centrosymmetric superconductor[120, 126] which makes it a prominent candidate for quantum computation. In the last 2 decades, GeTe is comprehensively studied due to its emerging phase change

features. The interest has boosted further with the discovery of topology in several Ge based chalcogenides[20, 127, 128, 129, 130, 131] and the presence of giant Rashba spin splitting[120, 124] in GeTe. With rising interest in the material system, the demand for high quality crystalline growth has also increased specifically for superconducting quantum and low power PCM applications (Section 5.2). The quest for pristine GeTe nanostructures is spiking[29, 53, 76] and acting as a bottleneck for the advanced material characterizations and in rapid application development.

GeTe crystal is reported to be prepared with various methods including the Bridgeman method[12, 21], PLD[71], ALD[132], CVD, sputter deposition[13, 70, 133] and MBE[15, 134]. Among them, MBE is the least studied technique with only a couple of reports in literature about the epitaxial growth on the non-reconstructed Si (111) surfaces. Various advantages including the precise thickness control of the epilayer, the least defect density and the probability of high quality nanostructures preparation via SAE designate MBE one of the unique tool to grow epilayers of such a sensitive material to ambient conditions (for details visit Chapter 6). To out knowledge, any information about the atomic scale-structural characterization of GeTe epilayer at Si (111) substrates including the interface, and the analysis of extended defects including twin domains, formation of TSFs and the behavior at substrate induced defects i.e. antiphase domains and screw dislocations, in a layer-free system of GeTe, are not available in the literature.

5.5.1 GeTe epitaxy on Si (111)

The epitaxy of GeTe binary system does not offer major growth challenges including the stoichiometric tuning and flux ratio adjustment, encountered during the epitaxial growth of GST and GBT alloys. Among all studied materials till now including 3D TIs (chapter 2) and Bi_xTe_y family (chapter 4), GeTe is the only material system that exists without the vdW based layer stacks. Such a structure brings the epitaxial growth of GeTe quite close to the classical epitaxy which would not be possible on Si (111) surface due to enormous lattice mismatch of approx. 8.5%. However, the capability of Te atoms to readily transform and support the vdW based layer architecture provides an avenue for the successful growth of GeTe.

The growth attempts of GeTe are started by keeping T_{sub} and T_{Te} constant at 300℃ and 320℃ respectively while T_{Ge} is gradually increased from 1220℃. With the increasing Ge flux, no growth of the epilayer is observed until T_{Ge} reached 1270℃. At this temperature, triangular shaped crystallites of GeTe (confirmed via XRD) are obtained; however, the density of these crystallites was too low. T_{Ge} is kept increasing until 1300℃ where each step of increased Ge flux resulted in an enhanced density of crystallites forming a semi-closed layer as depicted in Figure 5.17 while the achievement of a smooth epilayer remained unsuccessful.

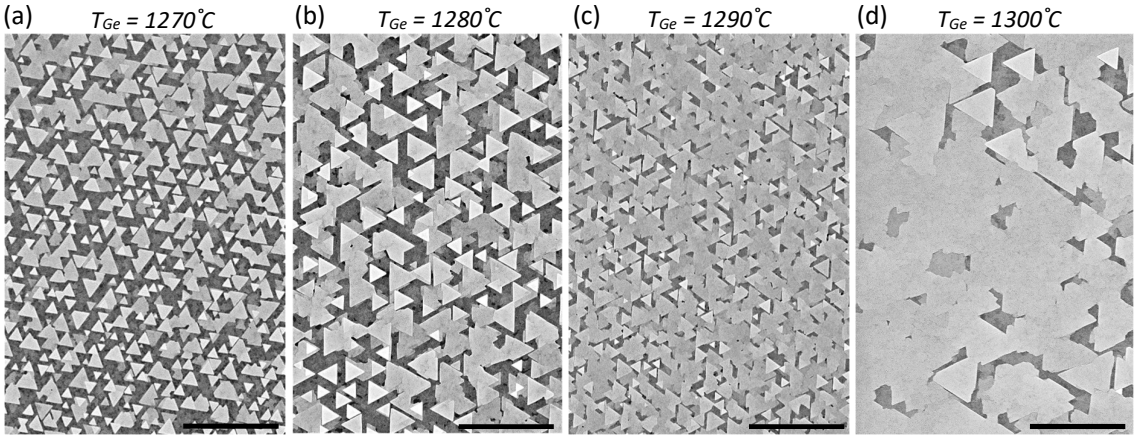

*Fig. 5.17: SEM images representing attempts to obtain epitaxial growth of GeTe on Si (111) non-reconstructed substrates. (a) Small sized triangular shaped crystallites of GeTe are observed at T_{Ge} = 1270℃. (b) Size of GeTe crystallites enhanced with increased Ge flux at T_{Ge} = 1280℃ although which further increment in Ge flux, overall coverage of GeTe increased with (c) T_{Ge} = 1290℃ without any change in size of crystallites. (d) Fully closed epilayer with high surface roughness of GeTe is obtained at T_{Ge} = 1300℃. (*scale bar = 1 µm)*

The continuously failing attempts to grow an entirely closed and smooth thin films of GeTe have raised a few questions. What can be the reason of such inhomogeneity? Why is it difficult to grow a thin film of GeTe on the non-reconstructed Si (111) surface in comparison to GSTs and GBTs via MBE? Why is the high quality thin film growth on non-reconstructed Si (111) surface reported only twice after two decades of research? Why do the reported growths of GeTe on 7 x 7 reconstructed Si (111) surfaces lack surface smoothness and occasionally exhibit the Peierls distortions[19, 134, 135]? Is it related to the non-vdW epitaxy where strain related issues arising from the substrate lattice mismatch result in defects and hinder a smooth growth or it is purely the matter of the incorrect growth parameters that require adjustments?

GeTe epitaxy on pseudo-substrates: In order to obtain smooth and high quality thin films of GeTe, it was necessary to answer the above mentioned questions. In order to do so, a few small set of experiments are conducted including the growth of GeTe on pseudo-substrate by introducing a thin layer of Bi_2Te_3 between Si (111) and GeTe interfaces. It is started with 3 nm thick epilayer of Bi_2Te_3 on which the growth of GeTe is conducted with unchanged previous parameters including T_{sub}, T_{Te} and T_{Ge} at 300 ℃, 320 ℃ and 1300 ℃ respectively. Surprisingly, entirely closed epilayer of GeTe with surface roughness of 1.8 ± 0.1 nm (rms value) is obtained. In the next steps, thickness of Bi_2Te_3 support layer is gradually decreased and the successful achievement of GeTe epilayer in each step is witnessed until the thickness of pseudo-substrate reached 0.3 nm (1/3 QL). Unexpectedly, even with such a low thickness of the support layer, GeTe epilayer remained entirely closed as depicted in Figure 5.18a. Moreover, no major changes in the surface roughness with reducing Bi_2Te_3 thickness is observed. Finally, the growth of GeTe is conducted again on Si (111) surface without Bi_2Te_3 support layer and once again, similar results with epilayer having high surface roughness (observed earlier in Figure 5.17d), are obtained.

With these successes and failures of achieving closed films of GeTe without the presence of a support layer, the focus is turned towards the epitaxy of GST and GBT alloys. During the growth optimization of GSTs, for the first time ADR dependency of Ge on T_{sub} is observed (Figure 5.2) which pointed out the discrepancy of parameter adjustment during GeTe growth, not to conduct the epitaxy with varying T_{sub}. If the high desorption rate of Ge is the real issue then it is obvious that optimum T_{sub} is required to be evaluated in order to achieve thin film epitaxy of GeTe. It also explains successful epitaxy of GeTe with Bi_2Te_3 support layer as Bi provides adhesive strength to Ge similar to the case of Sb, observed during the growth of BST alloys (Figure 2.7).

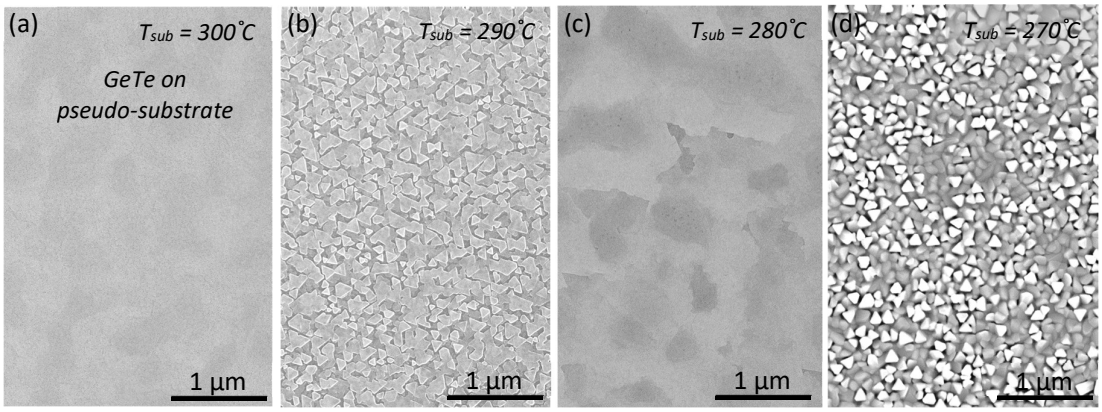

Fig. 5.18: SEM images representing epitaxial growth of GeTe for the search of optimum T_{sub} while T_{Ge} is kept constant at 1300˚C. (a) An entirely close epilayer of GeTe grown on top of 0.3 nm thick Bi_2Te_3 support layer at T_{sub} = 300˚C. Images representing changing coverage and textures of GeTe films grown on Si (111) without any support layer with decreasing T_{sub} at (b) 290˚C, (c) 280˚C and (d) 270˚C where best results are obtained at T_{sub} in vicinity of 280˚C.

In search of optimum T_{sub}, parameters T_{Ge} and T_{Te} are fixed at 1300 ℃ and 320 ℃ respectively while T_{sub} is decreased in gradual steps from 300 ℃ to 260 ℃. A soon as T_{sub} reached 290 ℃, the epilayer is observed to

exhibit slightly improved surface quality however, the surface roughness was still too high and not acceptable for the utilization into devices. With continuously decreasing T_{sub}, the optimum range with improved surface quality is observed between 280˚C - 285˚C while dropping below this range, epilayers once again resulted in heavily degraded surface quality. The effects of decreasing T_{sub} and the corresponding textures of epilayer can be visualized with the help of SEM images in Figure 5.18 (b-d). The identified range of T_{sub} still exhibited one major problem i.e. the relatively high value of R_{TF} (> 5 nm/h) that would lead to high defect density and therefore, the optimum flux (T_{Ge}) must also be adjusted to bring R_{TF} in the defect free zone (≤ 5 nm/h). The trend in R_{TF} and surface quality vs. T_{sub} is depicted in Figure 5.19a.

In order to optimize R_{TF}, parameters T_{sub} and T_{Te} are fixed at optimum values of 285˚C and 320˚C respectively while T_{Ge} is decreased is gradual steps from 1300˚C to 1260˚C. With decreasing T_{Ge}, the resulting changes in R_{TF} led to the improved crystal quality and enhanced surface smoothness of epilayers. The best growth is obtained at T_{Ge} = 1280˚C. Below this temperature, the ADR of Ge became too low and resulted in the defective (non-closed) films with the increased surface roughness that eventually started to evaporate as depicted in Figure 5.20. The trend in R_{TF} and surface quality vs. T_{Ge} is depicted in Figure 5.19b.

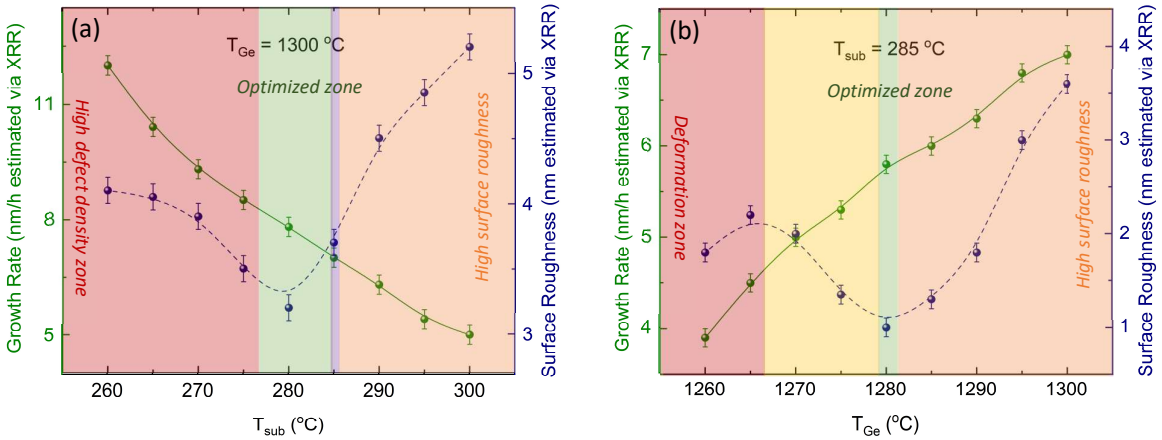

Fig. 5.19: The search for optimum T_{sub} and R_{TF} for GeTe epitaxy on Si (111) via MBE. (a) The trend of increasing R_{TF} and changing surface roughness with decreasing T_{sub} while all other parameters are fixed including T_{Ge} = 1300˚C. Entirely closed and smooth films are obtained with temperature range between 278˚C and 285˚C (identified with the green zone), (b) the trend of decreasing R_{TF} and changing surface roughness with decreasing T_{Ge} while T_{sub} is kept constant at 285˚C. Epilayer with the best surface quality is observed at T_{Ge} = 1280˚C (identified with the green zone).

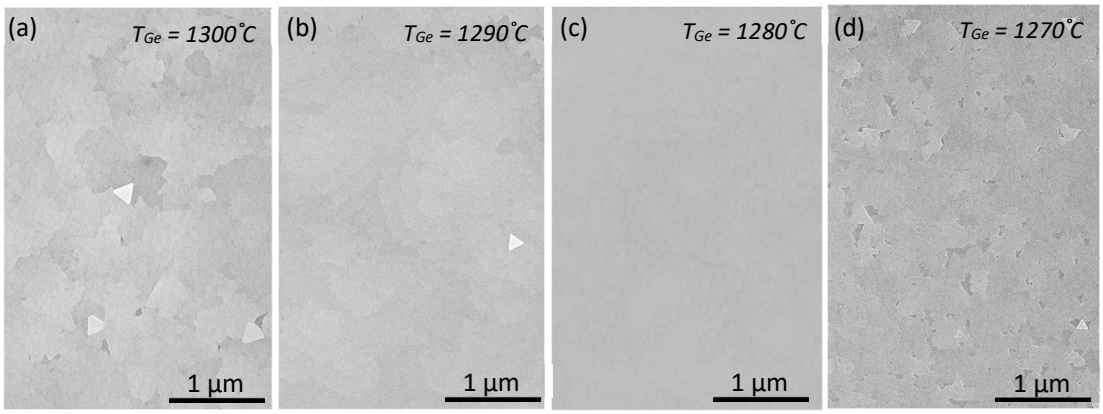

Fig. 5.20: SEM images representing epitaxial growth of GeTe for the search of optimum surface roughness and R_{TF} while T_{sub} is kept constant at 285˚C. The changing roughness of epilayer with changing ADR of Ge via applied Ge flux is evident where (a) represent epilayer prepared with T_{Ge} = 1300˚C, (b) with T_{Ge} = 1290˚C, (c) with T_{Ge} = 1280˚C and (d) with T_{Ge} = 1270˚C. Results with best surface quality are obtained at T_{Ge} = 1280˚C with R_{TF} = 5.6 nm/h.

After the evaluation of optimum parameters including T_{sub} and T_{Ge} at 285 ℃ and 1280 ℃ respectively with R_{TF} = 5.6 nm/h, high quality ultra-smooth films of GeTe are prepared. GeTe exhibits a trigonal crystal structure with R3m (160) space group[136] and a unit cell with 6 covalently bonded atomic layers comprising 3 blocks of GeTe with $c_{predicted}$ = 10.67 Å[13, 21, 31, 104, 132]. XRD characterizations have been performed on GeTe thin films similar to GST and GBT alloys. Figure 5.21 displays XRD 2θ-ω scan and RSM of GeTe confirming lattice parameters while XRD φ-scan revealed the domain free and high quality growth of GeTe.

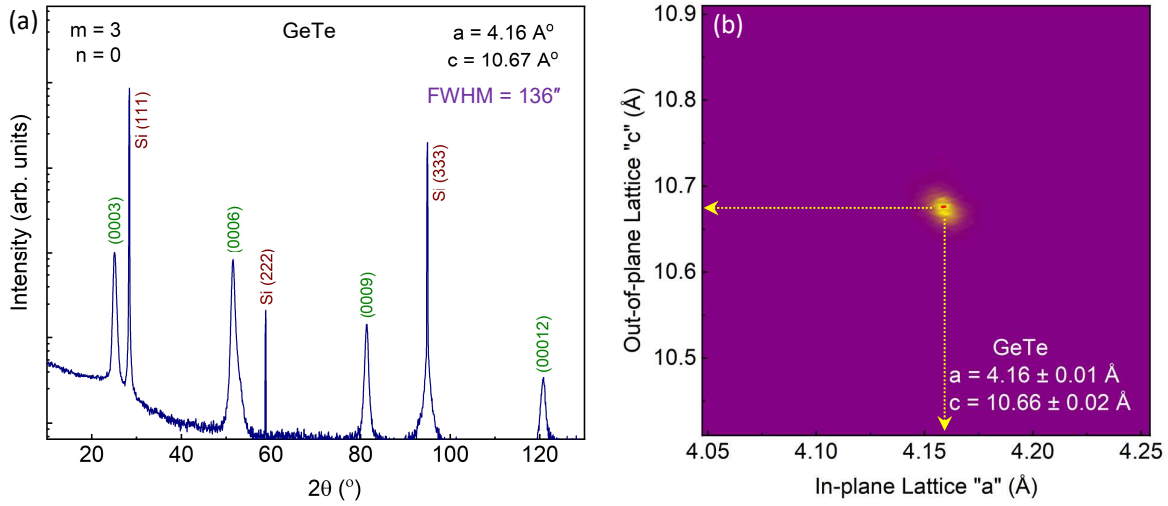

Fig. 5.21: Structural characterization of 42 nm thick epilayer of GeTe. (a) Diffraction peaks of GeTe with (m:n)=(3:0) exhibiting c = 10.67 Å. Δω scan revealed FWHM values of 136″ obtained at 2ϑ=52.61̊, the (000 6) peak indicating high structural quality of the epilayer. (b) Reciprocal space map (RSM) of GeTe epilayer acquired via XRD indicating lattice constants "a" and "c" in good agreement with literature.

GeTe vs. vdW systems: After successful growth of GeTe planar films, it has been realized that among all initially raised questions associated with recurrent failures of GeTe epitaxy, the selection of inappropriate parameters was the main cause of failure. However, if the wrong choice of parameters was the only reason of failure, how to justify the enhanced complexity in achieving GeTe epitaxy in comparison to other materials including GSTs, GBTs and 3D TIs? This complexity, as observed, can be linked to a very narrow window of parameters that allows the formation of entirely coalesced and smooth epilayers. Figure 5.19a indicates a very small range of T_{sub} with approx. 8 ℃ window that allowed fully-coalesced growth of GeTe (indicated by the green zone). This range is narrowed down further with the optimization of applied flux (T_{Ge}) to adjust R_{TF} in order to achieve defect free epilayers of GeTe. The parameters range, particularly to obtain entirely closed film in vdW based materials i.e. 3D TIs sometime exceeds even 50 ℃ in comparison to less than 8 ℃ for GeTe. This phenomenon signifies the growth complexity and also indicates how critical it is to tune the right parameters, in order to obtain the defect-free and smooth epilayers of GeTe.

5.5.2 Selective area epitaxy (SAE) of GeTe

After XRD characterization, focus is turned towards SAE. The optimized parameters of GeTe are subjected to pre-patterned substrates in order to obtain selectively grown nanostructures. All materials with high ADR dependency on T_{sub} always exhibit very low adhesive strength to amorphous surfaces, thus assist in achieving the selectivity. Ge, being a member of this group, also exhibited similar behavior and without the requirement of any modifications in T_{sub} or R_{TF}, selectively grown nanostructures are realized and depicted in Figure 5.22. The results obtained from SAE presented a couple of interesting observations mentioned below.

- Due to quite high L_D of Ge = 39 nm, R_{eff} in 50 nm wide trenches reached as high as 4 x R_{TF} (Figure 5.22b) that enhanced further to approx. 5 x R_{TF} in diamond array pattern (Figure 5.22c) and resulted in excessively overgrown nanostructures. Such a high R_{eff} will always result in nanostructures with high defect density.
- An important observation is the texture of overgrown GeTe epilayer, in comparison to all vdW based layered materials, is the avoidance of epilayer to grow laterally even after trenches were entirely filled. Unlike GSTs and GBTs, the overgrown GeTe films are observed to keep the pattern dimensions intact by growing only vertically without any considerable lateral expanse as depicted in Figure 5.22b and c.

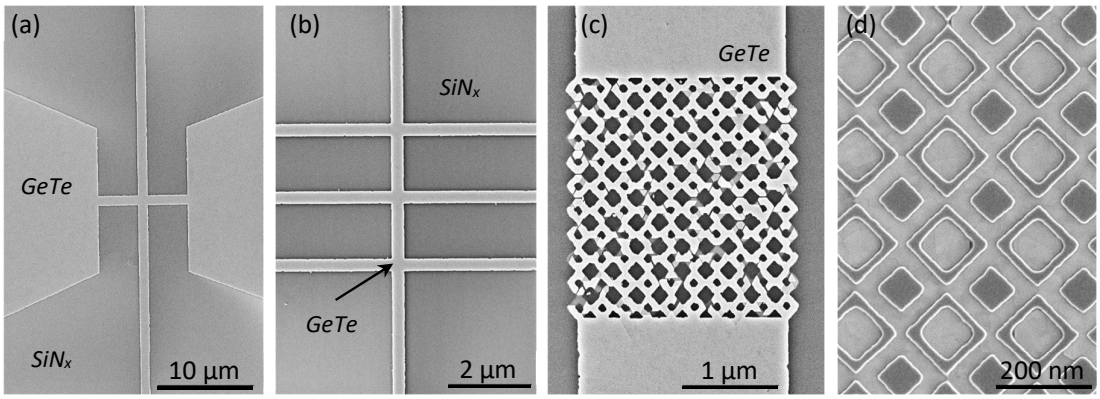

Fig. 5.22: SEM images representing SAE of GeTe on pre-patterned substrates with T_{sub} = 285˚C and T_{Ge} = 1280˚C. (a) Represents SAE on 1 µm wide Hallbar, (b) represents SAE in 500 nm wide Hallbar with slightly increased thickness of epilayer, (c) represents drastic increase in thickness of epilayer in 50 nm wide diamond array structures, while (d) also represents SAE in 50 nm wide diamond array structure similar to (c) although with increased T_{sub} = 300˚C resulting in reduced R_{eff}.

In order to reduce R_{eff} and to obtain defect-free nanostructures, two different approaches are exercised. In the first approach R_{TF} is lowered by decreasing T_{Ge} while in the second approach T_{Ge} is kept constant and T_{sub} is ramped up to 300˚C. Both approaches have been proven fatal for thin film epitaxy due to very low ADR as depicted in Figure 5.18 and 5.20. During SAE, the relatively high L_D of Ge compensated low ADR and did not allow epilayers to get defective. In general, results obtained with both approaches solved the problem of R_{eff} >> 5 nm/h during SAE; however, the second approach with constant T_{Ge} and increased T_{sub} proved to be more useful and easy to control. An example of SAE using the second approach is depicted in Figure 5.22d where epilayer is grown with similar parameters as other samples depicted in Figure 5.20(a-c), only T_{sub} is ramped up from 285˚C to 300˚C. It is evident that the second approach led to the drastic reduction in R_{eff} due to lowered $ADR_{(Ge)}$ and hence without probabilistic high defect density, selectively grown nanostructures are obtained.

5.5.3 STEM investigation of GeTe nanostructures

The detailed structural investigations of selectively grown GeTe nanostructures and interface studies with Si (111) are performed via STEM at the cross-section of three different GeTe samples mentioned below. Each lamella is extracted from 500 nm wide Hallbar.

- Sample 1: GeTe epilayer grown on 0.3 nm thick Bi_2Te_3 support layer.
  Limitation: Lamella is along Si [211] orientation.
- Sample 2: Pristine GeTe, selectively grown at T_{Ge} = 1260˚C at T_{sub} = 285˚C using the first approach to reduce R_{eff} by decreasing T_{Ge}. *Limitation: Lamella is along Si [211] orientation.*
- Sample 3: Pristine GeTe, selectively grown at T_{Ge} = 1280˚C at T_{sub} = 300˚C using the second approach to control R_{eff} by increasing T_{sub}.

Based on STEM measurements, key observations are stated below:

Sample 1: Figure 5.23a depicts Si – Bi_2Te_3 – GeTe interface. A monolayer of Te atoms, utilized to saturate Si dangling bonds, is visible. The presence of exotic trilayer architecture, observed during STEM investigations of GBT alloys, is witnessed once again at the interface. Such an exotic trilayer is always observed in epilayers containing Ge-Bi-Te elemental combinations. No such structures are observed in pure GeTe, GSTs or in Bi_xTe_y systems. The reason of the formation and exact stoichiometry of this structure are still unknown. The trilayer stacked with the vdW gap supported by Te monolayer at the interface. On top of trilayer, the growth of GeTe started with GBT infinite layer architecture. It means that Bi-Te dual layer started the formation of GBT layer (purple arrows in the Figure 5.23a) assisted by vdW epitaxy; however, with only incoming flux of Ge and Te, GeTe epilayer kept on growing without any vdW gaps and ending Bi-Te dual layer. Other than the appearance of exotic trilayer and GBT assisted start of GeTe epitaxy, no defects are observed; however, the lamella being along Si [211] orientation limited the observations of defects such as twins and TSFs.

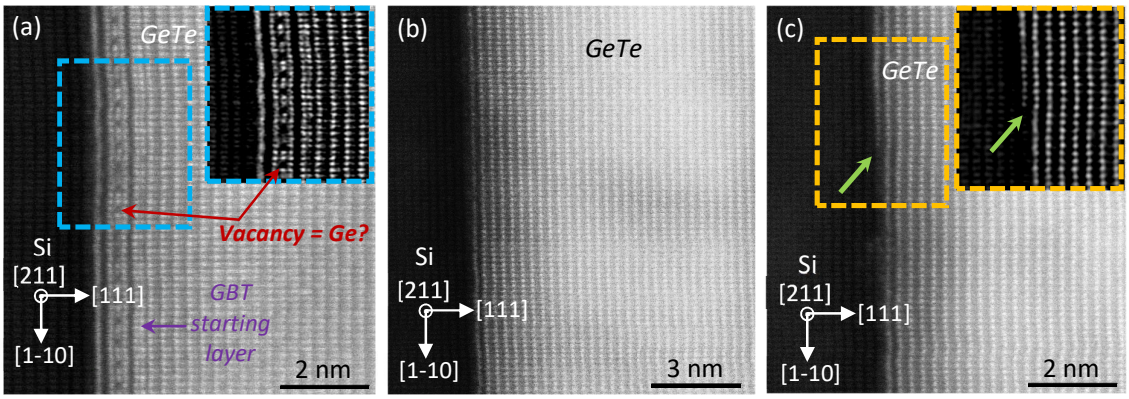

Fig. 5.23: STEM images of GeTe acquired along Si [211] projection. (a) HAADF image of sample 1 where GeTe is grown on top of 0.3 nm Bi_2Te_3 support layer. The presence of exotic trilayer structure at the interface is evident. On top of trilayer, GeTe epitaxy started with the GBT layer stack and continued in form of the layer-free architecture of GeTe due to unavailability of Bi atoms. The low-pass filtered image of marked area in (a) indicates the periodic appearance of low contrast structure in the exotic trilayer (inset). (b) HAADF image of sample 2 where GeTe epilayer is grown on Si (111) without any support layer. A completely relaxed and strain free growth of GeTe without any defects is witnessed. (c) GeTe epilayer (sample 2) passing through a Si step edge (green arrow). The discontinuity of step defect and growth of homogenous layer is evident without any presence of antiphase type domain or a screw dislocation.

Sample 2: Figure 5.23b depicts Si - GeTe interface where once again monoatomic layer of Te atoms, utilized to saturate Si dangling bonds, is visible. The layer-free architecture of GeTe with the periodic and regular arrangement of covalently bonded Ge and Te atoms without the presence of any vdW based layers is evident. Though, it is worth noticing that starting Te layer in GeTe block does not exhibit one to one relation with the saturated Te monolayer in a covalent type bond rather exhibits vdW type epitaxy with an incoherent interface at Si (111) surface similar to the vdW based layer structured materials i.e. 3D TIs, GSTs etc. Hence, a completely relaxed covalently bonded epilayer of GeTe acts as one solid block floating with weak vdW interaction on Te passivation layer, is observed. This attribute can be associated to the phenomenon of the resonant bonding[76, 86, 107, 119] that allows GeTe, even after having 8.5 % lattice mismatch, to grow uniformly and strain free not only on Si (111) surfaces but also on various other substrates. One of the key defects in 3D TIs i.e. the antiphase domain that forms at each periodic step edge of the substrate, is not observed in GeTe epilayer. At Si step edge, a single GeTe block (1/3 unit cell) with 3.6 Å in height matches in good approximation with the height of Si step edge as witnessed in Figure 5.23c. It discontinued the step induced effect (Figure 5.23c, green arrow) with a homogenous and continuous growth of GeTe epilayer and neutralized the formation of an antiphase domain or a screw dislocation.

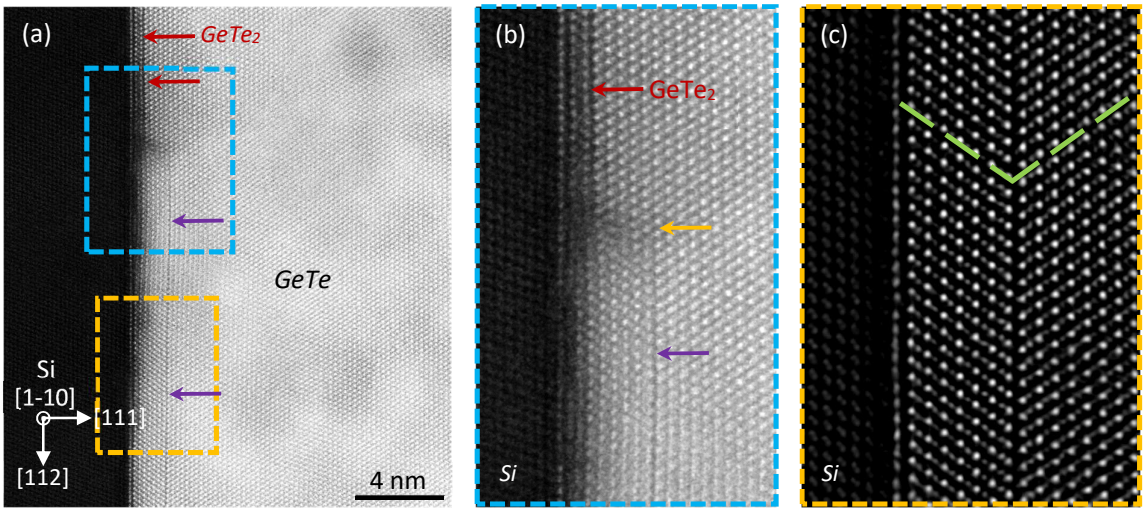

Fig. 5.24: STEM images of GeTe acquired along Si [1-10] projection. a) HAADF image of sample 3 where GeTe epilayer is grown without any support layer with relatively higher R_{eff}. The layer free architecture of GeTe block floating on Te passivated Si surface is evident. The presence of $GeTe_2$ TL structure at the interface is observed at a few places (red arrow). The presence and coalescence of rotation twin domains is observed (marked with blue box) where domain collinear with Si (311) engulfed the domain collinear with Si (220) giving rise to a TSF marked with purple arrows. (b) A magnified area marked in (a) depicts the phenomenon of twin domains coalescence that gave rise to a domain wall (indicated with yellow arrow) and a TSF. (c) Magnified and low pass filtered area marked in (a) depicting Ge vacancy layer assisted formation of a vdW gap to support a TSF.

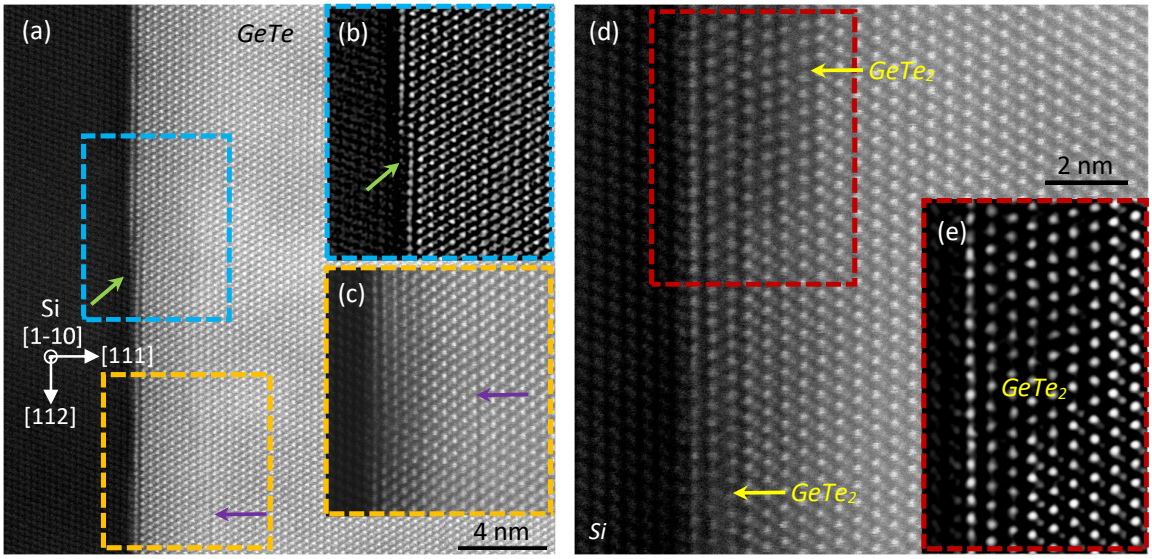

Fig. 5.25: STEM images of GeTe acquired along Si [1-10] projection. (a) HAADF image of sample 3 where GeTe epilayer passing through a Si step edge (indicated by green arrow) without the step induced defect continuity. The rare presence of Ge vacancy layer assisted formation of vdW gap without the presence of any defect is also witnessed (marked with yellow box). (b) Magnified and low pass filtered area marked in (a) depicts homogeneous growth of GeTe epilayer through a Si step edge where no antiphase type domain is observed. (c) Magnified area marked in (a) depicts the presence of a vdW gap without any neighboring defect. The vdW gap formation started after passing through a step edge due to slight height mismatch between GeTe block and Si substrate step. (d) The presence of multiple $GeTe_2$ TL structure at the interface is observed (marked with red box). The lattice sites of Ge atoms in trilayers seem cloudy where the position of Ge atoms could not be resolved as depicted also in (e) with a magnified and low pass filtered image however can be identified quite accurately in GeTe epilayer.

Sample 3: Figure 5.24a depicts Si - GeTe interface of sample 3, prepared at T_{sub} = 300℃ with R_{eff} = 8.8 nm/h. The floating GeTe epilayer on Te monolayer is evident. Due to relatively higher R_{eff} suppressed twin

domains are present where the dominant domain collinear with Si (311) engulfed the minor one. It resulted in the formation of a domain wall (magnified in Figure 5.24b) and a TSF (Figure 5.24c). It is quite interesting to visualize how the Ge vacancy layer assisted the formation of a TSF at coalescence of twin domains through vdW gap (indicated by purple arrows in Figure 5.24a and b).

Figure 5.25a depicts the behavior of GeTe epilayer at Si step edge similar to Figure 5.23c. Here with Si [1-10] projection, the formation of GeTe additional block at the step edge between upper and lower terraces and neutralizing the step defect continuity is witnessed (Figure 5.25b, green arrow). It also describes the ability of GeTe to grow across 2D defects without influencing the epilayer and ensuring high crystal quality. Figure 5.25c depicts occasionally appearing layer defect in GeTe where Ge vacancy layer forces neighboring Te atoms to form a vdW gap and continues the crystal formation (this is not a TSF as crystal formation continues along the same orientation after Ge vacancy layer). The reason for these layer defect formation is not entirely known. To our understanding, Ge vacancy layer assists GeTe to release out-of-plane strain caused by minor lattice mismatch after encountering defects such as a step edges. As discussed above that Si step edge height meets nicely with a block of GeTe; although, differs by 3.84 Å - 3.6 Å = 0.24 Å. This difference in the lattice pushes GeTe crystal to the interface after encountering a step edge and creates minor lattice strain. Such a strain can easily be released by a Ge vacancy layer that forces neighboring Te atoms to form a vdW gap and brings Te atoms closer. Hence, it helps the crystal to release strain and allows homogenous growth of the epilayer as indicated by purple arrow in 5.25c. After passing through such a vdW gap, the changes in Ge lattice positions relative to Te is also witnessed. This feature provides the ferroelectric behavior to GeTe crystal; however, is out of scope of this work and therefore not discussed here. While Figure 5.24a depicts the occasional formation of $GeTe_2$ layer at the interface, the formation of multi-layer stack of $GeTe_2$ at the interface makes it quite interesting (Figure 5.25d). The reason of $GeTe_2$ trilayer formation can be linked to Ge vacancies during the oxidation of GeTe in thin films, discussed in chapter 6 (Figure 6.4). One interesting observation is the delocalization of Ge atoms in trilayers. In GeTe crystal, Ge atoms are clearly visible while in $GeTe_2$ trilayers, the Ge positions seem like a cloud where the clear visibility of Ge atoms is not achieved.

In general, SAE of GeTe to fabricate pristine nanostructures along with the atomic resolution structural characterization to understand the formation of extended defects and interfaces has made the realization of low-power PCM and superconducting quantum applications more feasible.

5.6 Summary

The epitaxial growths of several key members of GST and GBT alloys along with GeTe, in form of high crystal quality thin films are achieved on planar Si (111) substrates. Using the technique of selective area epitaxy (SAE), stoichiometric nanostructures of these compositional alloys are prepared for the first time where the detailed structural characterizations are performed via XRD and STEM. The technique of SAE has facilitated the preparation of pristine nanostructures on one hand; while presented several challenges in form of unintentional stoichiometric shifts giving rise to the phenomena of selective stoichiometric shift (SSS) and selective dynamic stoichiometry (SDS). With the help of SAE growth model, the issues of SSS are resolved; however, the challenges of SDS can only be resolved partially. The phenomenon of SDS that results in the localized compositional variation based on changes in the geometrical pattern, can be utilized with the precise design modeling to engineer the in-plane electronic band structures and thus to fabricate novel devices such as quantum wells and topological switches. STEM based structural investigations facilitated the observation of inter-layer transition mechanisms including the Ge vacancy layer based vdW switching. Some novel layer structures at the interface are also observed; however, the deep understanding of those exotic structures and the layer architecture transformation mechanisms require further studies with the localized composition analysis via atomic resolution EDX and the image simulation techniques.

Chapter – 6
Surface Oxidation and Substrate Induced Effects

In the process of realizing any functional quantum device based on a topological material, the first step is to optimize the crystal quality of epilayers. Considering Si (111) as the standard substrate, the crystal growth optimization of 3D topological materials is conducted via MBE and discussed in chapter 2, 4 and 5 including the conventional 3D TIs i.e. Bi_2Te_3, Sb_2Te_3 and $Bi_xSb_{2-x}Te_3$, the exotic 3D topological materials i.e. Bi_xTe_y series and Ge based materials including GSTs, GBTs and GeTe respectively. Structural defects in those crystals such as domains and dislocations are systematically investigated, their sources are identified and neutralized with the optimization of growth parameters. Finally, high structural quality crystalline epilayers of all the above mentioned materials are prepared.

The next step is the optimization of surface quality. Topology is a surface related attribute and its successful utilization depends entirely on the reliability of surface quality, particularly in conventional 3D TIs that exhibit topological surface states (TSS) on all facets. This feature not only assigns critical importance to surfaces, it also indicates the inevitability to investigate surface reliability with possible degradation and ageing effects. Moreover, the development of an adoptable technique for the protection against the probable degradation is also of critical importance. A parallelepiped epilayer contains 6 surfaces in total; all of them become more prominent at nanoscale with the increased surface to volume ratio. Using the technique of selective area epitaxy (SAE), the 4 out of 6 surfaces are always protected by the side walls of the blocking material (SiN_x) while the remaining two i.e. the (0001) surfaces impact every aspect (i.e. structural and electronic characteristics) of the epilayer and, therefore, hold a key importance.

- The bottom (0001) surface is always in contact with the substrate and plays a significant role in the VdW epitaxy. It determines the probable band bending[1, 2] along with the electronic transfer at the interface with the substrate[3] and the propagation of substrate induced defects[4] in the epilayer such as antiphase domains and screw dislocations (for details refer to Figure 2.14).
- The top (0001) surface exhibits an interface with air (the ambient conditions) and is subject to surface degradation and ageing effects. Also, it is the top surface that determines the interface quality with the metallic electrodes required in almost all applications (for details visit Chapter 7).

This chapter is dedicated to investigate the effects arising from both TI (0001) surfaces.

- In the first part, the probable degradation of the top surfaces via oxidation along with the degradation mechanism in various material systems is investigated. The resulting changes such as structural reconfiguration near the surface along with the ageing effects are studied. Later, a solution for the protective measurement is devised and a comparative analysis between the protected and non-protected epilayers is performed.
- In the second part, the effects of the substrate material and its crystal structure on the bottom TI interface and the resulting changes in the electronic and structural characteristics of the TI epilayer are explored. Finally, a comparative analysis of TI epilayer being prepared at different substrates, is performed.

6.1 Surface inertness vs. rapid degradation

The topological community is largely divided on the issues of surface stability and degradation of 3D TIs under the exposure to ambient conditions. The existence of contradictory and in some cases, rather controversial reports have described the two extremely opposite behavior of 3D TIs that makes it quite challenging to summarize the general behavior of surface stability. These contradicting cases are:

- ***Stable surfaces in ambient conditions:*** The flat surface of 3D TIs i.e. top Te layer exhibits inertness towards oxidation, not only in ambient conditions but also in the controlled environment with relatively high humidity and oxygen rich conditions[5, 6, 7]. In general, 3D TIs exhibit no ageing effect.
- ***Degradation in UHV:*** 3D TI crystalline flakes that are exfoliated under vacuum conditions started to exhibit minor degradation after 1 hour of exfoliation while kept under UHV conditions without any exposure to the ambient conditions[8, 9, 10, 11].

The experimental observations in this study refute both of the above mentioned cases. In 3D TI epilayers, relatively stable and reliable surfaces without any noticeable degradation are realized that are grown and kept under UHV conditions for months while STM investigations are performed[12]. Similarly, as reported in earlier studies, no evident transformation is witnessed in ARPES measurements that are conducted on a freshly grown epilayer in comparison to samples that were kept under UHV conditions for longer durations[13, 14, 15]. However, as soon as the epilayer is exposed to ambient conditions, the resulting effects of the surface degradation are immediately observed via ARPES[16]. Such a fast degradation can be associated to the probable surface oxidation.

The observations of surface degradation, irrespective of the technique using which the TI epilayers are prepared, has been reported for Bi_2Te_3[19, 20, 21, 22, 23], Bi_2Se_3[17, 18, 19, 20], Sb_2Te_3[21, 22, 23], BST alloys[24], GST and GBT alloys[25, 26, 27] and GeTe[25, 28, 29, 30]. The oxidation process is reported not only to degrade the surface quality of epilayers, but to impact the structural and electronic characteristics of the bulk crystal as well. The impact of surface oxidation can be realized from the following few points.

- ***Surface degradation:*** The ARPES measurement, one of the most surface sensitive technique performed on 3D TI epilayers, lost the intensity and resolution as soon as the epilayer is exposed to ambient conditions for a few minutes (decreased signal to noise ratio) and could not be resolved at all when the exposure durations elongated until the surface is physically treated with Ar^+ plasma to remove the contaminated (oxidized) area[16].
- ***Non-functional interfaces:*** The Fermi velocity (v_F) is a critical parameter that impacts the induced superconducting coherence length and the interface transparency in a TI-SC hybrid junction. The Fermi velocity at the surface of Bi_2Te_3 epilayer has been observed to drop by an order of 2 from 4×10^5 m/s[31, 32, 33] (measured in an epilayer that was kept under UHV condition) to 3260 m/s[34] after the surface was exposed to the ambient conditions. Such a large degradation in v_F would not facilitate a high quality interface.
- ***Fermi shift and enhanced trivial carriers:*** After the exposure to ambient conditions, an unexpected shift in the Fermi level of the material along with the increment in the carrier concentration is observed in all 3D TIs including Sb_2Te_3, Bi_2Te_3 and Bi_2Se_3[17, 35, 36]. This phenomenon also decreases the overall contribution of TSS in magneto-transport investigations[17, 35].

The above mentioned points affirm that surface degradation via oxidation is a real problem that severely influences the crystal bulk characteristics and reduces the contribution of topological features. Earlier, the oxidation of various TI surfaces is reported where the investigation of oxidation states is conducted via X-ray photoemission spectroscopy (XPS)[25, 27, 37, 38]. The one critical information those reports lack is the structural investigation of surfaces after oxidation. The information about structural classification of the oxidized region, the oxidation rate and the probable structural changes in the non-oxidized crystal are primarily unknown. In the next section, STEM assisted structural characterizations of various oxidized layers are conducted and the electronic states of elements in the oxidized layer are investigated via XPS.

6.2 Surface oxidation of topological epilayers

The electronegativity difference between two elements indicates their reactivity[39]. When an atom of a certain element with higher electronegativity comes in contact with a compound containing elements with

relatively low electronegativity difference, the intruding atom chemically reacts with the compound resulting in the structural and chemical changes[39]. Oxygen exhibits the electronegativity of 3.5[39], the second highest in the periodic table and therefore, as soon as it gets in contact with any materials, there is always a very high probability for the oxidation process to occur. Based on the electronegativity difference with oxygen, all the elements involved in this study can be classified from the highest to the lowest reactivity as[39]: Ge > Bi > Sb > Te. This grading will help to understand the oxidation strength and the surface degradation rate in different compounds.

The oxidized layers of various topological materials are investigated via STEM where epilayers are exposed to the ambient conditions for various durations. The exposure time is varied from the shortest period of 1 hour ranging to the longest exposure of 4320 hours (6 months). In order to protect the epilayer surface from any unintended contamination i.e. dirt and other particles, the grown epilayers are kept in a clean plastic box with the lid closed and stored for the planned period of time in ambient environment. Based on the structural analysis of the oxidized layers, performed via STEM investigations, all materials can be divided into two categories.

- ***Amorphous oxidized layer:*** All material including Sb_2Te_3, Sb_xTe_y, $Bi_xSb_{2-x}Te_3$ alloys, GST and GBT alloys and GeTe exhibit oxidation with the formation of an amorphous oxidized layer.
- ***Crystalline oxidized layer:*** The pure Bi based material system such as Bi_2Se_3, Bi_2Te_3 and all Bi_xTe_y stoichiometric states exhibit the formation of a crystalline oxidized layer.

6.2.1 Oxidation with amorphous layer structure

The materials that belong to this group exhibited slight variations in the oxidation process from one another; however, they always resulted in an oxidized layer with amorphous structure under the exposure to ambient conditions. The summary of their oxidation processes is discussed below.

Sb based 3D TIs: Starting with Sb_2Te_3 (Figure 6.1), the oxidation process is observed to occur in the following three steps. The steps are:

- ***Physisorption:*** The oxygen molecules adsorbed on the epilayer surface. This process is relatively fast and generally occurs within a few seconds of exposure to ambient environment.
- ***Chemisorption:*** The adsorbed oxygen reacted with Sb and Te atoms forming the corresponding oxides i.e. Sb_2O_3 and TeO_2, witnessed via XPS measurements (Figure 6.2). This step was rapid; however, slower than physisorption and is observed to start in less than 15 minutes of exposure. (Figure 6.1a and b). Moreover, the homogenous oxidation of one complete QL throughout the surface is witnessed before the next QL started to oxidize (Figure 6.1c).
- ***Oxide layer growth:*** Diffusion limited growth of the oxide layer is observed where the oxygen kept on diffusing though the initially oxidized layer and simultaneously a small quantity of Te atoms kept on leaving the epilayer surface. This step is observed to be much slower than chemisorption.

The first two steps occurred rapidly and their effects can be easily seen via SEM images, depicted in Figure 6.1. The smooth surface with QL terraces suddenly transforms into a surface with numerous 5 – 10 nm wide holes of increasing density with the increasing exposure to ambient environment. These holes are believed to be the indication of the chemisorption process with Te atoms diffusing out and the oxygen molecules diffusing into the epilayer. After 2 hours of exposure to ambient conditions, a lamella at the cross-section of the epilayer is extracted; and via STEM investigation, the formation of an amorphous oxidized layer at the surface is observed as depicted in Figure 6.1c. After the oxidization of the first QL (≈ 1 nm), the decrement in the oxidation rate is witnessed as the oxidation process is now being controlled solely by the diffusion rate of oxygen into the epilayer through the pre-oxidized layer. The oxidation rate kept on decreasing with the increasing thickness of the oxidized layer.

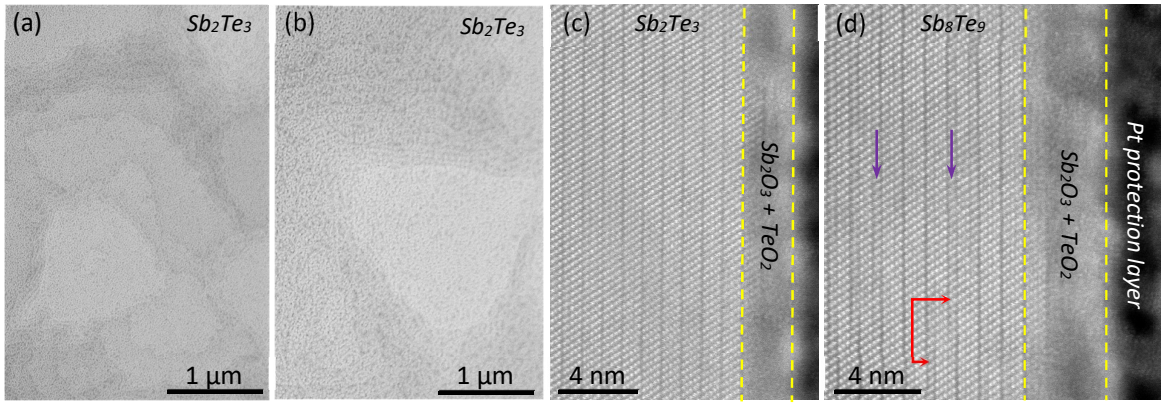

Fig. 6.1: Surface oxidation in Sb based materials. SEM images indicating the formation of holes on the surface of Sb_2Te_3 epilayer after exposure to ambient conditions for the duration of (a) 15 minutes and (b) 30 minutes. STEM-HAADF image, acquired along Si [1-10] projection, of (c) Sb_2Te_3 epilayer with approx. 2 nm of oxidized layer after exposure to ambient conditions for 2 hours. And (d) Sb_8Te_9 epilayer with approx. 2.5 nm of oxidized layer after exposure to ambient conditions for 90 minutes. The oxidized layers are marked with yellow lines. Purple arrows indicate the presence of Sb_2 bilayer while red arrows indicate the switching of bilayer structure through Sb-Te antisites.

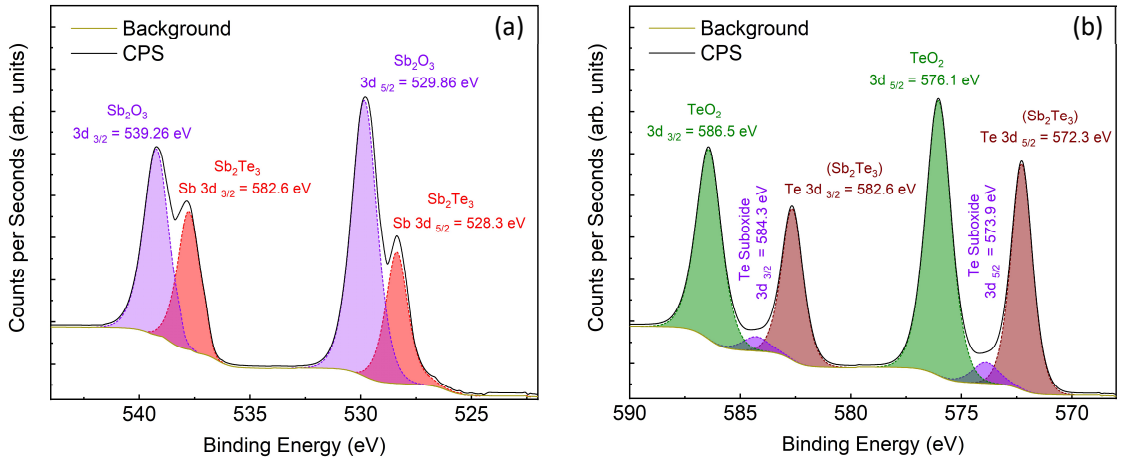

Fig. 6.2: XPS spectrum acquired under UHV conditions at the surface of Sb_2Te_3 epilayer after exposure to ambient conditions for 3 weeks. (a) The acquired spectrum between 520 eV and 545 eV along with the fitted 3d peaks of Sb based compounds. (b) The spectrum between 565 eV and 590 eV along with the fitted 3d peaks for Te compounds. The formation of Te sub oxide is witnessed in all samples until the homogenous stoichiometry of $Sb_2Te_2O_7$ is achieved.

The diffusion process continued for those samples which were exposed for longer durations to ambient environment until the homogenous stoichiometry of $Sb_2Te_2O_7$ (Sb_2O_3 + $2TeO_2$) in the oxidized layer is achieved. This behavior is confirmed via XPS measurements where the high resolution spectrum is acquired under UHV conditions and depicted in Figure 6.2. This is in-line with the earlier findings[21, 22, 23]. The similar oxidation behavior is also observed in BST alloys with the additional presence of Bi_2O_3. In Sb_xTe_y stoichiometric epilayers, the surface oxidation is witnessed to be slightly faster than Sb_2Te_3 due to relatively less availability of Te atoms (Figure 6.1d). In order to witness the extent of oxidation, STEM-HAADF images of Sb_2Te_3 and $Bi_{0.8}Sb_{1.2}Te_3$ epilayers after elongated exposures to ambient conditions with 3 weeks and 5 months respectively, are acquired and depicted in Figure 6.3.

GeTe: The oxidation process observed in the pristine GeTe epilayers is slightly different than other Ge containing alloys such as GSTs and GBTs; however, the oxidation in all Ge based materials is found to be mainly controlled by the self-diffusion of Ge atoms towards the surface followed by the structural reconfiguration[25, 29, 40]. The oxidation process in GeTe epilayers is observed to occur in the following steps.

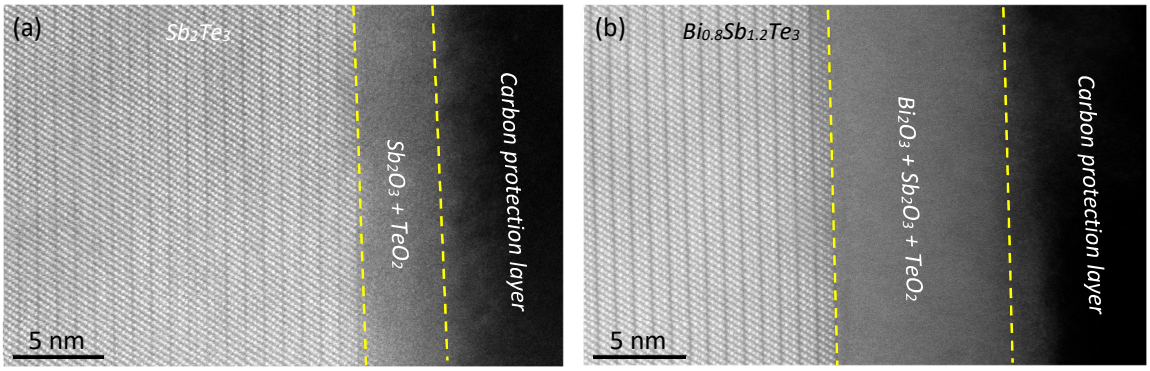

Fig. 6.3: Ageing effect in Sb based topological epilayers. STEM-HAADF image, acquired along Si [1-10] projection, of (a) Sb_2Te_3 epilayer after the exposure to ambient conditions for 3 weeks and (b) $Bi_{0.8}Sb_{1.2}Te_3$ epilayer after the exposure of 5 months with 4.5 nm and 9.8 nm thick oxidized layer respectively. The oxidized layers are marked with yellow lines.

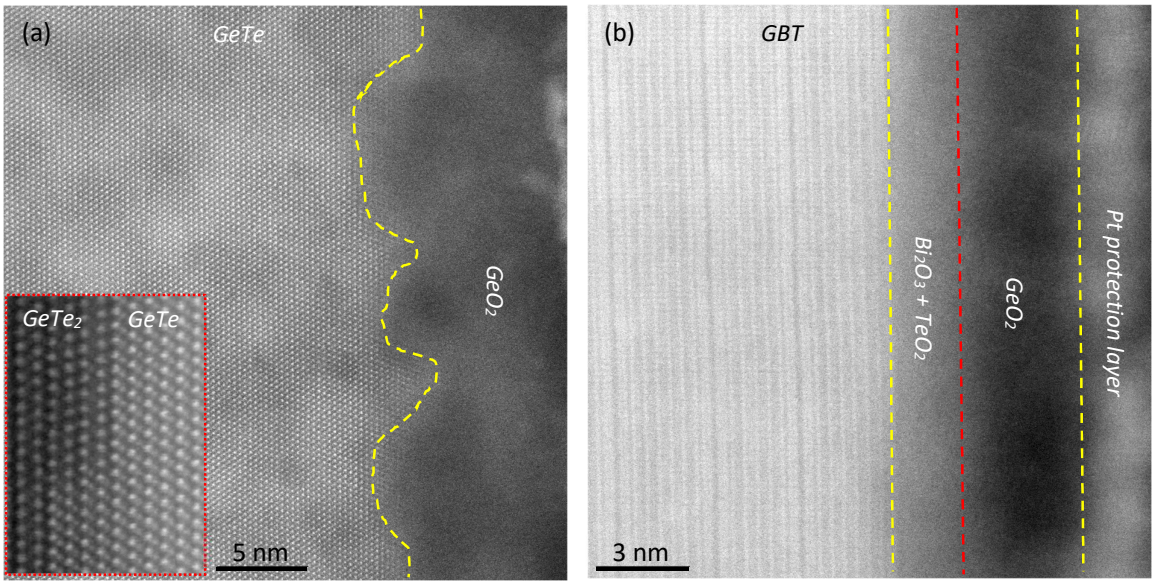

Fig. 6.4: Ageing effect in Ge based epilayers. STEM-HAADF image, acquired along Si [1-10] projection, of (a) GeTe epilayer after the exposure to ambient conditions for 2 months and (b) GBT epilayer after the exposure of 2 months. The oxidized layers are marked with yellow lines. The inhomogeneous thickness of GeO_x is evident in (a) where the high density of Ge vacancies in thin films led to the formation of GeTe2 layer structure (inset). The oxidized layer in GBT in (b) can be divided into two groups having different contrast due to difference in density.

- The surface oxidation in GeTe epilayer, similar to Sb based materials, occurred very rapidly where the oxidation of both elements i.e. Ge and Te atoms on the surface is observed.
- With the increasing exposure to the ambient conditions, Ge atoms are observed to migrate towards the oxidized surface where they reacted with the diffusing oxygen molecules and formed GeO_x that slowly and steadily transformed into GeO_2 (confirmed via XPS).
- The migration of Ge atoms to the surface left behind a Te rich epilayer that in thick films (> 20 nm) helped to fill Te vacancies. In thin films ranging in thickness 20 nm or below, however, these vacancies have forced the transformation of layer-free structure of GeTe into pockets of VdW based layered architecture of $GeTe_2$, as depicted in Figure 6.4a (inset) and observed in Figure 5.25.

The above mentioned oxidation steps are found to be in agreement with the proposed model[29]; however, the formation of $GeTe_2$ layered structure has never been predicted or observed during the oxidation process. The entire process is governed by the migration of Ge atoms forming Ge vacancies (V_{Ge}). V_{Ge} exhibits a very low formation energy of 0.08 eV[41] and has been confirmed by various theoretical models

as an agent to stabilize the structural transformations (amorphous ↔ crystalline) which makes GeTe a prominent phase change material (PCM)[42, 43, 44, 45, 46]. In GeTe epilayers, other than playing a crucial role in the crystal phase transformation; V_{Ge} is reported to be utilized as a tool to modify electronic band structures[47, 48], tune the Fermi level and alter bulk carrier concentration[48]. In agreement with the earlier reports[28, 29], the oxidized layer of GeTe is found to be comprised majorly of GeO_2 with smaller contents of TeO_2 forming (m x GeO_2 + n x TeO_2) where m >> n. GeTe epilayers, unlike all other investigated materials in this study, exhibited a non-uniform thickness of the oxidized layer throughout the sample surface, as depicted in Figure 6.4a.

GBT epilayers: The earlier stages of surface oxidation in GBT alloys occurred in a similar fashion to BST alloys where all the present elements i.e. Bi, Te and Ge exhibited oxidation and formed their corresponding oxides. However, after a few hours of oxidation; Ge atoms took control of the stoichiometry and the oxidation rate, just as observed in the case of GeTe. In GBT alloys, the oxidation rate is observed to be much slower than pristine GeTe. It is mostly due to the restricted diffusion of Ge atoms to the surface offered by the presence of relatively dense Bi_2O_3 which was not there in pristine GeTe epilayers. Based on the relative density of materials observed via STEM-HAADF images, the oxidized layer in GBT alloys can be divided into two separate layers as depicted in Figure 6.4b.

- The first layer is relatively thin, dense (bright contrast) and closer to the surface of the GBT epilayer. It consists heavily of Bi and Te oxides.
- The second layer is closer to the interface with air. It is relatively thicker, less dense (dark contrast) and consists heavily of GeO_x.

The segregation of two different stoichiometric oxidize layers was also indicated in earlier reports[25, 26, 27] where the investigation were performed via XPS. The order of stoichiometric oxide layers observed in this study is, however, found to be the exact opposite of the earlier reports. STEM investigations along with XPS measurements in this study, provided an undeniable evidence about the order of the oxides where Ge rich oxide layer is witnessed to exist much closer to the interface with air.

GST epilayers: Unlike GBTs, the surface oxidation of GST alloys is observed to happen in similar fashion to GeTe epilayers. A very interesting phenomenon of structural reconfiguration, initiated by the diffusion and resulting vacancies of Ge atoms, has been observed that has neither been witnessed in GBTs nor has ever been identified in earlier reports[25, 26, 27].

- At the exposure to ambient conditions, Ge atoms started to diffuse out of the current layer towards the exposed surface. It initiated the transformation of Ge rich layer architecture to Ge poor layers i.e. transformation of large layer structure to smaller ones as depicted in Figure 6.5a.
- The structural transformation continued until the layer architecture converted entirely in QLs (Figure 6.5b) while the surface oxide is observed to be comprised of GeO_x. The range of such structural transformations is observed to reach approx. 10 nm deep into the epilayer from the bottom of the oxidized surface (Figure 6.5b).

The one question arises at this point is why such a phenomenon is not witnessed in GBT epilayers while occurred in GSTs? It can be linked to higher energy requirements of Bi-Te antisites in GBTs in comparison to low energy formation of Sb-Te antisites (discussed in section 2.2.3). The combined phenomena of Ge migration (V_{Ge}) towards the surface and energetically favored Sb-Te antisites assisted the transformation of layer architecture and that is most probably why, such a behavior is witnessed in GSTs and not in GBT epilayers. Now, the question arises that how the oxidation will continue with the elongated exposure after the extraction of Ge from the top layers? This question cannot be answered at this point and requires more detailed investigations to understand the continuation of oxidation process in GSTs. The trend of increasing thickness with the ageing effect of all material systems that form amorphous oxidized layers, is summarized in Figure 6.6.

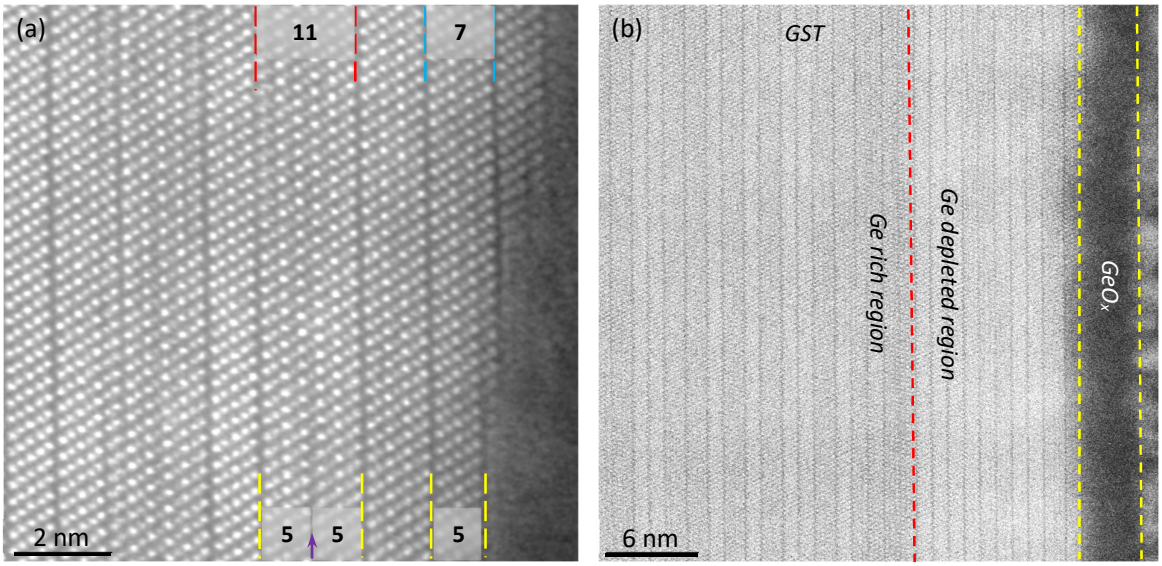

Fig. 6.5: STEM-HAADF images acquired along Si [1-10] projection, of (a) GST epilayer after the exposure to ambient conditions for 2 hours and (b) 1 month. The phenomenon of Ge vacancy assisted transformation of large layer architecture into smaller layer can be visualized in (a) where 11-atomic layer (red lines) is converting into 2 QLs with the central Ge atom layer forming a VdW gap (purple arrow). Similarly the conversion of SL into QL with Ge atoms gassing out is also evident. The formation of Ge poor region with Ge migration towards the surface and forming GeO_x can be visualized in (b) where the oxidized layer is presented by yellow lines.

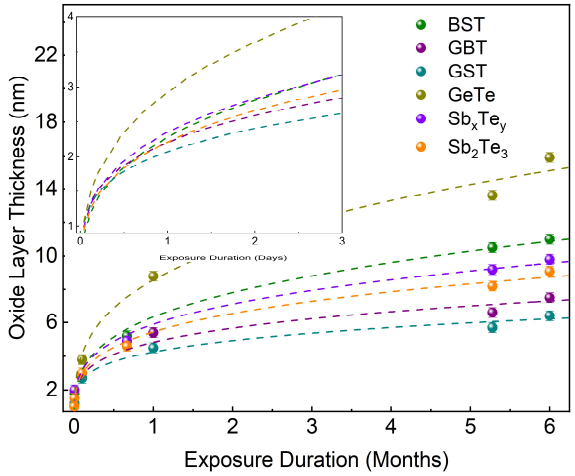

Fig. 6.6: Trend of ageing effect in various Sb and Ge based topological materials that structure in amorphous oxidized layer. The data is evaluated with multiple STEM investigations of epilayers that were exposed to ambient condition for different durations. The rapid surface oxidation and the resulting increment in thickness of oxide layer in the first 3 days is depicted in the inset. With increasing exposure, the oxidation rate of the epilayer decreases exponentially where the thickness of the oxide layer starts to saturate. The highest oxidation rate is exhibited by GeTe.

6.2.2 Oxidation with crystalline layer structure

The surface oxidation process in all pure Bi chalcogenides epilayers including Bi_2Te_3, Bi_xTe_y alloys and Bi_2Se_3 is witnessed to be similar where the oxidized surface exhibited the formation of a crystalline structure with the hexagonal surface. To our knowledge, the structural characterization of the oxidized layers in these material systems has never been reported until now; however, several studies have investigated the chemical composition via XPS [19, 37, 49, 50]. The combined investigation with STEM and XPS in this study shed light on an entirely different oxidation process and the chemical composition of the oxidized region.

As established earlier that after Ge, Bi exhibits the highest reactivity towards oxygen and that is why, a rapid surface oxidation in Bi chalcogenides is observed. The surface oxidation process is witnessed to occur in the following steps.

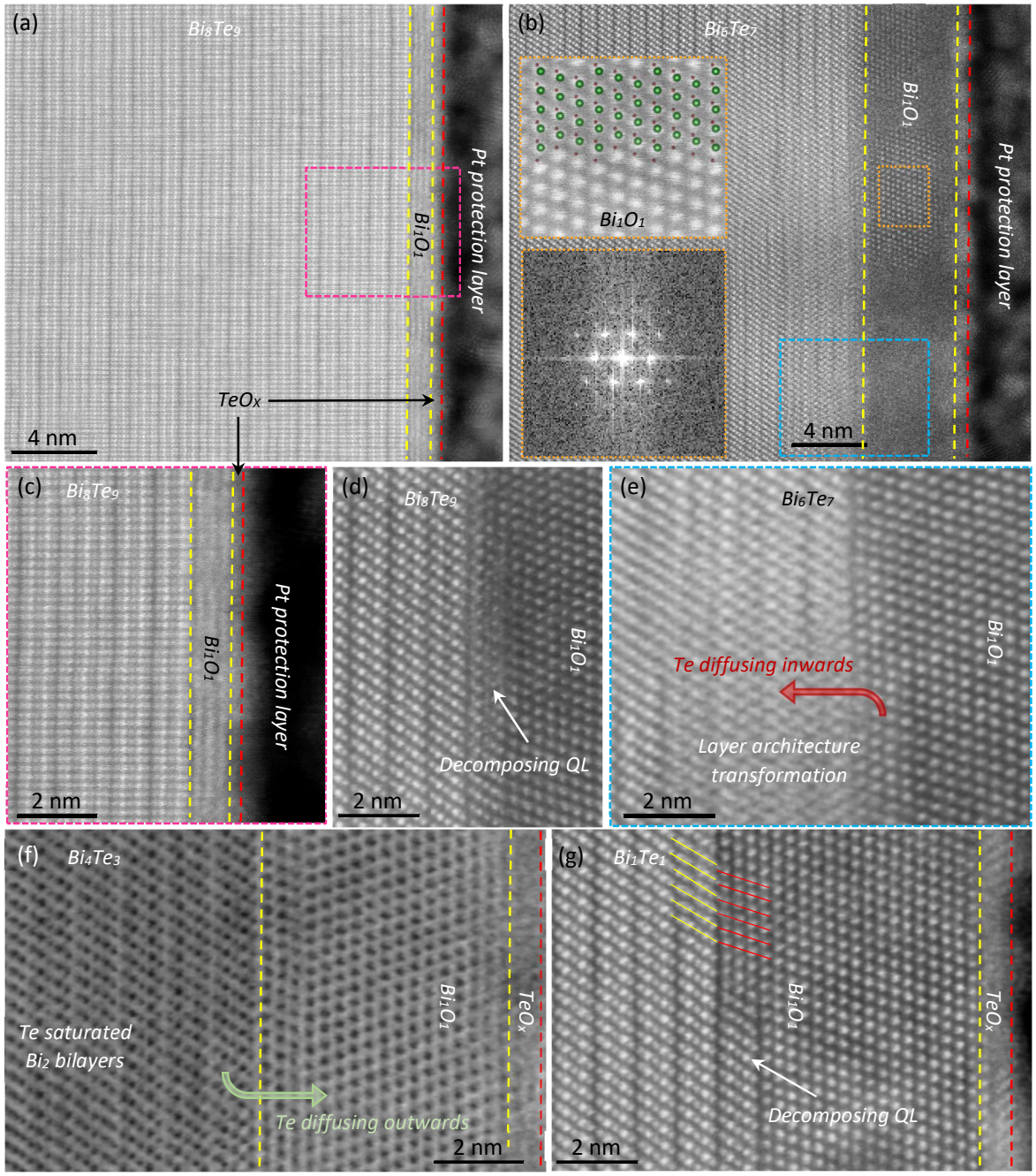

Fig. 6.7: STEM based structural investigations of crystalline Bi_1O_1 layer. (a) HAADF images of Bi_8Te_9 epilayer, acquired along Si [211] projection, after 1 hour of exposure to ambient conditions. The formation of three Bi_1O_1 layers and a very thin amorphous layer of TeO_x is evident (confirmed via XPS). (b) HAADF images of Bi_6Te_7 epilayer, acquired along Si [1-10] projection, after 1 month of exposure to ambient conditions. The increasing thickness of Bi_1O_1 layers have forced Te atoms to penetrate inwards where extra Te converted Bi_2 bilayers into QLs and altered the stoichiometric state of the epilayer. The inset images (orange boxes) in (b) represent magnified structure of the oxide layer where green and red atoms represent Bi and O respectively and FFT spectrum of the crystal structure. (c) A magnified image of the selected area in (a) depicting early stages of Bi_1O_1 layer. (d) The systematic decomposition of QL into Bi_1O_1 in a Bi_8Te_9 epilayer. (e) Representing the selected area in (b) where Bi_1O_1 layer has exceed the critical thickness of 4 nm and Te is diffusing inwards and converting Bi_2 bilayers into QLs. (f) Bright field image of oxidized layer observed in Bi_4Te_3 after 1 month of exposure to ambient conditions. The formation of TSF is also witnessed. (g) HAADF image of the oxidized layer observed in Bi_1Te_1 after 5 weeks of exposure. The relaxed layers of Bi_1O_1 are evident as they are not exhibiting one-to-one atomic correspondence (yellow vs. red lines) with the non-oxidized epilayer. The stoichiometric variations are witnessed in all (b, d, e, f and g) images due to elongated period of exposure.

- The physisorbed oxygen molecules diffused into Bi_2Te_3 (0001) surface and passed through Te basal planes and preferably interacted with Bi due to relatively higher interaction and bond strength between Bi-O than Te-O as reported earlier[51]. This feature provided unanticipated atomic processes with ultrafast transient mechanisms among Bi, Te and O at room temperature[37, 51].
- Bi atoms started to form hexagonal surface compatible crystal structure with oxygen and forced Te atoms from the first QL to be released and migrated to the surface. The newly formed Bi-O crystalline structure later confirmed to be Bi_1O_1 via XPS analysis (Figure 6.8a) and STEM measured lattice parameters (Figure 6.7) including a = 3.86 ± 0.04 Å and c = 9.76 ± 0.03 Å, is a trigonal crystal structure[52, 53, 54] that has never been observed in the oxidation process of Bi chalcogenides.
- The Bi atoms transformed the first QL into three Bi_1O_1 (0001) epitaxial layers (Figure 6.7a), witnessed earlier only in pure Bi crystals[55, 56, 57]. The newly formed Bi_1O_1 layers are yet chemically not pure and most probably contain Te atoms as antisites. However, the composition of Bi_1O_1 layers is observed to be improved in time with Te atoms gradually gassing out of the surface assisted by water vapors in the air (Figure 6.7b). On top of Bi_1O_1 self-organizing epilayer, the formation of a very thin and amorphous TeO_x layer is revealed by XPS and can also be observed in HAADF images (Figure 6.7a and c).
- After a rapid surface oxidation and the formation of three Bi_1O_1 epitaxial layers, the oxidation rate, in comparison to the amorphous oxidized layer, is observed to follow a linear trend. In time, the thickness of the oxide layer is observed to increase in gradual steps and simultaneously, the composition of Bi_1O_1 crystal became stoichiometrically purer with Te atoms leaving the surface.
- The oxidized layer thickness increased further as the oxygen molecules kept on diffusing inward through the crystalline Bi_1O_1 layers. The diffusing molecules reacted with Bi atoms of the non-oxidized epilayer and reconfigured the crystal structure (Figure 6.7d). Simultaneously, Te atoms through atomic bond transitions with Bi and oxygen, gradually migrated outwards through the crystalline Bi_1O_1 layers and degassed.
- After Bi_1O_1 layer reached a certain thickness (approx. 4 nm), another trend of Te atoms migration in Bi_xTe_y crystals is observed. Te atoms, instead of migrating outwards to the surface, are observed to be penetrating inwards to the non-oxidized region where they started to transform Bi_2 bilayers into Bi_2Te_3 QLs. This behaviors can be visualized via STEM image depicted in Figure 6.7e.
- With the increasing exposure to ambient conditions, the inward migrating Te atoms have saturated all nearby Bi_2 bilayers into QLs. Figures 6.7 b, f and g depict epilayers of Bi_6Te_7, Bi_4Te_3 and Bi_1Te_1 respectively where all neighboring Bi_2 bilayers, due to inward diffusing Te atoms, have converted into Bi_2Te_3 QLs and lost their stoichiometric identity. After reaching the saturation point, Te atoms, once again, are forced to migrate outwards to the top surface.
- With the increasing thickness of Bi_1O_1, both elements i.e. oxygen and Te atoms have to travel through crystal planes inwards and outwards respectively to continue the oxidation process. This is why, the oxidation rate is observed to deviate from the linear trend and decreased with the increasing thickness of the oxidized layer. This feature has also assisted in understanding the slightly higher oxidation rate in Bi rich alloys in comparison to the Te rich epilayers of Bi_xTe_y.

Bi_1O_1: Bismuth oxides exist in several stoichiometric states; however, the naturally occurring and the most stable form is Bi_2O_3[49, 50, 58, 59] that exhibits monoclinic crystal structure[60, 61] with a large bandgap ranging 2.78 – 3.31 eV[49, 50, 58]. Based on XPS investigations, all the earlier conducted studies on the oxidation of Bi_2Te_3 crystals have reported the formation of Bi_2O_3 with Bi^{3+} oxidation state[37, 38, 51, 62] while the structural characterization of the oxidized layers via XRD or TEM has never been reported. In this study, the formation of Bi_1O_1 (BiO), a crystalline bismuth oxide with Bi^{2+} oxidation state is witnessed via STEM investigations (Figure 6.7) and confirmed via XPS spectrum (Figure 6.8a). Bi_1O_1 is one of the rarest [56, 57] and only stable state of bismuth oxide that exhibits a hexagonal compatible crystal structure[52, 63]. It has been reported only a number of times as the result of Bi (0001) surface oxidation[53, 55, 56, 57]. It is an exotic oxide material that

exhibits semi-metallic behavior[56, 59, 64] and attracts the oxide community for its physical and electronic characteristics[54, 65]. However, due to its relatively challenging synthesis[56, 57, 66], it is also one of the least explored materials in the literature.

Bi_1O_1 vs. Bi_2O_3: Bi_1O_1 is a very stable compound in ambient conditions[53, 63, 67] that readily decomposes to (Bi_2O_3 + Bi) as soon as it is exposed to oxygen rich environment at high temperatures[49, 50, 58, 59, 65]. That is why, most of the oxidation studies of Bi based compounds e.g. Bi_2Te_3 and Bi_2Se_3 conducted under the controlled environment conditions always resulted in Bi_2O_3[37, 38, 51, 68] and Bi_1O_1 stoichiometry was never witnessed. In order to confirm this theory, Bi_8Te_9 epilayer is exposed to the ambient conditions for 2 weeks and as witnessed from STEM investigations (Figure 6.7d), the formation of Bi_1O_1 is observed and confirmed via XPS spectrum with the peak position at 158.45 eV (the characteristic peak for Bi^{2+} oxidation state[69, 70] as depicted in Figure 6.8a). The same sample is then exposed to the oxygen rich conditions at 200 ℃ for 2 hours and XPS investigations are performed again. The Bi_1O_1 characteristic peak that was observed at 158.45 eV has now shifted to 159.25 eV i.e. the characteristic peak of Bi_2O_3[38, 51, 58, 59] (Figure 6.8b). The higher temperature and oxygen rich conditions have facilitated the diffusion of oxygen molecules into the epilayer, enriched the oxygen deficient layer of Bi_1O_1 and transformed into Bi_2O_3.

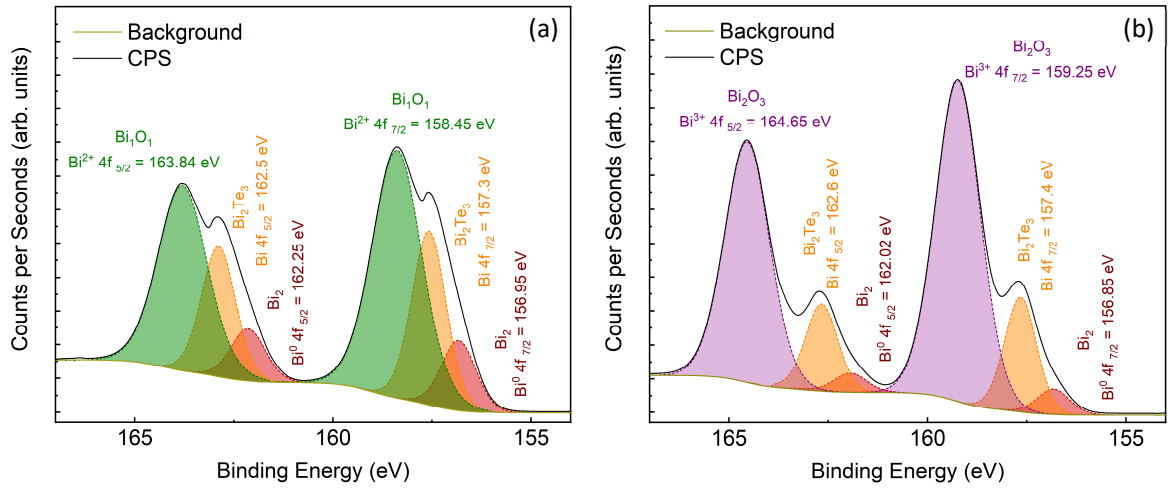

Fig. 6.8: XPS spectrum acquired at the surface of Bi_8Te_9 epilayer after exposure to ambient conditions for 2 weeks. (a) High resolution scans of 4f peaks of Bi between 150 eV and 170 eV depicting the Bi^{2+} oxidation state with the peaks position at 158.45 eV and 163.84 eV confirming Bi_1O_1. (b) Similar scan as (a) with thermal treatment of the oxidized layer, depicting the shift in Bi 4f peaks position to 159.25 eV and 164.65 eV confirming Bi^{3+} oxidation state with Bi_2O_3.

Crystalline Vs. amorphous oxidation rate: In all MBE grown epilayers of Bi_xTe_y in this study, irrespective of their stoichiometry, at the exposure to ambient conditions the formation of epitaxial Bi_1O_1 layer is witnessed. These Bi based epilayers exhibited rapid surface oxidation but unlike other materials with amorphous oxidized layers, the thickness of Bi_1O_1 is not observed to increase swiftly rather a linear trend for the first few days is witnessed. Later, a decline in the oxidation rate due to slower diffusion of oxygen with the increasing thickness of the oxidized layer, is observed. The trend of Bi_1O_1 layer thickness and a comparison with Sb_2Te_3 oxidation can be visualized in Figure 6.9.

Summary: In general, irrespective of the oxidized layer structure being amorphous or crystalline, at the exposure to ambient conditions, rapid surface oxidation is observed in all epilayers where a non-saturating oxidation process with continuously decreasing oxidation rate is witnessed to occur for months. The results of surface oxidation can be summarized as below:

- The oxidation process deformed the (000 1) surface quality and created challenges to fabricate high quality functional interfaces. In the amorphous oxidized layer with relatively large bandgaps,

the probable formation of a Schottky barrier at the interface can be extremely challenging to avoid. The crystalline, non-topological and semi-metallic Bi_1O_1 layers can act as a barrier between the connectivity of metallic electrodes and TSS.

- Apart from surface degradation, the oxidation process forced structural changes through layer architecture transformation. The stoichiometric variations in the non-oxidized layers are observed in GeTe (with the formation of $GeTe_2$), GST (Ge rich to Ge poor layers) and Bi_xTe_y (Bi_2 to QL transition) material systems.
- Surface oxidation resulting in structural changes and stoichiometric variations also altered the electronic characteristics of epilayers with the enhanced concentration of trivial carrier and unintentional deviations in the Fermi level. Such a trend is observed earlier with the enhanced n-type conductivity in Sb and Bi based materials due to loss of Te contents during the oxidation process. It can be witnessed by comparing the electronic transport parameters of the capped and non-capped samples of 3D TIs, listed in Table 3.3. Earlier reports have also confirmed the enhanced concentration of p-type carriers in Ge based alloys, after the exposure to ambient conditions[25, 71]. Hence, the surface oxidation of topological epilayers results in enhanced trivial carriers and suppresses the overall contribution of TSS in magneto-transport investigations.

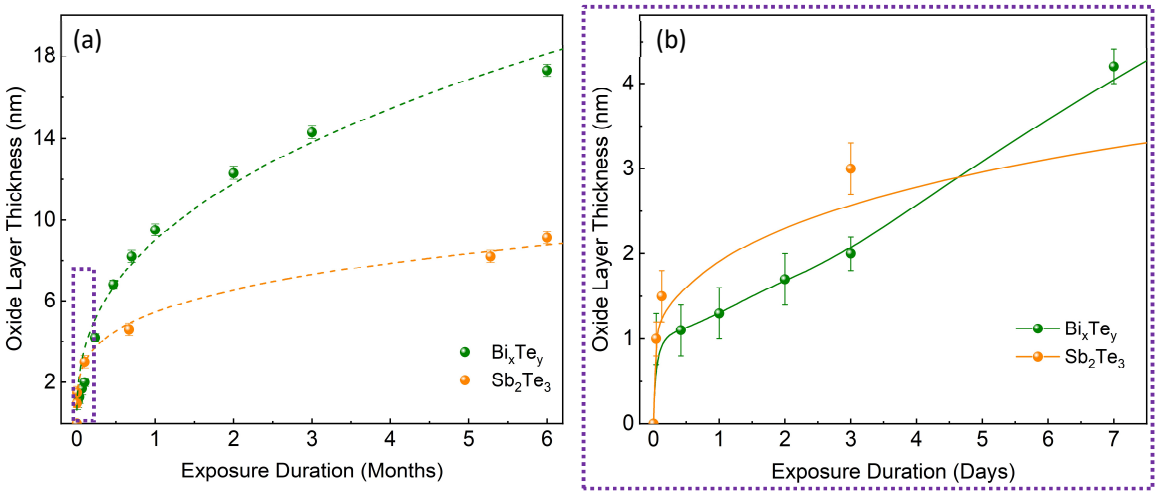

Fig. 6.9: Trend of ageing effect in Bi_xTe_y epilayers with the formation and increasing thickness of Bi_1O_1. The data is obtained with multiple STEM investigations of epilayers that were exposed to ambient condition for different durations. With increasing exposure, the oxidation rate of the epilayer decreases where the thickness of the oxide layer starts to saturate however in comparison to amorphous oxide layers, Bi_1O_1 exhibited enhanced oxidation rate and layer thickness. (b) The surface oxidation behavior in the first week of exposure is however different where the amorphous layers exhibited relatively higher rate that slowly and with linear like trend is overtaken by Bi_1O_1.

All the above mentioned issues act as limiting factors in the realization of high quality functional quantum devices. However, it is beneficial to know that all these issues arise from only one source, the non-protected and degraded surfaces of epilayers and can be completely neutralized by avoiding the surface degradation through oxidation. This phenomenon affirms the ultimate need to devise a suitable and adaptable technique with which the surfaces can be passivated from oxidation and the atomically clean interfaces with metallic electrodes, without the presence of any defects and Schottky traps, can be realized.

6.2.3 Surface passivation from oxidation

The passivation of epilayers to prevent the surface oxidation and ageing effects can be performed using several approaches[72, 73, 74, 75]; however, a suitable technique must exhibit the following characteristics:

- The approach must be capable of applying the passivation (capping material) *in situ*, right after the crystal growth and before the surfaces are exposed to the ambient conditions.
- The capping material should not diffuse into the epilayer and must not alter the structural or electronic characteristics of the crystal.
- The capping must be resistant to ambient conditions to prevent the surface oxidation and when desired, it must also be easily detachable in order to create metallic contacts with the epilayer etc.

Based on the above mentioned requirements, two types of passivation can be applied to epilayers for the specific purposes.

Soft/Temporary passivation: Soft passivation[76, 77] can be utilized to preserve epilayers for longer durations; however, mostly it is adapted for a short period of time particularly when a specimen is required to be transferred from one location to another for additional investigations such as STM and ARPES etc. in case where the vacuum transfer is not viable. A thin layer of Te/Se capping[76, 77] on top of their corresponding compounds acts as soft capping. When desired, the specimen can be loaded into a vacuum chamber and via thermal treatment, the extra Te/Se layer can be removed where the pristine and un-interacted (000 1) surface re-appears[76, 77]. In addition to surface passivation, this technique is also observed to help lowering Te/Se vacancies. The only challenge related by this technique is to manage the rate of thermal evaporation correctly while removing the passivation without damaging the epilayer. Moreover, this technique cannot be adapted with Bi_xTe_y, Bi_xSe_y and Sb_xTe_y stoichiometric alloys as Se/Te atoms will diffuse into the epilayers and subsequently, will modify the stoichiometry of the alloy.

Hard/Permanent passivation: Hard passivation[73, 78, 79] is the most common approach and generally implemented for permanent purposes to prevent the epilayer not only from oxidation but also from other chemicals during the device fabrication processes. It cannot be merely removed via thermal treatment; the removal process requires acidic or basic solution based wet etching or reactive ion assisted plasma based treatment. A thin layer of Al_2O_3 or HfO_2, both are considered as the best candidates for hard capping[73, 78, 79]. In cases where stoichiometric Al_2O_3 is not available, 2-3 nm thin layer of pure Al can be deposited as a capping layer[72, 79]. Pure Al, in comparison to stoichiometric Al_2O_3, exhibits one disadvantage of slightly diffusing (approx. 1 nm) into the applied epilayer; however, it readily oxidizes to AlO_x[80] at the exposure to ambient conditions and prevents the surface from further oxidation.

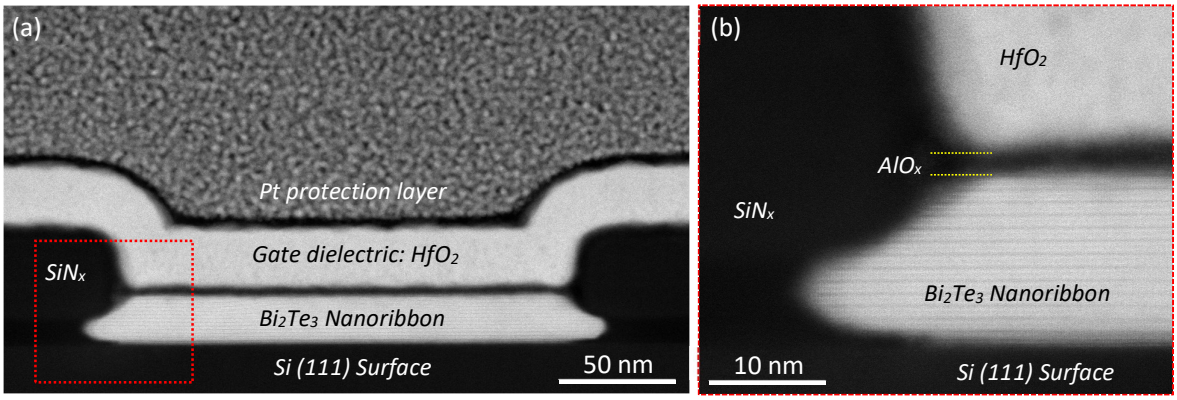

Fig. 6.10: (a) HAADF images acquired along Si [211] projection, depicting the cross-section of selectively grown Bi_2Te_3 nanoribbon after 1 year of exposure to ambient conditions. Epilayer was in situ deposited with 2 nm Al that converted in AlO_x at the exposure to ambient conditions and prevented TI surface from further oxidation or ageing effect. (b) Magnified images of the marked area in (a) depicting the nicely stacked QLs and approx. 3 nm thick formation of AlO_x on top.

The targeted epilayers/nanostructures prepared in this study for magneto-transport investigations (Section 3.6) were always capped via hard passivation by depositing 2 nm Al at approx. 0 ℃ on top of TI

epilayers as reported in Rosenbach *et al*[81]. After hard passivation, samples were processed through standard fabrications steps and finally encapsulated with 15 nm thick layer of HfO_2 deposited via ALD and utilized as the gate dielectric. The samples were then stored for 1 year in the ambient conditions and afterwards STEM investigations are performed at the cross-section of 200 nm wide T-junction to observe the unlikely ageing effect, the performance of Al capping layer and the diffusion extent of Al atoms into TI (Bi_2Te_3) epilayer. Figure 6.10 depicts HAADF image acquired at the cross-section of the capped TI epilayer. It is evident that after 1 year of storage in ambient conditions, the epilayer exhibited pristine surface quality with no ageing effect. The Al atoms, slightly diffused into TI epilayer during the deposition process, readily oxidized and formed approx. 3 nm thick layer of AlO_x (a capping layer) that has successfully passivated the surface from any further oxidation and degradation. Hence as witnessed, the crystal degradation and oxidations related challenges (section 6.2) can be unequivocally prevented with the surface passivation.

6.3 The substrate induced effects on TI epilayers

During the epitaxial growth process, the bottom surface of an epilayer develops an interface with the substrate and is always protected from degradation and other contaminations. It is, however, responsible for the band alignment between the epilayer and the substrate that may affect the doping level and the carrier density in the crystal. The epitaxial growth of 3D TIs on Si (111) substrates is conducted where the defect-free high quality crystalline and selectively grown nanostructures are prepared via SAE (Section 3.5). Despite the fact of achieving defect-free nanostructures (Figure 3.14), magneto-transport investigations, have confirmed the presence of an unexpectedly high carrier concentration (η_{3D} = 2 - 5 x 10^{19} cm^{-3}, for details visit Table 3.3) that is about 3 orders higher than the best reported values in literature[2, 82] with η_{3D} = 5 x 10^{16} cm^{-3} for Bi_2Se_3[83] and η_{3D} = 2 x 10^{16} cm^{-3} $Bi_2Te_{3-x}Se_x$ crystals[82]. The issues of high bulk carrier density measured in all 3D TIs prepared on Si (111) substrate and the non-improving carrier concentration in BST alloys (p- and n-type carriers neutralization) indicate the source of problem should be of external nature. It means, the growth itself may not be responsible for these unexpected results rather high density of trivial carriers must have originated at another source that must be identified.

A couple of theoretical studies have presented the possibility of electronic transfer at Si-TI interface due to band bending that later has been confirmed via ARPES[1, 2]. According to the presented model, the band bending at Si-TI interface results in high doping level of topological epilayer that, for sure, would increase the trivial carrier concentration of the whole system and would suppress the contribution of TSS. The similar behavior is observed during the electronic measurements of TI nanostructures (Section 3.6); however, before making a certain statement that band alignment at Si-TI interface is the source of high carrier concentration in all the performed measurements of 3D TIs, the experimental confirmations must be attained. This challenge is addressed by conducting the growth, structural characterization and magneto-transport analysis of BST alloy, where the epilayer is being prepared on another substrate. Later, a comparison of structural and electronic characteristics between the prepared epilayers on both substrates is conducted to deduce the source of the problem. For this purpose, it is decided to conduct the comparative study between Si (111) and an insulating substrate to make sure that electronic transfer will not occur at the interface. A thin layer (approx. 10 nm) of HfO_2 is selected as the substrate due to its high-k characteristics as the gate dielectric and the possibility to prepare ultra-clean and smooth films via ALD.

6.3.1 Growth and structural characterization of BST alloy on HfO_2

Substrate preparation: The HfO_2 substrate for the growth of BST alloy is prepared using the following steps.

- A highly conductive Si (111) wafer with 0.025 Ωcm resistivity is selected as a foundation for the possibility of using it as a global back gate during magneto-transport investigations.

- Si (111) wafer is RCA cleaned and native SiO_2 is removed via wet etching (detail steps are discussed in Table 2.2).
- The etched Si wafer is loaded into ALD chamber where it is thermally annealed at 500 ℃ for 15 minutes. The chamber is then set to the process temperature at 200 ℃ where 10 nm thick film of HfO_2 is thermally deposited. The detailed steps of ALD process can be found in Appendix 6A.
- The HfO_2 deposited wafer is then spin coated and diced into 1 x 1 cm^2 pieces. The resist is removed via organic solvents and samples are cleaned in Piranha solution before loading into MBE chamber to start the growth process.

Epitaxy on HfO_2: The optimum growth parameters of BST alloys are already discussed in Chapter 2 and 3. Using those parameters, all the growth attempts resulted in failures with the presence of a few BST crystals on HfO_2 surface. ALD prepared HfO_2 film at 200℃ exhibited amorphous structure that did not provide good adhesive strength to incoming adatoms and therefore, Bi and Sb adatoms exhibited a very low adsorption to desorption ratio (ADR). This behavior can be realized from the fact that in the early attempts to achieve selective area epitaxy (SAE) on Si (111), HfO_2 was utilized as a blocking surface to avoid the growth of TI epilayer (discussed in Section 3.1). Here, with an entirely opposite target of achieving high quality and fully coalesced epilayers of 3D TIs on HfO_2 (the blocking surface), in comparison to restrict the growth, drastic changes in the growth conditions are required.

The attempts to achieve entirely coalesced BST epilayers are started with the tuning of growth temperature (T_{sub}). T_{sub} is reduced in gradual steps from 300℃ until 200℃ where a fully coalesced yet very rough epilayer with extremely high density of structural defects (confirmed via scan Δω of XRD), is achieved. Various attempts to improve the structural quality are conducted that all resulted either in an improved structural quality with non-coalesced epilayers or in entirely closed films with high density of structural defects.

Finally, a multi-step growth process is developed. In the 1st step approx. 3 nm of topological material containing Bi, Sb and Te is deposited at T_{sub} = 100 ℃ in an amorphous state that after passing through several short annealing steps is slowly and steadily converted into crystalline layers. The controlled annealing process of TI epilayer is the most critical step as the amorphous substrate does not provide any azimuthal or rotational alignment to the forming crystals thus, there is always a high probability of forming structural defects such as domains and stacking faults. Secondly, the annealing rate can be fatal for thermal stability of topological layers as it causes adhesion challenges for the epilayer on an amorphous surface. After the controlled annealing process, T_{sub} is set to 220 ℃ in the 2nd stage where epilayer of the desired thickness is grown. In the 3rd stage, once again the process of controlled annealing steps is conducted at T_{sub} ranging from 250 ℃ - 270 ℃ in Te rich environment to get rid of any Te thermal vacancies (V_{Te}). At last, an entirely closed epilayer of BST alloy on HfO_2 with acceptable structural quality confirmed via XRD Δω scan (FWHM values below 500″) is achieved. The complete growth process containing the detailed steps with the corresponding T_{sub} and elemental fluxes are described in Appendix 6B. After the development of successful recipe to grow BST epilayers on amorphous HfO_2, various growths are conducted where relative contents of Bi and Sb in the epilayer are adopted to adjust the carrier concentration and to tune the Fermi level near the Dirac point. Later, the epitaxial growths of both binary compounds i.e. Bi_2Te_3 and Bi_2Se_3 are also conducted using the multi-step growth processes.

Structural characterization: The detailed structural investigations are conducted via XRD for each epilayer where rocking curve (Δω) analysis is utilized as a swift method to compare the structural quality among different growths that helped to optimize the final growth parameters. However, in order to analyze structural quality of the epilayer at atomic scale and to identify the type and density of defects, STEM investigations are conducted for $Bi_{0.8}Sb_{1.2}Te_3$ epilayer where a lamella is extracted along Si [1-10] orientation and some of the acquired HAADF images are depicted in Figure 6.11. The key observations are mentioned below:

- It is quite interesting to see how nicely QLs tend to arrange themselves parallel to the substrate without any support or crystalline orientation provided by the substrate (Figure 6.11a).
- At places the presence of stacking faults are observed where QLs are not stacked perfectly parallel to the substrate (Figure 6.11b).
- Most of the structural defects are found near the substrate where non-twinning domains (Figure 6.11c) and the presence of TSFs (yellow arrows in Figure 6.11c, d and e) are witnessed; most probably due to their deposition in an amorphous state during the 1st stage of growth process.

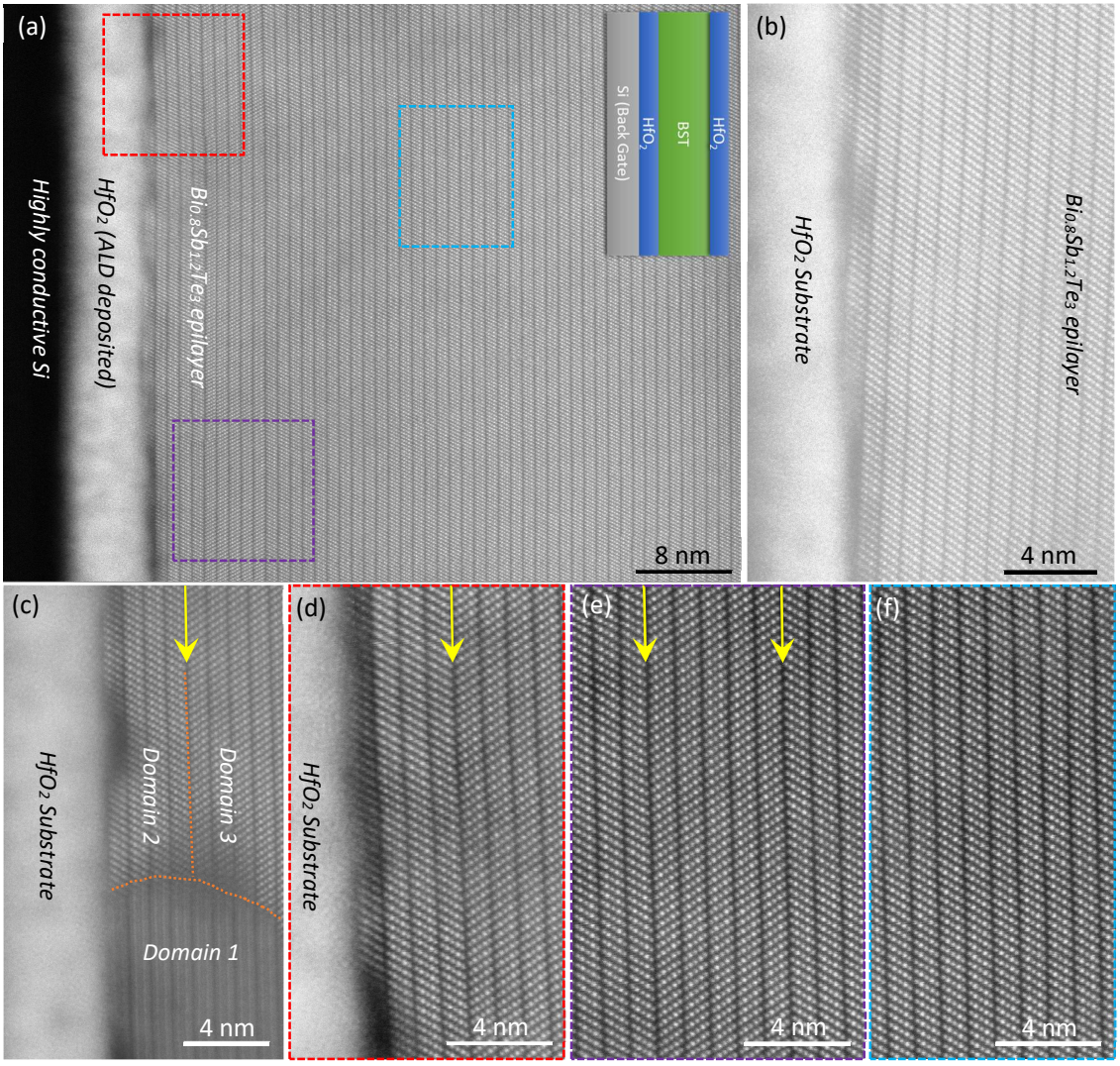

Fig. 6.11: (a) STEM-HAADF images acquired along Si [1-10] projection, at the cross-section of $Bi_{0.8}Sb_{1.2}Te_3$ epilayer grown on amorphous HfO_2 substrate. (b) An image representing the formation of stacking faults where QLs are not in perfectly parallel alignment with the substrate. (c) HfO_2-TI interface where epilayer is exhibiting structural defects including non-twinning domain and a TSF. HAADF images depicting the presence of TSF stacking fault near the substrate in (d) and in (e) with the presence of 2 TSFs indicated with yellow arrows. (f) Perfectly relaxed and defect free stacking of QLs on top of all defects observed in (b-e) that reside near the substrate.

In summary, STEM investigations have confirmed the structural quality of epilayer grown on HfO_2 is not comparably equivalent to Si surface as on Si (111), the defect-free epilayers were achieved (HAADF images are depicted in Figure 3.14). However, considering the crystalline growth of BST alloy on an amorphous substrate, an unexpectedly good structural quality of the epilayer is witnessed.

6.3.2 Electronic characterization of BST epilayer on HfO_2

In order to perform electronic characterization, a Hallbar structure is fabricated using the following steps:

- The grown epilayer is *in situ* capped with 2 nm Al as discussed in section 6.2.3 and exposed to air to form AlO_x. The epilayer is then loaded into ALD chamber and 15 nm of HfO_2 is deposited that is utilized as top gate dielectric.
- BST epilayer sandwiched between two HfO_2 films is structured via lithography and wet etching though top layer of HfO_2 and BST epilayer to create hallbar structure. Later, metallic depositions are performed to create contacts along with the top and bottom gate electrodes.

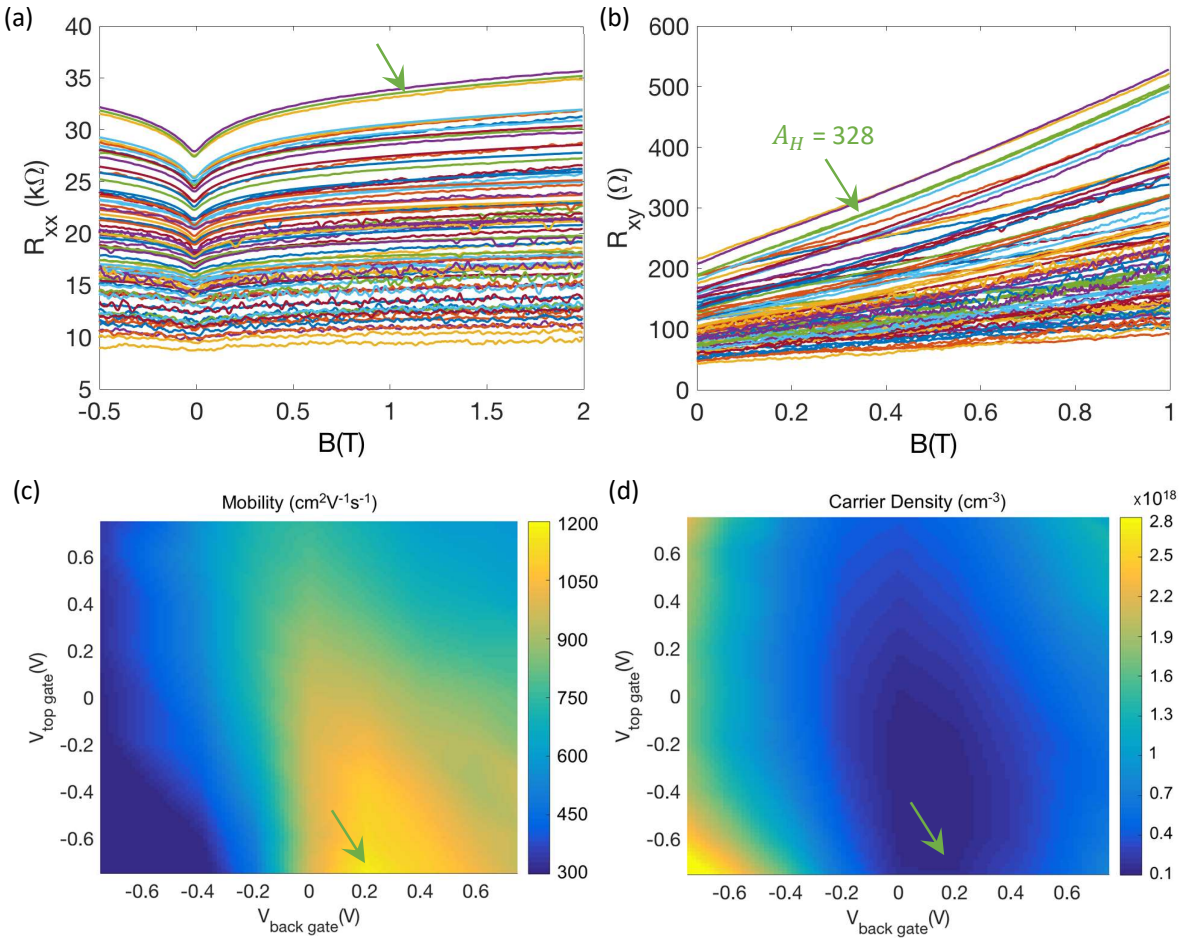

Fig. 6.12: Gate voltage dependent Hall measurement data of $Bi_{0.8}Sb_{1.2}Te_3$ on HfO_2. (a) Trend in longitudinal resistance (R_{xx}) vs. applied magnetic field where the optimum tuning of Fermi level obtained near the Dirac point with $V_{Top\ Gate}$ = -0.7 V and $V_{Back\ Gate}$ = 0.2 V (indicated with green arrow), (b) Trend in Hall resistance vs. applied field to extract Hall constant (A_H) in order to evaluate (c) mobility (μ) and (d) carrier concentration (η_{3D}) of the material system.

The fabricated dual-gated Hallbar structure is then investigated via magneto-transport analysis in similar fashion as selectively grown nanostructures on Si (111) substrates are measured (discussed in section 3.6). The Hall measurements of BST epilayer on HfO_2 are performed and here, only the summary of the key measurements including longitudinal resistance (R_{xx}), Hall resistance (R_{xy}), mobility (μ) and 3D carrier concentration (η_{3D}) are presented in Figure 6.12. The key observations are discussed below:

- Measurements without applying any gate voltage provided diminishing pattern of the weak anti-localization (WAL). This effect is observed to improve and weaken by applying a series of top and

back gate voltages due to Fermi shifts in and out of the bulk gap respectively, as depicted in Figure 6.12a. The best values are obtained where the Fermi level is tuned close to Dirac point in the bulk gap with $V_{Top\ Gate}$ = -0.7 V and $V_{Back\ Gate}$ = 0.2 V (indicated by a green arrow in Figure 6.12).

- It is interesting to observe that an epilayer with more structural defects on HfO_2 in comparison to the almost defect-free structure on Si (111) has exhibited much improved electronic parameters such as Hall constant (A_H) = 328 (Figure 6.12b), mobility (μ) = 1168 $cm^2V^{-1}s^{-1}$ (Figure 6.12c) and 3D carrier concentration (η_{3D}) = 1.7 x 10^{17} cm^{-3} (Figure 6.12d).

The 3D carrier concentration (η_{3D}) measured in BST epilayer grown on HfO_2 substrate is almost 1 order higher than the best reported values in the literature. However, the lower reported values are obtained from the binary Bi_2Se_3[83], the ternary $Bi_2Te_{3-x}Se_x$ crystals[82] and the quaternary $Bi_{2-x}Sb_xTe_{3-y}Se_y$[84, 85] TI films, all of them exhibit considerably large bandgap of approx. 300 meV in comparison to BST alloy ($Bi_{2-x}Sb_xTe_3$) with 170 meV. To our knowledge, the measured value of (η_{3D}) = 1.7 x 10^{17} cm^{-3} is one of the best obtained values for the BST alloy until now, that also can be slightly improved with the structural optimization of the epilayer by avoiding the observed crystal defects.

6.3.3 Comparison between Si (111) and HfO_2

The material parameters of BST alloy obtained from magneto-transport analysis while the structures being prepared on Si (111) and HfO_2 substrates, are compared in Table 6.1 where the values measured on Si (111) are adopted from Table 3.3. It is evident that BST alloy on HfO_2 with comparatively lower structural quality to Si (111), exhibited much improved electronic parameters particularly 3D charge carrier concentration (η_{3D}) is witnessed to improve by 2.5 orders while the mobility (μ) is improved by almost one order. In general, all parameters are observed to present enhanced performance that eventually are related to the lower bulk carrier concentration.

Table 6.1: A comparison of electronic characteristics of $Bi_{0.8}Sb_{1.2}Te_3$ structures obtained via magneto-transport investigations while the epilayers are prepared on Si (111) and HfO2 substrates.

Electronic Parameters – Units	BST on Si (111)	BST on HfO_2
Hall constant (A_H) – m^3C^{-1}	16	328
Mobility (μ) – $cm^2V^{-1}s^{-1}$	212	1168
2D charge carrier density (η_{2D}) – cm^{-2}	7.9 x 10^{13}	1.2 x 10^{12}
3D charge carrier density (η_{3D}) – cm^{-3}	5.4 x 10^{19}	1.7 x 10^{17}
Phase coherent length (l_Φ) – nm	169	358

The above mentioned results have confirmed the earlier reported phenomenon of band bending at Si-TI interface[1, 2]. It is the band bending and the resulting effects of high level doing in the topological epilayers that led to unexpected high density of trivial charge carriers in the nanostructures prepared on Si (111) substrates (Table 3.3) that ultimately suppressed the novel effects of TSS. Though, it is true that the phenomenon of band bending is the source of high carrier concentration in 3D TIs prepared on Si (111) but it does not provide any justification of the increased carrier density in Sb_2Te_3 in comparison to Bi_2Te_3 and particularly in BST alloy where p- and n-type carriers should have neutralized each other and among all materials, should have presented the lowest carrier concentration.

This question once again led to the detailed structural investigations of Si-TI interfaces via STEM. This interface was investigated in several samples during the structural characterization of 3D TIs and Bi_xTe_y alloys where a pristine and defect free interface between Si and TI epilayer with the existence of Te monolayer, is witnessed and also depicted in Figure 2.2. However, after the confirmation of high carrier density problem due to the band bending at Si-TI interface, the structural data of all the investigated material systems is analyzed again. It has been observed that Si-TI interfaces in Sb based materials are not

atomically sharp and well-defined as observed in case of Bi chalcogenides. With detailed investigations it has been observed that Sb diffuses approx. 3 – 4 nm into Si substrate (depicted in Figure 6.13) and thus creates a highly doped channel underneath the TI epilayer that certainly would have affected the carrier density in Sb based TIs and could be the reason of enhanced carriers in BST alloy in comparison to Bi_2Te_3.

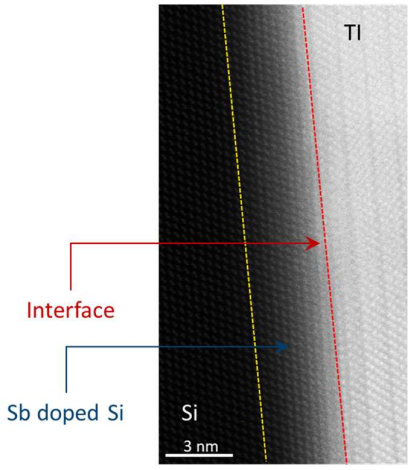

Fig. 6.13: STEM-HAADF image acquired along Si [1-10] projection, at the cross-section of $Bi_{0.1}Sb_{1.9}Te_3$ epilayer grown on Si (111) substrate. The diffusion of relatively heavy Sb atoms 3 – 4 nm into Si substrate is evident that would create a highly conductive channel in magneto-transport and enhance the bulk carrier concentration.

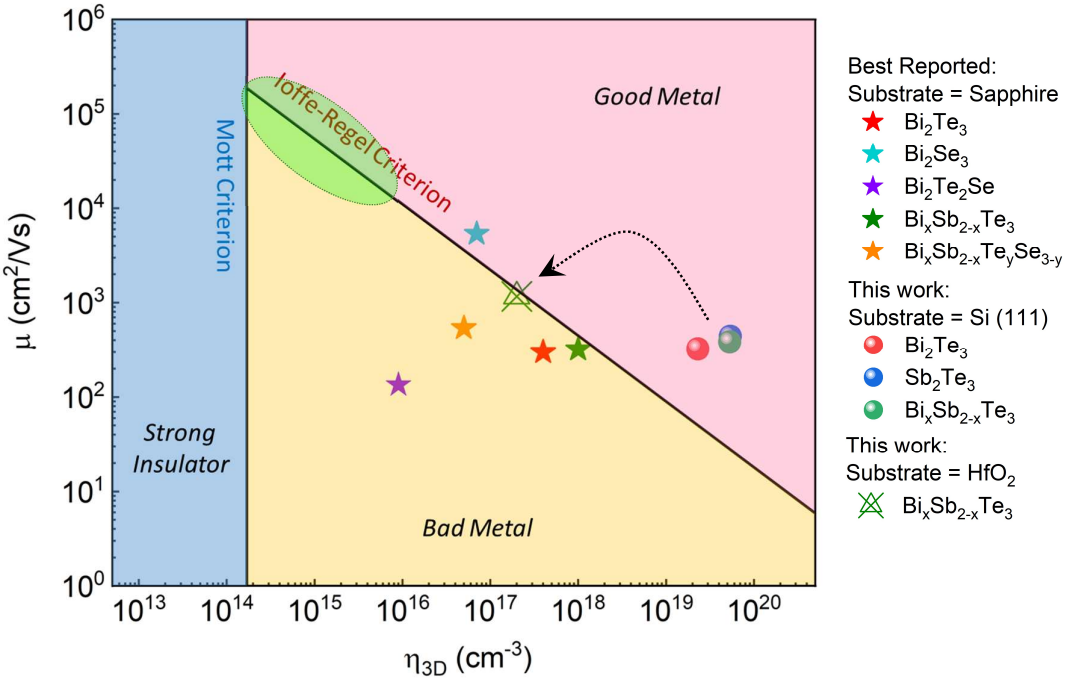

Fig. 6.14: Categorization of conventional 3D TIs based on their electronic characteristics according to Mott and Ioffe-Regel criteria. The best reported values are plotted and represented with the stars like shapes and compared with the data obtained in this work. A clear indication of high level of doping in Si based structures can be seen with respect to epilayer prepared on HfO_2.

Figure 6.14 represents the Mott[2, 45, 86, 87] and Ioffe-Regel[88, 89, 90] criteria to categorize materials on the basis of their electronic properties i.e. mobility and carrier concentration. Any material that exhibits 3D carrier concentration (η_{3D}) below 2 x 10^{14} cm^{-3} is regarded as a strong insulator according to Mott's law; all the other materials are considered as metals. The Ioffe-Regel criterion (IRC) presents further classification of metals between the good and the bad depending upon the electronic characteristics. In general, the high carrier concentration leads to low mobility and vice versa. The high performance TIs are expected to reside

at the border of IRC (region that identifies metal-insulator transition) and ideally at the crossing of Mott criterion, an area marked with the green colored zone. For the advanced quantum applications, the reduction in the bulk carrier density is not the only requirement, TIs must also exhibit the corresponding improvement in the mobility, as depicted Figure 6.14. Among most of the best reports values of carrier density (3D TIs) in the literature, the corresponding motilities are low and therefore, the data points reside below the Ioffe-Regel border. The observed deficiency in the mobility can be associated to point defects in the compositional alloys as the binary TI i.e. Bi_2Se_3 exhibits the higher mobility. Based on the results obtained in this work, following conclusions can be extracted:

- All TIs prepared on Si (111) exhibited an unexpected high carrier density and poor mobility; however, regarding the measured mobility values, the corresponding carrier density should have been 2 orders lower than the measured ones. This phenomenon can be explained via enhanced doping level of TI nanostructures due to the band bending at silicon substrates, discussed above. The corresponding higher values of mobility can be associated to the high quality of epitaxial growth and the *in situ* capping for the surface passivation.
- By replacing Si (111) substrate with an insulator (HfO_2), the issue of high bulk carriers due to band bending is avoided and the carrier concentration is improved by 2.5 orders resulting in an almost perfect placement on the IRC border.

In order to avoid these challenges in future and to utilize novel features of TSS, the substrate material must be switched from Si (111) to a crystalline insulator as the growth on an amorphous insulating substrate (HfO_2 or SiO_2) is extremely challenging and selective area epitaxy (SAE) is not possible. The crystalline insulators such as Sapphire, SiC, Mice, BaF (111), MgO (111), STO etc. in comparison to an amorphous insulators will not only provide support for epitaxy (azimuthal and rotation alignment to nucleating QLs), they will also enable the possibility of achieving SAE. With the SAE on crystalline insulators it will be possible to reconfigure the platform developed in earlier in chapter 3 that will provide reliable, dimensionally controllable and scalable architecture to achieve high quality nanostructures for advanced applications without the suppressed contribution of TSS.

Despite the fact of very high density of trivial carriers and suppressed contribution of TSS in 3D TIs on Si (111), the topological effects including SdH oscillations[81], AB oscillations[81, 91], resistive steering effect[92] (Section 3.6) and 4π-periodic contribution of Majorana bound states (MBS) in TI-SC hybrid junctions[93], are still observed. It was only possible due to high crystal quality of the grown epilayer on Si (111) and the *in situ* capping to avoid surface oxidation and ageing effects in the epilayer. As observed, the phenomenon of band bending and doping at Si-TI interface due to diffusion of Sb will always enhance the density of trivial carriers and suppress the effects of TSS; it will be extremely challenging to utilize novel features of topology to fabricate advanced devices such as a topological Qubit while conducting the epitaxy on Si (111).

6.4 Summary

A systematic study to investigate the surface stability of all materials prepared in chapter 2, 3, 4 and 5 is conducted, when the epilayers are exposed to the ambient environment. The structural characterization via STEM and chemical analysis via XPS have revealed that all epilayers are prone to aging. The surfaces belonging to all materials are observed to oxidize where a non-saturating process with a continually decreasing oxidation rate is observed. The oxidation process is observed to differ from one material system to another; however, based on the structural properties, all materials can be classified in two different groups. The first group contains Sb and Ge based alloys. These materials rapidly oxidize at the exposure to ambient conditions; however, after the oxidized layer reaches a thickness of couple of nanometers, the oxidation rates is observed to drop exponentially. These materials exhibit amorphous oxidized layers that can form Schottky-like barrier with metallic electrodes. Due to being amorphous in nature, however, the oxide layer can be removed via dry etching of Ar^+ plasma treatment. The second group contains pure Bi

based chalcogenides e.g. Bi_xTe_y alloys. The oxidized layer, in these materials, materializes into a semi-metallic and crystalline structure of Bi_1O_1 that cannot be removed easily and limits the connectivity of topological surfaces with the metallic electrodes. Irrespective of the oxidized layer being amorphous or crystalline, at the exposure to ambient conditions, the structural reconfiguration and stoichiometric deviations are observed in almost all the material systems. The passivation of epilayers is achieved with the *in situ* deposition of 2 nm thin layer of Al that readily transforms into AlO_x at the exposure to ambient conditions and prevents the epilayers from further oxidation and aging effects. Finally, the phenomenon of charge transfer due to band alignment at the Si (111) - TI bottom surface is investigated with a comparative growth, structural and transport analysis of TI epilayer prepared on HfO_2 substrate. The acquired results indicate caution and limit the utilization of Si substrates for the advanced quantum applications. These limitation can be addressed with the adaptation of a crystalline insulator (sapphire, SiC and STO etc.) as the substrate. With the development of a platform to achieve SAE of topological materials on the opted crystalline insulator at the nanoscale, the advanced material characterizations could be performed and the fabrication of quantum devices, without the suppressed contribution of TSS, would be more feasible.

Chapter – 7
Engineering Epitaxial Interfaces for TI-SC Hybrid Junctions

One of the most promising and immensely desired application of topology[1] is the fault tolerant quantum computation[2, 3, 4, 5] based on spatial braiding[4, 6, 7, 8] of Majorana quasiparticles that are predicted to emerge[4, 9, 10] in the vortex of a topological superconductor (TSC) as a zero energy excitation called Majorana zero mode[4, 11, 12] (introduced in section 1.3). According to Fu and Kane[9], a TSC can be artificially engineered based on a conventional s-wave superconductor (SC) and a strong topological insulator (STI) hybrid structure[13]. The building blocks of a TI-SC hybrid junction and the corresponding requirements are discussed in section 1.3. Among them, the most critical entity is the interface between the SC and STI[11]. This chapter is dedicated to perform the structural characterization of interfaces between STIs and s-wave SCs. At first, a preliminary study with STEM based structural investigations involving several s-wave SCs is performed and the challenges involved with the interface quality are identified. Later, several new hybrid junctions with the opted superconductor are prepared where the epitaxial interfaces are artificially engineered using the technique of self-epitaxy[14] and their interface transparencies, based on the Josephson junction (JJ) measurements, are evaluated.

7.1 Structural investigation of TI-SC hybrid structures

For the successful realization of an artificial TSC, the first requirement is the selection of an s-wave SC that would provide a suitable (i.e. defect-free, epitaxial and transparent) interface. In order to achieve this, several TI-SC hybrid junctions containing different s-wave SCs, are prepared. At the interface, STEM assisted atomic-scale structural investigations and the energy dispersive x-ray (EDX) based compositional analysis, are performed. Based on these investigations, the structural issues and challenges involved in attaining the epitaxial interfaces are identified and possible solutions for the structural optimization are addressed.

7.1.1 Generation – I interfaces

The first generation of hybrid structures are prepared with four different s-wave SCs including Sn, Pb, Nb and Al. With the purpose of avoiding any contamination at the interface and the surface degradation via oxidation (discussed in chapter 6), the hybrid structures are prepared *in situ* (without the exposure to ambient conditions). After the growth of TI epilayers via MBE, the samples are cooled down at approx. 0 ℃ where 40 nm thick layer of each SC is deposited and the TI-SC hybrid stacks are prepared, except for Nb which is deposited at 50 ℃. All selected SCs (Sn, Pb, Nb and Al) belong to the cubic crystal structure[15, 16], non-compatible with the hexagonal surface of 3D TIs and thus, are expected to exhibit the structural defects at the surface along with the formation of non-epitaxial interfaces. Based on STEM and EDX investigations of the interfaces between SC and TI epilayers, the main observations are discussed below:

- All prepared hybrid structures exhibited diffusion of SCs into the TI epilayers. The STEM-HAADF image acquired at the cross-section of Sb_2Te_3 – Nb junction along with the EDX spectrum is depicted in Figure 7.1. The cross-diffusion of Nb and Sb atoms to approx. 3 nm is witnessed that led to the formation of an amorphous layer at the interface. Both, the non-diffused region of Sb_2Te_3 (TI epilayer) and the Nb film on top of diffused amorphous region at the interface, exhibited crystalline structures.

- The STEM-HAADF image acquired at the cross-section of Sb_2Te_3 – Al junction along with the EDX spectrum is depicted in Figure 7.2. Similar to Nb, the cross-diffusion of Al and Sb atoms is observed; however, the diffused region is increased to approx. 4 nm. Unlike Nb, the diffused region resulted in the formation of a poly-crystalline structure that exhibited a semi-epitaxial interface with the non-diffused TI epilayer.
- Pb and Sn based hybrid structures are investigated where both atoms are observed to diffuse heavily into the TI epilayer (approx. 10 - 15 nm). Moreover, the diffused atoms are also witnessed to damage the trigonal crystal structure of the TI epilayer by forcing QLs to transform into the corresponding chalcogenides (cubic structure). Due to these reasons, both SCs are considered not suitable until a solution to block the diffusion of Sn and Pb atoms into the TI epilayers is found. The acquired TEM results along with the EDX profile of these stacks are depicted in Appendix 7A.

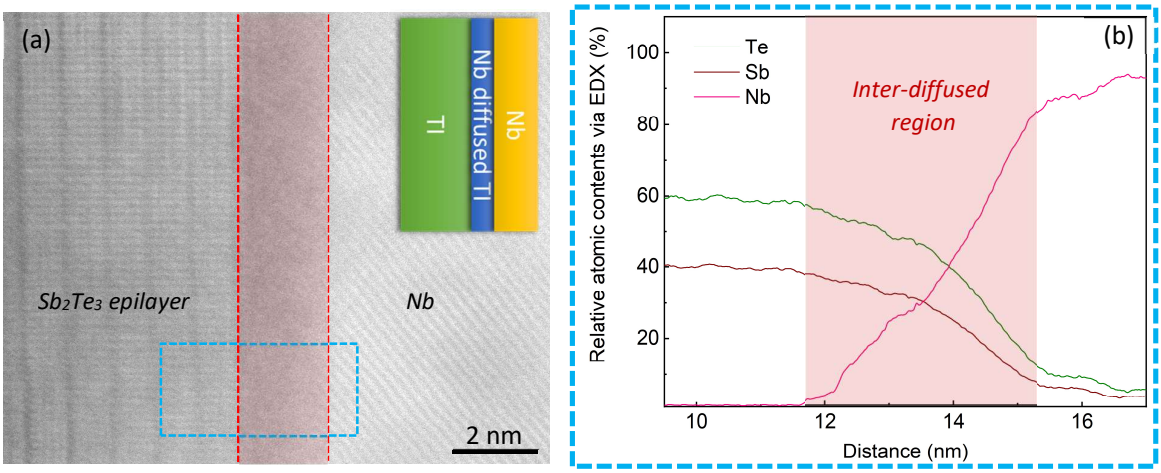

Fig. 7.1: (a) STEM-HAADF image acquired at the cross-section of Sb_2Te_3 – Nb hybrid junction along Si [211] projection. The formation of approx. 2 nm wide Nb diffused TI inter-mixed region with amorphous layer at the interface is evident. On top of mixed region crystalline Nb layer can be observed. (b) EDX profile in the marked area in (a) with the blue box representing the relative atomic contents of elements. The extent of Nb diffusion into the TI epilayer up to 3 nm, marked with the red zone, can be witnessed.

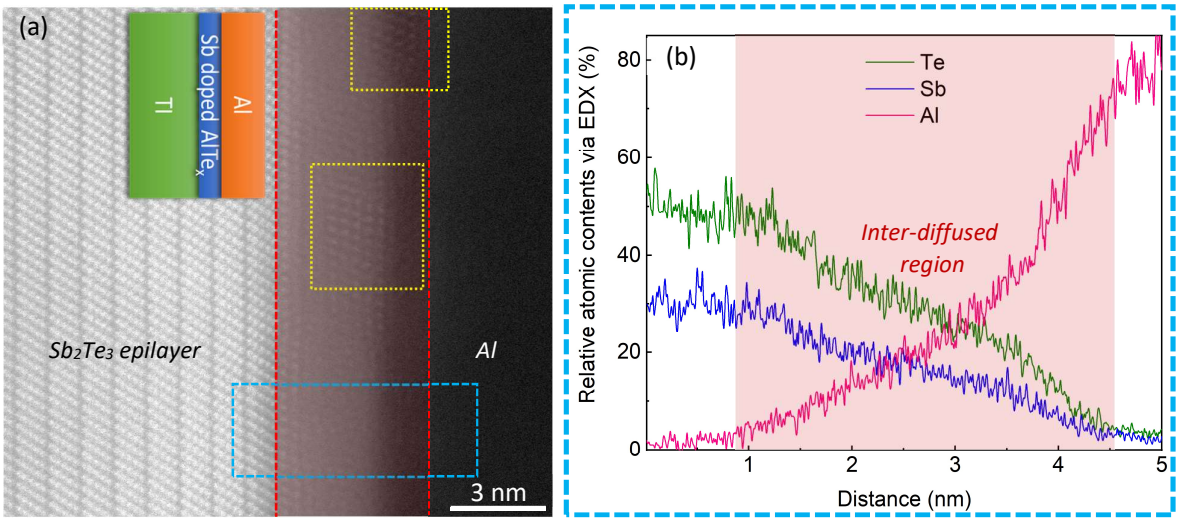

Fig. 7.2: (a) STEM-HAADF image acquired at the cross-section of Sb_2Te_3 – Al hybrid junction along Si [1-10] projection. Both elements i.e. Al and Sb are observed to diffuse at the interface and established approx. 4 nm wide inter-mixed region with polycrystalline structure containing AlSb alloy (yellow boxes) on top of TI epilayer before the Al layer is reached. (b) EDX profile in the marked area in (a) with the blue box representing the relative atomic contents of elements. The extent of Al diffusion into the TI epilayer up to 4 nm, marked with the red zone, can be witnessed.

7.1.2 Challenges in the first generation TI-SC hybrid structures

Among all SCs, Al exhibited the best structural results with the formation of a well-defined near epitaxial interface and a poly-crystalline diffused region at the surface. The EDX profile indicated the mixed contents of Al, Sb and Te in the polycrystalline region with the probable formation of $AlTe_x$[17, 18], a material with large trivial bandgap of 1.84 eV – 1.96 eV[19, 20] while HAADF image also confirmed the crystal structure of AlSb crystal[21, 22] (yellow boxes in Figure 7.2a), a III-V semiconductor with 1.66 eV bandgap[23]. Both materials $AlTe_x$ and AlSb with relatively large bandgap would contribute in the formation of a Schottky effect and limit the performance of the interface by resulting in a bad transparency. Such a behavior is reported earlier where the formation of $AlTe_x$ in GeTe[18] and the presence of a Schottky barrier in Bi_2Te_3 junctions[17] that has limited the electronic performance of the device. A similar trend is also reported in Al based JJs containing Bi_2Se_3 and Bi_2Te_3 as weak-links[24, 25, 26, 27] with a poor interface transparency of $\tau = 0.35$[24, 27]. Furthermore, the failure to achieve the induced superconductivity in Sb_2Te_3 – Al JJs is also reported by Schüffelgen *et al.*[28] It indicates that Al is not a suitable SC to fabricate an artificial TSC until further optimizations to avoid the formation of $AlTe_x$ and AlSb alloys (blocking the diffusion of Al into TI epilayer) are performed.

Nb, on the other hand, diffused into the TI epilayer with the formation of an amorphous layer on the surface where the composition can have two different possibilities i.e. the formation of $NbTe_x$ or the formation of $Sb_xNb_yTe_z$ ternary alloy. $NbTe_x$, in the stoichiometric state of $NbTe_2$, is a semi-metal[29] that exhibits superconductivity at 0.5 K[30, 31, 32] while $Sb_xNb_yTe_z$ alloy also exhibits semi-metal behavior that would not lead to the formation of a Schottky-like barrier. Due to the observed challenges in Al based junctions and the electronic compatibility of Nb, JJs based on BST alloy and Nb are prepared. The details of fabrication and measurements of JJs can be found in Schüffelgen *et al.*[28, 33] The superconducting measurements conducted on TI-Nb based Josephson junctions have indicated a high interface transparency along with the signatures of a TSC with the presence of Majorana bound state exhibiting 4π-periodic contributions of the supercurrent (I_c). Even after achieving such promising results, the realization of a topological qubit with Nb based junctions could be problematic due to some intrinsic properties of Nb as a SC. The Nb exhibits a large superconducting gap (Δ) = 1.43 ± 0.02 meV[34, 35] and the superconducting critical temperature (T_c) = 9.26 K[34, 35]; however, the superconducting phase coherent length (ξ)[36] is quite limited and can be evaluated using equation 7.1[37, 38] where $\hbar$ represents the reduced Planck constant and v_F is the Fermi velocity[39].

$$\xi_{Nb} = \frac{\hbar v_F}{\pi \Delta} = 41\ nm \tag{7.1}$$

The superconducting characteristics of Nb, in general, signify cautions that can be problematic for its utilization in the topological quantum computation. The major challenges include 1e instead of 2e periodicity[40, 41] of the supercurrent (I_c) and even parity instability[42, 43] along with the parity lifetime. During the manipulation of Majorana bound states in a JJ based circuit, these issues may result in the quasiparticle poisoning[40, 44]. In addition, the existence of several oxides of Nb[11, 44] and Abrikosov vortices (type-II superconductivity) may act as traps[11, 40] and make Nb more susceptible to poisoning. With the achievement of the defect-free and high crystal quality film along with the *in situ* surface passivation to avoid the oxidation, the overall challenges with Nb can be reduced; however, the parity stability and the lifetime still require major improvements. One such improvement has recently been achieved with NbTiN alloy where the parity lifetime exceeds a minute[45, 46]; however, the 1e periodicity of I_c still remains a critical challenge. In summary, though Nb based junctions have provided good interface transparencies, they can be problematic with the quasiparticle poisoning in the advanced functional devices. Moreover, the formation of amorphous region at the interface can be problematic in achieving the reproducible results.

All the issues encountered by the intrinsic characteristics of Nb can be solved with Al based junctions. Al exhibits type-1 superconductivity and in comparison to Nb, exhibits relatively small superconducting gap

(Δ) = 298 ± 2 μeV[47, 48], low critical temperature (T_c) = 1.20 K[47, 48] and lower critical magnetic field (H_c) = 10 mT[47, 48]. These shortcomings, however, are compensated with the enhanced superconducting phase coherent length (ξ) ≈ 1.2 to 1.5 μm, the 2e periodicity[40, 49, 50] of the supercurrent (I_c) and stable even parity[51], factors critical for Majorana based platform that are failed to be facilitated by Nb. Though, H_c = 10 mT is an inadequacy; however, by reducing the Al film thickness to approx. 10nm, the critical in-plane magnetic field and the critical temperature (T_c), both parameters can be improved to approx. 3 T[52, 53] and 2 K[52, 53] respectively. On one hand, Al exhibits quite promising superconducting characteristics while on the other hand, it results in the formation of an interface that exhibits a Schottky barrier and limits the realization of a high performance junction.

Based on above mentioned discussions, for the successful realization of advanced Majorana based circuits, Nb is required to be replaced with a more suitable SC i.e. Al; however, before Al can be utilized to fabricate TSC based circuits, the interface challenges must be addressed. Similar to Al, Sn and Pb also exhibit type-I superconductivity and theoretically, are more suitable to replace Nb; however, the challenges of diffusion into the TI epilayer also limit their utilization. Thus, for the realization of futuristic functional interfaces, the following challenges must be addressed.

- The most critical challenge is to devise a suitable technique to block the diffusion of Al/Sn/Pd atoms into the TI epilayers, so that the probabilistic formation of the Schottky barrier in form of $AlTe_x$ or AlSb and the structural damage of TI epilayers can be avoided.
- The adopted technique is preferred to provide a well-defined epitaxial interface with the TI epilayer. As observed in Nb based junctions, an epitaxial interface is not necessary to achieve high interface transparency; however, it ensures the low resistive noise at the junction[27] along with the reproducible results.

7.2 Interface engineering between SC and 3D TIs

Among the selected SCs, all have exhibited the diffusion into the TI epilayer; however, Nb is the only SC that can be utilized without any further optimization. Amongst the remaining three, Al is selected to conduct further optimization tests to find a suitable solution that, if successful, can be adopted for all SCs (Al, Sn and Pb). With the main objective of blocking the SC diffusion into the TI epilayer, a search for the possible solutions is started. One option is to insert an inter-diffusion barrier layer, a thin metallic film ranging 2 - 3 nm in thickness[24], between the SC and TI epilayer that would help in blocking the cross-diffusion and via restructuring the surface will result in the formation of new interfaces. The material selection for the inter-diffusion barrier is of critical importance as, along with blocking the SC atoms from diffusing into TI epilayer, it must not introduce any unintended deviations in the junction characteristics. Therefore, the selected material as the diffusion barriers must exhibit the following characteristics.

- It must block the SC from diffusing into TI epilayer.
- It should not diffuse itself into the TI and if the diffusion cannot be avoided, it must create a metallic or semi-metallic alloy at the interface to avoid the formation of a Schottky barrier.
- It should act as a highly transparent interface to the Cooper pair[27].
- If possible, it should configure a well-defined and epitaxial interface with the TI epilayer.

The approach of utilizing an inter-diffusion barrier between 3D TIs and Al junction is adopted by several groups[24, 25, 26, 27] where a measured poor interface transparency without any diffusion barrier τ = 0.35[24, 27] is witnessed to be improved to τ = 0.49[24, 27] and τ = 0.65[24, 27] with the addition of Ti and Pt thin films respectively. However, any structural characterization of the interface with or without the inter-diffusion barrier via XRD or STEM is not reported[24, 27], nor does the literature contain any information about the structural characterization, the dynamics or the probable surface reconfiguration at 3D TI - Al interfaces.

Using these reports as a starting point, a few metallic thin films are selected to be applied as the inter-diffusion barrier and the structural investigations are performed.

7.2.1 Inter-diffusion barrier and structural investigations

The elements Nb, Ti, Pt and Pd are selected to be investigated. A thin layer of these metals are utilized as the diffusion barrier and the structural changes at the interface along with the resulting surface reconfiguration at TI-B-Al hybrid junctions (here B represents the inter-diffusion barrier) are analyzed with the help of STEM and EDX investigations. The selected metals exhibit the following properties.

- All materials i.e. Nb, Ti, Pt and Pd, belong to the group of transitional metals and exhibit the cubic crystal structure[15, 54, 55] except for Ti that belongs to the hexagonal crystal family[56]. The feature of non-compatible crystal structure with 3D TIs indicates the probable strain issues, dislocations and defect formations at the surface without the possibility of realizing epitaxial and relaxed interfaces.
- Another feature of these materials is that all of them (Nb, Ti, Pt and Pd), in comparison to Bi and Sb, exhibit higher electronegativity difference[57] with Te. In other words, they exhibit higher reactivity and that is why, as soon as these materials will be introduced at the interface with TI epilayer, they most probably will interact with the Te atoms present at the surface and will restructure the interface by forming the corresponding tellurides[14].

Keeping the above mentioned factors in mind, both properties may lead to the high defect density and to the structural reconfiguration by forming new compounds at the interface. In order to avoid the formation of any unintended defects at the interface and to study pristine and un-interacted surfaces, the depositions of the inter-diffusion barrier and the Al film are conducted *in situ*. Al is known to arrange itself in an ultra-smooth crystalline film at lower than the ambient temperatures between -10 ℃ and -20 ℃[50, 58]. Right after the growth of TI epilayer via MBE, the sample is cooled down to approx. -10 ℃ where at first 3 nm of the barrier metal and subsequently, 30 nm of Al is deposited. Keeping in mind, the difference in the oxidation behavior and the interface formation with Si (111) substrates between Sb and Bi (discussed in chapter 6), it is decided to conduct the interface study separately for Bi_2Te_3 and Sb_2Te_3 as Sb tends to diffuse more actively and expected to behave differently from Bi_2Te_3. The overview of all the samples prepared for the interface investigations are listed in Table 7.1.

Table 7.1: An overview of the samples prepared to engineer epitaxial interfaces with the assistance of inter-diffusion barrier materials for structural characterization via STEM.

3D TI (Thickness)	Inter-diffusion Barrier (Thickness)	Superconductor (Thickness)
Bi_2Te_3 (15 nm)	Nb (3 nm)	Al (30 nm)
Bi_2Te_3 (15 nm)	Ti (3 nm)	Al (30 nm)
Bi_2Te_3 (15 nm)	Pd (3 nm)	Al (30 nm)
Bi_2Te_3 (15 nm)	Pt (3 nm)	Al (30 nm)
Sb_2Te_3 (15 nm)	Pt (3 nm)	Al (30 nm)
Sb_2Te_3 (15 nm)	Ti (3 nm)	Al (30 nm)

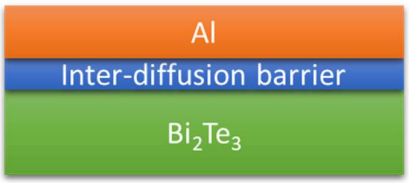

In order to investigate the interfaces, lamellae at the cross-section of each layer stacks, listed in Table 7.1, are prepared along Si [1-10] projection and the detailed STEM investigations are performed. With the help of HAADF and BF images, the structural reconfigurations at each interface are analyzed and via EDX spectrum, the compositional investigations including the diffusion of barrier metal into the TI and the performance of barrier layer to block Al atoms from reaching the TI epilayer, are conducted. The STEM images along with the corresponding EDX spectrum acquired at the interfaces of Bi_2Te_3 – B – Al based junctions where B = Nb, Ti, Pd and Pt are depicted in Figures 7.3, 7.4, 7.5 and 7.6 respectively.

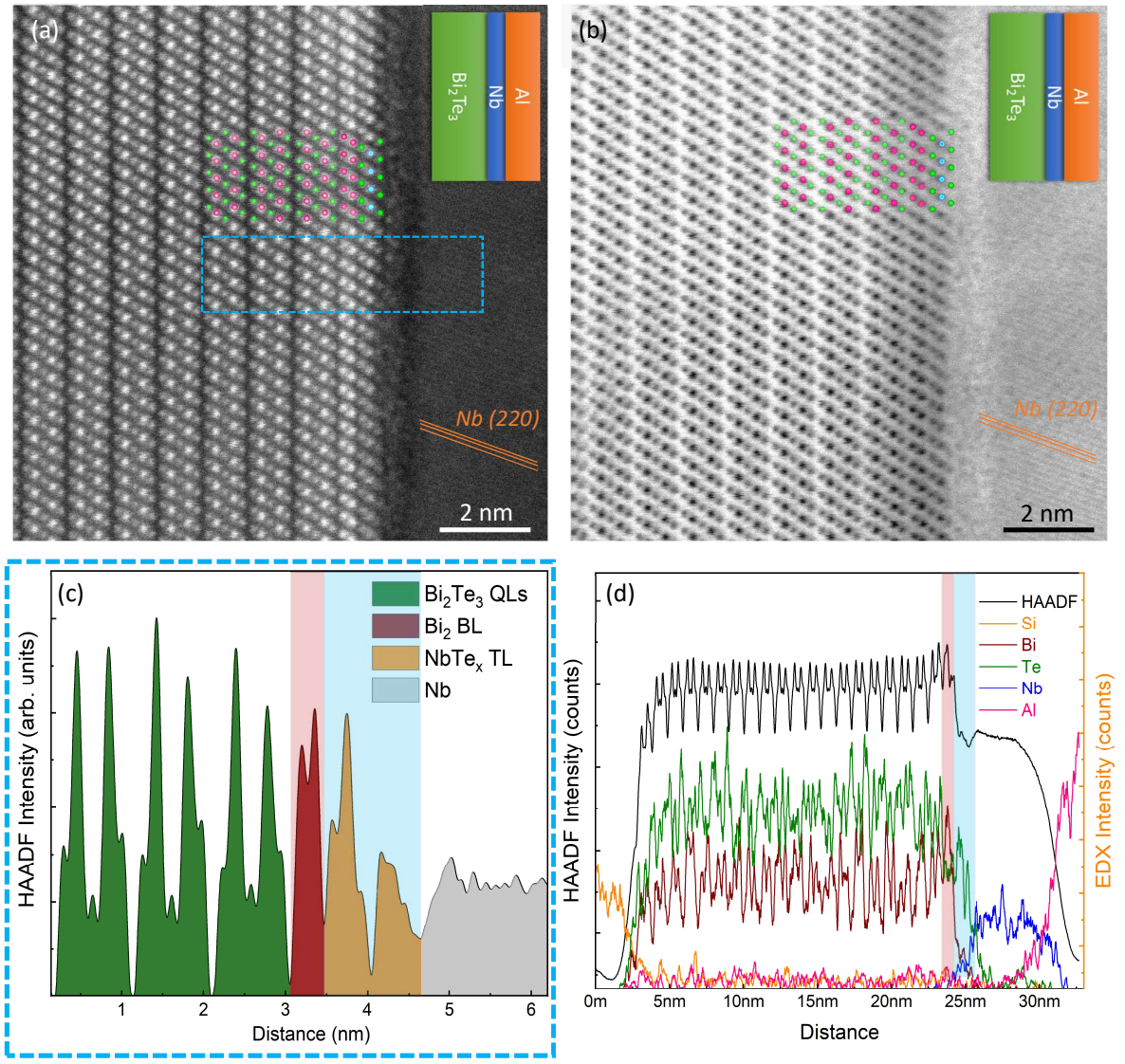

Fig. 7.3: Bi_2Te_3 – Nb – Al interface. (a) STEM-HAADF image acquired at the cross-section of TI epilayer along Si [1-10] projection. Nb atoms force the conversion of top Bi_2Te_3 QL into of Bi_2 bilayer and form $NbTe_2$ (TMDC) like structure that is damaged due to extensive lateral strain induced by the evolution of hybrid stacking introduced by Bi_2 bilayer and 19.5 % in-plane lattice mismatch between the stacking layers. The epitaxial interface is evident although the lateral strain damages the 0.7 nm wide intermediate region before crystalline Nb is witnessed. (b) BF image of (a). (c) Line profile at the interface of the reconstructed surface between Bi_2Te_3 and Nb along the marked area in (a). (d) EDX profile of the complete layer stack Si – Bi_2Te_3 – Nb – Al, indicating the formation of Bi_2 bilayer (red zone) and the intermediate region with $NbTe_x$ (blue zone). The diffusion of Al that is entirely blocked by the thin Nb layer is also evident in the profile.

Starting from the left in all these images, a defect-free and relaxed stacking of Bi_2Te_3 QLs is witnessed. Reaching near the interface at the end of QLs, slightly different behavior is observed from one barrier metal to another.

- In Nb based junction (Figure 7.3), the presence of a bilayer structure with relatively high contrast and smaller VdW gap is observed that can be associated to the presence of a Bi_2 bilayer as EDX spectrum also exhibits Bi rich composition in the specific region (red zone in Figure 7.3d). Followed by the Bi_2 bilayer, a trilayer like structure and an approx. 0.5 nm wide region with an amorphous

state is observed with the compositional presence of Nb and Te (blue zone in Figure 7.3d) that is followed by the crystalline film of Nb.

- The Ti based junction (Figure 7.4) exhibited quite similar behavior to Nb with the presence of a bilayer structure that is followed by a trilayer like structure with the compositional presence of Ti and Te, indicated by the blue zone in EDX spectrum (Figure 7.4d); however unlike Nb, the trilayer structure is followed by the hexagonal arrangement of Ti atoms without the presence of a thin amorphous layer.

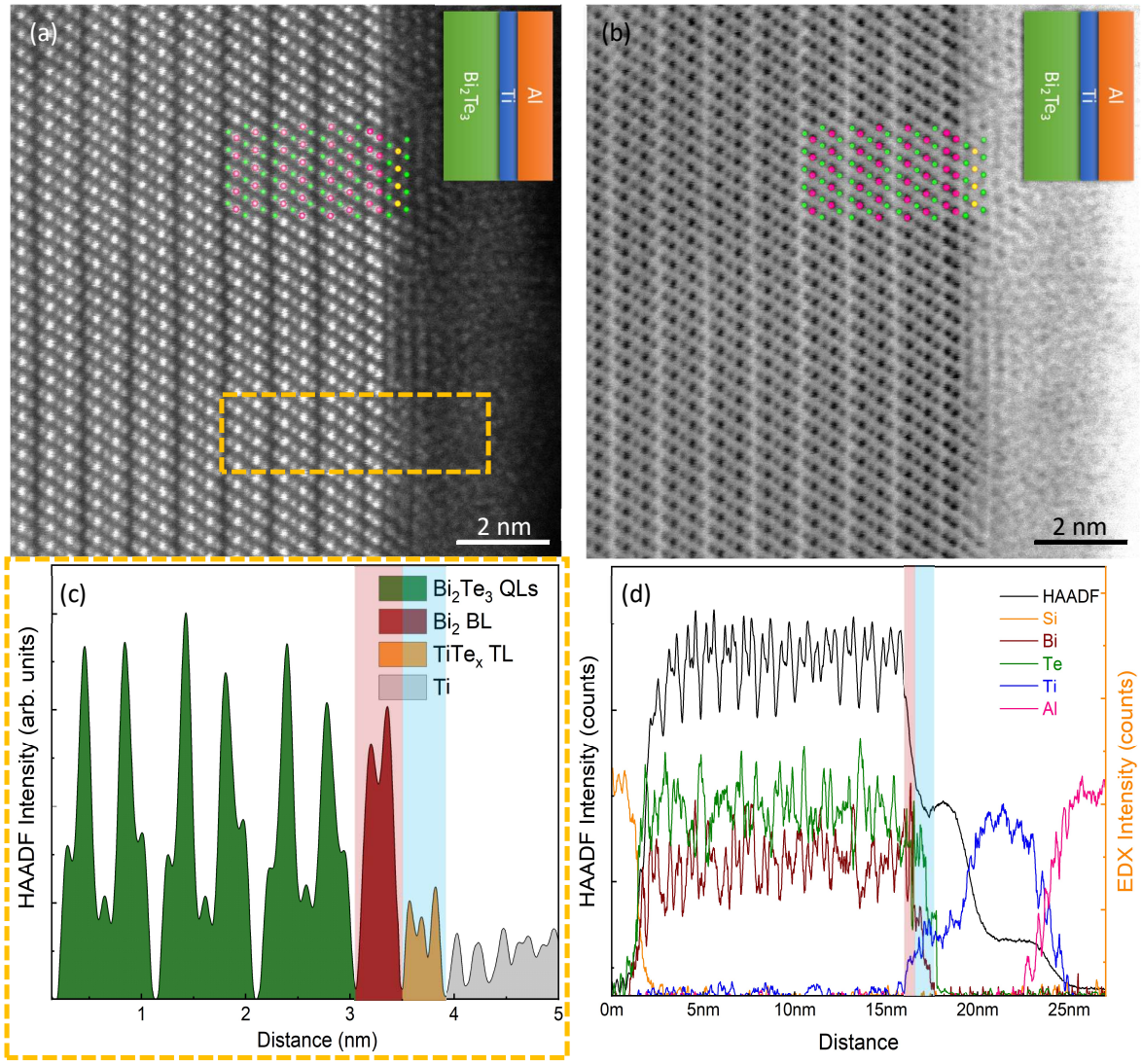

Fig. 7.4: Bi_2Te_3 – Ti – Al interfaces. (a) STEM-HAADF image acquired at the cross-section of TI epilayer along Si [1-10] projection. Ti atoms force the conversion of top Bi_2Te_3 QL into of Bi_2 bilayer and form $TiTe_2$ (TMDC) like structure that is damaged due to extensive lateral strain induced by the evolution of hybrid stacking introduced by Bi_2 bilayer and 16.7 % in-plane lattice mismatch between the stacking layers. The epitaxial interface is evident; although, the clear transformation from trigonal $TiTe_2$ to hexagonal Ti is not witnessed due to damaged TMDC layer ($TiTe_x$) by the lateral strain before the crystalline Ti is witnessed. (b) BF image of (a). (c) Line profile at the interface of the reconfigured surface between Bi_2Te_3 and Ti along the marked area in (a). (d) EDX profile of the complete layer stack Si – Bi_2Te_3 – Ti – Al, indicating the formation of Bi_2 bilayer (red zone) and the intermediate region with $TiTe_x$ (blue zone). Similar to the case of Nb, the diffusion of Al that is entirely blocked by the thin Ti layer is also evident in the profile.

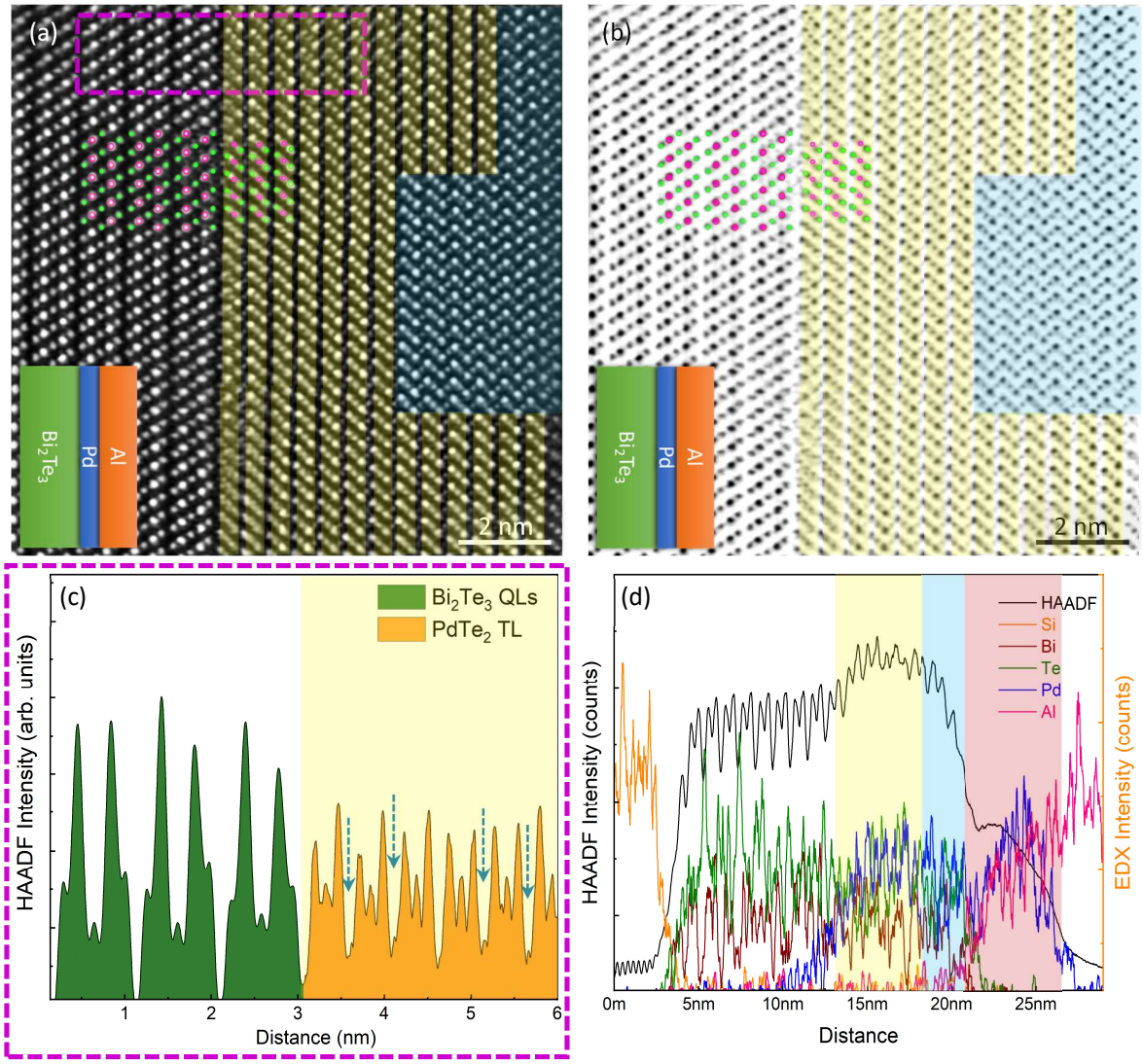

Fig. 7.5: Bi_2Te_3 – Pd – Al interfaces. (a) STEM-HAADF and (b) BF images acquired at the cross-section of TI epilayer along Si [1-10] projection. Pd atoms are observed to diffuse heavily and homogenously (approx. 7 nm) into the Bi_2Te_3 epilayer where they consumed Te atoms and formed $PdTe_2$ (TMDC). Some Pd atoms are intercalated in between $PdTe_2$ trilayers and created an exotic zig-zag like structure (indicated by blue box in a and b). A strain-free epitaxial interface between the diffused epilayer (now $PdTe_2$) and non-diffused TI epilayer is observed. (c) The line profile at the interface of the reconstructed surface between Bi_2Te_3 and Pd along the marked area in (a), the blue marked arrows identify the intercalated atoms. (d) EDX profile of the complete layer stack Si – Bi_2Te_3 – Pd – Al, indicating the heavily diffused TI region forming Bi containing $PdTe_2$ (yellow zone) and Pd_1Te_1 (blue zone). The diffusion of Al is not as efficiently blocked by the thin Pd layer as by Nb and Ti due to $AlPd_x$ alloy formation (red zone), as evident in the EDX profile.

- The Pd based junction (Figure 7.5) exhibited very different behavior than Nb and Ti. Without the presence of any Bi_2 bilayer, several trilayer like structures with the compositional presence of Pd, Te and Bi are observed having a well-defined interface with Bi_2Te_3 QL. This newly appeared interface between TI and trilayer structures exhibited the presence of a translation shear fault (TSF defect) that indicates the existence of weakly bonded and strain-free stacking of layers at the interface. At places, the formation of exotic zig-zag like structures with the intercalated atoms in the VdW gaps, is also observed (blue box in Figure 7.5a) before the crystalline Pd layer is reached.
- The Pt based junction (Figure 7.6) exhibited similar behavior to Pd where the presence of a structure containing three trilayers exhibiting a well-defined and epitaxial interface with Bi_2Te_3

epilayer is witnessed. Within the trilayer structures, the presence of a twin domain and a TSF (red oval and blue arrow in Figure 7.6a respectively) are also visible; however unlike Pd, the VdW gaps of trilayer structure exhibited no intercalated atoms. Following the trilayer structure, the epitaxial stacking of crystalline Pt thin film is also observed before the Pt-Al interface is reached.

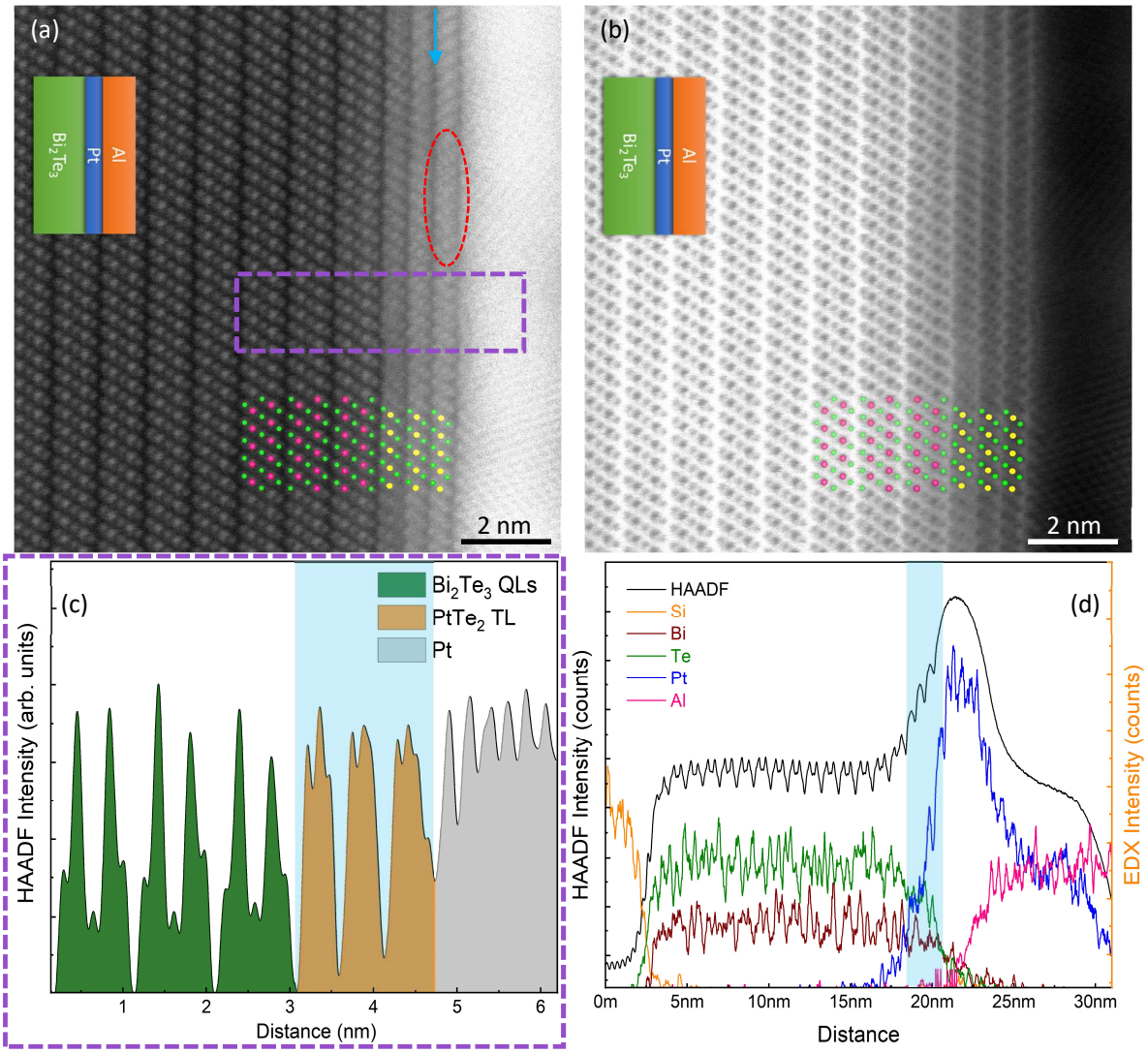

Fig. 7.6: Bi_2Te_3 – Pt – Al interfaces. (a) STEM-HAADF and (b) BF images acquired at the cross-section of TI epilayer along Si [1-10] projection. Pt atoms diffused slightly and homogenously (approx. 1 – 1.5 nm) into the Bi_2Te_3 epilayer, consumed Te atoms and formed $PtTe_2$ (TMDC) while the residual Bi atoms are also consumed and $PtBi_2$ trilayer structures are formed. That is why, no intercalated atoms are observed in Pt based TMDC layers. Both materials i.e. $PtTe_2$ and $PtBi_2$ exhibit a trigonal crystal structure and therefore, strain-free and epitaxial interfaces between the $PtTe_2$/$PtBi_2$ and Bi_2Te_3 epilayer, and between Pt and $PtTe_2$ trilayer are observed. (c) Line profile at the interface of the restructured surface between Bi_2Te_3 and Pt along the marked area in (a). (d) EDX profile of the complete layer stack Si – Bi_2Te_3 – Pt – Al, indicating the slightly diffused TI region forming Pt based TMDC like structures (blue zone). The diffusion of Al is blocked, not as efficiently as by Nb and Ti, though much improved with respect to Pd.

Considering the standard growth conditions, the presence of Bi_2 BL in the Nb and Ti based junctions is unexpected. The observed formation and compositions of trilayer like structures has confirmed the phenomenon of structural reconfiguration at the TI surface that are required to be understood along with the appearance of an amorphous region in the Bi_2Te_3 – Nb – Al junction.

7.2.2 Evolution of generation – II interfaces

All barrier metals are observed to diffuse into Bi_2Te_3 epilayer; however, the observed diffusion according to EDX profiles in Figures 7.3 - 7.6 is quite different from one metal to another. Nb and Ti exhibited the similar behavior with almost non-considerable diffusion. Pd diffused heavily up to 7 nm while Pt is observed to diffuse approx. 1.2 nm into Bi_2Te_3 epilayer. After the diffusion of barrier metal into the TI epilayer, the structural reconfigurations have occurred that led to the formation of new interfaces. The evolution of new interfaces must be understood separately for each materials and, is discussed below.

Based on the structural investigations of the interfaces via STEM and EDX spectrum of Nb and Ti based junctions (Figures 7.3 and 7.4), the surfaces have reconfigured in the following order:

- The incoming atoms of material X (Nb or Ti), due to their higher reactivity with Te than Bi, reacted with the top Te atomic layer of Bi_2Te_3 QL and eventually damaged it.
- This phenomenon forced the damaged/instable Bi_2Te_3 QL to transform into stable Bi_2 bilayer while Te atoms in that particular QL are extracted and consumed by the incoming atoms of material X to form XTe_2 (trilayer structures) as depicted in Figure 7.7.
- XTe_2, in general, known as the transition metal dichalcogenide (TMDC)[59, 60, 61] is a 2D material that exhibits a trigonal crystal structure with the VdW based trilayer architecture. The transformed TMDC layer rearranged itself via VdW interactions with the remaining TI epilayer. This phenomenon is known as the self-epitaxy[14, 62]. As a result of the self-epitaxy between the newly evolved TMDC layer and Bi_2 bilayer, a well-defined and epitaxial interface has evolved (Figure 7.7).

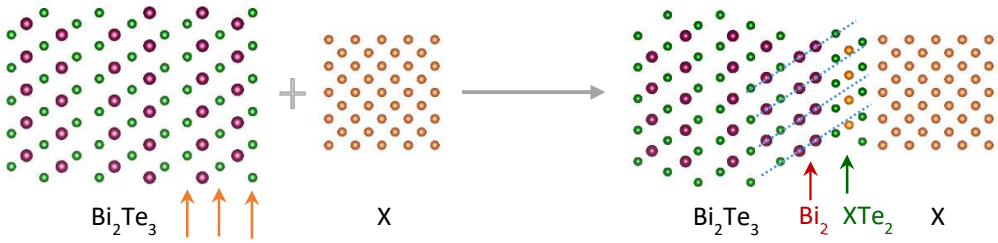

Fig. 7.7: A toy-model representation of the dynamics at the interface. (Left) The incoming atoms of material X interact with the exposed Te atoms of Bi_2Te_3 QL, damage the QL and force the transformation into Bi_2 bilayer. Meanwhile, they consume all Te atoms of the top QL and subsequently form TMDC trilayer structure of XTe_2 that align itself with the extra X atoms in the crystalline order. Considering the newly evolved interface between Bi_2 and XTe_2 being strain-free and relaxed, the one to one correspondence (coherent interface) will not be observed (indicated by blue dotted lines).

The interfaces of both materials (Nb and Ti) are witnessed to evolve in the exact same order as discussed above; however, certain deviations are observed including heavily damaged layer of XTe_2 (TMDC) and approx. 0.5 nm wide region of an amorphous state between crystalline XTe_2 and X before X-Al interface is reached. These deviations are discussed individually for each material X (Nb and Ti) in the next section. Before that, the interface evolution in Pd and Pt based junctions is discussed. Pd atoms are observed to diffuse heavily into the Bi_2Te_3 epilayer where a new interface has evolved at the edge of the diffusion limit (deep into the epilayer). Based on structural investigations via STEM and EDX spectrum (Figures 7.5), the evolution of a new interface have occurred in the following order.

- The incoming atoms of Pd diffused heavily into Bi_2Te_3 epilayer. STEM measurements indicated the extent of diffusion to approx. 7 nm.
- Due to higher reactivity of Pd towards Te than Bi, the diffused Pd atoms readily reacted with the existed Te atoms in the TI epilayer and transformed into $PdTe_2$ like trilayer architecture (indicated

by yellow shaded layers in Figure 7.5a) and exhibited the self-epitaxy with the remaining (non-diffused) TI epilayer via VdW stacking.

- At VdW gaps between $PdTe_2$ trilayer structures, the manifestation of relatively light atoms (most probably Pd) are observed to be intercalated in low density near the interface with TI epilayer. Their presence can also be witnessed in the line profile of HAADF image, depicted in Figure 7.5c (marked with blue arrows). Away from the interface, however, the density of intercalated Pd atoms seems to increase and resulted in the formation of a layer-free architecture with the exotic zig-zag structure (blue shaded region in Figure 7.6a), that after calculations of the atomic bond lengths seems to be a hexagonal structure of Pd_1Te_1.
- EDX spectrum indicates that both regions i.e. $PdTe_2$ trilayer area and Pd_1Te_1 layer-free structure, contain a substantial fraction of Bi as well (Figure 7.6d). To date, it is not known where exactly Bi is incorporated. Interestingly, the presence of Bi in Pd_1Te_1 region does not affect the structural characteristics of the region as $PdBi_x$ alloy also exhibits the hexagonal crystal structure[63, 64].

Pt, unlike Nb and Ti, diffused into the TI epilayer; however, the observed diffusion is quite limited in comparison to the Pd (Figure 7.6). The STEM investigations suggest that the evolution of a new interface has occurred in the following steps.

- The incoming atoms of Pt diffused slightly into the TI epilayer. STEM measurements indicated the extent of diffusion to approx. 1.2 nm uniformly throughout the sample.
- Due to higher reactivity of Pt towards Te than Bi, the diffused Pt atoms readily reacted with the nearby Te atoms into the TI epilayer and transformed into $PtTe_2$ like trilayer architecture (TMDC) and exhibited the self-epitaxy with the remaining (non-diffused) TI epilayer (Figure 7.6a and b).
- Pt, unlike all others barrier materials, utilized the residual Bi atoms in the diffused TI epilayer and transformed in $PtBi_2$ based trilayer structure along with $PtTe_2$ forming $Pt(Bi,Te)_2 = PtBi_xTe_{(2-x)}$ trilayer alloy. This trend is also evident in the EDX profile (Figure 7.7d) where the intensity of both elements i.e. Bi and Te is observed to drop gradually instead of an abrupt drop in the intensity, witnessed in the case of Nb and Ti. That is why, entirely clean VdW gaps without any intercalated atoms are observed in Pt based trilayers (Figure 7.6a and b).

7.2.3 Discussion

The evolution of generation-II interfaces due to the diffusion of barrier metals into the TI epilayer is discussed for each layer stack. The resulting chemical changes and structural reconfigurations at the surface, their electronic properties and the performance of the barrier materials to block Al from diffusion and reaching the TI epilayer must be understood and thus, is discussed below.

Structural reconfiguration in Nb layer stack: The Nb barrier at the TI surface results in the formation of $NbTe_2$ (TMDC) trilayer like structure (Figure 7.3). As mentioned earlier, $NbTe_2$ is a non-topological semi-metal[29] that exhibits superconductivity at 0.5 K[30, 31, 32]. Similar to most TMDCs, it exhibits a trigonal crystal structure with the in-plane lattice constant a = 3.68 Å[65, 66, 67] which results in approx. 19.5 % lattice mismatch with Bi_2Te_3 QL. One of the greatest advantage of VdW epitaxy is the structural support to construct heterostructures of various materials with diverse layer architecture (layer size) and different in-plane lattices that can be stacked on top of each other without any lateral strain or dislocations as long as two following conditions are fulfilled.

- The materials must belong to the compatible crystal structure.
- They must exhibit the pristine VdW stacking (between similar elements) for example Bi_2Te_3 (QL) and $NbTe_2$ (trilayer). Both materials exhibit Te at the starting and ending atomic positions (for details of pristine vs. hybrid VdW stacking visit chapter 4, Figure 4.7).

If both of above mentioned conditions are fulfilled, the structures with diverse in-plane lattice parameters can be stacked on top of each other where the atoms of different layers may not exhibit the in-plane one to one atomic correspondence with each other as depicted in Figure 7.7 (follow blue dotted lines). Such interfaces are called incoherent interfaces[68, 69, 70].

Unfortunately, the evolution of Bi_2 bilayer at the interface negates the second condition and introduces the hybrid stacking on both sides between Bi_2Te_3 QL - Bi_2 bilayer (Te-Bi) and Bi_2 bilayer - $NbTe_2$ trilayer (Bi-Te). As witnessed in chapter 4 (section 4.6), the hybrid stacking between Bi and Te atoms is strong enough to compress the entire Bi_xTe_y crystal vertically and stretch laterally. Here, the hybrid VdW interaction provides another example where Bi_2 bilayer forced the Te atoms of $NbTe_2$ layer to stretch and follow one to one stacking (forced the incoherent interface to be coherent) and in result introduced 19.5 % lateral strain in $NbTe_2$ layer and eventually damaged it (named $NbTe_x$). This phenomenon also results in the non-epitaxial stacking of crystalline Nb with the strained $NbTe_x$ through the formation of 0.5 nm wide amorphous region (Figure 7.3a and b). The amorphous region assists in neutralizing the lateral strain and on top of the amorphous region, the crystalline structure of Nb thin film is evident where Nb (220) planes can be observed in Figure 7.3. The hybrid stacking induced lateral strain provides only partial epitaxial interface (an epitaxial but strained interface). On the other hand, Nb provides good results as the blocking material and prevents Al atoms from reaching TI epilayer. Thus, the formation of any Schottky barrier is avoided as witnessed in the EDX profile (Figure 7.3d).

Structural reconfiguration in Ti layer stack: The Ti layer presents similar results as observed in Nb based heterostructures (Figure 7.4). Ti atoms do not diffuse into Bi_2Te_3 epilayer rather reconfigure the interface by transforming the top QL into Bi_2 bilayer and $TiTe_2$ like trilayer as depicted in Figure 7.4. $TiTe_2$ is a trivial semi-metal[71, 72] and exhibits a trigonal crystal structure with the in-plane lattice constant a = 3.77 Å[73, 74, 75] which brings it to approx. 16.7 % lattice mismatch with Bi_2Te_3 QL. Here, similar to $NbTe_x$, $TiTe_x$ represents the damaged $TiTe_2$ due to extreme lateral strain induced by the hybrid VdW stacking. On top of the strained $TiTe_x$, the hexagonal arrangement of Ti atoms is visible. Ti also provides suitable results as the blocking material and prevents the diffusion of Al atoms from reaching the TI epilayer as witnessed through the EDX profile in Figure 7.4d.

Modifications to avoid hybrid stacking: Nb and Ti, both materials present overwhelming results as the inter-diffusion barrier; however, their interfaces require minor modifications. One of the main drawback experienced while utilizing both materials, is the formation of Bi_2 bilayer and the appearance of hybrid stacking that laterally strains the TMDC layers and damage them. This phenomenon occurred due to only one reason, the unavailability of sufficient Te atoms at the surface to form the strain-free TMDC structures without damaging the Bi_2Te_3 QL, and it can be completely avoided by providing extra Te at the interface. These are two possibilities to achieve it *in situ* via MBE system.

- The first is the co-evaporation of Te along with Nb/Ti. The incoming flux of Te will assist the formation of $NbTe_2$/$TiTe_2$ without the requirement of utilizing Te atoms from the TI epilayer. The formation of Bi_2 bilayer will be avoided and strain-free epitaxial interfaces will be achieved.
- The second method is the substitution of the first approach if the co-evaporation of the materials is not possible. In this method, a couple of nm extra Te layer can be deposited on top of TI epilayer. The incoming Nb/Ti atoms will consume the extra Te atoms without affecting the TI epilayer and the relaxed stacking with the epitaxial interfaces will be achieved. This technique is already utilized in fabricating high quality $Bi_2Te_3 – TiTe_2$ heterostructures[76, 77, 78]. To the best of our knowledge, the high resolution or atomic-scale structural investigations have never been performed; however, the detailed XRD investigations have confirmed the formation of strain free heterostructures[77].

An unexpected advantage of the Bi_2 bilayer formation, as observed in Figure 7.3 and 7.4, is the capability of utilizing it as a tool to apply uniaxial strain to $NbTe_2$ and $TiTe_2$ layers as they are proposed to exhibit a

series of topological phase transitions under strain[79]. This feature is not the purpose of this study and therefore, any further experiments are not conducted; however, it provides a new experimental platform for the realization of topological phases in these materials that was not possible before and the investigations were limited only to the theoretical models.

Nb and Ti as diffusion barrier for Sb based TIs: The structural investigations are also conducted at the interface of Sb_2Te_3-Nb-Al and Sb_2Te_3-Ti-Al hybrid junctions. However, unlike Bi_2Te_3, Sb_2Te_3 do not present similar results rather both Nb and Ti are observed to diffuse into the TI epilayer. Due to diffusion, the formation of Sb_2 bilayer and the appearance of hybrid stacking is not witnessed.

- The interface at Sb_2Te_3-Nb-Al is found to be exactly similar to Figure 7.1 with the formation of approx. 3 nm thick amorphous inter-mixed region. Despite the shortcoming of an epitaxial interface, Nb displays the features of a strong inter-diffusion barrier and blocks the diffusion of Al atoms from reaching the TI epilayer thus, the formation of any Schottky barrier is avoided.
- Similar to Nb, Ti atoms are also observed to diffuse 3 nm in Sb_2Te_3 epilayer. Ti atoms form an approx. 4 nm wide region with a poly-crystalline structure containing Ti based binary Ti_xSb_{2-x} and ternary $Ti_xSb_{2-x}Te_3$ alloys[80, 81, 82]. Ti_xSb_{2-x} is a topological semi-metal[83, 84]; however, it exhibits the tetragonal crystal structure while the ternary $Ti_xSb_{2-x}Te_3$ alloy exhibits a meta-stable crystalline structure and is a well-known phase change material (PCM)[82]. It readily converts into an amorphous phase with a high resistive state and therefore, it may result in the formation of a Schottky like barrier. Ti film is failed to block the diffusion of Al atoms into Sb_2Te_3 due to diffusive nature of both Sb and Al. The STEM-HAADF image acquired at the interface of Sb_2Te_3-Ti-Al junction is depicted in Appendix 7A.

Structural reconfiguration in Pd layer stack: The Pd barrier at the Bi_2Te_3 results in the formation of several $PdTe_2$ (TMDC) trilayer and Pd_1Te_1 layer-free structures (Figure 7.5). $PdTe_2$ is a semi-metal that unlike $NbTe_2$ and $TiTe_2$ exhibits topologically non-trivial attributes and belongs to the class of type-II Dirac semi-metal (DSM) [85, 86, 87]. Along with the topology, $PdTe_2$ exhibits type-I superconductivity with T_C = 1.7 K [88, 89, 90, 91]. Both of these features render $PdTe_2$ itself a very conspicuous material for TSC[92]. However, here it is utilized as an intermediate source to block Al atoms from reaching TI epilayer and to engineer an epitaxial interface between Bi_2Te_3 and Al. Pd_1Te_1 and Pd_1Bi_1, both are semi-metals that exhibit a hexagonal crystal structure with P_{63}/mmc (194) space group[63, 64, 84, 93]. Pd_1Te_1 exhibits type-II superconductivity at 4.5 K[94] while Pd_1Bi_1, similar to $PdTe_2$, exhibits type-I superconductivity[95, 96] with T_C = 1.6 K. Moreover, $PdBi_x$ unlike $PdTe_2$, exhibits the non-centrosymmetric superconductivity[95, 96, 97] and recently reported to exhibit signatures of an odd-parity 3D topological superconductivity[98] in the tetragonal phase (β-$PdBi_2$).

The lattice parameters of the TMDC trilayer and the exotic zig-zag structures are measured via STEM. The parameters of the trilayer architectures are found to be a = 4.12 ± 0.04 Å and c = 5.14 ± 0.02 Å that are in good agreement with the earlier reported values $PdTe_2$ (a = 4.11 Å)[99, 100] and confirm the formation of TMDC structure. The parameters of the zig-zag structures are found to be a = 4.24 ± 0.04 Å and c = 5.68 ± 0.02 Å that that are in good agreement with the values of hexagonal Pd_1Te_1 (a = 4.22 Å)[84, 93] and Pd_1Bi_1 (a = 4.23 Å)[63, 64]. The formation of $PdTe_2$ and layer free architecture ($Pd_1Bi_xTe_{1-x}$) is observed to be dependent on the relative presence of Pd in the region. Near the interface with Bi_2Te_3 epilayer, the presence of Pd is less pronounced and therefore, only trilayer architecture of $PdTe_2$ is witnessed. However, 4 nm away from the interface, Pd is available in abundance and it facilitates the formation of the layer-free architecture. This trend can easily be observed in Figure 7.5a and b (blue colored zone).

As mentioned above, $PdTe_2$ exhibits a trigonal crystal structure with the in-plane lattice constant a = 4.11 Å[99, 100] which causes a lattice mismatch of 6.3 % with Bi_2Te_3 QL at the interface. Unlike the case of Nb and Ti where the presence of hybrid VdW stacking induces strain in the TMDC layers, $PdTe_2$ – Bi_2Te_3 interface exhibits the pristine vdW stacking i.e. the strain-free and entirely relaxed layer stacking between

Te-Te atoms. That is why, the one to one stacking (coherent interface) that can only be witnessed between the lattice matched layers or in the strained layers via hybrid vdW stacking, is not witnessed in $PdTe_2$. Also, the presence of a TSF at the newly evolved interface is another evidence of weakly bonded and strain-free layer stacking of Bi_2Te_3 – $PdTe_2$ layers. In general, Pd after diffusion forms $PdTe_2$ near the interface and exhibits a well-defined and epitaxial interface with the TI epilayer.

Pd unlike Nb and Ti, exhibits different behavior and diffuses in both regions i.e. in Bi_2Te_3 epilayer and in the Al film as well. Almost half of the deposited Pd is observed to diffuse into the TI epilayer where it transforms into the TMDC structure of $PdTe_2$ (in the less diffused regions) and into the layer-free architecture of $Pd_1Bi_xTe_{1-x}$ (in the heavy diffused regions) while the remaining Pd atoms are observed to diffuse into Al layer forming $AlPd_x$ alloy. Al, that is witnessed to be entirely blocked from diffusion by Nb and Ti thin films (Figure 7.3 and 7.4), is observed to slightly diffuse into TMDC structure of $PdTe_2$, depicted in Figure 7.5d; however, no formation of $AlTe_x$ is witnessed in HAADF images rather an intermediate states of $AlPd_x$ alloy is observed (red zone in Figure 7.5d). $AlPd_x$ exists in several stoichiometric states, all of them exhibit metallic behavior and therefore, should not be a problem for the formation of a Schottky barrier.

Pd as diffusion barrier for Sb based TIs: Sb_2Te_3-Pd-Al junction is not investigated as recently an STEM study on BST-Pd hybrid structure is conducted by Bai *et al*.[14] without the Al layer on top; however, it provides the relevant information about the interface. In case of Pd as the diffusion barrier, both Sb and Bi based TIs exhibit almost similar behavior. The only difference observed is in Sb based TIs with the diffusion of Pd into TI epilayer that is not homogeneous[14] while in the case of Bi_2Te_3, the diffusion of Pd and the formation of new interface is well-defined and uniform all over the sample. In general, Pd as the diffusion barrier between TI and Al, provides an atomically sharp and epitaxial interface and also blocks the formation of any Schottky barrier. The only drawback is the heavy diffusion of Pd into the TI epilayer that can be problematic for ultra-thin samples and the unexpected electronic behavior in the JJ based devices that might originate from the topological or superconductive nature of $PdTe_2$, Pd_1Te_1 or $PdBi_x$ alloys.

Structural reconfiguration in Pt layer stack: The Pt barrier at the Bi_2Te_3 results in the formation of three well-defined $PtTe_2$ (TMDC) and $PtBi_2$ trilayer-like structures (Figure 7.6). $PtTe_2$ is semi-metal[85] that similar to $TiTe_2$ does not exhibit superconductivity while its topology depends upon the thickness of the epilayer[101]. One monolayer (ML) of $PtTe_2$ (ML = trilayer structure of $PtTe_2$) is a very narrow bandgap semiconductor[102], 2 MLs become semi-metallic[103, 104] while 4 and more MLs crossover and start to exhibit topological attributes[102] and belong to the class of type-II Dirac semimetals (DSM) [101, 105, 106, 107]. $PtBi_2$ is also a semi-metal that exhibits Dirac surface states[108, 109] and conventional superconductivity below 600 mK[110, 111]. It exhibits hexagonal family compatible crystal structure in multiple phases including layered based structure in P-3 (147) [110, 112, 113] and P31m (157) [110, 112, 113] space groups; however, with the increasing availability of Pt atoms, it readily converts into the layer-free architecture of Pt_1Bi_1 with the zig-zag structure and exhibits P_{63}/mmc (194) space group[110, 114, 115], similar to the structure observed in Pd based junctions in Figure 7.5.

The lattice parameters of each TMDC trilayer are measured via STEM. The parameters of the trilayers are observed to deviate from each other indicating the localized compositional changes among them. The parameters of the first layer, in contact with Bi_2Te_3 epilayer, are found to be a = 4.11 ± 0.04 Å and c = 5.39 ± 0.03 Å while the parameters of the last layer, in contact with Pt, are found to be a = 4.23 ± 0.04 Å and c = 5.63 ± 0.03 Å that are much closer to reported values of $PtBi_2$[101, 106, 116, 117]. It indicates that the diffused Pt reacts readily with Te atoms and forms Te rich $PtBi_xTe_{(2-x)}$ trilayer closer to the TI epilayer while the trilayer in proximity to Pt is relatively Bi rich, indicated by the enhanced lattice parameters and confirmed via the EDX spectrum (Figure 7.6d).

$PtBi_2$ and $PtTe_2$, both exhibit the in-plane lattice constants a = 4.16 Å[110, 112] and 4.09 Å[101, 106, 116, 117] respectively which brings them to approx. 6.2 % lattice mismatch with Bi_2Te_3 QL at the interface. Similar to the case of $PdTe_2$, Pt based trilayers exhibit entirely strain-free and relaxed stacking forming a well-defined

epitaxial interface with the TI epilayer as depicted in Figure 7.6. It is interesting to notice that Pt similar to Pd utilizes Bi; however, it forms $PtBi_2$ trilayer structure allowing the possibility of achieving the perfectly relaxed and strain free interface. As observed, Pt also forms uniformly and homogenously only 3MLs of $PtTe_2$ (layers also contain Bi) that electronically act as a metal without any topological attributes. If required, with the co-evaporation of Te, the number of $PtTe_2$ layers can be increased and the topological attributes can be switched on. Pt as the diffusion barrier between Bi_2Te_3 and Al, allows self-diffusion; however, blocks Al atoms from reaching the TI epilayer and prevents the formation of any Schottky-like barrier. This trend can be visualized via EDX spectrum depicted in Figure 7.7d.

Pt as diffusion barrier for Sb based TIs: The interface investigations are conducted at Sb_2Te_3-Pt-Al junction as well. In case of Sb_2Te_3, almost similar behavior to Bi_2Te_3 is observed with a few minor differences.

- Unlike Bi, Sb atoms do not form layered structure of $PtSb_2$; however, the formation of layer-free architecture of Pt_1Sb_1 is possible but not observed.
- Due to diffusive nature of Sb, Pt is observed to diffuse further (up to 2.5 nm and inhomogeneously) into the TI epilayer and that is why, the total number of $PtTe_2$ layers, unlike Bi_2Te_3, is observed to be non-uniform and varies between 3 to 6 trilayers at different locations. The HAADF image is depicted in Appendix 7A.
- Unlike the case of Bi, the atomically clean vdW gaps between $PtTe_2$ trilayers are not observed mostly due to residual Sb atoms intercalated in between $PtTe_2$ layers, depicted in Appendix 7A.

7.2.4 Conclusions

As introduced earlier, all of the selected barrier metals i.e. Nb, Pt and Pd except Ti belong to the cubic crystal structure and thus, are expected to exhibit structural defects at the interface. The formation of such defects is not witnessed; however, as soon as these materials are introduced at the surface of the TI epilayer, they diffuse and interact with the Te atoms (present in the QLs), restructure the TI surface by forming the corresponding telluride i.e. $NbTe_2$, $TiTe_2$, $PtTe_2$ and $PdTe_2$ that are known as TMDCs. These trilayer structures (TMDCs) provide artificially engineered epitaxial interfaces through the vdW assisted self-alignment with the residual TI epilayer.

Based on the structural and chemical investigations of the diffusion barriers and their performance, the key observations are summarized individually for Bi_2Te_3 and Sb based TIs.

Engineering self-epitaxial interfaces for Bi_2Te_3: The structural investigations have revealed that the interaction of each blocking material with Bi_2Te_3 epilayer and the resulting structural reconfiguration occurs in slightly different fashion; however, the most critical feature that differentiates each material from one another is the extent of diffusion into Bi_2Te_3. Based on this feature, the barrier materials and the interface evolution in Bi_2Te_3 hybrid structures are categorized in following three groups.

- ***Diffusion-prohibited self-epitaxy of TMDC:*** Nb and Ti belong to this group. Both materials do not diffuse into the TI epilayer at all; however, the higher reactivity towards Te results in the forced transformation of top QL into Bi_2 bilayer and the hybrid vdW stacking induced strained TMDC layers that provide only partial-epitaxial interfaces. These materials exhibit the best capability to block Al atoms from reaching the TI epilayer. $NbTe_2$/$TiTe_2$ are not only preferred for the low temperature superconducting applications but also at higher temperatures they demonstrate a high resistance against diffusion and present ohmic contacts with the TI epilayers[118, 119].
- ***Diffusion-assisted self-epitaxy of TMDC:*** Pd belongs to this category. Pd atoms diffuse heavily into Bi_2Te_3 and transform the diffused TI into $PdTe_2$ trilayer and Pd_1Te_1 + $PdBi_x$ layer-free architectures. An atomically sharp (well-defined), epitaxial and strain-free interface establishes between $PdTe_2$

and the residual Bi_2Te_3. Pd exhibits relatively poor capability to block Al atoms from diffusion due to the formation of $AlPd_x$ alloy.

- ***Diffusion-limited self-epitaxy of TMDC:*** Pt belongs to this category. Pt atoms diffuse slightly into Bi_2Te_3 epilayer and consume both, Te and Bi atoms to transform into the trilayer architecture. The evolved layers of $PtTe_2$/$PtBi_2$ not only establishes a strain-free and well-defined epitaxial interface with Bi_2Te_3 but also with the crystalline Pt layer. Pt exhibits good capability to block Al atoms from reaching the TI epilayer.

Structurally, all barrier metals with Bi_2Te_3 exhibit the acceptable results (i.e. provide the formation of epitaxial interfaces and block Al atoms from diffusion and interacting with the TI epilayer). The observed shortcoming with Ti and Nb with the formation of Bi_2 bilayer can be easily avoided. The heavy diffusion of Pd into Bi_2Te_3 and the realization of $PdTe_2$ and Pd_1Te_1 with distinct topological and superconducting features can impact of the intrinsic junction characteristics and therefore, is the least recommended. However, the selection of the best barrier metal cannot be performed only on the basis of structural characteristics and therefore, JJs of each barrier materials with Bi_2Te_3 are fabricated and their electronic performance is investigated in section 7.3 to conduct a comparative analysis among them.

Engineering self-epitaxial interfaces for Sb based TIs: Due to the diffusive nature of Sb, Sb_2Te_3 and BST alloys exhibit similar behavior of the interface evolution with the barrier metals that differs from the above discussed results of Bi_2Te_3. The interface with Nb results in the formation of a diffused amorphous region (Figure 7.1). Similarly, Ti after diffusion forms a polycrystalline inter-mixed region at the interface that exhibits PCM characteristics. Both of them do not provide epitaxial interfaces. Pd and Pt with Sb containing TIs exhibit almost similar behavior to Bi_2Te_3 with minor differences and present a possibility to achieve epitaxial interfaces. Due to excessive diffusion of Pd, it is not recommended to use for the thin films and therefore structurally, Pt is ranked as the best material for Sb based TIs to engineer epitaxial interfaces.

Interface adaptations for Bi_xTe_y alloys: The epitaxial growth of the topologically rich family of Bi_xTe_y stoichiometric alloys is discussed in chapter 4. Due to the structural and observed similarity in growth mechanics (chapter 4) and oxidation process of Bi_xTe_y alloys with Bi_2Te_3 (chapter 6), the evolution of interfaces in Bi_xTe_y surfaces can be projected. One of the most critical requirement to fabricate devices containing Bi_xTe_y hybrid junctions is that the interface evolution must not alter the stoichiometry (composition) of the alloy. Based on this principle, Pd cannot be used as it diffuses heavily into the epilayer and thus, it will alter the composition of the alloy. Nb and Ti do not diffuse; however, they both force the transformation of the top QL into Bi_2 bilayer that will alter the composition locally on one hand, and would impact on the density of surface states and the topology on the other hand as witnessed in case of Bi_4Te_3, discussed in Figure 4.37. Using the modified approach of Te co-evaporation, discussed in section 7.2.3, this problem can be resolved for some stoichiometric alloys; however, the co-evaporation may lead to the stoichiometric deviations in other Bi_xTe_y alloys due to diffusion of Te into the epilayer. In cases, where the top layer of Bi_xTe_y film is Bi_2 bilayer instead of Bi_2Te_3 QL, Nb and Ti would present epitaxial interfaces without any transformations. Pt, on the other hand, is the only material that utilizes both elements i.e. Te and Bi and, in result, forms the vdW assisted trilayer architecture that provides epitaxial interfaces. In summary, all three materials i.e. Pt, Nb and Ti can be utilized to engineer epitaxial interfaces with Bi_xTe_y alloys with minor adjustments.

Interface adaptations for Bi_2Se_3: Though, the interface characterization of barrier metals with Bi_2Se_3 epilayers is not conducted, the information acquired from the structural characterization of other 3D TIs has provided a generalized platform to estimate the probable interface evolutions in Bi_2Se_3 epilayers. The selected barrier materials i.e. Nb, Ti, Pd and Pt after interacting with Bi_2Se_3 QL will most probably transform into the TMDC structures forming their corresponding selenides i.e. $NbSe_2$, $TiSe_2$, $PdSe_2$ and $PtSe_2$;

however, the realization of the above mentioned TMDCs depends upon the structural compatibility with Bi_2Se_3 and the chemical stability of the corresponding TMDC.

$NbSe_2$ belongs to the hexagonal crystal structure with P 63/mmc (194) space group[120, 121, 122, 123] having the in-plain lattice a = 3.46 Å. It is a semi-metal that exhibits superconductivity at 7.2 K[121, 124, 125, 126, 127]. $TiSe_2$ belongs to the trigonal crystal structure with P-3m1 (164) space group having the in-plain lattice a = 3.54 Å[128, 129, 130, 131]. It exhibits semi-metallic behavior[73, 132, 133, 134, 135] without any superconducting attributes. $PtSe_2$ similar to $TiSe_2$ belongs to the trigonal crystal structure with P-3m1 (164) space group having the in-plain lattice a = 3.73 Å[136, 137, 138, 139]; moreover, it is a semi-metal[103, 106, 140] that exhibits the conventional superconductivity at 2.15 K[141, 142]. It also exhibits the topologically non-trivial attributes and belong to the type-II DSM[142, 143, 144, 145, 146]. Pd forms $PdSe_2$ that unexpectedly exhibits the non-compatible i.e. the monoclinic crystal [147, 148, 149] and the non-metallic band structure[147, 148, 149]. The heavy diffusion of Pd and the structural non-compatibility designates Pd as an inappropriate material for the interface engineering. Except Pd, all barrier metals will most probably exhibit epitaxial interfaces with Bi_2Se_3 epilayers.

A few other adoptable barriers are Mo and W thin films. In Te based TIs, $MoTe_2$ is structurally compatible[150] while WTe_2 is non-compatible (Orthorhombic)[151, 152] and thus, cannot be utilized to acquire epitaxial interfaces. In Se based TIs both, Mo and W will readily transform into $MoSe_2$[153, 154, 155] and WSe_2[156, 157] that exhibit the hexagonal crystal structure with P 63/mmc (194) space group that would facilitate the self-aligned epitaxial interfaces with the Bi_2Se_3 epilayers.

7.2.5 Induced superconductivity in Bi_2Te_3 – B – Al hybrid junctions

In order to evaluate the electronic performance of the barrier metals, Al based JJs of all barrier metals (Nb, Ti, Pd and Pt) containing Bi_2Te_3 as the weak-link, are prepared. The JJs are fabricated *in situ* by combining the techniques of selective area epitaxy (SAE) and the on-chip stencil mask, a technique developed by Schüffelgen *et al*.[28, 33, 158] to shape the metallic electrodes *in situ*, without the requirement of post lithography process; and they are finally capped with 5 nm of Al_2O_3. Figure 7.8 depicts the SEM images of a few prepared junctions where Ti is utilized as the barrier material while the overview of all the fabrication steps can be found in Appendix 7B.

The detailed characterization of the prepared Josephson junctions (JJs) including the evolution and the temperature dependent behavior of Andreev bound states (ABS), temperature dependency of the supercurrent (I_C) to evaluate the diffusive and ballistic carrier contributions, topological signatures via radio frequency (RF) dependent Shapiro response to observe the contribution of 4π-periodic Majorana bound states (MBS) etc. are performed; however, they are not the part of this study. Some of those results along with the details of the measurement setup can be found in Wittl *et al*. while other will be reported in Schmitt *et al*. Here, the main purpose is to identify if the junctions exhibit the signatures of induced superconductivity, a feature that was failed to be achieved in junctions prepared without the inter-diffusion barrier, reported earlier[28]. Secondly, the aim is to compare the different barrier materials on the basis of the junction performance.

The junctions are loaded and cooled down in the Oxford Triton cryogenic system at the base temperature of 15 mK and the I-V measurements are performed. The signature of the induced superconductivity is witnessed with the junction resistance reaching 0 Ω. It can be observed with the help of the differential resistance dV/dI vs. V and I_c vs. V profiles, plotted in Figure 7.9. The similar trend is observed in all the measured junctions containing the entire set of barrier metals exhibiting minor deviations is the junction properties such as the critical temperature (T_c), the critical magnetic field (B_c), and the I_cR_n products etc.

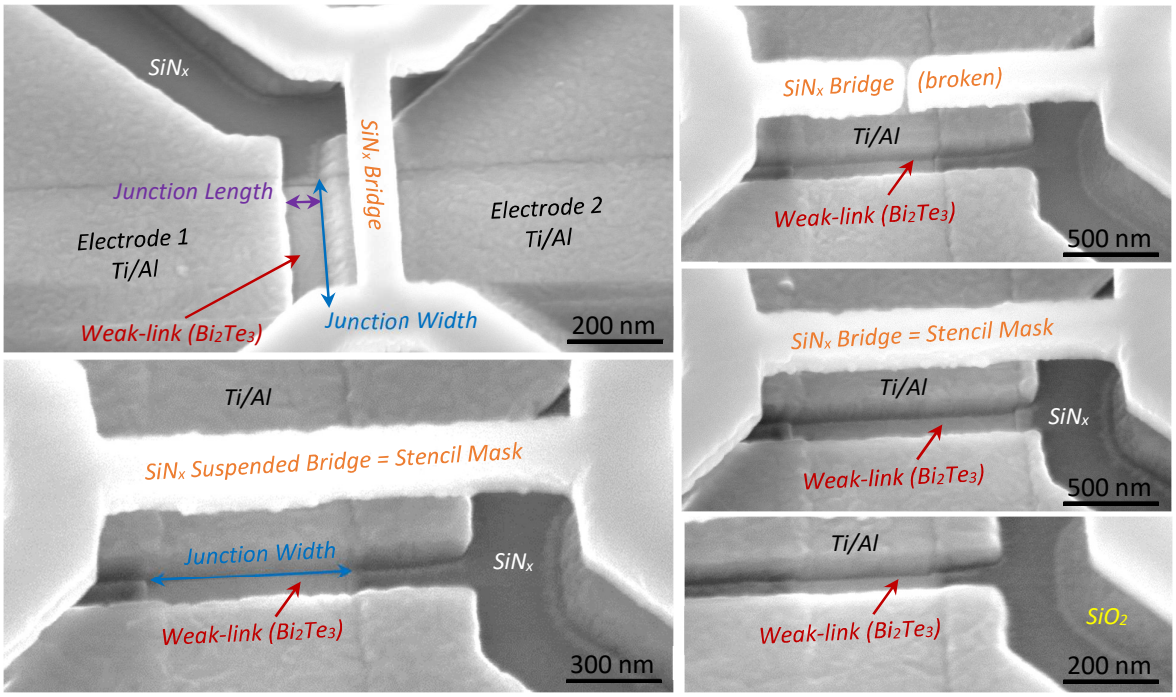

Fig. 7.8: Bird eye view of SEM images providing an overview of the fabricated Josephson junctions containing Bi_2Te_3 as the weak-link, Ti as the inter-diffusion barriers and Al as the superconducting electrodes. Various junctions having different dimensions with changing width and length are depicted. The on chip stencil mask is created with the combinational stack of PECVD based 300 nm SiO_2 and 100 nm SiN_x. The 100 nm thick SiN_x bridges are suspended being supported by 300 nm thick columns of SiO_2 that have facilitated to acquire the designed shape of the Al electrodes.

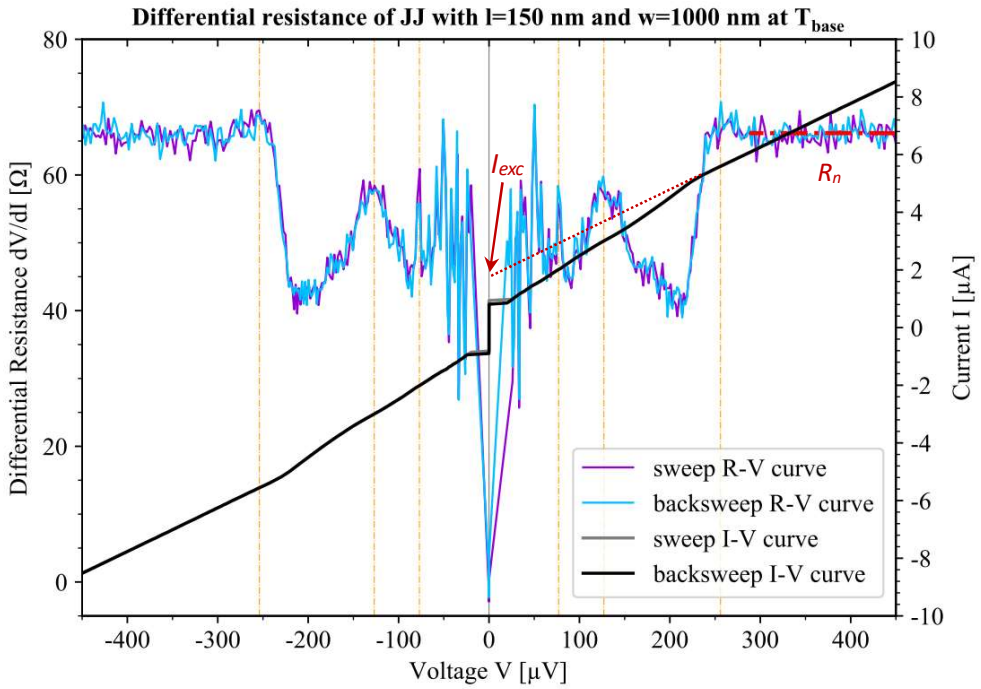

Fig. 7.9: A representation of the long range measurement of I_c vs. V and dV/dI vs. V acquired from a Bi_2Te_3 JJ prepared with Ti as the inter-diffusion barrier and Al as the superconducting electrode having width (W) = 1000 nm and length (L) = 150 nm. The parameters such as the normal states resistance (R_n), the switching current (I_c) and the excess current (I_{exc}) etc. are extracted. The dotted yellow lines are representing the multiple Andreev reflections. (Courtesy: W. Wittl)

Table 7.2: An overview of the measured junction characteristics for all barrier materials in Bi_2Te_3 – Al based JJs.

Junction Parameters [units]	Inter-diffusion Barrier			
	Nb	Ti	Pd	Pt
dimensions (length x width) [nm x nm]	*90 x 1000*	*150 x 1000*	*110 x 300*	*90 x 500*
I_c *= switching current [nA]*	*2206 ± 3*	*981 ± 4*	*7994 ± 15*	*451 ± 1*
R_n *= normal resistance [Ω]*	*58.19 ± 0.01*	*66.2 ± 0.01*	*40.4 ± 0.1*	*145.1 ± 0.01*
I_{exc} *= excess current [nA]*	*2284 ± 0.1*	*1921 ± 0.1*	*2800 ± 5*	*691 ± 3*
Δ' *= induced gap [μeV]*	*170 ± 10*	*123 ± 6*	*158 ± 10*	*180 ± 10*
B_c*= critical magnetic field [mT]*	*12 ± 1*	*19 ± 1*	*40 ± 2*	*26 ± 1*
T_c *= critical temperature [K]*	*0.91 ± 0.025*	*0.82 ± 0.025*	*1.3 ± 0.025*	*0.9 ± 0.025*
I_cR_n *[μV]*	*123 ± 1*	*65 ± 1*	*319 ± 1*	*66 ± 2*
$e\frac{I_{exc}R_n}{\Delta'}$	*0.78 ± 0.05*	*0.93 ± 0.05*	*0.71 ± 0.2*	*0.61 ± 0.1*
$e\frac{I_{exc}R_n}{\Delta}$	*0.44 ± 0.05*	*0.41 ± 0.05*	*0.39 ± 0.2*	*0.378 ± 0.1*
T_1/T_2 *= transparency (%)*	*72/60 ± 2*	*78/58 ± 2*	*68/57 ± 2*	*63/56 ± 1*

Multiple junctions having different dimensions for all barrier materials are measured and the best set of parameters are listed in Table 7.2. The listed parameters cannot be compared directly for different barrier metals as the junction dimensions differ. Also, the induced gap (Δ') cannot be evaluated with certainty as the behavior of the differential resistance at the switching current makes it quite challenging to extract the exact value and that is why, it is reported to perform such measurements in parallel with a shunted resistance[159, 160, 161]. The exact value of the induced gap (Δ') is important as, the parameter $eI_{exc}R_n/\Delta'$ can be evaluated that provides the corresponding value of Z[25, 162, 163, 164] and via Z, the junction transparency can be evaluated using $T = 1/(1+Z^2)$[165]. To have a more reliable comparison, the values of Z and the corresponding T are evaluated using both the Δ' and Δ named T_1 and T_2 in Table 7.2. Anyhow, the I_cR_n product and the transparency (T) are the two parameters that provide the figure of merit for a junction and thus, can be utilized to compare the barrier materials. Based on the obtained results the key observations are discussed below:

- Pd through the formation of $PdTe_2/Pd_1Te_1$, as expected, has heavily impacted the junction characteristics. It can be realized from the measured value of T_c exceeding the value of Al (1.2 K), most probably due to T_c of $PdTe_2$ (1.7 K). The switching current and the I_cR_n product also deviate from the junctions with other barrier metals. As $PdTe_2$ is observed to impact the superconducting properties of the junction, it may also influence the topological attributes of the weak-link and therefore, Pd is not recommended as a diffusion barrier.
- Other than Pd, all barrier metals have presented almost similar results. Nb, in general, always exhibits high I_c and therefore, larger I_cR_n product. The I_cR_n product provides the energy rating of a junction i.e. the maximum supercurrent that is alloyed by the junction before it converts into the normal resistive state. Both barrier materials i.e. Pt and Ti have exhibited the similar I_cR_n values along with the junction transparencies T_2, evaluated with the gap of Al (Δ).

Based on these results, the barrier metals Nb, Ti and Pt can be utilized to artificially engineer epitaxial interfaces with the successfully induced superconductivity in Al based Josephson junctions. The formation of TMDC assisted self-epitaxial interfaces have provided a platform that can be adopted with different TI materials on one hand, and s-wave SCs on the other hand to fabricate functional quantum devices. The TI-SC hybrid junctions that had failed earlier due to heavy diffusion of Sn and Pb, can now be refabricated with the incorporation of barrier metals, and the temperature limitation imposed by Al (T_c = 1.2 K) can be addressed by replacing Al with Sn (T_c = 3.7 K) and Pb (T_c = 7.2 K).

7.3 Summary

For the realization of topological superconductivity, the structural investigations at the interface between TI epilayers and various s-wave superconductors (SCs), are performed. Nb with BST alloy exhibits an amorphous though, highly transparent interface; however, it suffers from the 1e periodic supercurrent and is prone to quasiparticle poisoning that limits its utilization for the complex spintronics and Majorana based applications. To address this issue, Sn and Pb based interfaces are investigated. Both elements are observed to diffuse heavily into the TI epilayer where they deform the crystal structure by forming the corresponding chalcogenides (e.g. SnSe) with the non-compatible crystal structure (i.e. orthorhombic). Similarly, the interface with Al is also observed to be diffusive resulting in the formation of a polycrystalline region along with the appearance of a Schottky-like barrier at the interface that leads to failure in achieving the induced superconductivity in TI-SC hybrid structures. To counter the diffusion problem, a thin metallic film (3 nm) is introduced as the diffusion barrier between the TI epilayer (Bi_2Te_3/Sb_2Te_3) and SC (i.e. Al). Due to the behavioral difference between Sb and Bi based compounds, interfaces are individually investigated for Bi_2Te_3 and Sb_2Te_3 epilayers to compare the structural differences. The structural characterizations at the atomic-scale via STEM and compositional analysis via EDX are conducted for all TI-B-Al hybrid junctions. The selected barrier metals i.e. Nb, Ti, Pt and Pd, at the contact with TI epilayers switch into $NbTe_2$, $TiTe_2$, $PtTe_2$ and $PdTe_2$ like trilayer architecture respectively and establish the vdW based self-aligned epitaxial interfaces with the residual TI epilayers. They also successfully block the Al atoms from diffusing into the TI epilayer and hinder the formation of a Schottky-like barrier. Josephson junctions of Bi_2Te_3 - Al hybrid junctions based on all barrier materials are prepared and the induced superconductivity is successfully achieved in all of them. As Sb tends to diffuse into other materials, atomically sharp interfaces are not realized in most of the Sb based materials; however, Bi based TIs in almost all cases exhibit well-defined and epitaxial interfaces. Based on structural investigations, Pt is found to be best suited for Sb_2Te_3 while for Bi_2Te_3 all barrier materials exhibit the adoptable interfaces. The summary of best barrier metal for each TI is listed in Table 7.3. The other SCs that exhibit either the diffusion problems (with the formation of large bandgap alloys such as Al) or the non-compatible crystal structure (after diffusion into TI epilayer such as Sn and Pb) can now be utilized successfully with the incorporation of barrier materials that form epitaxial interfaces assisted by the self-epitaxy of TMDCs.

Table 7.3: An overview of the barrier materials incorporation with different 3D topological materials along with the recommendations based on the structural characterization to engineer the epitaxial interfaces.

3D Topological Materials	Inter-diffusion Barrier			
	Nb	Ti	Pd	Pt
Bi_2Te_3	Good	Good	Not recommended	Recommended
Sb_2Te_3 , BST alloys	-	Bad	Not recommended	Good
Bi_xTe_y	Good	Good	Bad	Recommended
Bi_2Se_3	Recommended	Good	Bad	Recommended

Chapter – 8

Conclusions and Outlook

In the perspective of crystal growth, there are certain challenges that limit the utilization of topologically protected Dirac surface states (TSS) of conventional 3D TIs into the futuristic quantum devices. This work is a modest attempt to systematically address those issues including the preparation of defect-free and high crystal quality epilayers, fabrication of pristine and integratable nanostructures, suppression of trivial carriers to enhance the contribution of TSS, and the realization of atomically transparent and epitaxial interfaces.

Starting with the epitaxial growth of 3D TIs, the relation between the growth parameters and the structural defect density is identified. The selection of optimum growth temperature (T_{sub}) and the control over thin film growth rate (R_{TF}) = 5 nm/h have facilitated the achievement of defect-free and high structural quality epilayers of all Te based 3D TIs. The demands of integratable complex nano-architecture are fulfilled with the selective growth of 3D TIs on the patterned Si (111) substrates. The development of plasma enhanced chemical vapor deposition (PECVD) based SiN_x to be resistant in HF based solutions has enabled the realization of combinational surfaces based patterned substrates. Furthermore, the technique of SAE has facilitated the achievement of a scalable network of topological nanostructures with adaptable dimensions. The encountered challenges of crystal defects in selectively grown nanostructures are addressed with the development of a specialized growth model. This model, by incorporating the pattern dimensions into account, has provided control over the effective growth rate (R_{eff}) of the crystal, and in succession, has facilitated the preparation of defect-free structures at the nanoscale.

Atomic scale structural characterizations conducted on selectively grown topological nanostructures have confirmed the high-quality of the grown crystals. Moreover, the magneto-transport investigations have revealed the improved electronic properties of 3D TIs, particularly the bulk carrier density (2×10^{-19} cm^3) is observed to decrease by almost 1 order, compared to the earlier reports (5×10^{-20} cm^3). Though improved results are obtained, the observed carrier density is still at least 2 orders higher than the utilizable conditions (10^{-17} cm^3) for most of the advanced quantum applications. This deficiency in electronic properties could not be associated to the crystal quality of 3D TIs, as almost defect-free nanostructures are realized. The detailed structural characterization via scanning transmission electron microscope (STEM) and chemical analysis via energy dispersive X-ray (EDX) spectroscopy have revealed the presence of a narrow channel created by the diffusion of Sb atoms into the silicon substrate that must have influenced the carrier density in Sb based TIs. Moreover, another source of high carrier density is identified in form of the probable charge transfer due to the band alignment of topological epilayer at the interface with the substrate. The presence of this phenomenon and the resulting impact on the bulk carrier density is revealed by conducting a comparative study with the crystal growth, the structural characterization and the magneto-transport investigations of $Bi_xSb_{2-x}Te_3$ (BST alloy) prepared on an insulating substrate of HfO_2. Unexpectedly, despite the relatively low structural quality of the epilayer on HfO_2 substrate, a decrement of almost two orders of magnitude in the bulk carrier density (1×10^{-17} cm^3) is observed. The obtained results have confirmed the phenomenon of the band alignment and the charge transfer that impacted the density of trivial carriers in the TI epilayers prepared on the silicon substrates. These observations indicate caution for the future utilization of silicon substrates to realize any advanced quantum device based on 3D TIs. Despite these limitations of TI nanostructures prepared on silicon substrates, the distinct phenomena in magneto-transport due to the presence of TSS including the weak anti-localization (WAL) effect, the Shubnikov-de Haas (SdH) and the Aharonov–Bohm (AB) oscillations, and the resistive steering effect are

witnessed. The observation of these effects can be associated to the high crystal quality of the selectively grown topological nanostructures.

One way to neutralize the issue of high density of trivial carriers (suppressed contribution of TSS) on the silicon substrates is the topological transformation of conventional 3D TIs into the topological Dirac semi-metal (TDSM) or into the Weyl semi-metal (WSM) phases. These phases exhibit topologically protected bulk states and thus, suppress the contribution of additional trivial carriers originating from the band alignment. Such phases can be contrived using the technique of topological band engineering (TBE). TBE is conducted by modifying the strength of spin-orbit coupling (SOC) with the van der Waals (vdW) epitaxy of topological-trivial heterostructures where the stoichiometry (relative contents of the trivial material) has provided control to tune the topological phase of the alloys. Two such systems are explored including $Bi_xTe_y = (Bi_2)_m(Bi_2Te_3)_n$ and GST/GBT = $(GeTe)_n(Sb_2Te_3/Bi_2Te_3)_m$ alloys.

In Bi_xTe_y, the gradual and controlled accumulation of Bi_2 bilayers in the stacking order allowed the epitaxial growth of 33 distinct states starting from Bi_2Te_3 and passing through the key compositions of Bi_3Te_4, Bi_4Te_5, Bi_6Te_7, Bi_8Te_9, $Bi_{10}Te_{11}$, Bi_1Te_1, $Bi_{10}Te_9$, Bi_8Te_7, Bi_6Te_5, Bi_4Te_3, Bi_3Te_2, and ending at Bi_2Te_1. The theoretical evaluations, performed combinedly in this and earlier study, have revealed the existence of dual topological phases in three evaluated states including Bi_2Te_3 and Bi_4Te_3 with the strong topological insulator (STI) and topological crystalline insulator (TCI) phases while Bi_1Te_1 exhibits the weak topological insulator (WTI) along with the TCI phase. The increasing contents of bismuth in these alloys impacts the strength of SOC and decreases the inverted bandgap from -210 meV (Bi_2Te_3) to almost -2 meV (Bi_4Te_3); however, most of these states are electronically and topologically unexplored. The detailed theoretical (DFT) investigations of all Bi_xTe_y alloys are required to have an overview of the trend in topology that would be able to provide an insight of the target stoichiometry that can be tuned exactly to engineer the electronic band structures of a TDSM phase. For the first time, a systematic atomic-scale structural characterization (via STEM) of Bi_xTe_y alloys has facilitated the observation of diverse variety of vdW stacks including the pristine (relatively weak) and the hybrid (relatively strong) vdW gaps. The localized variations in the bond lengths due to deviations in the atomic interactions with the changing vdW stacks, and the resulting impact on the dimensional changes in the corresponding unit cells are explored. These observations can be extremely helpful in understanding the classification of bonding (pseudo-vdW, metavalent etc…) and their impact on the structural and the electronic properties of the layer based material systems. Once again, the support of theoretical calculations and the simulations of structural models, are required.

The GST/GBT = $(GeTe)_n(Sb_2Te_3/Bi_2Te_3)_m$ heterostructures, similar to Bi_xTe_y alloys, have facilitated the achievement of TBE where the inverted bandgap, with the gradual accumulation of GeTe (trivial insulator) keeps on decreasing and finally transforms into a trivial phase. The successful epitaxy of various stoichiometric states including GST-147, GST-124, GST-225 and GST-326 along with their corresponding GBT states, are achieved. STEM based structural investigations of Ge based alloys have enabled the exploration of the vdW reconfiguration where the transformation of layer architecture is observed to occur via two distinct mechanisms. These mechanisms include Sb-Te antisite assisted bilayer swapping (zipper defect) and Ge vacancy/accumulation layer assisted vdW switching. These mechanism are not only the backbone of structural transformation from crystalline to amorphous state and vice versa, they also enabled the evolution of interfacial phase change (IPCMs) isomers in GST/GBT alloys.

The incorporation of these alloys belonging to both heterostructures i.e. Bi_xTe_y and GSTs/GBTs with the pre-patterned substrates is conducted, and via SAE nanostructures belonging to most of the stoichiometric states are successfully achieved. This achievement, on one hand, has paved a way to integrate the novel Bi_xTe_y materials with rich topological phases into the futuristic quantum devices. On the other hand, SAE of GST/GBT alloys has facilitated the preparation of compositional nanostructures that can be readily incorporated into the devices for low-power phase change applications. They can also be extremely useful

in future to realize the IPCMs based applications. At last, the layer-free architecture of GeTe is explored. The detailed structural characterization are performed on the selectively grown nanostructures of GeTe. SAE of these materials has fulfilled the long-awaited desire of obtaining the pristine nanostructures of materials that exhibit surface sensitivity to ambient conditions such as GeTe and Bi_xTe_y alloys.

Post growth optimization of nanostructures, the surface stability of all material systems in the ambient environment is investigated. The structural characterization via STEM and chemical analysis via x-ray photoemission spectroscopy (XPS) have revealed that all epilayers are prone to aging. The surfaces belonging to all materials are observed to oxidize where a non-saturating process with a continually decreasing oxidation rate is observed. The oxidation process is observed to differ from one material system to another; however based on structural properties, all materials can be classified in two different groups. The first group contains Sb and Ge based alloys. These materials rapidly oxidize at the exposure to ambient conditions; however, after the oxidized layer reaches a thickness of couple of nanometers, the oxidation rates is observed to drop exponentially. These materials exhibit amorphous oxidized layers that can form Schottky-like barrier with metallic electrodes. Due to being amorphous in nature, however, the oxide layer can be removed via dry etching of Ar^+ plasma treatment. The second group contains pure Bi based chalcogenides e.g. Bi_xTe_y alloys. The oxidized layer, in these materials, materializes into a semi-metallic and crystalline structure of Bi_1O_1 that cannot be removed easily and limits the connectivity of topological surfaces with the metallic electrodes. Irrespective of the oxidized layer being amorphous or crystalline, at the exposure to ambient conditions, the structural reconfiguration and stoichiometric deviations are observed in most of the material systems. The passivation of epilayers is achieved with the *in situ* deposition of 2 nm thin layer of Al that readily transforms into AlO_x at the exposure to ambient conditions and prevents the epilayers from further oxidation and aging effects.

Finally, for the realization of topological superconductivity, the structural investigations at the interface between TI epilayers and various s-wave superconducting (SC) materials, are performed. Keeping in mind the observation of surface oxidation, all interfaces are prepared *in situ* (without the exposure to ambient conditions). Due to the behavioral difference between Sb and Bi based compounds, observed during the oxidation process; interfaces are individually investigated for Bi_2Te_3 and Sb_2Te_3 epilayers to compare the structural differences. The formation of non-diffusive interface not just depends on TI epilayer; the SC materials also affect it. As reported earlier, Nb exhibits highly transparent interface; however, it suffers from the 1e periodic supercurrent and is prone to quasiparticle poisoning that limits its utilization for the complex spintronics and Majorana based applications. To resolve this issue, Sn and Pb are investigated and are observed to diffuse heavily into the TI epilayer where they deform the crystal structure by forming the corresponding chalcogenides (e.g. SnTe) with the non-compatible crystal structure (cubic). These results also restrict their utilization and therefore, the focus is shifted to other SC materials. At last, the interface investigations are conducted with Al where a slightly diffused region (4 nm) with the polycrystalline structure is observed. The appearance of a Schottky like barriers with the formation of large bandgap alloy (i.e. AlSb) at the interface resulted in devices with the non-induced superconductivity. To counter the diffusion problem, a thin metallic film (3 nm) is introduced as the diffusion barrier between the TI epilayer (Bi_2Te_3/Sb_2Te_3) and SC (i.e. Al). The atomic scale structural characterization via STEM and EDX analysis is conducted for all TI-B-SC hybrid junctions. The selected barrier metals i.e. Nb, Ti, Pt and Pd, at the contact with TI epilayers diffuse and react with Te atoms and transform into the corresponding transition metal dichalcogenides (TMDCs) forming $NbTe_2$, $TiTe_2$, $PtTe_2$ and $PdTe_2$ respectively. TMDCs are vdW based layered materials and therefore, they arrange themselves via self-epitaxy forming epitaxial interfaces. They also successfully blocked Al atoms from diffusing into TI epilayer and hinder the formation of a Schottky-like barrier. Josephson junctions of Bi_2Te_3 - Al hybrid junctions based on all barrier materials are prepared and the induced superconductivity is successfully achieved in all of them. As Sb tends to diffuse into other materials, atomically sharp interfaces are not realized in most of the Sb based materials; however, Bi based TIs in almost all cases exhibited well-defined and epitaxial interfaces. Based on structural investigations, Pt

is found to be best suited for Sb_2Te_3 while for Bi_2Te_3 all barrier materials exhibited the adoptable interfaces. The other SC materials that exhibit either the diffusion problems (with the formation of large bandgap alloys such as Al) or the non-compatible crystal structure (after diffusion into TI epilayer such as Sn and Pb) can now be utilized successfully with the incorporation of barrier materials that form epitaxial interfaces assisted by the self-epitaxy of TMDCs.

The knowledge acquired from this work can be incorporated into the future experiments to develop more efficient platform to fabricate nanostructures, to understand and investigate the electronic properties of materials with novel topologies and to explore advanced quantum devices with dynamic interfaces. Some of the examples are stated below:

- **SAE on the crystalline insulators:** Silicon substrates with the phenomenon of band alignment and charge transfer at the interface impose limitations for conventional 3D TIs. To neutralize the challenge of unintentional high density of trivial carriers, the best possibility is to adopt a crystalline insulator as the substrate such as sapphire (Al_2O_3), SiC, BaF_2 and STO. With minor modifications in the growth parameters, the scalable platform developed for SAE on Si (111), discussed in chapter 3, can be recalibrated to fabricate topological nanostructures on a crystalline insulator.
- **Probing strong side of WTIs and TDSMs:** The side surfaces (facets), in materials that exhibit novel topologies such as WTI and massive TDSM phases, are more important to probe/explore than the top surfaces. The planar epitaxial growth does not facilitate the investigation of side facets via scanning tunneling microscopy (STM) and angular resolved photoemission spectroscopy (ARPES) etc. An adaptable solution is the epitaxial growth (via SAE) of the desired crystal on the non-planar substrates. Si (100) surfaces offer the fabrication of such non-planar substrates. With the help of lithography and KOH based wet-etching processes, the angular Si (111) facets can be exposed and utilized for the crystal growth. The epitaxially grown non-planar/angular layers then present a possibility to investigate the side facets. A schematic representation of the substrate preparation and the results from the first growth test are depicted in Figure 8.1. This technique is valuable for the investigation of unexplored topologies in Bi_xTe_y superlattices that are already proposed to exhibit TCI, WTI and higher order topological insulator (HOTI) phases.

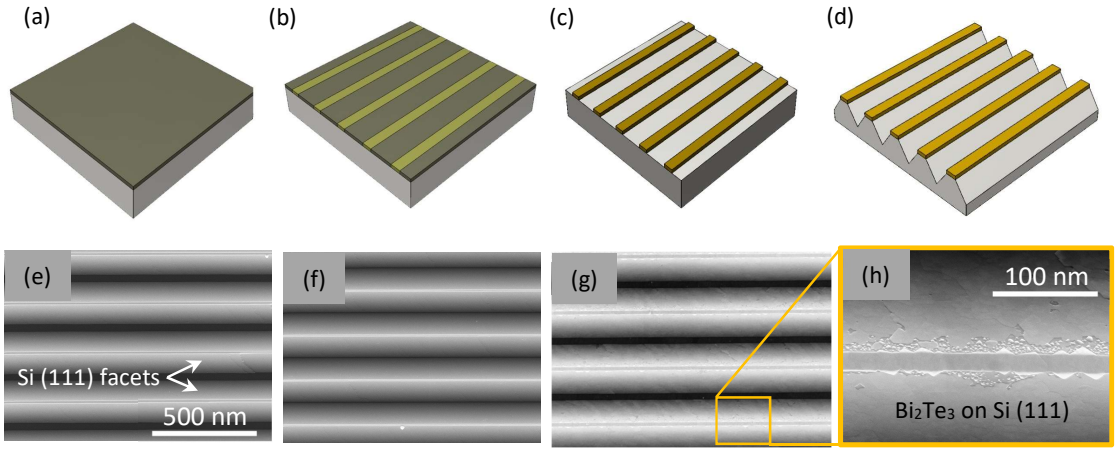

Fig. 8.1: (a-d) Schematic representation of fabricating Si (111) angular facets using Si (100) substrate via lithography and KOH based wet etching. (e-f) SEM images of the exposed Si (111) facets after KOH etching. (g) The first growth attempt of Bi_2Te_3 epilayer on Si (111) angular facets. (h) A higher magnification image of the marked area in (g) exhibiting the possibilities of growth and the characterization of the side surfaces in the non-planar epilayers.

- **Topological-trivial array for Majorana box qubits:** SAE of compositional alloys present many challenges where stoichiometric deviations are hard to control. In most cases, these problems can be resolved with the corresponding adjustments in the growth parameters. In the case of GST/GBT alloys, the controlled stoichiometric deviations can be helpful in the fabrication of topological-trivial switch arrays. The geometric changes (dimensions) in a pattern can be engineered to tune the localized variations in the topological phase of the alloy and thus, an array with the switching topological-trivial band structures can be prepared (For details visit Figure 5.16). Such structures can be incorporated with the superconducting electrodes to fabricate the Majorana box-like qubit circuits.
- **Neuromorphic computation:** The achievement of stoichiometric nanostructures of GST/GBT alloys via SAE has paved a path to utilize these materials in low-power PCM devices for non-volatile memory applications. With the development of IPCMs (control over stable growth of isomers), it will be possible to incorporate them into the complex quantum devices for the development of ultra-fast switching and low-energy processing units; the basic building blocks for the realization of neuromorphic computation.
- **Non-centrosymmetric superconductivity:** The non-centrosymmetric superconductivity with the absence of parity symmetry in crystal leads to several exotic properties. It is a topic of increasing interest in the community of superconducting and topological qubits. The discovery of non-centrosymmetric superconductivity in GeTe dramatically increased the demand of high quality and pristine nanostructures. In this work, the defect-free nanostructures of GeTe are prepared via SAE. These nanostructures can be utilized to explore the exotic and novel features of superconductivity and based on the observed/investigated phenomenon, they can be incorporated into the futuristic quantum circuits.
- **Multi-Terminal junctions and SQUID based proximity transistor (SQUIPT):** One of the basic device layout that requires the in-detail investigation for the successful braiding of Majorana quasiparticles in a topological qubit circuit is the multi-terminal Josephson junction. With the assistance of SAE and on-chip stencil mask, tri and quad-terminal junctions can be fabricated that with the incorporation of SQUID based circuits will enable the phase-sensitive measurements of 3D TIs based superconducting quantum circuits. An example of such a device fabrication is depicted in Figure 8.2.

In general, this study provides a platform where the desired TI martial via SAE can be incorporated into a scalable network of any complexity. Furthermore, it also provides a methodology of the *in situ* metallization via on-chip stencil mask to prepare any futuristic quantum circuits without the exposure of TI to the ambient conditions and to the fabrication chemicals. It could be visualized with the help of Figure 8.2 that provides an overview of any quantum device preparation in a “plug and play” mode.

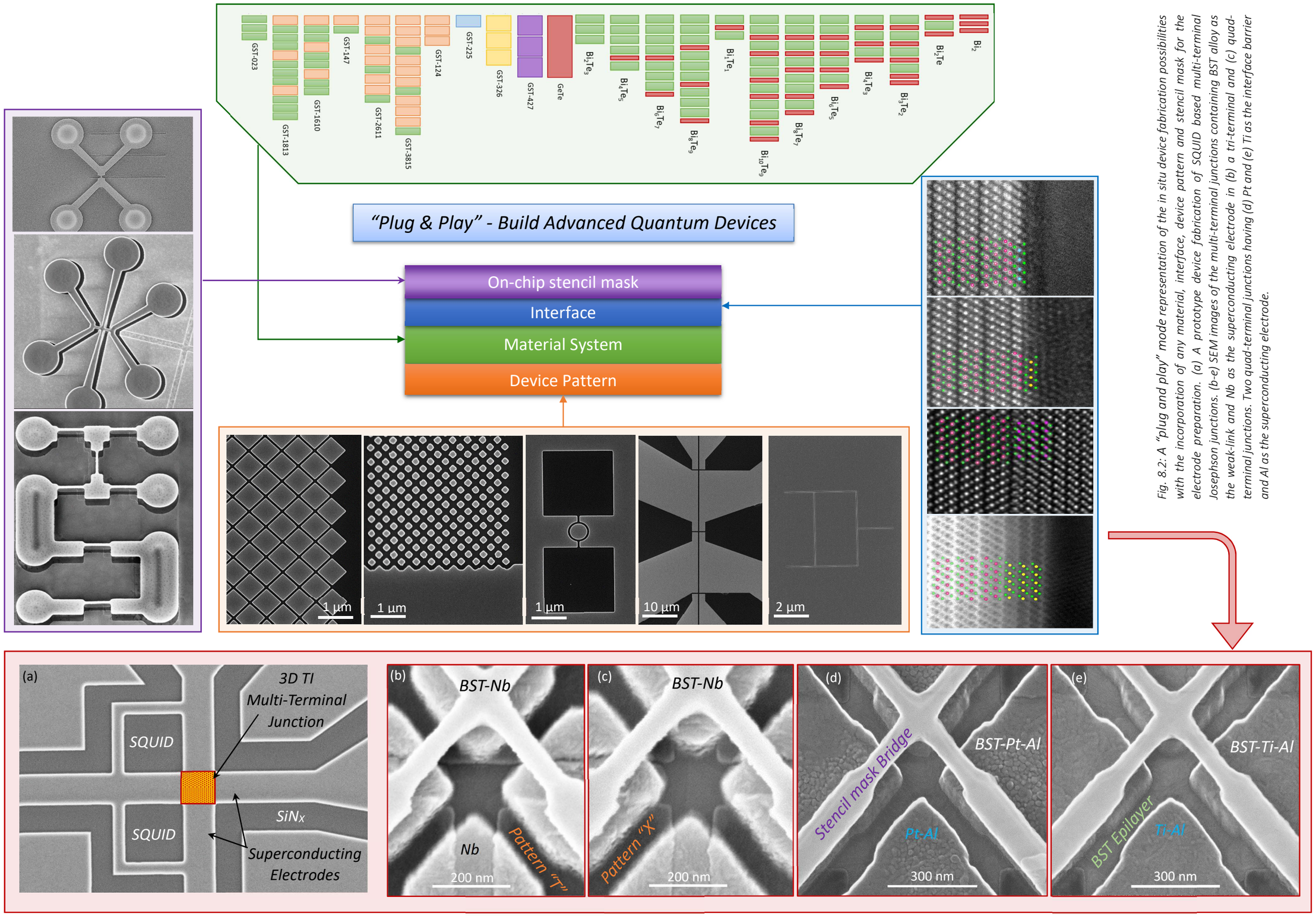

Fig. 8.2: A "plug and play" mode representation of the in situ device fabrication possibilities with the incorporation of any material, interface, device pattern and stencil mask for the electrode preparation. (a) A prototype device fabrication of SQUID based multi-terminal Josephson junctions. (b-e) SEM images of the multi-terminal junctions containing BST alloy as the weak-link and Nb as the superconducting electrode in (b) a tri-terminal and (c) quad-terminal junctions. Two quad-terminal junctions having (d) Pt and (e) Ti as the interface barrier and Al as the superconducting electrode.

Acknowledgements

I would like to thank all those who have contributed in this work and without whom this thesis would not have been completed.

Supervisors and Advisors:

Prof. Dr. Detlev Grützmacher: I am extremely obliged to you for giving me an opportunity to conduct this research study in PGI-9 particularly to a person like me who was away from any scientific work for more than 2 years and was not a safe bet due to the medical reasons. You have given me a hope to restructure my scientific carrier and introduced me to the Forschungszentrum Jülich, a place that has unbelievable resources and capabilities to conduct the state of the art research. The occasional discussions on the crystal growth challenges, fruitful sessions on the characterization methods and your insight into new ideas that should/must be explored have always kept me steady on my path. I am also thankful to you for encouraging several in-house and external fruitful collaborations that hopefully will lead to some interesting future experiments and results.

Prof. Dr. Markus Morgenstern: Thank you very much for being my second examiner. A couple of technical discussion with you in the start of my research and your insight into the field of topological insulators has guided me on various occasions during the course of this work.

Dr. Gregor Mussler: You are a great person and a good supervisor. I was extremely happy to meet you for the first time on the day of my interview and loved the opportunity to work here when you had given me a guided tour of the labs including MBE, nanocluster, HNF and ER-C. I was amazed to see the infrastructure and the future possibilities. Your non-challenging and always supportive attitude towards me is what every student dreams of. I am extremely thankful to learn a great deal of X-ray based structural characterization from an experienced scientist like you and hope that we will continue to work together in future.

Dr. Martina Luysberg: I do not have the proper words to appreciate you nicely. You were not just my technical supervisor for TEM studies, you were one of the strongest pillar of moral support and encouragement throughout my journey in this work. A perfectionist and an extremely brilliant scientist. You have helped me so much to understand and analyze the large set of topological materials that without you, I would not have been able to complete this work. And I hope that one day I will be able to acquire the level of knowledge you possess.

Prof. Dr. Thomas Schäpers: I have not seen a man so down to earth with such a high level of scientific knowledge as you Sir. You, despite of not being my supervisor have helped me on every step of the way and have provided your support on magneto-transport investigations that has facilitated the understanding of several unique phenomenon and the qualitative analysis of the crystal growth. I am eagerly looking forward to collaborate with you in the future.

Dr. Peter Schüffelgen: One of my colleague in the start of my Ph.D. and later with numerous interesting and productive long discussions, you have earned the place of an advisor to me. Exploiting your innovative stencil mask technique opened up the paths for so many futuristic and complex experiments that the PhD span started to seems too short. I hope that I will be able to continue working with you and together will explore several quantum devices based on scalable network of topological nanoribbons with stencil mask supported superconducting circuits for qubit applications.

Crystal Growth Team:

The crystal growth via MBE is the essence of my PhD work. While talking about MBE, the first person come to mind is Michael Schleenvoigt. He is one of my closest colleagues and also my teacher who has introduced me to the MBE system and assisted in laying the stepping stone of my work. Michael, you are a non-tiring, always supporting, ever smiling and a straight forward person. Your help in my work can never be ignored. Christoph Ringkamp is my second longest colleague. Though you are working on a different material system, you are an important member of the growth team. Several informal discussions with you about the growth problems and the challenges of new material systems kept the day's work interesting. With the extensive growth knowledge, the discussions with Dr. Mihail Lepsa and Dr. Alexander Pawlis help me occasionally to improve the crystal quality. During the last few years of this work, I would also like to thank several growth team members including Sarah Schmitt, Robert Müller, Max Vaßen-Carl, Qi Shu and Abbas Espiari for your help and contribution in this work.

Transmission Electron Microscopy Team:

The second major part of this study is comprised of atomic-scale structural characterization of topological epilayer via TEM/STEM. I cannot move forward without thanking Dr. Xiankui Wei who has collaborated in the investigation of TI-SC interfaces. Similarly, Helen Valencia has dedicatedly assisted in exploring the Bi_xTe_y material system and helped in pointing out various challenges in the lamella preparation that were the limiting factors in obtaining the high resolution STEM images. I esteem Lidia Kibkalo as one of my teachers. She has introduced me TEM for the first time and organized several training sessions that allowed me to work on my own later. I am extremely thankful for your help over the last few years. I would also like to offer my special thanks to Prof. Dr. Joachim Mayer for his precious time on several occasions and the fruitful discussions particularly on the coherent and incoherent interfaces that was extremely helpful in understanding the pristine and hybrid *van der Waals* interactions. I would also like to thank Dr. Doris Meertens and Dr. Elmar Neumann for preparation of hundreds of lamellas via focused ion beam throughout this work.

Fabrication Team:

One of the aims of this study is not just to grow new material systems via MBE but also to incorporate them into the scalable network of nanostructures via selective area epitaxy and build functional quantum devices using stencil lithography. This aim required an extensive fabrication work and none other than Tobias Schmitt comes to mind who has introduced me to the fabrication steps of the first generation of stencil mask. Several informal discussions and assistance over a period of time has helped me to design and fabricate several novel devices. Tobias is also the first person who has successfully demonstrated a function transmon qubit based on a conventional 3D TI (BST alloy) as the semiconductor weak-link. I wish you all the best for your future experiments. One of my other colleague Gerrit Behner has also assisted me heavily during the fabrication of selective masks. Several other teams members of HNF and PGI-9 including Luisa Koke, Erik Zimmermann, Kevin Jansen, Dr. Jürgen Moers, Georg Mathey, Janine Worbs and Natalie Bruger have guided and assisted me during the fabrication work. For the support of e-beam lithography, the efforts and services of Dr. Stefan Trellenkamp and Dr. Florian Lentz cannot be forgotten. I would also like to say special thanks to Benjamin Bennemann, Soraya Karimzadah and Christoph Krause who have presented their endless support in the nanocluster for metallic depositions and ALD processes.

A critical part of fabrication work, due to unavailability of LPCVD, is to optimize PECVD based SiN_x to be stable in HF based solutions and manage the extensive tensile strain for its utilization in the preparation of stencil masks. In task could not be completed without the assistance from Jana Brugger, Matthias Geitner, Andrea Trajcev, Thomas Grap, Anja Zass and Lars Petter.

Transport Team:

One of my colleagues who has assisted me a lot in the magneto-transport investigations of various materials is Dr. Daniel Rosenbach who was followed by Jonas Kölzer who also has helped me greatly in magneto-transport studies. Thinking of Jonas comes the word “order” into mind. Everything has to be properly managed and documented. I would like to thank for your support throughout the journey of this work. I would also like to thanks Frederik Marx, Jan Karthein, and Justus Teller for their help and assistance. For the assistance of supercomputing Josephson junction based devices measurements to investigate the interface transparency and the analysis, I would also like to appreciate the help of Benedikt Frohn and Willi Wittl. Without you this work would also be incomplete.

Theoretical Support Team:

I would like to acknowledge Dr. Kristof Moors, Dr. Gustav Bihlmayer, Peter Schmitz and Dr. Irene Aguilera for their support of theoretical calculations, electronic band evaluations and numerous technical discussions that guided me to design the path of this work.

I would also like to say special thanks to Prof. Dr. Matthias Wuttig and Prof. Dr. Rafal Dunin-Borkowsk for giving me time on several occasions out of your busy schedules and guiding me through various technical difficulties.

In the end, I would like to thank Silke Pieper, Christine Servo for their support in organizational stiff and the complete staff of PGI-9 and HNF for their kind assistance and support.

List of Abbreviations

2DEG	2-dimensional electron gas
ABO	Aharonov – Bohm oscillation
ABS	Andreev bound states
ADR	Adsorption to desorption ratio
AFM	Atomic force microscopy
ALD	Atomic layer deposition
ARPES	Angular resolved photoemission spectroscopy
BF	Bright field
BL	Bilayer
BQ	Bilayer – quintuple layer stack
BQB	Bilayer – quintuple layer – bilayer stack
BST	Bismuth antimony telluride ($Bi_xSb_{2-x}Te_3$)
CS	Crystal symmetry
CVD	Chemical vapor deposition
DF	Dark field
DFT	Density functional theory
DSM	Dirac semimetal
EBL	Electron beam lithography
EDX	Energy dispersive x-ray
FWHM	Full width at half maxima
HAADF	High angular annular dark field
HLN	Hikami – Larkin – Nagaoka
HRI	High resolution image (TEM)
HOTI	Higher order topological insulator
IRC	Ioffe-Regel criterion
IS	Inversion symmetry
IPCM	Interfacial phase change material
JJ	Josephson junction
LPCVD	Low pressure chemical vapor deposition
MBE	Molecular beam epitaxy
MBS	Majorana bound states
MOVPE	Metal-organic vapor phase epitaxy
MTI	Magnetic topological insulator
MTJ	Multi-terminal junction
NMR	Negative magnetoresistance
PCM	Phase change material
PECVD	Plasma enhanced chemical vapor deposition
PLD	Pulsed laser deposition
QAHI	Quantum anomalous Hall insulator
QL	Quintuple layer
QW	Quantum well
RBS	Rutherford backscattering spectrometry
RC	Rocking curve
RF	Radio frequency

RIE	Reactive ion etching
RS	Rotational symmetry
RSM	Reciprocal space map
RTA	Rapid thermal annealing
RTD	Rotational twin domains
SAE	Selective area epitaxy
SE	Self epitaxy
SEM	Scanning electron microscopy
SDS	Selective dynamic stoichiometry (2^{nd} order SSS)
SdH	Shubnikov-de Haas
SL	Septuple layer
SOC	Spin-orbit coupling
SSS	Selective stoichiometric shift
STEM	Scanning transmission electron microscopy
STM/STS	Scanning tunneling microscopy/Scanning tunneling spectroscopy
STI	Strong topological insulator
STZ	Selective temperature zone
TCI	Topological crystalline insulator
TEM	Transmission electron microscopy
TI	Topological insulator
TL	Trilayer
TLM	Transmission line model
TMDC	Transition metal dichalcogenide
TRS	Time-reversal symmetry
TSF	Translational shear fault
TRIM	Time-reversal invariant momenta
TSS	Topological surface states
TSC	Topological superconductor
TSM	Topological semimetal
TDSM	Topological Dirac semimetal
UHV	Ultra-high vacuum
vdW	van der Waals
VLS	Vapor – liquid – solid
VPE	Vapor phase epitaxy
WAL	Weak anti-localization
WTI	Weak topological insulator
WSM	Weyl semimetal
XPS	X-ray photoemission spectroscopy
XRD	X-ray diffraction

Appendix – 1
Scanning Transmission Electron Microscope (STEM)

Since the realization of aberration corrected lenses for the electron microscopes in 1990, the atomic-scale structural characterization and the chemical analysis has become a fundamental approach to investigate nanostructures. In this work different imaging modes and analytical techniques have been utilized in order to understand the structural properties and local chemical compositions of vdW assisted layer based materials. Fig A1.1 shows the different TEM imaging modes used during this work.

TEM: The basic characteristic of TEM is the parallel electron beam that elastically scatters at the lattice sites of the crystal (specimen). A complex system of magnetic lenses facilitate to project the image onto the viewing screen or a CCD camera to record. To conduct the structural investigations, the sample is mounted onto a double tilt holder for fine alignment and the investigations are conducted in the following order.

1. ***Bright field (BF) mode:*** In the first step, an overview of the sample is acquired using the bright field (BF) imaging mode (Fig. A1.1a). In the BF mode, the objective lens located underneath the specimen, focuses the parallel beams in the back focal plane. The objective aperture is then positioned in such a way that it transmits only the central beam (light blue rays), whereas all the diffracted beams (dark blue rays) are blocked and do not contribute in the projection of the image. A cross sectional view of a TI Film grown onto Si (111) substrate, covered with carbon protection layer, can be observed in Fig. A1.1a (underneath). The contrast in a BF image allows to distinguish different layers and is governed by two major imaging mechanisms:
    - Mass-thickness contrast causes the heavier elements (high Z value) and relatively thick areas of the specimen to appear darker. The heavy atoms e.g. Bi. Sb and Te (of which the TI is comprised), in comparison to the light atoms, scatter the electrons more strongly resulting in strongly diffracted beams that are blocked in the BF mode and the area appear darker. Considering the specimen having same composition throughout the projected area, the difference in the specimen thickness may also exhibit the similar result.
    - Bragg contrast is determined by the orientation of a crystal with respect to the electron beam. The Bragg law $2dSin(\theta) = n\lambda$ can be use to describe the constructive interference where n is a positive integer, λ is the wavelength of the incident wave and $2dSin(\theta)$ describes the path difference between the initial and the diffracted waves.
2. ***High resolution (HR) mode:*** The high resolution mode provides the information from both, the primary and the diffracted electron beams. The objective aperture is recalibrated in such a fashion that the diffracted beam that is blocked in the BF mode is now allowed to pass. Both beams interfere with each other and contribute in the projection of the image. The phase shift, caused by the defocus and the geometrical aberrations along with the diffraction conditions at the object determine the final electron wave. An example of the HR mode is depicted in Figure A1.1b where a lattice fringe pattern is observed within the area of the Si substrate. At the Si/TI interface the typical spectra contrast of an amorphous layer appears.
3. ***Diffraction Pattern (DP):*** By setting the intermediate lens on the back focal plane of the objective lens and with the selected area aperture located within the image plane a diffraction pattern can be imagined, see Figure A1.1 c. For amorphous materials a ring pattern and for crystalline specimen a spot pattern can be observed. In the image below the schematic, a diffraction pattern acquired at the Si substrate along [1-10] zone axis can be visualized.

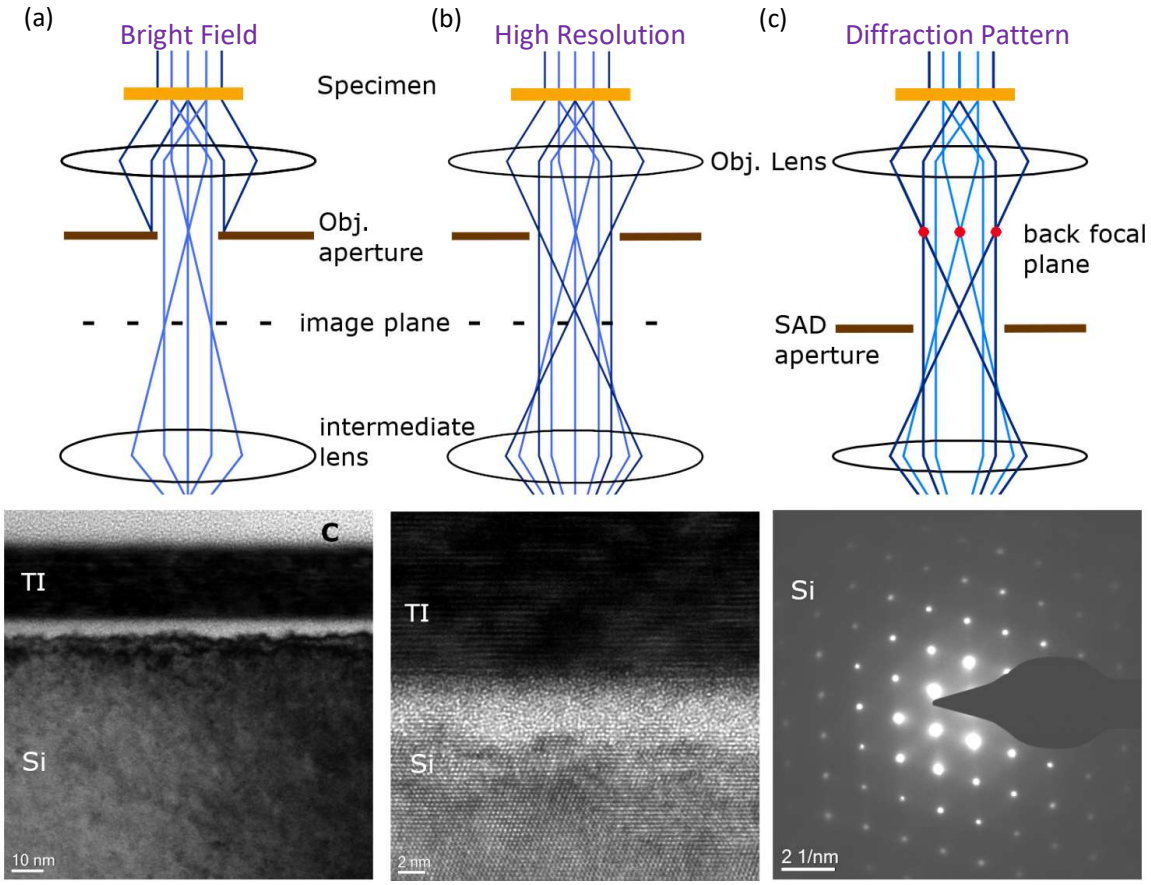

Fig. A1.1: Schematic of non-trivial electron beams near the specimen of interest. (a) Beam path to archive BF images, (b) HR image and (c) a diffraction pattern. Additionally, below the schematics the acquired images are displayed. (Image courtesy: Helen Valencia)

STEM: In STEM investigations, unlike TEM, the incident beam is not parallel instead a non-parallel beam is focused on a tiny spot of the specimen and scanned over the surface of the sample, see Figure A1.2. With the assistance of aberration correcting components it is possible to obtain a beam diameter of 0.8 Å, which determines the resolution. The beam is rastered across an area and the scattered electrons are detected with a bright field (Figure A1.2a) or an angular dark field (Figure A1.2b) detector. The image contrast of the bright field image is equivalent to a HR image in TEM and therefore, the contrast in Figure A1.2a is determined by mass-thickness contrast and Bragg-contrast, discussed above. In the depicted image, TI and Pt layers are darker then the Al, Al_2O_3 and Si substrate. In addition, the faint lines are visible in the Al region that can be attributed to the bending contours typical for the crystalline samples.

The contrast within the dark field image (Figure A1.2b) is determined by the scattered electrons at the higher angles (> 60 mrad) and hence, the image contrast is determined by the Rutherford scattering $\propto Z^2$. Hence, the atomic columns with the different atomic numbers lead to a distinct intensity distribution. Elements with a higher atomic number appear brighter, and therefore, Pt (Z = 78), Te (Z = 52) and Bi (Z = 83) have a brighter contrast than the Si substrate (Z = 14) or Al (Z = 13). Nonetheless, the differentiation between nearby atomic numbers is almost impossible. The diffracted signal is recorded by a high angle annular dark field (HAADF) detector and then is averaged over the whole detector area.

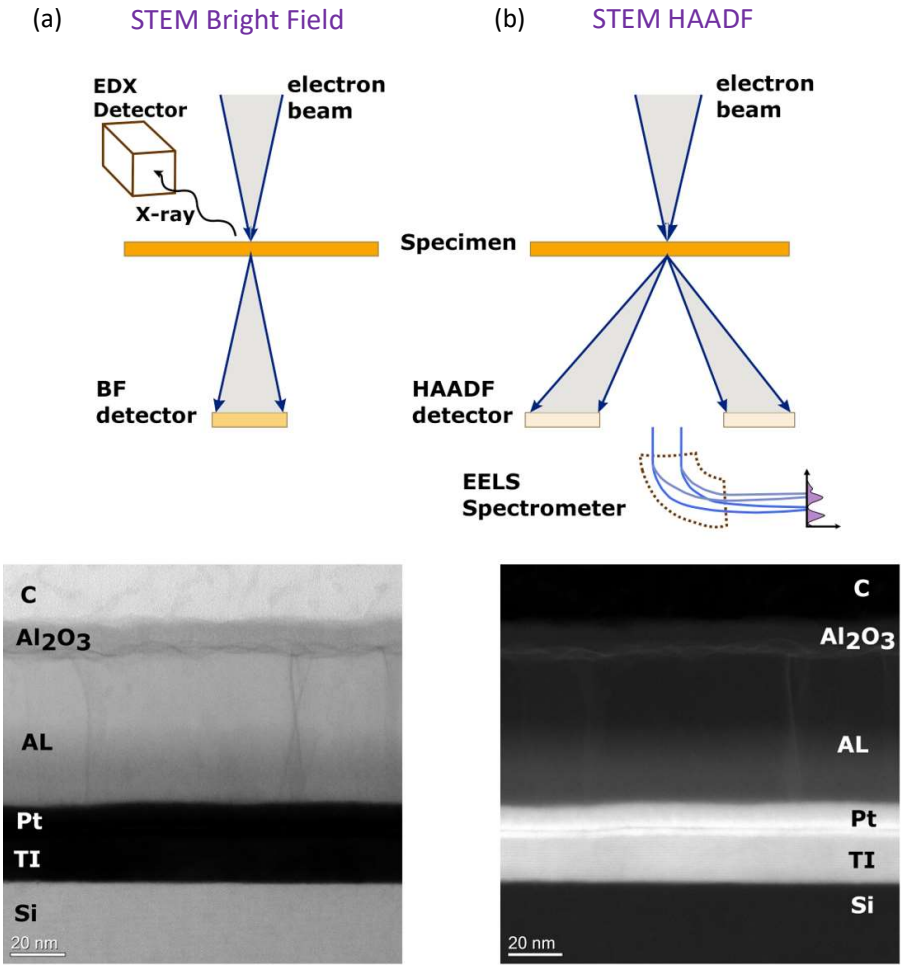

Fig. A1.2: Schematic of a STEM (a) bright field (BF) mode and (b) HAADF mode indicating the position of the corresponding detectors. Additionally the position of the EDX and EEL detector are marked. Below the schematic corresponding BF and HAADF images are shown. (Image courtesy: Helen Valencia)

Microscopes: During the course of this work, depending on the characteristics and limitations, different microscopes are utilized.

- For basic TEM investigations to acquire BF and HR images, the **Tecnai G2 F20** field emission is used. This system is optimized for imaging at the medium resolution. Using Tecnai, for an acceleration voltage of 200 kV, a point to point resolution of about 2 Å is reached.
- **FEI Titan G2 80-200 STEM (Chemi-STEM)** supplied with a high brightness Schottky Field emission gun. Due to its aberration corrector (monochromator and C_S probe corrector) for the condenser lens, it is possible to achieve a probe with a diameter of 0.8 Å which determines the resolution. Moreover, a **Super-X EDX** system, an **UltraScan 100XP-P** charge coupled digital camera, as well as a **Gatan Enfinium ER** (model 977) spectrometer with dual EELS option is also available in this system. To acquire images an on-axis BF and HAADF STEM detector is used. This instrument is used to perform atomic-scale structural characterization and to acquire EDX spectrums.

Appendix – 2A
Molecular Beam Epitaxy (MBE)

The MBE chamber used in this work "BST-MBE chamber" belongs to PGI-9 that is depicted in Figure A2.1. After the Piranha cleaning and HF etching, the samples are mounted on the holder and placed into the loading chamber. As the vacuum reached $1x10^{-6}$ mbar, the holder is moved into the transfer chamber that has a mobile extendable arm with 360° rotational freedom and later moved to the MBE main chamber where the epitaxy is performed.

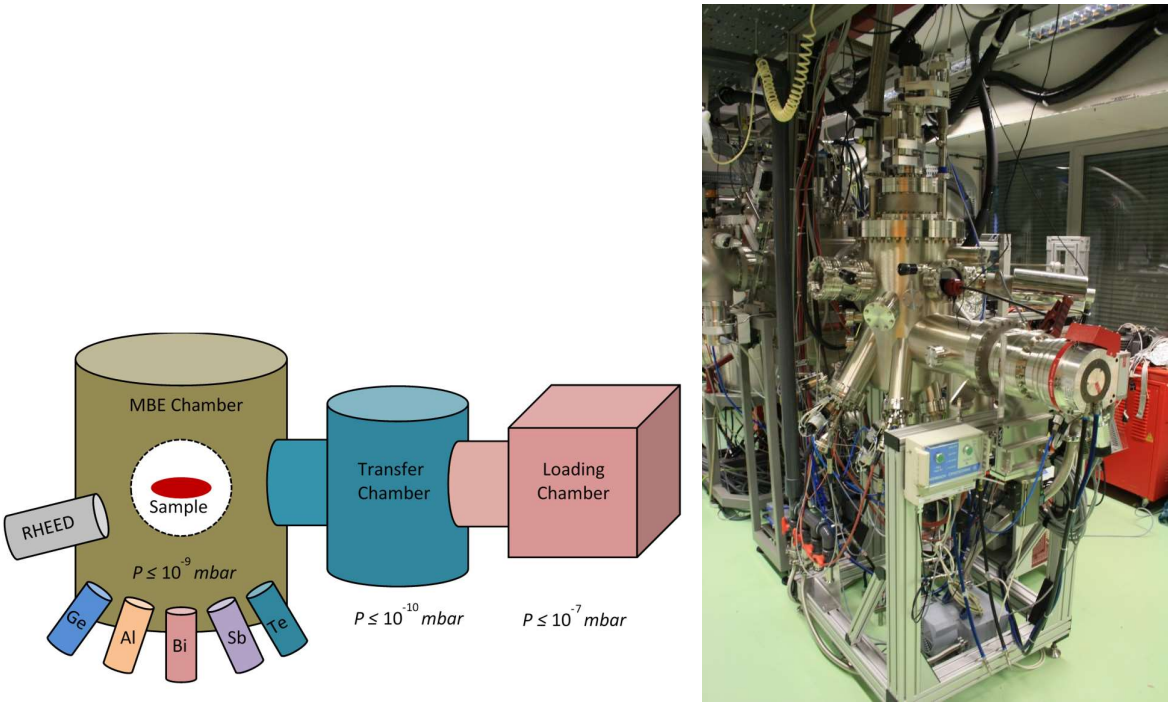

Fig. A2.1: (Left) A schematics of BST-MBE chamber connected with transfer and loading chambers. (Right) A real image of BST-MBR chamber.

The BST-MBE chamber contains 7 effusion cells including Bi, Sb, Te, Se, Ge, Al and Mn. All cells are standard high temperature effusion cells that facilitate the growth of conventional 3D TIs, the topological trivial heterostructures, phase change materials (GST and GBT) and magnetic TIs (MnBiTe).

In general, the epitaxial growth can be performed on a 100 mm (4 – inch) wide wafer; however, to avoid any post epitaxy dicing, in this work the epitaxial growth on the multiple samples having dimensions 10 x 10 mm^2 or 7 x 7 mm^2 is conducted at the same growth run. In this way, samples have similar growth parameters can be utilized to perform various investigations without having any major growth difference. The design of the sample holder used to perform multiple sample growth is depicted in Figure A2.2.

In order to perform the *in situ* metallic depositions as discussed in Appendix 7B or *in vacuo* characterization such as low temperature STM and ARPES, the epitaxy is performed using the omicron holder that allows the sample to be moved to other locations/chambers via the vacuum suitcase attachable to the transfer chamber as depicted in Figure A2.3.

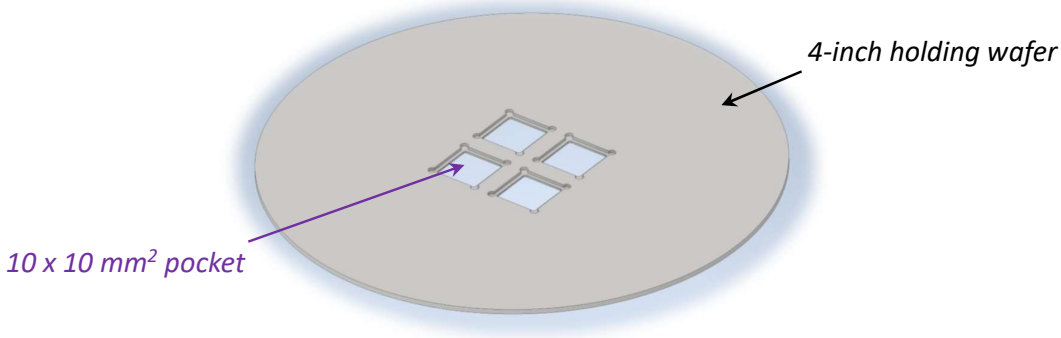

Fig. A2.2: The schematics of the multiple sample holder with a 100 mm diameter that allows to perform the epitaxial growth of 4 different sample at the same time.

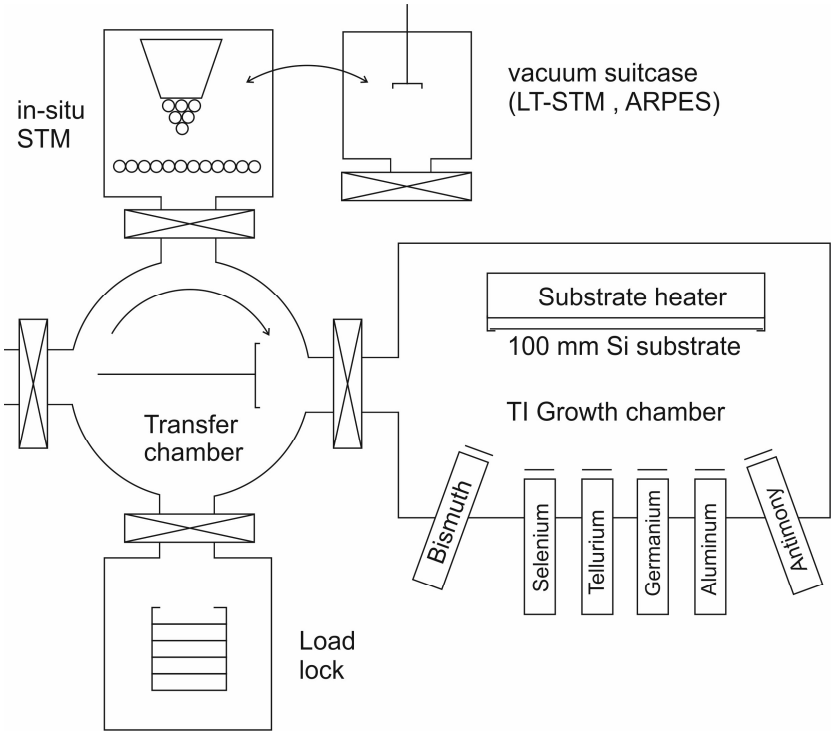

Fig. A2.3: The schematics of BST-MBE chamber connected to the vacuum suitcase via the transfer chambers.

Appendix – 2B
Beam Flux of Effusion Cells & Optimum Growth Parameters of 3D TIs

In this work, all growths are adjusted by the individual effusion cell temperatures. The reason for not using the elemental beam fluxes as growth parameters is the unavailability of flux measuring tool in the MBE chamber during early growths. It was, however, successfully installed into the chamber later and was utilized to monitor and adjust the beam fluxes. The individual beam fluxes for Bi and Sb cells are measured and plotted in the following graphs.

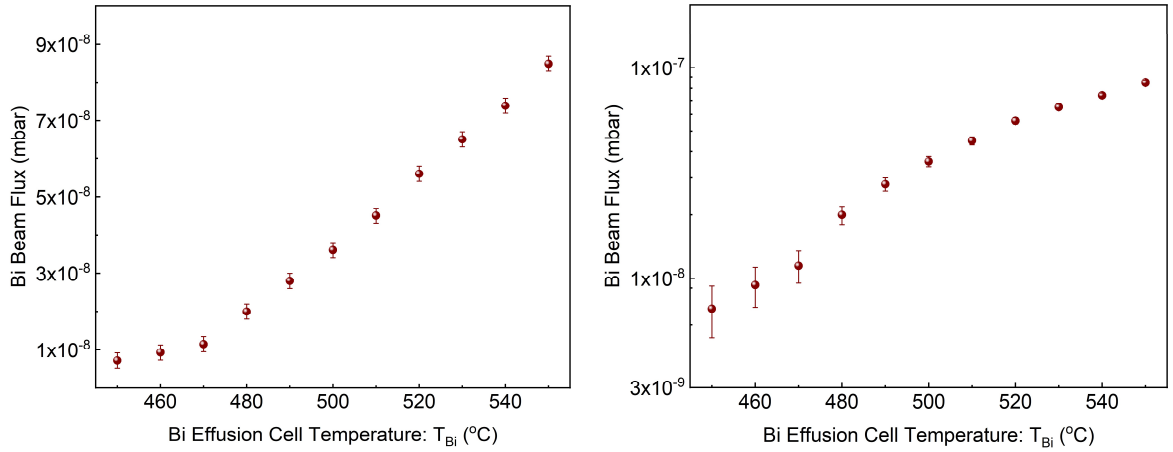

Fig. A2.4: The applied effusion cell temperature vs. the measured beam flux of Bi. The plots represent the trend of increasing beam flux with the incrementing T_{Bi} in a linear scale (left) and in a logarithmic scale (right).

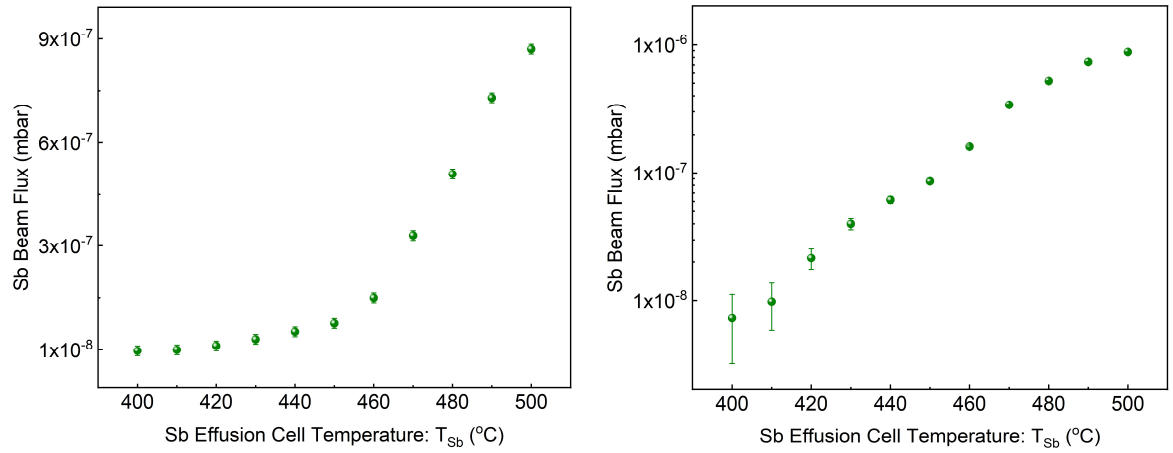

Fig. A2.5: The applied effusion cell temperature vs. the measured beam flux of Sb. The plots represent the trend of increasing beam flux with the incrementing T_{Bi} in a linear scale (left) and in a logarithmic scale (right).

Appendix – 2C
Compositional Analysis via Rutherford Backscattering Spectroscopy

The composition of the epilayer is investigated via Rutherford backscattering spectroscopy (RBS). A measured spectrum of BST alloy is depicted in Figure A2.6.

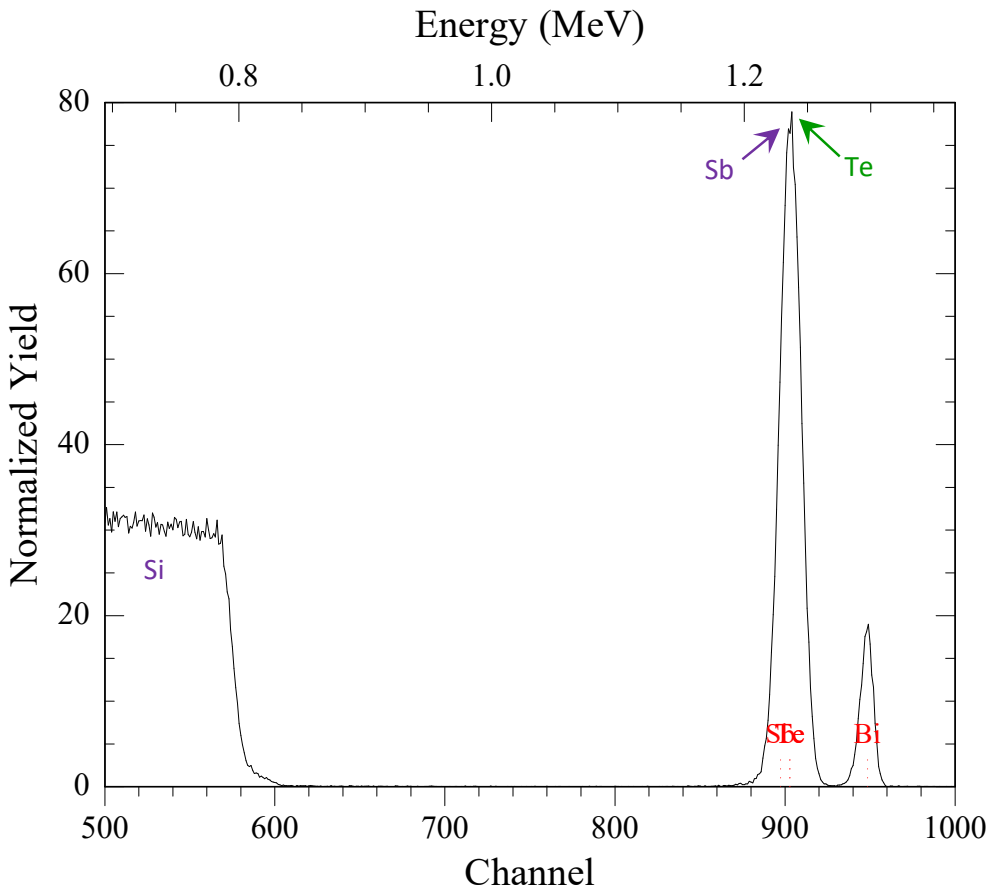

Fig. A2.6: A measured spectrum of BST epilayer via RBS. The expected peak positions of Bi, Sb and Te are marked.

The challenge in the analysis of the BST epilayers arise due to the elemental position of Sb and Te in the RBS spectrum that almost overlap. In BST, with the right configuration of Bi and the fixed amount of Te, quite accurate fittings and thus, the compositional investigations can be performed. Although, the RBS cannot be utilized to analyze Sb and Te contents in Sb_xTe_y alloys.

The acquired data is analyzed with a thickness and composition dependent simulation of an epilayer where the peak fitting provides the exact composition of the different elements. The acquired data of BST alloy along with the simulation can be observed in Figure A2.7.

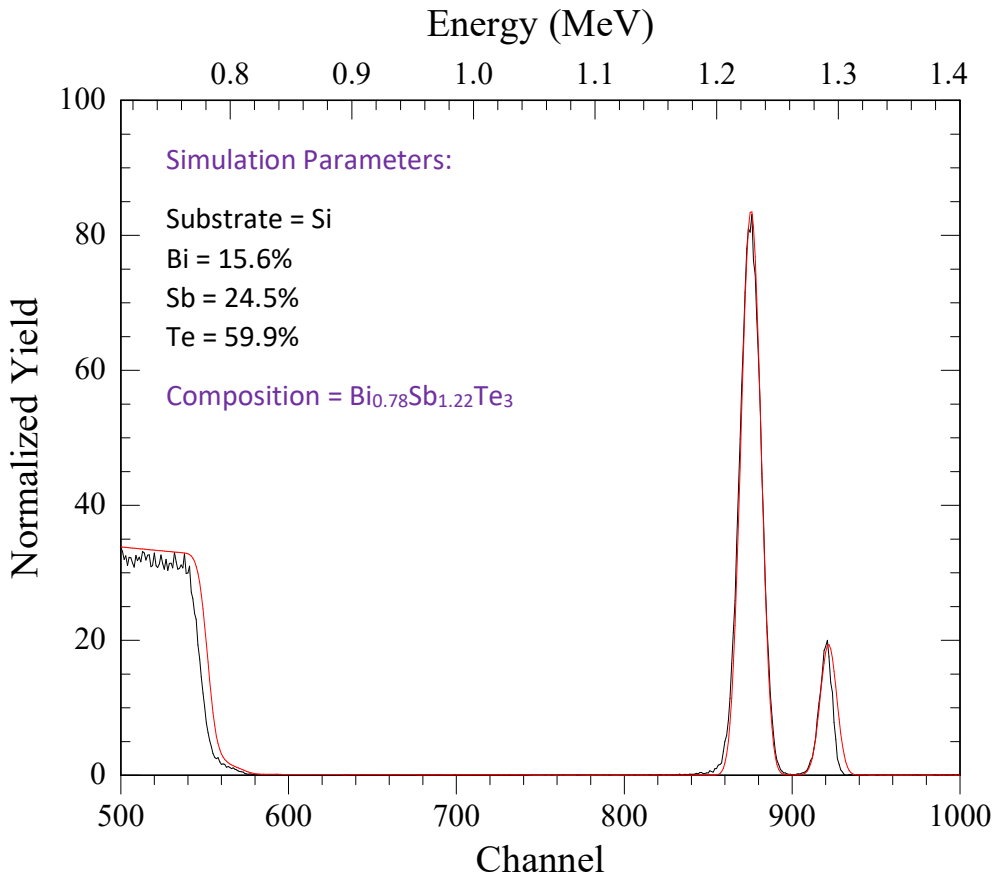

Fig. A2.7: A measured spectrum of BST epilayer along with the simulated data (in red) incorporating the epilayer thickness and the individual elemental contents providing the elemental composition.

Appendix – 3A
SiN_X deposition via PECVD

A 4-inch Si (111) wafer is cleaned with Piranha. The native SiO_2 is removed via wet etching using 1 % HF solution. The wafer is loaded into the Tempress oxidation furnace and 7 nm SiO_2 layer is prepared via dry oxidation process at 900℃. The oxidized wafer is then loaded into the Oxford PECVD reaction chamber and 30 nm of SiNx, using the mixed frequency procedure discussed below, is deposited.

PECVD Process Parameters:

The temperature of the reaction chamber is set to 350℃ and waited for 2 hour until the temperature is stable for homogenous deposition.

1. Pump down:
    - Duration = 1 min

2. Pre-heat and Purge:
    - Gas flow = N_2 at 500 sccm
    - Pressure = 1000 mTorr
    - Duration = 5 min

3. Pre-clean:
    - Gas flow = N_2 at 710 sccm
    - Pressure = 1000 mTorr
    - Duration = 1 min
    - Plasma frequency = HRF
    - Power = 20 W

4. Deposition (Mixed-frequency):
    - Gas flow = N_2 at 380 sccm
      SiH_4 at 20 sccm
      NH_3 at 30 sccm
    - Pressure = 1000 mTorr
    - Power = 35 W
    - Plasma frequency = periodic pulses
      HRF for 15 seconds
      LRF for 6 seconds
    - Total Duration = 1 min and 03 seconds

5. Pump down:
    - Duration = 1 min

Post Deposition Treatment:

The PECVD deposited SiN_x film is unstable in HF based solutions due to presence of H^+ ions in the film. In order to increase the stability of SiN_x, the deposited wafer is processed through rapid thermal annealing (RTA) to harden SiN_x film. This process is conducted in the following steps:

1. Ramp-up:
    - Starting Temp = 20˚C
    - Ending Temperature = 1000˚C
    - Ramp Rate: = 50˚C/second
    - Gas flow = N_2 at 5 liters/min
2. Bake-out:
    - Temperature = 1000˚C
    - Gas flow = N_2 at 5 liters/min
    - Duration = 5 min
3. Slow cool down:
    - Ending Temperature = 150˚C
    - Ramp Rate: = -100˚C/second
    - Gas flow = N_2 at 0.5 liters/min (wafer cools down in approx. 25 minutes to 150˚C before taking out of the chamber. See Figure A3.1)

After the annealing process, the etching rate of PECVD SiN_x drops from 25 nm/min to approx. 2 nm/min in the buffered HF.

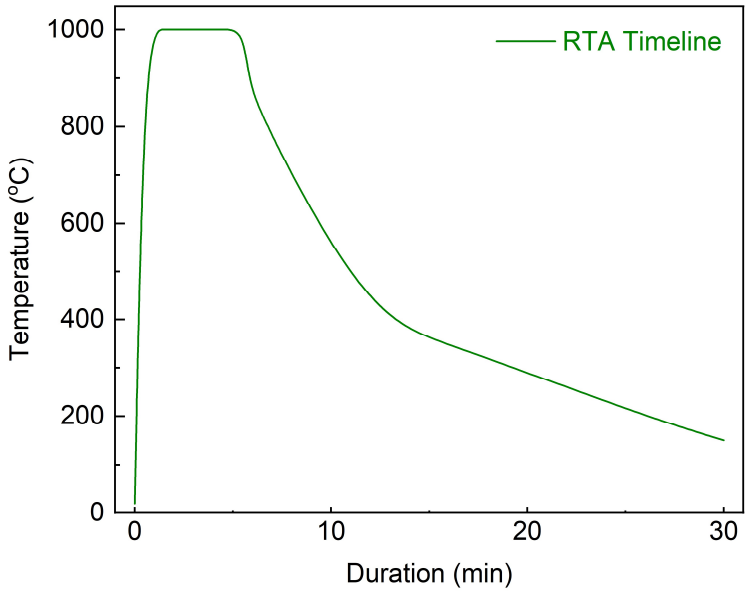

Fig. A3.1: RTA timeline representing all three process steps including ramp-up, bake-out and cool-down.

Appendix – 3B
Fabrication Steps:
Pre-patterned Samples for SAE

The major steps involved in the fabrication of pre-patterned substrates are discussed below.

Wafer-Scale Processing:

- Si (111) wafer is cleaned using process steps discussed in Table 2.2.
- After wet etching of Si native oxide, 7 nm thick layer of SiO_2 layer is prepared (Appendix 3A).
- 30 nm thick layer of SiN_x is prepared via PECVD using the process discussed in Appendix 3A.
- The wafer is RTA annealed at 1000˚C for 5 mins.
- The wafer is cleaned with solvents and spin coated for the first lithography step to prepare the global alignment markers on the wafer. The details of spin coating can be found in Table A3.1 while the e-beam lithography (EBL) steps and development parameters can be found in Table A3.2 and Table A3.3 respectively.

Table A3.1: A summary of the resist coating process on a 4-inch SiN_x + Si (111) wafer for the global marker preperation.

Sub-Process	Parameters
Cleaning	Acetone (5 min) + Isopropanol (5 min) + De-ionized (DI) water (10 min)
	Sample is dried with N2 blow gun
Pre-Bake	5 min @ 150˚C
	Sample is cooled down to 90˚C for resist coating
Resist	UV 6.06 (Positive e-beam resist)
Spin Coating	5 seconds @ 500 rpm + 30 seconds @ 4000 rpm
Soft-Bake	30 seconds @ 90˚C + 1 min @ 130˚C
	Dual-step soft bake step assisted in reducing the strain in UV 6.06 resist layer

Table A3.2: Summary of EBL parameters adopted to expose the global alignment markers on the above mentioned SiN_x + Si (111) 4-inch wafer.

EBL step	Parameters
Acceleration Voltage	100 KV
Step Size	5 nm
Dose $\left[\mu C/cm^2\right]$	58
Beam Current	1 nA
Defocus	+2
Proximity Correction	Yes

Table A3.3: Summary of development steps for the marker wafer.

Step	Parameters
Post-Bake	5 min @ 140˚C
Development	75 seconds in MF CD-26
Development Stop	10 mins in DI water
Hard Bake	1 min @ 90˚C

- The developed wafer is then treated with the reactive ion etching (RIE) to prepare 700 nm deep etched negative markers. The RIE dry etching parameters are listed in Table A3.4. These negative markers assure the accurate alignment of forthcoming lithography steps including pattern transfer, metallization and gate electrodes preparation with a maximum tolerance of ± 5 nm.

Table A3.4: Summary of RIE parameters to etch 30 nm SiNx and 700 nm Si to create negative markers on the 4-inch wafer. (RF = radio frequency, ICP = Inductive coupled plasma, sccm = standard cubic centimeters per minute)

	RIE Parameters	Values
Step 1	Target Material	SiN_x + SiO_2
	Temperature	20℃
	Gas flow	CHF_3 @ 55 sccm + O_2 @ 5 sccm
	RF Power	25 W
	(ICP) Power	100 W
	Duration	60 seconds
Step 2	Target Material	Si
	Temperature	20℃
	Gas flow	SF_6 @ 100 sccm + Ar @ 8 sccm
	RF Power	100 W
	(ICP) Power	0 W (off)
	Duration	100 seconds

- After the etching process, mentioned in Table A3.4, the wafer is cleaned and re-coated using the method listed in Table A3.1 and diced into 7 x 7 mm^2 pieces. Each sample is then processed individually to transfer the desired pattern.

Sample-Scale Processing (Pattern Transfer):

Each of the diced 7 x 7 mm^2 samples is processed individually for the pattern transfer to fabricate trenches on the blocking surface i.e. SiN_x. This step exposed the buried Si (111) surface into the etched trenches where the SAE is performed.

- In the first step the sample is coated with resist using Table A3.5.
- Then desired pattern is exposed on the sample using EBL parameters listed in Table A3.6 and the developments is performed (Table A3.7).
- The samples are finally etched via RIE (Table A3.8) and cleaned with Piranha (Table A3.7). Finally, SAE is performed using MBE.

Table A3.5: A summary of the resist coating process for the pattern transfer on a 7 x 7 mm^2 sample already containing alignment marker.

Sub-Process	Parameters
Cleaning	Acetone (5 min) + Isopropanol (5 min) + De-ionized (DI) water (10 min)
	Sample is dried with N2 blow gun
Pre-Bake	5 min @ 150℃
	Sample is cooled down to 90℃ for resist coating
Resist	Diluted CSAR 62 = (AR-P 6200.09 : AR 600-02) = (1:1) (Positive e-beam resist)
Spin Coating	30 seconds @ 4000 rpm
Soft-Bake	1 min @ 150℃

Table A3.6: Summary of EBL parameters adopted to transfer the nanoscale patterns on the sample for SAE of topological nanostructures.

EBL step	Parameters
Acceleration Voltage	100 KV
Step Size	2 nm
Dose $\left[\mu C/cm^2\right]$	4 x 120
In order to achieve the smooth edges and side walls of trenches at the nanoscale, multi-pass technique (four passes with a quarter dose factor) is utilized.	
Beam Current	200 pA
Special Correction	High resolution and follow geometry
This feature allows patterns with complex and round shaped patterns to be transferred (exposed) with the high resolution and least defective edges	
Proximity Correction	Yes

Table A3.7: Summary of development steps and resist removal for the step of pattern transfer via CSAR resist.

Step	Parameters
Post-Bake	Not required
Development	60 seconds in AR 600-546 *Special conditions (Temperature = 0˚C)*
Development Stop	60 seconds in Isopropanol
Resist removal after RIE etching process (Table A3.8)	
Resist Striping	5 mins (AR 600-71)
Sample Cleaning	Acetone (5 min) + Isopropanol (5 min) + De-ionized (DI) water (10 min)
Plasma Ashing	5 min @ 600 W (O_2 600 sccm)
Removing Organic Contaminations	Piranha Cleaning (Table 2.2)

Table A3.8: Summary of RIE parameters to etch 30 nm SiNx with precisely controlled etch rate to create trenches and expose buried Si (111) surface for SAE.

RIE Parameters	Values
Target Material	SiN_x + SiO_2
Temperature	0˚C *(lower temperatures help to achieve more physical than chemical etching and thus provide better profile of the side wall with lower undercut)*
Gas flow	CHF_3 @ 30 sccm + O_2 @ 2 sccm
RF Power	25 W
(ICP) Power	0 W (off)
Duration	2 min 20 seconds *(Trenches are 35 nm deep etched while 2 nm SiO_2 is left as a buffer to protect Si (111) surface from the exposure to plasma)*

Sample-Scale Processing (Metallization):

After SAE, the top surface of the grown sample is *in situ* passivated with 2 nm of Al deposition that readily oxidized into AlO_x at the exposure to ambient environment. This AlO_x layer protects the samples from further oxidation; however, it is required to etch properly in order to achieve ohmic contacts with the metallic electrodes. The metallization process is achieved in the following steps.

- The grown sample is cleaned using solvents and spin coated with multilayer stack of PMMA resist according to the parameters listed in Table A3.9.
- The spin coated sample is then exposed via EBL using the parameters mentioned in Table A3.10.
- The samples is then developed, the protection layer of AlO_x is wet etched and the metallization process is conducted using the parameters listed in Table A3.11.

Table A3.9: A summary of multi-layer PMMA resist coating process on the MBE grown sample to deposit the metallic contacts.

Sub-Process	Parameters
Cleaning	Acetone (5 min) + Isopropanol (5 min)
	Sample is dried with N2 blow gun
Pre-Bake	5 min @ 100℃
	Sample is cooled down to 90℃ for resist coating
Resist	PMMA (Multi-layer resist system) 50 K (639.03) + 50 K (639.03) + 950 K (679.03)
Spin Coating	30 seconds @ 4000 rpm (for all 3 steps)
Soft-Bake	5 min @ 160℃ (for all 3 steps)
Spin coating and soft bake process has been completed for the first layer before the second spin coating procedure is started. The total stack thickness of 700 nm is achieved.	

Table A3.10: Summary of EBL parameters to write the metallic contacts using multi-layer PMMA resist.

EBL step	Parameters
Acceleration Voltage	100 KV
Step Size	2 nm
Dose $\left[\mu C/_{cm^2}\right]$	490
Beam Current	200 pA
Proximity Correction	Yes

Table A3.11: Summary of development steps for PMMA resist and AlO_x etching.

Step	Parameters
Development	60 seconds in AR 600-55 (solvent)
Development Stop	3 mins in Isopropanol (IPA)
AlOx Etching	1 min in MF CD-26 (TMAH)
Etching Stop	1 mins in Isopropanol (IPA)

- The etched samples are loaded into the e-beam evaporation chamber.
- Using Ar^+ plasma with 10 sccm Ar flow and 30 W power, the surface is treated for 30 seconds with the plasma sputtering to remove any amorphous layers/contaminations.
- The metal is deposited and lift-off is conducted in the DMSO solution.
- After lift-off, the sample is loaded into ALD chamber and 15 nm of HfO_2 is deposited as the gate dielectric.
- Finally, the gate electrodes are prepared using similar steps mentioned above for the metallization process.

Appendix – 3C
Thickness Measurement of Selectively Grown Nanostructures

The thickness of the TI film in the selectively grown nanostructures is measured using the following three methods:

- ***Cross-sectional SEM:*** The selectively grown nanostructures are etched via focus ion beam (FIB) and at the cross-section of the grown nanoribbon, SEM images are acquired that have provided a rough estimate of the layer thickness (with ± 1 nm accuracy). An example of this techniques is depicted in Figure A3.2 where the SEM images are acquired at the cross-section of a 50 nm wide selectively grown Hallbar of Bi_2Te_3 along AA', BB' and CC' directions confirming a homogenous layer thickness of approx. 20 ± 1 nm.

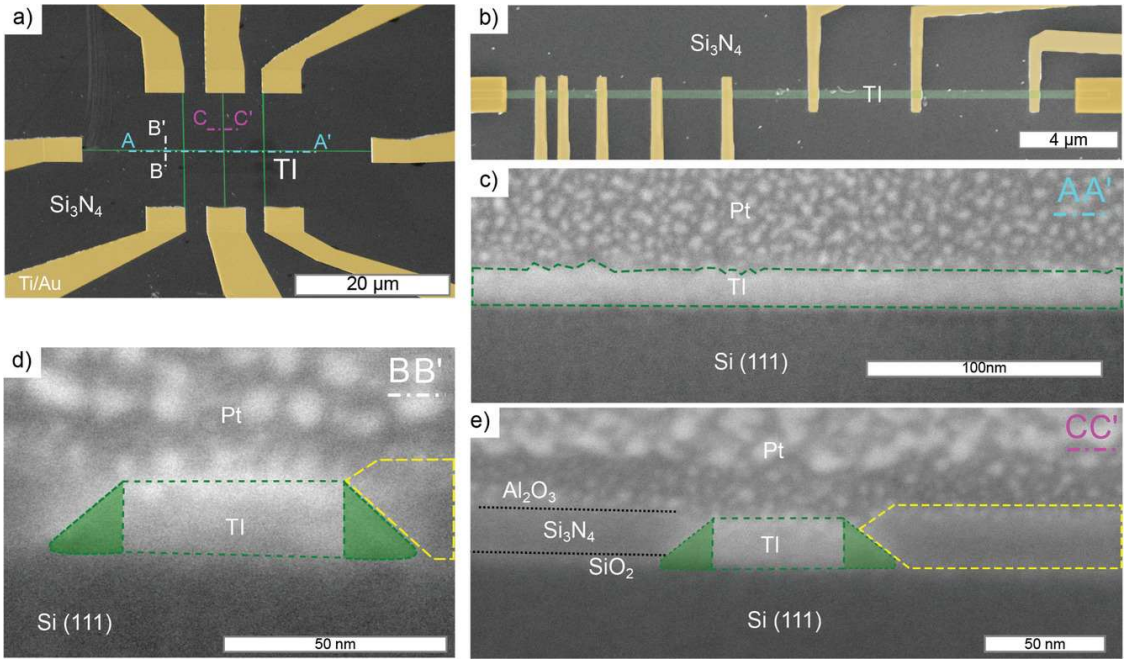

Fig. A3.2: False-colored SEM images of (a) 50 nm wide Hallbar and (b) 500 nm wide selectively grown nanoribbon of Bi_2Te_3. The cross-sectional investigation are conducted via SEM where the facets are prepared via FIB milling. (c) SEM image acquired at the cross-section of 50 nm Hall bar along AA' orientation indicating the layer thickness of 20 ± 1 nm. Similarly, the SEM images acquired along BB' and CC' directions are depicted in (d) and (e) respectively that confirm the homogenous thickness of Bi_2Te_3 epilayer along all directions.

- ***TEM and STEM***: A second approach adopted to measure the thickness of TI layer is the transmission electron microscopy (TEM) and scanning TEM (STEM). This is relatively an expensive and time consuming approach that cannot be utilized on the regular basis; however in this study, it is adopted to investigate the atomic-scale structural characterization of nanostructures after the growth optimization of each material system. This approach provides the high resolution measurements precise to a sub-nm scale. An example of this approach is depicted in Figure A3.3 where a couple of HAADF images indicate the QL stacking of Bi_2Te_3 and Sb_2Te_3 epilayers respectively along with the precise measurement of the layer thickness.

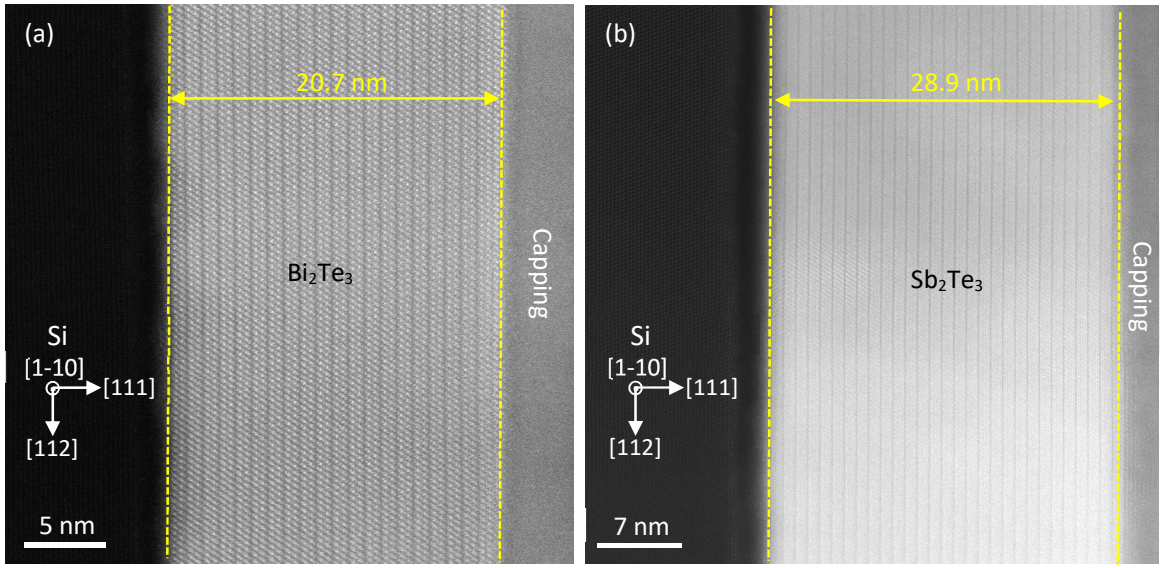

Fig. A3.3: STEM-HAADF images of (a) Bi_2Te_3 and (b) Sb_2Te_3, acquired at the cross-section of 500 nm wide selectively grown nanoribbons along Si [1-10] orientation.

- ***AFM:*** One of the easily adoptable and relatively accurate technique than SEM is the atomic force microscopy (AFM). In order to evaluate the layer thickness, AFM measurements are conducted on the pre-patterned substrates before and after the MBE growth. The difference in the trench depth provides the exact thickness of the TI epilayer in the particular nanostructure. A couple of examples containing AFM topographical images after SAE are depicted in Figure A3.4, while Figures A3.5 - A3.7 depict the line scans of the topographical images before and after SAE where the layer thicknesses of Bi_2Te_3, Sb_2Te_3 and BST epilayers are measured in 500 nm, 100 nm and 30 nm wide trenches respectively.

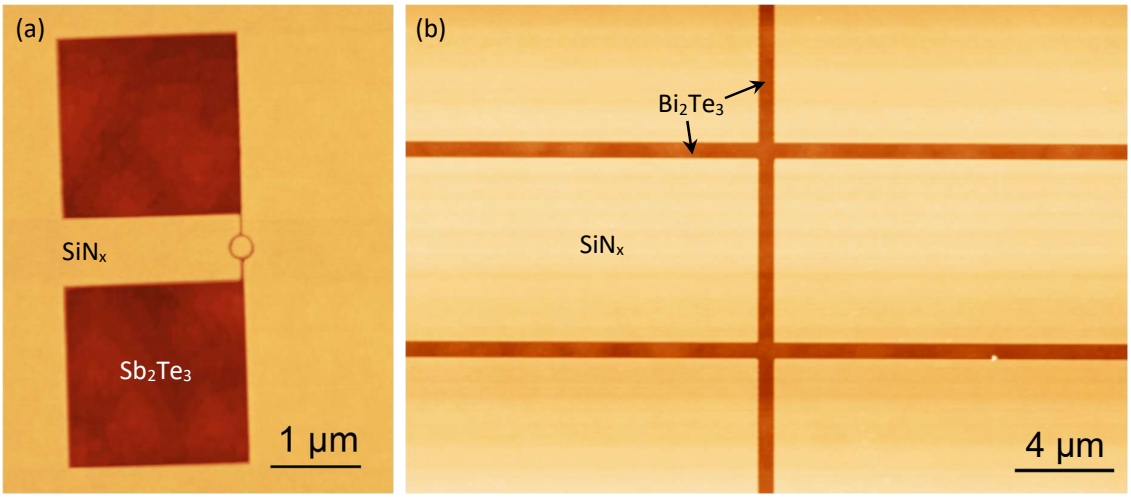

Fig. A3.4: AFM topographical images of selectively grown crystals of (a) Sb_2Te_3 and (b) Bi_2Te_3 on the Si (111) pre-patterned substrates.

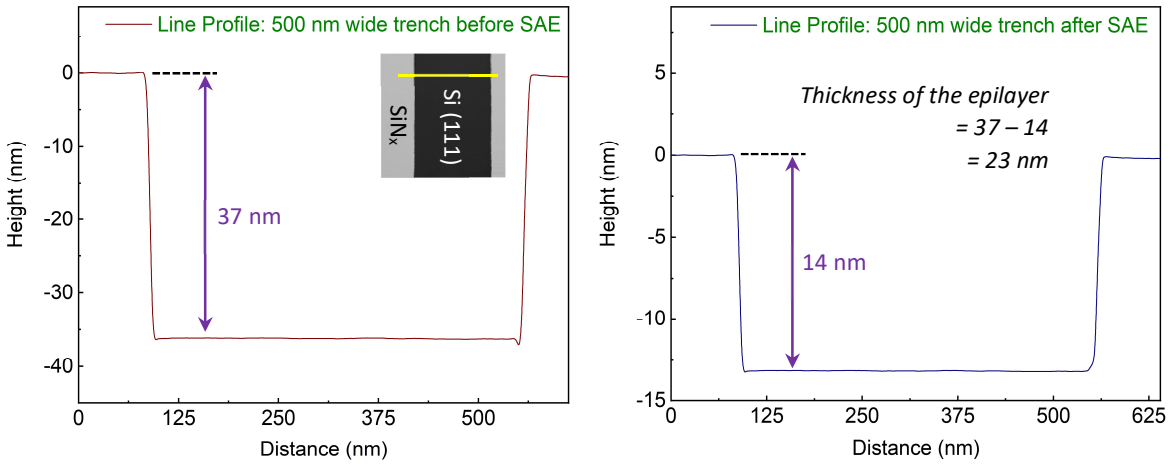

Fig. A3.5: The topographic line scans measured via AFM tapping mode in a 500 nm wide structure before and after the SAE of Bi_2Te_3 that provide the quite accurate measurement of the layer thickness.

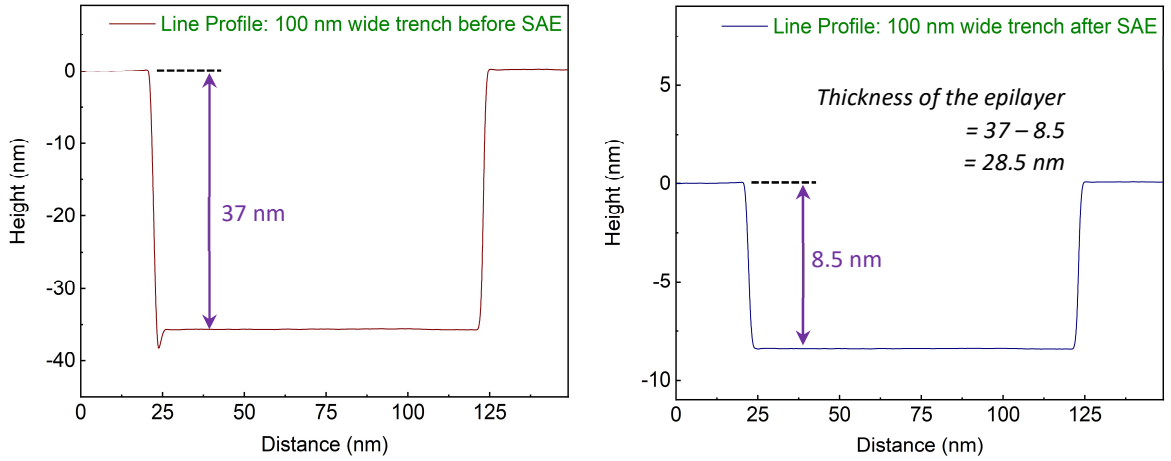

Fig. A3.6: The topographic line scans measured via AFM tapping mode in a 100 nm wide structure before and after the SAE of Sb_2Te_3 that provide the quite accurate estimate of the layer thickness.

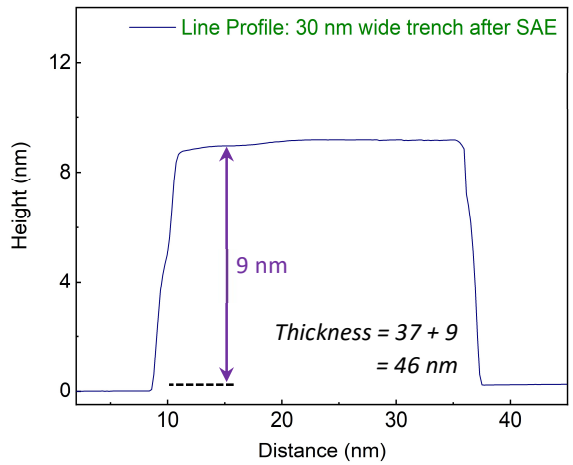

Fig. A3.7: The topographic line scan measured via AFM tapping mode in a 30 nm wide structure after the SAE of the BST alloy that indicates the excessive overgrowth in the nanostructure.

Appendix – 3D SAE Growth Model for Circular Objects and Rings

The growth model stablished in section 3.4 can be adopted for any desired geometry. In the main text, the model is represented specifically for the rectangular and square objects. Here, two examples for the non-conventional geometries are presented.

Circular Objects:

Consider a circular trench as represented in Figure A3.8 (left). During SAE, the impact of lateral diffusion of adatoms (L_D) will impact the geometry as represented in Figure A3.8 (right).

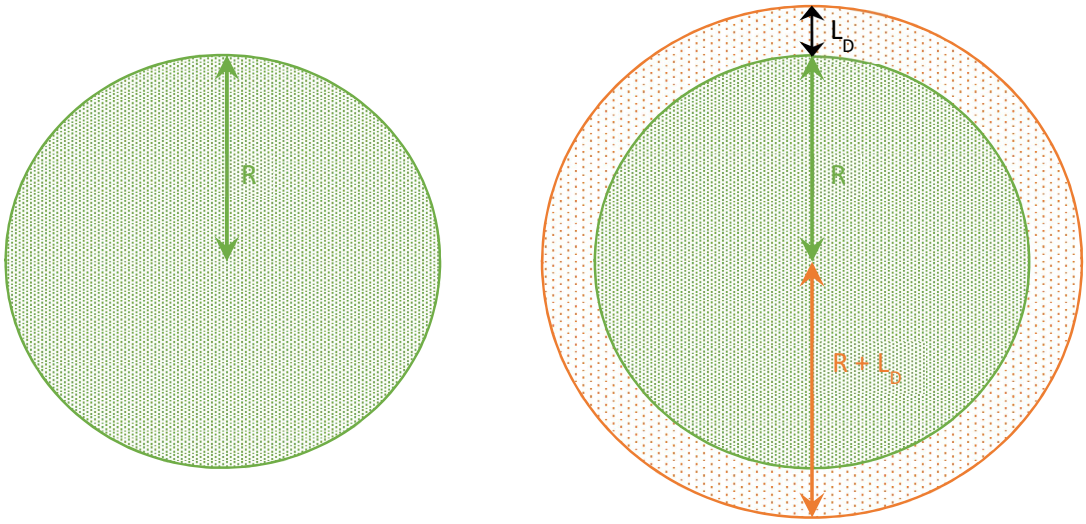

Fig. A3.8: Schematics of a circular trench and the representation of area before and during the selective growth (A_{eff}) due to lateral diffusion length of adatoms (L_D). The radius R of the object increased to ($R+L_D$) while evaluating A_{eff} during SAE.

The effective growth rates (R_{eff}) can be evaluated using the following equations.

$$A = \pi R^2$$

$$A_{eff} = \pi(R + L_D)^2$$

$$\frac{R_{eff}}{R_{TF}} = \frac{A_{eff}}{A}$$

$$R_{eff} = R_{TF}\left[1 + \frac{2L_D}{R} + \frac{\pi {L_D}^2}{A}\right] \quad \text{(A3.1)}$$

The value $\frac{\pi {L_D}^2}{A}$ is too small to have any impact until R = L_D, and thus can be ignored. Thus, R_{eff} can be represented as:

$$R_{eff} = R_{TF}\left[1 + \frac{2L_D}{R}\right] \quad \text{(A3.2)}$$

- If R >> 1 µm, $R_{eff} = R_{TF}$
- If R < 1 µm, R_{eff} can be evaluated using equation A3.2
- If R<< 1 µm, so much that R → L_D, R_{eff} can be evaluated using equation A3.1

Ring Structures:

Consider a circular ring trench as represented in Figure A3.9 (left). During SAE, the impact of lateral diffusion of adatoms (L_D) will impact the geometry as represented in Figure A3. 9 (right).

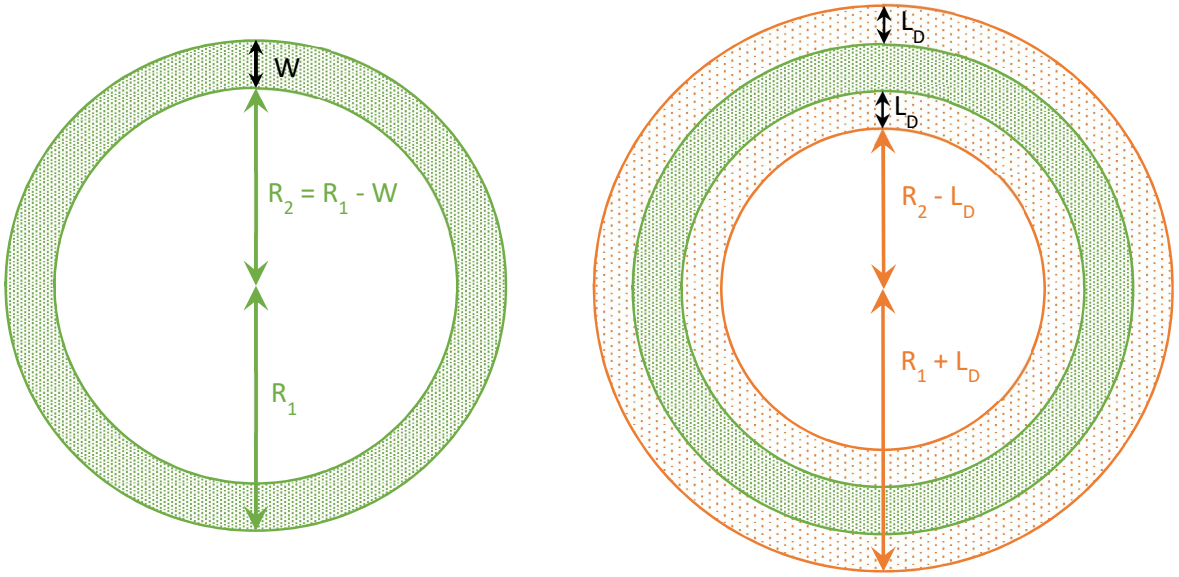

Fig. A3.7: Schematics of a circular ring trench and the representation of area before and during the selective growth (A_{eff}) due to lateral diffusion length of adatoms. The radii of external R_1 and internal rings R_2 of the ring structure will increase to R_1+L_D and R_2-L_D respectively while evaluating A_{eff} during SAE.

The effective growth rates (R_{eff}) can be evaluated using the following equations.

$$A = \pi {R_1}^2 - \pi {R_2}^2 = \pi {R_1}^2 - \pi(R_1 - W)^2$$

$$A = 2\pi R_1 W - \pi W^2$$

$$A_{eff} = \pi(R_1 + L_D)^2 - \pi(R_2 - L_D)^2$$

$$A_{eff} = 2\pi R_1 W - \pi W^2 + 4\pi R_1 L_D - 2\pi W L_D$$

$$\frac{R_{eff}}{R_{TF}} = \frac{A_{eff}}{A}$$

$$R_{eff} = R_{TF}\left[\frac{2\pi R_1 W - \pi W^2 + 4\pi R_1 L_D - 2\pi W L_D}{2\pi R_1 W - \pi W^2}\right]$$

$$R_{eff} = R_{TF}\left[\frac{2\pi R_1 W - \pi W^2}{2\pi R_1 W - \pi W^2} + \frac{4\pi R_1 L_D - 2\pi W L_D}{2\pi R_1 W - \pi W^2}\right]$$

$$R_{eff} = R_{TF}\left[1 + \frac{4\pi R_1 L_D - 2\pi W L_D}{2\pi R_1 W - \pi W^2}\right]$$

$$R_{eff} = R_{TF}\left[1 + \frac{4\pi R_1 L_D - 2\pi W L_D}{2\pi R_1 W - \pi W^2}\right]$$

$$R_{eff} = R_{TF}\left[1 + \frac{2\pi L_D\,(2R_1 - W)}{\pi W(2R_1 - W)}\right]$$

$$R_{eff} = R_{TF}\left[1 + \frac{2\pi L_D}{\pi W}\right]$$

$$R_{eff} = R_{TF}\left[1 + \frac{2L_D}{W}\right] \qquad \text{(A3.3)}$$

$$R_{eff} = R_{TF}\left[1 + \frac{2L_D}{(R_1 - R_2)}\right]$$

- If the width of the ring (W) is >> 1 µm, $R_{eff} = R_{TF}$
- If the width of the ring (W) is < 1 µm, R_{eff} can be estimated via the evaluated relation above.
- In case of ring structures, just W is not the only factor responsible for controlling R_{eff}, the overall value of R_1 and R_2 also govern the change.
    - If R_2 will be too small ($\rightarrow 0$), the impact will be slightly smaller and the trend will start to exhibit more close relation to the circular pattern, discussed in equation A3.2.
    - If R_2 will be large >> 1 µm, the equation A3.3 will provide the precise evaluation of R_{eff}.

Similarly, any pattern can be adopted and via SAE growth model the impact of geometrical patterns on R_{eff} can be easily evaluated.

Appendix – 4A
Stacking Sequences of Bi_xTe_y Stoichiometric States

Stacking sequences in a unit cell

Bi_8Te_9:

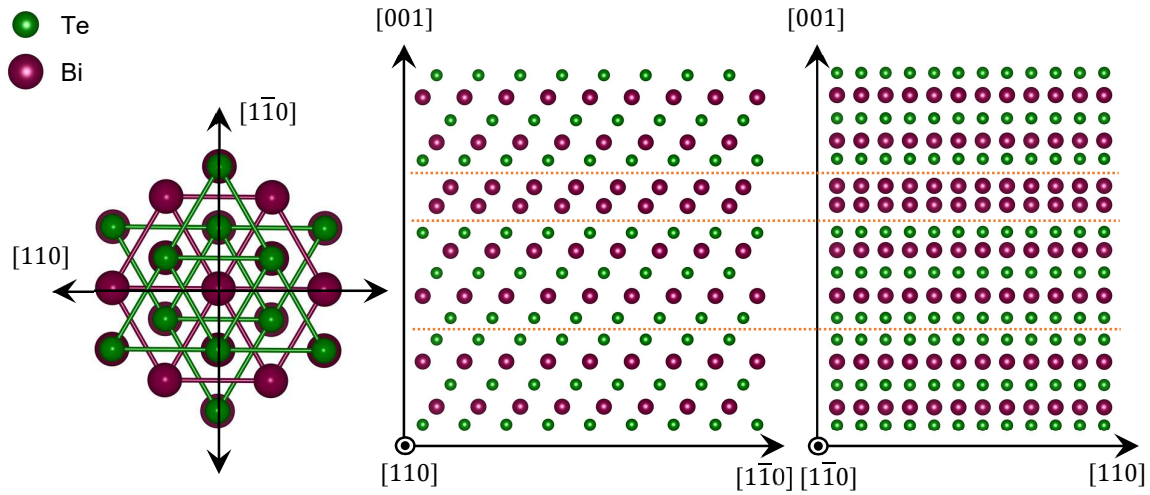

Fig. A4.1: A model representing the layer stacking sequence of Bi_8Te_9 characteristic cell along $[001]$, $[110]$ *and* $[1\bar{1}0]$ *orientations. The stacking order of QQBQ along* $[001]$ *orientation is evident where Q and B represent Bi_2Te_3 quintuple layer and Bi_2 bilayer respectively. As Bi_8Te_9 exhibits the multiple of 3 issue, the whole characteristic cell has to repeat 3 times periodically to complete a unit cell. The dotted orange lines are indicating the presence of Van-der-Waals interactions (VdW gaps).*

Bi_1Te_1:

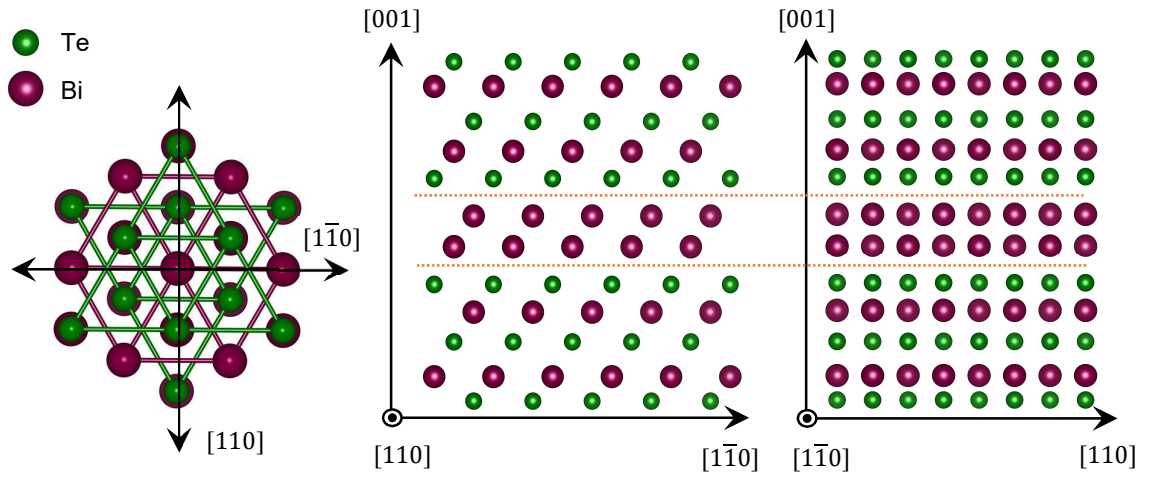

Fig. A4.2: A model representing the layer stacking sequence of Bi_1Te_1 unit cell along $[001]$, $[110]$ *and* $[1\bar{1}0]$ *orientations. The stacking order of QBQ along* $[001]$ *orientation is evident.*

$Bi_{10}Te_9$:

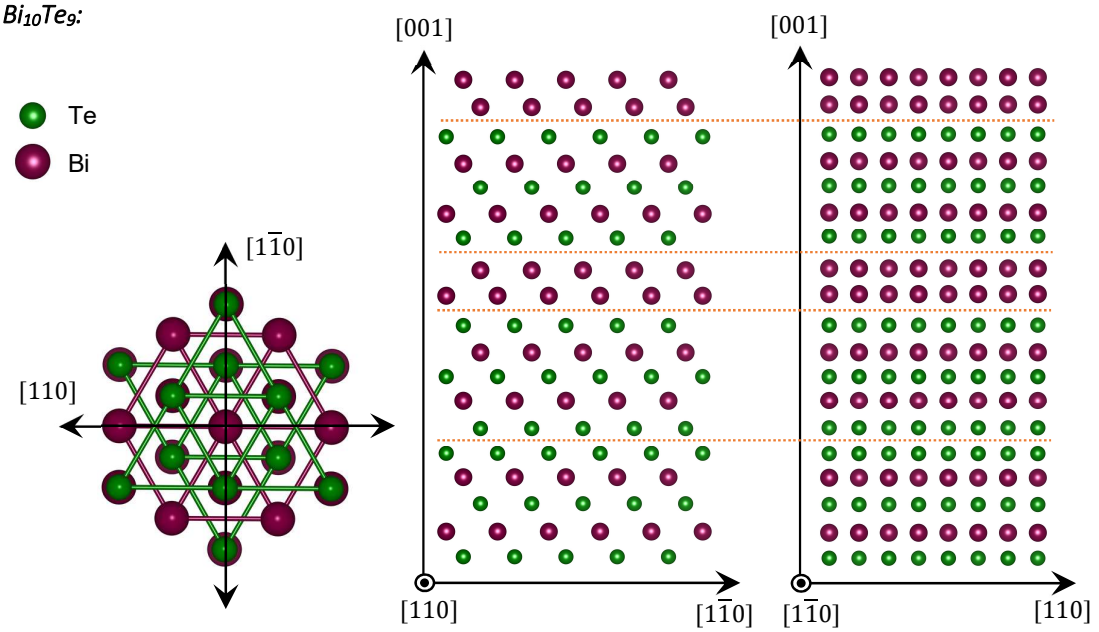

Fig. A4.3: A model representing the layer stacking sequence of $Bi_{10}Te_9$ characteristic cell along $[001]$, $[110]$ *and* $[1\bar{1}0]$ *orientations. The stacking order of QQB-QB along* $[001]$ *orientation is evident. As $Bi_{10}Te_9$ exhibits the multiple of 3 issue, the whole characteristic cell has to repeat itself 3 times to complete a unit cell.*

Bi_8Te_7:

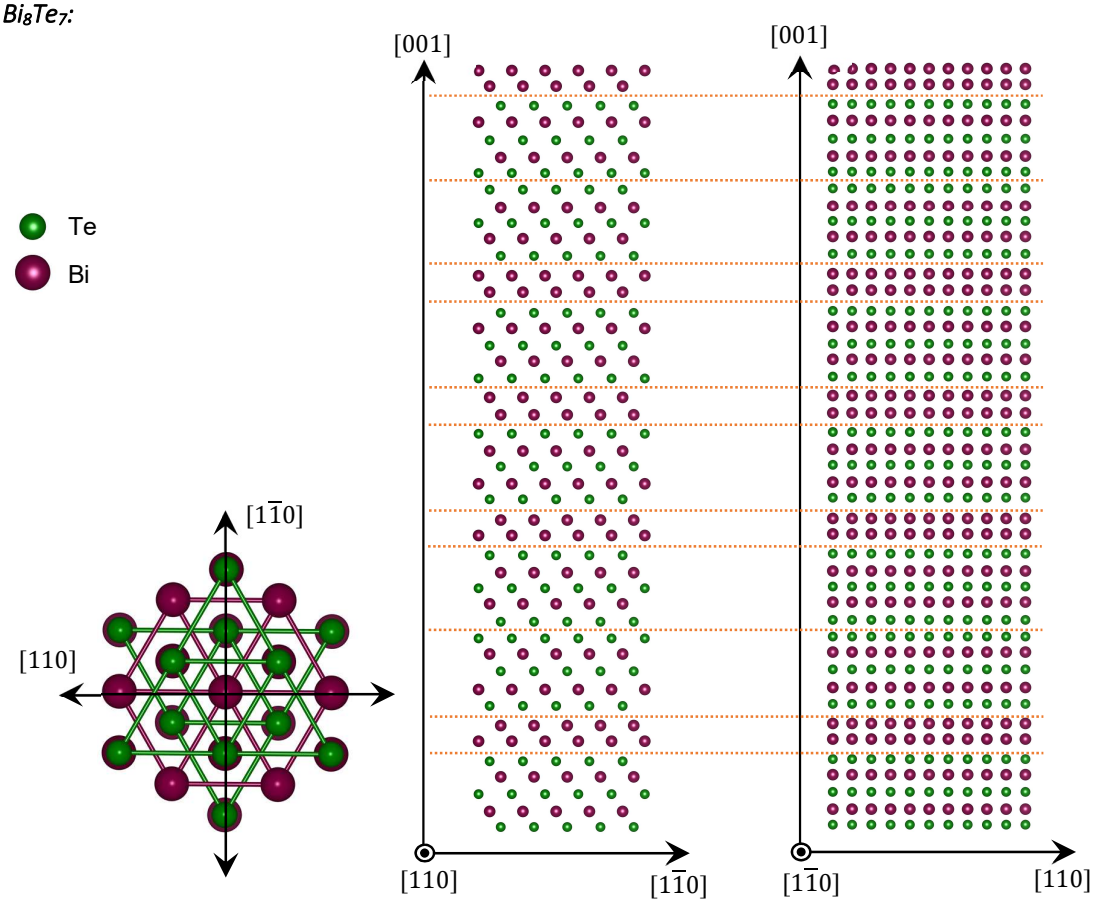

Fig. A4.4: A model representing the layer stacking sequence of $Bi_{10}Te_9$ unit cell along $[001]$, $[110]$ *and* $[1\bar{1}0]$ *orientations. The stacking order of QBQQB-QB-QBQQB along* $[001]$ *orientation is evident.*

Bi_7Te_6:

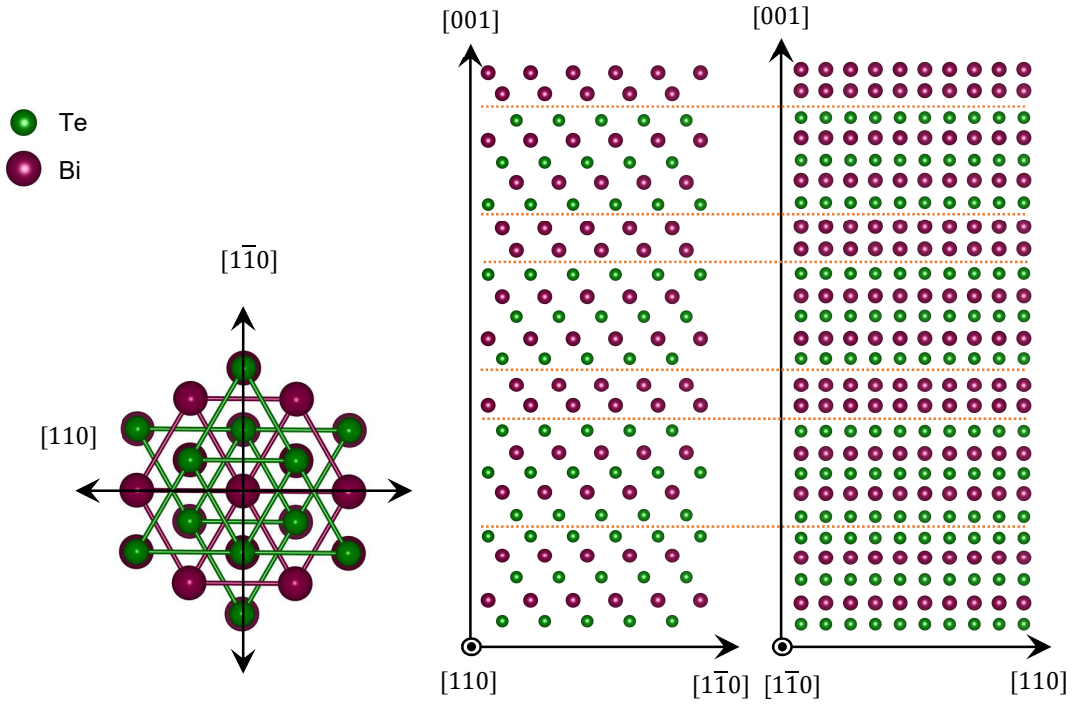

Fig. A4.5: A model representing the layer stacking sequence of Bi_7Te_6 characteristic cell along $[001]$, $[110]$ *and* $[1\bar{1}0]$ *orientations. The stacking order of QQB-QBQB along* $[001]$ *orientation is evident. As Bi_7Te_6 exhibits the multiple of 3 issue, the whole characteristic cell has to repeat itself 3 times to complete a unit cell.*

Bi_4Te_3:

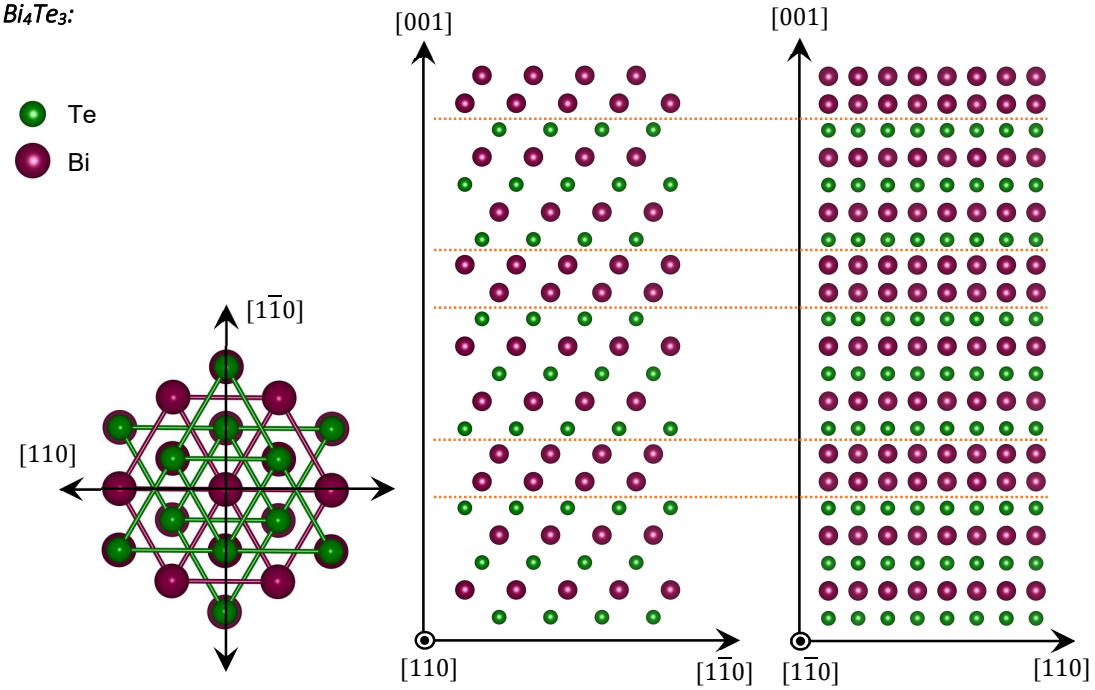

Fig. A4.6: A model representing the layer stacking sequence of Bi_4Te_3 unit cell along $[001]$, $[110]$ *and* $[1\bar{1}0]$ *orientations. The stacking order of QB-QB-QB along* $[001]$ *orientation is evident.*

Bi_2Te_1:

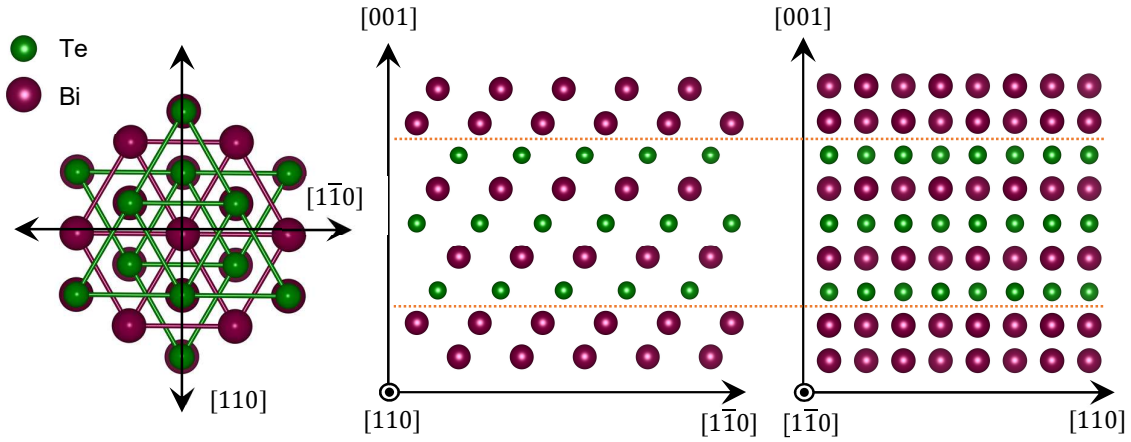

Fig. A4.7: A model representing the layer stacking sequence of Bi_2Te_1 unit cell along [001], [110] *and* [1$\bar{1}$0] *orientations. The stacking order of BQB along* [001] *orientation is evident.*

XRD – Reciprocal space maps (RSMs)

Bi_1Te_1:

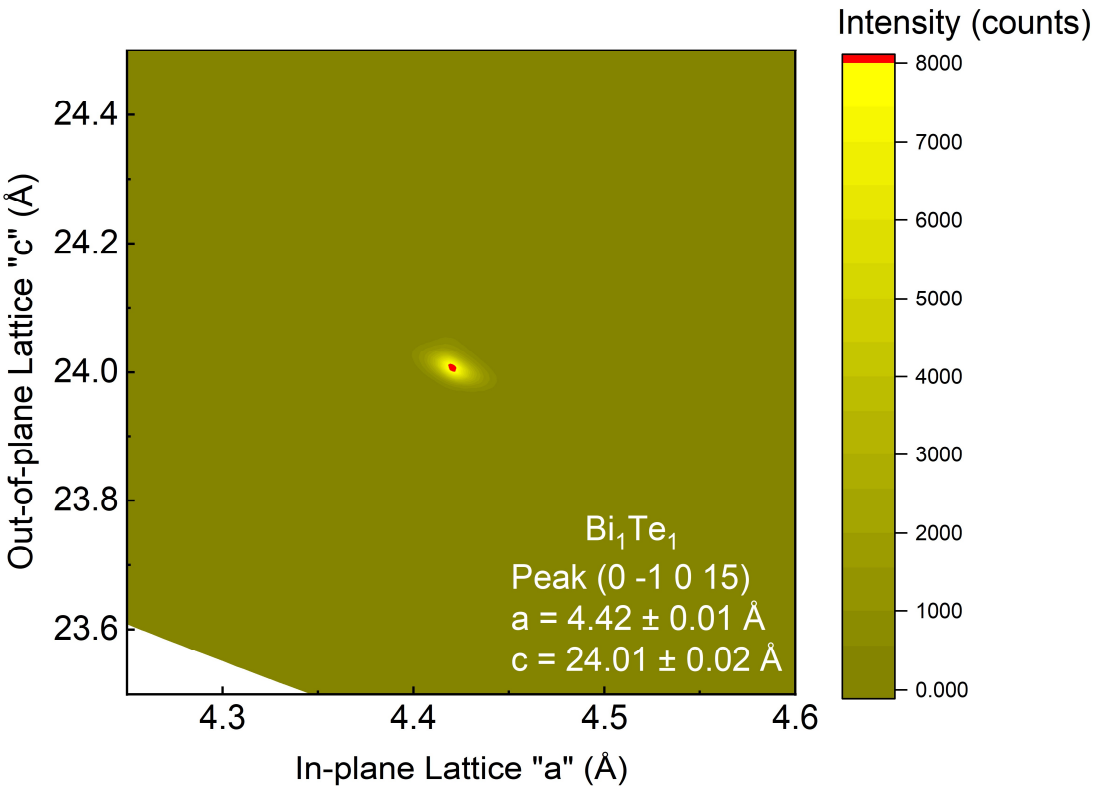

Fig. A4.8: XRD reciprocal space map, acquired along the (0 -1 0 15) peak of Bi_1Te_1 epilayer, providing the information about the lattice parameters of the crystal.

Bi_4Te_3:

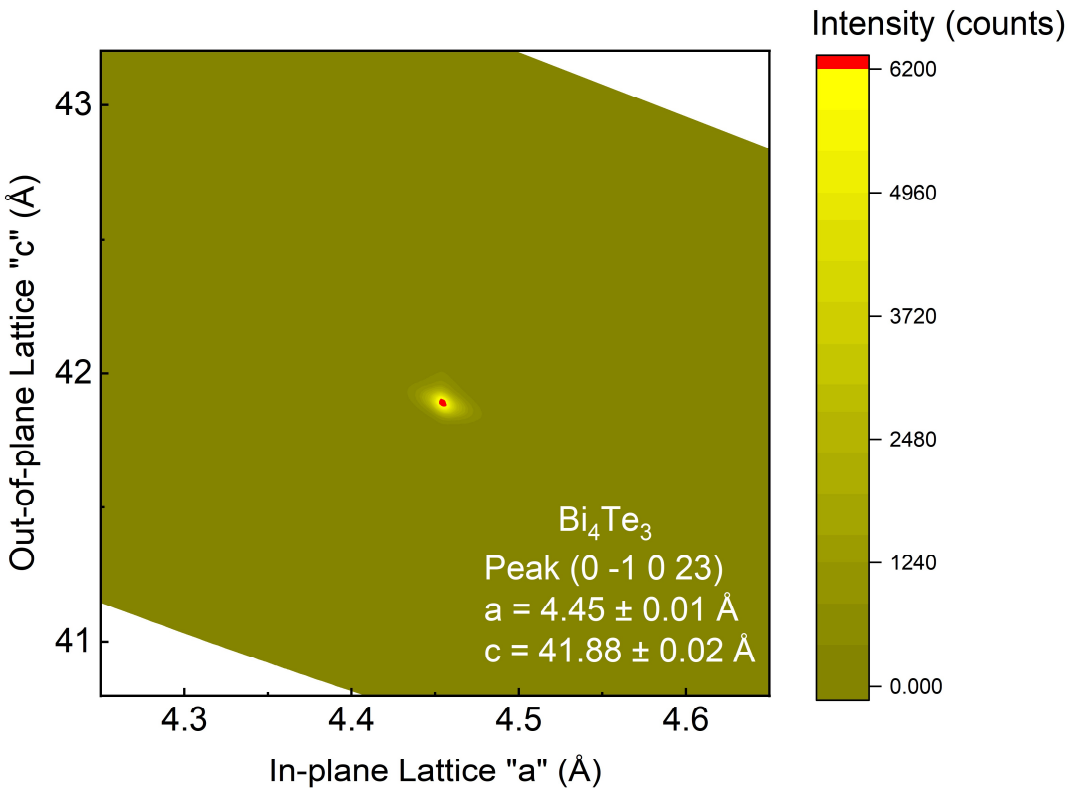

Fig. A4.8: XRD reciprocal space map, acquired along the (0 -1 0 23) peak of Bi_4Te_3 epilayer, providing the information about the lattice parameters of the crystal.

Appendix – 4B
Summary of Growth Parameters for all Bi_xTe_y Stoichiometric States

The summary of all growth parameters for all BixTey alloys is listed is Table A4.1.

Table A4.1: An overview of all Bi_xTe_y stoichiometric alloys prepared via MBE. For each state the relative contents of individual elements i.e. Bi and Te, the total number of individual layers of additive (m) and base (n) in a unit cell, the individual effusion cell temperatures, the growth temperature and the flux ratios are listed.

Bi_xTe_y	m	n	Bi (%)	Te (%)	T_{Bi} (°C)	T_{Te} (°C)	T_{sub} (°C)	Bi/Te Flux Ratio	Unit Cell Length (Å)
Bi_2Te_3	0	3	40.00	60.00	470	320	300	1 : 9.5	30.48
Bi_3Te_4	1	8	42.85	57.15	470	305	300	1 : 9	84.98
Bi_7Te_9	3	18	43.75	56.25	470	303	300	1 : 8.7	193.98
Bi_4Te_5	1	5	44.45	55.55	470	300	300	1 : 8.5	54.47
$Bi_{22}Te_{27}$	6	27	44.90	55.10	470	298	300	1 : 8.3	296.6
Bi_5Te_6	3	12	45.45	54.55	470	296	300	1 : 8	133.02
Bi_6Te_7	2	7	46.15	53.85	470	294	300	1 : 7.7	78.51
Bi_7Te_8	5	16	46.66	53.34	470	292	300	1 : 7.4	181.03
Bi_8Te_9	3	9	47.06	52.94	470	289	300	1 : 6.9	102.58
Bi_9Te_{10}	7	20	47.37	52.63	470	287	300	1 : 6.3	229.12
$Bi_{14}Te_{15}$	6	15	48.28	51.72	470	285	300	1 : 5.9	174.72
Bi_1Te_1	1	2	50.00	50.00	470	280	300	1 : 5	24.01
$Bi_{16}Te_{15}$	9	15	51.61	48.39	476	280	300	1 : 4.5	186.11
$Bi_{14}Te_{13}$	8	13	54.85	48.15	478	280	300	1 : 4.3	162.07
$Bi_{12}Te_{11}$	7	11	52.17	47.83	480	280	300	1 : 4	137.91
$Bi_{10}Te_9$	6	9	52.63	47.37	484	280	300	1 : 3.6	113.96
Bi_9Te_8	11	16	52.94	47.06	485	280	300	1 : 3.5	204.4
Bi_8Te_7	5	7	53.33	46.67	487	280	300	1 : 3.2	89.91
Bi_7Te_6	9	12	53.85	46.15	489	280	300	1 : 3	155.76
Bi_6Te_5	4	5	54.54	45.46	492	280	300	1 : 2.8	65.91
Bi_5Te_4	7	8	55.55	44.45	497	280	300	1 : 2.5	107.85
Bi_4Te_3	3	3	57.14	42.86	505	280	300	1 : 2	41.89
Bi_7Te_5	11	10	58.33	41.67	515	285	300	1 : 1.9	143.69
$Bi_{10}Te_7$	8	7	58.82	41.18	518	285	300	1 : 1.8	101.80
Bi_3Te_2	5	4	60	40	522	285	300	1 : 1.7	59.85
$Bi_{14}Te_9$	12	9	60.87	39.13	520	275	290	1 : 1.6	137.62
Bi_8Te_5	7	5	61.54	38.46	522	275	290	1 : 1.5	77.77
Bi_5Te_3	9	6	62.5	37.5	525	275	290	1 : 1.4	95.71
$Bi_{12}Te_7$	11	7	63.15	36.85	528	270	285	1 : 1.3	113.62
Bi_7Te_4	13	8	63.63	36.37	532	270	285	1 : 1.2	131.55
Bi_2Te_1	2	1	66.67	33.33	542	260	280	1 : 1	17.92
Bi_2	3	0	100	0	540	0	70	1 : 0	11.86

Appendix – 4C
Topology of individual Building Blocks in Bi_xTe_y System

Bi based compounds below the critical thickness of 3D TIs i.e. 6 nm exhibit a crossover between the 2D topological and trivial phases depending upon the thickness of the epilayer. This trend has been observed in the binary compound of Bi_2Te_3 and the ternary alloys of $Ge_1Bi_2Te_4$ (GBT-124) and $Pb_1Bi_2Te_4$ (PBT-124). The calculation of 2D topological invariant "ν", measured on the basis of the epilayer thickness i.e. total number of QLs and SLs, is listed in Table A4.2.

Table A4.2: Topological invariant v and bandgap of thin films of 3D TIs as a function of film thickness in quintuple layers (QL) or septuple layers (SL). Data acquired from "Ab-initio Calculations of Two-dimensional Topological Insulators by G. Bihlmayer"

Bi_2Te_3			$GeBi_2Te_4$			$PbBi_2Te_4$		
QLs	ν	gap (meV)	SLs	ν	gap (meV)	SLs	ν	gap (meV)
1	0	266	1	0	453	1	0	298
2	1	50	2	1	132	2	1	137
3	0	-	3	1	54	3	0	64
4	1	-	4	0	18	4	1	33
5	1	-	5	1	3	5	1	15

A similar trend is also observed in the basic building blocks of Bi_xTe_y alloys. An example of the observed trend of 2D topology with the change in the stacking sequence of layers is listed in Table A4.3 and the edge band structure for QB and QBQ building blocks is depicted in Figure A4.10.

Table A4.3: Topological invariant v and bandgap of thin films of 3D TIs as a function of film thickness in quintuple layers (QL) or septuple layers (SL). Calculations performed by "G. Bihlmayer"

Compound	Building Block	Stacking Sequence	Thickness (Å)	2D Topological invariant (ν)
Bi_2	BB	BL	3.95	1
Bi_2	BB	BL-BL	7.91	0
Bi_2Te_3	QQ	QL	10.15	0
Bi_4Te_3	QB	QL-BL	13.98	0
Bi_2Te_1	BQB	BL-QL-BL	17.94	0
Bi_2Te_3	QQ	QL-QL	20.31	1
Bi_1Te_1	QBQ	QL-BL-QL	24.01	1
Bi_4Te_3	QB	QL-BL-QL-BL	27.93	1
Bi_2Te_3	QQ	QL-QL-QL	30.48	0
Bi_2Te_3	QQ	QL-QL-QL-QL	40.64	1
Bi_1Te_1	QBQ	QL-BL-QL-QL-BL-QL	48.02	1
Bi_2Te_3	QQ	QL-QL-QL-QL-QL	50.80	1

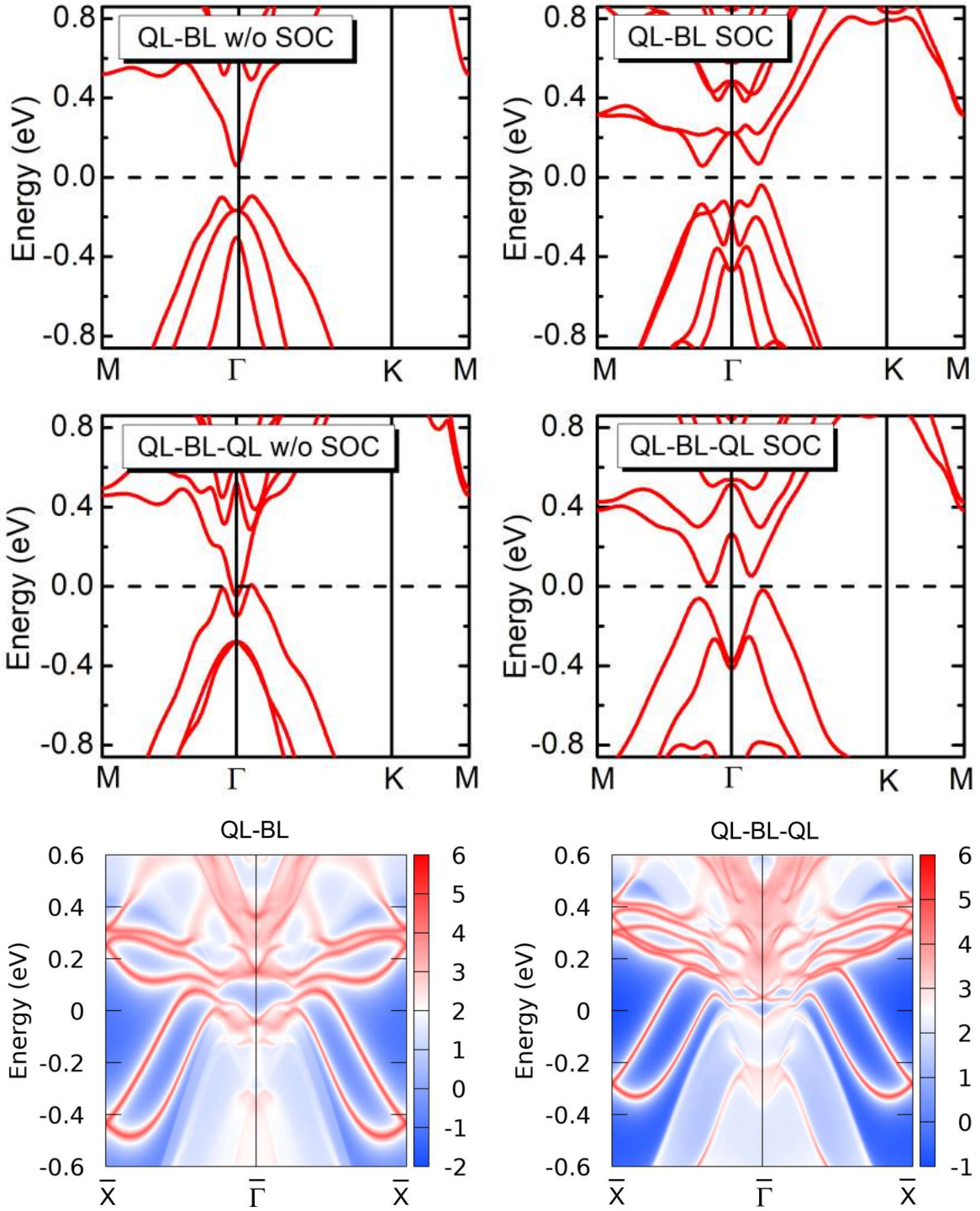

Fig. A4.10: Theoretical band calculations of the building blocks QB and QBQ with and without spin-orbit coupling. The bottom plots represent the edge band calculations to observe the 2D TI states that are absent in the QB block; however, can be observed in the QBQ block.

Appendix – 5A
Stacking Sequences in GST Stoichiometric Alloys

The stacking sequences of GST/GBT alloys along with the distribution of Ge in the layer architecture is describes below:

GXT-023 = (Sb_2Te_3 / Bi_2Te_3): Stacking order in a unit cell

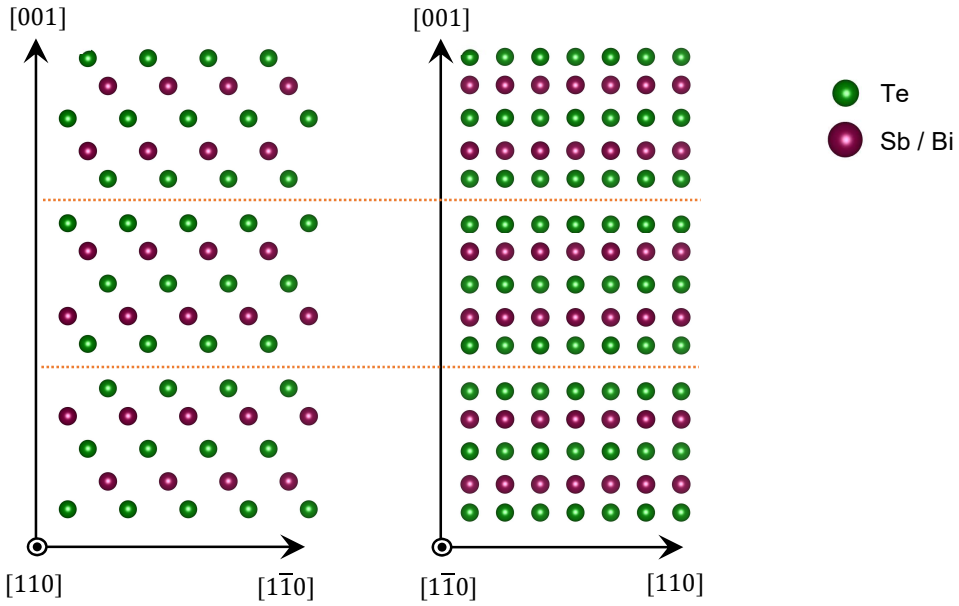

Fig. A5.1: A model representing Sb_2Te_3 / Bi_2Te_3 unit cell and the layer stacking sequence along $[110]$ *and* $[1\bar{1}0]$ *orientations. The maroon color represents Sb / Bi atoms while the green color indicates the locations of Te atoms. The stacking order of QQQ along* $[001]$ *orientation is evident where Q represents a quintuple layer. The dotted orange lines are indicating the presence of Van-der-Waals interactions (VdW gaps).*

GXT-147: Ge distribution and stacking order in a unit cell

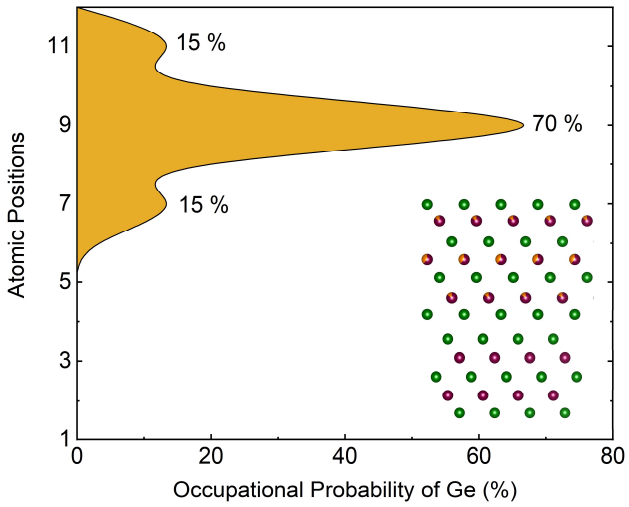

Fig. A5.2: Based on STEM investigations, the occupational probability of Ge atoms vs. atomic position in a unit cell, is plotted. The distribution of Ge contents in a septuple layer are derived from GST-1X4 while the quintuple layer does not contain Ge at all, except for the antisite defects.

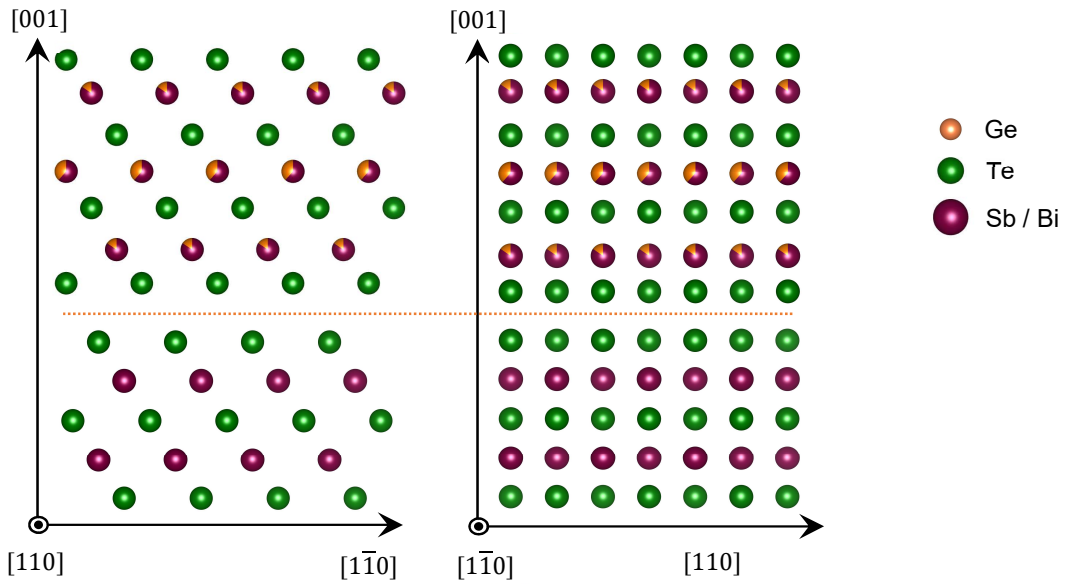

Fig. A5.3: A model representing GXT-147 unit cell and the layer stacking sequence along $[110]$ *and* $[1\bar{1}0]$ *orientations. The maroon color represents Sb / Bi atoms, the green color represents Te atoms while the orange color indicates the locations of Ge atoms. The stacking order of QS along* $[001]$ *orientation is evident where Q and S represent a quintuple layer and a septuple layer respectively. The dotted orange lines are indicating the presence of Van-der-Waals interactions (VdW gaps).*

GXT-124: Ge distribution and stacking order in a unit cell

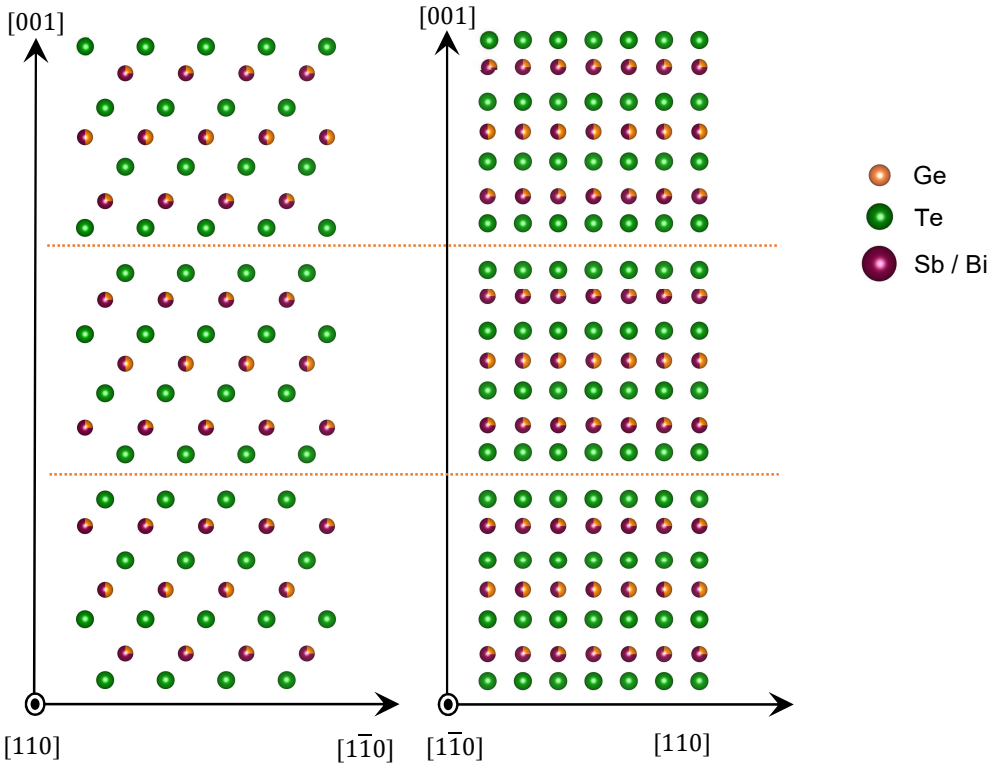

Fig. A5.4: A model representing GXT-124 unit cell and the layer stacking sequence along $[110]$ *and* $[1\bar{1}0]$ *orientations. The maroon color represents Sb / Bi atoms, the green color represents Te atoms while the orange color indicates the locations of Ge atoms. The stacking order of SSS along* $[001]$ *orientation is evident where S represents a septuple layer. The dotted orange lines are indicating the presence of Van-der-Waals interactions (VdW gaps).*

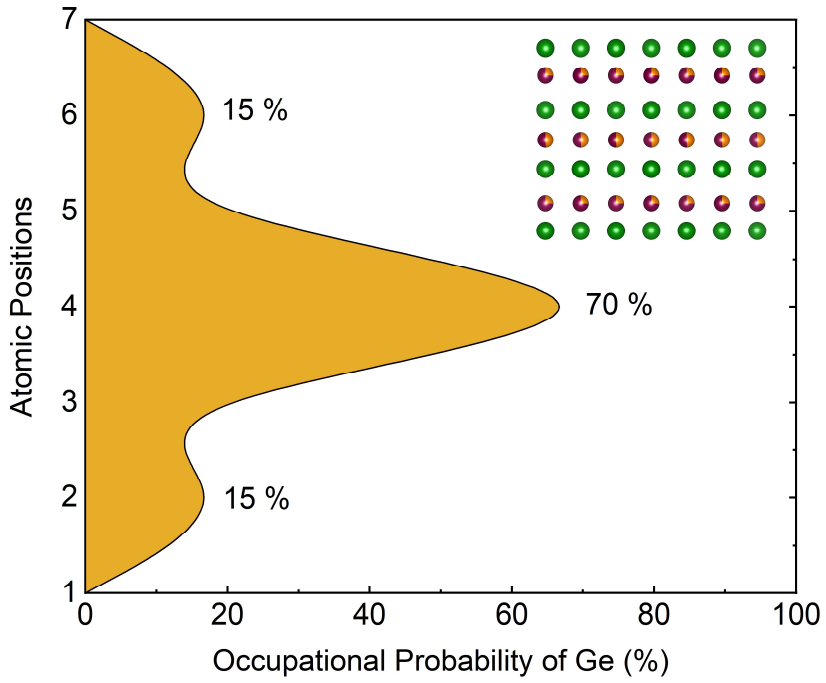

Fig. A5.5: Based on STEM investigations, the occupational probability of Ge atoms vs. atomic position in a septuple layer of GXT-124, is plotted. As GXT-124 suffers from the multiple of 3 issue, a unit cell contains 3 septuple layers with the depicted distribution.

GXT-225 = Ge distribution and stacking order in a unit cell

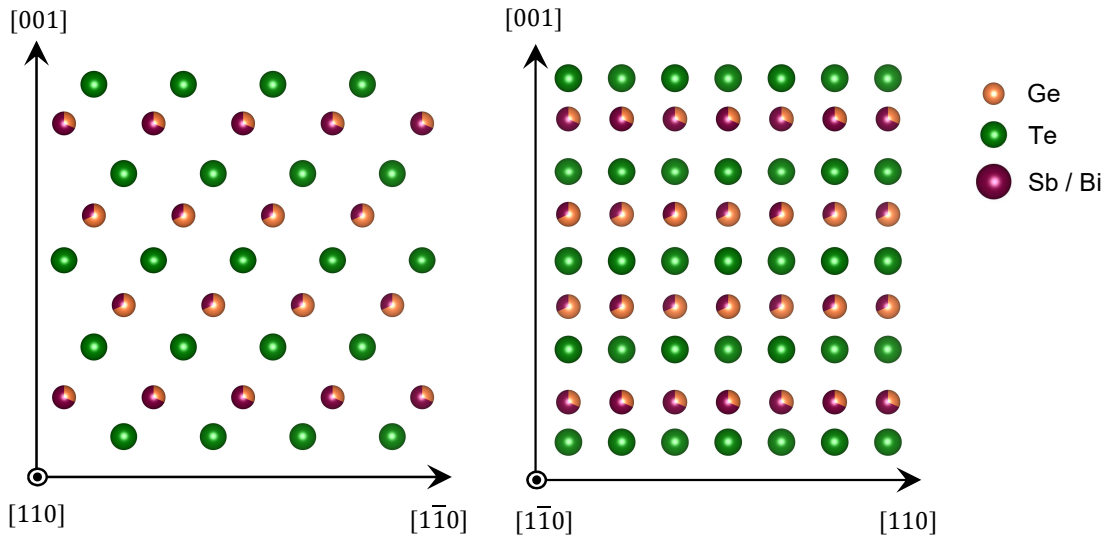

Fig. A5.6: A model representing GXT-225 unit cell and the layer stacking sequence along $[110]$ *and* $[1\bar{1}0]$ *orientations. The maroon color represents Sb / Bi atoms, the green color represents Te atoms while the orange color indicates the locations of Ge atoms. The stacking contains a single block of 9-atomic supercell along* $[001]$ *orientation. Each cell stacks with the other cells through weakly bonded Van-der-Waals interactions.*

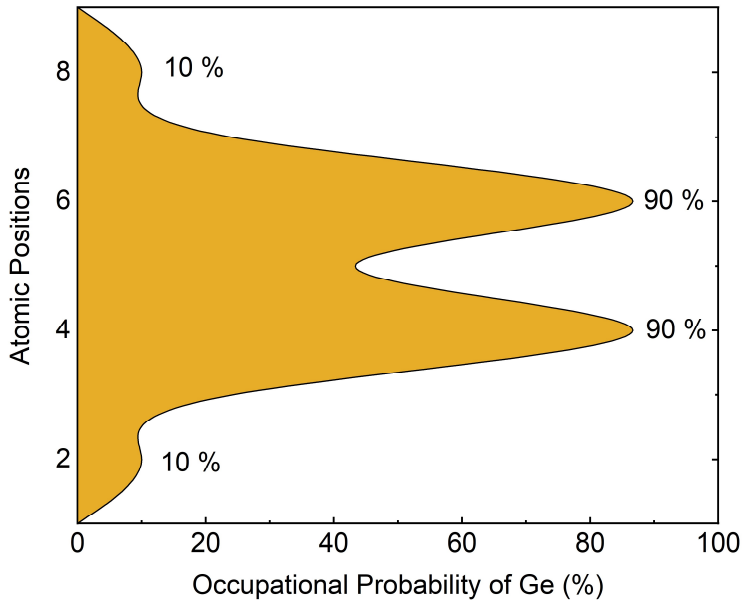

Fig. A5.7: Based on STEM investigations, the occupational probability of Ge atoms vs. atomic position in a 9-atomic cell of GXT-225, is plotted. As, a GST-225 supercell contains 9-atomic layer; 9 being a multiple of 3, this 9-atomic layer acts as a complete unit cell of GXT-225.

GXT-326: Ge distribution and stacking order in a unit cell

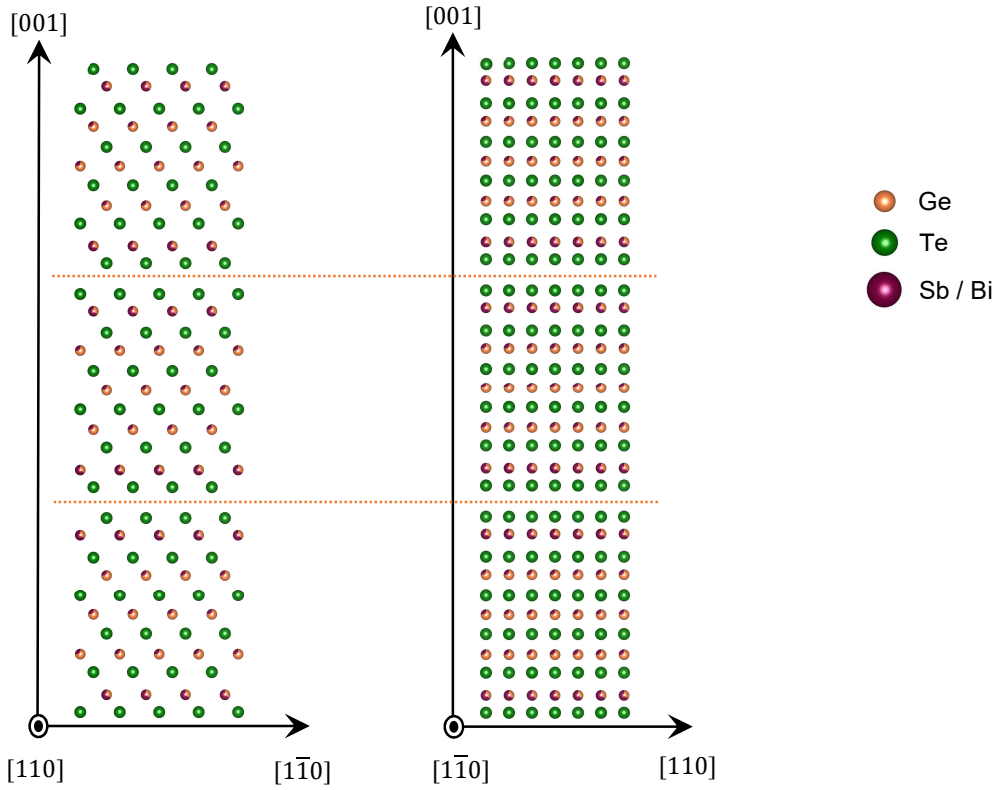

Fig. A5.8: A model representing GXT-326 unit cell and the layer stacking sequence along $[110]$ *and* $[1\bar{1}0]$ *orientations. The maroon color represents Sb / Bi atoms, the green color represents Te atoms while the orange color indicates the locations of Ge atoms. The stacking order of 3 periodic 11-atomic units along* $[001]$ *orientation is evident. The dotted orange lines are indicating the presence of Van-der-Waals interactions (VdW gaps).*

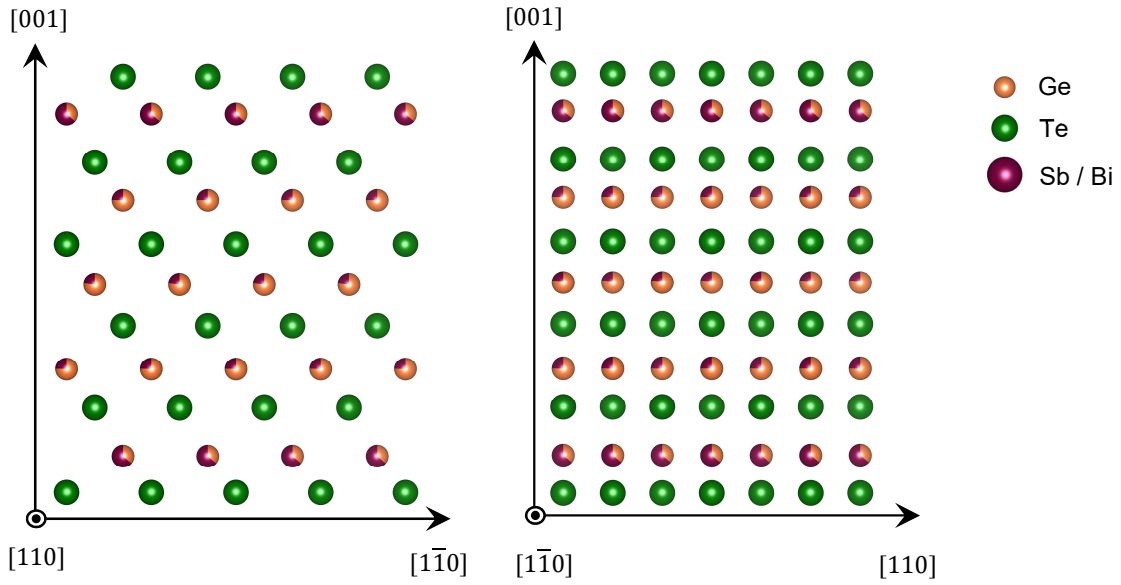

Fig. A5.9: A better resolved image of 11-atomic unit of GXT-326 depicted in Fig A5.8

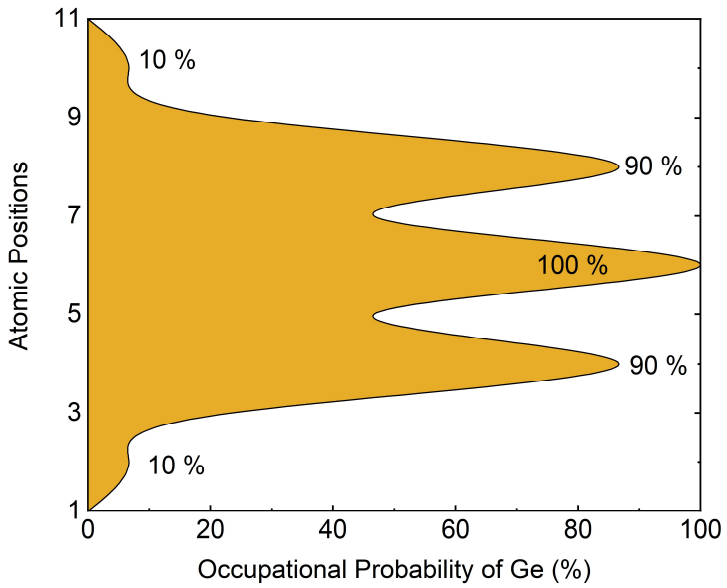

Fig. A5.10: Based on STEM investigations, the occupational probability of Ge atoms vs. atomic position in a 11-atomic cell of GXT-326, is plotted. As GXT-326 suffers from the multiple of 3 issue, a unit cell contains 3 stacks of 11-atomic supercells with the periodic distribution of Ge depicted above for a single cell.

GXT-225: Various proposed interatomic arrangements for IPCMs

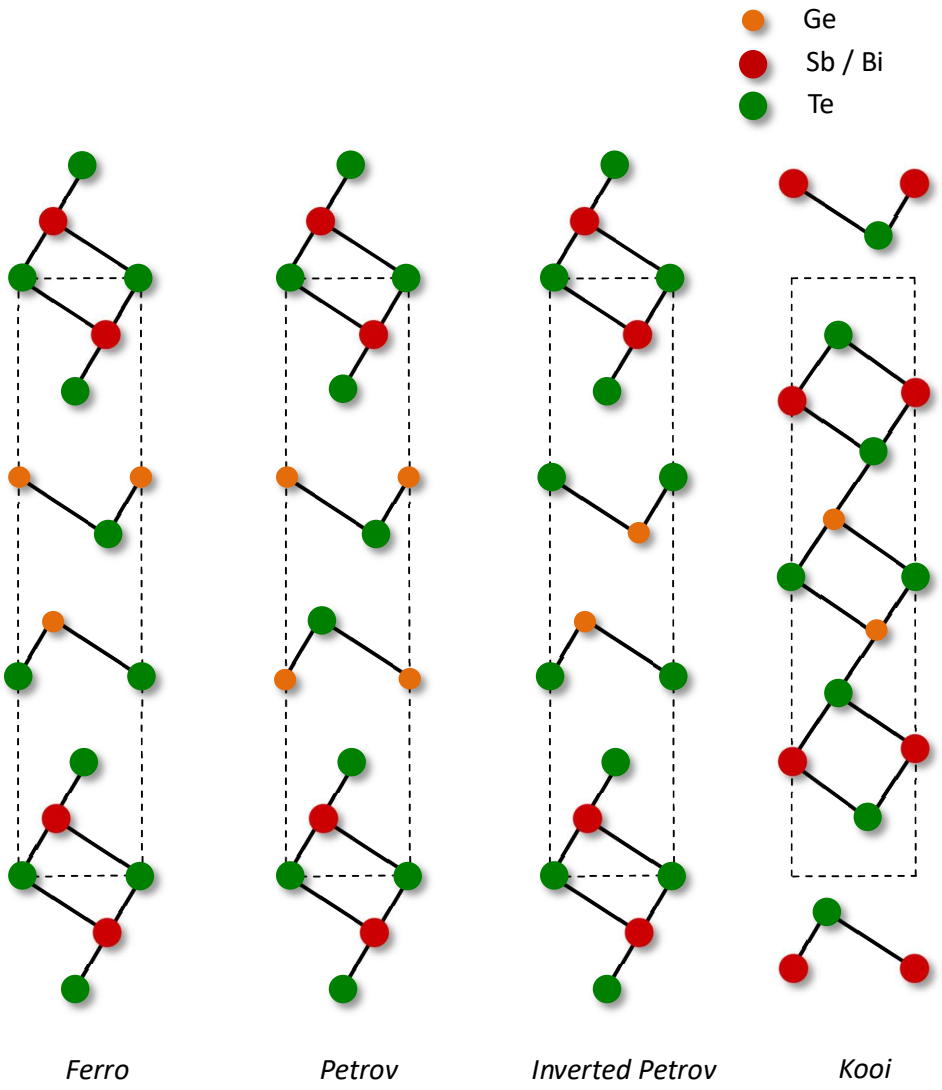

Fig. A5.11: Systematic illustrations of van der Waals reconfiguration at atomic scale resulting in various stacking arrangements of Sb_2Te_3 and GeTe within the trigonal crystal structure known as Ferro, Kooi, Petrov and inverted Petrov. They give rise to IPCMs and ferroelectric order in Dirac semi-metallic state of GST-225.

Appendix – 5B
Structural Investigations of GST Alloys

Addition information: Structural characterization of GST epilayers via XRD.

GST-147:

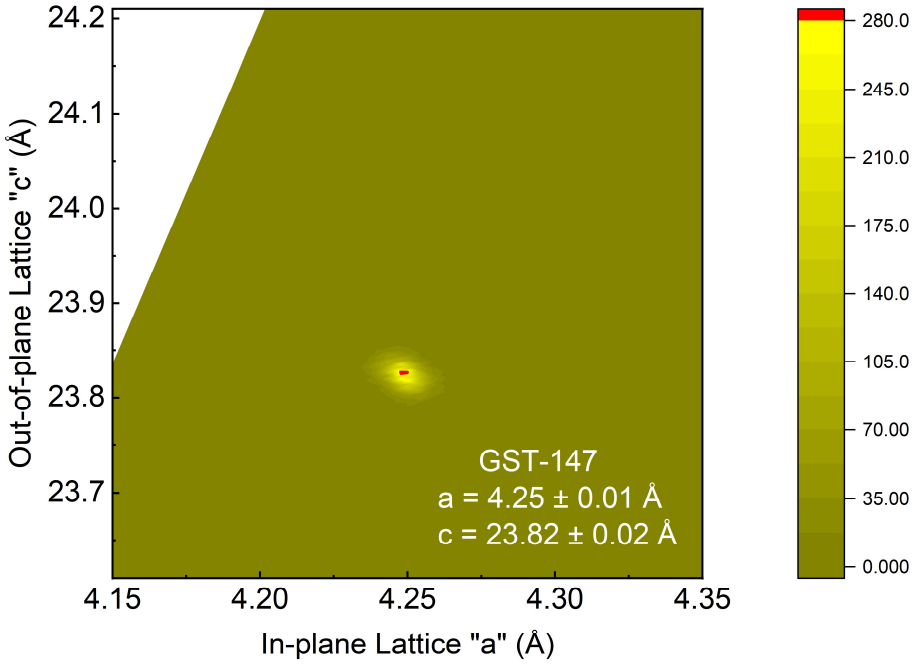

Fig. A5.12: Investigation of lattice parameters of GST-147 via XRD reciprocal space map (RSM).

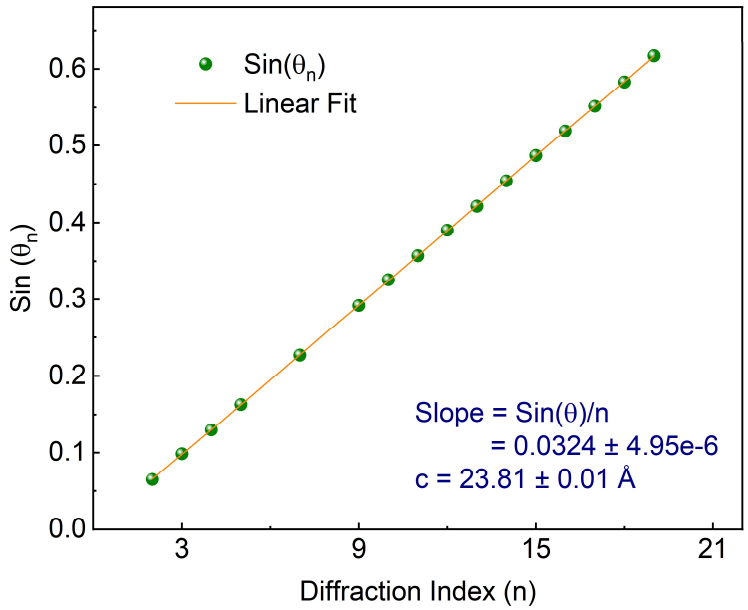

Fig. A5.13: Evaluation of unit cell length "c" for GST-147 epilayer according to the Bragg diffraction principle via XRD 2ϑ/ϑ scan.

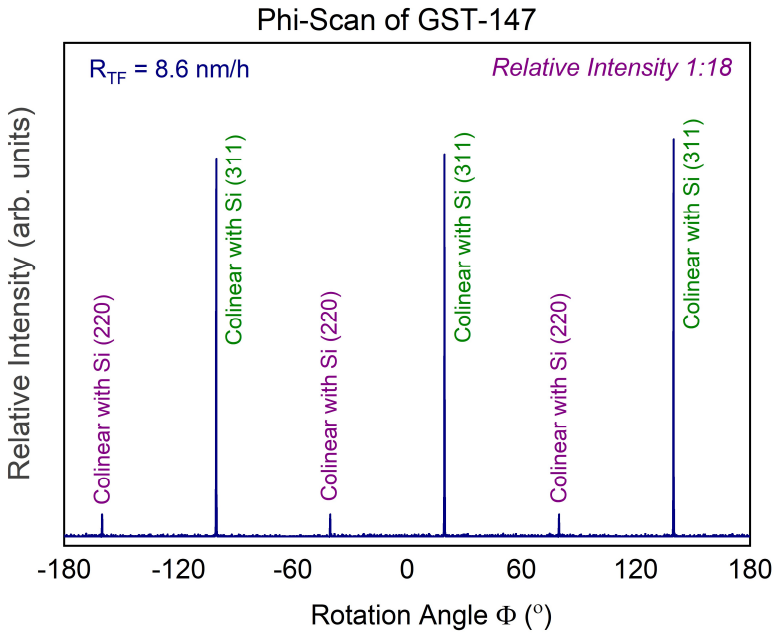

Fig. A5.14: Analysis of rotational twin domains via XRD φ-scan for GST-147 epilayer. The epilayer is prepared at moderate rate with R_{TF} = 8.6 nm/h and exhibited suppressed twin domains along Si (220) with relative abundance of 1:18 while the dominant domain is observed collinear with Si (311).

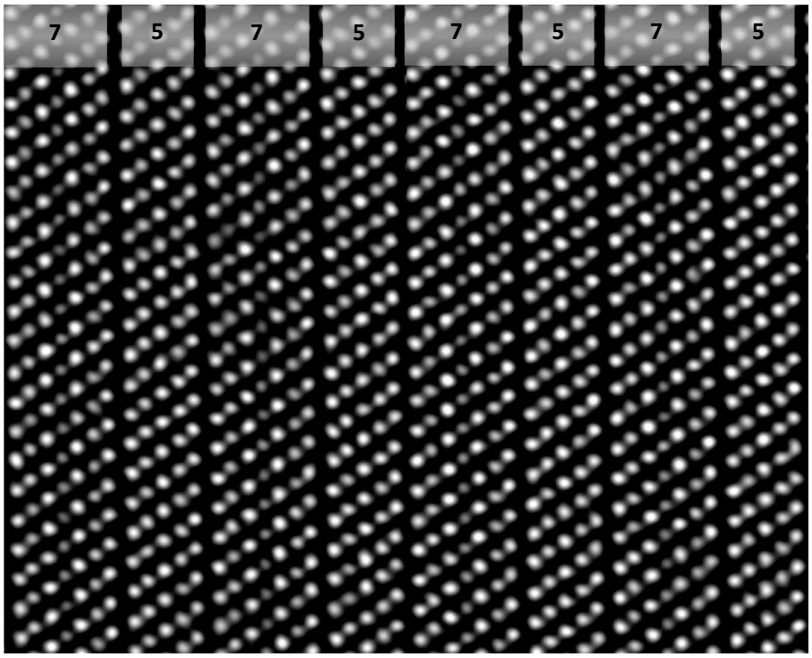

Fig. A5.15: STEM images acquired along Si [1-10] projection from selectively grown structures of GST-147 alloy. HAADF image acquired at the cross-section of 1000 nm wide structure. Layer stacking of SQ-SQ is evident confirming the stoichiometric state of GST-147.

GST-124:

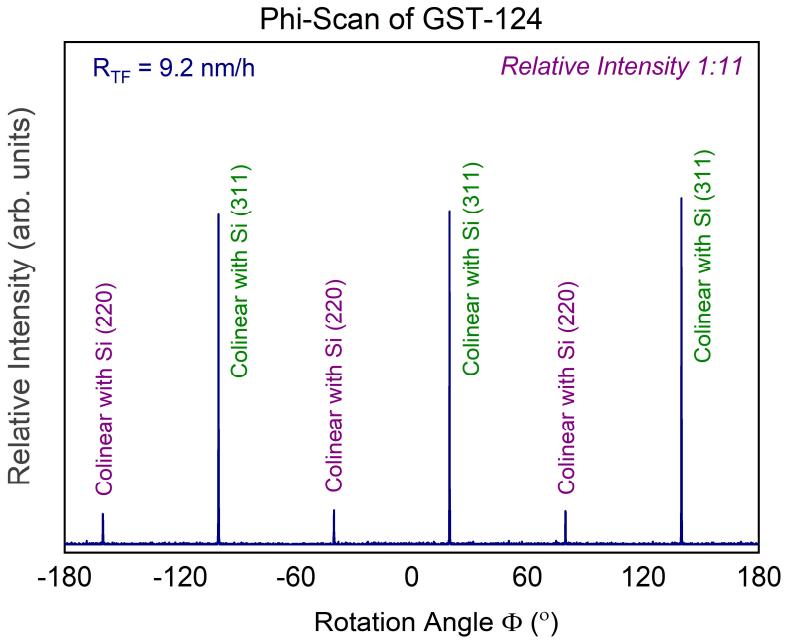

Fig. A5.15: Analysis of rotational twin domains via XRD φ-scan for GST-124 epilayer. The epilayer is prepared at moderate rate with R_{TF} = 9.2 nm/h and exhibited suppressed twin domains along Si (220) with relative abundance of 1:11 while the dominant domain is observed collinear with Si (311).

GST-225:

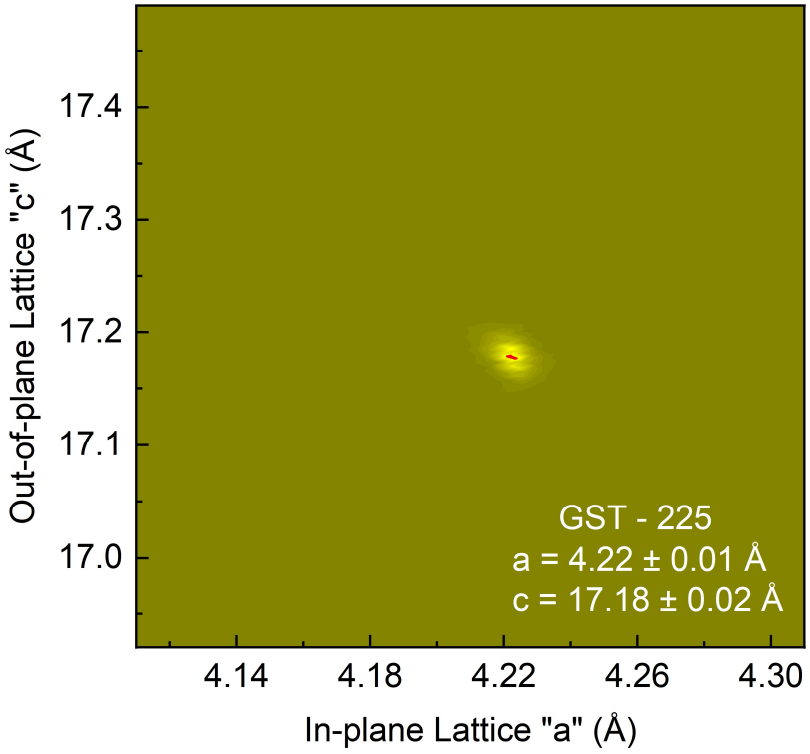

Fig. A5.16: Investigation of lattice parameters of GST-225 via XRD reciprocal space map (RSM).

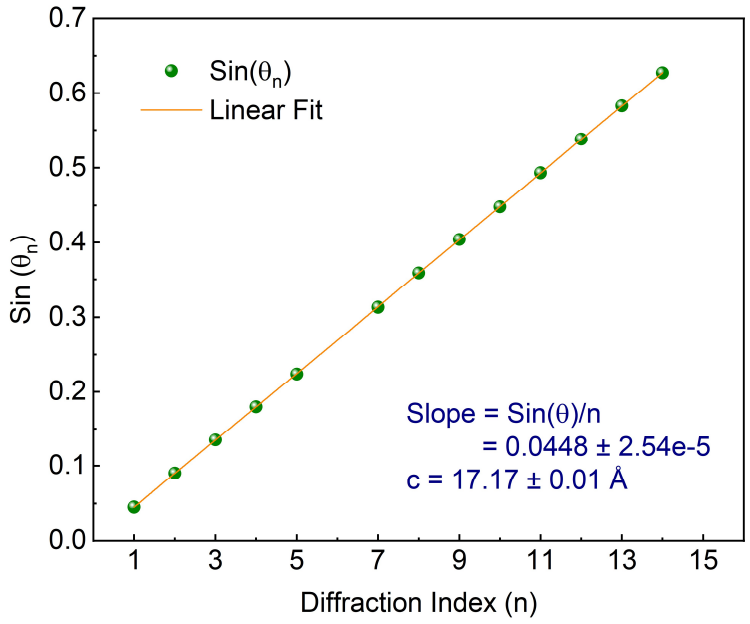

Fig A5.17: Evaluation of unit cell length "c" for GST-225 epilayer according to the Bragg diffraction principle via XRD 2ϑ/ϑ scan.

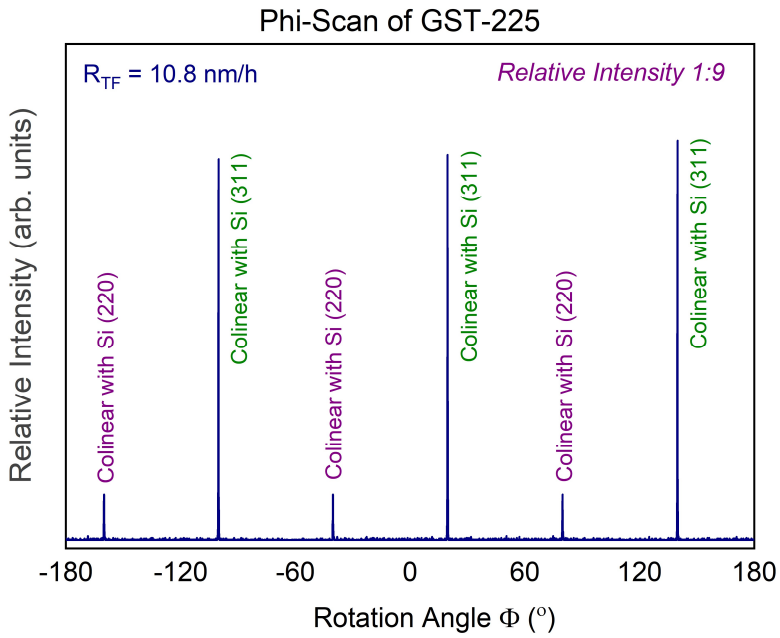

Fig. A5.18: Analysis of rotational twin domains via XRD φ-scan for GST-225 epilayer. The epilayer is prepared at moderate rate with R_{TF} = 10.8 nm/h and exhibited suppressed twin domains along Si (220) with relative abundance of 1:9 while the dominant domain is observed collinear with Si (311).

GST-326:

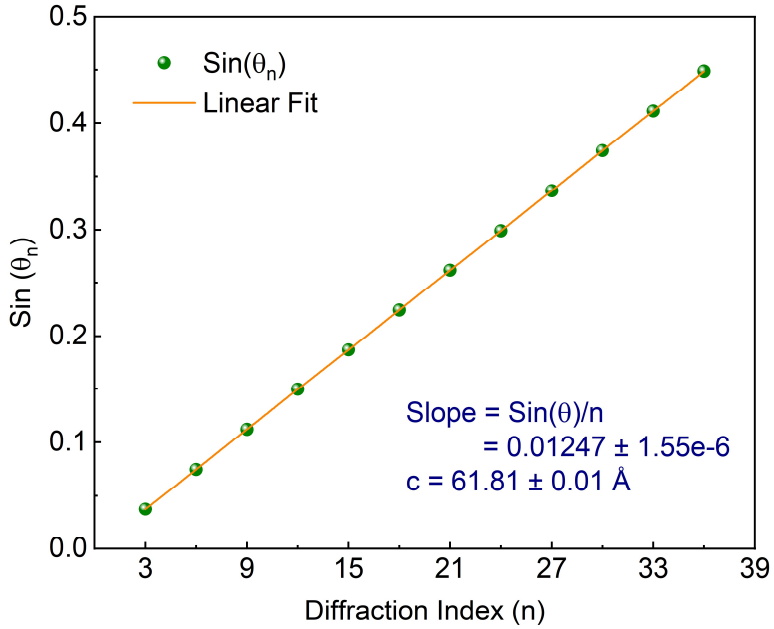

Fig. A5.19: Evaluation of unit cell length "c" for GST-225 epilayer according to the Bragg diffraction principle via XRD 2ϑ/ϑ scan.

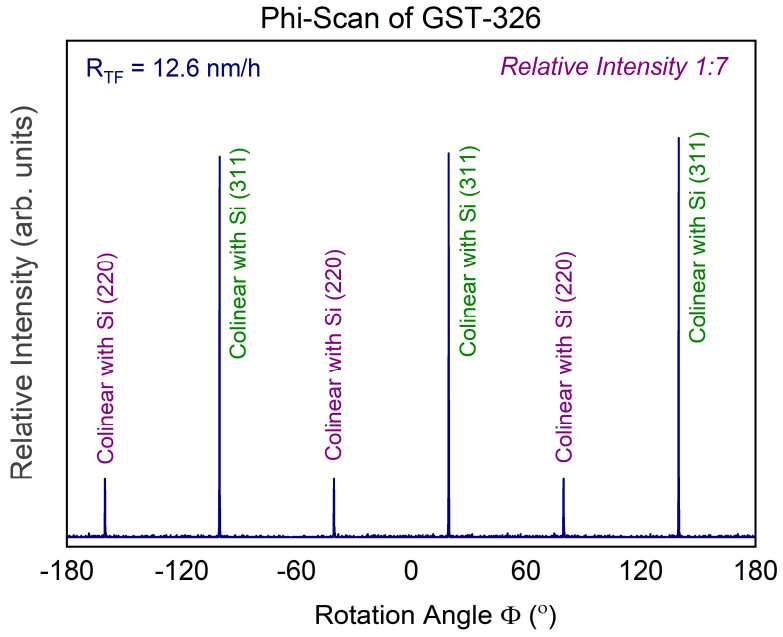

Fig. A5.20: Analysis of rotational twin domains via XRD φ-scan for GST-326 epilayer. The epilayer is prepared at moderate rate with R_{TF} = 12.6 nm/h and exhibited suppressed twin domains along Si (220) with relative abundance of 1:7 while the dominant domain is observed collinear with Si (311).

Appendix – 6A
HfO_2 Substrate Preparation via ALD

A 4-inch highly conductive Si (111) wafer with resistivity of 0.005 Ωcm is processed via RCA cleaning. The cleaned wafer is then loaded into the ALD chamber and 15 nm HfO_2 is deposited via the plasma process. The key material and process parameters are discussed in the following tables.

Table A6.1: Summary of chamber condition and the overview of the deposition settings.

Settings	Parameters/Conditions
Chamber	Oxford Vacuum Technologies
Table Temperature	200 °C
Manifold Temp	100 °C
Line Temp	120 °C
Wall Temp	120 °C
Base pressure	1.6 x 10^{-6} mbar
Substrate	Si (111) – 100 mm
Total Cycles	150
Process Duration	88 minutes

Table A6.2: Summary of the precursor parameter settings in one deposition cycle of the deposition process.

Process Step	Parameters
Precursor	TEMAH (**T**etrakis-(**E**thyl**M**ethyl**A**mido)-**H**afnium)
TEMAH Bubbler Temp	70 °C
1. TEMAH Step	
Ar Bubbler Flow	250 sccm
Ar Purge Flow	250 sccm
Chamber Pressure	0.11 mbar
TEMAH Dose Time	1 s
TEMAH Purge Time	15 s
TEMAH Pump Time	3 s
2. Plasma Step	
Plasma Strike Time	3 s
O2 Flow	60 sccm
Pressure during Plasma	0.2 mbar
ICP Power	250 W
Purge Time	6 s
3. Purge Step	
Post Plasma Purge Flow	250 sccm Ar
Post Plasma Chamber Pressure	0.106 mbar
Total Cycle Time	31 s
Final Pump	
Post Process Pump Duration	300 s

Appendix – 6B
Multi-Step Growth Recipe of 3D TIs for Amorphous Substrates

In order to obtain entirely coalesced and planar film of BST alloy on the amorphous HfO_2 substrates, a multi-step growth process is adopted. The details are as follow.

Cleaning:

The sample is cleaned in the piranha solution for 10 minutes and rinsed with the de-ionized water for several minutes. Later, the cleaned sample is loaded into the MBE chamber.

Step-1: Nucleation

1. T_{sub} = 550℃ (20 minutes)
2. T_{sub} = 100℃ (40 minutes)
   Set: T_{Bi} = 480℃, T_{Sb} = 460℃, T_{Te} = 330℃
3. Open shutter (Te) for 2 minutes
4. Open shutter (Bi and Sb)
5. After 5 minutes close shutter (Bi and Sb)

Step-2: Crystallization and Growth

1. Te Shutter is open
2. T_{sub} from 100℃ to 180℃, manually in 20 minutes
3. At T_{sub} = 180℃, Open shutter (Bi and Sb)
   At this stage if Bi and Sb shutters will not opened, holes will start to appear in the epilayer and will result in the non-uniform layer thickness.
4. T_{sub} from 180℃ to 220℃, manually in 10 minutes
5. Growth conducted for 2 hours
6. After 2 hours, close shutter (Bi and Sb)
   At this stage, the growth ends.

Step-3: Thermal Treatment with Te flux

1. Te Shutter is open
2. T_{sub} from 220℃ to 260℃, manually in 10 minutes
3. At T_{sub} = 260℃, T_{sub} → 220℃
4. T_{sub} from 220℃ to 260℃, manually in 10 minutes
5. At T_{sub} = 260℃, T_{sub} → 220℃
6. T_{sub} from 220℃ to 260℃, manually in 10 minutes
7. At T_{sub} = 260℃, T_{sub} → 220℃
   After 3 cycles
8. T_{sub} → 25℃
9. At T_{sub} = 200℃, close shutter (Te)

Appendix – 7A
TI-SC interfaces

Interface at Bi_2Se_3 – Sn hybrid structure: Sn is observed to diffuse so heavily into the TI epilayer that it penetrated almost 12 nm thick epilayer of Bi_2Se_3 entirely and reached the Si interface. Moreover, the diffused Sn atoms have transformed the vdW assisted QL based trigonal structure of TI into the disordered cubic structure where the vdW layers cannot be observed anymore.

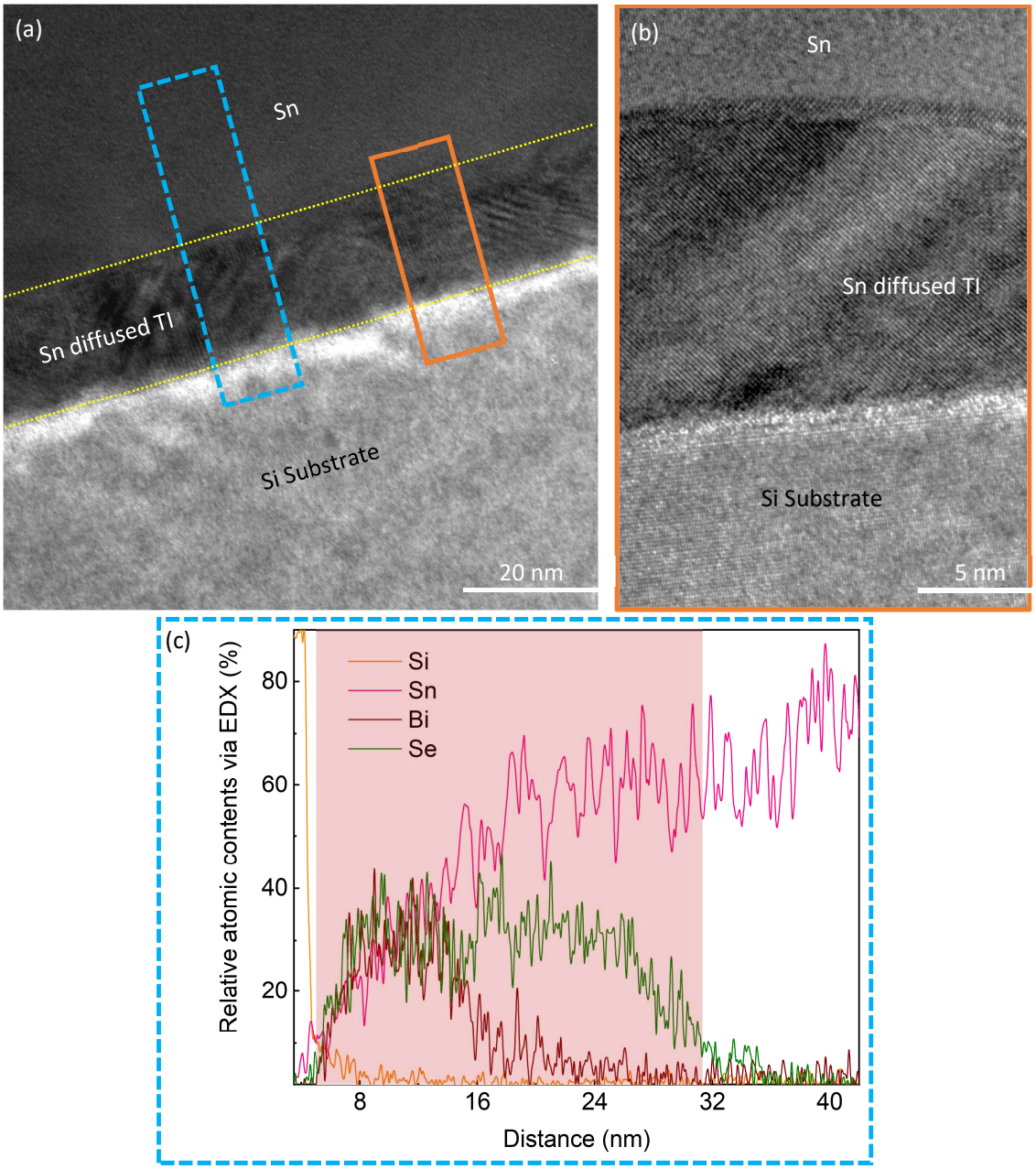

Fig. A7.1: (a) High resolution TEM image of Si (111) – Bi_2Se_3 – Sn hybrid stack. Sn is observed to diffuse into the TI epilayer and transformed into the disordered cubic crystal. (b) Magnified TEM image of the marked area in (a) that indicates the clean interface between Si (111) and Sn diffused TI crystal. (c) EDX spectrum acquired at the marked area in (a) confirming the Sn diffused till Si (111) interface.

Interface at Bi_2Se_3 – Pb hybrid structure: Similar to Sn, Pb is also observed to diffuse heavily into the TI epilayer and reached up to 10 nm deep into the TI epilayer. In the diffused region Pb has transformed the trigonal structure of TI into the disordered cubic structure; however, the non-diffused region exhibited the QLs with the trigonal crystal structure.

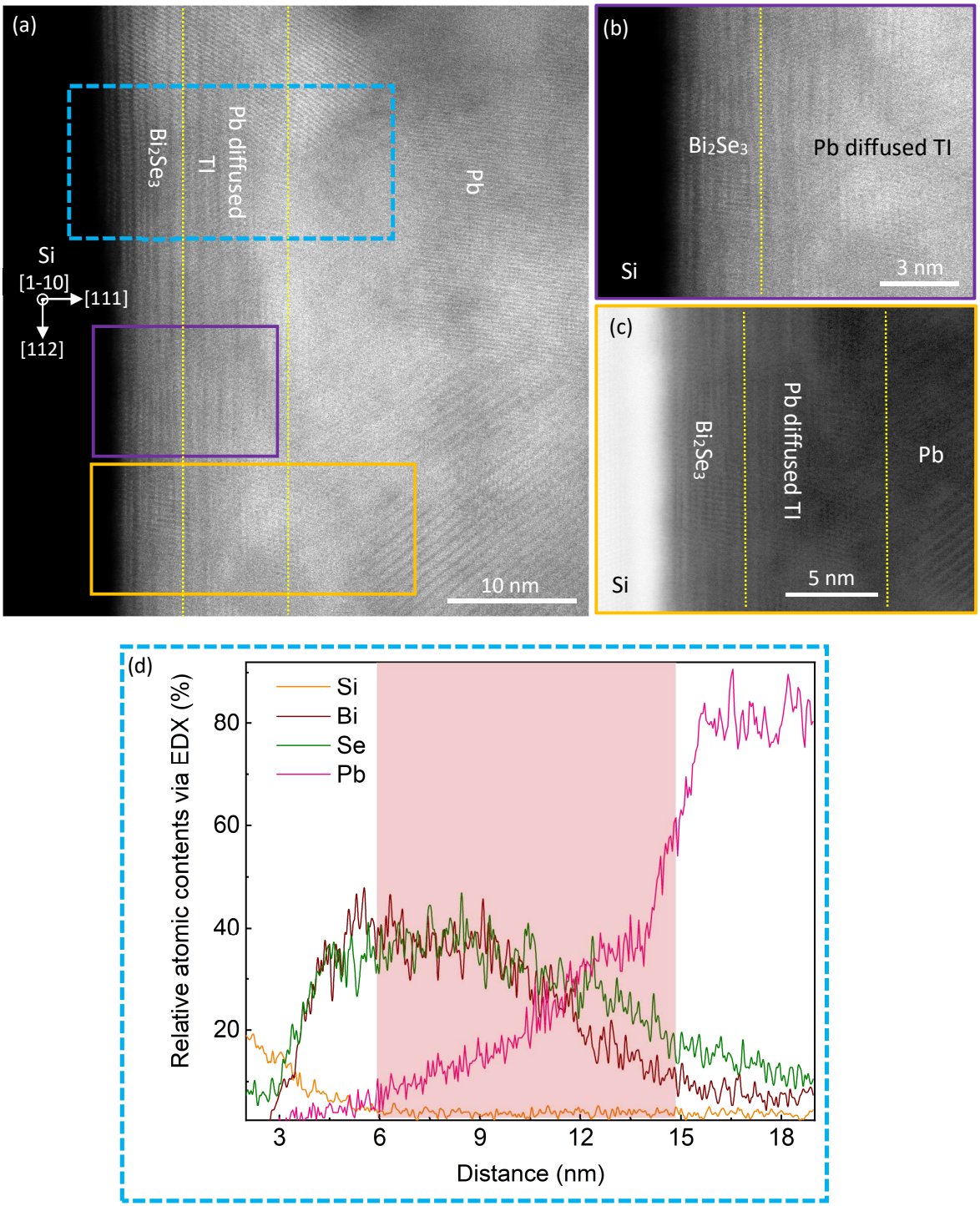

Fig. A7.2: (a) STEM-HAADF image of Si (111) – Bi_2Se_3 – Pb hybrid stack. (b-c) Magnified HAADF and bright field images of the marked areas in (a) respectively that depict the clean interface between Si (111) and TI QLs followed by the diffused TI region with crystalline Pb. (d) EDX spectrum acquired at the marked area in (a) confirming the Pb diffused almost 10 nm into the TI epilayer.

Interface at Sb_2Te_3 – Ti – Al hybrid structure: Sb forms alloy with Ti that can be observed in Figure A7.3. Due to the diffusion of Sb into Ti, the newly formed alloy failed to block Al atoms from diffusing into the TI epilayer. The formation of polycrystalline inter-mixed region followed by crystalline Al can be witnessed in Figure A7.3.

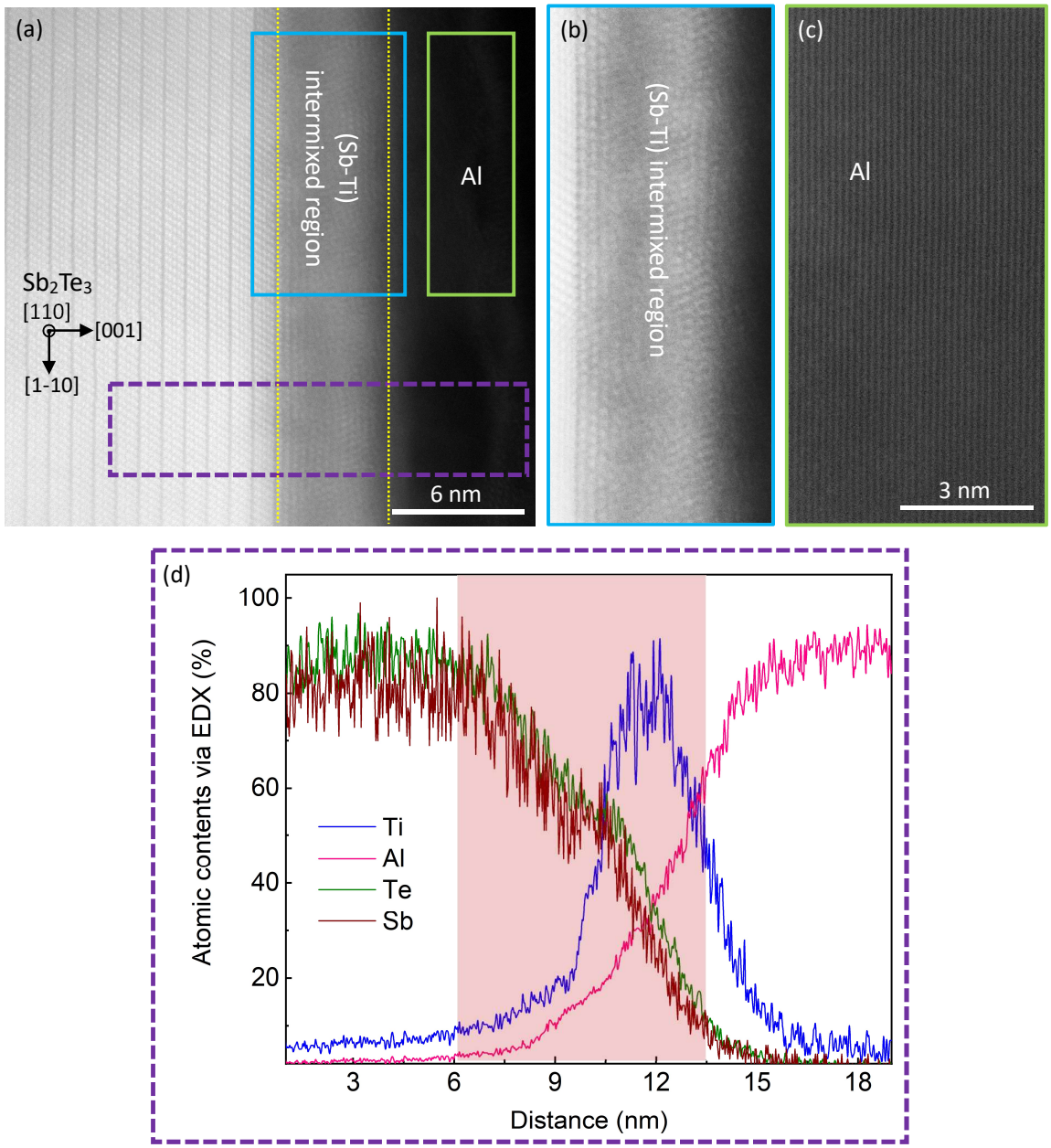

Fig. A7.3: (a) STEM-HAADF image of Sb_2Te_3 – Ti – Al hybrid stack. (b) Magnified HAADF image of the marked area in (a) representing the inter-mixed region. (c) High resolution image of an area marked in (a) depicting the crystalline stack of Al atoms. (d) EDX spectrum acquired at the marked area in (a) confirming the alloy formation of Ti and Sb while Al atoms are diffusing into the TI epilayer.

Interface at Sb_2Te_3 – Ti – Al hybrid structure: Pt is observed to diffuse up to 2.5 nm into Sb_2Te_3 epilayer where the Te atoms are consumed to form $PtTe_2$ trilayer structures of TMDC. However, the residual Sb atoms are observed to interfere in the formation of defect-free and homogenous trilayers. At places the formation three to six $PtTe_2$ are observed while in other areas, a high density of Sb atoms caused the formation of an amorphous structure that led to a non-epitaxial interface between Sb_2Te_3 and Pt.

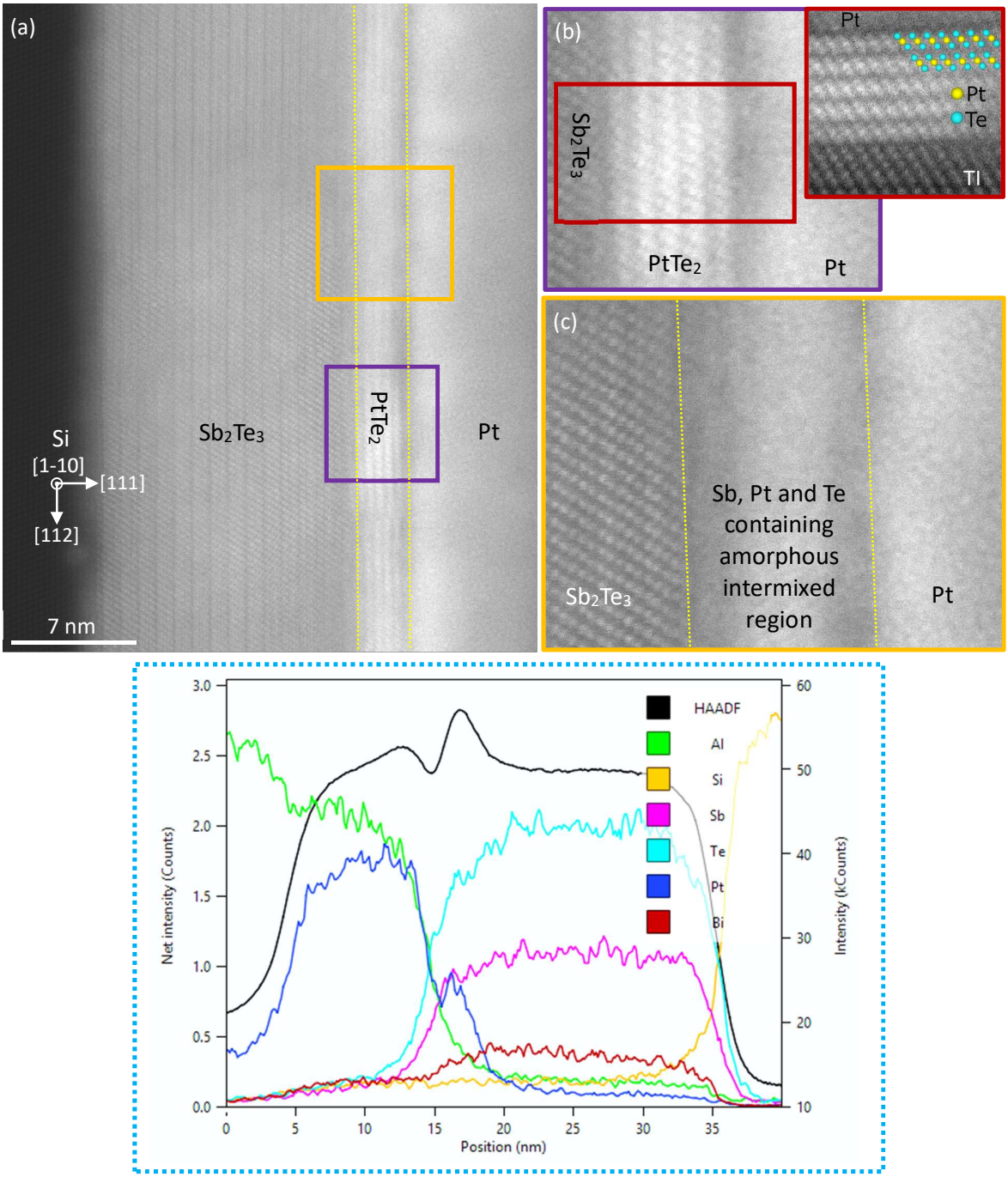

Fig. A7.4: (a) STEM-HAADF image of Si (111) – Sb_2Te_3 – Ti – Al hybrid stack along Si [1-10] orientation. (b) Magnified HAADF image of the marked area in (a) representing the crystalline formation of $PtTe_2$ layers. (c) High resolution image of an area marked in (a) depicting the formation of an amorphous region at the interface with TI epilayer. (d) EDX spectrum of the complete layer stack indicating the diffusion of Pt and Al into Sb_2Te_3.

Appendix – 7B
Incorporation of the pre-patterned Substrates and the Stencil Mask

Fabrication of on-chip stencil mask: The fabrication of on-chip stencil mask technique using LPCVD SiO_2 and SiN_x layers is developed by Peter Schüffelgen (PGI-9) in 2017. Due to the unavailability of LPCVD system, in this work, the technique is extended for PECVD based SiN_x. The PECVD deposited film quality due to excessive strain, inhomogeneous layer thickness and the presence of H^+ ions cannot be compared to LPCVD; however, with the systematic improvement of HF/LF mixed frequency deposition process and the post-deposition annealing steps (discussed in Appendix 3A), the layer quality is improved and the sustainable on-chip stencil masks are achieved. The schematics of the on-chip stencil mask and its utilization is depicted in Figure A7.5.

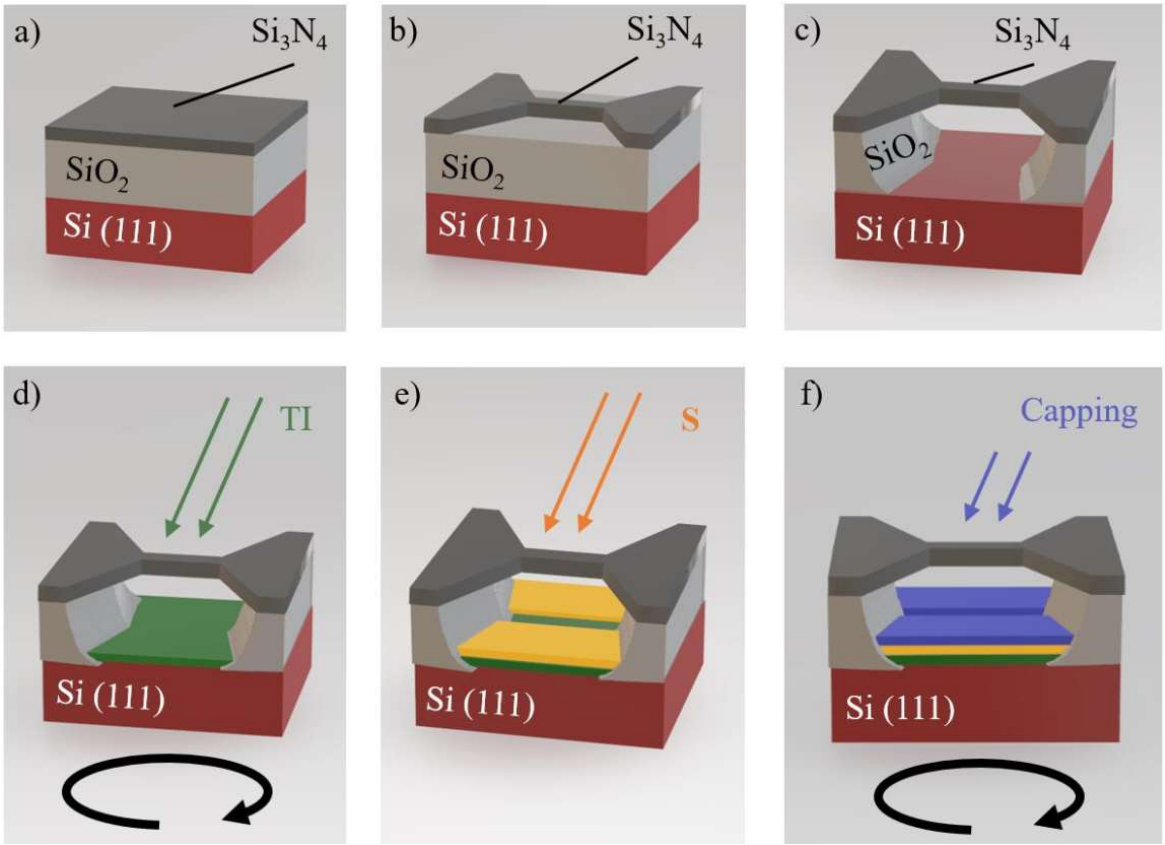

Fig. A7.5: The schematical representation of the on-chip stencil mask. (a) The preparation of thick (300 nm) SiO_2 and (100 nm) SiN_x layer stack. (b) e-beam lithography and RIE assisted dry etching of SiN_x layer to shape the stencil mask. (c) HF solution assisted isotropic wet etching of SiO_2 that assisted the formation of suspended bridge as the on-chip stencil mask of SiN_x. (d) Si (111) substrate with the patterned stencil mask is loaded into the MBE to perform the epitaxy. The sample is kept rotating during epitaxy to nullify the shadow effect of the bridge. (e) After the epitaxy, the rotation is stopped and the bridge is aligned in the desired orientation to the metallic molecular beam. This step allowed the formation of in situ metallic electrodes. After the metallic deposition, the rotation is started again and the entire layer stack is capped with Al_2O_3 to avoid the surface oxidation. (Image courtesy: Peter Schüffelgen)

The technique of stencil mask provides the ability of the *in vacuo* deposition of metallic electrodes. The incorporation of SAE with the stencil mask opens up the possibilities of achieving a scalable network of nanostructures that not only provides the pristine material with a high crystal quality but also the desired shape of nanostructures in any complexity of design. In order to fabricate such structures, the first step is to prepare the selective mask to achieve SAE in the desired dimensions and design. The wafer with the patterned substrate is then processed to prepare the on-chip stencil mask as discussed in Figure A7.5. The schematics of the whole fabrication steps can be observed in Figure A7.6.

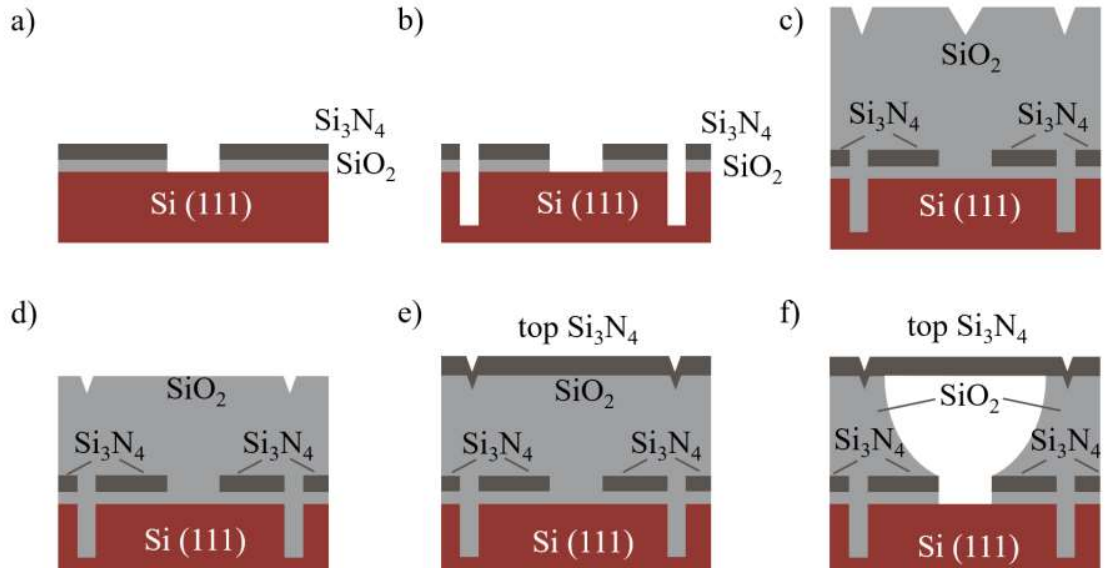

Fig. A7.6: The schematical representation of the on-chip stencil mask incorporated with the selective mask of the nanostructures. (a) The preparation of combinational layer stack and the fabrication of trenches to achieve SAE in the desired dimensions. (b) Preparation of the main markers to align the selective mask to stencil mask so that the nanostructures and the metallic electrodes could be achieved with ±5 nm accuracy. (c-e) The preparation of thick (300 nm) SiO_2 and (100 nm) SiN_x layer stack. Via e-beam lithography and RIE assisted dry etching of SiN_x layer to shape the stencil mask. (f) HF solution assisted isotropic wet etching of SiO_2 that assisted the formation of suspended bridge as the on-chip stencil mask of SiN_x and also exposed the buried selective mask to grow TI epilayer in the nanostructures. (Image courtesy: Tobias Schmitt)

Bibliography

Chapter – 1

1. *Montagnat J, Delingette H, Ayache N. A review of deformable surfaces: topology, geometry and deformation. Image and vision computing 2001,* ***19****(14):* *1023-1040.*

2. *Yang B-J, Nagaosa N. Classification of stable three-dimensional Dirac semimetals with nontrivial topology. Nature Communications 2014,* ***5****(1):* *4898.*

3. *Fradkin E. Field theories of condensed matter physics. Cambridge University Press, 2013.*

4. *Zhang H, Liu C-X, Qi X-L, Dai X, Fang Z, Zhang S-C. Topological insulators in Bi2Se3, Bi2Te3 and Sb2Te3 with a single Dirac cone on the surface. Nature Physics 2009,* ***5****(6):* *438-442.*

5. *Moore JE. The Birth of Topological Insulators. Nature 2010,* ***464:*** *194.*

6. *Hasan MZ, Kane CL. Colloquium: Topological insulators. Reviews of Modern Physics 2010,* ***82****(4):* *3045-3067.*

7. *Bernevig BA, Hughes TL, Zhang S-C. Quantum Spin Hall Effect and Topological Phase Transition in HgTe Quantum Wells. Science 2006,* ***314****(5806):* *1757-1761.*

8. *Hsieh D, Xia Y, Wray L, Qian D, Pal A, Dil JH, et al. Observation of Unconventional Quantum Spin Textures in Topological Insulators. Science 2009,* ***323****(5916):* *919-922.*

9. *Aguilera I. Private communications in Research Center Juelich 2020.*

10. *Schüffelgen P. Exploiting Topological Insulators for Majorana Devices and Physics Via Molecular Beam Epitaxy: Halbleiter-Nanoelektronik; 2018.*

11. *Fan Y, Wang KL. Spintronics Based on Topological Insulators. SPIN 2016,* ***06****(02):* *1640001.*

12. *Šmejkal L, Mokrousov Y, Yan B, MacDonald AH. Topological antiferromagnetic spintronics. Nature Physics 2018,* ***14****(3):* *242-251.*

13. *Pesin D, MacDonald AH. Spintronics and Pseudospintronics in Graphene and Topological Insulators. Nat Mater 2012,* ***11:*** *409.*

14. *Sarma SD, Freedman M, Nayak C. Majorana zero modes and topological quantum computation. npj Quantum Information 2015,* ***1****(1):* *15001.*

15. *Plugge S, Rasmussen A, Egger R, Flensberg K. Majorana box qubits. New Journal of Physics 2017,* ***19****(1):* *012001.*

16. *Franz M. Majorana's wires. Nature Nanotechnology 2013,* ***8****(3):* *149-152.*

17. *Xu C, Moore JE. Stability of the quantum spin Hall effect: Effects of interactions, disorder, and Z2 topology. Physical Review B 2006,* ***73****(4):* *045322.*

18. *Wu C, Bernevig BA, Zhang S-C. Helical Liquid and the Edge of Quantum Spin Hall Systems. Physical Review Letters 2006,* ***96****(10):* *106401.*

19. *Liu Q, Liu C-X, Xu C, Qi X-L, Zhang S-C. Magnetic Impurities on the Surface of a Topological Insulator. Physical Review Letters 2009,* ***102****(15):* *156603.*

20. *Rosenbach D, Oellers N, Jalil AR, Mikulics M, Kölzer J, Zimmermann E, et al. Quantum Transport in Topological Surface States of Selectively Grown Bi2Te3 Nanoribbons. Advanced Electronic Materials 2020,* ***n/a****(n/a):* *2000205.*

21. *Fu L, Kane CL. Topological insulators with inversion symmetry. Physical Review B 2007,* ***76****(4):* *045302.*

22. *Klein MJ. On a degeneracy theorem of Kramers. American Journal of Physics 1952,* ***20****(2):* *65-71.*

23. *Kane CL, Mele EJ. Quantum Spin Hall Effect in Graphene. Physical Review Letters 2005,* ***95****(22):* *226801.*

24. *Kane CL, Mele EJ. Z2 Topological Order and the Quantum Spin Hall Effect. Physical Review Letters 2005,* ***95****(14):* *146802.*

25. *Konig M, Wiedmann S, Brune C, Roth A, Buhmann H, Molenkamp LW, et al. Quantum Spin Hall Insulator State in HgTe Quantum Wells. Science 2007,* ***318:*** *766.*

26. *Hasan MZ, Moore JE. Three-Dimensional Topological Insulators. Annual Review of Condensed Matter Physics 2011,* ***2****(1):* *55-78.*

27. *Pauly C, Rasche B, Koepernik K, Richter M, Borisenko S, Liebmann M, et al. Electronic Structure of the Dark Surface of the Weak Topological Insulator Bi14Rh3I9. ACS Nano 2016,* ***10****(4):* *3995-4003.*

28. *Yoshimura Y, Matsumoto A, Takane Y, Imura K-I. Perfectly conducting channel on the dark surface of weak topological insulators. Physical Review B 2013,* ***88****(4):* *045408.*

29. *Eschbach M, Lanius M, Niu C, Młyńczak E, Gospodarič P, Kellner J, et al. Bi1Te1 is a dual topological insulator. Nature Communications 2017,* ***8****(1):* *14976.*

30. *Zhang P, Noguchi R, Kuroda K, Lin C, Kawaguchi K, Yaji K, et al. Observation and control of the weak topological insulator state in ZrTe5. Nature Communications 2021,* ***12****(1):* *406.*

31. *Noguchi R, Takahashi T, Kuroda K, Ochi M, Shirasawa T, Sakano M, et al. A weak topological insulator state in quasi-one-dimensional bismuth iodide. Nature 2019,* ***566****(7745):* *518-522.*

32. *Majhi K, Banerjee A, Ganesan R, Kumar PSA. Thickness-dependent electrical transport in weak topological insulator Bi1Se1. Journal of Applied Physics 2020,* ***128****(16):* *164305.*

33. *Majhi K, Pal K, Lohani H, Banerjee A, Mishra P, Yadav AK, et al. Emergence of a weak topological insulator from the BixSey family. Applied Physics Letters 2017,* ***110****(16):* *162102.*

34. *Fu L. Topological Crystalline Insulators. Physical Review Letters 2011,* ***106****(10):* *106802.*

35. *Hsieh TH, Lin H, Liu J, Duan W, Bansil A, Fu L. Topological crystalline insulators in the SnTe material class. Nature Communications 2012,* ***3****(1):* *982.*

36. *Liu J, Duan W, Fu L. Two types of surface states in topological crystalline insulators. Physical Review B 2013,* ***88****(24):* *241303.*

37. *Ando Y, Fu L. Topological Crystalline Insulators and Topological Superconductors: From Concepts to Materials. Annual Review of Condensed Matter Physics 2015, **6**(1): 361-381.*

38. *Lanius M. Topological Insulating Tellurides: How to tune Doping, Topology, and Dimensionality. Universitätsbibliothek der RWTH Aachen, 2018.*

39. *Hsieh D, Qian D, Wray L, Xia Y, Hor YS, Cava RJ, et al. A topological Dirac insulator in a quantum spin Hall phase. Nature 2008, **452**(7190): 970-974.*

40. *Roushan P, Seo J, Parker CV, Hor YS, Hsieh D, Qian D, et al. Topological surface states protected from backscattering by chiral spin texture. Nature 2009, **460**(7259): 1106-1109.*

41. *Teo JCY, Fu L, Kane CL. Surface states and topological invariants in three-dimensional topological insulators: Application to Bi(1-x)Sb(x). Physical Review B 2008, **78**(4): 045426.*

42. *Ando Y. Topological Insulator Materials. J Phys Soc Jpn 2013, **82**: 102001.*

43. *Sessi P, Di Sante D, Szczerbakow A, Glott F, Wilfert S, Schmidt H, et al. Robust spin-polarized midgap states at step edges of topological crystalline insulators. Science 2016, **354**(6317): 1269.*

44. *Tanaka Y, Ren Z, Sato T, Nakayama K, Souma S, Takahashi T, et al. Experimental realization of a topological crystalline insulator in SnTe. Nature Physics 2012, **8**(11): 800-803.*

45. *Schindler F, Cook AM, Vergniory MG, Wang Z, Parkin SSP, Bernevig BA, et al. Higher-order topological insulators. Science Advances 2018, **4**(6): eaat0346.*

46. *Rauch T, Flieger M, Henk J, Mertig I, Ernst A. Dual Topological Character of Chalcogenides: Theory for Bi2Te3. Physical Review Letters 2014, **112**(1): 016802.*

47. *Benalcazar WA, Bernevig BA, Hughes TL. Quantized electric multipole insulators. Science 2017, **357**(6346): 61-66.*

48. *Schindler F, Wang Z, Vergniory MG, Cook AM, Murani A, Sengupta S, et al. Higher-order topology in bismuth. Nature Physics 2018, **14**(9): 918-924.*

49. *Noguchi R, Kobayashi M, Jiang Z, Kuroda K, Takahashi T, Xu Z, et al. Evidence for a higher-order topological insulator in a three-dimensional material built from van der Waals stacking of bismuth-halide chains. Nature Materials 2021, **20**(4): 473-479.*

50. *Ni X, Weiner M, Alù A, Khanikaev AB. Observation of higher-order topological acoustic states protected by generalized chiral symmetry. Nature Materials 2019, **18**(2): 113-120.*

51. *Ruchira VB, Soumya B. Out of equilibrium chiral higher order topological insulator on a π-flux square lattice. Journal of Physics: Condensed Matter 2021.*

52. *Nayak AK, Reiner J, Queiroz R, Fu H, Shekhar C, Yan B, et al. Resolving the topological classification of bismuth with topological defects. Science Advances 2019, **5**(11): eaax6996.*

53. *Oostinga JB, Maier L, Schüffelgen P, Knott D, Ames C, Brüne C, et al. Josephson Supercurrent through the Topological Surface States of Strained Bulk HgTe. Physical Review X 2013, **3**(2): 021007.*

54. *Zaheer S, Young SM, Cellucci D, Teo JCY, Kane CL, Mele EJ, et al. Spin texture on the Fermi surface of tensile-strained HgTe. Physical Review B 2013, **87**(4): 045202.*

55. *Zhao H, Chen X, Lu J, Shu H, Lu W. Band gap tuning in HgTe through uniaxial strains. Solid State Communications 2013, **166**: 1-5.*

56. *Brüne C. HgTe based topological insulators. 2014.*

57. *Liu ZK, Zhou B, Zhang Y, Wang ZJ, Weng HM, Prabhakaran D, et al. Discovery of a Three-Dimensional Topological Dirac Semimetal, Na₃Bi. Science 2014, **343**(6173): 864-867.*

58. *Gibson QD, Schoop LM, Muechler L, Xie LS, Hirschberger M, Ong NP, et al. Three-dimensional Dirac semimetals: Design principles and predictions of new materials. Physical Review B 2015, **91**(20): 205128.*

59. *Liu ZK, Jiang J, Zhou B, Wang ZJ, Zhang Y, Weng HM, et al. A stable three-dimensional topological Dirac semimetal Cd3As2. Nature Materials 2014, **13**(7): 677-681.*

60. *Neupane M, Xu S-Y, Sankar R, Alidoust N, Bian G, Liu C, et al. Observation of a three-dimensional topological Dirac semimetal phase in high-mobility Cd 3 As 2. Nature communications 2014, **5**(1): 1-8.*

61. *Borisenko S, Gibson Q, Evtushinsky D, Zabolotnyy V, Büchner B, Cava RJ. Experimental realization of a three-dimensional Dirac semimetal. Physical review letters 2014, **113**(2): 027603.*

62. *Cheng H, Sha Y, Liu R, Fang C, Lu L. Discovering Topological Surface States of Dirac Points. Physical Review Letters 2020, **124**(10): 104301.*

63. *Tabert CJ, Carbotte JP. Optical conductivity of Weyl semimetals and signatures of the gapped semimetal phase transition. Physical Review B 2016, **93**(8): 085442.*

64. *Murakami S, Hirayama M, Okugawa R, Miyake T. Emergence of topological semimetals in gap closing in semiconductors without inversion symmetry. Science Advances 2017, **3**(5): e1602680.*

65. *Armitage NP, Mele EJ, Vishwanath A. Weyl and Dirac semimetals in three-dimensional solids. Reviews of Modern Physics 2018, **90**(1): 015001.*

66. *Lv B, Weng H, Fu B, Wang XP, Miao H, Ma J, et al. Experimental discovery of Weyl semimetal TaAs. Physical Review X 2015, **5**(3): 031013.*

67. *Wang S, Lin B-C, Wang A-Q, Yu D-P, Liao Z-M. Quantum transport in Dirac and Weyl semimetals: a review. Advances in Physics: X 2017, **2**(3): 518-544.*

68. *Xu S-Y, Belopolski I, Alidoust N, Neupane M, Bian G, Zhang C, et al. Discovery of a Weyl fermion semimetal and topological Fermi arcs. Science 2015, **349**(6248): 613-617.*

69. *Pal PB. Dirac, Majorana, and Weyl fermions. American Journal of Physics 2011, **79**(5): 485-498.*

70. *Huang S-M, Xu S-Y, Belopolski I, Lee C-C, Chang G, Wang B, et al. A Weyl Fermion semimetal with surface Fermi arcs in the transition metal monopnictide TaAs class. Nature Communications 2015, **6**(1): 7373.*

71. *Li Y-Y, Wang G, Zhu X-G, Liu M-H, Ye C, Chen X, et al. Intrinsic Topological Insulator Bi2Te3 Thin Films on Si and Their Thickness Limit. Advanced Materials 2010, **22**(36): 4002-4007.*

72. *Xu S-Y, Xia Y, Wray LA, Jia S, Meier F, Dil JH, et al. Topological Phase Transition and Texture Inversion in a Tunable Topological Insulator. Science 2011, **332**(6029): 560-564.*

73. *Young SM, Chowdhury S, Walter EJ, Mele EJ, Kane CL, Rappe AM. Theoretical investigation of the evolution of the topological phase of Bi2Se3 under mechanical strain. Physical Review B 2011, **84**(8): 085106.*

74. *Wang Z, Liu Q, Luo J-W, Zunger A. Digging for topological property in disordered alloys: the emergence of Weyl semimetal phase and sequential band inversions in PbSe–SnSe alloys. Materials Horizons 2019, **6**(10): 2124-2134.*

75. *Wang Z, Sun Y, Chen X-Q, Franchini C, Xu G, Weng H, et al. Dirac semimetal and topological phase transitions in ${A}_{3}$Bi ($A=\text{Na}$, K, Rb). Physical Review B 2012, **85**(19): 195320.*

76. *Wang Z, Weng H, Wu Q, Dai X, Fang Z. Three-dimensional Dirac semimetal and quantum transport in Cd${}_{3}$As${}_{2}$. Physical Review B 2013, **88**(12): 125427.*

77. *Singh B, Sharma A, Lin H, Hasan MZ, Prasad R, Bansil A. Topological electronic structure and Weyl semimetal in the TlBiSe${}_{2}$ class of semiconductors. Physical Review B 2012, **86**(11): 115208.*

78. *Halász GB, Balents L. Time-reversal invariant realization of the Weyl semimetal phase. Physical Review B 2012, **85**(3): 035103.*

79. *Steinberg JA, Young SM, Zaheer S, Kane CL, Mele EJ, Rappe AM. Bulk Dirac Points in Distorted Spinels. Physical Review Letters 2014, **112**(3): 036403.*

80. *Young SM, Zaheer S, Teo JCY, Kane CL, Mele EJ, Rappe AM. Dirac Semimetal in Three Dimensions. Physical Review Letters 2012, **108**(14): 140405.*

81. *Morimoto T, Furusaki A. Weyl and Dirac semimetals with ${\mathbb{Z}}_{2}$ topological charge. Physical Review B 2014, **89**(23): 235127.*

82. *Ma J, Deng K, Zheng L, Wu S, Liu Z, Zhou S, et al. Experimental progress on layered topological semimetals. 2D Materials 2019, **6**(3): 032001.*

83. *Burkov A, Balents L. Weyl semimetal in a topological insulator multilayer. Physical review letters 2011, **107**(12): 127205.*

84. *Yang B-J, Kim YB. Topological insulators and metal-insulator transition in the pyrochlore iridates. Physical Review B 2010, **82**(8): 085111.*

85. *Wan X, Turner AM, Vishwanath A, Savrasov SY. Topological semimetal and Fermi-arc surface states in the electronic structure of pyrochlore iridates. Physical Review B 2011, **83**(20): 205101.*

86. *Liang T, Gibson Q, Ali MN, Liu M, Cava RJ, Ong NP. Ultrahigh mobility and giant magnetoresistance in the Dirac semimetal Cd3As2. Nature Materials 2015, **14**(3): 280-284.*

87. *Singh S, Süß V, Schmidt M, Felser C, Shekhar C. Strong correlation between mobility and magnetoresistance in Weyl and Dirac semimetals. Journal of Physics: Materials 2020, **3**(2): 024003.*

88. *Li H, He H, Lu H-Z, Zhang H, Liu H, Ma R, et al. Negative magnetoresistance in Dirac semimetal Cd3As2. Nature Communications 2016,* ***7****(1):* *10301.*

89. *Zhang X, Jin L, Dai X, Liu G. Topological Type-II Nodal Line Semimetal and Dirac Semimetal State in Stable Kagome Compound Mg3Bi2. The Journal of Physical Chemistry Letters 2017,* ***8****(19):* *4814-4819.*

90. *Hosen MM, Dimitri K, Belopolski I, Maldonado P, Sankar R, Dhakal N, et al. Tunability of the topological nodal-line semimetal phase in $\mathrm{ZrSi}X$-type materials ($X=\mathrm{S}, \mathrm{Se}, \mathrm{Te}$). Physical Review B 2017,* ***95****(16):* *161101.*

91. *Zhang Q, Zhang Z, Zhu Z, Schwingenschlögl U, Cui Y. Exotic Topological Insulator States and Topological Phase Transitions in Sb2Se3–Bi2Se3 Heterostructures. ACS Nano 2012,* ***6****(3):* *2345-2352.*

92. *Matetskiy AV, Mararov VV, Kibirev IA, Zotov AV, Saranin AA. Trivial band topology of ultra-thin rhombohedral Sb2Se3 grown on Bi2Se3. Journal of Physics: Condensed Matter 2020,* ***32****(16):* *165001.*

93. *Kyono A, Hayakawa A, Horiki M. Selenium substitution effect on crystal structure of stibnite (Sb2S3). Physics and Chemistry of Minerals 2015,* ***42****(6):* *475-490.*

94. *Jeon JH, Song M, Kim H, Jang W-J, Park J-Y, Yoon S, et al. Quintuple layer Bi2Se3 thin films directly grown on insulating SiO2 using molecular beam epitaxy. Applied Surface Science 2014,* ***316:*** *42-45.*

95. *Park K, Xiao F, Yoo BY, Rheem Y, Myung NV. Electrochemical deposition of thermoelectric SbxTey thin films and nanowires. Journal of Alloys and Compounds 2009,* ***485****(1):* *362-366.*

96. *Kifune K, Kubota Y, Matsunaga T, Yamada N. Extremely long period-stacking structure in the Sb-Te binary system. Acta Crystallographica Section B 2005,* ***61****(5):* *492-497.*

97. *Takagaki Y, Giussani A, Tominaga J, Jahn U, Calarco R. Transport properties in a Sb–Te binary topological-insulator system. Journal of Physics: Condensed Matter 2013,* ***25****(34):* *345801.*

98. *Nonaka T, Ohbayashi G, Toriumi Y, Mori Y, Hashimoto H. Crystal structure of GeTe and Ge2Sb2Te5 meta-stable phase. Thin Solid Films 2000,* ***370****(1):* *258-261.*

99. *Lazzarini L, Rotunno E, Grillo V, Longo M. Determination of the atomic stacking sequence of Ge-Sb-Te nanowires by HAADF STEM. MRS Proceedings 2013,* ***1512:*** *mrsf12-1512-ff1510-1506.*

100. *Wang J-J, Xu Y-Z, Mazzarello R, Wuttig M, Zhang W. A Review on Disorder-Driven Metal-Insulator Transition in Crystalline Vacancy-Rich GeSbTe Phase-Change Materials. Materials (Basel) 2017,* ***10****(8):* *862.*

101. *Li P, Ding T, Li J, Zhang C, Dou Y, Li Y, et al. Positive Effect of Ge Vacancies on Facilitating Band Convergence and Suppressing Bipolar Transport in GeTe-Based Alloys for High Thermoelectric Performance. Advanced Functional Materials 2020,* ***30****(15):* *1910059.*

102. *Liu Z, Sato N, Guo Q, Gao W, Mori T. Shaping the role of germanium vacancies in germanium telluride: metastable cubic structure stabilization, band structure modification, and stable N-type conduction. NPG Asia Materials 2020,* ***12****(1):* *66.*

103. *Bos JWG, Zandbergen HW, Lee MH, Ong NP, Cava RJ. Structures and thermoelectric properties of the infinitely adaptive series (Bi2)m(Bi2Te3)n. Physical Review B 2007, **75**(19): 195203.*

104. *Bos JWG, Faucheux F, Downie RA, Marcinkova A. Phase stability, structures and properties of the (Bi2)m (Bi2Te3)n natural superlattices. Journal of Solid State Chemistry 2012, **193**: 13-18.*

105. *Saito Y, Fons P, Makino K, Mitrofanov KV, Uesugi F, Takeguchi M, et al. Compositional tuning in sputter-grown highly-oriented Bi–Te films and their optical and electronic structures. Nanoscale 2017, **9**(39): 15115-15121.*

106. *Li J, Li Y, Du S, Wang Z, Gu B-L, Zhang S-C, et al. Intrinsic magnetic topological insulators in van der Waals layered MnBi₂Te₄-family materials. Science Advances 2019, **5**(6): eaaw5685.*

107. *Luo W, Qi X-L. Massive Dirac surface states in topological insulator/magnetic insulator heterostructures. Physical Review B 2013, **87**(8): 085431.*

108. *Eremeev SV, Men'shov VN, Tugushev VV, Echenique PM, Chulkov EV. Magnetic proximity effect at the three-dimensional topological insulator/magnetic insulator interface. Physical Review B 2013, **88**(14): 144430.*

109. *Hirahara T, Otrokov MM, Sasaki TT, Sumida K, Tomohiro Y, Kusaka S, et al. Fabrication of a novel magnetic topological heterostructure and temperature evolution of its massive Dirac cone. Nature Communications 2020, **11**(1): 4821.*

110. *He L, Kou X, Wang KL. Review of 3D topological insulator thin-film growth by molecular beam epitaxy and potential applications. physica status solidi (RRL) – Rapid Research Letters 2013, **7**(1-2): 50-63.*

111. *Jiang Z, Chang C-Z, Tang C, Zheng J-G, Moodera JS, Shi J. Structural and proximity-induced ferromagnetic properties of topological insulator-magnetic insulator heterostructures. AIP Advances 2016, **6**(5): 055809.*

112. *Yang SR, Fanchiang YT, Chen CC, Tseng CC, Liu YC, Guo MX, et al. Evidence for exchange Dirac gap in magnetotransport of topological insulator--magnetic insulator heterostructures. Physical Review B 2019, **100**(4): 045138.*

113. *Liu T, Kally J, Pillsbury T, Liu C, Chang H, Ding J, et al. Changes of Magnetism in a Magnetic Insulator due to Proximity to a Topological Insulator. Physical Review Letters 2020, **125**(1): 017204.*

114. *Zou J, He Z, Xu G. The study of magnetic topological semimetals by first principles calculations. npj Computational Materials 2019, **5**(1): 96.*

115. *Popkin G. Quest for qubits. Science 2016, **354**(6316): 1090.*

116. *Walter Ogburn R, Preskill J. Topological Quantum Computation. In: Williams CP, editor. Quantum Computing and Quantum Communications; 1999 1999//; Berlin, Heidelberg: Springer Berlin Heidelberg; 1999. p. 341-356.*

117. *Ayukaryana NR, Fauzi MH, Hasdeo EH. The Quest and Hope of Majorana Zero Modes in Topological Superconductor for Fault Tolerant Quantum Computing: An Introductory Overview. arXiv preprint arXiv:200907764 2020.*

118. *He M, Sun H, He QL. Topological insulator: Spintronics and quantum computations. Frontiers of Physics 2019,* ***14****(4):* *43401.*

119. *Kauffman L, Lomonaco S. Braiding with Majorana fermions, vol. 9873. SPIE, 2016.*

120. *Ma X, Reichhardt CJO, Reichhardt C. Braiding Majorana fermions and creating quantum logic gates with vortices on a periodic pinning structure. Physical Review B 2020,* ***101****(2):* *024514.*

121. *Fu L, Kane CL. Superconducting Proximity Effect and Majorana Fermions at the Surface of a Topological Insulator. Physical Review Letters 2008,* ***100****(9):* *096407.*

122. *Leijnse M, Flensberg K. Introduction to topological superconductivity and Majorana fermions. Semiconductor Science and Technology 2012,* ***27****(12):* *124003.*

123. *Sun H-H, Jia J-F. Detection of Majorana zero mode in the vortex. npj Quantum Materials 2017,* ***2****(1):* *34.*

124. *Jäck B, Xie Y, Li J, Jeon S, Bernevig BA, Yazdani A. Observation of a Majorana zero mode in a topologically protected edge channel. Science 2019,* ***364****(6447):* *1255-1259.*

125. *Lutchyn RM, Sau JD, Das Sarma S. Majorana Fermions and a Topological Phase Transition in Semiconductor-Superconductor Heterostructures. Physical Review Letters 2010,* ***105****(7):* *077001.*

126. *Wang M-X, Li P, Xu J-P, Liu Z-L, Ge J-F, Wang G-Y, et al. Interface structure of a topological insulator/superconductor heterostructure. New Journal of Physics 2014,* ***16****(12):* *123043.*

127. *Lutchyn RM, Bakkers EPAM, Kouwenhoven LP, Krogstrup P, Marcus CM, Oreg Y. Majorana zero modes in superconductor–semiconductor heterostructures. Nature Reviews Materials 2018,* ***3****(5):* *52-68.*

128. *Trang CX, Shimamura N, Nakayama K, Souma S, Sugawara K, Watanabe I, et al. Conversion of a conventional superconductor into a topological superconductor by topological proximity effect. Nature Communications 2020,* ***11****(1):* *159.*

129. *Das A, Ronen Y, Most Y, Oreg Y, Heiblum M, Shtrikman H. Zero-bias peaks and splitting in an Al–InAs nanowire topological superconductor as a signature of Majorana fermions. Nature Physics 2012,* ***8****(12):* *887-895.*

130. *Deng M, Yu C, Huang G, Larsson M, Caroff P, Xu H. Anomalous zero-bias conductance peak in a Nb–InSb nanowire–Nb hybrid device. Nano letters 2012,* ***12****(12):* *6414-6419.*

131. *Finck A, Van Harlingen D, Mohseni P, Jung K, Li X. Anomalous modulation of a zero-bias peak in a hybrid nanowire-superconductor device. Physical review letters 2013,* ***110****(12):* *126406.*

132. *Mourik V, Zuo K, Frolov SM, Plissard S, Bakkers EP, Kouwenhoven LP. Signatures of Majorana fermions in hybrid superconductor-semiconductor nanowire devices. Science 2012,* ***336****(6084):* *1003-1007.*

133. *Nadj-Perge S, Drozdov IK, Li J, Chen H, Jeon S, Seo J, et al. Observation of Majorana fermions in ferromagnetic atomic chains on a superconductor. Science 2014,* ***346****(6209):* *602-607.*

134. *Wang M-X, Liu C, Xu J-P, Yang F, Miao L, Yao M-Y, et al. The Coexistence of Superconductivity and Topological Order in the Bi₂Se₃ Thin Films. Science 2012, **336**(6077): 52.*

135. *Xu J-P, Liu C, Wang M-X, Ge J, Liu Z-L, Yang X, et al. Artificial Topological Superconductor by the Proximity Effect. Physical Review Letters 2014, **112**(21): 217001.*

136. *Xu J-P, Wang M-X, Liu ZL, Ge J-F, Yang X, Liu C, et al. Experimental detection of a Majorana mode in the core of a magnetic vortex inside a topological insulator-superconductor Bi 2 Te 3/NbSe 2 heterostructure. Physical review letters 2015, **114**(1): 017001.*

137. *Beenakker C. Search for non-Abelian Majorana braiding statistics in superconductors. arXiv preprint arXiv:190706497 2020.*

138. *Frolov SM, Manfra MJ, Sau JD. Topological superconductivity in hybrid devices. Nature Physics 2020, **16**(7): 718-724.*

139. *Ioselevich PA, Feigel'man MV. Anomalous Josephson Current via Majorana Bound States in Topological Insulators. Physical Review Letters 2011, **106**(7): 077003.*

140. *Chuburin YP, Tinyukova TS. The emergence of bound states in a superconducting gap at the topological insulator edge. Physics Letters A 2020, **384**(27): 126694.*

141. *Schulz F, Plekhanov K, Loss D, Klinovaja J. Majorana bound states in topological insulators with hidden Dirac points. Physical Review Research 2020, **2**(3): 033215.*

142. *Schüffelgen P, Rosenbach D, Li C, Schmitt TW, Schleenvoigt M, Jalil AR, et al. Selective area growth and stencil lithography for in situ fabricated quantum devices. Nature Nanotechnology 2019, **14**(9): 825-831.*

143. *Schüffelgen P, Rosenbach D, Li C, Schmitt T, Schleenvoigt M, Jalil AR, et al. Boosting transparency in topological josephson junctions via stencil lithography. arXiv preprint arXiv:171101665 2017.*

144. *Qi X-L, Hughes TL, Raghu S, Zhang S-C. Time-Reversal-Invariant Topological Superconductors and Superfluids in Two and Three Dimensions. Physical Review Letters 2009, **102**(18): 187001.*

145. *Alicea J. New directions in the pursuit of Majorana fermions in solid state systems. Reports on Progress in Physics 2012, **75**(7): 076501.*

146. *Beenakker CWJ. Search for Majorana Fermions in Superconductors. Annual Review of Condensed Matter Physics 2013, **4**(1): 113-136.*

147. *Alicea J, Oreg Y, Refael G, von Oppen F, Fisher MPA. Non-Abelian statistics and topological quantum information processing in 1D wire networks. Nature Physics 2011, **7**(5): 412-417.*

148. *Yang G, Lyu Z, Wang J, Ying J, Zhang X, Shen J, et al. Protected gap closing in Josephson trijunctions constructed on ${\mathrm{Bi}}_{2}{\mathrm{Te}}_{3}$. Physical Review B 2019, **100**(18): 180501.*

149. *Li Z-Z, Zhang F-C, Wang Q-H. Majorana modes in a topological insulator/s-wave superconductor heterostructure. Scientific Reports 2014, **4**(1): 6363.*

150. *Krzyzosiak M, Gonczarek R, Gonczarek A, Jacak L. Interplay between spin-singlet and spin-triplet order parameters in a model of an anisotropic superconductor with cuprate planes. Journal of Physics: Conference Series 2009,* ***152:*** *012057.*

151. *Bai M, Yang F, Luysberg M, Feng J, Bliesener A, Lippertz G, et al. Novel self-epitaxy for inducing superconductivity in the topological insulator (Bi 1− x Sb x) 2 Te 3. Physical Review Materials 2020,* ***4****(9):* *094801.*

152. *Wang E, Ding H, Fedorov AV, Yao W, Li Z, Lv Y-F, et al. Fully gapped topological surface states in Bi2Se3 films induced by a d-wave high-temperature superconductor. Nature Physics 2013,* ***9****(10):* *621-625.*

153. *Roy B. Higher-order topological superconductors in $\mathcal{P}$-, $\mathcal{T}$-odd quadrupolar Dirac materials. Physical Review B 2020,* ***101****(22):* *220506.*

154. *Shen J, Heedt S, Borsoi F, van Heck B, Gazibegovic S, Op het Veld RLM, et al. Parity transitions in the superconducting ground state of hybrid InSb–Al Coulomb islands. Nature Communications 2018,* ***9****(1):* *4801.*

155. *Savin AM, Meschke M, Pekola JP, Pashkin YA, Li TF, Im H, et al. Parity effect in Al and Nb single electron transistors in a tunable environment. Applied Physics Letters 2007,* ***91****(6):* *063512.*

156. *Loder F, Kampf AP, Kopp T, Mannhart J, Schneider CW, Barash YS. Magnetic flux periodicity of h/e in superconducting loops. Nature Physics 2008,* ***4****(2):* *112-115.*

157. *Hyun J, Jeong MY, Kim S, Jung M-C, Lee Y, Lim C-y, et al. A weak topological insulator state in quasi-one-dimensional superconductor TaSe $ _3$. arXiv preprint arXiv:200905917 2020.*

158. *Wiedenmann J, Bocquillon E, Deacon RS, Hartinger S, Herrmann O, Klapwijk TM, et al. 4π-periodic Josephson supercurrent in HgTe-based topological Josephson junctions. Nature Communications 2016,* ***7****(1):* *10303.*

159. *Schüffelgen P, Rosenbach D, Pang Y, Kampmeier J, Luysberg M, Kibkalo L, et al. Signatures of induced superconductivity in AlOx-capped topological heterostructures. Solid-State Electronics 2019,* ***155:*** *111-116.*

160. *Galletti L, Charpentier S, Iavarone M, Lucignano P, Massarotti D, Arpaia R, et al. Influence of topological edge states on the properties of $\mathrm{Al}/{Bi}_{2}{\mathrm{Se}}_{3}/\mathrm{Al}$ hybrid Josephson devices. Physical Review B 2014,* ***89****(13):* *134512.*

161. *Ghatak S, Breunig O, Yang F, Wang Z, Taskin AA, Ando Y. Anomalous Fraunhofer Patterns in Gated Josephson Junctions Based on the Bulk-Insulating Topological Insulator BiSbTeSe2. Nano Letters 2018,* ***18****(8):* *5124-5131.*

162. *Charpentier S, Galletti L, Kunakova G, Arpaia R, Song Y, Baghdadi R, et al. Induced unconventional superconductivity on the surface states of Bi2Te3 topological insulator. Nature Communications 2017,* ***8****(1):* *2019.*

163. *Kunakova G, Bauch T, Trabaldo E, Andzane J, Erts D, Lombardi F. High transparency Bi2Se3 topological insulator nanoribbon Josephson junctions with low resistive noise properties. Applied Physics Letters 2019,* ***115****(17):* *172601.*

164. *Borisova S. Fabrication and in-situ STM investigation of growth dynamics of semiconductor nanostructures grown by MBE. Available from INIS: http://inis.iaea.org/search/search.aspx?orig_q=RN:44111367 thesis, 2012.*

165. *Kampmeier J, Morgenstern M, Grützmacher D. Molecular Beam Epitaxy of Topological Insulator Thin Films. RWTH Aachen University, 2018.*

Chapter – 2

1. *Teo JCY, Fu L, Kane CL. Surface states and topological invariants in three-dimensional topological insulators: Application to Bi(1-x)Sb(x). Physical Review B 2008,* ***78****(4):* *045426.*

2. *Hasan MZ, Moore JE. Three-Dimensional Topological Insulators. Annual Review of Condensed Matter Physics 2011,* ***2****(1):* *55-78.*

3. *Rosenbach D, Oellers N, Jalil AR, Mikulics M, Kölzer J, Zimmermann E, et al. Quantum Transport in Topological Surface States of Selectively Grown Bi2Te3 Nanoribbons. Advanced Electronic Materials 2020,* ***n/a****(n/a):* *2000205.*

4. *Fan Y, Wang KL. Spintronics Based on Topological Insulators. SPIN 2016,* ***06****(02):* *1640001.*

5. *Šmejkal L, Mokrousov Y, Yan B, MacDonald AH. Topological antiferromagnetic spintronics. Nature Physics 2018,* ***14****(3):* *242-251.*

6. *Pesin D, MacDonald AH. Spintronics and Pseudospintronics in Graphene and Topological Insulators. Nat Mater 2012,* ***11:*** *409.*

7. *Akhmerov AR, Nilsson J, Beenakker CWJ. Electrically Detected Interferometry of Majorana Fermions in a Topological Insulator. Phys Rev Lett 2009,* ***102:*** *216404.*

8. *Schüffelgen P, Rosenbach D, Li C, Schmitt TW, Schleenvoigt M, Jalil AR, et al. Selective area growth and stencil lithography for in situ fabricated quantum devices. Nature Nanotechnology 2019,* ***14****(9):* *825-831.*

9. *Lutchyn RM, Sau JD, Das Sarma S. Majorana Fermions and a Topological Phase Transition in Semiconductor-Superconductor Heterostructures. Physical Review Letters 2010,* ***105****(7):* *077001.*

10. *Fu L, Kane CL. Superconducting Proximity Effect and Majorana Fermions at the Surface of a Topological Insulator. Physical Review Letters 2008,* ***100****(9):* *096407.*

11. *Leijnse M, Flensberg K. Introduction to topological superconductivity and Majorana fermions. Semiconductor Science and Technology 2012,* ***27****(12):* *124003.*

12. *Sarma SD, Freedman M, Nayak C. Majorana zero modes and topological quantum computation. npj Quantum Information 2015,* ***1****(1):* *15001.*

13. *Plugge S, Rasmussen A, Egger R, Flensberg K. Majorana box qubits. New Journal of Physics 2017,* ***19****(1):* *012001.*

14. *Franz M. Majorana's wires. Nature Nanotechnology 2013,* ***8****(3):* *149-152.*

15. *Kong D, Cui Y. Opportunities in chemistry and materials science for topological insulators and their nanostructures. Nature Chemistry 2011, **3**(11): 845-849.*

16. *Xu J-P, Wang M-X, Liu ZL, Ge J-F, Yang X, Liu C, et al. Experimental detection of a Majorana mode in the core of a magnetic vortex inside a topological insulator-superconductor Bi 2 Te 3/NbSe 2 heterostructure. Physical review letters 2015, **114**(1): 017001.*

17. *He QL, Pan L, Stern AL, Burks EC, Che X, Yin G, et al. Chiral Majorana fermion modes in a quantum anomalous Hall insulator–superconductor structure. Science 2017, **357**(6348): 294-299.*

18. *Deng Y, Yu Y, Shi MZ, Guo Z, Xu Z, Wang J, et al. Quantum anomalous Hall effect in intrinsic magnetic topological insulator MnBi₂Te₄. Science 2020, **367**(6480): 895-900.*

19. *Dziom V, Shuvaev A, Pimenov A, Astakhov GV, Ames C, Bendias K, et al. Observation of the universal magnetoelectric effect in a 3D topological insulator. Nature Communications 2017, **8**(1): 15197.*

20. *Mogi M, Kawamura M, Yoshimi R, Tsukazaki A, Kozuka Y, Shirakawa N, et al. A magnetic heterostructure of topological insulators as a candidate for an axion insulator. Nature Materials 2017, **16**(5): 516-521.*

21. *Xu S-Y, Xia Y, Wray LA, Jia S, Meier F, Dil JH, et al. Topological Phase Transition and Texture Inversion in a Tunable Topological Insulator. Science 2011, **332**(6029): 560-564.*

22. *Koumoulis D, Leung B, Chasapis TC, Taylor R, King Jr. D, Kanatzidis MG, et al. Understanding Bulk Defects in Topological Insulators from Nuclear-Spin Interactions. Advanced Functional Materials 2014, **24**(11): 1519-1528.*

23. *Menshchikova TV, Otrokov MM, Tsirkin SS, Samorokov DA, Bebneva VV, Ernst A, et al. Band Structure Engineering in Topological Insulator Based Heterostructures. Nano Letters 2013, **13**(12): 6064-6069.*

24. *Jin K-H, Yeom HW, Jhi S-H. Band structure engineering of topological insulator heterojunctions. Physical Review B 2016, **93**(7): 075308.*

25. *Li H, Gao L, Li H, Wang G, Wu J, Zhou Z, et al. Growth and band alignment of Bi2Se3 topological insulator on H-terminated Si(111) van der Waals surface. Applied Physics Letters 2013, **102**(7): 074106.*

26. *Berntsen MH, Götberg O, Wojek BM, Tjernberg O. Direct observation of decoupled Dirac states at the interface between topological and normal insulators. Physical Review B 2013, **88**(19): 195132.*

27. *Bos JWG, Faucheux F, Downie RA, Marcinkova A. Phase stability, structures and properties of the (Bi2)m (Bi2Te3)n natural superlattices. Journal of Solid State Chemistry 2012, **193**: 13-18.*

28. *Bos JWG, Zandbergen HW, Lee MH, Ong NP, Cava RJ. Structures and thermoelectric properties of the infinitely adaptive series (Bi2)m(Bi2Te3)n. Physical Review B 2007, **75**(19): 195203.*

29. *Concepción O, Galván-Arellano M, Torres-Costa V, Climent-Font A, Bahena D, Manso Silván M, et al. Controlling the Epitaxial Growth of Bi2Te3, BiTe, and Bi4Te3 Pure Phases by Physical Vapor Transport. Inorganic Chemistry 2018, **57**(16): 10090-10099.*

30. *Kong D, Randel JC, Peng H, Cha JJ, Meister S, Lai K, et al. Topological Insulator Nanowires and Nanoribbons. Nano Letters 2010,* ***10****(1):* *329-333.*

31. *Kuznetsov PI, Yapaskurt VO, Shchamkhalova BS, Shcherbakov VD, Yakushcheva GG, Luzanov VA, et al. Growth of Bi2Te3 films and other phases of Bi-Te system by MOVPE. Journal of Crystal Growth 2016,* ***455:*** *122-128.*

32. *Saito Y, Fons P, Makino K, Mitrofanov KV, Uesugi F, Takeguchi M, et al. Compositional tuning in sputter-grown highly-oriented Bi–Te films and their optical and electronic structures. Nanoscale 2017,* ***9****(39):* *15115-15121.*

33. *Zayachuk DM, Slynko VE, Csik A. Peculiar properties of preferential sputtering of PbTe, SnTe, and GeTe by Ar+ ion plasma. Materials Science in Semiconductor Processing 2018,* ***88:*** *103-108.*

34. *Yamada N, Matsunaga T. Structure of laser-crystallized Ge2Sb2+xTe5 sputtered thin films for use in optical memory. Journal of Applied Physics 2000,* ***88****(12):* *7020-7028.*

35. *Bulai G, Pompilian O, Gurlui S, Nemec P, Nazabal V, Cimpoesu N, et al. Ge-Sb-Te Chalcogenide Thin Films Deposited by Nanosecond, Picosecond, and Femtosecond Laser Ablation. Nanomaterials (Basel) 2019,* ***9****(5):* *676.*

36. *Hilmi I, Lotnyk A, Gerlach JW, Schumacher P, Rauschenbach B. Influence of substrate dimensionality on the growth mode of epitaxial 3D-bonded GeTe thin films: From 3D to 2D growth. Materials & Design 2019,* ***168:*** *107657.*

37. *Le PH, Liao C-N, Luo CW, Leu J. Thermoelectric properties of nanostructured bismuth–telluride thin films grown using pulsed laser deposition. Journal of Alloys and Compounds 2014,* ***615:*** *546-552.*

38. *Eschbach M, Lanius M, Niu C, Młyńczak E, Gospodarič P, Kellner J, et al. Bi1Te1 is a dual topological insulator. Nature Communications 2017,* ***8****(1):* *14976.*

39. *Collins-McIntyre LJ, Wang W, Zhou B, Speller SC, Chen YL, Hesjedal T. Growth of BiSe and BiTe on amorphous fused silica by MBE. physica status solidi (b) 2015,* ***252****(6):* *1334-1338.*

40. *Jerng S-K, Joo K, Kim Y, Yoon S-M, Lee JH, Kim M, et al. Ordered growth of topological insulator Bi2Se3 thin films on dielectric amorphous SiO2 by MBE. Nanoscale 2013,* ***5****(21):* *10618-10622.*

41. *Fülöp A, Song Y, Charpentier S, Shi P, Ekström M, Galletti L, et al. Phase transition of bismuth telluride thin films grown by MBE. Applied Physics Express 2014,* ***7****(4):* *045503.*

42. *Nakamura H, Rungger I, Sanvito S, Inoue N, Tominaga J, Asai Y. Resistive switching mechanism of GeTe–Sb2Te3 interfacial phase change memory and topological properties of embedded two-dimensional states. Nanoscale 2017,* ***9****(27):* *9386-9395.*

43. *He L, Kou X, Wang KL. Review of 3D topological insulator thin-film growth by molecular beam epitaxy and potential applications. physica status solidi (RRL) – Rapid Research Letters 2013,* ***7****(1-2):* *50-63.*

44. *Kampmeier J, Weyrich C, Lanius M, Schall M, Neumann E, Mussler G, et al. Selective area growth of Bi2Te3 and Sb2Te3 topological insulator thin films. Journal of Crystal Growth 2016,* ***443:*** *38-42.*

45. *Chen X, Ma X-C, He K, Jia J-F, Xue Q-K. Molecular Beam Epitaxial Growth of Topological Insulators. Advanced Materials 2011,* ***23****(9):* *1162-1165.*

46. *Borisova S, Krumrain J, Luysberg M, Mussler G, Grützmacher D. Mode of Growth of Ultrathin Topological Insulator Bi2Te3 Films on Si (111) Substrates. Crystal Growth & Design 2012,* ***12****(12):* *6098-6103.*

47. *Mussler G. Molecular-Beam Epitaxy of 3D Topological Insulator Thin Films and Devices on Si Substrates. physica status solidi (b) 2021,* ***258****(1):* *2000007.*

48. *Schäpers T, Weyrich C, Rosenbach D, Kölzer J, Schmitt T, Schüffelgen P, et al. Phase-coherent transport in topological insulator nanocolumns and nanoribbons. Spintronics XI; 2018: International Society for Optics and Photonics; 2018. p. 107320V.*

49. *Weyrich C, Drögeler M, Kampmeier J, Eschbach M, Mussler G, Merzenich T, et al. Growth, characterization, and transport properties of ternary (Bi1− xSbx) 2Te3 topological insulator layers. Journal of Physics: Condensed Matter 2016,* ***28****(49):* *495501.*

50. *Weyrich C, Lanius M, Schüffelgen P, Rosenbach D, Mussler G, Bunte S, et al. Phase-coherent transport in selectively grown topological insulator nanodots. Nanotechnology 2018,* ***30****(5):* *055201.*

51. *Weyrich CP, Schäpers T. Electrical transport and magnetoresistance in MBE-grown 3D topological insulator thin films and nanostructures: Fachgruppe Physik; 2020.*

52. *Plucinski L, Herdt A, Fahrendorf S, Bihlmayer G, Mussler G, Döring S, et al. Electronic structure, surface morphology, and topologically protected surface states of Sb2Te3 thin films grown on Si(111). Journal of Applied Physics 2013,* ***113****(5):* *053706.*

53. *Chen Y, Analytis JG, Chu J-H, Liu Z, Mo S-K, Qi X-L, et al. Experimental realization of a three-dimensional topological insulator, Bi2Te3. science 2009,* ***325****(5937):* *178-181.*

54. *Fang T, Li X, Hu C, Zhang Q, Yang J, Zhang W, et al. Complex Band Structures and Lattice Dynamics of Bi2Te3-Based Compounds and Solid Solutions. Advanced Functional Materials 2019,* ***29****(28):* *1900677.*

55. *Zhang Y, He K, Chang C-Z, Song C-L, Wang L-L, Chen X, et al. Crossover of the three-dimensional topological insulator Bi2Se3 to the two-dimensional limit. Nature Physics 2010,* ***6****(8):* *584-588.*

56. *Zhang H, Liu C-X, Qi X-L, Dai X, Fang Z, Zhang S-C. Topological insulators in Bi2Se3, Bi2Te3 and Sb2Te3 with a single Dirac cone on the surface. Nature Physics 2009,* ***5****(6):* *438-442.*

57. *Eschbach M, Młyńczak E, Kellner J, Kampmeier J, Lanius M, Neumann E, et al. Realization of a vertical topological p–n junction in epitaxial Sb2Te3/Bi2Te3 heterostructures. Nature Communications 2015,* ***6****(1):* *8816.*

58. *Kellner J, Eschbach M, Kampmeier J, Lanius M, Młyńczak E, Mussler G, et al. Tuning the Dirac point to the Fermi level in the ternary topological insulator (Bi1−xSbx)2Te3. Applied Physics Letters 2015,* ***107****(25):* *251603.*

59. *Lanius M, Kampmeier J, Weyrich C, Kölling S, Schall M, Schüffelgen P, et al. P–N Junctions in Ultrathin Topological Insulator Sb2Te3/Bi2Te3 Heterostructures Grown by Molecular Beam Epitaxy. Crystal Growth & Design 2016,* ***16****(4):* *2057-2061.*

60. *Fornari CI, Rappl PHO, Morelhão SL, Abramof E. Structural properties of Bi2Te3 topological insulator thin films grown by molecular beam epitaxy on (111) BaF2 substrates. Journal of Applied Physics 2016,* ***119****(16):* *165303.*

61. *Kim K-C, Lee J, Kim BK, Choi WY, Chang HJ, Won SO, et al. Free-electron creation at the 60° twin boundary in Bi 2 Te 3. Nature communications 2016,* ***7****(1):* *1-6.*

62. *Bi2Te3 Crystal Structure: Datasheet from "PAULING FILE Multinaries Edition – 2012" in SpringerMaterials (https://materials.springer.com/isp/crystallographic/docs/sd_0309161). Springer-Verlag Berlin Heidelberg & Material Phases Data System (MPDS), Switzerland & National Institute for Materials Science (NIMS), Japan.*

63. *Ploog KH. Heteroepitaxy—new challenges and opportunities for materials engineering through molecular beam epitaxy. Journal of Crystal Growth 2002,* ***237-239:*** *2028-2034.*

64. *Koma A. Van der Waals epitaxy—a new epitaxial growth method for a highly lattice-mismatched system. Thin Solid Films 1992,* ***216****(1):* *72-76.*

65. *Koma A. Van der Waals epitaxy for highly lattice-mismatched systems. Journal of Crystal Growth 1999,* ***201-202:*** *236-241.*

66. *Lanius M. Topological Insulating Tellurides: How to tune Doping, Topology, and Dimensionality. Universitätsbibliothek der RWTH Aachen, 2018.*

67. *Schüffelgen P. Exploiting Topological Insulators for Majorana Devices and Physics Via Molecular Beam Epitaxy: Halbleiter-Nanoelektronik; 2018.*

68. *Kim C, Kim DH, Han YS, Chung JS, Park S, Park S, et al. Development of bismuth tellurium selenide nanoparticles for thermoelectric applications via a chemical synthetic process. Materials Research Bulletin 2011,* ***46****(3):* *407-412.*

69. *Kim C, Kim DH, Kim JT, Han YS, Kim H. Investigation of Reaction Mechanisms of Bismuth Tellurium Selenide Nanomaterials for Simple Reaction Manipulation Causing Effective Adjustment of Thermoelectric Properties. ACS Applied Materials & Interfaces 2014,* ***6****(2):* *778-785.*

70. *Nagao T, Doi T, Sekiguchi T, Hasegawa S. Epitaxial Growth of Single-Crystal Ultrathin Films of Bismuth on Si(111). Japanese Journal of Applied Physics 2000,* ***39****(Part 1, No. 7B):* *4567-4570.*

71. *Momand J, Boschker JE, Wang R, Calarco R, Kooi BJ. Tailoring the epitaxy of Sb2Te3 and GeTe thin films using surface passivation. CrystEngComm 2018,* ***20****(3):* *340-347.*

72. *Lotnyk A, Hilmi I, Ross U, Rauschenbach B. Van der Waals interfacial bonding and intermixing in GeTe-Sb2Te3-based superlattices. Nano Research 2018,* ***11****(3):* *1676-1686.*

73. *Lotnyk A, Ross U, Dankwort T, Hilmi I, Kienle L, Rauschenbach B. Atomic structure and dynamic reconfiguration of layered defects in van der Waals layered Ge-Sb-Te based materials. Acta Materialia 2017,* ***141:*** *92-96.*

74. *Hilmi I, Lotnyk A, Gerlach JW, Schumacher P, Rauschenbach B. Research Update: Van-der-Waals epitaxy of layered chalcogenide Sb2Te3 thin films grown by pulsed laser deposition. APL Materials 2017,* ***5****(5):* *050701.*

75. *Seong S, Albright TA, Zhang X, Kanatzidis M. Te-Te bonding in copper tellurides. Journal of the American Chemical Society 1994,* ***116****(16):* *7287-7293.*

76. *Lanius M, Kampmeier J, Kölling S, Mussler G, Koenraad PM, Grützmacher D. Topography and structure of ultrathin topological insulator Sb2Te3 films on Si(111) grown by means of molecular beam epitaxy. Journal of Crystal Growth 2016,* ***453:*** *158-162.*

77. *Esposito L, Bietti S, Fedorov A, Nötzel R, Sanguinetti S. Ehrlich-Schw\"obel effect on the growth dynamics of GaAs(111)A surfaces. Physical Review Materials 2017,* ***1****(2):* *024602.*

78. *Schönherr P, Tilbury T, Wang H, Haghighirad AA, Srot V, van Aken PA, et al. Step-Flow Growth of Bi2Te3 Nanobelts. Crystal Growth & Design 2016,* ***16****(12):* *6961-6966.*

79. *Borisova S. Fabrication and in-situ STM investigation of growth dynamics of semiconductor nanostructures grown by MBE. Available from INIS: http://inis.iaea.org/search/search.aspx?orig_q=RN:44111367 thesis, 2012.*

80. *Kampmeier J, Morgenstern M, Grützmacher D. Molecular Beam Epitaxy of Topological Insulator Thin Films. RWTH Aachen University, 2018.*

81. *Schleenvoigt M. Quality Improvement of Molecular Beam Epitaxy Grown Topological Insulator Thin Films and in situ Fabrication of Devices. 2017.*

82. *Ungár T. Microstructural parameters from X-ray diffraction peak broadening. Scripta Materialia 2004,* ***51****(8):* *777-781.*

83. *Wong CS. X-ray diffraction techniques for future advanced CMOS metrology challenges. Dublin City University, 2013.*

84. *Bismuth: Inorganic Chemistry. Encyclopedia of Inorganic and Bioinorganic Chemistry, pp 1-32.*

85. *Beladi-Mousavi SM, Pumera M. 2D-Pnictogens: alloy-based anode battery materials with ultrahigh cycling stability. Chemical Society Reviews 2018,* ***47****(18):* *6964-6989.*

86. *Sturala J, Sofer Z, Pumera M. Chemistry of Layered Pnictogens: Phosphorus, Arsenic, Antimony, and Bismuth. Angewandte Chemie International Edition 2019,* ***58****(23):* *7551-7557.*

87. *Wu W, Chen S, Zhai J. Study on the physical properties and structure of titanium antimony thin films for phase change memory application. Journal of Materials Science 2017,* ***52****(19):* *11598-11607.*

88. *Perrière J. Rutherford backscattering spectrometry. Vacuum 1987,* ***37****(5):* *429-432.*

89. *Jeynes C, Barradas NP, Szilágyi E. Accurate Determination of Quantity of Material in Thin Films by Rutherford Backscattering Spectrometry. Analytical Chemistry 2012,* ***84****(14):* *6061-6069.*

90. *Schinzel AAGL, Smith DW, Miller JR. Monozygotic twinning and structural defects. The Journal of Pediatrics 1979,* ***95****(6):* *921-930.*

91. *Cava RJ, Ji H, Fuccillo MK, Gibson QD, Hor YS. Crystal structure and chemistry of topological insulators. Journal of Materials Chemistry C 2013,* ***1****(19):* *3176-3189.*

92. *Heremans JP, Cava RJ, Samarth N. Tetradymites as thermoelectrics and topological insulators. Nature Reviews Materials 2017,* ***2****(10):* *17049.*

93. *Randle V. Grain boundary engineering: an overview after 25 years. Materials Science and Technology 2010,* ***26****(3):* *253-261.*

94. *Kampmeier J, Borisova S, Plucinski L, Luysberg M, Mussler G, Grützmacher D. Suppressing Twin Domains in Molecular Beam Epitaxy Grown Bi2Te3 Topological Insulator Thin Films. Cryst Growth Des 2015,* ***15:*** *390.*

95. *Levy I, Garcia TA, Shafique S, Tamargo MC. Reduced twinning and surface roughness of Bi2Se3 and Bi2Te3 layers grown by molecular beam epitaxy on sapphire substrates. Journal of Vacuum Science & Technology B 2018,* ***36****(2):* *02D107.*

96. *Harrison SE, Li S, Huo Y, Zhou B, Chen YL, Harris JS. Two-step growth of high quality Bi2Te3 thin films on Al2O3 (0001) by molecular beam epitaxy. Applied Physics Letters 2013,* ***102****(17):* *171906.*

97. *Schreyeck S, Tarakina NV, Karczewski G, Schumacher C, Borzenko T, Brüne C, et al. Molecular Beam Epitaxy of High Structural Quality Bi2Se3 on Lattice Matched InP(111) Substrates. Appl Phys Lett 2013,* ***102:*** *041914.*

98. *Utama MIB, de la Mata M, Magen C, Arbiol J, Xiong Q. Twinning-, Polytypism-, and Polarity-Induced Morphological Modulation in Nonplanar Nanostructures with van der Waals Epitaxy. Advanced Functional Materials 2013,* ***23****(13):* *1636-1646.*

99. *Mortelmans W, Nalin Mehta A, Balaji Y, El Kazzi S, Sergeant S, Houssa M, et al. Fundamental limitation of van der Waals homoepitaxy by stacking fault formation in WSe2. 2D Materials 2020,* ***7****(2):* *025027.*

100. *Chen K-C, Lai S-M, Wu B-Y, Chen C, Lin S-Y. Van der Waals Epitaxy of Large-Area and Single-Crystalline Gold Films on MoS2 for Low-Contact-Resistance 2D–3D Interfaces. ACS Applied Nano Materials 2020,* ***3****(3):* *2997-3003.*

101. *Mio AM, Konze PM, Meledin A, Küpers M, Pohlmann M, Kaminski M, et al. Impact of Bonding on the Stacking Defects in Layered Chalcogenides. Advanced Functional Materials 2019,* ***29****(37):* *1902332.*

102. *Alden JS, Tsen AW, Huang PY, Hovden R, Brown L, Park J, et al. Strain solitons and topological defects in bilayer graphene. Proceedings of the National Academy of Sciences 2013,* ***110****(28):* *11256.*

103. *Zhao X, Ding Z, Chen J, Dan J, Poh SM, Fu W, et al. Strain Modulation by van der Waals Coupling in Bilayer Transition Metal Dichalcogenide. ACS Nano 2018,* ***12****(2):* *1940-1948.*

104. *Akshay VR, Suneesh MV, Vasundhara M. Tailoring Thermoelectric Properties through Structure and Morphology in Chemically Synthesized n-Type Bismuth Telluride Nanostructures. Inorganic Chemistry 2017,* ***56****(11):* *6264-6274.*

105. *Witting IT, Chasapis TC, Ricci F, Peters M, Heinz NA, Hautier G, et al. The Thermoelectric Properties of Bismuth Telluride. Advanced Electronic Materials 2019,* ***5****(6):* *1800904.*

106. *Wang Y, Liu W-D, Shi X-L, Hong M, Wang L-J, Li M, et al. Enhanced thermoelectric properties of nanostructured n-type Bi2Te3 by suppressing Te vacancy through non-equilibrium fast reaction. Chemical Engineering Journal 2020,* ***391:*** *123513.*

107. *Wiendlocha B. Resonant Levels, Vacancies, and Doping in Bi2Te3, Bi2Te2Se, and Bi2Se3 Tetradymites. Journal of Electronic Materials 2016,* ***45****(7):* *3515-3531.*

108. *Li CH, van 't Erve OMJ, Li YY, Li L, Jonker BT. Electrical Detection of the Helical Spin Texture in a p-type Topological Insulator Sb2Te3. Scientific Reports 2016,* ***6****(1):* *29533.*

109. *Pyykkö P, Atsumi M. Molecular Single-Bond Covalent Radii for Elements 1–118. Chemistry – A European Journal 2009,* ***15****(1):* *186-197.*

110. *Chuang P-Y, Su S-H, Chong C-W, Chen Y-F, Chou Y-H, Huang J-C-A, et al. Anti-site defect effect on the electronic structure of a Bi2Te3 topological insulator. RSC Advances 2018,* ***8****(1):* *423-428.*

111. *Hashibon A, Elsässer C. First-Principles Density Functional Theory Study of Native Point Defects in Bi2Te3. Phys Rev B: Condens Matter Mater Phys 2011,* ***84:*** *144117.*

112. *Scanlon DO, King PDC, Singh RP, de la Torre A, Walker SM, Balakrishnan G, et al. Controlling Bulk Conductivity in Topological Insulators: Key Role of Anti-Site Defects. Advanced Materials 2012,* ***24****(16):* *2154-2158.*

113. *Horák J, Čermák K, Koudelka L. Energy formation of antisite defects in doped Sb2Te3 and Bi2Te3 crystals. Journal of Physics and Chemistry of Solids 1986,* ***47****(8):* *805-809.*

114. *Starý Z, Horák J, Stordeur M, Stölzer M. Antisite defects in Sb2−xBixTe3 mixed crystals. Journal of Physics and Chemistry of Solids 1988,* ***49****(1):* *29-34.*

115. *Termentzidis K, Pokropivny A, Xiong S-Y, Chumakov Y, Cortona P, Volz S. Structural Engineering of Vacancy Defected Bismuth Tellurides for Thermo-electric Applications. EPJ Web of Conferences 2012,* ***33:*** *02012.*

Chapter – 3

1. *Yue C, Jiang S, Zhu H, Chen L, Sun Q, Zhang DW. Device Applications of Synthetic Topological Insulator Nanostructures. Electronics 2018,* ***7****(10):* *225.*

2. *Xiu F-X, Zhao T-T. Topological insulator nanostructures and devices. Chinese Physics B 2013,* ***22****(9):* *096104.*

3. *Liu P, Williams JR, Cha JJ. Topological nanomaterials. Nature Reviews Materials 2019,* ***4****(7):* *479-496.*

4. *Wang A-Q, Ye X-G, Yu D-P, Liao Z-M. Topological Semimetal Nanostructures: From Properties to Topotronics. ACS Nano 2020,* ***14****(4):* *3755-3778.*

5. *Li H, Peng H, Dang W, Yu L, Liu Z. Topological insulator nanostructures: Materials synthesis, Raman spectroscopy, and transport properties. Frontiers of Physics 2012,* ***7****(2):* *208-217.*

6. *Rosenbach D, Oellers N, Jalil AR, Mikulics M, Kölzer J, Zimmermann E, et al. Quantum Transport in Topological Surface States of Selectively Grown Bi2Te3 Nanoribbons. Advanced Electronic Materials 2020,* ***n/a****(n/a):* *2000205.*

7. *Kölzer J, Rosenbach D, Weyrich C, Schmitt TW, Schleenvoigt M, Jalil AR, et al. Phase-coherent loops in selectively-grown topological insulator nanoribbons. Nanotechnology 2020,* ***31****(32):* *325001.*

8. *Bardarson JH, Brouwer PW, Moore JE. Aharonov-Bohm Oscillations in Disordered Topological Insulator Nanowires. Physical Review Letters 2010,* ***105****(15):* *156803.*

9. *Dufouleur J, Veyrat L, Dassonneville B, Xypakis E, Bardarson JH, Nowka C, et al. Weakly-coupled quasi-1D helical modes in disordered 3D topological insulator quantum wires. Scientific Reports 2017,* ***7****(1):* *45276.*

10. *Moors K, Schüffelgen P, Rosenbach D, Schmitt T, Schäpers T, Schmidt TL. Magnetotransport signatures of three-dimensional topological insulator nanostructures. Physical Review B 2018,* ***97****(24):* *245429.*

11. *Kölzer J, Moors K, Jalil AR, Zimmermann E, Rosenbach D, Kibkalo L, et al. In-plane magnetic field-driven symmetry breaking in topological insulator-based three-terminal junctions. arXiv preprint arXiv:201215118 2020.*

12. *Jing Y, Huang S, Wu J, Meng M, Li X, Zhou Y, et al. A Single-Electron Transistor Made of a 3D Topological Insulator Nanoplate. Advanced Materials 2019,* ***31****(42):* *1903686.*

13. *Qi XL, Zhang SC. Topological Insulators and Superconductors. Rev Mod Phys 2011,* ***83:*** *1057.*

14. *Galletti L, Charpentier S, Lucignano P, Massarotti D, Arpaia R, Tafuri F, et al. Josephson effect in Al/Bi2Se3/Al coplanar hybrid devices. Physica C: Superconductivity and its Applications 2014,* ***503:*** *162-165.*

15. *Jäck B, Xie Y, Li J, Jeon S, Bernevig BA, Yazdani A. Observation of a Majorana zero mode in a topologically protected edge channel. Science 2019,* ***364****(6447):* *1255-1259.*

16. *Bernevig BA, Hughes TL. Topological insulators and topological superconductors. Princeton university press, 2013.*

17. *Schüffelgen P, Rosenbach D, Li C, Schmitt TW, Schleenvoigt M, Jalil AR, et al. Selective area growth and stencil lithography for in situ fabricated quantum devices. Nature Nanotechnology 2019,* ***14****(9):* *825-831.*

18. *Awschalom DD, Bassett LC, Dzurak AS, Hu EL, Petta JR. Quantum Spintronics: Engineering and Manipulating Atom-Like Spins in Semiconductors. Science 2013,* ***339****(6124):* *1174-1179.*

19. *Tian J, Childres I, Cao H, Shen T, Miotkowski I, Chen YP. Topological insulator based spin valve devices: Evidence for spin polarized transport of spin-momentum-locked topological surface states. Solid State Communications 2014,* ***191:*** *1-5.*

20. *Wang KL, Lang M, Kou X. Spintronics of Topological Insulators. In: Xu Y, Awschalom DD, Nitta J (eds). Handbook of Spintronics. Springer Netherlands: Dordrecht, 2016, pp 431-462.*

21. *He M, Sun H, He QL. Topological insulator: Spintronics and quantum computations. Frontiers of Physics 2019,* ***14****(4):* *43401.*

22. *Osterhage H, Gooth J, Hamdou B, Gwozdz P, Zierold R, Nielsch K. Thermoelectric properties of topological insulator Bi2Te3, Sb2Te3, and Bi2Se3 thin film quantum wells. Applied Physics Letters 2014,* ***105****(12):* *123117.*

23. *Heremans JP, Cava RJ, Samarth N. Tetradymites as thermoelectrics and topological insulators. Nature Reviews Materials 2017, **2**(10): 17049.*

24. *Xu N, Xu Y, Zhu J. Topological insulators for thermoelectrics. npj Quantum Materials 2017, **2**(1): 51.*

25. *Serrano-Sánchez F, Gharsallah M, Nemes NM, Biskup N, Varela M, Martínez JL, et al. Enhanced figure of merit in nanostructured (Bi,Sb)2Te3 with optimized composition, prepared by a straightforward arc-melting procedure. Scientific Reports 2017, **7**(1): 6277.*

26. *Sarma SD, Freedman M, Nayak C. Majorana zero modes and topological quantum computation. npj Quantum Information 2015, **1**(1): 15001.*

27. *Walter Ogburn R, Preskill J. Topological Quantum Computation. In: Williams CP, editor. Quantum Computing and Quantum Communications; 1999 1999//; Berlin, Heidelberg: Springer Berlin Heidelberg; 1999. p. 341-356.*

28. *Kong D, Cha JJ, Lai K, Peng H, Analytis JG, Meister S, et al. Rapid Surface Oxidation as a Source of Surface Degradation Factor for Bi2Se3. ACS Nano 2011, **5**(6): 4698-4703.*

29. *Green AJ, Dey S, An YQ, O'Brien B, O'Mullane S, Thiel B, et al. Surface oxidation of the topological insulator Bi2Se3. Journal of Vacuum Science & Technology A 2016, **34**(6): 061403.*

30. *Thomas CR, Vallon MK, Frith MG, Sezen H, Kushwaha SK, Cava RJ, et al. Surface Oxidation of Bi2(Te,Se)3 Topological Insulators Depends on Cleavage Accuracy. Chemistry of Materials 2016, **28**(1): 35-39.*

31. *Gehring P, Reusch FB, Mashhadi SS, Burghard M, Kern K. Surface oxidation effect on the electrical behaviour of Bi2Te2Se nanoplatelets. Nanotechnology 2016, **27**(28): 285201.*

32. *Bando H, Koizumi K, Oikawa Y, Daikohara K, Kulbachinskii VA, Ozaki H. The time-dependent process of oxidation of the surface of Bi2Te3studied by x-ray photoelectron spectroscopy. Journal of Physics: Condensed Matter 2000, **12**(26): 5607-5616.*

33. *Lang M, He L, Xiu F, Yu X, Tang J, Wang Y, et al. Revelation of Topological Surface States in Bi2Se3 Thin Films by In Situ Al Passivation. ACS Nano 2012, **6**(1): 295-302.*

34. *Lee JS, Brittman S, Yu D, Park H. Vapor–Liquid–Solid and Vapor–Solid Growth of Phase-Change Sb2Te3 Nanowires and Sb2Te3/GeTe Nanowire Heterostructures. Journal of the American Chemical Society 2008, **130**(19): 6252-6258.*

35. *Kong D, Randel JC, Peng H, Cha JJ, Meister S, Lai K, et al. Topological Insulator Nanowires and Nanoribbons. Nano Letters 2010, **10**(1): 329-333.*

36. *Zhu H, Richter CA, Zhao E, Bonevich JE, Kimes WA, Jang H-J, et al. Topological Insulator Bi2Se3 Nanowire High Performance Field-Effect Transistors. Scientific Reports 2013, **3**(1): 1757.*

37. *Schönherr P, Collins-McIntyre LJ, Zhang S, Kusch P, Reich S, Giles T, et al. Vapour-liquid-solid growth of ternary Bi2Se2Te nanowires. Nanoscale Research Letters 2014, **9**(1): 127.*

38. *Jeon JH, Song M, Kim H, Jang W-J, Park J-Y, Yoon S, et al. Quintuple layer Bi2Se3 thin films directly grown on insulating SiO2 using molecular beam epitaxy. Applied Surface Science 2014, **316**: 42-45.*

39. *Sun L, Lin Z, Peng J, Weng J, Huang Y, Luo Z. Preparation of Few-Layer Bismuth Selenide by Liquid-Phase-Exfoliation and Its Optical Absorption Properties. Scientific Reports 2014, **4**(1): 4794.*

40. *Ambrosi A, Sofer Z, Luxa J, Pumera M. Exfoliation of Layered Topological Insulators Bi2Se3 and Bi2Te3 via Electrochemistry. ACS Nano 2016, **10**(12): 11442-11448.*

41. *Li CH, van 't Erve OMJ, Li YY, Li L, Jonker BT. Electrical Detection of the Helical Spin Texture in a p-type Topological Insulator Sb2Te3. Scientific Reports 2016, **6**(1): 29533.*

42. *Childres I, Tian J, Miotkowski I, Chen Y. AFM and Raman studies of topological insulator materials subject to argon plasma etching. Philosophical Magazine 2013, **93**(6): 681-689.*

43. *Gao L, Li H, Ren W, Wang G, Li H, Zhou Z, et al. Patterning Bi2Se3 single-crystalline thin films on Si(111) substrates using strong oxidizing acids. RSC Advances 2017, **7**(51): 32294-32299.*

44. *Kampmeier J, Weyrich C, Lanius M, Schall M, Neumann E, Mussler G, et al. Selective area growth of Bi2Te3 and Sb2Te3 topological insulator thin films. Journal of Crystal Growth 2016, **443**: 38-42.*

45. *Cho A. Advances in molecular beam epitaxy (MBE). Journal of crystal growth 1991, **111**(1-4): 1-13.*

46. *Stringfellow GB. Organometallic vapor-phase epitaxy: theory and practice. Elsevier, 1999.*

47. *Barbos C, Blanc-Pelissier D, Fave A, Blanquet E, Crisci A, Fourmond E, et al. Characterization of Al2O3 thin films prepared by thermal ALD. Energy Procedia 2015, **77**: 558-564.*

48. *Zhang X-Y, Hsu C-H, Lien S-Y, Wu W-Y, Ou S-L, Chen S-Y, et al. Temperature-Dependent HfO2/Si Interface Structural Evolution and its Mechanism. Nanoscale research letters 2019, **14**(1): 1-8.*

49. *Schüffelgen P, Rosenbach D, Pang Y, Kampmeier J, Luysberg M, Kibkalo L, et al. Signatures of induced superconductivity in AlOx-capped topological heterostructures. Solid-State Electronics 2019, **155**: 111-116.*

50. *Schüffelgen P. Exploiting Topological Insulators for Majorana Devices and Physics Via Molecular Beam Epitaxy: Halbleiter-Nanoelektronik; 2018.*

51. *Lanius M. Topological Insulating Tellurides: How to tune Doping, Topology, and Dimensionality. Universitätsbibliothek der RWTH Aachen, 2018.*

52. *EerNisse EP. Stress in thermal SiO2 during growth. Applied Physics Letters 1979, **35**(1): 8-10.*

53. *Liu L, Liu W-g, Cao N, Cai C-l. Study on The Performance of PECVD Silicon Nitride Thin Films. Defence Technology 2013, **9**(2): 121-126.*

54. *Luhmann N, Jachimowicz A, Schalko J, Sadeghi P, Sauer M, Foelske-Schmitz A, et al. Effect of oxygen plasma on nanomechanical silicon nitride resonators. Applied Physics Letters 2017, **111**(6): 063103.*

55. *Bagolini A, Savoia AS, Picciotto A, Boscardin M, Bellutti P, Lamberti N, et al. PECVD low stress silicon nitride analysis and optimization for the fabrication of CMUT devices. Journal of Micromechanics and Microengineering 2014, **25**(1): 015012.*

56. *Claassen W, Valkenburg W, Wijgert W, Willemsen M. On the relation between deposition conditions and (mechanical) stress in plasma silicon nitride layers. Thin Solid Films 1985, **129**(3-4): 239-247.*

57. *Blaauw C. Preparation and Characterization of Plasma-Deposited Silicon Nitride. Journal of The Electrochemical Society 1984,* ***131****(5):* *1114.*

58. *Wright DN, Marstein ES, Rognmo A, Holt A. Plasma-enhanced chemical vapour-deposited silicon nitride films; The effect of annealing on optical properties and etch rates. Solar energy materials and solar cells 2008,* ***92****(9):* *1091-1098.*

59. *Lapeyrade M, Besland M, Meva'a C, Sibai A, Hollinger G. Silicon nitride thin films deposited by electron cyclotron resonance plasma-enhanced chemical vapor deposition. Journal of Vacuum Science & Technology A: Vacuum, Surfaces, and Films 1999,* ***17****(2):* *433-444.*

60. *Knotter DM, Denteneer TD. Etching mechanism of silicon nitride in HF-based solutions. Journal of The Electrochemical Society 2001,* ***148****(3):* *F43.*

61. *Ritala H, Kiihamäki J, Puukilainen E. Correlation Between Film Properties and Anhydrous HF Vapor Etching Behavior of Silicon Oxide Deposited by CVD Methods. Journal of The Electrochemical Society 2011,* ***158****(6):* *D399.*

62. *Longjuan T, Yinfang Z, Jinling Y, Yan L, Wei Z, Jing X, et al. Dependence of wet etch rate on deposition, annealing conditions and etchants for PECVD silicon nitride film. Journal of Semiconductors 2009,* ***30****(9):* *096005.*

63. *Schmitt T. Low-dimensional Josephson junctions based on molecular beam epitaxy grown topolgical insulator thin films. Master's thesis, RWTH Aachen 2017.*

64. *Bansal N, Koirala N, Brahlek M, Han M-G, Zhu Y, Cao Y, et al. Robust topological surface states of Bi2Se3 thin films on amorphous SiO2/Si substrate and a large ambipolar gating effect. Applied Physics Letters 2014,* ***104****(24):* *241606.*

65. *Jerng S-K, Joo K, Kim Y, Yoon S-M, Lee JH, Kim M, et al. Ordered growth of topological insulator Bi2Se3 thin films on dielectric amorphous SiO2 by MBE. Nanoscale 2013,* ***5****(21):* *10618-10622.*

66. *Borisova S, Krumrain J, Luysberg M, Mussler G, Grützmacher D. Mode of Growth of Ultrathin Topological Insulator Bi2Te3 Films on Si (111) Substrates. Crystal Growth & Design 2012,* ***12****(12):* *6098-6103.*

67. *Lanius M, Kampmeier J, Kölling S, Mussler G, Koenraad PM, Grützmacher D. Topography and structure of ultrathin topological insulator Sb2Te3 films on Si(111) grown by means of molecular beam epitaxy. Journal of Crystal Growth 2016,* ***453:*** *158-162.*

68. *Peng H, Lai K, Kong D, Meister S, Chen Y, Qi XL, et al. Aharonov-Bohm Interference in Topological Insulator Nanoribbons. Nat Mater 2009,* ***9:*** *225.*

69. *Aharonov Y, Bohm D. Significance of electromagnetic potentials in the quantum theory. Physical Review 1959,* ***115****(3):* *485.*

70. *Weyrich CP, Schäpers T. Electrical transport and magnetoresistance in MBE-grown 3D topological insulator thin films and nanostructures: Fachgruppe Physik; 2020.*

71. *Behner G. Towards the detection of Majorana zero-modes using interferometric methods. Master's thesis, RWTH Aachen 2020.*

72. *Weyrich C, Lanius M, Schüffelgen P, Rosenbach D, Mussler G, Bunte S, et al. Phase-coherent transport in selectively grown topological insulator nanodots. Nanotechnology 2018,* ***30****(5):* *055201.*

73. *Weyrich C, Drögeler M, Kampmeier J, Eschbach M, Mussler G, Merzenich T, et al. Growth, characterization, and transport properties of ternary (Bi1− xSbx) 2Te3 topological insulator layers. Journal of Physics: Condensed Matter 2016,* ***28****(49):* *495501.*

74. *Brahlek M, Koirala N, Bansal N, Oh S. Transport properties of topological insulators: Band bending, bulk metal-to-insulator transition, and weak anti-localization. Solid State Communications 2015,* ***215-216:*** *54-62.*

75. *Rischau CW, Ubaldini A, Giannini E, Beek CJvd. Charge puddles in a completely compensated topological insulator. New Journal of Physics 2016,* ***18****(7):* *073024.*

Chapter – 4

1. *Aguilera I. Private communications in Research Center Juelich 2020.*

2. *Yang B-J, Nagaosa N. Classification of stable three-dimensional Dirac semimetals with nontrivial topology. Nature Communications 2014,* ***5****(1):* *4898.*

3. *Eschbach M, Lanius M, Niu C, Młyńczak E, Gospodarič P, Kellner J, et al. Bi1Te1 is a dual topological insulator. Nature Communications 2017,* ***8****(1):* *14976.*

4. *Rauch T, Flieger M, Henk J, Mertig I, Ernst A. Dual Topological Character of Chalcogenides: Theory for Bi2Te3. Physical Review Letters 2014,* ***112****(1):* *016802.*

5. *Schindler F, Cook AM, Vergniory MG, Wang Z, Parkin SSP, Bernevig BA, et al. Higher-order topological insulators. Science Advances 2018,* ***4****(6):* *eaat0346.*

6. *Schindler F, Wang Z, Vergniory MG, Cook AM, Murani A, Sengupta S, et al. Higher-order topology in bismuth. Nature Physics 2018,* ***14****(9):* *918-924.*

7. *Saito Y, Fons P, Makino K, Mitrofanov KV, Uesugi F, Takeguchi M, et al. Compositional tuning in sputter-grown highly-oriented Bi–Te films and their optical and electronic structures. Nanoscale 2017,* ***9****(39):* *15115-15121.*

8. *Drozdov IK, Alexandradinata A, Jeon S, Nadj-Perge S, Ji H, Cava RJ, et al. One-dimensional topological edge states of bismuth bilayers. Nature Physics 2014,* ***10****(9):* *664-669.*

9. *Nayak AK, Reiner J, Queiroz R, Fu H, Shekhar C, Yan B, et al. Resolving the topological classification of bismuth with topological defects. Science Advances 2019,* ***5****(11):* *eaax6996.*

10. *Witting IT, Chasapis TC, Ricci F, Peters M, Heinz NA, Hautier G, et al. The Thermoelectric Properties of Bismuth Telluride. Advanced Electronic Materials 2019,* ***5****(6):* *1800904.*

11. *Bos JWG, Faucheux F, Downie RA, Marcinkova A. Phase stability, structures and properties of the (Bi2)m (Bi2Te3)n natural superlattices. Journal of Solid State Chemistry 2012,* ***193:*** *13-18.*

12. *Bos JWG, Zandbergen HW, Lee MH, Ong NP, Cava RJ. Structures and thermoelectric properties of the infinitely adaptive series (Bi2)m(Bi2Te3)n. Physical Review B 2007,* ***75****(19):* *195203.*

13. *Le PH, Liao C-N, Luo CW, Leu J. Thermoelectric properties of nanostructured bismuth–telluride thin films grown using pulsed laser deposition. Journal of Alloys and Compounds 2014,* ***615:*** *546-552.*

14. *Fang Y, Cano J. Higher-order topological insulators in antiperovskites. Physical Review B 2020,* ***101****(24):* *245110.*

15. *Sessi P, Di Sante D, Szczerbakow A, Glott F, Wilfert S, Schmidt H, et al. Robust spin-polarized midgap states at step edges of topological crystalline insulators. Science 2016,* ***354****(6317):* *1269.*

16. *Canvel Y, Lagrasta S, Boixaderas C, Barnola S, Mazel Y, Dabertrand K, et al. Modification of Ge-rich GeSbTe surface during the patterning process of phase-change memories. Microelectronic Engineering 2020,* ***221:*** *111183.*

17. *Di Biagio F, Cecchi S, Arciprete F, Calarco R. Crystallization Study of Ge-Rich (GeTe)m(Sb2Te3)n Using Two-Step Annealing Process. physica status solidi (RRL) – Rapid Research Letters 2019,* ***13****(4):* *1800632.*

18. *Golovchak R, Choi YG, Kozyukhin S, Chigirinsky Y, Kovalskiy A, Xiong-Skiba P, et al. Oxygen incorporation into GST phase-change memory matrix. Applied Surface Science 2015,* ***332:*** *533-541.*

19. *Huang W-H, Gao T-L, Huang C-W, Chang C-F, Wu W-W, Tuan H-Y. Synthesis of single-crystalline Ge1Sb2Te4 nanoplates in solution phase. CrystEngComm 2016,* ***18****(13):* *2244-2246.*

20. *Lazzarini L, Rotunno E, Grillo V, Longo M. Determination of the atomic stacking sequence of Ge-Sb-Te nanowires by HAADF STEM. MRS Proceedings 2013,* ***1512:*** *mrsf12-1512-ff1510-1506.*

21. *Sa B, Zhou J, Sun Z, Ahuja R. Strain-induced topological insulating behavior in ternary chalcogenide Ge 2 Sb 2 Te 5. EPL (Europhysics Letters) 2012,* ***97****(2):* *27003.*

22. *Sangeetha BG, Joseph CM, Suresh K. Preparation and characterization of Ge1Sb2Te4 thin films for phase change memory applications. Microelectronic Engineering 2014,* ***127:*** *77-80.*

23. *Deng Y, Yu Y, Shi MZ, Guo Z, Xu Z, Wang J, et al. Quantum anomalous Hall effect in intrinsic magnetic topological insulator MnBi₂Te₄. Science 2020,* ***367****(6480):* *895-900.*

24. *Li J, Li Y, Du S, Wang Z, Gu B-L, Zhang S-C, et al. Intrinsic magnetic topological insulators in van der Waals layered MnBi₂Te₄-family materials. Science Advances 2019,* ***5****(6):* *eaaw5685.*

25. *(Bi2)m(Bi2Te3)n, m= 2, n= 1 (Bi2Te) Crystal Structure: Datasheet from "PAULING FILE Multinaries Edition – 2012" in SpringerMaterials (https://materials.springer.com/isp/crystallographic/docs/sd_1934381). Springer-Verlag Berlin Heidelberg & Material Phases Data System (MPDS), Switzerland & National Institute for Materials Science (NIMS), Japan.*

26. *Bi45Te55 (Bi6Te7) Crystal Structure: Datasheet from "PAULING FILE Multinaries Edition – 2012" in SpringerMaterials (https://materials.springer.com/isp/crystallographic/docs/sd_0531044). Springer-Verlag Berlin Heidelberg & Material Phases Data System (MPDS), Switzerland & National Institute for Materials Science (NIMS), Japan.*

27. *Bi2Te2 (BiTe) Crystal Structure: Datasheet from "PAULING FILE Multinaries Edition – 2012" in SpringerMaterials (https://materials.springer.com/isp/crystallographic/docs/sd_1006412). Springer-Verlag Berlin Heidelberg & Material Phases Data System (MPDS), Switzerland & National Institute for Materials Science (NIMS), Japan.*

28. *Bi49Te51 (BiTe) Crystal Structure: Datasheet from "PAULING FILE Multinaries Edition – 2012" in SpringerMaterials (https://materials.springer.com/isp/crystallographic/docs/sd_0531042). Springer-Verlag Berlin Heidelberg & Material Phases Data System (MPDS), Switzerland & National Institute for Materials Science (NIMS), Japan.*

29. *Bi43Te57 (Bi4Te5) Crystal Structure: Datasheet from "PAULING FILE Multinaries Edition – 2012" in SpringerMaterials (https://materials.springer.com/isp/crystallographic/docs/sd_0531043). Springer-Verlag Berlin Heidelberg & Material Phases Data System (MPDS), Switzerland & National Institute for Materials Science (NIMS), Japan.*

30. *Li Y-Y, Wang G, Zhu X-G, Liu M-H, Ye C, Chen X, et al. Intrinsic Topological Insulator Bi2Te3 Thin Films on Si and Their Thickness Limit. Advanced Materials 2010, **22**(36): 4002-4007.*

31. *Steiner H, Volobuev V, Caha O, Bauer G, Springholz G, Holy V. Structure and composition of bismuth telluride topological insulators grown by molecular beam epitaxy. Journal of Applied Crystallography 2014, **47**(6): 1889-1900.*

32. *Mansour AN, Wong-Ng W, Huang Q, Tang W, Thompson A, Sharp J. Structural characterization of Bi2Te3 and Sb2Te3 as a function of temperature using neutron powder diffraction and extended X-ray absorption fine structure techniques. J Appl Phys 2014, **116:** 083513.*

33. *Fornari CI, Rappl PHO, Morelhão SL, Abramof E. Structural properties of Bi2Te3 topological insulator thin films grown by molecular beam epitaxy on (111) BaF2 substrates. Journal of Applied Physics 2016, **119**(16): 165303.*

34. *Bayliss P. Crystal chemistry and crystallography of some minerals in the tetradymite group. American Mineralogist 1991, **76**(1-2): 257-265.*

35. *Medlin DL, Erickson KJ, Limmer SJ, Yelton WG, Siegal MP. Dissociated $$ \frac{1}{3}\langle 0\bar{1}11\rangle $$13 ⟨01¯11⟩ dislocations in Bi2Te3 and their relationship to seven-layer Bi3Te4 defects. Journal of Materials Science 2014, **49**(11): 3970-3979.*

36. *Bi4Te5 Crystal Structure: Datasheet from "PAULING FILE Multinaries Edition – 2012" in SpringerMaterials (https://materials.springer.com/isp/crystallographic/docs/sd_1006415). Springer-Verlag Berlin Heidelberg & Material Phases Data System (MPDS), Switzerland & National Institute for Materials Science (NIMS), Japan.*

37. *Massalski T, Subramanian P. Hf (Hafnium) Binary Alloy Phase Diagrams. ASM international Cleveland, 1990.*

38. *Hamdou B, Kimling J, Dorn A, Pippel E, Rostek R, Woias P, et al. Thermoelectric Characterization of Bismuth Telluride Nanowires, Synthesized Via Catalytic Growth and Post-Annealing. Advanced Materials 2013, **25**(2): 239-244.*

39. *Anandan P, Omprakash M, Azhagurajan M, Arivanandhan M, Rajan Babu D, Koyama T, et al. Tailoring bismuth telluride nanostructures using a scalable sintering process and their thermoelectric properties. CrystEngComm 2014, **16**(34): 7956-7962.*

40. *Bragg WH, Bragg WL. The reflection of X-rays by crystals. Proceedings of the Royal Society of London Series A, Containing Papers of a Mathematical and Physical Character 1913,* ***88****(605):* *428-438.*

41. *Bi8Te9 Crystal Structure: Datasheet from "PAULING FILE Multinaries Edition – 2012" in SpringerMaterials (https://materials.springer.com/isp/crystallographic/docs/sd_1300266). Springer-Verlag Berlin Heidelberg & Material Phases Data System (MPDS), Switzerland & National Institute for Materials Science (NIMS), Japan.*

42. *Feutelais Y, Legendre B, Rodier N, Agafonov V. A study of the phases in the bismuth - tellurium system. Materials Research Bulletin 1993,* ***28****(6):* *591-596.*

43. *Sejkora J, Litochleb J, Plasil J, Bures B. Tsumoite and associated tellurides from the Au deposit Libcice near Novy Knin, Czech Republic: mineralogy and genetic significance. Journal of Geosciences 2009,* ***54****(1):* *73-82.*

44. *Cook NJ, Ciobanu CL, Wagner T, Stanley CJ. Minerals of the system Bi–Te–Se–S related to the tetradymite archetype: review of classification and compositional variation. The Canadian Mineralogist 2007,* ***45****(4):* *665-708.*

45. *Kifune K, Kubota Y, Matsunaga T, Yamada N. Extremely long period-stacking structure in the Sb-Te binary system. Acta Crystallographica Section B 2005,* ***61****(5):* *492-497.*

46. *BiTe Crystal Structure: Datasheet from "PAULING FILE Multinaries Edition – 2012" in SpringerMaterials (https://materials.springer.com/isp/crystallographic/docs/sd_0531055). Springer-Verlag Berlin Heidelberg & Material Phases Data System (MPDS), Switzerland & National Institute for Materials Science (NIMS), Japan.*

47. *Yamana K, Kihara K, Matsumoto T. Bismuth tellurides: BiTe and Bi4Te3. Acta Crystallographica Section B 1979,* ***35****(1):* *147-149.*

48. *Kuznetsov PI, Yapaskurt VO, Shchamkhalova BS, Shcherbakov VD, Yakushcheva GG, Luzanov VA, et al. Growth of Bi2Te3 films and other phases of Bi-Te system by MOVPE. Journal of Crystal Growth 2016,* ***455:*** *122-128.*

49. *Concepción O, Galván-Arellano M, Torres-Costa V, Climent-Font A, Bahena D, Manso Silván M, et al. Controlling the Epitaxial Growth of Bi2Te3, BiTe, and Bi4Te3 Pure Phases by Physical Vapor Transport. Inorganic Chemistry 2018,* ***57****(16):* *10090-10099.*

50. *Kim Y, Cho S, DiVenere A, Wong GKL, Ketterson JB. Composition-dependent layered structure and transport properties in BiTe thin films. Physical Review B 2001,* ***63****(15):* *155306.*

51. *Hulliger F, Lévy F, L¿ FA, Lévy F. Structural Chemistry of Layer-Type Phases. Springer, 1976.*

52. *Sharma ALL, Spataru DC, Medlin DL, Sharma PA, Morales AM. Extreme Solid State Refrigeration using Nanostructured Bi-Te alloys. 2009; 2009.*

53. *Bi8Te7 Crystal Structure: Datasheet from "PAULING FILE Multinaries Edition – 2012" in SpringerMaterials (https://materials.springer.com/isp/crystallographic/docs/sd_1006417). Springer-Verlag Berlin Heidelberg & Material Phases Data System (MPDS), Switzerland & National Institute for Materials Science (NIMS), Japan.*

54. *Sugihara S, Kawashima S, Yonekura I, Suzuki H, Sekine R. Doping effects on the electronic structures of Bi/sub 2/Te/sub 3/ and thermoelectric property. XVI ICT '97. Proceedings ICT'97. 16th International Conference on Thermoelectrics (Cat. No.97TH8291); 1997 26-29 Aug. 1997; 1997. p. 63-67.*

55. *Gaspard J-P. Structure of covalently bonded materials: From the Peierls distortion to Phase-Change Materials. Comptes Rendus Physique 2016, **17**(3): 389-405.*

56. *Villars P, Cenzual K, Gladyshevskii R. Handbook. De Gruyter, 2013.*

57. *Lee J, Wagstaff S, Lambotte G, Allanore A, Tesfaye F. Materials Processing Fundamentals 2020. Springer International Publishing, 2020.*

58. *Weber A. Gasphasen- und lösungsbasierte Synthese von thermoelektrischen Materialien. 2014.*

59. *Imamov R, Semiletov S. Crystal Structure of the Phases in the Systems Bi-Se, Bi-Te and Sb-Te. Sov Phys Crystallogr 1971, **15**(5): 845-850.*

60. *Loa I, Bos JWG, Downie RA, Syassen K. Atomic ordering in cubic bismuth telluride alloy phases at high pressure. Physical Review B 2016, **93**(22): 224109.*

61. *Bi4Te3 Crystal Structure: Datasheet from "PAULING FILE Multinaries Edition – 2012" in SpringerMaterials (https://materials.springer.com/isp/crystallographic/docs/sd_1006413). Springer-Verlag Berlin Heidelberg & Material Phases Data System (MPDS), Switzerland & National Institute for Materials Science (NIMS), Japan.*

62. *Wang G, Lok SK, Wong GKL, Sou IK. Molecular beam epitaxy-grown Bi4Te3 nanowires. Applied Physics Letters 2009, **95**(26): 263102.*

63. *Wu J, Jian J, Wang S, Guo S, Lei R, Liu H. Preparation of Bi4Te3 highly oriented nanopillars array film with enhanced electrical properties. Powder Diffraction 2018, **33**(2): 115-120.*

64. *Fülöp A, Song Y, Charpentier S, Shi P, Ekström M, Galletti L, et al. Phase transition of bismuth telluride thin films grown by MBE. Applied Physics Express 2014, **7**(4): 045503.*

65. *Jeffries JR, Lima Sharma AL, Sharma PA, Spataru CD, McCall SK, Sugar JD, et al. Distinct superconducting states in the pressure-induced metallic structures of the nominal semimetal Bi${}_{4}$Te${}_{3}$. Physical Review B 2011, **84**(9): 092505.*

66. *Akshay VR, Suneesh MV, Vasundhara M. Tailoring Thermoelectric Properties through Structure and Morphology in Chemically Synthesized n-Type Bismuth Telluride Nanostructures. Inorganic Chemistry 2017, **56**(11): 6264-6274.*

67. *Baker H. Alloy Phase Diagrams, vol. 3, 1992.*

68. *Park K, Xiao F, Yoo BY, Rheem Y, Myung NV. Electrochemical deposition of thermoelectric SbxTey thin films and nanowires. Journal of Alloys and Compounds 2009, **485**(1): 362-366.*

69. *Lippert W, Banse H, Bohne-Neuber A, Golder H, Hantke G, Kirschstein G, et al. Wismut: System-Nummer. Springer Berlin Heidelberg, 2019.*

70. *Brankovic S. Electrodeposition for Energy Applications. Electrochemical Society, 2008.*

71. *Macia E. Thermoelectric Materials: Advances and Applications. Jenny Stanford Publishing, 2015.*

72. *Gardner W, Cooke EI, Cooke RWI. Handbook of Chemical Synonyms and Trade Names. CRC Press, 2019.*

73. *Deb M, Sarkar SC. Minerals and Allied Natural Resources and their Sustainable Development: Principles, Perspectives with Emphasis on the Indian Scenario. Springer Singapore, 2017.*

74. *Amstutz GC, Goresy AE, Frenzel G, Kluth C, Moh G, Wauschkuhn A, et al. Ore Genesis: The State of the Art. Springer Berlin Heidelberg, 2012.*

75. *Ramdohr P. The Ore Minerals and Their Intergrowths. Elsevier Science, 2013.*

76. *Tomashyk V, Feychuk P, Shcherbak L. Ternary Alloys Based on II-VI Semiconductor Compounds. CRC Press, 2013.*

77. *Stillwell RL, Jenei Z, Weir ST, Vohra YK, Jeffries JR. Superconducting $\mathrm{B}{\mathrm{i}}_{2}\mathrm{Te}$: Pressure-induced universality in the ${({\mathrm{B}{\mathrm{i}}_{2}})}_{m}{({\mathrm{B}{\mathrm{i}}_{2}\mathrm{T}{\mathrm{e}}_{3}})}_{n}$ series. Physical Review B 2016,* ***93****(9):* *094511.*

78. *Bi2Te3 Crystal Structure: Datasheet from "PAULING FILE Multinaries Edition – 2012" in SpringerMaterials (https://materials.springer.com/isp/crystallographic/docs/sd_0309161). Springer-Verlag Berlin Heidelberg & Material Phases Data System (MPDS), Switzerland & National Institute for Materials Science (NIMS), Japan.*

79. *Wuttig M, Deringer VL, Gonze X, Bichara C, Raty J-Y. Incipient Metals: Functional Materials with a Unique Bonding Mechanism. Advanced Materials 2018,* ***30****(51):* *1803777.*

80. *Zhu M, Cojocaru-Mirédin O, Mio AM, Keutgen J, Küpers M, Yu Y, et al. Unique Bond Breaking in Crystalline Phase Change Materials and the Quest for Metavalent Bonding. Advanced Materials 2018,* ***30****(18):* *1706735.*

81. *Raty J-Y, Wuttig M. The interplay between Peierls distortions and metavalent bonding in IV–VI compounds: comparing GeTe with related monochalcogenides. Journal of Physics D: Applied Physics 2020,* ***53****(23):* *234002.*

82. *Cheng Y, Wahl S, Wuttig M. Metavalent Bonding in Solids: Characteristic Representatives, Their Properties, and Design Options. physica status solidi (RRL) – Rapid Research Letters 2021,* ***15****(3):* *2000482.*

83. *Wuttig M, Yamada N. Phase-change materials for rewriteable data storage. Nature materials 2007,* ***6 11:*** *824-832.*

84. *Zhang W, Thiess A, Zalden P, Zeller R, Dederichs PH, Raty JY, et al. Role of vacancies in metal–insulator transitions of crystalline phase-change materials. Nature Materials 2012,* ***11****(11):* *952-956.*

85. *Rodrigues-Junior G, Marçal LAB, Ribeiro GAS, Rappl PHdO, Abramof E, Sciammarella PV, et al. Direct observation of large strain through van der Waals gaps on epitaxial $\mathrm{B}{\mathrm{i}}_{2}\mathrm{T}{\mathrm{e}}_{3}$/graphite: Pseudomorphic relaxation and the role of $\mathrm{B}{\mathrm{i}}_{2}$ layers on the*

*$\mathrm{B}{\mathrm{i}}_{x}\mathrm{T}{\mathrm{e}}_{y}$ topological insulator series. Physical Review Materials 2020, **4**(2): 023602.*

86. *Rosenbach D, Oellers N, Jalil AR, Mikulics M, Kölzer J, Zimmermann E, et al. Quantum transport in topological surface states of Bi $ _2 $ Te $ _3 $ nanoribbons. arXiv preprint arXiv:200109028 2020.*

87. *Bhilmayer G. Private communications in Research Center Juelich (PGI-1). 2020.*

88. *Kölzer J, Rosenbach D, Weyrich C, Schmitt TW, Schleenvoigt M, Jalil AR, et al. Phase-coherent loops in selectively-grown topological insulator nanoribbons. Nanotechnology 2020, **31**(32): 325001.*

89. *Rosenbach D, Oellers N, Jalil AR, Mikulics M, Kölzer J, Zimmermann E, et al. Quantum Transport in Topological Surface States of Selectively Grown Bi2Te3 Nanoribbons. Advanced Electronic Materials 2020, **n/a**(n/a): 2000205.*

90. *Breunig O, Wang Z, Taskin AA, Lux J, Rosch A, Ando Y. Gigantic negative magnetoresistance in the bulk of a disordered topological insulator. Nature Communications 2017, **8**(1): 15545.*

91. *Andrei N, Furuya K, Lowenstein J. Solution of the Kondo problem. Reviews of modern physics 1983, **55**(2): 331.*

92. *Hanaki Y, Ando Y, Ono S, Takeya J. Zn-doping effect on the magnetotransport properties of Bi 2 Sr 2− x La x CuO 6+ δ single crystals. Physical Review B 2001, **64**(17): 172514.*

93. *Ramirez A. Colossal magnetoresistance. Journal of Physics: Condensed Matter 1997, **9**(39): 8171.*

94. *Burkov A. Chiral anomaly and diffusive magnetotransport in Weyl metals. Physical review letters 2014, **113**(24): 247203.*

95. *Li H, He H, Lu H-Z, Zhang H, Liu H, Ma R, et al. Negative magnetoresistance in Dirac semimetal Cd3As2. Nature Communications 2016, **7**(1): 10301.*

96. *Son D, Spivak B. Chiral anomaly and classical negative magnetoresistance of Weyl metals. Physical Review B 2013, **88**(10): 104412.*

97. *Aji V. Adler-Bell-Jackiw anomaly in Weyl semimetals: Application to pyrochlore iridates. Physical Review B 2012, **85**(24): 241101.*

98. *Zhang H, Li H, Wang H, Cheng G, He H, Wang J. Linear positive and negative magnetoresistance in topological insulator Bi2Se3 flakes. Applied Physics Letters 2018, **113**(11): 113503.*

99. *Galanakis D, Stanescu TD. Electrostatic effects and band bending in doped topological insulators. Physical Review B 2012, **86**(19): 195311.*

100. *Mahatha SK, Menon KSR. Inhomogeneous band bending on MoS2(0001) arising from surface steps and dislocations. Journal of Physics: Condensed Matter 2012, **24**(30): 305502.*

101. *Singh R, Gangwar VK, Daga DD, Singh A, Ghosh AK, Kumar M, et al. Unusual negative magnetoresistance in Bi2Se3–ySy topological insulator under perpendicular magnetic field. Applied Physics Letters 2018, **112**(10): 102401.*

102. *Yadav R, Bhattacharyya B, Pandey A, Kaur M, Aloysius RP, Gupta A, et al. Accessing topological surface states and negative MR in sculpted nanowires of Bi2Te3 at ultra-low temperature. Journal of Physics: Condensed Matter 2020,* ***33****(8):* *085301.*

103. *Skinner B, Chen T, Shklovskii B. Why is the bulk resistivity of topological insulators so small? Physical review letters 2012,* ***109****(17):* *176801.*

104. *Skinner B, Chen T, Shklovskii B. Effects of bulk charged impurities on the bulk and surface transport in three-dimensional topological insulators. Journal of Experimental and Theoretical Physics 2013,* ***117****(3):* *579-592.*

105. *Behner G. Towards the detection of Majorana zero-modes using interferometric methods. Master's thesis, RWTH Aachen 2020.*

Chapter – 5

1. *Lippert W, Banse H, Bohne-Neuber A, Golder H, Hantke G, Kirschstein G, et al. Wismut: System-Nummer. Springer Berlin Heidelberg, 2019.*

2. *Yamana K, Kihara K, Matsumoto T. Bismuth tellurides: BiTe and Bi4Te3. Acta Crystallographica Section B 1979,* ***35****(1):* *147-149.*

3. *Schindler F, Wang Z, Vergniory MG, Cook AM, Murani A, Sengupta S, et al. Higher-order topology in bismuth. Nature Physics 2018,* ***14****(9):* *918-924.*

4. *Bismuth: Inorganic Chemistry. Encyclopedia of Inorganic and Bioinorganic Chemistry, pp 1-32.*

5. *Ilzycer D, Sinvani M, Dukhan R, Weingarten R, Shiloh M. Controlled segregation of dopant in Bridgman-grown n-type thermoelectric alloys. Journal of crystal growth 1988,* ***87****(1):* *107-112.*

6. *Weber A. Gasphasen- und lösungsbasierte Synthese von thermoelektrischen Materialien. 2014.*

7. *Collins-McIntyre LJ, Wang W, Zhou B, Speller SC, Chen YL, Hesjedal T. Growth of BiSe and BiTe on amorphous fused silica by MBE. physica status solidi (b) 2015,* ***252****(6):* *1334-1338.*

8. *Bos JWG, Faucheux F, Downie RA, Marcinkova A. Phase stability, structures and properties of the (Bi2)m (Bi2Te3)n natural superlattices. Journal of Solid State Chemistry 2012,* ***193:*** *13-18.*

9. *Macia E. Thermoelectric Materials: Advances and Applications. Jenny Stanford Publishing, 2015.*

10. *Witting IT, Chasapis TC, Ricci F, Peters M, Heinz NA, Hautier G, et al. The Thermoelectric Properties of Bismuth Telluride. Advanced Electronic Materials 2019,* ***5****(6):* *1800904.*

11. *Di Biagio F, Cecchi S, Arciprete F, Calarco R. Crystallization Study of Ge-Rich (GeTe)m(Sb2Te3)n Using Two-Step Annealing Process. physica status solidi (RRL) – Rapid Research Letters 2019,* ***13****(4):* *1800632.*

12. *Nonaka T, Ohbayashi G, Toriumi Y, Mori Y, Hashimoto H. Crystal structure of GeTe and Ge2Sb2Te5 meta-stable phase. Thin Solid Films 2000,* ***370****(1):* *258-261.*

13. *King MR, Wagner BP, Jones EB, El-Hinnawy N, Borodulin P, McLaughlin SR, et al. Development of cap-free sputtered GeTe films for inline phase change switch based RF circuits. Journal of Vacuum Science & Technology B 2014,* ***32****(4):* *041204.*

14. *Cao T, Cen M. Fundamentals and Applications of Chalcogenide Phase-Change Material Photonics. Advanced Theory and Simulations 2019,* ***2****(8):* *1900094.*

15. *Boschker JE, Wang R, Calarco R. GeTe: a simple compound blessed with a plethora of properties. CrystEngComm 2017,* ***19****(36):* *5324-5335.*

16. *Kellner J, Bihlmayer G, Liebmann M, Otto S, Pauly C, Boschker JE, et al. Mapping the band structure of GeSbTe phase change alloys around the Fermi level. Communications Physics 2018,* ***1****(1):* *5.*

17. *Bruns G, Merkelbach P, Schlockermann C, Salinga M, Wuttig M, Happ TD, et al. Nanosecond switching in GeTe phase change memory cells. Applied Physics Letters 2009,* ***95****(4):* *043108.*

18. *Nakamura H, Rungger I, Sanvito S, Inoue N, Tominaga J, Asai Y. Resistive switching mechanism of GeTe–Sb2Te3 interfacial phase change memory and topological properties of embedded two-dimensional states. Nanoscale 2017,* ***9****(27):* *9386-9395.*

19. *Gaspard J-P. Structure of covalently bonded materials: From the Peierls distortion to Phase-Change Materials. Comptes Rendus Physique 2016,* ***17****(3):* *389-405.*

20. *Momand J, Boschker JE, Wang R, Calarco R, Kooi BJ. Tailoring the epitaxy of Sb2Te3 and GeTe thin films using surface passivation. CrystEngComm 2018,* ***20****(3):* *340-347.*

21. *Lefkowitz I, Shields M, Dolling G. Crystal growth and neutron studies of large single crystals of the alloy series SnTe-GeTe. Journal of Crystal Growth 1970,* ***6****(2):* *143-146.*

22. *Tran NT, Chang YC, Faragalli DA, Roberts SS, Josefowicz JY, Shing YH. GeTe thin films: Amorphous and crystalline characteristics. Journal of Vacuum Science & Technology A 1983,* ***1****(2):* *345-347.*

23. *Yang B-J, Nagaosa N. Classification of stable three-dimensional Dirac semimetals with nontrivial topology. Nature Communications 2014,* ***5****(1):* *4898.*

24. *Murakami S, Hirayama M, Okugawa R, Miyake T. Emergence of topological semimetals in gap closing in semiconductors without inversion symmetry. Science Advances 2017,* ***3****(5):* *e1602680.*

25. *Schindler F, Cook AM, Vergniory MG, Wang Z, Parkin SSP, Bernevig BA, et al. Higher-order topological insulators. Science Advances 2018,* ***4****(6):* *eaat0346.*

26. *Lotnyk A, Behrens M, Rauschenbach B. Phase change thin films for non-volatile memory applications. Nanoscale Advances 2019,* ***1****(10):* *3836-3857.*

27. *Huang S-m, Sun Z, Jin C-x, Huang S-y, Chen Y-w. Phase changes in Ge1Sb2Te4 films induced by single femtosecond laser pulse irradiation. Transactions of Nonferrous Metals Society of China 2006,* ***16:*** *s226-s231.*

28. *Wuttig M, Yamada N. Phase-change materials for rewriteable data storage. Nature materials 2007,* ***6 11:*** *824-832.*

29. *Schmitz PC, Mazzarello R. Topological phases in interfacial phase change materials. 2015.*

30. *Burr GW, Brightsky MJ, Sebastian A, Cheng H, Wu J, Kim S, et al. Recent Progress in Phase-Change Memory Technology. IEEE Journal on Emerging and Selected Topics in Circuits and Systems 2016, **6**(2): 146-162.*

31. *Matsunaga T, Yamada N. Crystallographic Studies on High-Speed Phase-Change Materials Used for Rewritable Optical Recording Disks. Japanese Journal of Applied Physics 2004, **43**(7B): 4704-4712.*

32. *Ronneberger I, Zanolli Z, Wuttig M, Mazzarello R. Changes of Structure and Bonding with Thickness in Chalcogenide Thin Films. Advanced Materials, **n/a**(n/a): 2001033.*

33. *GeTe Crystal Structure: Datasheet from "PAULING FILE Multinaries Edition – 2012" in SpringerMaterials (https://materials.springer.com/isp/crystallographic/docs/sd_0547914). Springer-Verlag Berlin Heidelberg & Material Phases Data System (MPDS), Switzerland & National Institute for Materials Science (NIMS), Japan.*

34. *GeSb2Te4 Crystal Structure: Datasheet from "PAULING FILE Multinaries Edition – 2012" in SpringerMaterials (https://materials.springer.com/isp/crystallographic/docs/sd_1407163). Springer-Verlag Berlin Heidelberg & Material Phases Data System (MPDS), Switzerland & National Institute for Materials Science (NIMS), Japan.*

35. *Karpinsky OG, Shelimova LE, Kretova MA, Fleurial JP. An X-ray study of the mixed-layered compounds of (GeTe)n (Sb2Te3)m homologous series. Journal of Alloys and Compounds 1998, **268**(1): 112-117.*

36. *Nurmamat M, Okamoto K, Zhu S, Menshchikova TV, Rusinov IP, Korostelev VO, et al. Topologically Nontrivial Phase-Change Compound GeSb2Te4. ACS Nano 2020.*

37. *Bayliss P. Crystal chemistry and crystallography of some minerals in the tetradymite group. American Mineralogist 1991, **76**(1-2): 257-265.*

38. *Medlin DL, Erickson KJ, Limmer SJ, Yelton WG, Siegal MP. Dissociated $$ \frac{1}{3}\langle 0\bar{1}11\rangle $$13 ⟨01¯11⟩ dislocations in Bi2Te3 and their relationship to seven-layer Bi3Te4 defects. Journal of Materials Science 2014, **49**(11): 3970-3979.*

39. *Shelimova LE, Karpinskii OG, Kretova MA, Kosyakov VI, Shestakov VA, Zemskov VS, et al. Homologous series of layered tetradymite-like compounds in the Sb-Te and GeTe-Sb2Te3 systems. Inorganic Materials 2000, **36**(8): 768-775.*

40. *Matsunaga T, Yamada N. Structural investigation of ${\mathrm{GeSb}}_{2}{\mathrm{Te}}_{4}:$ A high-speed phase-change material. Physical Review B 2004, **69**(10): 104111.*

41. *Huang W-H, Gao T-L, Huang C-W, Chang C-F, Wu W-W, Tuan H-Y. Synthesis of single-crystalline Ge1Sb2Te4 nanoplates in solution phase. CrystEngComm 2016, **18**(13): 2244-2246.*

42. *Lazzarini L, Rotunno E, Grillo V, Longo M. Determination of the atomic stacking sequence of Ge-Sb-Te nanowires by HAADF STEM. MRS Proceedings 2013, **1512:** mrsf12-1512-ff1510-1506.*

43. *Longo M, Fallica R, Wiemer C, Salicio O, Fanciulli M, Rotunno E, et al. Metal Organic Chemical Vapor Deposition of Phase Change Ge1Sb2Te4 Nanowires. Nano Letters 2012, **12**(3): 1509-1515.*

44. *Hardtdegen H, Rieß S, Schuck M, Keller K, Jost P, Du H, et al. A model structure for interfacial phase change memories: Epitaxial trigonal Ge1Sb2Te4. Journal of Alloys and Compounds 2016,* ***679:*** *285-292.*

45. *Ratajczak A, von der Ahe M, Du H, Mussler G, Grützmacher D. Metal organic vapor phase epitaxy of $$\hbox {Ge}_{1}\hbox {Sb}_{2}\hbox {Te}_{4}$$Ge1Sb2Te4 thin films on Si(111) substrate. Applied Physics A 2019,* ***125****(3):* *163.*

46. *Xu L, Tong L, Geng L, Yang F, Xu J, Su W, et al. A comparative study on electrical transport properties of thin films of Ge1Sb2Te4 and Ge2Sb2Te5 phase-change materials. Journal of Applied Physics 2011,* ***110****(1):* *013703.*

47. *Volker H, Jost P, Wuttig M. Low-Temperature Transport in Crystalline Ge1Sb2Te4. Advanced Functional Materials 2015,* ***25****(40):* *6390-6398.*

48. *Wełnic W, Wuttig M. Reversible switching in phase-change materials. Materials Today 2008,* ***11****(6):* *20-27.*

49. *Sangeetha BG, Joseph CM, Suresh K. Preparation and characterization of Ge1Sb2Te4 thin films for phase change memory applications. Microelectronic Engineering 2014,* ***127:*** *77-80.*

50. *Bragaglia V, Jenichen B, Giussani A, Perumal K, Riechert H, Calarco R. Structural change upon annealing of amorphous GeSbTe grown on Si(111). Journal of Applied Physics 2014,* ***116****(5):* *054913.*

51. *Wang J-J, Xu Y-Z, Mazzarello R, Wuttig M, Zhang W. A Review on Disorder-Driven Metal-Insulator Transition in Crystalline Vacancy-Rich GeSbTe Phase-Change Materials. Materials (Basel) 2017,* ***10****(8):* *862.*

52. *Boschker JE, Boniardi M, Redaelli A, Riechert H, Calarco R. Electrical performance of phase change memory cells with Ge3Sb2Te6 deposited by molecular beam epitaxy. Applied Physics Letters 2015,* ***106****(2):* *023117.*

53. *Schmitz[1] PC, Zhang W, Mokrousov Y, Mazzarello[1] R. Topological phases in interfacial GeSbTe phase change materials. Phys Rev Lett 2011,* ***107:*** *127205.*

54. *Park Y-J, Cho J-Y, Jeong M-W, Na S, Joo Y-C. New pathway for the formation of metallic cubic phase Ge-Sb-Te compounds induced by an electric current. Scientific Reports 2016,* ***6****(1):* *21466.*

55. *von Rohr F, Schilling A, Cava RJ. Single-crystal growth and thermoelectric properties of Ge(Bi,Sb)4Te7. Journal of Physics: Condensed Matter 2013,* ***25****(7):* *075804.*

56. *Frumar M, Tichý L, Matyáš M, Želízko J. Some physical properties of semiconducting GeSb4Te7 crystals. physica status solidi (a) 1974,* ***22****(2):* *535-541.*

57. *Rausch P. Investigations of binary and ternary phase change alloys for future memory applications. 2012.*

58. *Rocca J, García JL, Ureña MA, Fontana M, Arcondo B. Temperature Dependence of Electrical Resistance in Ge-Sb-Te Thin Films. Materials Research 2019,* ***22****.*

59. *Mihailescu IN. Synthesis and Modification of Nanostructured Thin Films. MDPI AG, 2020.*

60. *Bulai G, Pompilian O, Gurlui S, Nemec P, Nazabal V, Cimpoesu N, et al. Ge-Sb-Te Chalcogenide Thin Films Deposited by Nanosecond, Picosecond, and Femtosecond Laser Ablation. Nanomaterials (Basel) 2019, **9**(5)**:** 676.*

61. *Park J-W, Eom SH, Lee H, Da Silva JLF, Kang Y-S, Lee T-Y, et al. Optical properties of pseudobinary GeTe, ${\text{Ge}}_{2}{\text{Sb}}_{2}{\text{Te}}_{5}$, ${\text{GeSb}}_{2}{\text{Te}}_{4}$, ${\text{GeSb}}_{4}{\text{Te}}_{7}$, and ${\text{Sb}}_{2}{\text{Te}}_{3}$ from ellipsometry and density functional theory. Physical Review B 2009, **80**(11)**:** 115209.*

62. *Behrens M. Structural, optical and switching properties of epitaxial Ge-Sb-Te thin films.*

63. *Shelimova L, Karpinskii O, Zemskov V, Konstantinov P. Structural and electrical properties of layered tetradymite-like compounds in the GeTe—Bi 2 Te 3 and GeTe—Sb 2 Te 3 systems. Inorganic materials 2000, **36**(3)**:** 235-242.*

64. *Matsunaga T, Kojima R, Yamada N, Kifune K, Kubota Y, Takata M. Structural Features of Ge1Sb4Te7, an Intermetallic Compound in the GeTe-Sb2Te3 Homologous Series. Chemistry of Materials 2008, **20**(18)**:** 5750-5755.*

65. *GeSb4Te7 Crystal Structure: Datasheet from "PAULING FILE Multinaries Edition – 2012" in SpringerMaterials (https://materials.springer.com/isp/crystallographic/docs/sd_1102023). Springer-Verlag Berlin Heidelberg & Material Phases Data System (MPDS), Switzerland & National Institute for Materials Science (NIMS), Japan.*

66. *Petrov AK, Sechkarev AV. Temperature dependence of infrared spectra. Soviet Physics Journal 1965, **8**(5)**:** 62-64.*

67. *Klechkovskaya VV, Imamov RM. Electron diffraction structure analysis—from Vainshtein to our days. Crystallography Reports 2001, **46**(4)**:** 534-549.*

68. *Kozyukhin S, Lazarenko P, Vorobyov Y, Baranchikov A, Glukhenkaya V, Smayev M, et al. Laser-induced modification and formation of periodic surface structures (ripples) of amorphous GST225 phase change materials. Optics & Laser Technology 2019, **113:** 87-94.*

69. *Behera JK, Wang W, Zhou X, Guan S, Weikang W, Shengyuan YA, et al. Resistance modulation in Ge2Sb2Te5. Journal of Materials Science & Technology 2020, **50:** 171-177.*

70. *Yamada N, Matsunaga T. Structure of laser-crystallized Ge2Sb2+xTe5 sputtered thin films for use in optical memory. Journal of Applied Physics 2000, **88**(12)**:** 7020-7028.*

71. *Hilmi I, Lotnyk A, Gerlach JW, Schumacher P, Rauschenbach B. Influence of substrate dimensionality on the growth mode of epitaxial 3D-bonded GeTe thin films: From 3D to 2D growth. Materials & Design 2019, **168:** 107657.*

72. *Le PH, Liao C-N, Luo CW, Leu J. Thermoelectric properties of nanostructured bismuth–telluride thin films grown using pulsed laser deposition. Journal of Alloys and Compounds 2014, **615:** 546-552.*

73. *Ge2Sb2Te5 Crystal Structure: Datasheet from "PAULING FILE Multinaries Edition – 2012" in SpringerMaterials (https://materials.springer.com/isp/crystallographic/docs/sd_1102022). Springer-Verlag Berlin Heidelberg & Material Phases Data System (MPDS), Switzerland & National Institute for Materials Science (NIMS), Japan.*

74. *c-Ge2Sb2Te5 (Ge2Sb2Te5) Crystal Structure: Datasheet from "PAULING FILE Multinaries Edition – 2012" in SpringerMaterials (https://materials.springer.com/isp/crystallographic/docs/sd_1218546). Springer-Verlag Berlin Heidelberg & Material Phases Data System (MPDS), Switzerland & National Institute for Materials Science (NIMS), Japan.*

75. *Kolobov AV, Fons P, Saito Y, Tominaga J. Atomic Reconfiguration of van der Waals Gaps as the Key to Switching in GeTe/Sb2Te3 Superlattices. ACS Omega 2017, **2**(9): 6223-6232.*

76. *Simpson RE, Fons P, Kolobov AV, Fukaya T, Krbal M, Yagi T, et al. Interfacial phase-change memory. Nature Nanotechnology 2011, **6**(8): 501-505.*

77. *Behrens M, Lotnyk A, Gerlach JW, Hilmi I, Abel T, Lorenz P, et al. Ultrafast interfacial transformation from 2D- to 3D-bonded structures in layered Ge–Sb–Te thin films and heterostructures. Nanoscale 2018, **10**(48): 22946-22953.*

78. *Cecchi S, Zallo E, Momand J, Wang R, Kooi BJ, Verheijen MA, et al. Improved structural and electrical properties in native Sb2Te3/GexSb2Te3+x van der Waals superlattices due to intermixing mitigation. APL Materials 2017, **5**(2): 026107.*

79. *Kooi B, Groot W, De Hosson JTM. In situ transmission electron microscopy study of the crystallization of Ge 2 Sb 2 Te 5. Journal of Applied Physics 2004, **95**(3): 924-932.*

80. *Chen B, ten Brink GH, Palasantzas G, Kooi BJ. Crystallization kinetics of GeSbTe phase-change nanoparticles resolved by ultrafast calorimetry. The Journal of Physical Chemistry C 2017, **121**(15): 8569-8578.*

81. *Pandian R, Kooi BJ, Oosthoek JL, van den Dool P, Palasantzas G, Pauza A. Polarity-dependent resistance switching in GeSbTe phase-change thin films: The importance of excess Sb in filament formation. Applied Physics Letters 2009, **95**(25): 252109.*

82. *Ohyanagi T, Kitamura M, Araidai M, Kato S, Takaura N, Shiraishi K. GeTe sequences in superlattice phase change memories and their electrical characteristics. Applied Physics Letters 2014, **104**(25): 252106.*

83. *Takaura N, Ohyanagi T, Tai M, Kinoshita M, Akita K, Morikawa T, et al. 55-μA GexTe1−x/Sb2Te3 superlattice topological-switching random access memory (TRAM) and study of atomic arrangement in Ge-Te and Sb-Te structures. 2014 IEEE International Electron Devices Meeting; 2014 15-17 Dec. 2014; 2014. p. 29.22.21-29.22.24.*

84. *Egami T, Johguchi K, Yamazaki S, Takeuchi K. Investigation of multi-level-cell and SET operations on super-lattice phase change memories. Japanese Journal of Applied Physics 2014, **53**(4S): 04ED02.*

85. *Yu X, Robertson J. Modeling of switching mechanism in GeSbTe chalcogenide superlattices. Scientific reports 2015, **5**: 12612-12612.*

86. *Bang D, Awano H, Tominaga J, Kolobov AV, Fons P, Saito Y, et al. Mirror-symmetric Magneto-optical Kerr Rotation using Visible Light in [(GeTe)2(Sb2Te3)1]n Topological Superlattices. Scientific Reports 2014, **4**(1): 5727.*

87. *Wang X-P, Li X-B, Chen N-K, Chen Q-D, Han X-D, Zhang S, et al. Element-specific amorphization of vacancy-ordered GeSbTe for ternary-state phase change memory. Acta Materialia 2017, **136**: 242-248.*

88. *Akola J, Jones RO. Structural phase transitions on the nanoscale: The crucial pattern in the phase-change materials ${\mathrm{Ge}}_{2}{\mathrm{Sb}}_{2}{\mathrm{Te}}_{5}$ and GeTe. Physical Review B 2007,* ***76****(23):* *235201.*

89. *Yang F, Chen T, Wang M, Yan B, Wan L, Ke D, et al. First-principles study of the properties for crystal Ge2Sb2Te5 with Ge vacancy. AIP Advances 2018,* ***8****(6):* *065223.*

90. *Ge3Sb2Te6 Crystal Structure: Datasheet from "PAULING FILE Multinaries Edition – 2012" in SpringerMaterials (https://materials.springer.com/isp/crystallographic/docs/sd_1818188). Springer-Verlag Berlin Heidelberg & Material Phases Data System (MPDS), Switzerland & National Institute for Materials Science (NIMS), Japan.*

91. *Matsunaga T, Kojima R, Yamada N, Kifune K, Kubota Y, Takata M. Structural investigation of Ge3Sb2Te6, an intermetallic compound in the GeTe–Sb2Te3 homologous series. Applied Physics Letters 2007,* ***90****(16):* *161919.*

92. *Wang Z, Liu Q, Luo J-W, Zunger A. Digging for topological property in disordered alloys: the emergence of Weyl semimetal phase and sequential band inversions in PbSe–SnSe alloys. Materials Horizons 2019,* ***6****(10):* *2124-2134.*

93. *Sa B, Zhou J, Sun Z, Ahuja R. Strain-induced topological insulating behavior in ternary chalcogenide Ge 2 Sb 2 Te 5. EPL (Europhysics Letters) 2012,* ***97****(2):* *27003.*

94. *Pauly C, Liebmann M, Giussani A, Kellner J, Just S, Sánchez-Barriga J, et al. Evidence for topological band inversion of the phase change material Ge2Sb2Te5. Applied Physics Letters 2013,* ***103****(24):* *243109.*

95. *Tominaga J. Topological memory using phase-change materials. MRS Bulletin 2018,* ***43****(5):* *347.*

96. *Kim J, Kim J, Jhi S-H. Prediction of topological insulating behavior in crystalline Ge-Sb-Te. Physical Review B 2010,* ***82****(20):* *201312.*

97. *Silkin IV, Koroteev YM, Bihlmayer G, Chulkov EV. Influence of the Ge–Sb sublattice atomic composition on the topological electronic properties of Ge2Sb2Te5. Applied Surface Science 2013,* ***267:*** *169-172.*

98. *Kim J, Jhi S-H. Emerging topological insulating phase in Ge□Sb□Te compounds. physica status solidi (b) 2012,* ***249****(10):* *1874-1879.*

99. *Kim J, Jhi S-H. Disorder-induced structural transitions in topological insulating Ge-Sb-Te compounds. Journal of Applied Physics 2015,* ***117****(19):* *195701.*

100. *Sa B, Zhou J, Sun Z, Tominaga J, Ahuja R. Topological Insulating in $\mathrm{GeTe}/{\mathrm{Sb}}_{2}{\mathrm{Te}}_{3}$ Phase-Change Superlattice. Physical Review Letters 2012,* ***109****(9):* *096802.*

101. *ODHIAMBO HO. Computational study of the structural, Electronic, optical and thermal properties of Hexagonal and cubic Germanium-antimony-telluride. Maseno University, 2016.*

102. *Pauly C. Identification of Tellurium based Phase-Change Materials as Strong Topological Insulators. Strong and Weak Topology Probed by Surface Science. Springer, 2015, pp 59-103.*

103. *Singh B, Lin H, Prasad R, Bansil A. Topological phase transition and two-dimensional topological insulators in Ge-based thin films. Physical Review B 2013, **88**(19): 195147.*

104. *Wang J, Ronneberger I, Zhou L, Lu L, Deringer VL, Zhang B, et al. Unconventional two-dimensional germanium dichalcogenides. Nanoscale 2018, **10**(16): 7363-7368.*

105. *Rosenbach D, Oellers N, Jalil AR, Mikulics M, Kölzer J, Zimmermann E, et al. Quantum Transport in Topological Surface States of Selectively Grown Bi2Te3 Nanoribbons. Advanced Electronic Materials 2020, **n/a**(n/a): 2000205.*

106. *Kim J, Kim J, Kim K-S, Jhi S-H. Topological Phase Transition in the Interaction of Surface Dirac Fermions in Heterostructures. Physical Review Letters 2012, **109**(14): 146601.*

107. *Sterzi A, Manzoni G, Crepaldi A, Cilento F, Zacchigna M, Leclerc M, et al. Probing band parity inversion in the topological insulator GeBi2Te4 by linear dichroism in ARPES. Journal of Electron Spectroscopy and Related Phenomena 2018, **225**: 23-27.*

108. *Arita M, Sato H, Shimada K, Namatame H, Taniguchi M, Sasaki M, et al. Angle resolved photoemission study of GeBi₂Te₄. Proceedings of the 12th Asia Pacific Physics Conference (APPC12), vol. 1. Journal of the Physical Society of Japan, 2014.*

109. *Xu S-Y, Wray L, Xia Y, Shankar R, Petersen A, Fedorov A, et al. Discovery of several large families of topological insulator classes with backscattering-suppressed spin-polarized single-Dirac-cone on the surface. arXiv preprint arXiv:10075111 2010.*

110. *Mihara T, Kojima R, Tsuchino A, Sato S, Hisada K, Furumiya S, et al. Crystallization properties of Ge2Bi2Te5and Ge10Sb90amorphous nanoparticles subjected to pulsed laser irradiation. Applied Physics Express 2014, **7**(5): 055001.*

111. *Sun CW, Lee JY, Kim YT. Phase Transition Behavior of Ge–Bi–Te Thin Films from an NaCl to Rhombohedral Structure. Japanese Journal of Applied Physics 2008, **47**(10): 7983-7985.*

112. *Matsunaga T, Kojima R, Yamada N, Kifune K, Kubota Y, Takata M. Structures of stable and metastable Ge2Bi2Te5, an intermetallic compound in a GeTe-Bi2Te3 pseudobinary system. Acta Crystallographica Section B 2007, **63**(3): 346-352.*

113. *Sun C, Lee J, Kim Y. TEM study of the structural similarity between NaCl and rhombohedral phase of Te-based ternary chalcogenide materials. physica status solidi (a) 2009, **206**(1): 50-53.*

114. *Plugge S, Rasmussen A, Egger R, Flensberg K. Majorana box qubits. New Journal of Physics 2017, **19**(1): 012001.*

115. *Kooi BJ, Wuttig M. Chalcogenides by Design: Functionality through Metavalent Bonding and Confinement. Advanced Materials 2020, **32**(21): 1908302.*

116. *Wuttig M, Deringer VL, Gonze X, Bichara C, Raty J-Y. Incipient Metals: Functional Materials with a Unique Bonding Mechanism. Advanced Materials 2018, **30**(51): 1803777.*

117. *Raty J-Y, Wuttig M. The interplay between Peierls distortions and metavalent bonding in IV–VI compounds: comparing GeTe with related monochalcogenides. Journal of Physics D: Applied Physics 2020, **53**(23): 234002.*

118. *Zhu M, Cojocaru-Mirédin O, Mio AM, Keutgen J, Küpers M, Yu Y, et al. Unique Bond Breaking in Crystalline Phase Change Materials and the Quest for Metavalent Bonding. Advanced Materials 2018,* ***30****(18):* *1706735.*

119. *Wang R, Zhang W, Momand J, Ronneberger I, Boschker JE, Mazzarello R, et al. Formation of resonant bonding during growth of ultrathin GeTe films. NPG Asia Materials 2017,* ***9****(6):* *e396-e396.*

120. *Di Sante D, Barone P, Bertacco R, Picozzi S. Electric Control of the Giant Rashba Effect in Bulk GeTe. Advanced Materials 2013,* ***25****(4):* *509-513.*

121. *Elmers HJ, Wallauer R, Liebmann M, Kellner J, Morgenstern M, Wang RN, et al. Spin mapping of surface and bulk Rashba states in ferroelectric $\ensuremath{\alpha}$-GeTe(111) films. Physical Review B 2016,* ***94****(20):* *201403.*

122. *Krempaský J, Volfová H, Muff S, Pilet N, Landolt G, Radović M, et al. Disentangling bulk and surface Rashba effects in ferroelectric $\ensuremath{\alpha}$-GeTe. Physical Review B 2016,* ***94****(20):* *205111.*

123. *Plachkova SK, Georgieva OG, Odin IN. Solid State Transformations and Electrophysical Properties of GeTe-Rich Solid Solutions in the GeTe-Ag2Te-Bi2Te3 System. physica status solidi (a) 1991,* ***128****(2):* *361-368.*

124. *Liebmann M, Rinaldi C, Di Sante D, Kellner J, Pauly C, Wang RN, et al. Giant Rashba-Type Spin Splitting in Ferroelectric GeTe(111). Advanced Materials 2016,* ***28****(3):* *560-565.*

125. *Hein RA, Gibson JW, Mazelsky R, Miller RC, Hulm JK. Superconductivity in Germanium Telluride. Physical Review Letters 1964,* ***12****(12):* *320-322.*

126. *Narayan V, Verpoort PC, Dann JRA, Backes D, Ford CJB, Lanius M, et al. Long-lived nonequilibrium superconductivity in a noncentrosymmetric Rashba semiconductor. Physical Review B 2019,* ***100****(2):* *024504.*

127. *Li Y-Y, Wang G, Zhu X-G, Liu M-H, Ye C, Chen X, et al. Intrinsic Topological Insulator Bi2Te3 Thin Films on Si and Their Thickness Limit. Advanced Materials 2010,* ***22****(36):* *4002-4007.*

128. *Wang G, Zhu XG, Sun YY, Li YY, Zhang T, Wen J, et al. Topological Insulator Thin Films of Bi2Te3 with Controlled Electronic Structure. Adv Mater 2011,* ***23:*** *2929.*

129. *Seixas L, Abdalla LB, Schmidt TM, Fazzio A, Miwa RH. Topological States Ruled by Stacking Faults in Bi2Se3 and Bi2Te3. J Appl Phys 2013,* ***113:*** *023705.*

130. *He L, Kou X, Wang KL. Review of 3D topological insulator thin-film growth by molecular beam epitaxy and potential applications. physica status solidi (RRL) – Rapid Research Letters 2013,* ***7****(1-2):* *50-63.*

131. *Kampmeier J, Weyrich C, Lanius M, Schall M, Neumann E, Mussler G, et al. Selective area growth of Bi2Te3 and Sb2Te3 topological insulator thin films. Journal of Crystal Growth 2016,* ***443:*** *38-42.*

132. *Gwon T, Eom T, Yoo S, Lee H-K, Cho D-Y, Kim M-S, et al. Atomic Layer Deposition of GeTe Films Using Ge{N[Si(CH3)3]2}2, {(CH3)3Si}2Te, and Methanol. Chemistry of Materials 2016,* ***28****(19):* *7158-7166.*

133. *Zayachuk DM, Slynko VE, Csik A. Peculiar properties of preferential sputtering of PbTe, SnTe, and GeTe by Ar+ ion plasma. Materials Science in Semiconductor Processing 2018,* ***88:*** *103-108.*

134. *Wang R, Campi D, Bernasconi M, Momand J, Kooi BJ, Verheijen MA, et al. Ordered Peierls distortion prevented at growth onset of GeTe ultra-thin films. Scientific Reports 2016,* ***6****(1):* *32895.*

135. *Wang R, Boschker JE, Bruyer E, Sante DD, Picozzi S, Perumal K, et al. Toward Truly Single Crystalline GeTe Films: The Relevance of the Substrate Surface. The Journal of Physical Chemistry C 2014,* ***118****(51):* *29724-29730.*

136. *Schulz S, Heimann S, Kaiser K, Prymak O, Assenmacher W, Brüggemann JT, et al. Solution-Based Synthesis of GeTe Octahedra at Low Temperature. Inorganic Chemistry 2013,* ***52****(24):* *14326-14333.*

Chapter – 6

1. *Berntsen MH, Götberg O, Wojek BM, Tjernberg O. Direct observation of decoupled Dirac states at the interface between topological and normal insulators. Physical Review B 2013,* ***88****(19):* *195132.*

2. *Brahlek M, Koirala N, Bansal N, Oh S. Transport properties of topological insulators: Band bending, bulk metal-to-insulator transition, and weak anti-localization. Solid State Communications 2015,* ***215-216:*** *54-62.*

3. *Chen X, Ma X-C, He K, Jia J-F, Xue Q-K. Molecular Beam Epitaxial Growth of Topological Insulators. Advanced Materials 2011,* ***23****(9):* *1162-1165.*

4. *Borisova S, Krumrain J, Luysberg M, Mussler G, Grützmacher D. Mode of Growth of Ultrathin Topological Insulator Bi2Te3 Films on Si (111) Substrates. Crystal Growth & Design 2012,* ***12****(12):* *6098-6103.*

5. *Yashina LV, Sánchez-Barriga J, Scholz MR, Volykhov AA, Sirotina AP, Neudachina VS, et al. Negligible Surface Reactivity of Topological Insulators Bi2Se3 and Bi2Te3 towards Oxygen and Water. ACS Nano 2013,* ***7****(6):* *5181-5191.*

6. *Atuchin VV, Golyashov VA, Kokh KA, Korolkov IV, Kozhukhov AS, Kruchinin VN, et al. Formation of Inert Bi2Se3(0001) Cleaved Surface. Crystal Growth & Design 2011,* ***11****(12):* *5507-5514.*

7. *Golyashov VA, Kokh KA, Makarenko SV, Romanyuk KN, Prosvirin IP, Kalinkin AV, et al. Inertness and degradation of (0001) surface of Bi2Se3 topological insulator. Journal of Applied Physics 2012,* ***112****(11):* *113702.*

8. *Chen Y, Analytis JG, Chu J-H, Liu Z, Mo S-K, Qi X-L, et al. Experimental realization of a three-dimensional topological insulator, Bi2Te3. science 2009,* ***325****(5937):* *178-181.*

9. *Park SR, Jung WS, Kim C, Song DJ, Kim C, Kimura S, et al. Quasiparticle scattering and the protected nature of the topological states in a parent topological insulator ${\text{Bi}}_{2}{\text{Se}}_{3}$. Physical Review B 2010,* ***81****(4):* *041405.*

10. *Zhou B, Liu ZK, Analytis JG, Igarashi K, Mo SK, Lu DH, et al. Controlling the carriers of topological insulators by bulk and surface doping. Semiconductor Science and Technology 2012,* ***27****(12):* *124002.*

11. *Hoefer K, Becker C, Rata D, Swanson J, Thalmeier P, Tjeng LH. Intrinsic conduction through topological surface states of insulating Bi2Te3epitaxial thin films. Proc Natl Acad Sci USA 2014,* ***111:*** *14979.*

12. *Leis A, Schleenvoigt M, Jalil AR, Cherepanov V, Mussler G, Grützmacher D, et al. Room temperature in-situ measurement of the spin voltage of a BiSbTe3 thin film. Scientific Reports 2020,* ***10****(1):* *2816.*

13. *Kellner J, Eschbach M, Kampmeier J, Lanius M, Młyńczak E, Mussler G, et al. Tuning the Dirac point to the Fermi level in the ternary topological insulator (Bi1−xSbx)2Te3. Applied Physics Letters 2015,* ***107****(25):* *251603.*

14. *Lüpke F, Eschbach M, Heider T, Lanius M, Schüffelgen P, Rosenbach D, et al. Electrical resistance of individual defects at a topological insulator surface. Nature Communications 2017,* ***8****(1):* *15704.*

15. *Lüpke F, Just S, Eschbach M, Heider T, Młyńczak E, Lanius M, et al. In situ disentangling surface state transport channels of a topological insulator thin film by gating. npj Quantum Materials 2018,* ***3****(1):* *46.*

16. *Plucinski L, Mussler G, Krumrain J, Herdt A, Suga S, Grützmacher D, et al. Robust surface electronic properties of topological insulators: Bi2Te3 films grown by molecular beam epitaxy. Applied Physics Letters 2011,* ***98****(22):* *222503.*

17. *Kong D, Cha JJ, Lai K, Peng H, Analytis JG, Meister S, et al. Rapid Surface Oxidation as a Source of Surface Degradation Factor for Bi2Se3. ACS Nano 2011,* ***5****(6):* *4698-4703.*

18. *Green AJ, Dey S, An YQ, O'Brien B, O'Mullane S, Thiel B, et al. Surface oxidation of the topological insulator Bi2Se3. Journal of Vacuum Science & Technology A 2016,* ***34****(6):* *061403.*

19. *Yeh Y-C, Ho P-H, Wen C-Y, Shu G-J, Sankar R, Chou F-C, et al. Growth of the Bi2Se3 Surface Oxide for Metal–Semiconductor–Metal Device Applications. The Journal of Physical Chemistry C 2016,* ***120****(6):* *3314-3318.*

20. *Salehi M, Brahlek M, Koirala N, Moon J, Wu L, Armitage NP, et al. Stability of low-carrier-density topological-insulator Bi2Se3 thin films and effect of capping layers. APL Materials 2015,* ***3****(9):* *091101.*

21. *Volykhov AA, Sánchez-Barriga J, Sirotina AP, Neudachina VS, Frolov AS, Gerber EA, et al. Rapid Surface Oxidation of Sb2Te3 as Indication for a Universal Trend in the Chemical Reactivity of Tetradymite Topological Insulators. Chemistry of Materials 2016,* ***28****(24):* *8916-8923.*

22. *Arun P, Tyagi P, Vedeshwar AG, Kumar Paliwal V. Ageing effect of Sb2Te3 thin films. Physica B: Condensed Matter 2001,* ***307****(1):* *105-110.*

23. *Somdock N, Harnwunggmoung A, Sakulkalavek A, Sakdanuphab R. Effect of real working environment/formation of oxide phase on thermoelectric properties of flexible Sb2Te3 films. Ceramics International 2019,* ***45****(13):* *15860-15865.*

24. *Lwin ML, Dharmaiah P, Madavali B, Lee C-H, Shin D-w, Song G, et al. Oxide formation mechanism and its effect on the microstructure and thermoelectric properties of p-type Bi0.5Sb1.5Te3 alloys. Intermetallics 2018,* ***103:*** *23-32.*

25. *Gourvest E, Pelissier B, Vallée C, Roule A, Lhostis S, Maitrejean S. Impact of Oxidation on Ge2Sb2Te5and GeTe Phase-Change Properties. Journal of The Electrochemical Society 2012, **159**(4): H373-H377.*

26. *Canvel Y, Lagrasta S, Boixaderas C, Barnola S, Mazel Y, Dabertrand K, et al. Modification of Ge-rich GeSbTe surface during the patterning process of phase-change memories. Microelectronic Engineering 2020, **221:** 111183.*

27. *Golovchak R, Choi YG, Kozyukhin S, Chigirinsky Y, Kovalskiy A, Xiong-Skiba P, et al. Oxygen incorporation into GST phase-change memory matrix. Applied Surface Science 2015, **332:** 533-541.*

28. *Krbal M, Kolobov AV, Fons P, Nitta K, Uruga T, Tominaga J. Investigation of the oxidation process in GeTe-based phase change alloy using Ge K-edge XANES spectroscopy. Pure and Applied Chemistry 2019, **91**(11): 1769-1775.*

29. *Berthier R, Bernier N, Cooper D, Sabbione C, Hippert F, Noé P. In situ observation of the impact of surface oxidation on the crystallization mechanism of GeTe phase-change thin films by scanning transmission electron microscopy. Journal of Applied Physics 2017, **122**(11): 115304.*

30. *Kolb AND, Bernier N, Robin E, Benayad A, Rouvière J-L, Sabbione C, et al. Understanding the Crystallization Behavior of Surface-Oxidized GeTe Thin Films for Phase-Change Memory Application. ACS Applied Electronic Materials 2019, **1**(5): 701-710.*

31. *Qu D-X, Hor YS, Xiong J, Cava RJ, Ong NP. Quantum Oscillations and Hall Anomaly of Surface States in the Topological Insulator Bi₂Te<sub>3</sub&gt. Science 2010, **329**(5993): 821.*

32. *Li Y-Y, Wang G, Zhu X-G, Liu M-H, Ye C, Chen X, et al. Intrinsic Topological Insulator Bi2Te3 Thin Films on Si and Their Thickness Limit. Advanced Materials 2010, **22**(36): 4002-4007.*

33. *Hajlaoui M, Papalazarou E, Mauchain J, Lantz G, Moisan N, Boschetto D, et al. Ultrafast Surface Carrier Dynamics in the Topological Insulator Bi2Te3. Nano Letters 2012, **12**(7): 3532-3536.*

34. *Wolos A, Szyszko S, Drabinska A, Kaminska M, Strzelecka SG, Hruban A, et al. Landau-Level Spectroscopy of Relativistic Fermions with Low Fermi Velocity in the ${\mathrm{Bi}}_{2}{\mathrm{Te}}_{3}$ Three-Dimensional Topological Insulator. Physical Review Letters 2012, **109**(24): 247604.*

35. *Brahlek M, Kim YS, Bansal N, Edrey E, Oh S. Surface versus bulk state in topological insulator Bi2Se3 under environmental disorder. Applied Physics Letters 2011, **99**(1): 012109.*

36. *Edmonds MT, Hellerstedt JT, Tadich A, Schenk A, O'Donnell KM, Tosado J, et al. Stability and Surface Reconstruction of Topological Insulator Bi2Se3 on Exposure to Atmosphere. The Journal of Physical Chemistry C 2014, **118**(35): 20413-20419.*

37. *Bando H, Koizumi K, Oikawa Y, Daikohara K, Kulbachinskii VA, Ozaki H. The time-dependent process of oxidation of the surface of Bi2Te3studied by x-ray photoelectron spectroscopy. Journal of Physics: Condensed Matter 2000, **12**(26): 5607-5616.*

38. *Guo J-H, Qiu F, Zhang Y, Deng H-Y, Hu G-J, Li X-N, et al. Surface Oxidation Properties in a Topological Insulator Bi 2 Te 3 Film. Chinese Physics Letters 2013, **30**(10): 106801.*

39. *Boeyens JC. The periodic electronegativity table. Zeitschrift für Naturforschung B 2008, **63**(2): 199-209.*

40. *Yashina LV, Püttner R, Neudachina VS, Zyubina TS, Shtanov VI, Poygin MV. X-ray photoelectron studies of clean and oxidized α-GeTe(111) surfaces. Journal of Applied Physics 2008, **103**(9): 094909.*

41. *Yang F, Chen T, Wang M, Yan B, Wan L, Ke D, et al. First-principles study of the properties for crystal Ge2Sb2Te5 with Ge vacancy. AIP Advances 2018, **8**(6): 065223.*

42. *Nonaka T, Ohbayashi G, Toriumi Y, Mori Y, Hashimoto H. Crystal structure of GeTe and Ge2Sb2Te5 meta-stable phase. Thin Solid Films 2000, **370**(1): 258-261.*

43. *Matsunaga T, Kojima R, Yamada N, Kifune K, Kubota Y, Takata M. Structures of stable and metastable Ge2Bi2Te5, an intermetallic compound in a GeTe-Bi2Te3 pseudobinary system. Acta Crystallographica Section B 2007, **63**(3): 346-352.*

44. *Park Y-J, Cho J-Y, Jeong M-W, Na S, Joo Y-C. New pathway for the formation of metallic cubic phase Ge-Sb-Te compounds induced by an electric current. Scientific Reports 2016, **6**(1): 21466.*

45. *Wang J-J, Xu Y-Z, Mazzarello R, Wuttig M, Zhang W. A Review on Disorder-Driven Metal-Insulator Transition in Crystalline Vacancy-Rich GeSbTe Phase-Change Materials. Materials (Basel) 2017, **10**(8): 862.*

46. *Zhang W, Thiess A, Zalden P, Zeller R, Dederichs PH, Raty JY, et al. Role of vacancies in metal–insulator transitions of crystalline phase-change materials. Nature Materials 2012, **11**(11): 952-956.*

47. *Li P, Ding T, Li J, Zhang C, Dou Y, Li Y, et al. Positive Effect of Ge Vacancies on Facilitating Band Convergence and Suppressing Bipolar Transport in GeTe-Based Alloys for High Thermoelectric Performance. Advanced Functional Materials 2020, **30**(15): 1910059.*

48. *Liu Z, Sato N, Guo Q, Gao W, Mori T. Shaping the role of germanium vacancies in germanium telluride: metastable cubic structure stabilization, band structure modification, and stable N-type conduction. NPG Asia Materials 2020, **12**(1): 66.*

49. *Leontie L, Caraman M, Alexe M, Harnagea C. Structural and optical characteristics of bismuth oxide thin films. Surface Science 2002, **507-510**: 480-485.*

50. *Risold D, Hallstedt B, Gauckler LJ, Lukas HL, Fries SG. The bismuth-oxygen system. Journal of Phase Equilibria 2007, **16**(3): 223.*

51. *Music D, Chang K, Schmidt P, Braun FN, Heller M, Hermsen S, et al. On atomic mechanisms governing the oxidation of Bi2Te3. Journal of Physics: Condensed Matter 2017, **29**(48): 485705.*

52. *BiO Crystal Structure: Datasheet from "PAULING FILE Multinaries Edition – 2012" in SpringerMaterials (https://materials.springer.com/isp/crystallographic/docs/sd_1701355). Springer-Verlag Berlin Heidelberg & Material Phases Data System (MPDS), Switzerland & National Institute for Materials Science (NIMS), Japan.*

53. *Zavyalova A, Imamov R, Pinsker Z. An electron-diffraction study of thin films in the Bi-O system. SOVIET PHYS CRYSTALLOGR 1965, **9**(6): 724-728.*

54. *Zav'yalova A, Imamov R. Special features of the crystal structure of bismuth oxides. Journal of Structural Chemistry 1973,* ***13****(5):* *811-814.*

55. *Abdelmoula K, Renard D, Nihoul G. Study of a bismuth (001) surface compound by analysis of high resolution electron microscope images. Surface Science 1990,* ***225****(3):* *397-406.*

56. *Campbell CT, Taylor TN. The coadsorption of potassium and oxygen on Bi(0001): Accelerated oxidation. Surface Science 1982,* ***118****(3):* *401-414.*

57. *Taylor TN, Campbell CT, Rogers JW, Ellis WP, White JM. The interaction of oxygen with Bi(0001): Kinetic, electronic, and structural features. Surface Science 1983,* ***134****(2):* *529-546.*

58. *Medernach JW. On the structure of evaporated bismuth oxide thin films. Journal of Solid State Chemistry 1975,* ***15****(4):* *352-359.*

59. *Moiseev G, Vatolin N, Belousova N. Thermodynamic Investigations in the Bi-O System. Journal of Thermal Analysis and Calorimetry 2000,* ***61****(1):* *289-303.*

60. *Ivanov SA, Tellgren R, Rundlo¨f H, Orlov VG. Structural studies of α-Bi2O3 by neutron powder diffraction. Powder Diffraction 2001,* ***16****(4):* *227-230.*

61. *Prekajski M, Kremenović A, Babić B, Rosić M, Matović B, Radosavljević-Mihajlović A, et al. Room-temperature synthesis of nanometric α-Bi2O3. Materials Letters 2010,* ***64****(20):* *2247-2250.*

62. *Rogacheva EI, Budnik AV, Dobrotvorskaya MV, Fedorov AG, Krivonogov SI, Mateychenko PV, et al. Growth and structure of thermally evaporated Bi2Te3 thin films. Thin Solid Films 2016,* ***612:*** *128-134.*

63. *Zavyalova A, Imamov R, Pinsker Z. Crystal structure of hexagonal BiO. SOVIET PHYS CRYSTALLOGR 1966,* ***10****(4):* *401-403.*

64. *Villars P, Cenzual K, Daams J, Gladyshevskii R, Shcherban O, Dubenskyy V, et al. Structure Types. Part 6: Space Groups (166) R-3m - (160) R3m · BiO: Datasheet from Landolt-Börnstein - Group III Condensed Matter · Volume 43A6: "Structure Types. Part 6: Space Groups (166) R-3m - (160) R3m" in SpringerMaterials (https://doi.org/10.1007/978-3-540-44752-8_545). Springer-Verlag Berlin Heidelberg.*

65. *Zhukov VP, Zhukovskii VM, Zainullina VM, Medvedeva NI. Electronic structure and chemical bonding in bismuth sesquioxide polymorphs. Journal of Structural Chemistry 1999,* ***40****(6):* *831-837.*

66. *Lyamkin SA. Initial stages of bismuth oxide formation. Russian Metallurgy (Metally) 2010,* ***2010****(2):* *105-107.*

67. *Bayliss P. Crystal chemistry and crystallography of some minerals in the tetradymite group. American Mineralogist 1991,* ***76****(1-2):* *257-265.*

68. *Atuchin VV, Golyashov VA, Kokh KA, Korolkov IV, Kozhukhov AS, Kruchinin VN, et al. Crystal growth of Bi2Te3 and noble cleaved (0001) surface properties. Journal of Solid State Chemistry 2016,* ***236:*** *203-208.*

69. *Guan H, Zhang X, Xie Y. Soft-Chemical Synthetic Nonstoichiometric Bi2O2.33 Nanoflower: A New Room-Temperature Ferromagnetic Semiconductor. The Journal of Physical Chemistry C 2014, **118**(46): 27170-27174.*

70. *Peng Y, Wang KK, Liu T, Xu J, Xu BG. Synthesis of one-dimensional Bi2O3-Bi2O2.33 heterojunctions with high interface quality for enhanced visible light photocatalysis in degradation of high-concentration phenol and MO dyes. Applied Catalysis B: Environmental 2017, **203:** 946-954.*

71. *Ronneberger I, Zanolli Z, Wuttig M, Mazzarello R. Changes of Structure and Bonding with Thickness in Chalcogenide Thin Films. Advanced Materials, **n/a**(n/a): 2001033.*

72. *Lang M, He L, Xiu F, Yu X, Tang J, Wang Y, et al. Revelation of Topological Surface States in Bi2Se3 Thin Films by In Situ Al Passivation. ACS Nano 2012, **6**(1): 295-302.*

73. *Chen J, Kim J, Poudel N, Hou B, Shen L, Shi H, et al. Enhanced thermoelectric efficiency in topological insulator Bi2Te3 nanoplates via atomic layer deposition-based surface passivation. Applied Physics Letters 2018, **113**(8): 083904.*

74. *Jenkins GS, Schmadel DC, Sushkov AB, Drew HD, Bichler M, Koblmueller G, et al. Dirac cone shift of a passivated topological Bi${}_{2}$Se${}_{3}$ interface state. Physical Review B 2013, **87**(15): 155126.*

75. *Song E, Baranovskiy A, Xu E, Busani T, Swartzentruber B, Zhang S, et al. Manipulating thermal and electronic transports in thermoelectric Bi2Te3 nanowires by porphyrin adsorption. AIP Advances 2018, **8**(10): 105010.*

76. *Dai J, Wang W, Brahlek M, Koirala N, Salehi M, Oh S, et al. Restoring pristine Bi2Se3 surfaces with an effective Se decapping process. Nano Research 2015, **8**(4): 1222-1228.*

77. *Hoefer K, Becker C, Wirth S, Hao Tjeng L. Protective Capping of Topological Surface States of Intrinsically Insulating Bi2Te3. AIP Adv 2015, **5:** 097139.*

78. *Hilmi I, Lotnyk A, Gerlach JW, Schumacher P, Rauschenbach B. Research Update: Van-der-Waals epitaxy of layered chalcogenide Sb2Te3 thin films grown by pulsed laser deposition. APL Materials 2017, **5**(5): 050701.*

79. *Schüffelgen P, Rosenbach D, Pang Y, Kampmeier J, Luysberg M, Kibkalo L, et al. Signatures of induced superconductivity in AlOx-capped topological heterostructures. Solid-State Electronics 2019, **155:** 111-116.*

80. *Evertsson J, Bertram F, Zhang F, Rullik L, Merte LR, Shipilin M, et al. The thickness of native oxides on aluminum alloys and single crystals. Applied Surface Science 2015, **349:** 826-832.*

81. *Rosenbach D, Oellers N, Jalil AR, Mikulics M, Kölzer J, Zimmermann E, et al. Quantum Transport in Topological Surface States of Selectively Grown Bi2Te3 Nanoribbons. Advanced Electronic Materials 2020, **n/a**(n/a): 2000205.*

82. *Ren Z, Taskin AA, Sasaki S, Segawa K, Ando Y. Fermi level tuning and a large activation gap achieved in the topological insulator Bi${}_{2}$Te${}_{2}$Se by Sn doping. Physical Review B 2012, **85**(15): 155301.*

83. *Butch NP, Kirshenbaum K, Syers P, Sushkov AB, Jenkins GS, Drew HD, et al. Strong surface scattering in ultrahigh-mobility ${\text{Bi}}_{2}{\text{Se}}_{3}$ topological insulator crystals. Physical Review B 2010, **81**(24): 241301.*

84. *Pan Y, Wu D, Angevaare J, Luigjes H, Frantzeskakis E, De Jong N, et al. Low carrier concentration crystals of the topological insulator Bi2− xSbxTe3− ySey: a magnetotransport study. New journal of physics 2014, **16**(12): 123035.*

85. *Han K-B, Chong SK, Oliynyk AO, Nagaoka A, Petryk S, Scarpulla MA, et al. Enhancement in surface mobility and quantum transport of Bi2−xSbxTe3−ySey topological insulator by controlling the crystal growth conditions. Scientific Reports 2018, **8**(1): 17290.*

86. *Rischau CW, Ubaldini A, Giannini E, Beek CJvd. Charge puddles in a completely compensated topological insulator. New Journal of Physics 2016, **18**(7): 073024.*

87. *Pergament A, Stefanovich G, Markova N. The Mott criterion: So simple and yet so complex. arXiv preprint arXiv:14114372 2014.*

88. *Gurvitch M. Ioffe-Regel criterion and resistivity of metals. Physical Review B 1981, **24**(12): 7404-7407.*

89. *Beltukov YM, Kozub VI, Parshin DA. Ioffe-Regel criterion and diffusion of vibrations in random lattices. Physical Review B 2013, **87**(13): 134203.*

90. *Graham MR, Adkins CJ, Behar H, Rosenbaum R. Experimental study of the Ioffe-Regel criterion for amorphous indium oxide films. Journal of Physics: Condensed Matter 1998, **10**(4): 809-819.*

91. *Behner G. Towards the detection of Majorana zero-modes using interferometric methods. Master's thesis, RWTH Aachen 2020.*

92. *Kölzer J, Moors K, Jalil AR, Zimmermann E, Rosenbach D, Kibkalo L, et al. In-plane magnetic field-driven symmetry breaking in topological insulator-based three-terminal junctions. arXiv preprint arXiv:201215118 2020.*

93. *Schüffelgen P, Rosenbach D, Li C, Schmitt TW, Schleenvoigt M, Jalil AR, et al. Selective area growth and stencil lithography for in situ fabricated quantum devices. Nature Nanotechnology 2019, **14**(9): 825-831.*

Chapter – 7

1. *Popkin G. Quest for qubits. Science 2016, **354**(6316): 1090.*

2. *Walter Ogburn R, Preskill J. Topological Quantum Computation. In: Williams CP, editor. Quantum Computing and Quantum Communications; 1999 1999//; Berlin, Heidelberg: Springer Berlin Heidelberg; 1999. p. 341-356.*

3. *Ayukaryana NR, Fauzi MH, Hasdeo EH. The Quest and Hope of Majorana Zero Modes in Topological Superconductor for Fault Tolerant Quantum Computing: An Introductory Overview. arXiv preprint arXiv:200907764 2020.*

4. *Sarma SD, Freedman M, Nayak C. Majorana zero modes and topological quantum computation. npj Quantum Information 2015, **1**(1): 15001.*

5. *He M, Sun H, He QL. Topological insulator: Spintronics and quantum computations. Frontiers of Physics 2019, **14**(4): 43401.*

6. *Kauffman L, Lomonaco S. Braiding with Majorana fermions, vol. 9873. SPIE, 2016.*

7. *Plugge S, Rasmussen A, Egger R, Flensberg K. Majorana box qubits. New Journal of Physics 2017, **19**(1): 012001.*

8. *Ma X, Reichhardt CJO, Reichhardt C. Braiding Majorana fermions and creating quantum logic gates with vortices on a periodic pinning structure. Physical Review B 2020, **101**(2): 024514.*

9. *Fu L, Kane CL. Superconducting Proximity Effect and Majorana Fermions at the Surface of a Topological Insulator. Physical Review Letters 2008, **100**(9): 096407.*

10. *Leijnse M, Flensberg K. Introduction to topological superconductivity and Majorana fermions. Semiconductor Science and Technology 2012, **27**(12): 124003.*

11. *Sun H-H, Jia J-F. Detection of Majorana zero mode in the vortex. npj Quantum Materials 2017, **2**(1): 34.*

12. *Jäck B, Xie Y, Li J, Jeon S, Bernevig BA, Yazdani A. Observation of a Majorana zero mode in a topologically protected edge channel. Science 2019, **364**(6447): 1255-1259.*

13. *Wang M-X, Liu C, Xu J-P, Yang F, Miao L, Yao M-Y, et al. The Coexistence of Superconductivity and Topological Order in the Bi₂Se₃ Thin Films. Science 2012, **336**(6077): 52.*

14. *Bai M, Yang F, Luysberg M, Feng J, Bliesener A, Lippertz G, et al. Novel self-epitaxy for inducing superconductivity in the topological insulator (Bi 1− x Sb x) 2 Te 3. Physical Review Materials 2020, **4**(9): 094801.*

15. *Nb Crystal Structure: Datasheet from "PAULING FILE Multinaries Edition – 2012" in SpringerMaterials (https://materials.springer.com/isp/crystallographic/docs/sd_1215974). Springer-Verlag Berlin Heidelberg & Material Phases Data System (MPDS), Switzerland & National Institute for Materials Science (NIMS), Japan.*

16. *Cooper A. Precise lattice constants of germanium, aluminum, gallium arsenide, uranium, sulphur, quartz and sapphire. Acta Crystallographica 1962, **15**(6): 578-582.*

17. *Sathyamoorthy R, Dheepa J, Subbarayan A. Electrical conduction studies on Bi2Te3 thin films. Journal of Crystal Growth 2005, **281**(2): 563-570.*

18. *Cooley KA, Mohney SE. Reactivity in metal-Ge-Te systems: Thermodynamic predictions and experimental observations. Journal of Vacuum Science & Technology A 2019, **37**(6): 061510.*

19. *Conrad O, Schiemann A, Krebs B. Die Kristallstruktur von β-Al2Te3. Zeitschrift für anorganische und allgemeine Chemie 1997, **623**(1-6): 1006-1010.*

20. *Debbichi L, Kim H, Björkman T, Eriksson O, Lebègue S. First-principles investigation of two-dimensional trichalcogenide and sesquichalcogenide monolayers. Physical Review B 2016, **93**(24): 245307.*

21. *Balakrishnan G, Huang S, Dawson LR, Xin YC, Conlin P, Huffaker DL. Growth mechanisms of highly mismatched AlSb on a Si substrate. Applied Physics Letters 2005, **86**(3): 034105.*

22. *Ripalda JM, Sanchez AM, Taboada AG, Rivera A, Alén B, González Y, et al. Relaxation dynamics and residual strain in metamorphic AlSb on GaAs. Applied Physics Letters 2012, **100**(1): 012103.*

23. *Ali MA, Aleem H, Sarwar B, Murtaza G. First-principles calculations for optoelectronic properties of AlSb and GaSb under influence of spin–orbit interaction effect. Indian Journal of Physics 2020, **94**(4): 477-484.*

24. *Galletti L, Charpentier S, Iavarone M, Lucignano P, Massarotti D, Arpaia R, et al. Influence of topological edge states on the properties of $\mathrm{Al}/{Bi}_{2}{\mathrm{Se}}_{3}/\mathrm{Al}$ hybrid Josephson devices. Physical Review B 2014, **89**(13): 134512.*

25. *Ghatak S, Breunig O, Yang F, Wang Z, Taskin AA, Ando Y. Anomalous Fraunhofer Patterns in Gated Josephson Junctions Based on the Bulk-Insulating Topological Insulator BiSbTeSe2. Nano Letters 2018, **18**(8): 5124-5131.*

26. *Charpentier S, Galletti L, Kunakova G, Arpaia R, Song Y, Baghdadi R, et al. Induced unconventional superconductivity on the surface states of Bi2Te3 topological insulator. Nature Communications 2017, **8**(1): 2019.*

27. *Kunakova G, Bauch T, Trabaldo E, Andzane J, Erts D, Lombardi F. High transparency Bi2Se3 topological insulator nanoribbon Josephson junctions with low resistive noise properties. Applied Physics Letters 2019, **115**(17): 172601.*

28. *Schüffelgen P. Exploiting Topological Insulators for Majorana Devices and Physics Via Molecular Beam Epitaxy: Halbleiter-Nanoelektronik; 2018.*

29. *Brixner L. Preparation and properties of the single crystalline AB2-type selenides and tellurides of niobium, tantalum, molybdenum and tungsten. Journal of Inorganic and Nuclear Chemistry 1962, **24**(3): 257-263.*

30. *Nagata S, Abe T, Ebisu S, Ishihara Y, Tsutsumi K. Superconductivity in the metallic layered compound NbTe2. Journal of Physics and Chemistry of Solids 1993, **54**(8): 895-899.*

31. *Chen H, Li Z, Fan X, Guo L, Chen X. Quantum linear magnetoresistance in NbTe2. Solid State Communications 2018, **275**: 16-20.*

32. *Zhang X, Luo T, Hu X, Guo J, Lin G, Li Y, et al. Superconductivity and Fermi Surface Anisotropy in Transition Metal Dichalcogenide NbTe2. Chinese Physics Letters 2019, **36**(5): 057402.*

33. *Schüffelgen P, Rosenbach D, Li C, Schmitt TW, Schleenvoigt M, Jalil AR, et al. Selective area growth and stencil lithography for in situ fabricated quantum devices. Nature Nanotechnology 2019, **14**(9): 825-831.*

34. *Eisenstein J. Superconducting Elements. Reviews of Modern Physics 1954, **26**(3): 277-291.*

35. *Matthias BT, Geballe TH, Compton VB. Superconductivity. Reviews of Modern Physics 1963,* ***35****(1):* *1-22.*

36. *Mourachkine A. Determination of the Coherence Length and the Cooper-Pair Size in Unconventional Superconductors by Tunneling Spectroscopy. Journal of Superconductivity 2004,* ***17****(6):* *711-724.*

37. *Svistunov BV, Babaev ES, Prokof'ev NV. Superfluid states of matter. Crc Press, 2015.*

38. *Annett JF. Superconductivity, superfluids and condensates, vol. 5. Oxford University Press, 2004.*

39. *Pronin AV, Dressel M, Pimenov A, Loidl A, Roshchin IV, Greene LH. Direct observation of the superconducting energy gap developing in the conductivity spectra of niobium. Physical Review B 1998,* ***57****(22):* *14416-14421.*

40. *Savin AM, Meschke M, Pekola JP, Pashkin YA, Li TF, Im H, et al. Parity effect in Al and Nb single electron transistors in a tunable environment. Applied Physics Letters 2007,* ***91****(6):* *063512.*

41. *Sharon O, Shaulov AA, Berger J, Sharoni A, Berkovits R, Yeshurun Y. Current-Induced Crossover of Flux Periodicity from h/2e to h/e in a Superconducting Nb Nano-Ring. Nano Letters 2018,* ***18****(12):* *7851-7855.*

42. *Amado M, Fornieri A, Carillo F, Biasiol G, Sorba L, Pellegrini V, et al. Electrostatic tailoring of magnetic interference in quantum point contact ballistic Josephson junctions. Physical Review B 2013,* ***87****(13):* *134506.*

43. *Oostinga JB, Maier L, Schüffelgen P, Knott D, Ames C, Brüne C, et al. Josephson Supercurrent through the Topological Surface States of Strained Bulk HgTe. Physical Review X 2013,* ***3****(2):* *021007.*

44. *Marín-Suárez M, Peltonen JT, Pekola JP. Active Quasiparticle Suppression in a Non-Equilibrium Superconductor. Nano Letters 2020,* ***20****(7):* *5065-5071.*

45. *Ménard GC, Malinowski FK, Puglia D, Pikulin DI, Karzig T, Bauer B, et al. Suppressing quasiparticle poisoning with a voltage-controlled filter. Physical Review B 2019,* ***100****(16):* *165307.*

46. *van Woerkom DJ, Geresdi A, Kouwenhoven LP. One minute parity lifetime of a NbTiN Cooper-pair transistor. Nature Physics 2015,* ***11****(7):* *547-550.*

47. *Court NA, Ferguson AJ, Clark RG. Energy gap measurement of nanostructured aluminium thin films for single Cooper-pair devices. Superconductor Science and Technology 2007,* ***21****(1):* *015013.*

48. *Cochran JF, Mapother DE. Superconducting Transition in Aluminum. Physical Review 1958,* ***111****(1):* *132-142.*

49. *Espy C, Sharon OJ, Braun J, Garreis R, Strigl F, Shaulov A, et al. Flux-periodicity crossover fromh/2e to h/e in aluminium nano-loops. Journal of Physics: Conference Series 2018,* ***969:*** *012063.*

50. *Shen J, Heedt S, Borsoi F, van Heck B, Gazibegovic S, Op het Veld RLM, et al. Parity transitions in the superconducting ground state of hybrid InSb–Al Coulomb islands. Nature Communications 2018,* ***9****(1):* *4801.*

51. *Yamamoto T, Nakamura Y, Pashkin YA, Astafiev O, Tsai JS. Parity effect in superconducting aluminum single electron transistors with spatial gap profile controlled by film thickness. Applied Physics Letters 2006,* ***88****(21):* *212509.*

52. *Prestigiacomo JC, Liu TJ, Adams PW. Asymmetric avalanches in the condensate of a Zeeman-limited superconductor. Physical Review B 2014, **90**(18): 184519.*

53. *Adams PW, Nam H, Shih CK, Catelani G. Zeeman-limited superconductivity in crystalline Al films. Physical Review B 2017, **95**(9): 094520.*

54. *Huang X, Li F, Zhou Q, Wu G, Huang Y, Wang L, et al. In situ synchrotron X-ray diffraction with laser-heated diamond anvil cells study of Pt up to 95 GPa and 3150 K. RSC Advances 2015, **5**(19): 14603-14609.*

55. *King HW, Manchester FD. A low-temperature X-ray diffraction study of Pd and some Pd-H alloys. Journal of Physics F: Metal Physics 1978, **8**(1): 15-26.*

56. *Sabeena M, Murugesan S, Anees P, Mohandas E, Vijayalakshmi M. Crystal structure and bonding characteristics of transformation products of bcc β in Ti-Mo alloys. Journal of Alloys and Compounds 2017, **705**: 769-781.*

57. *Boeyens JC. The periodic electronegativity table. Zeitschrift für Naturforschung B 2008, **63**(2): 199-209.*

58. *Narayanan LA, Samuel FH, Gruzleski JE. Crystallization behavior of iron-containing intermetallic compounds in 319 aluminum alloy. Metallurgical and Materials Transactions A 1994, **25**(8): 1761-1773.*

59. *Mattheiss LF. Band Structures of Transition-Metal-Dichalcogenide Layer Compounds. Physical Review B 1973, **8**(8): 3719-3740.*

60. *Chhowalla M, Shin HS, Eda G, Li L-J, Loh KP, Zhang H. The chemistry of two-dimensional layered transition metal dichalcogenide nanosheets. Nature Chemistry 2013, **5**(4): 263-275.*

61. *Manzeli S, Ovchinnikov D, Pasquier D, Yazyev OV, Kis A. 2D transition metal dichalcogenides. Nature Reviews Materials 2017, **2**(8): 17033.*

62. *Bhattacharya A, Bansal B. 26 - Self-Assembly in Semiconductor Epitaxy: From Growth Mechanisms to Device Applications. In: Kuech TF (ed). Handbook of Crystal Growth (Second Edition). North-Holland: Boston, 2015, pp 1057-1099.*

63. *Bayliss P. Revised unit-cell dimensions, space group, and chemical formula of some metallic minerals. The Canadian Mineralogist 1990, **28**(4): 751-755.*

64. *Schubert K, Anderko K, Kluge M, Beeskow H, Ilschner M, Dˆrre E, et al. Strukturuntersuchung der Legierungsphasen Cu 2 Te, CuTe, Cu 3 Sb, InTe, Bi 2 Se 3, Pd 5 Sb 3 und Pd 5 Bi 3. Naturwissenschaften 1953, **40**(9): 269-269.*

65. *van Landuyt J, van Tendeloo G, Amelinckx S. Electron diffraction study of inter- and intrapolytypic phase transitions in transition metal dichalcogenides. II. Shear transformations in TaS2, TaTe2, and NbTe2. physica status solidi (a) 1974, **26**(2): 585-592.*

66. *Bhatt N, Vaidya R, Patel SG, Jani AR. X-ray diffraction studies of NbTe2 single crystal. Bulletin of Materials Science 2004, **27**(1): 23-25.*

67. *Barajas-Aguilar AH, Irwin JC, Garay-Tapia AM, Schwarz T, Paraguay Delgado F, Brodersen PM, et al. Crystalline structure, electronic and lattice-dynamics properties of NbTe2. Scientific Reports 2018,* ***8****(1):* *16984.*

68. *Zbib HM, Overman CT, Akasheh F, Bahr D. Analysis of plastic deformation in nanoscale metallic multilayers with coherent and incoherent interfaces. International Journal of Plasticity 2011,* ***27****(10):* *1618-1639.*

69. *Zhang RF, Wang J, Beyerlein IJ, Germann TC. Dislocation nucleation mechanisms from fcc/bcc incoherent interfaces. Scripta Materialia 2011,* ***65****(11):* *1022-1025.*

70. *Kang K, Wang J, Zheng SJ, Beyerlein IJ. Minimum energy structures of faceted, incoherent interfaces. Journal of Applied Physics 2012,* ***112****(7):* *073501.*

71. *Claessen R, Anderson RO, Gweon GH, Allen JW, Ellis WP, Janowitz C, et al. Complete band-structure determination of the quasi-two-dimensional Fermi-liquid reference compound ${\mathrm{TiTe}}_{2}$. Physical Review B 1996,* ***54****(4):* *2453-2465.*

72. *Reshak AH, Auluck S. Electronic and optical properties of the $1T$ phases of ${\mathrm{TiS}}_{2},$ ${\mathrm{TiSe}}_{2},$ and ${\mathrm{TiTe}}_{2}$. Physical Review B 2003,* ***68****(24):* *245113.*

73. *Arnaud Y, Chevreton M. Etude comparative des composés TiX2 (X = S, Se, Te). Structures de TiTe2 et TiSeTe. Journal of Solid State Chemistry 1981,* ***39****(2):* *230-239.*

74. *Bayliss P. Crystal chemistry and crystallography of some minerals in the tetradymite group. American Mineralogist 1991,* ***76****(1-2):* *257-265.*

75. *De Boer D, Van Bruggen C, Bus G, Coehoorn R, Haas C, Sawatzky G, et al. Titanium ditelluride: Band structure, photoemission, and electrical and magnetic properties. Physical Review B 1984,* ***29****(12):* *6797.*

76. *Harris FR, Standridge S, Feik C, Johnson DC. Design and Synthesis of [(Bi2Te3)x(TiTe2)y] Superlattices. Angewandte Chemie International Edition 2003,* ***42****(43):* *5296-5299.*

77. *Harris FR, Standridge S, Johnson DC. The Synthesis of [(Bi2Te3)x{(TiTe2)y}1.36] Superlattices from Modulated Elemental Reactants. Journal of the American Chemical Society 2005,* ***127****(21):* *7843-7848.*

78. *Westover R, Atkins RA, Falmbigl M, Ditto JJ, Johnson DC. Self-assembly of designed precursors: A route to crystallographically aligned new materials with controlled nanoarchitecture. Journal of Solid State Chemistry 2016,* ***236:*** *173-185.*

79. *Zhang Q, Cheng Y, Schwingenschlögl U. Series of topological phase transitions in TiTe${}_{2}$ under strain. Physical Review B 2013,* ***88****(15):* *155317.*

80. *Drašar Č, Steinhart M, Lošťák P, Shin HK, Dyck JS, Uher C. Transport coefficients of titanium-doped Sb2Te3 single crystals. Journal of Solid State Chemistry 2005,* ***178****(4):* *1301-1307.*

81. *Zhu M, Wu L, Rao F, Song Z, Ren K, Ji X, et al. Uniform Ti-doped Sb2Te3 materials for high-speed phase change memory applications. Applied Physics Letters 2014,* ***104****(5):* *053119.*

82. *Zhu M, Xia M, Rao F, Li X, Wu L, Ji X, et al. One order of magnitude faster phase change at reduced power in Ti-Sb-Te. Nature Communications 2014,* ***5****(1):* *4086.*

83. *Vergniory MG, Elcoro L, Felser C, Regnault N, Bernevig BA, Wang Z. A complete catalogue of high-quality topological materials. Nature 2019, **566**(7745): 480-485.*

84. *Bradlyn B, Elcoro L, Cano J, Vergniory MG, Wang Z, Felser C, et al. Topological quantum chemistry. Nature 2017, **547**(7663): 298-305.*

85. *Orders PJ, Liesegang J, Leckey RCG, Jenkin JG, Riley JD. Angle-resolved photoemission from the valence bands of NiTe2, PdTe2and PtTe2. Journal of Physics F: Metal Physics 1982, **12**(11): 2737-2753.*

86. *Leng H, Paulsen C, Huang YK, de Visser A. Type-I superconductivity in the Dirac semimetal ${\mathrm{PdTe}}_{2}$. Physical Review B 2017, **96**(22): 220506.*

87. *Noh H-J, Jeong J, Cho E-J, Kim K, Min BI, Park B-G. Experimental Realization of Type-II Dirac Fermions in a ${\mathrm{PdTe}}_{2}$ Superconductor. Physical Review Letters 2017, **119**(1): 016401.*

88. *Liu Y, Zhao J-Z, Yu L, Lin C-T, Liang A-J, Hu C, et al. Identification of Topological Surface State in PdTe 2 Superconductor by Angle-Resolved Photoemission Spectroscopy. Chinese Physics Letters 2015, **32**(6): 067303.*

89. *Clark OJ, Neat MJ, Okawa K, Bawden L, Marković I, Mazzola F, et al. Fermiology and Superconductivity of Topological Surface States in ${\mathrm{PdTe}}_{2}$. Physical Review Letters 2018, **120**(15): 156401.*

90. *Das S, Amit, Sirohi A, Yadav L, Gayen S, Singh Y, et al. Conventional superconductivity in the type-II Dirac semimetal ${\mathrm{PdTe}}_{2}$. Physical Review B 2018, **97**(1): 014523.*

91. *Liu C, Lian C-S, Liao M-H, Wang Y, Zhong Y, Ding C, et al. Two-dimensional superconductivity and topological states in ${\mathrm{PdTe}}_{2}$ thin films. Physical Review Materials 2018, **2**(9): 094001.*

92. *Zhang J, Huang GQ. The superconductivity and topological surface state of type-II Dirac semimetal NiTe2. Journal of Physics: Condensed Matter 2020, **32**(20): 205702.*

93. *Kim WS, Chao GY, Cabri LJ. Phase relations in the Pd-Te system. Journal of the Less Common Metals 1990, **162**(1): 61-74.*

94. *Tiwari B, Goyal R, Jha R, Dixit A, Awana VPS. PdTe: a 4.5 K type-II BCS superconductor. Superconductor Science and Technology 2015, **28**(5): 055008.*

95. *Mitra S, Okawa K, Kunniniyil Sudheesh S, Sasagawa T, Zhu J-X, Chia EEM. Probing the superconducting gap symmetry of $\ensuremath{\alpha}\ensuremath{-}{\mathbf{PdBi}}_{2}$: A penetration depth study. Physical Review B 2017, **95**(13): 134519.*

96. *Sakano M, Okawa K, Kanou M, Sanjo H, Okuda T, Sasagawa T, et al. Topologically protected surface states in a centrosymmetric superconductor β-PdBi2. Nature Communications 2015, **6**(1): 8595.*

97. *Dimitri K, Hosen MM, Dhakal G, Choi H, Kabir F, Sims C, et al. Dirac state in a centrosymmetric superconductor $\ensuremath{\alpha}\text{\ensuremath{-}}{\mathrm{PdBi}}_{2}$. Physical Review B 2018, **97**(14): 144514.*

98. *Kolapo A, Li T, Hosur P, Miller JH. Possible transport evidence for three-dimensional topological superconductivity in doped β-PdBi2. Scientific Reports 2019, **9**(1): 12504.*

99. *Finlayson TR, Reichardt W, Smith HG. Lattice dynamics of layered-structure compounds: ${\mathrm{PdTe}}_{2}$. Physical Review B 1986, **33**(4): 2473-2480.*

100. *Pell MA, Mironov YV, Ibers JA. PdTe2. Acta Crystallographica Section C: Crystal Structure Communications 1996, **52**(6): 1331-1332.*

101. *Ma H, Chen P, Li B, Li J, Ai R, Zhang Z, et al. Thickness-Tunable Synthesis of Ultrathin Type-II Dirac Semimetal PtTe2 Single Crystals and Their Thickness-Dependent Electronic Properties. Nano Letters 2018, **18**(6): 3523-3529.*

102. *Deng K, Yan M, Yu C-P, Li J, Zhou X, Zhang K, et al. Crossover from 2D metal to 3D Dirac semimetal in metallic PtTe2 films with local Rashba effect. Science Bulletin 2019, **64**(15): 1044-1048.*

103. *Guo GY, Liang WY. The electronic structures of platinum dichalcogenides: PtS2, PtSe2and PtTe2. Journal of Physics C: Solid State Physics 1986, **19**(7): 995-1008.*

104. *Politano A, Chiarello G, Kuo C-N, Lue CS, Edla R, Torelli P, et al. Tailoring the Surface Chemical Reactivity of Transition-Metal Dichalcogenide PtTe2 Crystals. Advanced Functional Materials 2018, **28**(15): 1706504.*

105. *Yan M, Huang H, Zhang K, Wang E, Yao W, Deng K, et al. Lorentz-violating type-II Dirac fermions in transition metal dichalcogenide PtTe2. Nature Communications 2017, **8**(1): 257.*

106. *Chia X, Adriano A, Lazar P, Sofer Z, Luxa J, Pumera M. Layered Platinum Dichalcogenides (PtS2, PtSe2, and PtTe2) Electrocatalysis: Monotonic Dependence on the Chalcogen Size. Advanced Functional Materials 2016, **26**(24): 4306-4318.*

107. *Politano A, Chiarello G, Ghosh B, Sadhukhan K, Kuo C-N, Lue CS, et al. 3D Dirac Plasmons in the Type-II Dirac Semimetal ${\mathrm{PtTe}}_{2}$. Physical Review Letters 2018, **121**(8): 086804.*

108. *Thirupathaiah S, Kushnirenko Y, Haubold E, Fedorov AV, Rienks EDL, Kim TK, et al. Possible origin of linear magnetoresistance: Observation of Dirac surface states in layered ${\mathrm{PtBi}}_{2}$. Physical Review B 2018, **97**(3): 035133.*

109. *Nie X-A, Li S, Yang M, Zhu Z, Xu H-K, Yang X, et al. Robust Hot Electron and Multiple Topological Insulator States in PtBi2. ACS Nano 2020, **14**(2): 2366-2372.*

110. *Shipunov G, Kovalchuk I, Piening BR, Labracherie V, Veyrat A, Wolf D, et al. Polymorphic ${\mathrm{PtBi}}_{2}$: Growth, structure, and superconducting properties. Physical Review Materials 2020, **4**(12): 124202.*

111. *Xu CQ, Xing XZ, Xu X, Li B, Chen B, Che LQ, et al. Synthesis, physical properties, and band structure of the layered bismuthide ${\mathrm{PtBi}}_{2}$. Physical Review B 2016, **94**(16): 165119.*

112. *Gao W, Zhu X, Zheng F, Wu M, Zhang J, Xi C, et al. A possible candidate for triply degenerate point fermions in trigonal layered PtBi2. Nature Communications 2018, **9**(1): 3249.*

113. *Kaiser M, Baranov AI, Ruck M. Bi2Pt(hP9) by Low-Temperature Reduction of Bi13Pt3I7: Reinvestigation of the Crystal Structure and Chemical Bonding Analysis. Zeitschrift für anorganische und allgemeine Chemie 2014, **640**(14): 2742-2746.*

114. *Zhuravlev N, Stepanova A. AN X-RAY INVESTIGATION OF SUPERCONDUCTING ALLOYS OF BISMUTH WITH PLATINUM IN THE RANGE 20-640C. Soviet Phys-Cryst(English Transl) 1962,* ***7****.*

115. *Qin Y, Luo M, Sun Y, Li C, Huang B, Yang Y, et al. Intermetallic hcp-PtBi/fcc-Pt Core/Shell Nanoplates Enable Efficient Bifunctional Oxygen Reduction and Methanol Oxidation Electrocatalysis. ACS Catalysis 2018,* ***8****(6):* *5581-5590.*

116. *Lin M-K, Villaos RAB, Hlevyack JA, Chen P, Liu R-Y, Hsu C-H, et al. Dimensionality-Mediated Semimetal-Semiconductor Transition in Ultrathin ${\mathrm{PtTe}}_{2}$ Films. Physical Review Letters 2020,* ***124****(3):* *036402.*

117. *Zhang K, Wang M, Zhou X, Wang Y, Shen S, Deng K, et al. Growth of large scale PtTe, PtTe2 and PtSe2 films on a wide range of substrates. Nano Research 2020.*

118. *Mortensen CD, Johnson D. Interdiffusion of Bi and Sb in Superlattices Built from Blocks of Bi2Te3, Sb2Te3 and TiTe2. MRS Proceedings 2009,* ***1166:*** *1166-N1102-1102.*

119. *Mortensen C, Zschack P, Johnson DC. The Evaluation of TiTe2 as a Diffusion Barrier in the Formation of Low Thermal Conductivity Nanolaminates with Bi2Te3 and Sb2Te3. Advances in Science and Technology; 2010: Trans Tech Publ; 2010. p. 38-47.*

120. *Marezio M, Dernier PD, Menth A, Hull GW. The crystal structure of NbSe2 at 15°K. Journal of Solid State Chemistry 1972,* ***4****(3):* *425-429.*

121. *Wang M-X, Li P, Xu J-P, Liu Z-L, Ge J-F, Wang G-Y, et al. Interface structure of a topological insulator/superconductor heterostructure. New Journal of Physics 2014,* ***16****(12):* *123043.*

122. *Brown BE, Beerntsen DJ. Layer structure polytypism among niobium and tantalum selenides. Acta Crystallographica 1965,* ***18****(1):* *31-36.*

123. *Meerschaut A, Deudon C. Crystal structure studies of the 3R-Nb1.09S2 and the 2H-NbSe2 compounds: correlation between nonstoichiometry and stacking type (= polytypism). Materials Research Bulletin 2001,* ***36****(9):* *1721-1727.*

124. *Garoche P, Veyssié JJ, Manuel P, Molinié P. Experimental investigation of superconductivity in 2H-NbSe2 single crystal. Solid State Communications 1976,* ***19****(5):* *455-460.*

125. *El-Bana MS, Wolverson D, Russo S, Balakrishnan G, Paul DM, Bending SJ. Superconductivity in two-dimensional NbSe2field effect transistors. Superconductor Science and Technology 2013,* ***26****(12):* *125020.*

126. *Xi X, Wang Z, Zhao W, Park J-H, Law KT, Berger H, et al. Ising pairing in superconducting NbSe2 atomic layers. Nature Physics 2016,* ***12****(2):* *139-143.*

127. *Lian C-S, Si C, Duan W. Unveiling Charge-Density Wave, Superconductivity, and Their Competitive Nature in Two-Dimensional NbSe2. Nano Letters 2018,* ***18****(5):* *2924-2929.*

128. *Borghesi A, Chen-jia C, Guizzetti G, Nosenzo L, Reguzzoni E, Stella A, et al. Thermoreflectance studies of transition-metal dichalcogenides between 1 and 9 eV. Physical Review B 1986,* ***33****(4):* *2422-2428.*

129. *Greenaway DL, Nitsche R. Preparation and optical properties of group IV–VI2 chalcogenides having the CdI2 structure. Journal of Physics and Chemistry of Solids 1965,* ***26****(9):* *1445-1458.*

130. *Observation of intermediate phases during the lithium intercalation of TiX2 (X = S, Se). Zeitschrift für Kristallographie - Crystalline Materials 1983,* ***164****(3-4):* *273-278.*

131. *Rimmington HPB, Balchin AA. The growth by iodine vapour transport techniques and the crystal structures of layer compounds in the series TiSxSe2−x, TiSxTe2−x, TiSexTe2−x. Journal of Crystal Growth 1974,* ***21****(2):* *171-181.*

132. *Friend RH, Jerome D, Liang WY, Mikkelsen C, Yoffe AD. Semimetallic character of TiSe2and semiconductor character of TiS2under pressure. Journal of Physics C: Solid State Physics 1977,* ***10****(24):* *L705-L708.*

133. *Wilson JA. Concerning the semimetallic characters of TiS2 and TiSe2. Solid State Communications 1977,* ***22****(9):* *551-553.*

134. *Levy F, Froidevaux Y. Journal of Physics C: Solid State Physics 1979,* ***12****(3):* *473-487.*

135. *Di Salvo FJ, Moncton DE, Waszczak JV. Electronic properties and superlattice formation in the semimetal ${\mathrm{TiSe}}_{2}$. Physical Review B 1976,* ***14****(10):* *4321-4328.*

136. *Gronvold F, Haraldsen H, Kjekshus A. On the sulfides, selenides and tellurides of platinum. Acta Chem Scand 1960,* ***14****(9):* *1879-1893.*

137. *Furuseth S, Selte K, Kjekshus A. Redetermined crystal structures of nite2 pdte2 pts2 ptse2 and ptte2. MUNKSGAARD INT PUBL LTD 35 NORRE SOGADE, PO BOX 2148, DK-1016 COPENHAGEN …; 1965. pp. 257-&.*

138. *Soled S, Wold A, Gorochov O. Crystal growth and characterization of several platinum sulfoselenides. Materials Research Bulletin 1976,* ***11****(8):* *927-932.*

139. *Kliche G. Far-infrared and X-ray investigations of the mixed platinum dichalcogenides PtS2−xSex, PtSe2−xTex, and PtS2−xTex. Journal of Solid State Chemistry 1985,* ***56****(1):* *26-31.*

140. *Zhao X, Niu W, Zhang H, Dai X, Wei S, Yang L. Effects of interlayer coupling and electric field on the electronic properties of PtSe2/ZrSe2 van der Waals heterojunctions. Applied Surface Science 2020,* ***510:*** *145316.*

141. *Yuan Y, Duan Y, Wang Z, Sun J. Filamentary superconductivity in wrinkled PtSe2. Journal of Physics D: Applied Physics 2021,* ***54****(21):* *215302.*

142. *Cheng C, Sun J-T, Liu M, Chen X-R, Meng S. Tunable electron-phonon coupling superconductivity in platinum diselenide. Physical Review Materials 2017,* ***1****(7):* *074804.*

143. *Qu D-X, Hor YS, Xiong J, Cava RJ, Ong NP. Quantum Oscillations and Hall Anomaly of Surface States in the Topological Insulator Bi₂Te<sub>3</sub&gt. Science 2010,* ***329****(5993):* *821.*

144. *Clark OJ, Mazzola F, Feng J, Sunko V, Marković I, Bawden L, et al. Dual quantum confinement and anisotropic spin splitting in the multivalley semimetal ${\mathrm{PtSe}}_{2}$. Physical Review B 2019,* ***99****(4):* *045438.*

145. *Zhang K, Yan M, Zhang H, Huang H, Arita M, Sun Z, et al. Experimental evidence for type-II Dirac semimetal in ${\mathrm{PtSe}}_{2}$. Physical Review B 2017,* ***96****(12):* *125102.*

146. *Li Y, Xia Y, Ekahana SA, Kumar N, Jiang J, Yang L, et al. Topological origin of the type-II Dirac fermions in $\mathrm{PtSe}{}_{2}$. Physical Review Materials 2017,* ***1****(7):* *074202.*

147. *Grønvold F, Røst E. The crystal structure of PdSe2 and PdS2. Acta Crystallographica 1957,* ***10****(4):* *329-331.*

148. *Ijjaali I, Ibers JA. Crystal structure of palladium selenide, PdSe. Zeitschrift für Kristallographie-New Crystal Structures 2001,* ***216****(1-4):* *519-520.*

149. *Selb E, Tribus M, Heymann G. Verbeekite, the Long-Unknown Crystal Structure of Monoclinic PdSe2. Inorganic Chemistry 2017,* ***56****(10):* *5885-5891.*

150. *Champion JA. Some properties of (Mo, W) (Se, Te) 2. British Journal of Applied Physics 1965,* ***16****(7):* *1035-1037.*

151. *Mentzen BF, Sienko MJ. Preparation and x-ray study of mixed-anion tungsten dichalcogenides. Inorganic Chemistry 1976,* ***15****(9):* *2198-2202.*

152. *Mar A, Jobic S, Ibers JA. Metal-metal vs tellurium-tellurium bonding in WTe2 and its ternary variants TaIrTe4 and NbIrTe4. Journal of the American Chemical Society 1992,* ***114****(23):* *8963-8971.*

153. *Bronsema KD, De Boer JL, Jellinek F. On the structure of molybdenum diselenide and disulfide. Zeitschrift für anorganische und allgemeine Chemie 1986,* ***540****(9-10):* *15-17.*

154. *Davis BD, Robinson WR. The structure of α-Mo15Se19, a binary molybdenum selenidecontaining Mo6Se8 and Mo9Se11 clusters. Journal of Solid State Chemistry 1990,* ***85****(2):* *332-336.*

155. *Agarwal MK, Talele LT. Growth conditions and structural characterization of molybdenum sulphoselenide single crystals: (MoSxSe2−x, 0≦x≦2). Materials Research Bulletin 1985,* ***20****(3):* *329-336.*

156. *Schutte WJ, De Boer JL, Jellinek F. Crystal structures of tungsten disulfide and diselenide. Journal of Solid State Chemistry 1987,* ***70****(2):* *207-209.*

157. *Brixner LH. X-ray Study and Thermoelectric Properties of the W[sub x]Ta[sub 1−x]Se[sub 2] System. Journal of The Electrochemical Society 1963,* ***110****(4):* *289.*

158. *Schüffelgen P, Rosenbach D, Li C, Schmitt T, Schleenvoigt M, Jalil AR, et al. Boosting transparency in topological josephson junctions via stencil lithography. arXiv preprint arXiv:171101665 2017.*

159. *Cawthorne AB, Whan CB, Lobb CJ. Influence and evaluation of parasitic inductance in shunted Josephson junctions. IEEE Transactions on Applied Superconductivity 1997,* ***7****(2):* *2355-2358.*

160. *Belogolovskii M, Zhitlukhina E, Lacquaniti V, Leo ND, Fretto M, Sosso A. Intrinsically shunted Josephson junctions for electronics applications. Low Temperature Physics 2017,* ***43****(7):* *756-765.*

161. *Kupriyanov MY, Brinkman A, Golubov AA, Siegel M, Rogalla H. Double-barrier Josephson structures as the novel elements for superconducting large-scale integrated circuits. Physica C: Superconductivity 1999,* ***326-327:*** *16-45.*

162. *Qu F, Yang F, Shen J, Ding Y, Chen J, Ji Z, et al. Strong Superconducting Proximity Effect in Pb-Bi2Te3 Hybrid Structures. Scientific Reports 2012,* ***2****(1):* *339.*

163. *Veldhorst M, Snelder M, Hoek M, Gang T, Guduru VK, Wang XL, et al. Josephson supercurrent through a topological insulator surface state. Nature Materials 2012,* ***11****(5):* *417-421.*

164. *Williams JR, Bestwick AJ, Gallagher P, Hong SS, Cui Y, Bleich AS, et al. Unconventional Josephson Effect in Hybrid Superconductor-Topological Insulator Devices. Physical Review Letters 2012,* ***109****(5):* *056803.*

165. *Flensberg K, Hansen JB, Octavio M. Subharmonic energy-gap structure in superconducting weak links. Physical Review B 1988,* ***38****(13):* *8707-8711.*